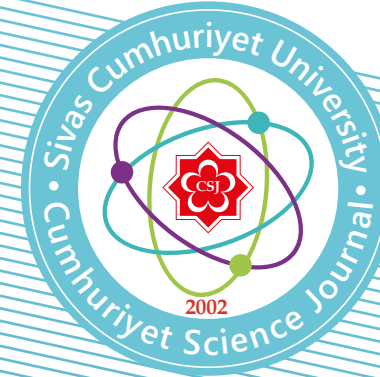




Cumhuriyet Science Journal
Faculty of Science, Cumhuriyet University
58140 - Sivas - Türkiye
Phone: +90(346) 487 13 72
Fax: +90(346) 219 11 86
e-mail: csj@cumhuriyet.edu.tr
<http://csj.cumhuriyet.edu.tr/en>
<http://dergipark.org.tr/en/pub/csaj>

Cumhuriyet Science Journal Vol: 43 No: 1 Year 2022

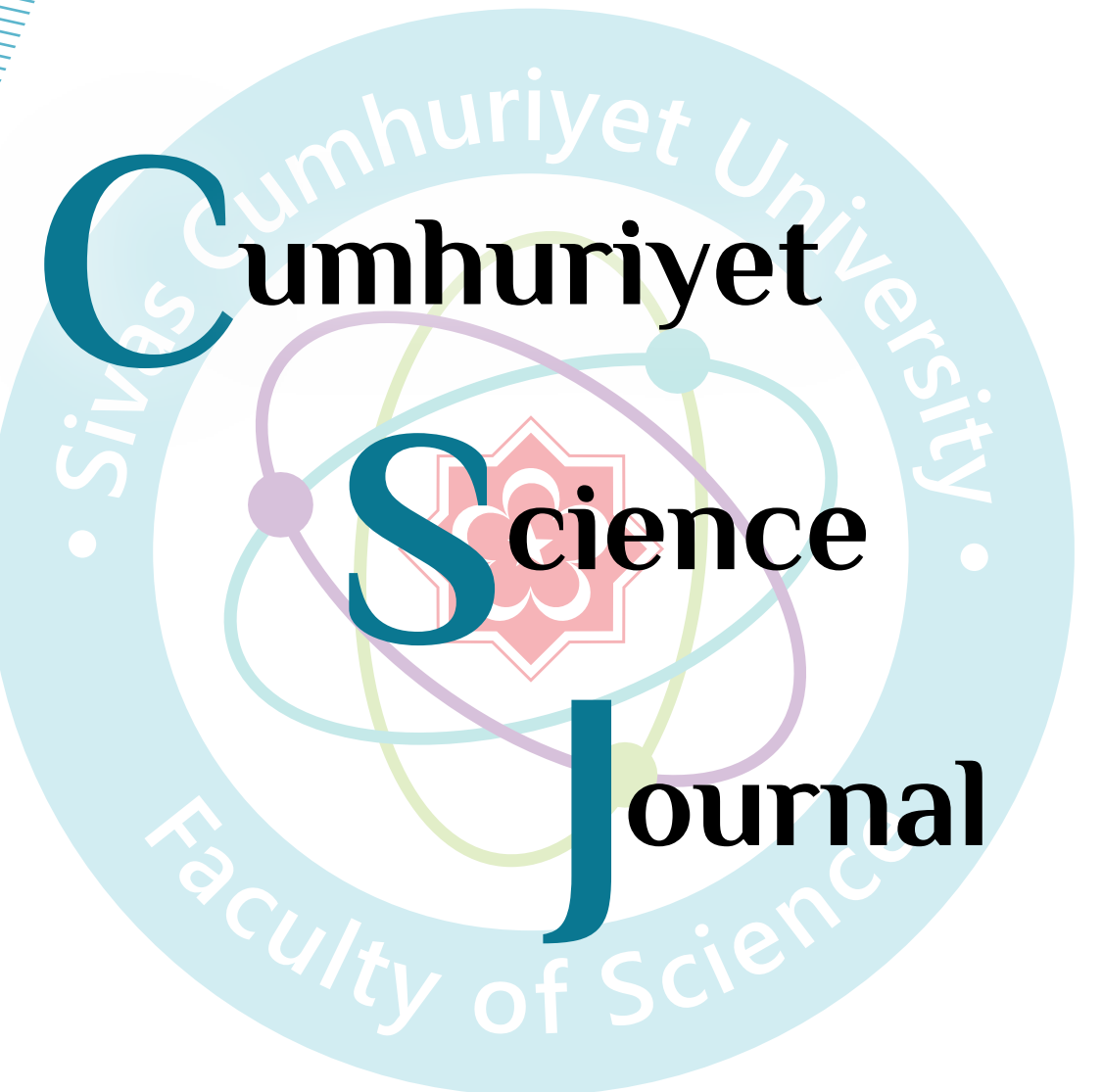


Sivas Cumhuriyet University

ISSN : 2680-2587

e-ISSN : 246-2587X

dergipark.org.tr/tr/pub/csaj
e-mail: csj@cumhuriyet.edu.tr



Cumhuriyet Science Journal (CSJ) is an official publication of Sivas Cumhuriyet University, Science Faculty. The high quality research papers related to the natural sciences are published as online four times a year. CSJ is an open access, free of charge journal and all articles in CSJ have undergone peer review and upon acceptance are immediately and permanently free for everyone to read and download.

Volume: 43

Number: 1

Year: 2022



ISSN:2587-2680
e-ISSN:2587-246X
Period:Quarterly
Founded:2002
Publisher:Sivas Cumhuriyet
University

Cumhuriyet Science Journal (CSJ)

Journal Previous Name: Cumhuriyet Üniversitesi Fen-Edebiyat Fakültesi Fen Bilimleri Dergisi

Old ISSN: 1300-1949

Owner on behalf of the Sivas Cumhuriyet University, Faculty of Science

Prof. Dr. İdris ZORLUTUNA (Sivas Cumhuriyet University)

Editor in Chief

Prof. Dr. İdris ZORLUTUNA (Sivas Cumhuriyet University)

Managing Editor

Assoc. Prof. Dr. Adil ELİK (Sivas Cumhuriyet University)

Editors

Prof. Dr. Baki KESKİN

bkeskin@cumhuriyet.edu.tr

Subjects: Mathematics and Statistics

Institution: Sivas Cumhuriyet University

Assoc. Prof. Dr. Adil ELİK

elik@cumhuriyet.edu.tr

Subjects: Chemistry and Chemical Engineering,
Environmental Sciences, Basic Sciences (General)

Institution: Sivas Cumhuriyet University

Prof. Dr. Nilüfer TOPSAKAL

ntopsakal@cumhuriyet.edu.tr

Subjects: Applied Mathematics

Institution: Sivas Cumhuriyet University

Prof. Dr. Serkan AKKOYUN

sakkoyun@cumhuriyet.edu.tr

Subjects: Physics and Physical Engineering

Institution: Sivas Cumhuriyet University

Prof. Dr. Halil İbrahim ULUSOY

hiulusoy@cumhuriyet.edu.tr

Subjects: Chemistry, Analytical Chemistry, Drug Analysis, Pharmacy

Institution: Sivas Cumhuriyet University

Prof. Dr. Fatih UNGAN

fungan@cumhuriyet.edu.tr

Subjects: Optics, Phonotics and Fiber optics

Institution: Sivas Cumhuriyet University

Assoc. Prof. Dr. Nail ALTUNAY

naltunay@cumhuriyet.edu.tr

Subjects: Bioanalytical Chemistry, Chemometric Analysis

Institution: Sivas Cumhuriyet University

Section Editors

Prof. Dr. Natalia BONDARENKO

bondarenkonp@info.sgu.ru

Subjects: Applied Mathematics and Physics

Institution: Samara University

Prof. Dr. Marcello LOCATELLI

marcello.locatelli@unich.it

Subjects: Analytical Chemistry

Institution: University "G. d'Annunzio" of Chieti-Pescara

Prof. Dr. Konstantin P. KATIN

kpkatin@yandex.ru

Subjects: Theoretical Chemistry, Computational design of nanostructures, nanodevices and nanotechnologies

Institution: National Research Nuclear University

Assoc. Prof. Dr. Duran KARAKAŞ

dkarakas@cumhuriyet.edu.tr

Subjects: Inorganic Chemistry, Theoretical Chemistry

Institution: Sivas Cumhuriyet University

Assoc. Prof. Dr. Yaşar ÇAKMAK

ycakmak@cumhuriyet.edu.tr

Subjects: Applied Mathematics

Institution: Sivas Cumhuriyet University

Assoc. Prof. Dr. Sevgi DURNA DAŞTAN

sdurna@cumhuriyet.edu.tr

Subjects: Molecular Biology

Institution: Sivas Cumhuriyet University

Assist. Prof. Dr. Yener ÜNAL

uyener@cumhuriyet.edu.tr

Subjects: Statistics

Institution: Sivas Cumhuriyet University

Abstracted&Indexing

ULAKBİM TR-Dizin

Index Copernicus (ICI Journals Master List)

Clarivate Analytics Zoological Record

Crossref

WorldCat

Akademik Dizin

Arastirmax Bilimsel Yayın İndeksi

Bielefeld Academic Search Engine (BASE)

Directory of Research Journal Indexing (DRJI)

Google Scholar

Research Gate

Idealonline

Editorial Board

Prof. Dr. Sezai ELAGÖZ (ASELSAN)
Prof. Dr. Mustafa SOYLAK (Erciyes University)
Prof. Dr. Chuan Fu Yang (Nanjing University of Science and Technology)
Prof. Dr. Münevver SÖKMEN (KGTU)
Prof. Dr. Hüseyin MERDAN (TOBB ETU)
Prof. Dr. Mehmet AKKURT (Erciyes University)
Prof. Dr. Mustafa KAVUTÇU (Gazi University)
Prof. Dr. Francois VOS (The University of Queensland)
Prof. Dr. Abuzar KABIR (International Forensic Research Institute)
Prof. Dr. Mustafa TÜZEN (GOP University)
Prof. Dr. Songül KAYA MERDAN (METU)
Prof. Dr. Jose Javier Valiente-Dobon (INFN-LNL, Padova University)
Prof. Dr. Yeşim SAĞ AÇIKEL (Hacettepe University)
Prof. Dr. Mehmet ŞİMŞİR (Sivas Cumhuriyet University)
Prof. Dr. Atalay SÖKMEN (KGTU)
Prof. Dr. Ricardo I. JELDRES (Universidad de Antofagasta)
Prof. Dr. Mustafa YILDIRIM (Sivas Cumhuriyet University)
Prof. Dr. Ali DELİCEOĞLU (Erciyes University)
Prof. Dr. Tuncay BAYRAM (Karadeniz Technical University)
Prof. Dr. Gökhan KOÇAK (Erciyes University)
Prof. Dr. Nadjat Laouet (Freres Mentouri Constantine-1 University)
Assoc. Prof. Dr. Savaş KAYA (Sivas Cumhuriyet University)

Layout Editors:

Lecturer Aykut HASBEK

Copyeditors:

Assist. Prof. Dr. Doğa Can SERTBAŞ
Assist. Prof. Dr. Hacı Ahmet KARADAŞ
Research Assistant Özgür İNCE

Proofreader:

Assist. Prof. Dr. Yener ÜNAL
Lecturer Aykut HASBEK

Publication Type: Peer Reviewed Journal

Cite Type: Cumhuriyet Sci. J.

Contact Information

Faculty of Science Cumhuriyet University
58140 Sivas- TURKEY
Phone: +90(346)2191010-1522
Fax: +90(346)2191186
e-mail: csj@cumhuriyet.edu.tr
<http://dergipark.gov.tr/csj>

CONTENTS

PAGES

Gülşah ALBAYRAK

Bortezomib Potentiates the Effect of Roscovitine Via Dna Damage Induced Apoptosis in A549 Lung Cancer Cells (Research Article).....

1 - 5

Esen ÇAKMAK

A Bioinformatics Approach to Identify Potential Biomarkers in Non-Small Cell Lung Cancer (Research Article).....

6 - 13

Meltem AŞAN ÖZÜSAĞLAM, Songül TACER, Safia BOULECHFAR, Amar ZELLAGUI

An Investigation of the Bactericidal and Fungicidal Effects of Algerian Propolis Extracts and Essential Oils (Research Article)

14 - 19

Emrah SARIYER

Free Energy Decomposition of CarO Outer Membrane Protein of Acinetobacter baumannii (Research Article).....

20 - 26

Murat DOĞAN, Duygu TAŞKIN, Mizgin ERMANOĞLU, Turan ARABACI

Characterization of Nanoparticles Containing Achillea Phrygia and Their Antioxidant and Antiproliferative Properties (Research Article).....

27 - 32

Işıl Nihan KORKMAZ

In Vitro Inhibition Effects of 2-Amino Thiazole Derivatives on Lactoperoxidase Enzyme Activity (Research Article).....

33 - 37

Yasemin IŞIKVER, Ali IŞIKVER

Synthesis and Characterization of Cationic P(AAm-AETAC) Hydrogels, and Their Uses in Adsorption of Titan Yellow (Research Article)

38 - 44

Asuman UÇAR, Mükerrerem FINDIK, Emine AKGEMCİ

CT-DNA/BSA Binding Studies of Thiosemicarbazone-Derived Zn(II) Complex (Research Article).....

45 - 52

Adil ELİK, Nail ALTUNAY

Chemometric-Based Optimization of Ionic Liquid-Based Dispersive Liquid-Liquid Microextraction for Separation and Preconcentration of Erythrosine from Real Matrices (Research Article).....

53 - 60

Ersen YILMAZ

Blending Effect of Maleic Anhydride-Styrene-Methyl Methacrylate Terpolymer on Polyvinylchloride (Pvc)/Polystyrene (Ps) Mixtures (Research Article).....

61 - 65

Yasemin CAMADAN, Ebru AKKEMİK

Searching for New Natural Inhibitors of Acetylcholinesterase Enzyme (Research Article).....

66 - 71

Prasun Kumar SANTRA

Mathematical Analysis of Discrete Fractional Prey-Predator Model with Fear Effect and Square Root Functional Response (Research Article).....

72 - 76

Zuhal KUCUKARSLAN YUZBASİ

Surfaces Using a Common Geodesic Curve With an Alternative Moving Frame in The 3-Dimensional Lie Group (Research Article)

77 - 81

Arfah ARFAH

On Involutives of Admissible Non-Lightlike Curves in Pseudo-Galilean 3-Space (Research Article)

82 - 87

Figen KANGALGİL, Feda İLHAN

Period-doubling Bifurcation and Stability in a Two Dimensional Discrete Prey-predator Model with Allee Effect and Immigration Parameter on Prey (Research Article)

88 - 97

Gülten TORUN, Meliha MERCAN BOYRAZ, Ülkü DİNLEMEZ KANTAR

Investigation of the Asymptotic Behavior of Generalized Baskakov-Durrmeyer-Stancu Type Operators (Research Article)

98 - 104

Damla YILMAZ <i>Orthogonal Semiderivations and Symmetric Bi-semiderivations in Semiprime Rings (Research Article).....</i>	105 - 112
Ebru ÇOPUROĞLU <i>Calculating Entropy of Some Solid Metals by Using n-Dimensional Debye Approximation(Research Article).....</i>	113 - 115
Murat KAPLAN <i>On the Lyapunov Time Estimations For Comet 1/P Halley (Research Article).....</i>	116 - 122
Ekrem ÇİÇEK <i>The Modeling of Radioactive Cobalt Adsorption on Molecular Sieves (Research Article).....</i>	123 - 125
Aysevil SALMAN DURMUŞLAR <i>Effect of Ring Radius and Electric Field on the Relative Refractive Index of a GaAs Quantum Ring (Research Article)....</i>	126 - 131
Evrin Ersin KANGAL <i>Dynamics of the Dirac Particle in an Anisotropic Rainbow Universe (Research Article)</i>	132 - 136
Serap YİĞİT GEZGİN, Amina HOUIMI, Bedrettin MERCİMEK, Hamdi Şükür KILIÇ <i>The Investigation of Photovoltaic and Electrical Properties of Bi Doped CTS/Si Hetero-Junction Structure for the Solar Cell Application (Research Article).....</i>	137 - 145
Muhammet Oğuzhan YALÇIN, Nevin GÜLER DİNCER, Öznur İŞÇİ GÜNERİ <i>Investigating the COVID19 Characteristics of the Countries Based on Time Series Clustering (Research Article)</i>	146 - 164

Bortezomib Potentiates the Effect of Roscovitine Via Dna Damage Induced Apoptosis in A549 Lung Cancer Cells

Gülşah Albayrak^{1,a,*}¹ Department of Medical Biology, Faculty of Medicine, Ufuk University, Ankara, Turkey

*Corresponding author

Research Article

History

Received: 11/03/2021

Accepted: 29/12/2021

Copyright

©2022 Faculty of Science,
Sivas Cumhuriyet Universityalbayrakgulsah@gmail.com<https://orcid.org/0000-0001-9106-5798>

ABSTRACT

The adoption of new treatment modalities remains crucial as lung cancer has one of the lowest survival rates, along with liver and pancreatic cancer. Bortezomib is a proteasome inhibitor that has higher anticancer effect in combination therapies. Therefore, the aim of this study is to investigate whether bortezomib could have additional anticancer effect when combined with cyclin-dependent kinase (CDK) inhibitor-roscovitine in vitro. Apoptosis related gene expression levels of p53, Noxa, Puma, Bcl-xL, Bak, Casp-3 and Casp-7 were measured by quantitative PCR (qPCR) upon treatment with 10-20µM roscovitine and in combination with 30nM bortezomib for 24 hours. Synergistic effect on apoptosis was also investigated at protein levels by analyzing p53, Cleaved Casp-3 and Cleaved Parp expressions. Induction of autophagy was determined by western blotting of B-catenin and LC3B I-II. Roscovitine combined bortezomib treatment induced apoptosis by upregulating p53 pathway and its downstream mediators. Bortezomib increased Parp and Caspase3 cleavage significantly at 24h. Bortezomib inhibited B-catenin and triggered autophagy induction at 24 and 48hours. As cancer cells evade programmed cell death, CDK inhibitors might be used to direct cancer cells into apoptosis. This study concludes that bortezomib potentiates the effect of roscovitine via DNA damage induced apoptosis in A549 lung cancer cells.

Keywords: CDK inhibitor, Lung cancer, Bortezomib, Apoptosis, Roscovitine.

Introduction

Lung cancer remains to be the leading cause of deaths worldwide and it has one of the lowest survival rates, along with liver and pancreatic cancer [1,2]. Survival rates are low due to diagnosis at an advanced stage of the disease [3]. Therefore the adoption of new treatment modalities is indispensable.

Roscovitine is a small molecule that targets various CDKs (CDK2, CDK7 and CDK9) in cell cycle [4]. Roscovitine is an investigational drug that is currently in phase trials for the treatment of solid cancers, cushings syndrome and active ulcerative colitis [5]. Roscovitine derivatives are also being used in order to increase the efficacy of the drug [6]. As cancer cells reprogramme cell death by evading apoptosis, cyclin-dependent kinase inhibitors might be used in treatment to direct cells into apoptosis.

Bortezomib is a proteasome inhibitor that is used in the treatment of multiple myeloma and mantle cell lymphoma [7]. It inhibits 26S proteasome where ubiquitinated proteins are degraded [8]. The ubiquitin-proteasome pathway maintains homeostatic intracellular concentrations of proteins which is a crucial mechanism that promotes protein degradation [9]. As ubiquitin-proteasome pathway is dysregulated during cancer progression, targeting this pathway is crucial in treatment [10]. Bortezomib became the first FDA approved proteasome inhibitor and clinical trials are ongoing since to investigate its anticancer activity in solid tumors [11]. Bortezomib is also found to increase the effect of traditional anticancer agents [doxorubicin, cisplatin, paclitaxel, irinotecan, and radiation etc] [12]. Therefore, the aim of this study was to investigate

whether bortezomib could potentiate the anticancer effect of cyclin-dependent kinase [CDK] inhibitor-roscovitine in vitro. Bortezomib and roscovitines' anti-proliferative effect on A549 lung cancer cells were previously identified as single treatment agent and IC50 values were identified as 30nM for bortezomib and 10µM for roscovitine in A549 cells [13,14] However their synergistic effect in lung cancer cells has not been studied before. To investigate the synergic effect, A549 cells were treated with 10 and 20µM roscovitine +30 nM bortezomib for 24 and 48 hours. Previous researches identified that roscovitine requires higher IC50 concentration (10-20µM) than bortezomib [30nM]. Therefore lower (10µM) and higher (20µM) roscovitine alone and their combination with the constant concentration of bortezomib (30nM) was used in order to leverage roscovitine's effect.

Apoptosis related gene expressions (p53, Noxa, Puma, Bcl-xL, Bak, Casp-3 and Casp7) were measured by qPCR at 24 hours. In order to shed more light into the molecular mechanism of these drugs, P53, Parp and Casp-3 cleavage were detected by western blot. Induction of autophagy was also determined by measuring LC3BI, LC3B-II and B-Catenin protein expression profiles by western blot.

Materials and Methods

Cell Culture and Chemicals

A549 cells were grown in DMEM medium supplemented with 10% Fetal bovine serum (FBS) (Sigma-Aldrich, St Louis, MO, USA). Cells were grown in an

incubator in 5% CO₂ at 37°C. Roscovitine and bortezomib were supplied from Santa Cruz, Texas, USA. Roscovitine and bortezomib were dissolved in DMSO, the maximum concentration of DMSO was used as a vehicle control. A549 cells were treated with 10-20µM roscovitine and in combination with 30nM bortezomib for 24 and 48 hours.

Protein Expression Analysis by Western Blotting

Protein lysates were collected after 24 and 48 hours treatment with the indicated drugs and quantified by using the BCA Assay Kit (Thermo Pierce, Rockford, IL, USA). Lysates (20 µg) were denatured for 5 minutes at 95°C in LDS non-reducing sample buffer (Pierce, Rockford, IL, USA) and then loaded to the 10% Tris-glycine gels. The gels were transferred to the PVDF membrane (Merck Millipore, Darmstadt, Germany) at 300 mA for 90 minutes. Membranes were blocked with 5% non-fat milk powder in TBS-T for 1 hour at room temperature and incubated overnight at 4°C with the primary antibodies for P53, cleaved Parp, cleaved Casp-3, LC3B, B-Catenin and B-actin at 1:1000 dilution (Thermo Pierce, Rockford, IL, USA). Blots were washed with TBS-T subsequently. Protein bands were detected by using the secondary antibody (Thermo Pierce, Rockford, IL, USA) and the blots were visualized by BioVision ECL Western Blotting Substrate Kit (Biovision, California, USA).

Gene Expression Analysis by RT-qPCR

RNA was isolated by using Trizol reagent (Invitrogen, Thermo Fischer Scientific, USA) 2000 ng total RNA was reverse transcribed by Superscript III cDNA Synthesis Kit (Invitrogen, Thermo Fischer Scientific, USA) Forward and reverse primer sequences was provided in the appendix. 10–20 cycles of specific target amplification was performed by SYBR Green qPCR master mix. RT- qPCR analysis was performed in Roche LightCycler qPCR. Gapdh was used as internal control when calculating Cq value. $\Delta\Delta Cq$ method was used to quantify the gene expression levels. mRNA expression levels for p53, Noxa, Puma, Bcl-xL, Bak, Casp-3 and Casp7 were measured by qPCR. Data was analyzed and plotted in Graphpad prism software.

Statistical Analysis

Experiments were performed in three different replicates. Statistical analysis was performed by using GraphPad Prism software. Differences between the

control and treatment groups were compared by t-test. The results were expressed as the mean \pm standard error mean. Western blot image densities were calculated by Imagej. Statistical analysis and plotting of the data was performed in GraphPad Prism software.

Results and Discussion

Bortezomib and Roscovitines' Effects on Apoptosis

P53 pathway and related downstream target genes that are involved in apoptosis were quantified by qPCR in order to assess roscovitine's anticancer activity and its synergic effect with bortezomib. A549 cells were treated with 10 and 20µM roscovitine and in combination with 30nM bortezomib for 24 hours. mRNA expression levels for p53, Noxa, Puma, Bcl-xL, Bak, Casp-3 and Casp-7 were quantified by qPCR. mRNA expression were normalized to the Gapdh housekeeping control for each gene.

Roscovitine treatment decreased p53 levels but when bortezomib was added p53 gene expression levels were upregulated (Figure 1a). Noxa mRNA expression levels were downregulated upon 10, 20µM roscovitine and 10 µM+30nM bortezomib treatment, however it increased with 20µM+30nM bortezomib treatment (Figure 1b). Puma is known as p53 upregulated modulator of apoptosis, consistent with the p53 upregulation, Puma levels increased at all treatment conditions (Figure 1c). Bortezomib induced Bcl-xL upregulation at 24 hours (Figure 1d). Bak is also a member of the BCL2 protein family. Bak mRNA levels increased upon 20µM roscovitine, 10 and 20µM roscovitine+30nM bortezomib (Figure 1e). Caspases are crucial mediators of apoptosis. Caspase 3 mRNA expression levels upregulated with all treatment conditions (Figure 1f), whereas Caspase 7 remained unchanged or decreased (Figure 1g).

To further investigate the induction of apoptosis upon roscovitine and bortezomib treatment; p53, cleaved parp and cleaved caspase 3 protein expression levels were determined by western blotting at 24 hours. Consistent with the mRNA expression, p53 protein expression levels were upregulated upon treatment. Cleaved caspase 3 is an indicator of apoptosis. Cleaved caspase 3 levels increased in a dose-dependent manner. It was found that bortezomib potentiated the effect of roscovitine via Parp cleavage (Figure 2).

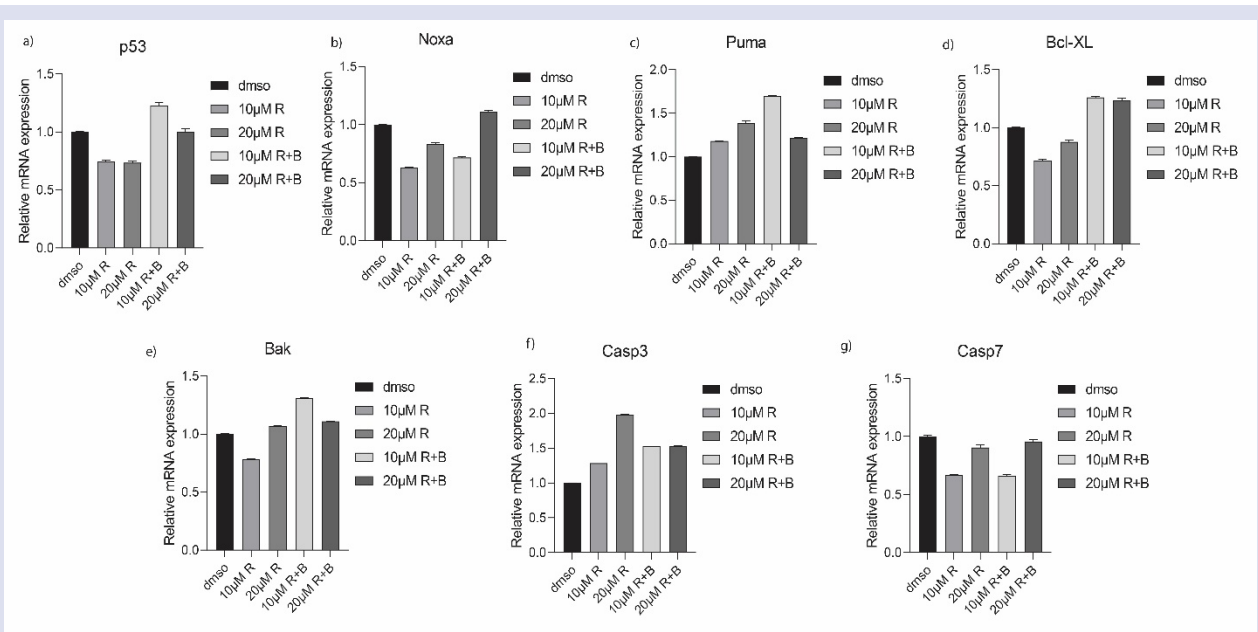


Figure 1. P53 pathway and related downstream target genes that are involved in apoptosis were quantified by qPCR. A549 cells were treated with 10 and 20µM Roscovitine and plus 30nM Bortezomib for 24 h. mRNA expression levels for p53, Noxa, Puma, Bcl-xL, Bak, Casp-3 and Casp7 were measured by qPCR. mRNA expression values were normalized to the Gapdh housekeeping control.

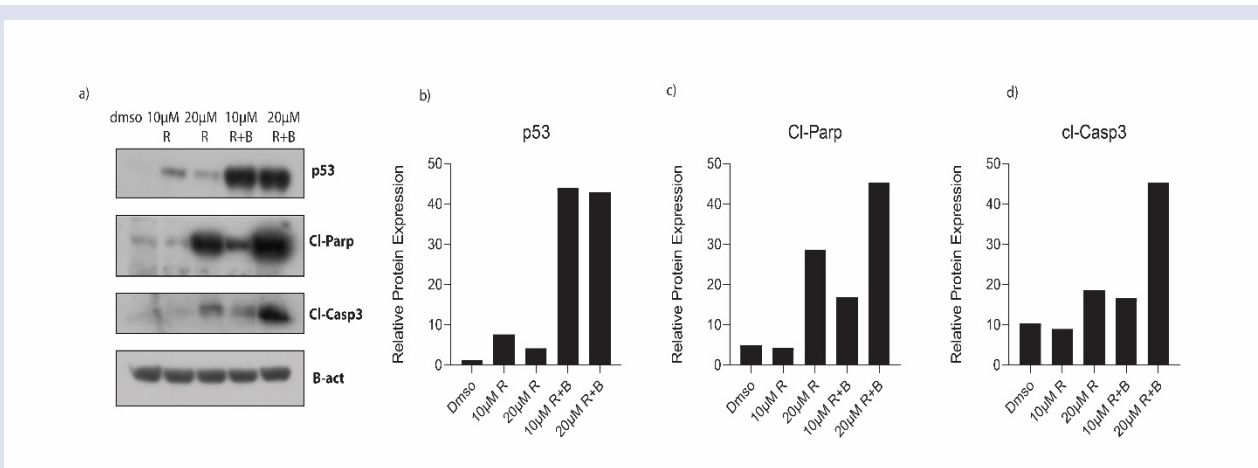


Figure 2. a) A549 cells were treated with indicated concentrations of Roscovitine and Bortezomib for 24 h and 48h. Roscovitine and Bortezomib combination increased p53 protein expression in A549 cells. Parp and Casp3 cleavages were detected by western blot analysis upon Roscovitine and Bortezomib treatment for 24 h. b) Relative protein expression were represented as fold change for p53 normalized to β-Actin. c) Relative protein expression were represented as fold change of the PARP cleavage normalized to β-Actin d) Relative protein expression were represented as fold change of the Casp-3 cleavage normalized to β-Actin

Roscovitine and Bortezomid Induce Autolysosomal β-Catenin Degradation in A549 Cells

A549 cells were treated with indicated concentrations of roscovitine and bortezomib for 24 h and 48h, the induction of autophagy was determined by western blotting of LC3B protein expression. B-catenin protein expression levels were also investigated to question its

role in autophagy. 10 µM roscovitine+30nM bortezomib and and 20µM roscovitine+30nM bortezomib concentrations inhibited B-catenin protein expression significantly at 24h. 20µM roscovitine+30nM bortezomib treatment decreased B-catenin levels at 48h. LC3-II is an autophagy indicator. Bortezomib increased the induction of autophagy at both 24 and 48 h (Figure3).

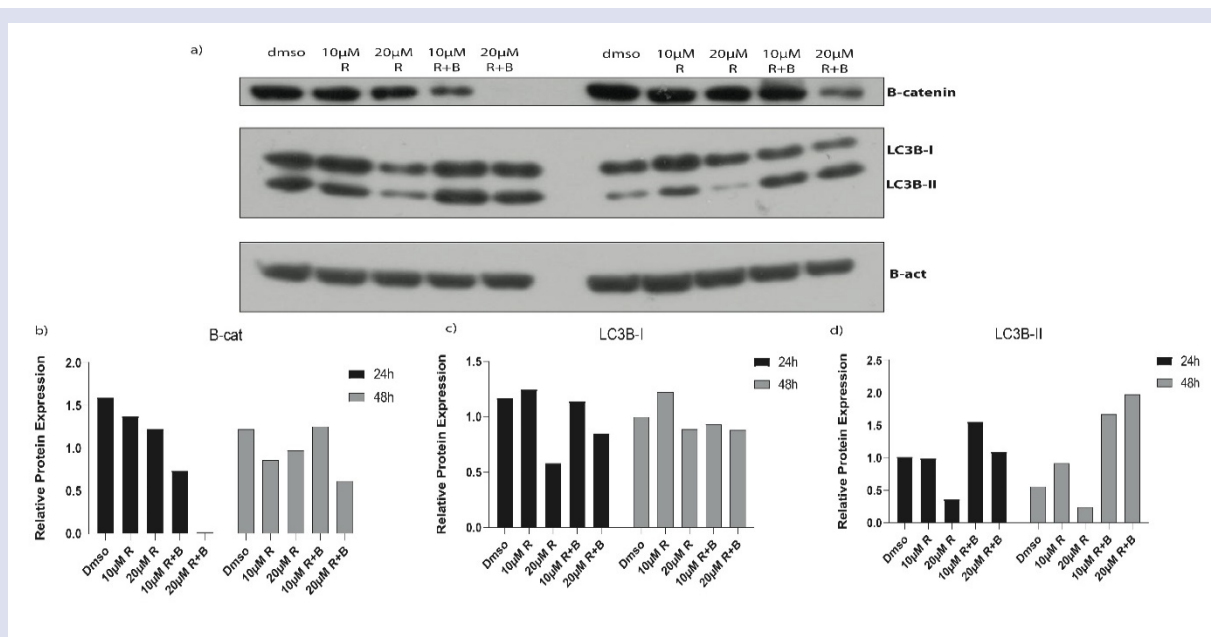


Figure 3. a) A549 cells were treated with indicated concentrations of Roscovitine and Bortezomib for 24 h and 48h. Roscovitine and Bortezomib combination decreased B-catenin protein expression in A549 cells. The induction of autophagy was determined by LC3B protein expression. B-actin was used as loading control. b) Relative protein expressions were represented as fold change for B-catenin normalized to β -Actin. c) Relative protein expression were represented as fold change for LC3B-I normalized to β -Actin. d) Relative protein expression were represented as fold change for LC3B-II normalized to β -Actin.

Discussion

The CDKs are critical regulators of cell cycle control and have other important cellular functions such as transcription [15]. As cancer cells have uncontrolled proliferation and CDKs are a central regulator of the cell cycle control; developing CDK inhibitors as anticancer agents gained interest [16]. However, targeting human kinome is a challenging task as human genome encodes 538 different protein kinases and many of them are associated with cancer progression [17]. Bortezomib is a proteasome inhibitor that has synergic effect when used in combination with the other anticancer agents [18]. Therefore, Bortezomib was evaluated in combination with roscovitine to assess their potential for the development of new treatment modalities in lung cancer treatment.

Although the number of ongoing clinical trials with roscovitine remained limited, recently it was found that roscovitine enhanced antitumor activity of temozolomide in vitro and in vivo by regulating autophagy and Caspase-3 dependent apoptosis in glioblastoma [19]. p53 acts as a tumor suppressor and reacts to stress signals with diverse responses. One of the most important p53 functions is to induce apoptosis [20]. In this study, bortezomib potentiated the effect of roscovitine via p53 dependent pathway of apoptosis.

Bcl-xL is a Bcl-2 protein family member that modulates apoptosis by controlling mitochondrial membrane

permeability [21]. It was found that bortezomib treatment increased the gene expression of the Bcl-2 protein family members involved in apoptosis [Puma, Bcl-xL, Bak]. Bortezomib also induced Caspase 3 cleavage both at mRNA and protein levels. Caspase-3 catalyzes the cleavage of many key cellular proteins during apoptosis [22]. PARP cleavage is observed during programmed cell death induced by a variety of apoptotic stimuli [23]. The protein expression profiles of p53, cleaved Casp-3 and cleaved Parp were consistent with the mRNA expression data. The results revealed that using bortezomib in combination with the CDK inhibitor roscovitine promoted apoptosis both at the mRNA and protein levels. Increasing cleaved Parp protein expression levels upon combination treatment suggests that more DNA damage accumulated when cells were treated with the proteasome inhibitor. Bortezomib treatment induced more autophagy via B-catenin-LC3B axis when compared to the control treatment. Although this study is limited with a single cell line in vitro, a large body of evidence demonstrates that roscovitine and bortezomib have synergic anticancer effect via DNA damage induced apoptosis.

Conflicts of Interest

The author declares no conflicts of interest. No competing financial interests exist.

References

- [1] Barta J.A., Powell C.A., Wisnivesky J.P., Global epidemiology of lung cancer, *Annals of Global Health*, 85(1) (2019).
- [2] de Groot P.M., Wu C.C., Carter B.W., Munden R.F., The epidemiology of lung cancer, *Translational Lung Cancer Research*, 7(3) (2018) 220.
- [3] Luo Y.H., Luo L., Wampfler J.A., Wang Y., Liu D., Chen Y.M., Adjei A.A., Midthun D.E., Yang P., 5-year overall survival in patients with lung cancer eligible or ineligible for screening according to US Preventive Services Task Force criteria: a prospective, observational cohort study, *The Lancet Oncology*, 20(8) (2019) 1098-1108.
- [4] Cicenäs J., Kalyan K., Sorokinas A., Stankunas E., Levy J., Meskinyte I., Stankevicius V., Kaupinis A., Valius M., Roscovitine in cancer and other diseases, *Annals of Translational Medicine*, 3(10) (2015).
- [5] Langlois F., Chu J., Fleseriu M., Pituitary-directed therapies for Cushing's disease, *Frontiers in Endocrinology*, 9 (2018) 164.
- [6] Bettayeb K., Oumata N., Echaliér A., Ferandin Y., Endicott J.A., Galons H., Meijer L., CR8, a potent and selective, roscovitine-derived inhibitor of cyclin-dependent kinases, *Oncogene*, 27(44) (2008) 5797-5807.
- [7] Chen D., Frezza M., Schmitt S., Kanwar J., P Dou Q., Bortezomib as the first proteasome inhibitor anticancer drug: current status and future perspectives, *Current Cancer Drug Targets*, 11(3) (2011) 239-253.
- [8] Thibaudeau T.A., Smith D.M., A practical review of proteasome pharmacology, *Pharmacological Reviews*, 71(2) (2019) 170-197.
- [9] Shang F., Taylor A., Ubiquitin-proteasome pathway and cellular responses to oxidative stress, *Free Radical Biology and Medicine*, 51(1) (2011) 5-16.
- [10] Soave C.L., Guerin T., Liu J., Dou Q.P., Targeting the ubiquitin-proteasome system for cancer treatment: discovering novel inhibitors from nature and drug repurposing, *Cancer and Metastasis Reviews*, 36(4) (2017) 717-736.
- [11] Ping Dou Q., A Zonder J., Overview of proteasome inhibitor-based anti-cancer therapies: perspective on bortezomib and second generation proteasome inhibitors versus future generation inhibitors of ubiquitin-proteasome system, *Current Cancer Drug Targets*, 14(6) (2014) 517-536.
- [12] Kapoor P., Ramakrishnan V., Rajkumar S.V., Bortezomib combination therapy in multiple myeloma, *In Seminars in Hematology*, 49(3) (2012) 228-242.
- [13] Taromi S., Lewens F., Arsenic R., Sedding D., Sängér J., Kunze A., Moebis M., Benecke J., Freitag H., Christen F., Kaemmerer D., Proteasome inhibitor bortezomib enhances the effect of standard chemotherapy in small cell lung cancer, *Oncotarget* 8(57) (2017) 97061.
- [14] Zhang T., Jiang T., Zhang F., Li C., Zhou Y.A., Zhu Y.F., Li X.F., Involvement of p21Waf1/Cip1 cleavage during roscovitine-induced apoptosis in non-small cell lung cancer cells, *Oncology reports*, 23(1) (2010) 239-245.
- [15] Bertoli C., Skotheim J.M., De Bruin R.A., Control of cell cycle transcription during G1 and S phases, *Nature Reviews Molecular Cell Biology*, 14(8) (2013) 518-528.
- [16] Law M.E., Corsino P.E., Narayan S., Law B.K., Cyclin-dependent kinase inhibitors as anticancer therapeutics, *Molecular Pharmacology*, 88(5) (2015) 846-852.
- [17] Bhullar K.S., Lagarón N.O., McGowan E.M., Parmar I., Jha A., Hubbard B.P., Rupasinghe H.V., Kinase-targeted cancer therapies: progress, challenges and future directions, *Molecular Cancer*, 17(1) (2018) 1-20.
- [18] Sooman L., Gullbo J., Bergqvist M., Bergström S., Lennartsson J., Ekman S., Synergistic effects of combining proteasome inhibitors with chemotherapeutic drugs in lung cancer cells, *BMC Research Notes*, 10(1) (2017) 1-9.
- [19] Pandey V., Ranjan N., Narne P., Babu P.P., Roscovitine effectively enhances antitumor activity of temozolomide in vitro and in vivo mediated by increased autophagy and Caspase-3 dependent apoptosis, *Scientific Reports*, 9(1) (2019) 1-13.
- [20] Fridman J.S., Lowe S.W., Control of apoptosis by p53, *Oncogene*, 22(56) (2003) 9030-9040.
- [21] Stevens M., Oltean S., Modulation of the apoptosis gene Bcl-x function through alternative splicing, *Frontiers in Genetics*, 10 (2019) 804.
- [22] Porter A.G., Jänicke R.U., Emerging roles of caspase-3 in apoptosis, *Cell Death & Differentiation*, 6(2) (1999) 99-104.
- [23] Herceg Z., Wang Z.Q., Failure of poly (ADP-ribose) polymerase cleavage by caspases leads to induction of necrosis and enhanced apoptosis, *Molecular and Cellular Biology*, 19(7) (1999) 5124-5133.

A Bioinformatics Approach to Identify Potential Biomarkers in Non-Small Cell Lung Cancer

Esen ÇAKMAK^{1,a,*}

¹ Medical Laboratory Techniques Program, Department of Medical Services and Techniques, Health Services Vocational School, Kahramanmaraş Sütçü İmam University, Kahramanmaraş, Turkey.

*Corresponding author

Research Article

History

Received: 21/05/2021

Accepted: 27/01/2022

Copyright



©2022 Faculty of Science,
Sivas Cumhuriyet University

ABSTRACT

Non-small cell lung cancer (NSCLC) is responsible for about 85% of lung cancer types. The molecular mechanism of NSCLC has not been completely elucidated. The current study aims to explore the potential biomarkers and targets for NSCLC. The gene and miRNA expression profiles were downloaded from the Gene Expression Omnibus (GEO) database. The differentially expressed miRNAs (DEMs) and genes (DEGs) were determined and used for further analysis. Functional enrichment analyses were applied using the DAVID program. Moreover, the miRNA targets were predicted based on the miRWalk. The STRING software was constructed protein-protein interaction (PPI) and miRNA-mRNA networks and Cytoscape software was used to visualize PPI and miRNA-mRNA networks and to identify hub genes. As a result of bioinformatic analysis, a total of 159 DEGs and 22 DEMs were identified and DEGs were mostly enriched in the terms like ECM receptor interaction, signal transduction and leukocyte transendothelial migration. The identified hub genes were IL6, COL1A1, CLDN5, CAV1, CDH5, SPP1, GNG11, PPBP, CXCL2 and CXCR2. A total of 239 target genes were identified as potential mRNAs. The most significantly identified genes and miRNAs could serve as potential biomarkers for NSCLC.

Keywords: Non-small cell lung cancer, miRNA, mRNA, Bioinformatics analysis.

^a esencakmak1820@gmail.com

 <https://orcid.org/0000-0001-8805-3315>

Introduction

Lung cancer is the crucial cause of cancer-related deaths in worldwide. Diagnosis and treatment of lung cancer are of critical importance to improve survival of cancer patients, especially earlier stages [1]. In particular, smokers are more likely to develop lung cancer and therefore smoking is one of the most important causes in lung cancer. However, several researchers have been reported that non-smokers also get lung cancer. The incidence of lung cancer in men is higher than in women [2]. Lung cancer is histopathologically divided into two groups as small cell lung cancer (SCLC) and non-small cell lung cancer (NSCLC) and NSCLC is accounting for 85 % of lung cancers with two major subtypes: adenocarcinoma (AD) and squamous cell carcinoma (SCC) [3]. Despite significant improvements in NSCLC treatments, the overall survival rate (20%) and the 5-year survival rate (16%) is still very low for NSCLC patients [4]. The lack of effective tools and methods are major problems in early detection of lung cancer. Therefore, it is urgent to screen new potential molecular markers and methods for understanding of the molecular mechanisms underlying lung cancer.

MicroRNAs (miRNAs) are small (19–25 nt long), single stranded and highly conserved non-coding RNA molecules that are a critical regulator in the gene expression. miRNAs regulate posttranscriptionally gene expression through binding to complementary sequences in target mRNAs. They suppress gene expression by translation inhibition or degradation of mRNA. MicroRNAs recognize with 3'

region (3'-UTR) of their target mRNAs which are generally complementary nucleotides by 5' region of miRNAs. These small RNAs are involved in several types of cellular activities like apoptosis, cell proliferation or differentiation, development and progression [6]. MicroRNAs have been discovered to be connected with different cancer types. Especially, the changes in miRNA expression profiles play an important role in cancer pathogenicity. Comparison of miRNA expression profiles between tumor and healthy tissues is a crucial approach for an early detection, diagnosis, prognostic and therapy.

Microarray data analysis and bioinformatics methods have been widely applied to identify new molecular targets using gene expression data in many cancer types. Cai et al. [7] identified 8 miRNAs and 211 common genes using gene expression datasets via bioinformatic analysis for NSCLC. As a result of the bioinformatic analysis, they reported that identified miRNAs and genes can be a major regulator in the occurrence and development of NSCLC. In a different study, the differential expression levels of mRNA and miRNA between cancer tissues and healthy tissues were compared and the key miRNA-gene pairs were identified. The related genes were presented as potential biomarkers and as potential drug targets [8].

It was determined to differentially expressed genes (DEGs) and miRNAs (DEMs) between NSCLC tissues and healthy lung tissues using bioinformatic analyses in the current study. Subsequently, functional enrichment analysis, PPI network, prediction of miRNA targets and

survival analysis were applied and miRNA–mRNA regulatory network was finally constructed to identified genes in NSCLC. The aim of this study was to identified key miRNAs and genes as potential biomarkers in NSCLC and to contribute to the clarification of the molecular mechanism in NSCLC.

Materials and Methods

Microarray Data

Two genes (GSE18842 and GSE19804) and two miRNAs (GSE19945 and GSE102286) expression profiles were obtained from the Gene Expression Omnibus (GEO, <http://www.ncbi.nlm.nih.gov/geo>) database. The GSE18842 datasets contain 46 NSCLC and 45 healthy lung tissues. GSE19804 datasets include 60 NSCLC and 60 healthy lung tissues. In the present study, it was randomly selected 9 tumor and 8 healthy tissues for the GSE19945 datasets and 40 tumor and 40 healthy tissues for the GSE102286 datasets.

Data Processing

In the microarray datasets, GEO2R (www.ncbi.nlm.nih.gov/geo/geo2r) was used to identify differentially expressed genes (DEGs) and differentially expressed miRNAs (DEMs) between NSCLC and healthy lung tissues [9]. GEO2R includes a huge number of experimental datasets and an adjusted P-value (adj. P) is applied to correct false-positive rates. The adjusted p value cutoff was set as $P < 0.05$ and $|\log_2\text{FC}| > 2$ for DEGs selection and $|\log_2\text{FC}| > 1$ for DEMs selection. Following, the overlapping DEGs and DEMs in these datasets were analyzed and drawn Venn diagrams using Venny online tool (<http://bioinformatics.psb.ugent.be/webtools/Venny/>)

Gene Ontology (GO) and Pathway Analysis

Database for Annotation Visualization and Integrated Discovery (DAVID) software (<https://david.ncifcrf.gov/> Version 6.8) was used to explore the potential functions of the overlapping DEGs and DEMs for Gene Ontology (GO) and Kyoto Encyclopedia of Genes and Genomes (KEGG) pathway enrichment analysis. The cut-off value was set as $P < 0.05$.

Establishment of PPI Network

A PPI network was constructed for DEGs using The Search Tool of the Retrieval of Interacting Genes (STRING) database (<https://string-db.org/cgi/>) and was visualized by Cytoscape tool (www.cytoscape.org) with cut-off criterion of confidence score > 0.4 . Moreover, DEGs were analyzed to determine hub genes with the significant degree of nodes ($> 5\%$ degree) by Cytohubba algorithm.

Survival Analysis

Differentially expressed genes were entered into the Kaplan Meier (KM) plotter in order to assess the effect of these genes on survival in the lung cancer

(<http://kmplot.com/analysis/index.php?p=background>). A 95% confidence interval for the hazard ratio and log-rank P value were determined and showed on the KM plotter tool.

Prediction of miRNA targets

Target genes of the overlapped DEMs among miRNA datasets were predicted from the miRWalk database (http://mirwalk.umm.uni-heidelberg.de/search_mirnas Version 3.0) [10]. TargetScan, miRDB and miRTarBase algorithms in MiRWalk database were performed to increase the accuracy in miRNA target prediction. Putative mRNAs were selected from target genes only recognized by all three databases.

Construction of miRNA–mRNA Regulatory Network

The regulatory network was constructed using a combination of overlapped miRNAs and putative mRNAs and visualized using by Cytoscape software (version 3.8.2).

Results

Identification of DEGs and DEMs

A total of 1022 and 265 genes showed significantly deregulation in the GSE18842 and GSE19804 microarray datasets, respectively. Among them, 607 and 213 upregulated genes for GSE18842 and 415 and 52 downregulated genes for GSE19804 were identified in NSCLC tissues. In addition, a total of 130 upregulated and 29 downregulated genes were determined common in both microarray datasets (Figure 1).

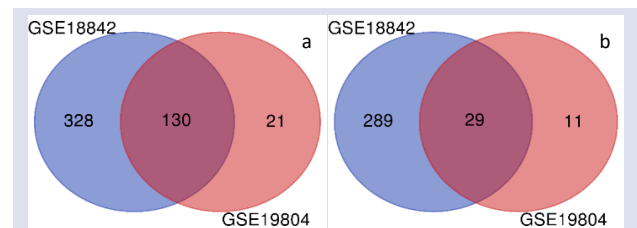


Figure 1. Venn Diagrams of identified DEGs in NSCLC. (a) upregulated (b) downregulated DEGs.

According to the results of GEO2R analysis, it was determined 118 DEMs from GSE19945 (65 upregulated and 53 downregulated DEMs) and 51 DEMs from GSE102286 (19 upregulated and 32 downregulated DEMs). A total of 12 upregulated DEMs (hsa-miR-30d-5p, hsa-miR-30a-5p, hsa-miR-1-3p, hsa-miR-145-5p, hsa-miR-144-5p, hsa-miR-30b-5p, hsa-miR-126-5p, hsa-miR-218-5p, hsa-miR-551b, hsa-miR-223-5p, hsa-miR-451 and hsa-miR-195-5p) and 10 downregulated DEMs (hsa-miR-93-5p, hsa-miR-130b-5p, hsa-miR-193b-5p, hsa-miR-183-5p, hsa-miR-196b, hsa-miR-9-5p, hsa-miR-21-5p, hsa-miR-96-5p, hsa-miR-18a and hsa-miR-135b) were found to overlap in both miRNA datasets (Figure 2).

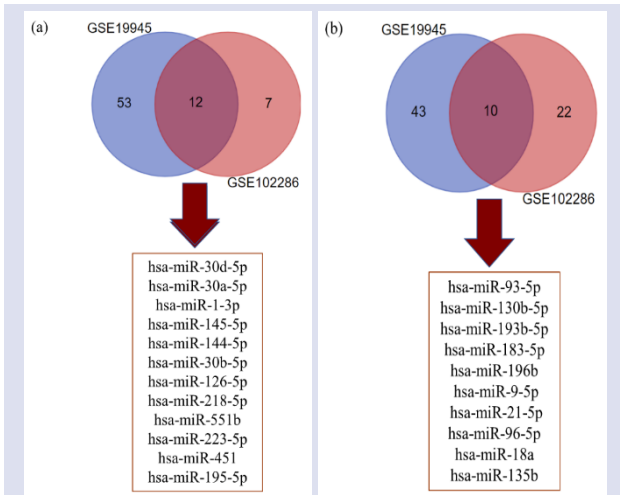


Figure 2. Venn Diagrams of identified DEMs in NSCLC. (a) upregulated (b) downregulated DEMs.

Functional Enrichment Analysis

The GO ontology contains three terms as biological process (BP), cellular component (CC) and molecular

function (MF) [8]. GO classification and KEGG pathway enrichment analysis were conducted to investigate the function of the DEGs with the DAVID software. According to the results of the GO analysis, 88 % (110/179) of the upregulated DEGs were mainly enriched in signal transduction, inflammatory response and negative regulation of transcription from RNA polymerase II promoter. In total, 94.4 % (118) and 81.6 % (102) upregulated DEGs were importantly enriched in cellular components and molecular functions, respectively. In addition, 96.6 % (28) involved genes for biological processes, 96.6 % (28) involved genes for cellular components and 93.1 % (27) involved genes for molecular functions were enriched in total of 36 downregulated DEGs. The KEGG pathway analysis showed that several disease-related pathways including leukocyte transendothelial migration, adrenergic signaling in cardiomyocytes, focal adhesion and ECM receptor interaction played an essential role in NSCLC pathogenesis. The some of the most significant GO categories and the KEGG pathways analysis are showed in Table 1.

Table 1. Some of the most significant DEGs in NSCLC

Category	Term	Description	Gene Counts	P-value
Up regulated gene				
GO:0007165	GOTERM_BP_DIRECT	signal transduction	10	3,40E-01
GO:0000122	GOTERM_BP_DIRECT	negative regulation of transcription from RNA polymerase II promoter	9	9,60E-02
GO:0006954	GOTERM_BP_DIRECT	inflammatory response	8	1,20E-02
GO:0043547	GOTERM_BP_DIRECT	positive regulation of GTPase activity	8	1,20E-02
GO:0045944	GOTERM_BP_DIRECT	positive regulation of transcription from RNA polymerase II promoter	8	7,50E-02
GO:0001525	GOTERM_BP_DIRECT	angiogenesis	8	4,50E-01
GO:0016021	GOTERM_CC_DIRECT	integral component of membrane	44	2,90E-02
GO:0005886	GOTERM_CC_DIRECT	plasma membrane	40	5,10E-03
GO:0005576	GOTERM_CC_DIRECT	extracellular region	31	6,60E-08
GO:0070062	GOTERM_CC_DIRECT	extracellular exosome	26	5,30E-02
GO:0005515	GOTERM_MF_DIRECT	protein binding	64	2,30E-02
GO:0008201	GOTERM_MF_DIRECT	heparin binding	9	5,20E-06
GO:0038023	GOTERM_MF_DIRECT	signaling receptor activity	6	9,80E-03
hsa05144	KEGG_PATHWAY	Malaria	5	5,50E-04
hsa05143	KEGG_PATHWAY	Leukocyte transendothelial migration	4	6,10E-02
hsa04670	KEGG_PATHWAY	Adrenergic signaling in cardiomyocytes	4	9,40E-02
hsa04261	KEGG_PATHWAY	Cell adhesion molecules (CAMs)	4	1,00E-01
Down regulated gene				
GO:0030574	GOTERM_BP_DIRECT	collagen catabolic process	6	5,2E-8
GO:0030199	GOTERM_BP_DIRECT	collagen fibril organization	4	3,3E-5
GO:0022617	GOTERM_BP_DIRECT	extracellular matrix disassembly	4	2,4E-4
GO:0005576	GOTERM_CC_DIRECT	extracellular region	11	5,8E-5
GO:0005615	GOTERM_CC_DIRECT	extracellular space	9	5,4E-4
GO:0031012	GOTERM_CC_DIRECT	proteinaceous extracellular matrix	6	4,1E-5
GO:0005581	GOTERM_CC_DIRECT	collagen trimer	5	9,8E-6
GO:0005509	GOTERM_MF_DIRECT	calcium ion binding	5	2,3E-2
GO:0004252	GOTERM_MF_DIRECT	serine type endopeptidase activity	4	6,9E-3
GO:0004222	GOTERM_MF_DIRECT	metalloendopeptidase activity	3	1,3E-2
hsa04512	KEGG_PATHWAY	ECM receptor interaction	4	5,1E-4
hsa04510	KEGG_PATHWAY	Focal adhesion	4	6,1E-3
hsa04151	KEGG_PATHWAY	PI3K Akt signaling pathway	4	2,5E-2

PPI Network

The two PPI networks were constructed for significantly up regulated DEGs (Figure 3a) and down regulated DEGs (Figure 3b). Nine DEGs with the significant

degree of nodes (> 5% degree) were determined by Cytohubba algorithm with ranked method "degree". These DEGs were identified as hub genes including IL6, COL1A1, CLDN5, CAV1, CDH5, SPP1, GNG11, PPBP, CXCL2 and CXCR2.

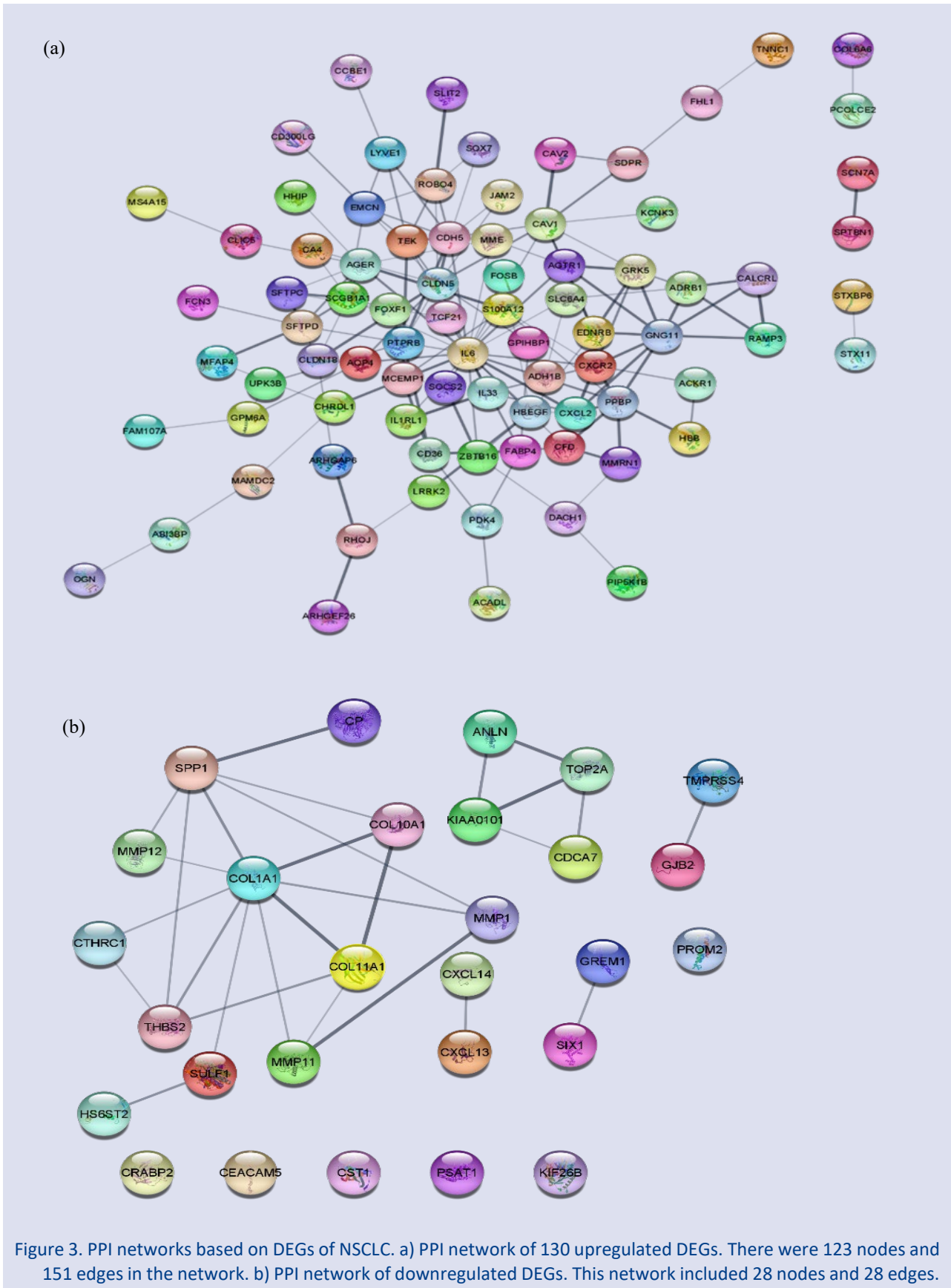


Figure 3. PPI networks based on DEGs of NSCLC. a) PPI network of 130 upregulated DEGs. There were 123 nodes and 151 edges in the network. b) PPI network of downregulated DEGs. This network included 28 nodes and 28 edges.

Survival Analysis

The identified hub genes were analyzed to evaluate the prognostic value by Kaplan-Meier plotter. The low and high expression level of the hub genes were used to define features of overall survival in NSCLC patients. Survival curves were plotted for the NSCLC patients (n=1,925) with adenocarcinoma (n=865) and squamous cell carcinoma (675). According to results of KM analysis, the high expression levels of IL6, PPBP, CXCR2, SPP1 and COL1A1 hub genes predicted worse prognosis of patients with NSCLC (P<0,005). In addition, low expression levels of CLDN5, CAV1, CDH5, GNG11 and CXCL2 were associated with poor overall survival (P<0,005) (Figure 4).

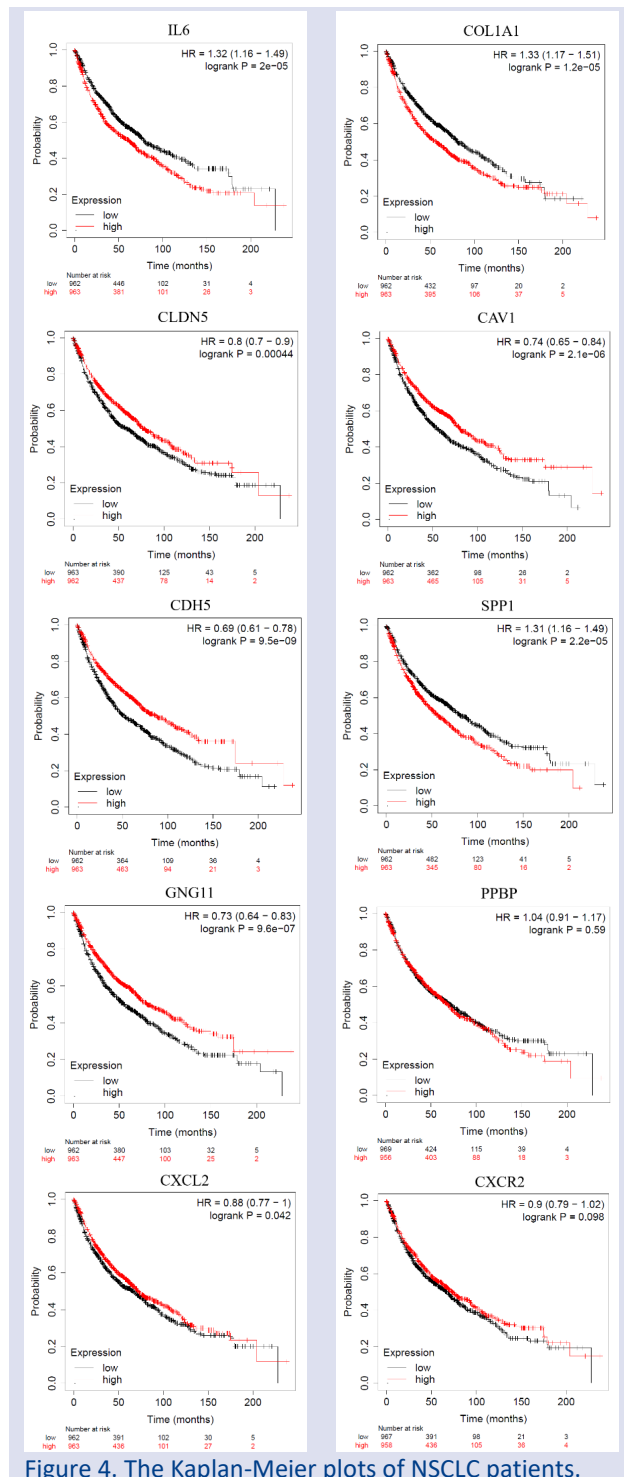


Figure 4. The Kaplan-Meier plots of NSCLC patients.

Prediction of miRNA Target

Target genes of the overlapped DEMs were predicted using TargetScan, miRDB and miRTarBase databases in MiRWalk. A total of 239 target genes were determined as potential mRNAs. When compared target genes with DEGs, hsa-miR-1-3p and hsa-miR-145-5p upregulated DEMs presented the same expression trend compared to their predicted targets in NSCLC. In this study, hsa-miR-1-3p was the most upregulated miRNAs and predicted to target the upregulated ANKRD29 gene. Similarly, hsa-miR-145-5p was upregulated and predicted to target the upregulated two genes including MYRF and ERG genes. However, hsa-miR-195-5p (an upregulated DEMs) and hsa-miR-93-5p (a downregulated DEMs) showed the opposite expression trend compared to their predicted targets in NSCLC. For example, hsa-miR-195-5p was predicted to target one upregulated (TGFB3 gene) and two downregulated genes (CHEK1 and RASEF genes). Also, hsa-miR-93-5p was predicted to target one upregulated (RAB11FIP1 gene) and one downregulated gene (RACGAP1 gene).

miRNA-mRNA Regulatory Network

miRNA-mRNA Regulatory Network showed that a mRNA may be targeted by two or more miRNA. PPP1R12A gene had interactions with hsa-miR-30b-5p and hsa-miR-96-5p (Supplementary Figure 1). In addition, REST (hsa-miR-93-5p and hsa-miR-9-5p), YOD1 (hsa-miR-93-5p and hsa-miR-30b-5p), ATXN1 (hsa-miR-96-5p and hsa-miR-93-5p), GID4 (hsa-miR-21-5p and hsa-miR-93-5p) and PURA genes (hsa-miR-195-5p and hsa-miR-93-5p) had interactions with two different miRNAs.

Discussions

With the introduction to molecular targeted therapy of cancer, miRNAs and genes have emerged as important molecules used in the diagnosis and treatment for cancer patients. These molecules have widely used to find new approaches and treatments for NSCLC. The proliferation of NSCLC is slower than SCLC, however, it is generally diagnosed at the later stages of disease [4]. The 5-year survival rate of NSCLC patients is reported to be less than 20% [11]. Therefore, understanding the molecular mechanisms of NSCLC progression is very important. Also, identifying the potential biomarkers and therapeutic targets is a critical factor for early diagnosis and treatment of NSCLC.

Considering many studies conducted in recent years, it is seen that bioinformatics approaches are a new trend especially in cancer research. Large biological data obtained through experimental analyzes are used in bioinformatics approaches. These data sets are analyzed and transformed into meaningful information with computational methods. Large amounts of biological data stored in public databases such as Gene Expression Omnibus (GEO) and The Cancer Genome Atlas (TCGA) are invaluable resources for researchers to use in bioinformatics analysis. By comparing the gene expression

profiles between normal and tumor tissues with bioinformatics approaches, a lot of information can be obtained about tumor progression and development. Moreover, with these applications, new potential biomarkers can be discovered for the diagnosis and treatment of the diseases. These potential biomarkers can be guiding especially in clinical applications. In many recent studies on lung cancer, new molecular markers have been identified among miRNAs, mRNAs and circRNAs using bioinformatics approaches and their interactions with each other have been investigated. In a recent study, differentially expressed circRNAs (DECs), miRNAs (DEMs), and genes (DEGs) between NSCLC tumor and healthy lung tissues are examined via bioinformatics analysis. A circRNA-miRNA-mRNA network was conducted using DECs, DEMs, and DEGs for NSCLC. Furthermore, the researchers reported that identified molecule networks (hsa_circ_0001947/hsa-miR-637/RRM2 and hsa_circ_0072305/hsa-miR-127-5p/DTL) have a critical role in the occurrence and development of NSCLC [7]. Bioinformatic approaches have been used to explore the genes involved in the development of SCLC and their molecular mechanisms. Gene and miRNA expression profiles were compared between lung cancer tissues and normal lung tissues using transcription sequencing data and non-coding RNA data stored in geodatabase and differentially expressed miRNAs and genes were determined. In addition, some hub genes such as KIF11, MSH2 and RAD21, which were predicted to be regulated by miRNAs, were identified and it was estimated that these hub genes could be a potential biomarker in the diagnosis and treatment of SCLC [8]. The findings are very promising and guide for further research. Similarly, in the present study, it was aimed to identify new molecular markers in lung cancer using bioinformatics approaches. The obtained data have a promising potential for the diagnosis and treatment of NSCLC.

Functional enrichment analysis of the DEGs showed that these genes have an important relationship with lung cancer and these findings are validated with literature researches. For example, caveolin 1, CAV1 gene product, interferes cell growth of lung cancer by interacting with phospho-ERK1/2, estrogen receptor and progesterin receptor [12]. Similarly, many studies have been showed that this protein is an important factor for the metastasis, proliferation, cell migration and invasion of lung cancer [13-15]. Interleukin-6 (IL-6) has a strong positive association with C-reactive protein and is a prognostic factor for NSCLC patients [16]. As a result of GO enrichment analysis for DEGs, it is determined to many significant terms including integral component of membrane, extracellular region, cell adhesion, protein binding and integral component of membrane. GNG11, FABP4 and IL33 genes act as tumor suppressors in lung adenocarcinoma similar to the current study. GNG11 is a lipid-anchored protein and FABP4 have a role in fatty acids metabolism. IL33 is responsible for many biological

processes as a cytokine and is known to be an important factor in cancer progression [17].

In the present study, the results of KEGG pathways analysis indicate that the many DEGs were frequently clustered in cell adhesion molecules, leukocyte transendothelial migration, protein digestion and absorption, focal adhesion and ECM-receptor interaction pathway. Similar to the current study, Lu et al. [18] developed and validated a novel gene expression signature in NSCLC patients. They have showed that many pathways (e.g. leukocyte transendothelial migration and cell adhesion) were associated with recurrence free survival. In addition, determination of CAMs expression was proposed as biomarker for cancer therapy.

In survival analysis applied for identified hub genes, the high expression of IL6, PBP, IL8RB, SPP1 and COL1A1 genes was correlated with worse overall survival and low mRNA expression of CLDN5, CAV1, CDH5, GNG11 and CXCL2 were correlated with poor overall survival for NSCLC patients. Consistent with these results, the low expression of CDH5 associates with poor prognosis in NSCLC [19]. In addition, the key genes were recognized by constructing the PPI network for NSCLC patients. IL6, COL1A1, CLDN5, CAV1, CDH5, SPP1, GNG11, PPBP, CXCL2 and CXCR2 genes were identified as hub genes.

The 22 DEMs and target genes of them were recognized for NSCLC in the current study. Among the miRNAs, hsa-miR-1-3p found to be one of the most miRNAs and predicted to target the ANKRD29 gene. miR-1-3p play a role as a remarkable tumor suppressor in different types of cancers such as lung cancer [20], prostate cancer [21] and colorectal cancer [22]. Among the miRNAs, the expression of miR-9 was considerably lower than other downregulated miRNAs, while miR-451a was markedly upregulated in NSCLC tissues. In a different a study, it is reported that upregulation of miR-451a increases the sensitivity to radiotherapy in A549 cells by enhancing of apoptosis [23]. Additionally, Kim et al. [24] showed that downregulation of miR-9 associates with poor prognosis in colorectal cancer. These findings are consistent with our findings. However, Piao et al. [19] reported that the miR-451a was identified as tumor suppressors, while miR-9 was oncogenes.

According to the present study, hsa-miR-195-5p targets TGFBR3, CHEK1 and RASEF genes, while EGLN3, RACGAP1 and RAB11FIP1 genes are identified as target genes of hsa-miR-93-5p in NSCLC tissues. TGFBR3 (Transforming growth factor beta receptor type III) has shown to be a key molecule in progression and metastasis of cancer as a suppressor for breast, prostate, ovarian, pancreatic, renal and NSCLC [25]. Overexpression of CHEK1 gene (Cell cycle checkpoint kinase 1) has the potential to be an important factor in the development of human malignant tumors [26]. Oshita et al. [27] have reported that the higher expression of RASEF was associated with the poorer prognosis and suggested that RASEF is a new molecular marker and target for lung cancer patients.

In the current study, the bioinformatic analyses are only performed by comparison of NSCLC and health lung tissues. The 10 most significantly hub genes and 22 miRNAs could be considered as potential prognostic biomarkers and therapeutic targets. Moreover, bioinformatic analysis may present different ways to explore function of miRNAs and mRNAs and to clarify the underlying mechanisms of NSCLC. Therefore, the results of the current study may considerably provide benefit to NSCLC patients in clinical studies.

Conclusions

In conclusions, mRNA and miRNA expression profiles between NSCLC and healthy lung tissues were analyzed using microarray datasets downloaded from the GEO database and differentially expressed genes and miRNAs were identified in NSCLC. Pathogenesis and therapeutic targets of NSCLC were explored using bioinformatics approaches. The identified genes, miRNAs and miRNA targets have significant potential for the occurrence and development of NSCLC. These target molecules could serve as prognostic biomarkers and therapeutic targets. However, these findings need to be supported by further studies.

Conflicts of interest

The author declare that they have no conflict of interests

References

- [1] Li C., Yin Y., Liu X., Xi X., Xue W., Qu Y., Non-small cell lung cancer associated microRNA expression signature: Integrated bioinformatics analysis, validation and clinical significance, *Oncotarget*, 8 (15) (2017) 24564–24578.
- [2] Shi K., Li N., Yang M., Li W., Identification of key genes and pathways in female lung cancer patients who never smoked by a bioinformatics analysis, *J. Cancer*, 10(1) (2019) 51–60.
- [3] Chen Y.J., Guo Y.N., Shi K., Huang H.M., Huang S.P., Xu W.Q., Li Z.Y., Wei K.L., Gan T.Q., Chen G., Down-regulation of microRNA-144-3p and its clinical value in non-small cell lung cancer: A comprehensive analysis based on microarray, miRNA-sequencing, and quantitative real-time PCR data, *Respir. Res.*, 20(1) (2019) 1–18.
- [4] Yu H., Pang Z., Li G., Gu T., Bioinformatics analysis of differentially expressed miRNAs in non-small cell lung cancer, *J. Clin. Lab. Anal.*, 35(2) (2021) 1–11.
- [5] Chen Y., Min L, Ren C, Xu X., Yang J., Sun X., Wang T., Wang F., Sun C., Zhang X., MiRNA-148a serves as a prognostic factor and suppresses migration and invasion through Wnt1 in non-small cell Lung cancer, *PLoS One*, 12(2) (2017) 1–17.
- [6] Si W., Shen J., Zheng H., Fan W., The role and mechanisms of action of microRNAs in cancer drug resistance, *Clin. Epigenetics*, 11 (1) (2019) 1–24.
- [7] Cai X., Lin L., Zhang Q., Wu W., Su A., Bioinformatics analysis of the circRNA-miRNA-mRNA network for non-small cell lung cancer, *J. Int. Med. Res.*, 48(6) (2020) 1-15.
- [8] Mao Y., Xue P., Li L., Xu P., Cai Y., Chu X., Jiang P., Zhu S., Bioinformatics analysis of mRNA and miRNA microarray to identify the key miRNA-gene pairs in small-cell lung cancer, *Mol. Med. Rep.*, 20(3) (2019) 2199–2208.
- [9] Bao M., Jiang G., Differential expression and functional analysis of lung cancer gene expression datasets: A systems biology perspective, *Oncol. Lett.*, 18(1) (2019) 776–782.
- [10] Sticht C., De La Torre C., Parveen A., Gretz N., Mirwalk: An online resource for prediction of microRNA binding sites, *PLoS One*, 13 (10) (2018) 1–6.
- [11] Wang K., Chen M., Wu W., Analysis of microRNA (miRNA) expression profiles reveals 11 key biomarkers associated with non-small cell lung cancer, *World J. Surg. Oncol.*, 15(1) (2017) 1–10.
- [12] Sun M.Z., Guan Z., Liu S., Zhou X., Wang N., Shao S., Lin D., Caveolin-1 interferes cell growth of lung cancer NCI-H446 cell through the interactions with phospho-ERK1/2, estrogen receptor and progesterin receptor, *Biomed. Pharmacother.*, 66(4) (2012) 242–248.
- [13] Yeh D., Chen C., Sun M.Z., Shao S., Hao L., Song Y., Gong L., Hu J., Wang Q., Caveolin-1 is an important factor for the metastasis and proliferation of human small cell lung cancer NCI-H446 cell, *Anat. Rec.*, 292(10) (2009) 1584–1592.
- [14] Luanpitpong S., Talbott S.J., Rojanasakul Y., Nimmanit U., Pongrakhananon V., Wang L., Chanvorachote P., Regulation of lung cancer cell migration and invasion by reactive oxygen species and caveolin-1, *J. Biol. Chem.*, 285(50) (2010) 38832–38840.
- [15] Chen H.L., Fan L.F., Gao J., Ouyang J.P., Zhang Y.X., Differential expression and function of the caveolin-1 gene in non-small cell lung carcinoma, *Oncol. Rep.*, 25(2) (2011) 359–366.
- [16] McKeown D.J., Brown D.J.F., Kelly A., Wallace A.M., McMillan D.C., The relationship between circulating concentrations of C-reactive protein, inflammatory cytokines and cytokine receptors in patients with non-small-cell lung cancer, *Br. J. Cancer*, 91 (12) (2004) 1993–1995.
- [17] Hsu Y.L., Hung J.Y., Lee Y.L., Chen F.W., Chang K.F., Chang W.A., Tsai Y.M., Chong I.W., Kuo P.L., Identification of novel gene expression signature in lung adenocarcinoma by using next-generation sequencing data and bioinformatics analysis, *Oncotarget*, 8(62) (2017) 104831–104854.
- [18] Lu Y., Wang L., Liu P., Yang P., You M., Gene-expression signature predicts postoperative recurrence in stage I non-small cell lung cancer patients, *PLoS One*, 7(1) (2012) 1-9.
- [19] Piao J., Sun J., Yang Y., Jin T., Chen L., Lin Z., Target gene screening and evaluation of prognostic values in non-small cell lung cancers by bioinformatics analysis, *Gene*, 647 (2018) 306–311.
- [20] Li T., Wang X., Jing L., Li Y., MiR-1-3p inhibits lung adenocarcinoma cell tumorigenesis via targeting protein regulator of cytokinesis 1, *Front. Oncol.*, 9(120) (2019) 1–11.
- [21] Li S.M., Wu H.L., Yu X., Tang K., Wang S.G., Ye Z.Q., Hu J., The putative tumour suppressor miR-1-3p modulates prostate cancer cell aggressiveness by repressing E2F5 and PFTK1, *J. Exp. Clin. Cancer Res.*, 37(1) (2018) 1–15.
- [22] Du G., Yu X., Chen Y., Cai W., MiR-1-3p Suppresses Colorectal Cancer Cell Proliferation and Metastasis by Inhibiting YWHAZ-Mediated Epithelial-Mesenchymal Transition, *Front. Oncol.*, 11 (2) (2021)1–8.
- [23] Tian F., Han Y., Yan X., Zhong D., Yang G., Lei J., Li X., Wang X., Upregulation of microRNA-451 increases the sensitivity of A549 cells to radiotherapy through enhancement of apoptosis, *Thorac. Cancer*, 7(2) (2016) 226–231.

- [24] Kim H., Kim T., Jaygal G., Woo J., Kim C.J., Baek M.J., Jeong D., Downregulation of miR-9 correlates with poor prognosis in colorectal cancer, *Pathol. Res. Pract.*, 216(8), (2020) 1-7.
- [25] Liu X.L., Xiao K., Xue B., Yang D., Lei Z., Shan Y., Zhang H.T., Dual role of TGFBR3 in bladder cancer, *Oncol. Rep.*, 30(3) (2013) 1301–1308.
- [26] Wu M., Pang J.S., Sun Q., Huang Y., Hou J.Y., Chen G., Zeng J.J., Feng Z.B., The clinical significance of CHEK1 in breast cancer: a high-throughput data analysis and immunohistochemical study., *Int. J. Clin. Exp. Pathol.*, 12 (1) (2019) 1–20.
- [27] Oshita H., Nishino R., Takano A., Fujitomo T., Aragaki M., Kato T., Akiyama H., Tsuchiya E., Kohno N., Nakamura Y., Daigo Y., RASEF is a novel diagnostic biomarker and a therapeutic target for lung cancer, *Mol. Cancer Res.*, 11(8) (2013) 937–951.

An Investigation of the Bactericidal and Fungicidal Effects of Algerian Propolis Extracts and Essential Oils

Meltem Asan-Ozusaglam^{1,a,*}, Songul Tacer^{1,b}, Safia Boulechfar^{2,3,c}, Amar Zellaoui^{2,d}

¹Department of Molecular Biology and Genetic, Faculty of Science and Letters, University of Aksaray, Aksaray / Turkey

²Laboratory of Biomolecules and Plant Breeding, Life Science and Nature Department, Faculty of Exact Science and Life Science and Nature, University of Larbi Ben Mhidi Oum El Bouaghi, Algeria

³Department of Biochemistry, Molecular and Cellular Biology, Faculty of Nature and Life Sciences, Mentouri University, Constantine / Algeria

*Corresponding author

Research Article

History

Received: 21/05/2021

Accepted: 27/01/2022

Copyright



©2022 Faculty of Science,
Sivas Cumhuriyet University

ABSTRACT

Natural products have been used in medicine for variety of purposes for centuries. As a natural product, propolis is gaining increasing importance today due to its antimicrobial activity against pathogenic microorganisms. Hence, the aim of the present study was to investigate the antimicrobial activity of extracts and essential oils of propolis collected from various regions of Algeria against food-borne and clinically pathogen microorganisms including *Salmonella enteritidis* RSKK 171, *Shigella sonnei* MU:57 and *Candida glabrata* RSKK 04019. The antimicrobial activity of the propolis extracts and essential oils were evaluated using disc diffusion method. The results showed that all propolis extracts and essential oils exhibited antimicrobial activity against the tested microorganisms with inhibition zones varied from 8.31 mm to 14.53 mm. The minimal inhibitory concentration (MIC) and minimal bactericidal or fungicidal concentration (MBC or MFC) of the samples were determined by microdilution-broth method. The MIC and MBC or MFC values were in the range of 0.25-2 µg/µl and 0.25-4 µg/µl. Therefore, propolis extracts and essential oils from different regions of Algeria have potential to be used as a natural additive for food and pharmaceutical industries.

Keywords: Propolis, Antimicrobial, Bactericidal, Fungicidal.

^a meltemozusaglam@gmail.com

^b <https://orcid.org/0000-0002-3638-1306>

^c saf.bio@hotmail.fr

^d <https://orcid.org/0000-0002-2716-0261>

^b songultacer@outlook.com.tr

^b <https://orcid.org/0000-0002-7035-8134>

^d zellaouiuniv@yahoo.com

^d <https://orcid.org/0000-0002-6515-8103>

Introduction

In the last 20 years, due to the existence of side effects of synthetic medicines and the resistance of microorganisms to these drugs, the tendency towards the use of drugs with natural ingredients has increased. [1]. Today, many of the microorganisms that cause foodborne infections gain resistance over time due to antimicrobial drugs and misuse. Therefore, people tend to prefer products with natural antimicrobial properties [2]. Natural products are increasingly used as they are better tolerated in the human body [3]. Propolis is a natural bee product that honey bees (*Apis mellifera* L.) obtain by adding salivary enzymes to the resin they collect from sprouts, leaves, buds and shell cracks in trees and plants [4-6]. It contains plant resin (50%), beeswax (30%), essential oils (10%) and other components (5%) [7]. Propolis have wide biological properties such as antibacterial [8], antifungal [9], anti-inflammatory [10], anticarcinogen [11], anti-allergic, anti-diabetic [12], cytostatic, hepatoprotective and photoprotective effects [13, 14].

Candida species are opportunistic species that cause certain infections when the host's immune and defense system is weakened [15]. Clinically, *Candida* strains have difficulties in their treatment as they become resistant to antifungals [16, 17]. Shigellosis, also known as bacillary dysentery, is an infectious disease caused by *Shigella*. *S. dysenteriae*, *S. boydii*, *S. sonnei* and *S. flexneri* are all pathogens for humans in the genus *Shigella* [18]. Infection

is mainly spread from person to person through fecal-oral route or contaminated food and water consumption. [19]. *Salmonella* genus is one of the most important causes of foodborne bacterial and diseases in the world [20]. *Salmonella* species can be transmitted to humans in a variety of ways, but most infections result from the consumption of contaminated food of animal origin [21].

To date, the antimicrobial activities of propolis extracts and essential oils against various bacterial and fungal strains have been studied. However, the composition of propolis varies considerably according to the climate, season, geographical region, collection time and source of plant [22, 23]. As a result, the chemical composition and biological properties of propolis vary greatly depending on the sources from which it is collected. In the current study, it is aimed to investigate the antimicrobial activities of propolis extracts and essential oils collected from different regions of Algeria against two food-borne Gram-negative bacteria and one clinical yeast.

Materials and Methods

Test Microorganisms

In vitro antimicrobial activity of propolis extracts and essential oils were tested against two Gram negative bacteria (*S. enteritidis* RSKK 171 and *S. sonnei* MU: 57) and

one yeast (*C. glabrata* RSKK 04019). The strains of bacteria and yeast were cultured at 37°C in nutrient broth/agar and at 30°C in YPD (Yeast Peptone Dextrose) broth/agar mediums.

Propolis Samples

The samples of propolis were collected from *Apis mellifera* hives located at different geographical regions of Northeast Algeria (Collo, El harrouch, Taref, Konstantin, Setif, Mila, Batna, Oum el Bouaghi) (Table 1).

Table 1. Collection regions of propolis samples

Samples name	Samples	Collection Region	City
1	Methanolic extract	Menia	Constantine
2	Methanolic extract	Grarem	Mila
3	Methanolic extract	Collo	Skikda
4	Methanolic extract	Mestaoua & Chelala mountains	Batna
5	Methanolic extract	El Harrouch	Skikda
6	Methanolic extract	Bouteldja	Taref
7	Aqueous fraction of methanolic extract	Babor	Sétif
8	Methanolic extract	Babor	Sétif
9	Methanolic extract	Oum el Bouaghi	Oum el Bouaghi
M	Essential oil	Menia	Constantine
H	Essential oil	El Harrouch	Skikda
C	Essential oil	Collo	Skikda
B	Essential oil	Mestaoua & Chelala mountains	Batna
X	Essential oil	Oum el Bouaghi	Oum el Bouaghi

Preparation of Propolis Extracts and Essential Oils

The collected propolis samples were pulverized after separation of impurities. The powdered propolis samples (20 g) were extracted with 200 ml of hydroalcoholic solution (80% MeOH, 20% distilled water) in three times for 72 h. After the extraction, the obtained extracts were filtered, evaporated and then kept at 4°C under dry conditions until use [24]. However, propolis essential oils were obtained by hydrodistillation of crude powdered propolis (100 g) using a Clevenger type apparatus for 3 h. The obtained oils were dried over anhydrous sodium sulphate and then stored at 4°C. Prior to determine the antimicrobial activity, propolis extracts and essential oils (10 mg) were dissolved in 1 ml of Dimethyl sulphoxide (DMSO) to obtain a final concentration of 10 µg/µl. Then, the obtained solutions were sterilized by 0.45 µm Millipore filters.

Determination of antimicrobial activity

Disc diffusion assay

The disc diffusion method was used to determine the antimicrobial activity of propolis extracts and essential oils [25]. The culture suspensions were adjusted by comparing with 0.5 McFarland. Then, a volume of 100 µl of suspension was spread on agar plates. Thereafter, sterile 6 mm diameter filter discs (Whatman paper no 3) were placed on the inoculated plates and impregnated with 15 µl (150 µg/disc) of propolis extracts and essential oils. The plates were kept at 4°C for 1 h to enable prediffusion of propolis samples into the agar. The inoculated plates were then incubated at 37°C for 24 h for bacterial strains and 30°C for 48 h for yeast. The results were obtained by measuring the diameter of growth inhibition zone diameter around the discs and expressed in mm.

Microdilution assay

The two-fold microdilution method was used to determine the minimum inhibitory (MIC), minimum bactericidal (MBC) and minimum fungicidal (MFC) concentrations of propolis extracts and essential oils. The propolis extracts and essential oils were added to each growth medium to obtain a final concentration of 4 µg/µl and 8 µg/µl, respectively and diluted to 4, 2, 1, 0.5 and 0.25 µg/µl in tubes. Then, the content of the tubes was mixed and they were incubated at appropriate temperatures for 24 h for bacterial strains and for 48 h for yeast. The MIC value was defined as the lowest concentration of propolis extracts and essential oils, which inhibited bacterial or fungal growth. MBC and MFC were determined by spot dropping from each clear tube on solid growth medium and incubating for 24 h and 48 h at appropriate temperature. The lowest concentration that did not show bacterial or fungal growth was defined as the MBC or MFC value. The results are expressed as µg/µl.

Results and Discussion

One of the most researched activities of propolis is its antimicrobial activity. Many scientific studies have proved the effect of propolis extracts and essential oils on various bacteria, fungi, viruses and other microorganisms [22, 23, 26]. Thus, in this study we investigated the antibacterial and antifungal activities of propolis extracts and essential oils, against some pathogenic microorganisms, by two methods: disc diffusion and microdilution assays. The results of disc diffusion revealed the ability of propolis extracts and essential oils to inhibit the growth of all tested microorganisms with inhibition zone diameters

ranged from 8.71 ± 0.19 mm to 14.53 ± 0.27 mm (Table 2, Figure 1).

Table 2. Antimicrobial activity of propolis extracts and essential oils

Samples	Inhibition zone diameter (mm)		
	<i>C. glabrata</i> RSKK 04019	<i>S. enteritidis</i> RSKK 171	<i>S. sonnei</i> MU:57
1	12.07±0.23	10.15±0.21	9.23±0.07
2	10.49±0.25	9.60±0.54	9.08±0.08
3	11.45±0.51	8.96±0.33	9.81±0.30
4	9.89±0.28	9.53±0.20	9.20±0.01
5	10.64±0.16	9.21±0.23	8.31±0.44
6	12.02±0.27	9.93±0.16	9.03±0.34
7	14.53±0.27	8.95±0.44	9.84±0.18
8	8.87±0.89	8.78±0.90	8.46±0.64
9	12.95±0.51	9.67±0.40	9.24±0.31
B	10.24±0.34	9.12±0.21	9.39±0.08
C	9.41±0.28	9.51±0.37	9.34±0.41
H	11.47±0.30	8.71±0.19	8.76±0.33
M	10.78±0.64	8.97±0.20	8.87±0.73
X	11.29±0.53	9.14±0.19	9.44±0.50

Regarding antibacterial activity, the highest inhibition effect was exhibited by Sample 1 against *S. enteritidis* RSKK 171 (10.15 ± 0.21 mm) and Sample 7 against *S. sonnei* MU:57 (9.84 ± 0.18 mm). Sample 8, however, was the less active against *S. enteritidis* RSKK 171 and *S. sonnei* MU:57 with inhibition zone diameter values of 8.78 ± 0.90 mm and 8.46 ± 0.64 mm, respectively. Among propolis essential oils, Sample C and X were more active against *S. enteritidis* RSKK 171 (9.51 ± 0.37 mm) and *S. sonnei* MU:57 (9.44 ± 0.50), respectively, while Sample H and M exerted the lowest activity.

The results of antifungal activity of propolis extracts and essential oils against *C. glabrata* RSKK 04019 revealed that the highest inhibition zone diameter against *C. glabrata* RSKK 04019 was exerted by Sample 7 (14.53 ± 0.27 mm) and Sample 9 (12.95 ± 0.51 mm). Sample 8, however, recorded the lowest inhibition effect with inhibition zone diameter of (8.87 ± 0.89 mm). The MFC values varied from 0.25 to 2 $\mu\text{g}/\mu\text{l}$ for propolis extracts and from 1 to 4 $\mu\text{g}/\mu\text{l}$ for propolis essential oil. Sample 7 recorded the lowest MFC (0.25 $\mu\text{g}/\mu\text{l}$).

The determination of MIC values by microdilution method showed that among all propolis extracts and fatty acids, sample 7 was the most effective extract with MIC value of 1 $\mu\text{g}/\mu\text{l}$ against the two Gram-negative bacteria

(Table 3). The MBC values varied between 1 $\mu\text{g}/\mu\text{l}$ and 4 $\mu\text{g}/\mu\text{l}$. The lowest MBC value was recorded by Sample 7 (1 $\mu\text{g}/\mu\text{l}$) against *S. enteritidis* RSKK 171 and *S. sonnei* MU:57 (Table 3). All of the fatty acid samples (B, C, H, M, X) showed the same MBC value (4 $\mu\text{g}/\mu\text{l}$).

Antimicrobials are usually regarded as bactericidal or fungicidal if the MBC/MIC or MFC/MIC ratio is ≤ 4 and bacteriostatic or fungistatic if the MBC/MIC or MFC/MIC ratio is >4 [27, 28]. The ratios obtained for all the test microorganisms were below 4 which indicated that all propolis extracts and essential oils were bactericidal in action against *S. enteritidis* RSKK 171 and *S. sonnei* MU:57 and fungicidal against *C. glabrata* RSKK 04019 (Table 4).



Figure 1a. Sample 7 against *C. glabrata* RSKK 04019



Figure 1b. Sample 4 against *S. enteritidis* RSKK 171

Figure 1. Antimicrobial activity of the propolis samples

Some studies stated that propolis is active only against Gram-positive bacteria and some fungi [29, 30], while in others it showed weak activity against Gram-negative [31, 32]. It has been also reported that Gram-positive bacteria are generally more sensitive to propolis than Gram-negative bacteria [33].

Table 3. MIC, MBC and MFC values of propolis methanolic extracts and essential oils

Samples	MIC ($\mu\text{g}/\mu\text{l}$)			MFC ($\mu\text{g}/\mu\text{l}$)		MBC ($\mu\text{g}/\mu\text{l}$)	
	<i>C. glabrata</i> RSKK 04019	<i>S. enteritidis</i> RSKK 171	<i>S. sonnei</i> MU:57	<i>C. glabrata</i> RSKK 04019	<i>S. enteritidis</i> RSKK 171	<i>S. sonnei</i> MU:57	
1	2	2	2	2	2	4	
2	2	2	2	2	4	4	
3	2	2	2	2	4	4	
4	2	2	2	1	4	4	
5	1	2	2	2	4	4	
6	1	2	2	2	2	2	
7	0.25	1	1	0.25	1	1	
8	1	2	2	2	4	4	
9	1	2	2	2	2	2	
B	2	2	2	2	4	4	
C	2	2	2	4	4	4	
H	2	2	2	4	4	4	
M	2	2	2	4	4	4	
X	1	2	2	1	4	4	

Table 4. MBC/MIC and MFC/MIC ratios values of propolis methanolic extracts and essential oils

Samples	MBC/MIC or MFC/MIC		
	<i>C. glabrata</i> RSKK 04019	<i>S. enteritidis</i> RSKK 171	<i>S. sonnei</i> MU:57
1	1	1	2
2	1	2	2
3	1	2	2
4	0.5	2	2
5	2	2	2
6	2	1	1
7	1	1	1
8	2	2	2
9	2	1	1
B	1	2	2
C	2	2	2
H	2	2	2
M	2	2	2
X	1	2	2

Overall, in the current study, the test of antimicrobial activity of Algerian propolis has shown that propolis extracts and essential oils are more effective against yeast than Gram-negative bacteria. This could be due to the difference of membrane structure of bacteria and yeast. The antimicrobial effect mechanisms of propolis can be considered as its action on the permeability of the microbial cell membrane, the deterioration of the membrane potential, the reduction of ATP production and the decrease of the bacterial motility [34]. In a study conducted by Al-Ani et al, ethanolic extracts of propolis from Germany, Ireland, and Czech Republic showed moderate activity with MIC values ranging from 0.6 mg/ml to 5 mg/ml against Gram-negative bacteria and 0.6 mg/ml to 2.5 mg/ml against *Candida* species [35]. These results are quite higher than our findings. Gür et al. found that propolis from Turkey exhibited antibacterial effect on both Gram-positive and Gram-negative bacteria [36]. Mohdaly et al. [37] reported that methanolic extract of

propolis from Egypt had a nearly MIC value (1.35 mg/ml) and generally lower MBC value (MBC 1.45 mg/ml) against *Salmonella enterica* when compared to the MIC and MBC values of propolis extracts against *S. enteritidis* RSKK 171 in our study. Additionally, ethanolic extract of propolis from other regions in Algeria (El Mechrouha and Ouled Driss regions) presented no antibacterial activity against the tested Gram-negative bacteria [38]. Seidel et al. [39] reported that propolis ethanolic extract from various countries showed bacteriostatic activity against Gram-negative bacteria, which is different from our results that revealed the bactericidal effect of both propolis extracts and essential oils on Gram-negative bacteria tested. This difference, however, may be due to the difference in the chemical composition of propolis, which is linked to the difference of geographical origins of propolis. It is noteworthy that the composition of propolis varies considerably according to the climate, season, geographical region, and collection time and source plant [22, 23].

Conclusion

The antimicrobial activity of propolis extracts and essential oils collected from different regions of Algeria against two food-borne Gram-negative bacteria and one clinical yeast were studied to reveal their potentials properties as natural antimicrobial additive. The results of the study indicated that the propolis samples showed a good antimicrobial activity on the test microorganisms. In addition, it has been determined that the propolis samples have bactericidal and fungicidal effects on the test microorganisms. Therefore, the propolis extracts and essential oils from various regions of Algeria can be used as a potential bioactive additive for pharmaceutical and food industries.

Conflicts of Interest

The authors state that there is no conflict of interests.

References

- [1] Tajkarimi M.M., Ibrahim S.A., Cliver D.O., Antimicrobial herb and spice compounds in food, *Food Control*, 21 (2010) 1199–1218.
- [2] Karatepe P., Patir B., The effect of eugenol and thymol on chemical, microbiological and sensory quality of pasteurized butter, *Firat University Medical Journal of Health Sciences*, 26 (2012) 35-46.
- [3] Oskay M., Tamer A.U., Ay G., Sari D., Akta K., Antimicrobial activity of the leaves of *Lippia triphylla* (L'Her) O. Kuntze (Verbenaceae) against on bacteria and yeasts, *J. Biol. Sci.*, 5(5) (2005) 620-622.
- [4] da Silva C., Prasniewski A., Calegari M.A., de Lima V.A., Oldoni T.L., Determination of total phenolic compounds and antioxidant activity of ethanolic samples of propolis using ATR–FT-IR spectroscopy and chemometrics, *Food Anal. Methods*, 11(7) (2018) 2013-2021.
- [5] Segueni N., Khadraoui F., Rhouati S., Volatile compounds as propolis characterization markers. In Euro-Mediterranean Conference for Environmental Integration, November, Springer, (2017) 1271-1273.
- [6] Ghisalberti E.L., Propolis: a review, *Bee World*, 60 (1979) 59–84.
- [7] El-Ghamdi A.A., Bayaqoob N.I., Rushdi A.I., Alattal Y., Simoneit B.R., El-Mubarak A.H., Al-Mutlaq K.F., Chemical compositions and characteristics of organic compounds in propolis from Yemen, *Saudi J. Biol. Sci.*, 24(5) (2017) 1094-1103.
- [8] Kumazawa S., Hamasaka T., Nakayama T., Antioxidant activity of propolis of various geographic origins, *Food Chem.*, 84 (2004) 329–339.
- [9] Yadav H., Mungara P., Jivrajani M., Nivsarkar M., Anandjiwala S., TLC-densitometric quantification of negundoside, ursolic acid, eugenol, lupeol, and β -sitosterol using HPTLC from vitex negundo leaves, *J. Liq. Chromatogr. Relat. Technol.*, 35(11) (2012) 1565-1584.
- [10] Piccinelli A.L., Mencherini T., Celano R., Mouhoubi Z., Tamendjari A., Aquino R.P., Rastrelli L., Chemical composition and antioxidant activity of Algerian propolis, *J. Agric. Food Chem.*, 61(21) (2013) 5080-5088.
- [11] de Moura S.A.L., Negri G., Salatino A., Lima L.D.C., Dourado L.P.A., Mendes J.B., Aqueous sample Brazilian propolis: primary components, evaluation of inflammation and wound healing by using subcutaneous implanted sponges, *Evid. Based Complement. Alternat. Med.*, 18 (2009) 1–9.
- [12] Wang R., Ding S., Zhao D., Wang Z., Wu J., Hu W., Effect of dehydration methods on antioxidant activities, phenolic contents, cyclic nucleotides, and volatiles of jujube fruits, *Food Sci. Biotechnol.*, 25(1) (2016) 137-143.
- [13] Kang L.J., Lee H.B., Bae H.J., Lee S.G., Antidiabetic effect of propolis: reduction of expression of glucose-6-phosphatase through inhibition of Y279 and Y216 autophosphorylation of GSK-3 α/β in HepG2 cells. *Phytother. Res.*, 24(10) (2010) 1554-1561.
- [14] de Castro P.A., Savoldi M., Bonatto D., Malavazi I., Goldman M.H., Berretta A.A., Transcriptional profiling of *Saccharomyces cerevisiae* exposed to propolis, *BMC Complement. Altern. Med.*, 12 (2012) 194.
- [15] Silva F., Domingues F.C., Antimicrobial activity of coriander oil and its effectiveness as food preservative, *Crit. Rev. Food Sci. Nutr.*, 57 (2017) 35-47.
- [16] Martins N., Ferreira I.C.F.R., Barros L., Silva S., Henriques M., Candidiasis: predisposing factors, prevention, diagnosis and alternative treatment, *Mycopathologia*, 177(5–6) (2014) 223-240
- [17] Douglas L.J., Candida biofilms and their role in infection, *Trends Microbiol.*, 11(1) (2003) 30-36.
- [18] Wu F.M., Doyle M.P., Beuchat L.A., Wells J.G., Mintz E.D., Swaminathan B. Fate of *Shigella sonnei* on parsley and methods of disinfection, *J. Food Prot.*, 63 (2000) 568-572.
- [19] Lampel, K.A., Maurelli, A.T., 2002. Shigella. In: Cliver, D.O., Riemann, H.P. (Eds.), *Foodborne Diseases*. 2nd ed. London: Elsevier Science Ltd, (2002) 69-77.
- [20] Gouws P.A., Visser M., Brözel V.S., A polymerase chain reaction procedure for the detection of *Salmonella* sp. within 24 hours, *J. Food Prot.* 61(8) (1998) 1039-1042.
- [21] Akpınar M., Salmonella ile bakteriyofajlarının çeşitli köy kümes folluklarından izolasyonu ve karakterizasyonu. Yüksek Lisans Tezi, Fen Bilimleri Enstitüsü, Ankara Üniversitesi, Ankara (2020).
- [22] Sforcin J.M., Fernandes Jr., Lopes C.A.M., Bankova V., Funari S.R.C., Seasonal effect on Brazilian propolis antibacterial activity, *J. Ethnopharmacol.*, 73 (2000) 243–249.
- [23] Hegazi A.G., Abd El Hady F.K., Abd Allah F.A., Chemical composition and antimicrobial activity of European propolis, *Z. Naturforsch. C*, 55 (2000) 70–75.
- [24] Park Y.K., Ikegaki M., Preparation of water and ethanolic extracts of propolis and evaluation of the preparations, *Bioscience, Biotechnology and Biochemistry*, 62(11) (1998) 2230–2232.
- [25] Murray P.R., Baron E.J., Pfaller M.A., Tenevor F.C., Tenover R.H., *Manual of Clinical Microbiology*. 6th ed. Washington: ASM Press, (1995) 457–464.
- [26] Kujumgiev A., Bankova V., Ignatova A., Popov S., Antibacterial activity of propolis, some of its components and analogs, *Pharmazie*, 48 (1993) 785-786.
- [27] Krishnan N., Ramanathan S., Sasidharan S., Murugaiyah V., Mansor S.M., Antimicrobial activity evaluation of *Cassia spectabilis* leaf samples, *Int. J. Pharmacol.*, 6(4) (2010) 510–514.
- [28] Hazen K.C., Fungicidal versus fungistatic activity of terbinafine and itraconazole: An in vitro comparison, *J. Am. Acad. Dermatol.*, 38(5) (1998) 37-41.
- [29] Marcucci M.C., Propolis: Chemical composition, biological properties and therapeutic activity, *Apidologie*, 26 (1995) 83-99.
- [30] De Castro S.L., Higashi K.O., Effect of different formulations of propolis on mice infected with *Trypanosoma cruzi*, *J. Ethnopharmacol.*, 46 (1995) 55–58.
- [31] Bhavaniramy S., Vishnupriya S., Al-Aboody M.S., Vijayakumar R., Baskaran D., Role of essential oils in food safety: Antimicrobial and antioxidant applications, *Grain & Oil Science and Technology*, 2(2) (2019) 49-55.
- [32] Nieva M.M.I., Isla M.I., Cudmani N.G., Vattuone M.A., Sampietro A.R., Screening of antibacterial activity of Amaicha del Valle (Tucuman, Argentina) propolis, *J. Ethnopharmacol.*, 68 (1999) 97–102.
- [33] Grange J.M., Davey R.W., Antibacterial properties of propolis (bee glue), *Journal of the Royal Society of Medicine*, 83 (1990) 159–161.
- [34] Przybytek I., Karpinski T.M. Antibacterial properties of propolis, *Molecules*, 24(11) (2019) 2047.
- [35] Al-An I., Zimmermann S., Reichling J., Wink M., Antimicrobial activities of European propolis collected from various geographic origins alone and in combination with antibiotics, *Medicines*, (1) (2018) 2.
- [36] Gür N., Bayrak N., Topdemir A., Determination of antimicrobial activity and some biochemical properties of honey and propolis in Turkish markets, *Prog. Nutr.*, 22(3) (2020) e2020040.

- [37] Mohdaly A.A.A., Mahmoud A.A., Roby M.H.H., Smetanska I., Ramadan M.F., Phenolic extract from propolis and bee pollen: composition, antioxidant and antibacterial activities, *J. Food Biochem.*, 39 (2015) 538–547.
- [38] Bouzahouane H., Ayari A., Guehria I., Riah O., Propolis: Antimicrobial activity and chemical composition analysis: Properties of propolis, *J. Microbiol. Biotech. Food Sci.*, 10(6) (2021) e3211.
- [39] Seidel V., Peyfoon E., Watson D.G., Fearnley J., Comparative study of the antibacterial activity of propolis from different geographical and climatic zones, *Phytother. Res.*, 22(2008) 1256–1263.

Free Energy Decomposition of CarO Outer Membrane Protein of *Acinetobacter baumannii*

Emrah Sariyer^{1,a,*}

¹ Medical Laboratory Techniques, Vocational School of Health Services, Artvin Çoruh University, Artvin, Turkey.

*Corresponding author

Research Article

History

Received: 11/11/2021

Accepted: 14/03/2022

Copyright



©2022 Faculty of Science,
Sivas Cumhuriyet University

^a esariyer@yahoo.com

^{id} <https://orcid.org/0000-0003-1721-0314>

ABSTRACT

The increase in the number of antibiotic-resistant microorganisms reported today has made this issue one of the main topics of all institutes. *Acinetoebacter baumannii* is a species that is on the list of the WHO and plays an important role, especially in hospital-acquired infections. CarO outer membrane protein, which regulates the passage of small molecules and some antibiotics into the periplasmic space and is associated with carbapenem resistance, has been identified in *A. baumannii*. In this study, residues that contribute to the binding energy of imipenem to different types of CarO proteins were identified. In addition, energy decomposition was compared when Biapenem, Ertapenem, Imipenem, Faropenem, and Meropenem were docked to ATCC-17978 CarO protein separately. As a result of this study, it was determined that generally charged residues had a negative effect on binding affinity, but hydrophobic and uncharged residues had a positive effect. In addition, in ertapenem, faropenem, and meropenem-bound complexes, charged residues increased the affinity and caused the interaction between carbapenems and CarO to be continuous and tight. It was predicted that the residues determined in this study would be precursors to mutagenesis studies and could also be an example for similar studies.

Keywords: *Acinetobacter baumannii*, CarO, Imipenem, Binding affinity, Energy decomposition.

Introduction

Acinetoebacter baumannii is a non-motile, aerobic, gram-negative bacterium and mostly causes infection in the liver, blood, urinary system, and wounds [1]. It is common in hospital-acquired infections in recent years and the World Health Organization has declared it among the ESKAPE organisms (*Enterococcus faecium*, *Staphylococcus aureus*, *Klebsiella pneumoniae*, *A. baumannii*, *Pseudomonas aeruginosa*, and *Enterobacter spp*) to be considered [2]. A carbapenem group of antibiotics is generally used against this bacterium, and multiple resistance mechanisms are developing rapidly against these antibiotics [3]. Carbapenem-Resistant *A. baumannii* was announced among the species that should be emphasized by the WHO in 2018 [4].

Since *A. baumannii* is a gram negative bacterium, it has a membrane consisting of an inner and an outer membrane, and the outer membrane has different structures and properties, including lipopolysaccharides (LPS) or lipooligosaccharides (LOS) [5, 6]. Thanks to the asymmetric outer membrane, it adheres to other cells or regulates the passage of small molecules, lipids or antibiotics from the outside into the periplasmic space [7]. The outer membrane contains the integral membrane proteins BamA, LptD, Omp33–36, OmpW, CarO and OprD, among which CarO has been related with the carbapenem resistance of the outer membrane protein [8]. CarO has a molecular weight of 29 kDa, consists of 8 β -barrel structures, and the 3-dimensional crystal structure of this protein has been defined for three different isoforms [9].

Decreased expression and structural changes of CarO have been reported to render *A. baumannii* resistant to Imipenem [10, 11].

There are clinical studies on the relationship of CarO-Imipenem resistance, but it was limited studies on the protein at the structural and molecular level [12]. Structural studies at the molecular level are both time-consuming and costly processes. For this reason, computational studies, which are powerful and useful methods of today, continue to dominate [13]. From these methods, protein ligand interactions can be analyzed quickly with molecular docking and molecular dynamics simulations [14]. Molecular dynamics simulations can simulate the movements of molecules at the atomic level according to classical mechanical rules. Generally, regional observations such as protein ligand interactions, loop mobility, secondary structure formation can be made in the ns time interval. However, computation times become excessively long in the case of large molecules. Today, this problem is overcome by using GPU processors instead of CPU processors. Simulations in the μ s time interval have been reduced to 10-15 days with this technical infrastructure [15].

In our previous study, homology models of ATCC-17978, Type 1, Type 2, Type 3, and Type 4 CarO proteins were generated, carbapenems were docked to the binding site of CarO proteins, and complexes were simulated by molecular dynamics methods for the analysis of CarO-carbapenem interaction (unpublished data). In

this study, a free energy decomposition study, which is a post-process analysis, was performed following molecular dynamics simulations. In this context, the affinities of Imipenem for 5 different CarO isoforms ATCC-17978, Type 1, Type 2, Type 3, and Type 4, as well as the affinity of the different Carbapenems Biapenem, Ertapenem, Faropenem, and Meropenem to ATCC-17978 were analysed. This study aims to determine the important residues that will regulate the passage of carbapenems through the CarO channel by calculating the contribution of each residue to the binding energy. It is thought that the critical residues determined by this study will lead to mutation studies and also to lead to similar studies related to other CarO isoforms.

Materials and Methods

Free Energy Decomposition

Molecular mechanics-generalized Born surface area (MMGBSA) method was used for free energy decomposition. This method is based on molecular dynamics simulation and is MD trajectory analysis. MD simulation was performed in the explicit water model, but in the MMGBSA method, implicit water was added by deleting the explicit water [16]. The binding energy is generally calculated by subtracting the apo-protein and ligand energies from the total bond energy in the complex (1). MMGBSA calculates the free energy of binding by combining gas phase energy (MM), electrostatic solvation energy (GB), and nonelectrostatic contribution to solvation energy (SA) (2). ΔE_{MM} shows gas-phase interaction energy between protein and ligand; $\Delta G_{GB} + \Delta G_{nonpolar}$ shows the polar and nonpolar components of the desolvation free energy; $T\Delta S$ is the change of conformational entropy on ligand binding [17].

$$\Delta G_{bind} = G_{complex} - G_{protein} - G_{ligand} \quad (1)$$

$$\Delta E_{MM} + \Delta G_{GB} + \Delta G_{nonpolar} - T\Delta S \quad (2)$$

In this study, Imipenem docked to five different types of CarO and five different carbapenems docked to ATCC 17978 CarO were analyzed. Binding energy decomposition was performed on the trajectory files generated using 800 ns of simulation as a post processing MD. These binding energy contributions were calculated by taking a snapshot every 40 ns throughout the simulation using the MMPSA.py application [18]. The decomposition of the total account was calculated using the per-residue scheme. In the calculation, all residues that contributed or did not contribute to the binding energy were taken into account, and then those that did not contribute were eliminated and the results were given graphically.

Results and Discussion

The Energy Contribution per Residue in ATCC 17978-Carbapenem Complexes

In this part of the study, the trajectory of ATCC-17978 CarO-carbapenem complexes as a result of 800 ns simulation was analyzed. The residues that contributed to the binding energy were analyzed by making separately energy decomposition for the 5 types of carbapenems such as Biapenem, Ertapenem, Faropenem, Meropenem, and Imipenem. First of all, the contribution of all residues was carefully examined and only the residues that contributed to the binding energy were determined to simplify the graph. The energy contribution was given in kcal/mol in the drawn graph and residues were indicated on the x-axis (Figure 1).

According to these results, the residues that contributed most to the binding energy in the ATCC 17978-Biapenem complex were listed as Tyr54, Leu98, Lys100, Leu164, Glu185, and Ile189, respectively. Besides, Asp45, which is a negatively charged residue, stands out as the residue that reduces the binding affinity. In the ATCC 17978-Ertapenem complex, Leu47, Asp193, Lys194, Tyr195, Trp197, and Pro199 residues were the residues that contribute most to the binding energies. The most striking among these residues is the positively charged residue Lys194. The residues with the highest contribution to the binding energy in the ATCC 17978-Faropenem complex were listed as Tyr54, Leu98, Leu164, Glu185, Lys188, Ile189, and Lys194, respectively. The residue that contributed most to the binding of Faropenem to CarO was found to be positively charged Lys188 and Lys194, and also the residue that negatively affected the binding energy was expressed as negatively charged residues Lys100 and Asp192. In another complex, ATCC 17978-Meropenem, Arg44, Asp55, Asp59, Asp97, Thr99, Lys196, and Val200 were listed as residues that contributed to the binding energies. These residues usually stand out as positive and negative charged residues. In the last complex, ATCC 17978-Imipenem, it was noted that Tyr54, Val56, Tyr96, Leu98, Glu186, Arg190, Lys196, and Val200 residues contributed the most to the binding energy. These residues were generally hydrophobic and besides Lys100 residue reduced the binding affinity.

Although the residues that contribute to the binding energy vary according to the carbapenem type, the regions where the residues were located and the physical properties of the residues were similar. It was only seen as an Imipenem that differed from the others because the residues it interacted with were mostly hydrophobic. The residue that reduced the binding affinity was generally detected as the negatively charged residue Asp45-46.

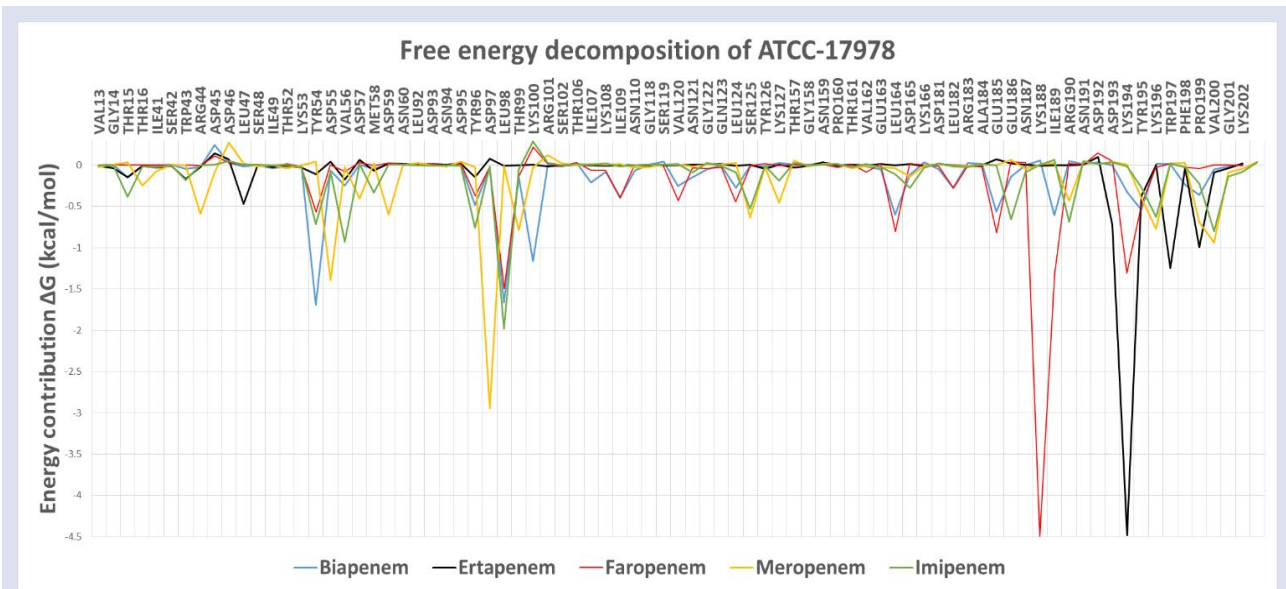


Figure 1. Per-residue free energy decomposition of ATCC 17978-Carbapenem complexes

The Energy Contribution Per Residue in Imipenem-CarO's Complexes

The common residues contributing to the binding energy in ATCC-17978 CarO-carbapenem complexes were determined, then the same properties were analysed in different CarO isoforms. Only Imipenem docked CarO types were used in these analyses because clinically an Imipenem-CarO resistance relationship has been reported [12]. For this reason, residues affecting the binding affinity of Imipenem were determined separately in Type 1, Type 2, type 3, and Type 4 CarO isoforms.

First of all, the energy decomposition in the Type 1-Imipenem complex was listed as Leu98, Lys100, Ser109, Val126, Met130, Leu170, Glu192 and Glu196 respectively (Figure 2). Among these residues, hydrophobic residues Leu98 and Ile196, positively charged Lys100, and negatively charged Glu192 were found to contribute the most. Charged residues Lys191 and Arg197 were residues that reduced the binding affinity of Imipenem to Type 1 CarO.

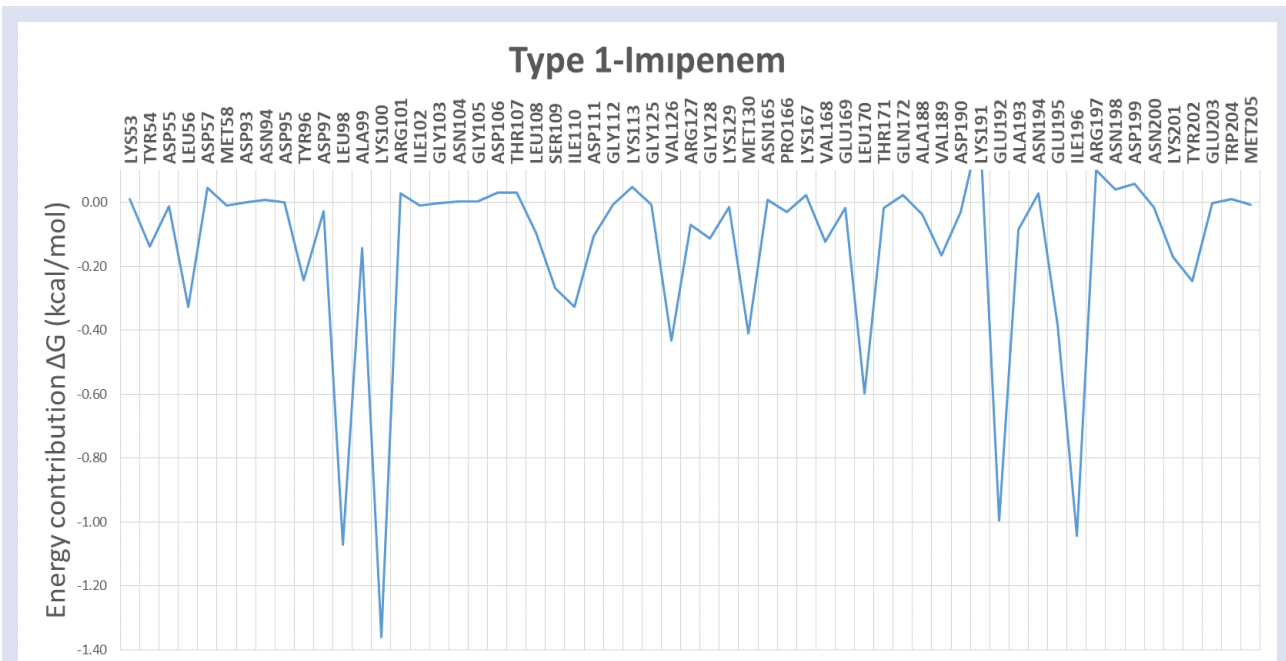


Figure 2. Per-residue free energy decomposition of Type 1-Imipenem

The residues contributing to the binding energy in the Type 2-Imipenem complex were Trp44, Ser45, Tyr55, Met57, Pro205, and Val206, respectively (Figure 3). All of

these residues were uncharged and on the other hand, the charged residues Glu110, and Lys208 negatively affected the binding affinity of Imipenem to Type 2 CarO.

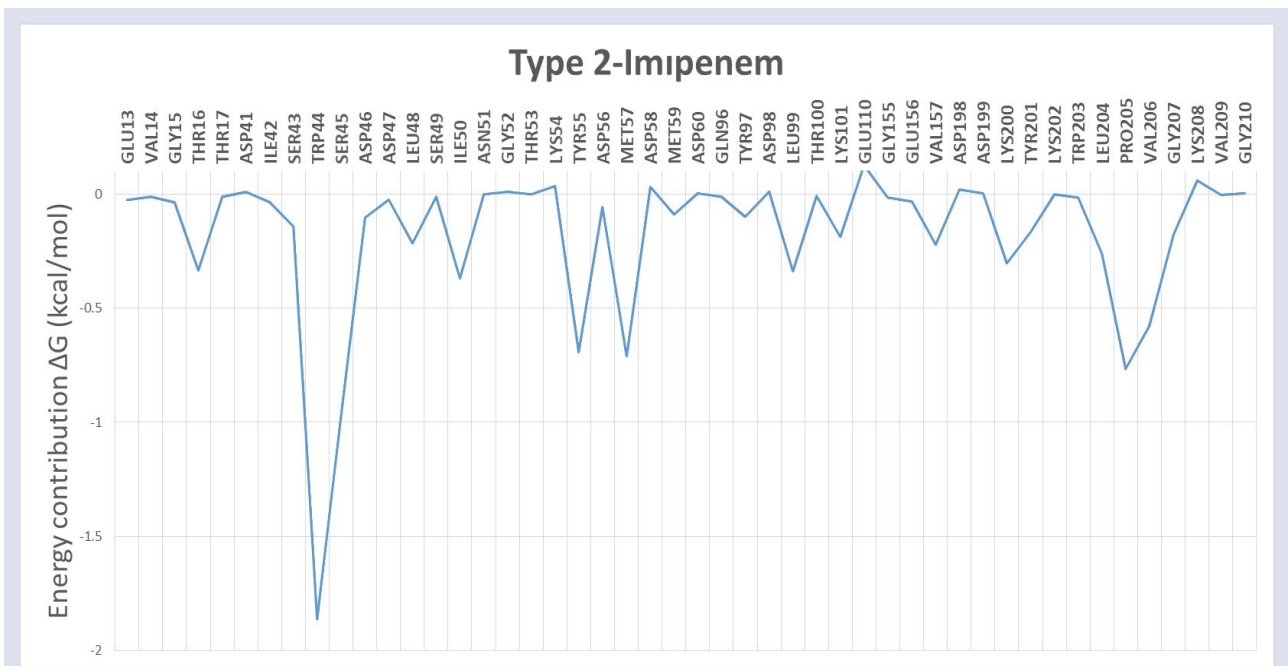


Figure 3. Per-residue free energy decomposition of Type 2-Imipenem

In the Type 3-Imipenem complex, the residues contributing to the binding energy of Imipenem were listed as Val50, Asn51, Ser53, Arg101, Phe109, and Arg110

(Figure 4). Similar to Type 1 and Type 2, the charged residues that reduce the binding affinity of Imipenem were Asp46, Glu190, and Lys193.

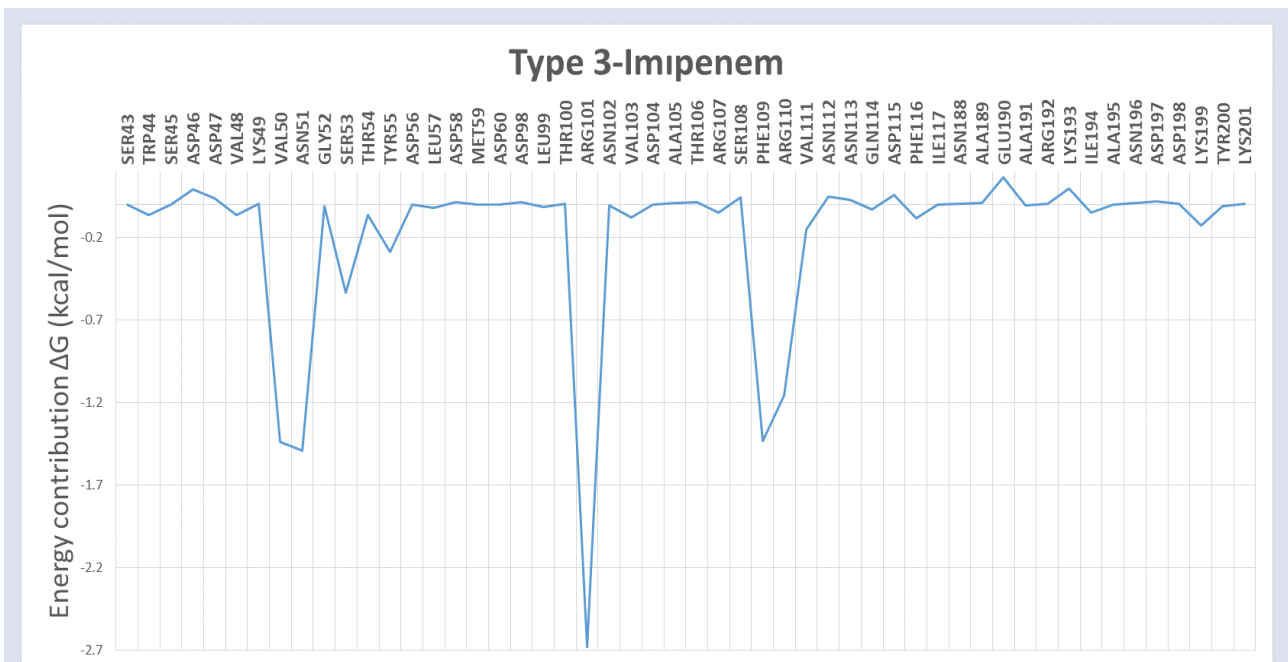


Figure 4. Per-residue free energy decomposition of Type 3-Imipenem

The residues contributing to the binding energy of Imipenem in the Type 4-Imipenem complex were listed as Trp44, Ile50, Tyr55, Lys101, Ile190, Lys195, and Tyr196, respectively (Figure 5). Except for the Lysine residue, the

residues were hydrophobic and the charged residues Lys54, Glu186, and Asp193 were residues that weakened the binding affinity of Imipenem to Type 4 CarO

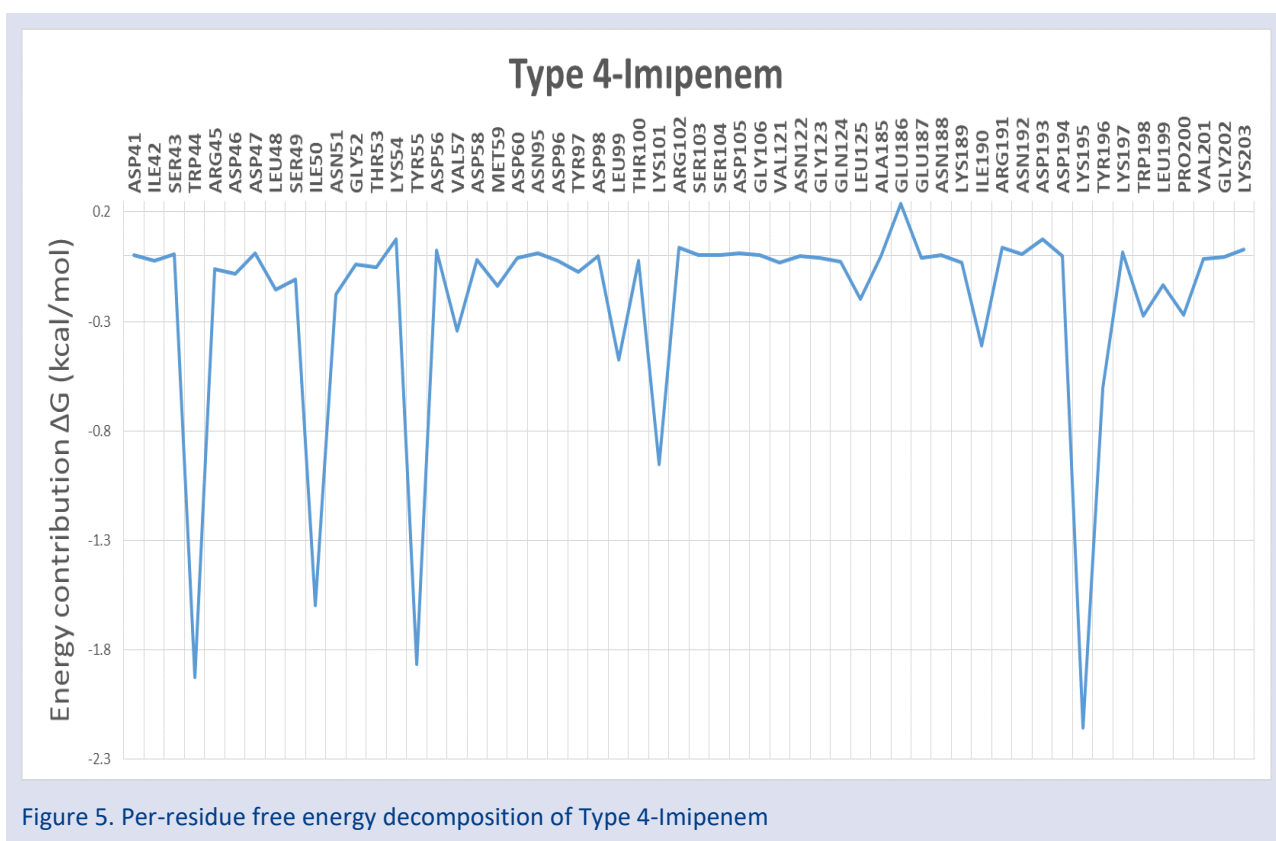


Figure 5. Per-residue free energy decomposition of Type 4-Imipenem

Conclusion

In this study, 9 different energy decompositions were performed and these were given comparatively for themselves. The residues contributing to the binding energy of carbapenems in the ATCC-17978 CarO outer membrane protein were evaluated in general. Theoretically, in order for a compound to be taken into the periplasmic space after binding to the outer membrane protein, it should not contain very tight and continuous bonds [10]. For this reason, the physical properties of the residues expressed in this study and their contribution to the binding energies were critical. To simplify the comparison, the residues that contribute to the binding energy in each complex and their physical properties are given in Table 1. As can be seen from this table, almost all of the residues were negatively or positively charged and hydrophobic residues. On the other hand, all of the residues that reduced the binding affinity were found to be negatively or positively charged residues.

When we look at Table 1 in conclusion, it appears to be different residues as the protein and carbapenem types change. If the imipenem-bound complexes were evaluated within themselves, it was observed that the meropenem-bound complex had a different interaction motif. Mostly, these residues were different than the others with charged residues. Biapenem and faropenem showed nearly identical interactions, with the most similar partially imipenem-bound complex. It was also observed that Faropenem, Ertapenem, and Meropenem

made strong bonds with ATCC17978 CarO residues. However, Imipenem generally travels in a hydrophobic pocket and, unlike the others, charged residues reduce the binding energy of Imipenem. Faropenem and Ertapenem. Charged residues such as Lys188 in the faropenem complex, Lys194 in the ertapenem complex, and Asp97 in the meropenem complex contributed highly to the affinity of these carbapenems for CarO. However, hydrophobic residues such as Tyr54 in the biapenem complex and Leu98 in the imipenem complex contributed relatively more to their affinity for CarO. The most outstanding residue was the result that Leu98 contributed significantly to the binding energy in all complexes except the Meropenem complex.

As a further comparison, different types of CarO outer membrane protein were compared with each other. In this comparison, Imipenem, which is the Carbapenem-CarO resistance relationship was reported [19], was analysed.

When the residues that contributed to each complex were compared, it was noticed that the Type2 CarO complex was differentiated from the others. The residues that increased the binding affinity were hydrophobic and polar, while those that decreased it were charged residues. In this sense, when all the complexes were examined, it was observed that the residues that increased the binding energy were generally Lysine and Arginine residues. The result in the graphics is residues Lys100, which contributes highly to the binding affinity in Type1 CarO. While Trp44 and Ser45 were in Type 2, Arg101 in Type 3 stood out, and finally, it was expressed as Lys195 in Type 4.

Table 1 The energy contribution of residues in the complex. (Common residues were shown as an underlined and R indicates "Reducing affinity")

Complexes	Hydrophobic	Charged	Polar and uncharged
ATCC17978-Biopenem	<u>Tyr54, Leu98, Leu164, and Ile189</u>	<u>Lys100, Glu185</u> and <u>Asp45(R)</u>	
ATCC17978-Ertapenem	Leu47, Tyr195 and Trp197	Asp193, <u>Lys194</u> , Asp45(R)	Pro199
ATCC17978-Faropenem	<u>Tyr54, Leu98, Leu164 and Ile189</u>	<u>Glu185</u> , Lys188, <u>Lys194</u> , <u>Lys100(R)</u> and Asp192(R)	
ATCC17978-Meropenem	<u>Val200</u>	Arg44, Asp46(R) Asp55, Asp59, Asp97, Arg101(R) and <u>Lys196</u>	Thr99
ATCC17978-Imipenem	<u>Tyr54</u> , Val56, Tyr96, <u>Leu98</u> , and <u>Val200</u>	<u>Lys100(R)</u> , Glu186, Arg190 and <u>Lys196</u>	
Type 1-Imipenem	Leu98, Val126, Met130 and Leu170	Glu192, Glu196, and Arg197, Lys100, Lys191(R) and Arg197(R)	Ser109
Type 2-Imipenem	Trp44, Tyr55, Met57 and Val206	Glu110(R), and Lys208(R)	Ser45 and Pro205
Type 3-Imipenem	Val50 and Phe109	Asn51, Arg101, Arg110 Asp46(R), Glu190(R) and Lys193(R)	Ser53
Type 4-Imipenem	Trp44, Ile50, Tyr55, Ile190 and Tyr196	Lys101, Lys195, Lys54(R), Glu186(R), and Asp193(R)	

The literature says the extracellular glove-shaped extensions do not have a specific binding motif and it consist of cationic channel [10]. When all the results are evaluated together, in order for antibiotics or other molecules to be taken up by the outer membrane proteins, they must first bind to this channel and then move towards the channel and be taken into the periplasmic space. For this reason, strong and fixed bonds either completely stop this progress or slow it down. When the samples in this study were compared, it was concluded that Imipenem was most likely to pass through the channel and that other carbapenem may or may not pass more difficult. In the comparison between CarO isoforms, it was observed that the more charged residues in the protein, the tighter and more stable bonds were formed. Among these types, it was concluded that the most likely ATCC-17978 CarO outer membrane protein Imipenem would get into the periplasmic space. In addition, it was predicted that the residues expressed in this study would be a source for mutagenesis studies. Moreover, it was thought that it would lead to studies related to different carbapenems or different types of CarO proteins.

Acknowledgment

The numerical calculations reported in this paper were fully/partially performed at TUBITAK ULAKBIM, High Performance and Grid Computing Centre (TRUBA resources).

The authors received no specific grant from any funding agency.

Conflicts of interest

The authors declare that they have no conflicts of interest.

References

- [1] Eliopoulos G. M., Maragakis L. L., Perl T. M., Acinetobacter baumannii: epidemiology, antimicrobial resistance, and treatment options, *Clinical Infectious Diseases*, 46 (2008) 1254-1263.
- [2] Chen L.K., Kuo S.C., Chang K.C., Cheng C.C., Yu P.Y., Chang C.H., Clinical antibiotic-resistant Acinetobacter baumannii strains with higher susceptibility to environmental phages than antibiotic-sensitive strains, *Scientific Reports*, 7 (2017) 1-10.
- [3] Lee C.-R., Lee J. H., Park M., Park K. S., Bae I. K., Kim Y. B. *et al*, Biology of Acinetobacter baumannii: pathogenesis, antibiotic resistance mechanisms, and prospective treatment options, *Frontiers in Cellular and Infection Microbiology*, 7 (2017) 55.
- [4] Kyriakidis I., Vasileiou E., Pana Z. D., Tragiannidis A., Acinetobacter baumannii Antibiotic Resistance Mechanisms, *Pathogens*, 10 (2021) 373.
- [5] Kamischke C., Fan J., Bergeron J., Kulasekara H. D., Dalebroux Z. D., Burrell A. *et al*, The Acinetobacter baumannii Mla system and glycerophospholipid transport to the outer membrane, *Elife*, 8 (2019) e40171.

- [6] Hua M., Liu J., Du P., Liu X., Li M., Wang H., The novel outer membrane protein from OprD/Occ family is associated with hypervirulence of carbapenem resistant *Acinetobacter baumannii* ST2/KL22, *Virulence*, 12 (2021) 1-11.
- [7] Nie D., Hu Y., Chen Z., Li M., Hou Z., Luo X., Outer membrane protein A (OmpA) as a potential therapeutic target for *Acinetobacter baumannii* infection, *Journal of Biomedical Science*, 27 (2020) 1-8.
- [8] Vila-Farrés X., Ferrer-Navarro M., Callarisa A. E., Martí S., Espinal P., Gupta S., Loss of LPS is involved in the virulence and resistance to colistin of colistin-resistant *Acinetobacter nosocomialis* mutants selected in vitro, *Journal of Antimicrobial Chemotherapy*, 70 (2015) 2981-2986.
- [9] Zahn M., D'agostino T., Eren E., Baslé A., Ceccarelli M., Van Den Berg B., Small-molecule transport by CarO, an abundant eight-stranded β -barrel outer membrane protein from *Acinetobacter baumannii*, *Journal of Molecular Biology*, 427 (2015) 2329-2339.
- [10] Siroy A., Molle V., Lemaître-Guillier C., Vallenet D., Pestel-Caron M., Cozzone A. J., Channel formation by CarO, the carbapenem resistance-associated outer membrane protein of *Acinetobacter baumannii*, *Antimicrobial Agents and Chemotherapy*, 49 (2005) 4876-4883.
- [11] Uppalapati S. R., Sett A., Pathania R., The outer membrane proteins OmpA, CarO, and OprD of *Acinetobacter baumannii* confer a two-pronged defense in facilitating its success as a potent human pathogen, *Frontiers in Microbiology*, 11 (2020).
- [12] Zhu L. J., Chen X. Y., Hou P. F., Mutation of CarO participates in drug resistance in imipenem-resistant *Acinetobacter baumannii*, *Journal of Clinical Laboratory Analysis*, 33 (2019) e22976.
- [13] Baxevanis A. D., Bader G. D., Wishart D. S., *Bioinformatics*. John Wiley & Sons, (2020).
- [14] Morris G. M., Huey R., Olson A. J., Using autodock for ligand-receptor docking, *Current Protocols in Bioinformatics*, 24 (2008) 8.14. 11-18.14. 40.
- [15] Gotz A. W., Williamson M. J., Xu D., Poole D., Le Grand S., Walker R. C., Routine microsecond molecular dynamics simulations with AMBER on GPUs. 1. Generalized born, *Journal of Chemical Theory and Computation*, 8 (2012) 1542-1555.
- [16] Genheden S., Ryde U., The MM/PBSA and MM/GBSA methods to estimate ligand-binding affinities, *Expert Opinion on Drug Discovery*, 10 (2015) 449-461.
- [17] Ylilauri M., Pentikäinen O. T., MMGBSA as a tool to understand the binding affinities of filamin-peptide interactions, *Journal of Chemical Information and Modeling*, 53 (2013) 2626-2633.
- [18] Miller III B. R., McGee Jr T. D., Swails J. M., Homeyer N., Gohlke H., Roitberg A. E., MMPBSA. py: an efficient program for end-state free energy calculations, *Journal of Chemical Theory and Computation*, 8 (2012) 3314-3321.
- [19] Catel-Ferreira M., Coadou G., Molle V., Mugnier P., Nordmann P., Siroy A. *et al*, Structure-function relationships of CarO, the carbapenem resistance-associated outer membrane protein of *Acinetobacter baumannii*, *Journal of Antimicrobial Chemotherapy*, 66 (2011) 2053-2056.

Characterization of Nanoparticles Containing *Achillea Phrygia* and Their Antioxidant and Antiproliferative Properties

Murat Doğan^{1,a,*}, Duygu Taşkın^{2,b}, Mizgin Ermanoğlu^{3,c}, Turan Arabacı^{4,d}

¹ Department of Pharmaceutical Biotechnology, Faculty of Pharmacy, Sivas Cumhuriyet University, Sivas/Turkey

² Department of Analytical Chemistry, Faculty of Pharmacy, University of Health Science, Istanbul, Turkey

³ Department of Pharmacognosy, Faculty of Pharmacy, Marmara University, Istanbul, Turkey

⁴ Department of Pharmaceutical Botany, Faculty of Pharmacy, Inonu University, Malatya, Turkey

*Corresponding author

Research Article

History

Received: 12/01/2022

Accepted: 14/03/2022

Copyright



©2022 Faculty of Science,
Sivas Cumhuriyet University

ABSTRACT

In this study, antioxidant and antiproliferative properties of "*Achillea phrygia*" were investigated. Since the antioxidant and antiproliferative activity of B sub-extract from plant's chloroform extract is higher than other extracts, B sub-extract of *Achillea phrygia* was used in the preparation of nanoparticles. Characterization of nanoparticles was made, antiproliferative activities and IC₅₀ values of nanoparticles and only chloroform extract was calculated by cell culture studies and XTT cell viability test. According to the results, it was observed that the extract-loaded chitosan nanoparticles had a strong antiproliferative activity in both MCF 7 and HT29 cells. The results of this study support that bioactive extract of the *Achillea phrygia* plant can be prepared as an herbal medicine candidate by preparing formulations with biopolymers and being investigated in cancer studies.

Keywords: Cytotoxic activity, Antioxidant activity, Nanoparticle, Bioactive material, MCF 7 cell line.

^a mdogan@cumhuriyet.edu.tr
^c mizginerm@hotmail.com

^{ib} <https://orcid.org/0000-0003-2794-0177>
^{id} <https://orcid.org/0000-0003-3146-1988>

^b duygu.taskin@sbu.edu.tr
^d turan.arabaci@inonu.edu.tr

^{id} <https://orcid.org/0000-0002-5279-0900>
^{id} <https://orcid.org/0000-0003-3869-4557>

Introduction

Developing effective drug and treatment strategies has excellent importance in maintaining the human healthy. Therefore, significant scientific studies and financial support are used to discover and design new effective substances and treatment methods. In addition, due to the serious side effects of traditional treatment strategies and synthetic chemotherapeutics, it is widely accepted that natural herbal active substances are the leading and key sources for patient prosperity [1]. Angiogenesis plays significant role in the mechanism of many diseases. Therefore, scientists mind to use natural and medicinal herbal extracts to modulate angiogenesis [2].

Bioactive materials have drawn attention for their pharmacological effects, which can be of great interest in treating cancer. Bioactive medicinal plants with anticancer potential not only ensure nutritional benefits, but also prevent the progression of cancer through various mechanisms of action in the human body [3]. Various bioactive substances of plant, animal and microbial sources show recognizable anticancer potential with various mechanisms of action such as antimetastatic, antioxidant, etc. Bioactive extracts have a high efficacy potential in the treatment of cancer, and they can be alternative treatments for the treatment of various carcinogenesis [4]. Natural compounds are very important as interesting repositories of biologically active compounds. Historically, natural products for anticancer studies have led to significant success. More than 60% of the clinical use of antitumor drugs consists of natural

products, including marine organisms, plants, and bacteria, while more than 3000 plant species are used to fight neoplasms [5, 6]. Scientific study results provide new hopes for the joint use of natural compounds and chemotherapeutics in tumor treatment [7]. In the light of the evidence obtained from the studies, it is aimed to characterize the interactions and efficacy of natural compounds and classical chemotherapy drug combinations against various types of cancer. The promising results can be shown as a new hope for the combined use of natural compounds and chemotherapeutics in cancer treatment [8, 9].

Significant developments were performed to the cancer treatments. However, undesirable effect of cancer proceeds to rise and is becoming one of the most destructive diseases. Therefore, studies to prevent cancer have become an important way in which the fight against cancer can be possible [10]. To cite a few examples, curcumin, the active ingredient in turmeric, can prevent cancer formation, suppress proliferation, and induce apoptosis in tumor cells. Curcumin shows its anticancer activities via using multiple constituents such as transcription factors, antiapoptotic proteins, protein kinases, and cell cycle proteins [11]. Some studies have been conducted on the ability of the *Achillea sp.*, which we used in this study, to show anticancer activity in various types of cancer. However, the studies and the results obtained are not sufficient to elucidate these activities. Many medicinal plant extracts with determined biological activities are widely used in the treatment of

various diseases [12, 13]. Extracts and essential oils, which are thought to be effective in these extracts, are obtained as a result of various extraction and distillation processes. These active substances are used for various purposes such as cancer, cardiovascular diseases, central nervous system diseases, digestive system diseases [13]. In addition to the benefits of biological active substances obtained from plants, there are also various undesirable effects. At the beginning of these effects are the lack of targeted therapy, dosing problem and toxic effects on healthy tissues and cells [14]. Nanoparticle drug delivery systems are used to prevent or correct the undesirable effects of bioactive medicinal plant extracts. Targeting bioactive components used in the treatment of diseases, having the desired drug release profile, reducing the toxic effects of drugs, and preventing multi-drug resistance are the most important advantages of these systems [15, 16, 17]. Biocompatible polymers are widely used in the preparation of nanoparticulate systems. The most important advantages of chitosan are that it does not show toxic properties, is biocompatible, and has high encapsulation efficiency [18, 19]. In this study, chitosan nanoparticles containing *A. phrygia* extract were prepared. In addition, characterization studies of nanoparticles were performed, and their anticancer activities were evaluated by cell culture studies.

Materials and Methods

Plant Material and Extraction Procedures

Prof. Dr Turan Arabacı determined the *A. phrygia* specimens acquired during field experiments. For future reference, a voucher specimen (T.Arabacı 2962) was deposited in the herbarium of Inonu University, Faculty of Pharmacy, Department of Pharmaceutical Botany. The plant's aerial parts were dried in the shade (at 25 °C) and ground into a fine powder in a mechanic grinder. The maceration procedure was used to extract the powdered samples with organic solvents (methanol and chloroform) until they were colourless. Under reduced pressure, the organic phase was evaporated to dryness. For future analysis, all extracts were kept at 4°C. On the MCF-7 cell line, the cytotoxic activities of chloroform (IC₅₀ = 0.041 mg/mL) and methanol (IC₅₀ = 127.65 mg/mL) extracts were tested, and chloroform extract was found to be more potent than methanol extract. Column chromatography was used in this investigation to separate the probable active chemicals found in the effective chloroform extract based on their polarity. The chloroform sub-extract (5 g) was inserted to a silica gel column and eluted with toluene, petroleum ether and methanol mixture of increasing polarity of petroleum ether (100%, 1500 mL), petroleum ether /chloroform (75:25, 1500 mL), petroleum ether /chloroform (1:1, 1500 mL), chloroform (100%, 1500 mL), chloroform/methanol (75:25, 1500 mL), chloroform/ methanol (1:1, 1500 mL), chloroform/methanol (25:75, 1500 mL), and methanol (100%, 1000 mL) to obtain eight (A-H) fractions.

Cell Culture

Dulbecco's modified Eagle's medium (DMEM), and fetal bovine serum (FBS) were obtained from Merck Millipore (United States). Penicillin-Streptomycin-L-glutamine solution was purchased from Sigma-Aldrich (Germany). Chitosan (400 kDa, DD 87) and tripolyphosphate (TPP) were purchased from Fluka (Germany). Colorectal adenocarcinoma cells (HT29) and breast cancer cells (MCF 7) were used in this study. XTT reagent was purchased Roche Diagnostic. Cells were seeded in DMEM including FBS (10 %), penicillin (100 IU/mL), streptomycin (10 mg/mL).

Cytotoxicity Assay

Cytotoxic activity of *A. phrygia* extracts was evaluated using the XTT assay against the MCF7 and HT29 cells. Cells were seeded in 96-well plates with DMEM (100 µL) and incubated overnight. *A. phrygia* extracts were dissolved in DMSO for using cytotoxicity assay. Extracts suspended in DMEM were added to each well (40 µg/mL) and same amount of DMSO was inserted to the control group. The cells were incubated for 24 h. Following each well were washed with PBS, XTT (50 µL) mixture and colorless DMEM (100 µL) were inserted to wells and the cells were incubated for 4 h. Micro plate ELISA reader was used to measure absorbance of XTT-formazan at 450 nm. Antiproliferative activity of extracts were calculated compared to control. According to the assessment of XTT results, nanoparticle which indicate the greatest antiproliferative activity against MCF 7 and HT29 cancer cells, were synthesised. XTT assays of nanoparticles with extract and only extract were repeated to calculate the IC₅₀ values.

Antioxidant Assays

DPPH assay

The extracts' DPPH free radical scavenging abilities were assessed using an experimental technique reported in the literature [20]. In a nutshell, 240 microliters of DPPH solution (0.1 mM) were mixed with 10 microliters of compounds made at various doses (0.5-5 mg/mL). After that, the mixture was allowed to rest for 30 minutes at room temperature. Using a microplate reader (AMR-100) at 517 nm, the absorbance of the combination was compared to the reference. The experiment was done three times and the IC₅₀ values (mg/mL) are used to express the results.

FRAP assay

The FRAP technique was used to assess the effectiveness of compounds (0.5-5 mg/mL) to reduce ferric. After mixing 190 µL of FRAP reagent with 10 µL of compound for 4 minutes, the absorbance of the combination was measured against a reference using a microplate reader (AMR-100) set to 593 nm. FeSO₄.7H₂O was used to create the standard curve and the compounds FRAP values were expressed as a mM Fe²⁺/mg extract.

CUPRAC assay

In CUPRAC method, 60 microliters of copper (II) solution, neocuproin solution, and ammonium acetate buffer (1 M) were mixed in this experiment. Shake the solution after adding 10 μL of ethanol and 60 μL of compound. For 60 minutes, the solutions were maintained at room temperature with their mouths closed. Absorbance values at 450 nm were measured at the conclusion of this period against a reference solution that did not include a sample [21, 22]. The CUPRAC findings were expressed as mMTE/mg extract.

Preparation of Chitosan Nanoparticles

Nanoparticles containing *A. phrygia* were prepared using the ionic gelation method. In order to determine the features and differences of nanoparticles, nanoparticles with and without extract were prepared. Initially, a certain amount of chitosan was dissolved in acetic acid (0.5 %) at 1000 rpm under magnetic stirring. Tripolyphosphate solution (0.5% w/v) containing the extract dropped into chitosan solution (0.5% w/v). Nanoparticle solutions were centrifuged at 10,000 rpm for 30 minutes. The supernatant was removed and the pellet was washed with bidistilled water. This process was performed three times. After lyophilization, nanoparticles were stored at +4 $^{\circ}\text{C}$.

Measurement of Particle Size And Zeta (Z) Potential

The size and ζ potential measurements were evaluated via a Zetasizer Nano ZS instrument.

Statistical Analysis

All experiments were performed in triplicate. All data from the study were given as the mean \pm SD and analysed using Graphpad Prism 5. Statistical differences between the study groups were analysed using a two-way analysis of variance (ANOVA) followed by Tukey's multiple comparison test. Mean values were considered statistically significant if $p < 0.05$.

Results and Discussion

Characterization of Chitosan Nanoparticles

Properties of nanoparticles such as particle size and ζ potential are very important in terms of biological activity studies. Therefore, these features should be at desired values. Particles were investigated for this purpose. Results of nanoparticles containing extract and pure nanoparticles were shown in Table 1. According to the results, size of nanoparticle (228.34 ± 1.9 nm) including *A. phrygia* extract had higher size than pure nanoparticle (207.56 ± 2.6 nm). In addition, polydispersity index (PDI) values of chitosan nanoparticle with extract (0.187 ± 0.05) were smaller than pure nanoparticle (0.21 ± 0.03). ζ potential of extract loaded nanoparticle and non-extract nanoparticle were 8.2 ± 0.06 mV and 7.6 ± 0.03 mV respectively. According to the results size homogeneity and zeta potential values of both nanoparticles (pure and extract loaded) are suitable for use.

Table 1. Particle size, ζ potential, and PDI index values of nanoparticles

Samples	ζ potential (mV) \pm SD	Size (nm) \pm SD	PDI \pm SD
*CNPCE	8.2 ± 0.06	228.34 ± 1.9	0.187 ± 0.05
**CNPE	7.6 ± 0.03	207.26 ± 2.6	0.211 ± 0.03

*CNPCE shows extract containing chitosan nanoparticle,

**CNPE shows pure chitosan nanoparticles.

Results of Antiproliferative Activity

Cancer is called an incurable disease because of late diagnosis of the disease and poor awareness of the disease. In addition to the existence of various treatment mechanisms for cancer treatment, there are also many undesirable effects of these treatments. Using the knowledge and experience gained in these treatments, characterization studies of active substances of biological origin and investigation of their activities in cancer treatment constitute very important fields of study [4, 6]. Antiproliferative effect of *A. phrygia* extracts were investigated on HT29 and MCF7 cell lines. Cytotoxic activity results of extracts were indicated in Figure 1 and Figure 2. On Figure 1 results, it was shown that cell viability ranged from 58.27 ± 0.26 % to 79.10 ± 0.34 % in HT29 cells. The results show that the extracts have significant antiproliferative effects on cancer cells. Especially, B extract decreased the proliferation of HT29 cells about half. According to the result it can be concluded that the extracts of *A. phrygia* have significant cytotoxic activity on HT29 cells.

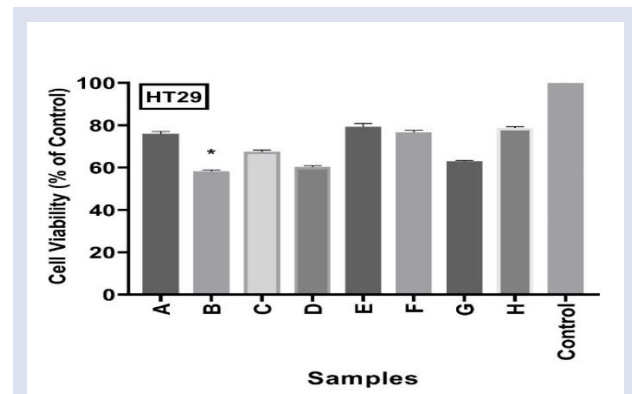


Figure 1. Cytotoxic activities of sub-chloroform extracts of *A. phrygia* on HT29 cell line. *B extract showed the most antiproliferative activity on HT29 cells.

Figure 2 results showed that cell viability ranged from 56.67 ± 0.32 % to 87.92 ± 0.47 % in MCF 7 cells. It can be said that these extracts have a significant cytotoxic effect on MCF 7 cancer cells, since the cell viability is below 70 % in MCF 7 cells to which A, B, D and G extracts were treated. B extract of *A. phrygia* showed the highest anticancer activity, significantly reducing the viability of cancer cells in both MCF 7 (56.67 ± 0.32 %) and HT29 (58.27 ± 0.26 %) cell lines. In the light of these results, nanoparticles of the B extract were prepared and applied to MCF 7 and HT29 cancer cells and their IC_{50} values were calculated.

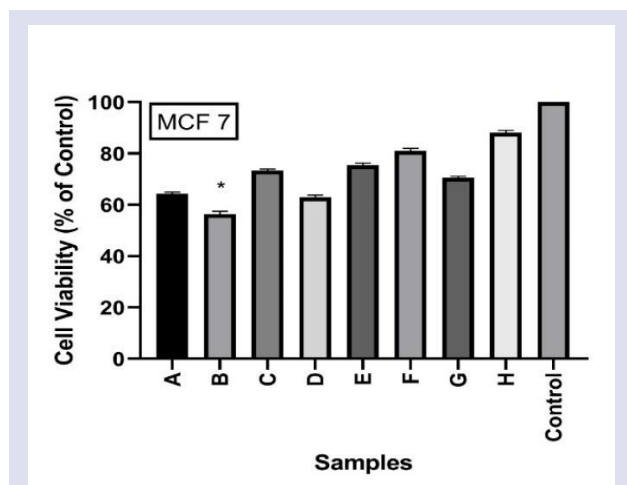


Figure 2. Cytotoxic activities of sub-chloroform extract of *A. phrygia* on MCF 7 cell line. *B extract showed the most antiproliferative activity on MCF7 cells.

IC₅₀ values were calculated by applying B extract and nanoparticle containing B extract to HT29 cells at certain concentrations and performing XTT test. Figure 3 results indicated that both the nanoparticle with B extract and only B extract showed significant antiproliferative activity on HT29 cells associated with an increase in concentration. When the B extract and the nanoparticle containing the extract were treated with HT29 cells at a concentration 100 µg/ml, cell viability was observed as 46.87±0.43 % and 45.90±0.23 % respectively. On only B extract, the viability of the HT29 cells was between 46.8±0.43 % and 71.96±0.34 %. In addition, cell viability of nanoparticle with B extract, ranged from 45.90±0.23 % to 65.48±0.37 %. IC₅₀ values of nanoparticle with B extract and only B extract were 58.28 µg/mL and 66.32 µg/mL respectively. This result shows that our samples formed by coating B extract with nanoparticles significantly reduced HT29 cancer cell proliferation and increased the cytotoxic effect compared to the extract alone. In addition, nanoparticle loaded with B extract had higher cytotoxic activity on HT29 cell line than only B extract.

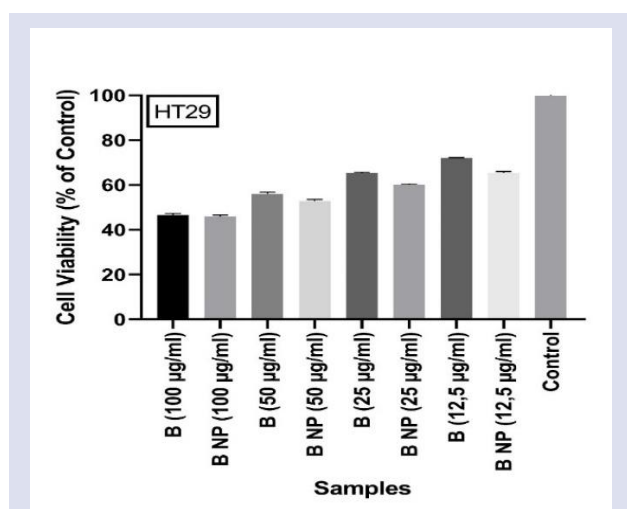


Figure 3. Concentration-related antiproliferative activities of B extract and nanoparticles containing B extract. B NP indicates nanoparticle include B extract.

XTT assay results showed that B extract and B extract loaded nanoparticles had stronger antiproliferative effect. Cell viability of B extract was between 35.29±0.18 % and 54.70±0.26 %. Cell viability of B extract loaded nanoparticle was between 29.47±0.32 % and 51.27±0.18 % depending on the concentration. Taking advantage of these valuable results it can be said that *A. phrygia* extracts have significant cytotoxic and antiproliferative effects on HT29 and MCF 7 cell lines. Especially, D extract loaded with nanoparticle showed the highest antiproliferative effect on both cell lines.

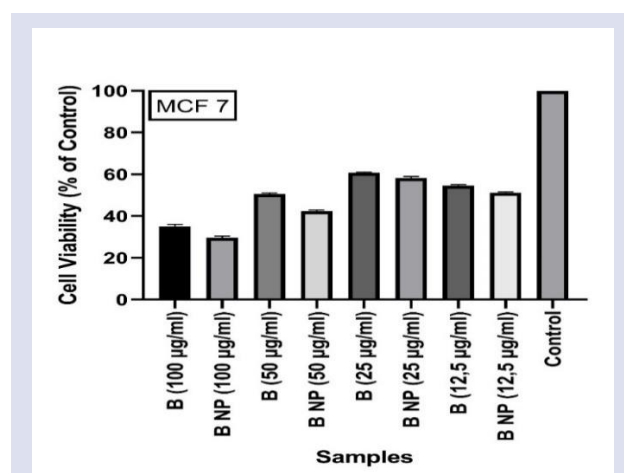


Figure 4. Concentration-related antiproliferative activities of B extract and nanoparticles containing B extract. B NP indicates nanoparticle include B extract.

Results of Antioxidant Activity

Antioxidant activities of 8 different sub-extracts obtained from the plant were evaluated using DPPH, CUPRAC and FRAP methods (Table 2). For DPPH activity, the extracts had IC₅₀ values ranging from 0.399 to 1.399 mg/mL. The findings showed that the B extract (IC₅₀:0.399 mg/mL) had higher DPPH radical scavenging activity compared to the other extracts. In addition, in this study, it was determined that the radical scavenging activity of all extracts showed lower radical scavenging activity than the ascorbic acid (IC₅₀:0.0028 mg/mL). When the FRAP values obtained as a result of this study were compared among themselves, it was determined that the B extract (40.984 mM FeSO₄/mg extract) of plant showed stronger iron (III) ion reduction potential compared to the other extracts. In addition, it was determined that all extracts had lower FRAP values than the BHT compound (86.004 mMFeSO₄/mg). The extracts have CUPRAC values ranging from 0.422 mM to 2.149 mM. The D (2.149 mMTE/mg extract) and B (1.713 mMTE/mg extract) extracts obtained from the plant have higher the potential to reduce Cu(II) to Cu(I) compared to other extracts. In this study, all extracts were found to have a lower CUPRAC value than the ascorbic acid compound (3.213 mMTE/mg). As a result, the findings obtained from the study showed that the B extract had the strongest antioxidant activity potential compared to the other extracts.

Table 2. Antioxidant activities of 8 different sub-extracts obtained from the plant

<i>A. phrygia</i> Chloroform sub-extract	DPPH (IC ₅₀ : mg/mL)	FRAP (mMFeSO ₄ /mg extract)	CUPRAC (mMTE/mg extract)
A	1.399±0.929	36.307±0.698	0.422±0.008
B	0.399±0.091	40.984±0.201	1.713±0.065
C	0.573±0.094	38.694±1.007	1.681±0.078
D	0.621±0.017	32.501±0.550	2.149±0.108
E	0.861±0.123	36.372±0.806	1.609±0.088
F	0.565±0.095	32.050±0.349	1.351±0.065
G	1.189±0.335	29.018±0.403	0.779±0.025
H	0.650±0.123	28.050±0.201	0.682±0.003
Ascorbic acid	0.0028±0.0004	-	3.213±0.076
BHT	-	86.004± 4.914	-

Conclusions

In this study, antioxidant and antiproliferative properties of sub-chloroform extracts from *Achillea phrygia* were investigated. It was determined that the B extract obtained from the plant had strong antioxidant and antiproliferative effects compared to other extracts. Nanoparticles with B extract, which has the highest antiproliferative activity in HT29 and MCF 7 cancer cells, were prepared by cell culture studies. Appropriate formulations were determined by performing particle size, zeta potential and polydispersity index tests of nanoparticles, and the anticancer activities of these formulations were evaluated with the XTT test. According to the results, it was observed that nanoparticles containing B extract showed significantly higher antiproliferative activity compared to only B extract.

Acknowledgement

The authors would like to thank the CUTFAM Research Center, Sivas Cumhuriyet University, School of Medicine, Sivas, Turkey, for providing the necessary facilities to conduct this study and Scientific and Technological Research Council of Turkey (TÜBİTAK) for the financial support of this research (Project No: 116S509) and Serkan Köstekci for help during the field studies.

Conflict of Interest

The authors declare that they have no conflict of interest.

References

- Demirci B., Tabanca N., Wedge D.E., Khan S.I., Khan I.A., Aytac Z., Baser K.H.C., Chemical Composition and Biological Activities of Four *Achillea* Essential Oils from Turkey, *Planta Medica*, 75(4) (2009) 420-421.
- Azaz A. D., Arabaci T., Sangun M. K., Essential Oil Composition and Antimicrobial Activities of *Achillea biserrata* M. Bieb. and *Achillea salicifolia* Besser subsp *salicifolia* Collected in Turkey, *Asian Journal of Chemistry*, 21(4) (2009) 3193-3198.
- Chin Y., Chin W., Balunas M.J., Chai H.B., Kinghorn A.D. Drug discovery from natural sources, *AAPS J.*, 8 (2006) E239–E253.
- DeSantis C.E., Lin C.C., Mariotto A.B., Siegel R.L., Stein K.D., Kramer J.L., Cancer treatment and survivorship statistics, *CA Cancer J. Clin.*, 64 (2014) 252–271.
- Martinho N., Damgé C., Reis C.P., Recent advances in drug delivery systems, *J. Biomater Nanobiotechnol.*, 2 (2011) 510-526.
- Rodrigues T., Reker D., Schneider P., Schneider G. Counting on natural products for drug design, *Nat. Chem.*, 8 (2016) 531-541.
- Alfatemi S.M.H., Rad J.S., Rad M.S., Mohsenzadeh S., Teixeira da Silva J.A., Chemical composition, antioxidant activity and in vitro antibacterial activity of *Achillea wilhelmsii* C. Koch essential oil on methicillin-susceptible and methicillin-resistant *Staphylococcus aureus* spp., *Biotech.*, 5(1) (2015) 39-44.
- Akcin A., Akcin T.A., Seyis F., Coban A.Y., Durupinar B. Antimicrobial and Antioxidant Activity of the Essential Oil of the Turkish Endemic Species *Achillea phrygia* Boiss. & Bal., *Journal of Essential Oil Bearing Plants*, 17(2) (2014) 219-227.
- Ghani A., Azizi M., Hassanzadeh-Khayyat M., Pahlavanpour A.A., Essential oil composition of *Achillea eriophora*, *A. nobilis*, *A. biebersteinii* and *A. wilhelmsii* from Iran, *J. Essent. Oil Bear, Plants*, 11 (5) (2008) 460–467.
- Ghasemi Y., Khalaj A., Mohagheghzadeh A., Khosarav A., Composition and in vitro antimicrobial activity of the essential oil of *Achillea eriophora*, *Chem. Nat. Comp.*, 44 (5) (2008) 663–665.
- Kesdek M., Kordali S., Usanmaz A., Ercisli S., The toxicity of essential oils of some plant species against adults of colorado potato beetle, *Leptinotarsa decemlineata* Say (Coleoptera: Chrysomelidae), *Comptes Rendus De L., Academie Bulgare Des Sciences*, 68(1) (2015) 127-136.
- Kocak A., Bagci E., & Bakoglu A. Chemical Composition of Essential Oils of *Achillea teretifolia* Willd. and *A. millefolium* L. subsp *millefolium* Growing in Turkey, *Asian Journal of Chemistry*, 22(5) (2010) 3653-3658.
- Toncer O., Basbag S., Karaman S., Diraz E., Basbag M., Chemical Composition of the Essential Oils of some *Achillea* Species Growing Wild in Turkey, *International Journal of Agriculture and Biology*, 12(4) (2010) 527-530.
- Turkmenoglu F.P., Agar O.T., Akaydin G., Hayran M., Demirci B., Characterization of volatile compounds of eleven *Achillea* species from Turkey and biological activities of essential oil and methanol extract of *A. hamzaoglu* Arabaci et Budak, *Molecules*, 20 (2015) 11432-11458.

- [15] Calvo P., Remunan-Lopez C., Vila-Jato J.L., Alonso M.J., Novel hydrophilic chitosan-polyethylene oxide nanoparticles as protein carriers, *J. Appl. Polym. Sci.*, 63 (1997) 125-32.
- [16] Sun Y., Wan A., Preparation of nanoparticles composed of chitosan and its derivatives as delivery systems for macromolecules, *J. Appl. Polym. Sci.*, 105 (2007) 552–61.
- [17] Song C., Yu H., Zhang M., Yang Y., Zhang G., Physicochemical properties and antioxidant activity of chitosan from the blowfly *Chrysomya megacephala* larvae, *Int. J. Biol. Macromol.*, 60 (2013) 347–354.
- [18] Csaba N., Koping Hoggard M., Alonso M. J., Ionically cross-linked chitosan/ tripolyphosphate nanoparticles for oligonucleotide and plasmid DNA delivery, *Int. J. Pharmaceutics*, 382 (2009) 05- 14.
- [19] Wolf N.B., Kuchler S., Radowski M.R., Blaschke T., Kramer K.D., Weindi G., Influences of opioids and nanoparticles on in vitro wound healing models, *European Journal of Pharmaceutics and Biopharmaceutics*, 73 (2009) 34-42.
- [20] Wei F., Jinglou C., Yaling C., Yongfang L., Liming C., Lei P., Zhou D., Liang X., Ruan J., Antioxidant, free radical scavenging, antiinflammatory and hepatoprotective potential of the extract from *Parathelypteris nipponica* (Franch. et Sav.) Ching, *J. Ethnopharmacol.*, 130 (2010) 521–528.
- [21] Apak R., Güclü K., Ozyurek M., Karademir S.E., Novel total antioxidant capacity index for dietary polyphenols and vitamins C and E, using their cupric ion reducing capability in the presence of neocuproine: CUPRAC Method, *J. Agric. Food Chem.*, 52 (2004) 7970–81.
- [22] Benzie I.F., Strain J.J., The ferric reducing ability of plasma (FRAP) as a measure of "antioxidant power": the FRAP assay, *Anal. Biochem.*, 239 (1996) 70–6.

In Vitro Inhibition Effects of 2-Amino Thiazole Derivatives on Lactoperoxidase Enzyme Activity

İşil Nihan Korkmaz^{1,a,*}

¹ Department of Chemistry, Faculty of Science, Atatürk University, Erzurum, Turkey.

*Corresponding author

Research Article

History

Received: 01/11/2021

Accepted: 25/01/2022

Copyright



©2022 Faculty of Science,
Sivas Cumhuriyet University

^a isil.krkmz@gmail.com

^{id} <https://orcid.org/0000-0003-4896-5226>

ABSTRACT

Lactoperoxidase (LPO E.C. 1.11.1.7) is a member of the peroxidase family and is an important glycoprotein containing heme group in its structure and showing the antimicrobial effect on disease causing microorganisms in the digestive system of newborn babies. Thiazoles are the simplest members of heterocyclic compounds containing nitrogen and sulfur atoms in their structure. Many active pharmaceutical substances such as vitamin B1, penicillin, and those obtained by synthesis, contain a thiazole ring. It is desirable to evaluate the biological activities of thiazole derivatives, such as antiprotozoal antibacterial, antifungal, antituberculosis, and anthelmintic, with emphasis on their potential medical applications. The aim of this study was to determine the in vitro inhibition profiles of 2-amino thiazole derivatives against bovine LPO enzyme. In this study it was determined that all amino thiazole derivatives inhibited the LPO enzyme competitively. When the results were compared with each other, the 2-Amino-4-(4-chlorophenyl) thiazole compound showed the best inhibition effect against LPO with the K_i value of 250 ± 100 nM.

Keywords: Lactoperoxidase, Amino thiazole, Pharmaceutical, Inhibition.

Introduction

Peroxidases (POD: E.C.1.11.1.7), is a member of the oxidoreductase enzyme family, which has the potential to be used in many fields; one of the most common enzymes in all cell types [1]. Peroxidases is found in many sources, including bacteria, yeast, and higher plants, fungi, milk, and dairy products. Hydrogen peroxide (H_2O_2), which is formed during biotransformation in biological systems and has oxidizing properties, must be removed from the environment. This task in ensuring the removal of H_2O_2 from the environment in metabolism; It performs enzymes such as catalase and peroxidase, which are enzymes that show antioxidant properties in cells [2].

Lactoperoxidase (LPO); found in milk, saliva, tears, and the digestive system of newborns. It is a glycoprotein consisting of a single polypeptide chain containing the heme group (protoheme 9) as a prosthetic group [3]. This enzyme, which is found in large amounts in milk and dairy products, has a very important position in the prevention of pathogens in the gastro tract of infants during the lactation process. In other words, the lactoperoxidase system functions as a natural defense mechanism against invading microorganisms [4]. Thiazoles, one of the most important representatives of the quintuple natural ring system carrying sulfur and nitrogen. They are functional groups that are frequently encountered in the structure of drug molecules. It is an important component of the pharmacophores of many molecules of medical importance. The fact that the thiazole ring system is in the structure of compounds with important physiological

effects such as penicillin and vitamin B1 and its similarities with other heterocyclic ring systems and the role of the ring in different pharmacological activities have increased the studies on ring structure and derivatives [5,6].

For the thiazole ring system, antimicrobial [7,8], antiviral [9], antiprotozoal [10], anticancer [11], antioxidant [12], anticonvulsant [13], antidiabetic [14], antihypertensive [15], anticholinesterase [16, 17], analgesic and anti-inflammatory [18] activities have been reported.

In this study, the inhibition effects of 2-amino thiazole derivatives on the LPO enzyme activity were determined. The IC_{50} , K_i values and the inhibition type of 2-amino thiazole derivatives were found.

Materials and Methods

Chemicals and Experimental Procedure

LPO enzyme was isolated by procuring bovine milk from local dairy farms in Erzurum. 2,2'-Azino-bis(3-ethylbenzthiazoline-6-sulfonic acid) (ABTS) used for activity studies, hydrogen peroxide and 2-Amino-4-(2,4-difluorophenyl) thiazole [a], 2-Amino-4-(4-bromophenyl) thiazole [b], 2-Amino-5-(methyl)-4-phenyl thiazole [c], 2-Amino-4-(5,6,7,8-tetrahydro-2-naphthyl)thiazole [d], 2-Amino-4-(4-chlorophenyl)thiazole [e], 4-(3,4-difluorophenyl)-1,3-thiazol-2-amino [f] compounds were commercially available from Sigma-Aldrich.

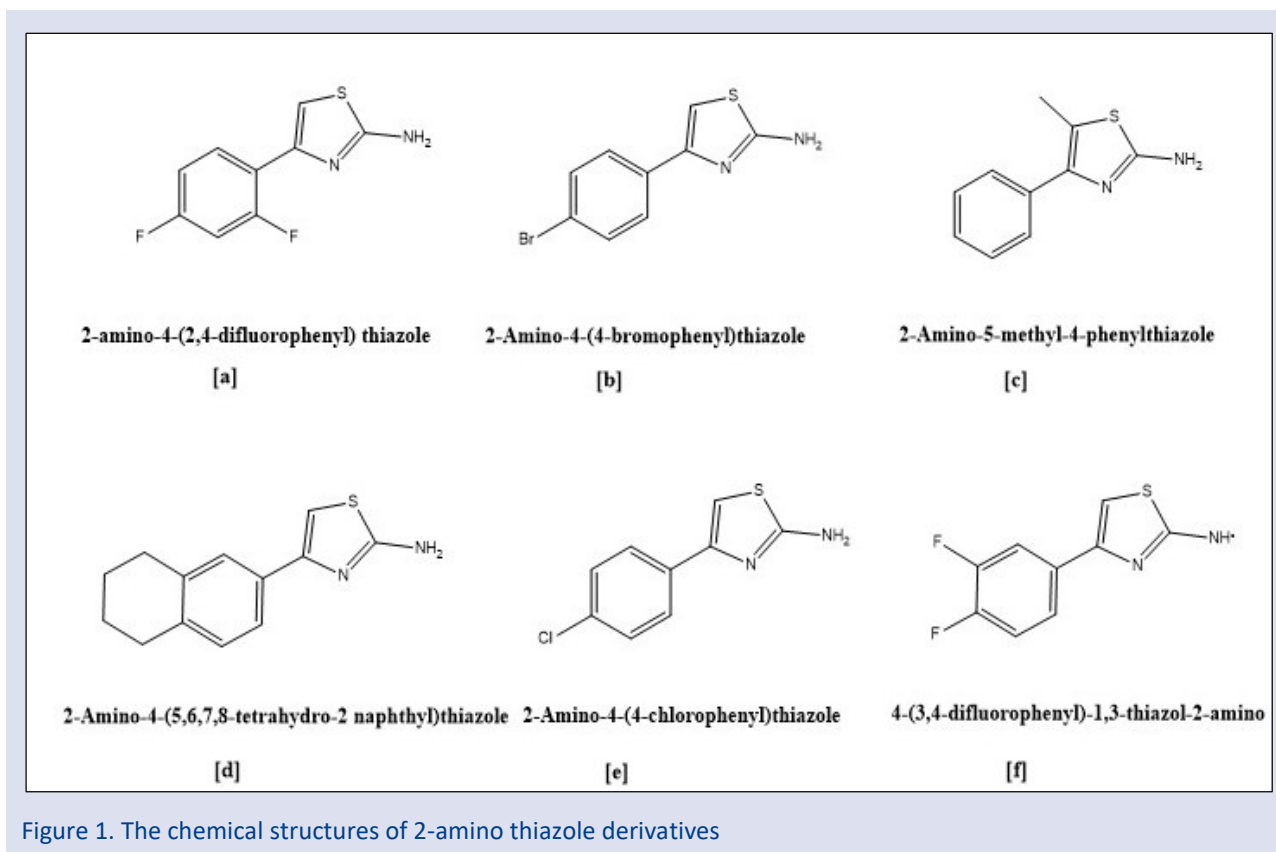


Figure 1. The chemical structures of 2-amino thiazole derivatives

Measurement of LPO Activity

LPO activity was determined by making minor modifications to the procedure performed by Shindler and Bardsley. According to previous study, 2.895 mL of ABTS (1.0 mM) in KH_2PO_4 (100 mM, pH 6.0) was mixed with 0.1 mL of 3.2 mM H_2O_2 with 0.005 mL of enzyme. It is determined according to the increase in absorbance at 412 nm of the compound formed as a result of oxidation of the ABTS molecule, which is the substrate that provides the formation of pigment or colorant [19,20]. An enzyme unit (E.Ü.); It is defined as the amount of enzyme that catalyzes the oxidation of 1 μmol ABTS at 298 K° in 1 minute (ϵ : 32.600 M⁻¹ cm⁻¹) [21].

Purification of LPO

As reported in our previous study, the LPO enzyme was isolated from Sepharose 4B-L-tyrosine-sulfanilamide column. The prepared affinity column was equilibrated with the 10 mM, pH 6.8 Na_2HPO_4 solution. The homogenate was then packed onto the column and the column was washed with Na_2HPO_4 400 mL, 25 mM, pH 6.8. In the last step, eluents were collected by elution with $\text{NaCl}/\text{Na}_2\text{HPO}_4$ solution (1 M/0.25 M, pH:6.8) [22].

The Inhibition Studies of 2-Amino Thiazole Derivatives on LPO

Inhibition of 2-amino thiazole derivatives was determined from the graph of % Activity-inhibitor concentration drawn by working at five different inhibitor concentrations. IC_{50} values were determined for inhibitors with inhibitory effect, and the Lineweaver-Burk plot was drawn from the results with the activity measurements carried out at three different 2-amino thiazole derivatives

and five different ABTS concentrations, and the K_i values and inhibition types of 2-Amino thiazole derivatives were determined [23].

Results and Discussion

The benefits of compounds containing milk and dairy products to human health at every stage of human life are known to date. Milk has many components that protect itself and the newborn from harmful microorganisms. The most important of these components is LPO [21]. LPO is an enzyme found in abundance in milk, which is responsible for forming an antimicrobial compound that catalyzes the reaction of thiocyanate ion and hydrogen peroxide in the living body [24-28]. LPO obtained from many animal sources contributes greatly to the destruction of bacteria by suppressing growth by causing bacterial inhibition [29].

In the literature, it was seen that there is no study to determine the inhibition parameters on LPO in studies involving thiazoles. In the light of this information, the parameters of the effects of amino thiazole derivatives on LPO enzyme activity were determined (Table 1).

Table 1. Inhibition data of 2-Amino thiazole derivatives

Compound	R ²	IC ₅₀ (nM)	K _i (nM)	Inhibition type
[a]	0.9068	340	390±50	Competitive
[b]	0.9968	490	670±60	Competitive
[c]	0.9175	890	480±50	Competitive
[d]	0.9132	470	540±140	Competitive
[e]	0.9035	320	250±100	Competitive
[f]	0.9418	550	600±290	Competitive

2-Amino-4-(2,4-difluorophenyl) thiazole [a], 2-Amino-4-(4-bromophenyl) thiazole [b], 2-Amino-5-(methyl)-4-phenyl) thiazole [c], 2-Amino-4-(5,6,7,8-tetrahydro-2-naphthyl) thiazole [d], 2-Amino-4-(4-chlorophenyl) thiazole [e], 4-(3,4-difluorophenyl)-1,3-thiazol-2-amino

[f] IC₅₀ values were found from the graphs drawn from the activity measurements of the compounds at different dose concentrations (Table 1). These values are (a), (b), (c), (d), (e) and (f); 340, 490, 890, 470, 320 and 550 nM for amino molecules, respectively.

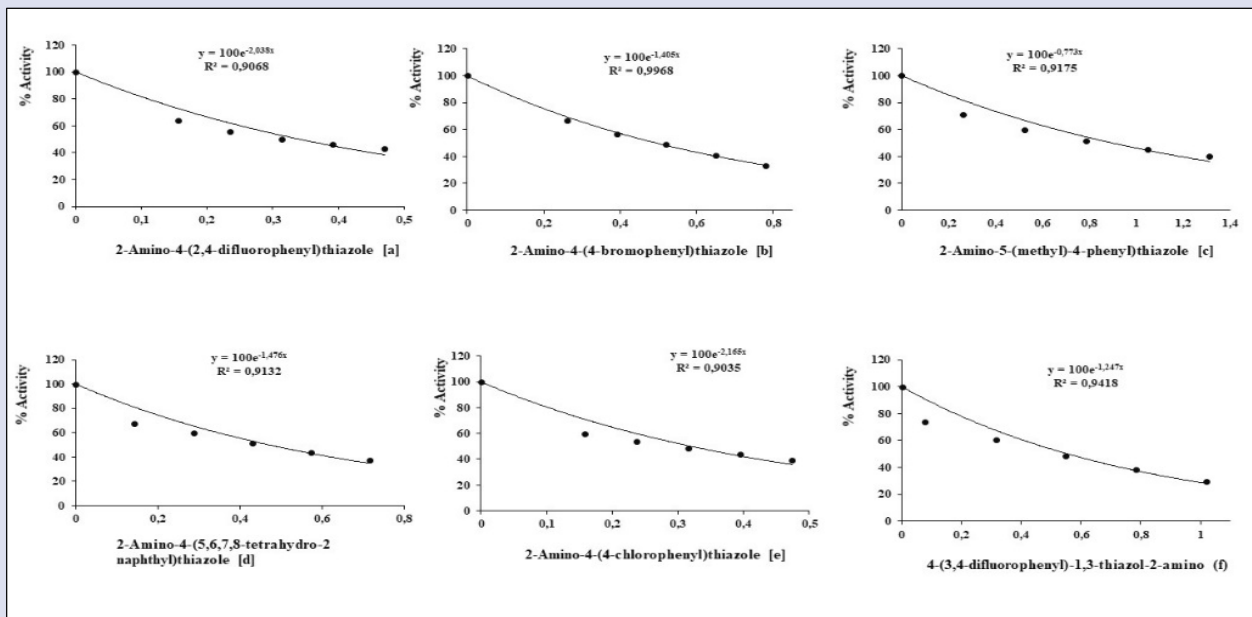


Figure 2. Activity(%)-[Inhibitor] graphs of 2-Amino thiazole derivatives with LPO enzyme

As a result of the activity measurements, the K_i values and inhibition types of 2-amino thiazole derivatives were determined by the Lineweaver-Burk curves (Figure 2). K_i values are (a), (b), (c), (d), (e) and (f); 390±50, 670±60,

480±0.05, 540±140, 250±100 and 600±290 nM for amino molecules, respectively. It was determined from the graphs that the inhibition types were competitive for all studied thiazole compounds.

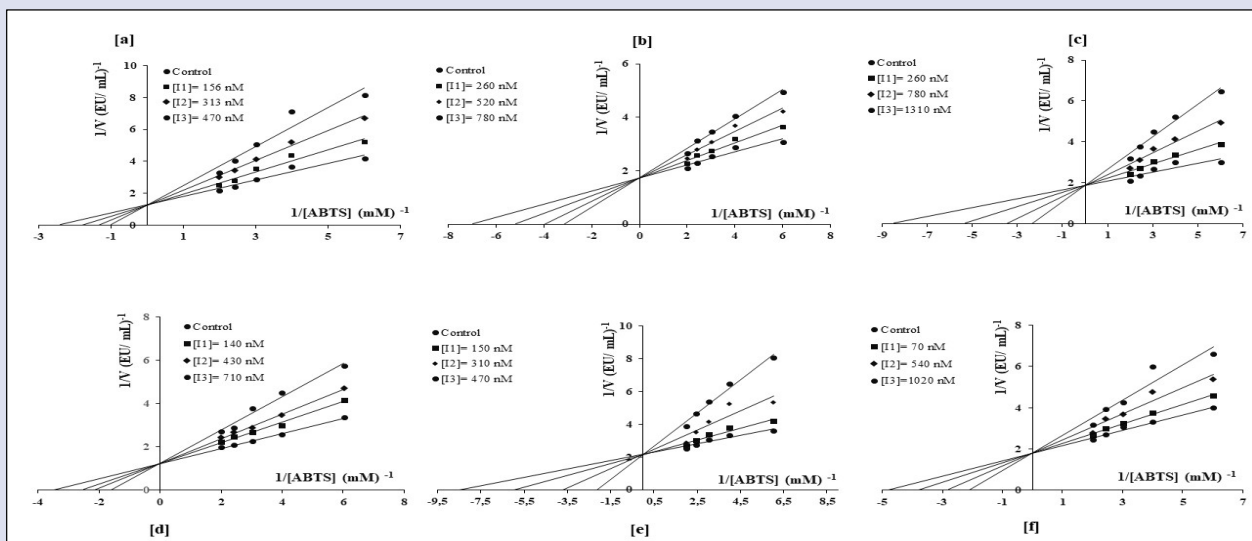


Figure 3. Graphs of 1/V and 1/[S] for 2-amino thiazole derivatives of LPO enzyme ([a]: 2-Amino-4-(2,4-difluorophenyl) thiazole; [b]: 2-Amino-4-(4-) bromophenyl) thiazole [c]: 2-Amino-5-(methyl)-4-phenyl) thiazole; [d]: 2-Amino-4-(5,6,7,8-tetrahydro-2-naphthyl) thiazole; [e]: 2-Amino-4-(4-chlorophenyl) thiazole; [f]: Lineweaver-Burk plots for 4-(3,4-difluorophenyl)-1,3-thiazol-2-amino)

In a study by Wang et al., the α -glucosidase inhibitory activities of several coumarin thiazole derivatives were evaluated. When the results were compared with

acarbose used as a standard inhibitor, it was determined that coumarin thiazole compounds exhibited potent inhibitory activities at the micromolar level [30].

The effect of pyrazolyl-thiazole compounds on the inhibition of aldose reductase and α -glycosidase, which is accepted as a standard approach in the treatment of diabetic complications, was investigated. It was reported from the results that all compounds exhibited an inhibition profile at the micromolar level [31].

LPO, which has the potential to be used in many areas, is abundant in milk and dairy products because it reduces microflora [32,33]. It has an important position in the prevention of bacterial growth and is considered a very important compound in the natural defense mechanism against bacterial infections [29,34].

In another study, secondary sulfonamides containing acetoxycarbazamide, triacetoxycarbazamide, hydroxycarbazamide and trihydroxycarbazamide and containing thiazole, pyrimidine, pyridine, isoxazole and thiadiazole groups were synthesized. In vitro inhibitory effects of these synthesized derivatives against LPO were investigated. The results obtained determined that secondary sulfonamide derivatives are effective LPO inhibitors [35].

Xanthine oxidase (XO) inhibitors are widely used in the treatment of gout. In another study, a series of new tri-substituted 2-(indol-5-yl) thiazole derivatives with an indole skeleton were synthesized and their in vitro inhibitory activities against xanthine oxidase were determined. It has been reported that the 2-(3-cyano-2-isopropylindol-5-yl)-4-methylthiazole-5-carboxylic acid derivative exhibits the strongest XO inhibitory activity at the nm level [36].

The synthesis of sulfonamide-containing thiazole compounds and the inhibitory effects of these derivatives on the activity of human carbonic anhydrase I and II were evaluated by Kılıçbaşlan et al. The inhibitory effects of 12 synthesized sulfonamides on the hydratase and esterase activities of these isoenzymes (hCA-I and hCA-II) were investigated in vitro. They observed that all synthesized compounds inhibited CA isoenzyme activity at μ M level [37].

In a different study, in vitro inhibition parameters of sesamol on bovine lactoperoxidase system were determined.

LPO enzyme was purified 467.51 fold with 75.99% yield in one step by an affinity chromatography technique using sulfanilamide as ligand. It was determined that sesamol strongly inhibited the LPO enzyme at the nM level and showed a competitive inhibition effect [38].

Conclusion

Newborn health needs to determine how and in what way this enzyme will act if chemicals are used in living things. As a result, the inhibitory effects of 2-amino thiazole derivatives on the purified LPO enzyme *in vitro* were investigated in detail. As can be seen here in the study, some 2-amino thiazole derivatives seem to inhibit lactoperoxidase at the micromolar level. The LPO enzyme found in milk and dairy products, which is important for the innate immune system, plays an important role in breaking down bacteria and removing them. A problem in the LPO system triggers the immune system significantly.

Although it is not a desirable situation especially for newborn babies, parents in the lactation process must be careful against the problems caused by inhibitions to keep the immune system of the babies strong.

Conflicts of interest

The authors state that did not have conflict of interests.

References

- [1] Erdem H.U., Kalin R., Özdemir N., Özdemir H., Purification and Biochemical Characterization of Peroxidase Isolated From White Cabbage (*Brassica oleracea* Var. Capitata F. Alba), *International Journal of Food Properties.*, 18 (2015) 2099- 2109.
- [2] Halliwell B., Oxygen radicals: A Commonsense Look at Their Nature and Medical Importance, *Medical Biology*, 62 (1984) 71-77.
- [3] Wolfson LM., Sumner SS., Antibacterial Activity of the Lactoperoxidase System: A Review, *Journal of Food Protection*, 56 (1993) 887-892.
- [4] Reiter B., Review of the Progress of Dairy Science: Antimicrobial Systems in Milk, *Journal of Dairy Research*, 45 (1978) 131-147.
- [5] Mayhoub A.S., Marler L., Kondratyuk T.P., Park E.J., Pezzuto J.M., Cushman M., Optimizing thiadiazole analogues of resveratrol versus three chemopreventive targets, *Bioorg. Med. Chem.*, 20(1) (2012) 510-20.
- [6] Mayhoub A.S., Marler L., Kondratyuk T.P., Park E.J., Pezzuto J.M., Cushman M., Optimization of the aromatase inhibitory activities of pyridylthiazole analogues of resveratrol, *Bioorg. Med. Chem.*, 20(7) (2012) 2427-34.
- [7] Ozadali K., Tan O.U., Yogeewari P., Dharmarajan S., Balkan A., Synthesis and antimycobacterial activities of some new thiazolylhydrazone derivatives, *Bioorganic & Medicinal Chemistry Letters*, 24(7) (2014) 1695-1697.
- [8] Qin Y.J., Wang P.F., Makawana J.A., Wang Z.C., Wang Z.N., Jiang A.Q., Zhu H., Design, synthesis and biological evaluation of metronidazole-thiazole derivatives as antibacterial inhibitors, *Bioorganic & Medicinal Chemistry Letters*, 24(22) (2014) 5279-5283.
- [9] Xu Z., Guo J., Yang Y., Zhang M., Ba M., Li Z., Guo C., 2, 4, 5-Trisubstituted thiazole derivatives as HIV-1 NNRTIs effective on both wild-type and mutant HIV-1 reverse transcriptase: optimization of the substitution of positions 4 and 5, *European Journal of Medicinal Chemistry*, 123 (2014) 309-316.
- [10] Makam P., Thakur P.K., Kannan T., In vitro and in silico antimalarial activity of 2-(2-hydrazinyl) thiazole derivatives, *European Journal of Pharmaceutical Sciences*, 52 (2014) 138-145.
- [11] Popsavin M., Kojić V., Torović L., Svirčev M., Spaić S., Jakimov D., Popsavin V., Synthesis and in vitro antitumour activity of tiazofurin analogues with nitrogen functionalities at the C-2' position, *European Journal of Medicinal Chemistry*, 111 (2016) 114-125.
- [12] Geronikaki A.A., Pitta E.P., Liaras K.S., Thiazoles and thiazolidinones as antioxidants, *Curr. Med. Chem.*, 20, 4460-4480 (2013).
- [13] Mishra C.B., Kumari S., Tiwari M., Thiazole: A promising heterocycle for the development of potent CNS active agents, *European Journal of Medicinal Chemistry*, 92 (2015) 1-34.

- [14] Xu Q., Huang L., Liu J., Ma L., Chen T., Chen J., Chen L., Design, synthesis and biological evaluation of thiazole-and indole-based derivatives for the treatment of type II diabetes, *European Journal of Medicinal Chemistry*, 52 (2012) 70-81.
- [15] Turan-Zitouni G., Chevallet P., Kilic FS., Erol K., Synthesis of some thiazolyl-pyrazoline derivatives and preliminary investigation of their hypotensive activity, *European Journal of Medicinal Chemistry*, 35(6) (2000) 635-641.
- [16] Turan-Zitouni G., Ozdemir A., Kaplancikli Z.A., Altintop M.D., Temel H.E., Akalın Çiftçi G., Synthesis and biological evaluation of some thiazole derivatives as new cholinesterase inhibitors. *Enzyme Inhib. Med. Chem.*, 28(3) (2013) 509-514.
- [17] Rahim F., Javed M.T., Ullah H., Wadood A., Taha M., Ashraf M., Khan K.M., Synthesis, molecular docking, acetylcholinesterase and butyrylcholinesterase inhibitory potential of thiazole analogs as new inhibitors for Alzheimer disease, *Bioorganic Chemistry*, 62 (2015) 106-116.
- [18] El -Achkar G.A., Jouni M., Mrad M.F., Hirz T., El Hachem N., Khalaf A., Habib A., Thiazole derivatives as inhibitors of cyclooxygenases in vitro and in vivo, *European Journal of Pharmacology*, 750 (2015) 66-73.
- [19] Shindler J.S., Bardsley W., Steady-State Kinetics of Lactoperoxidase With ABTS as Chromogens, *Biochemical and Biophysical Research Communications*, 67 (1975) 1307-1312.
- [20] Kalin R., Köksal Z., Bayrak S., Gerni S., Ozyürek I.N., Usanmaz H., Gülçin İ., Molecular docking and inhibition profiles of some antibiotics on lactoperoxidase enzyme purified from bovine milk, *Journal of Biomolecular Structure and Dynamics*, (2020) 1-10.
- [21] Atasever A., Ozdemir H., Gulcin I., Kufrevioglu O.I., One step purification of lactoperoxidase from bovine milk by affinity chromatography, *Food Chemistry*, 136(2) (2013) 864-870.
- [22] Özyürek I.N., Kalın R., Özdemir H., D-Penisilamin, D-Penisilamin disülfid ve N-Asetil-D-penisilamin'in Laktoperoksidaz Enzim Aktivitesi Üzerine İnhibisyon Etkileri, *Journal of the Institute of Science and Technology*, 10(2) (2020) 1146-1153.
- [23] Lineweaver H., Burk D.J., The Determination of Enzyme Dissociation Constants, *Journal of the American Chemical Society*, 56 (1934) 658-66.
- [24] Berg J., Tymoczko J.L., Stryer L., W. H. Freeman and Company ISBN, *Biochemistry*, (2002) 0- 7167-4955-6.
- [25] Berg J.M., Tymoczko J.L., Stryer L., *Biochemistry* 6th ed. New York: W. H. Freeman and Company (2007).
- [26] Hussain S., Slikker J.R., W., Ali S.F., Age-related changes in antioxidant enzymes, superoxide dismutase, catalase, glutathione peroxidase and glutathione in different regions of mouse brain, *International Journal of Developmental Neuroscience*, 13(8) (1995) 811-817
- [27] Sievers G., Structure of milk lactoperoxidase. A study using circular dichroism and difference absorption spectroscopy, *Biochimica et Biophysica Acta*, (1980) 624: 249
- [28] Singh AK., Singh N., Sharma S., Kaur P., Srinivasan A., Singh T.P., Crystal structure of lactoperoxidase at 2.4Å resolution, *J. Mol. Biol.*, 376(1) (2007) 1060- 1075.
- [29] Jacob B.M., Antony K.E., Sreekumar B., Haridas M., Thiocyanate mediated antifungal and antibacterial property of goat milk lactoperoxidase, *Life Sciences*, 66 (25) (2000) 2433-2439.
- [30] Wang G., He D., Li X., Li J., Peng Z., Design, synthesis and biological evaluation of novel coumarin thiazole derivatives as α -glucosidase inhibitors, *Bioorganic Chemistry*, 65 (2016) 167-174.
- [31] Demir Y., Taslimi P., Koçyiğit Ü.M., Akkuş M., Özasan M.S., Duran H.E., Beydemir Ş., Determination of the inhibition profiles of pyrazolyl-thiazole derivatives against aldose reductase and α -glycosidase and molecular docking studies, *Archiv der Pharmazie.*, 353(12) (2020) 2000118.
- [32] Barrett N.E., Grandison A.S., Lewis M.J., Contribution of the lactoperoxidase system to the keeping quality of pasteurized milk, *Journal of Dairy Research.*, 66(1) (1999) 73-80.
- [33] Reiter B., Härnolv G., Lactoperoxidase antibacterial system: natural occurrence, biological functions and practical applications, *Journal of Food Protection*, 47(9) (1984) 724-732.
- [34] Kussendrager K.D., Van Hooijdonk A.C.M., Lactoperoxidase: physico-chemical properties, occurrence, mechanism of action and applications, *British Journal of Nutrition*, 84(S1) (2000) 19-25.
- [35] Köksal Z., Kalin R., Camadan Y., Usanmaz H., Almaz Z., Gülçin İ., Ozdemir H., Secondary sulfonamides as effective lactoperoxidase inhibitors, *Molecules*, 22(6) (2017) 793.
- [36] Song J.U., Choi S.P., Kim T.H., Jung C.K., Lee J.Y., Jung S.H., Kim G.T., Design and synthesis of novel 2-(indol-5-yl) thiazole derivatives as xanthine oxidase inhibitors, *Bioorganic & Medicinal Chemistry Letters*, 25(6) (2015) 1254-1258.
- [37] Kılıçaslan S., Arslan M., Ruya Z., Bilen Ç., Ergün A., Gençer N., Arslan O., Synthesis and evaluation of sulfonamide-bearing thiazole as carbonic anhydrase isoforms hCA I and hCA II, *Journal of Enzyme Inhibition and Medicinal Chemistry*, 31(6) (2016) 1300-1305.
- [38] Kalın R., Laktoperoksidaz Sistemine Karşı Sesamolün İnhibisyon Kinetiği, *Gümüşhane Üniversitesi Sağlık Bilimleri Dergisi*, 9(4), 389-395.

Synthesis and Characterization of Cationic P(AAm-AETAC) Hydrogels, and Their Uses in Adsorption of Titan Yellow

Yasemin Işıkvır ^{1,a,*}, Ali Işıkvır ^{2,b}

¹ Department of Chemistry, Faculty of Science, Sivas Cumhuriyet University, Sivas, Turkey.

² MEB Ulaş ÇPAL, Sivas, Turkey

*Corresponding author

Research Article

History

Received: 24/09/2021

Accepted: 27/01/2022

Copyright



©2022 Faculty of Science,
Sivas Cumhuriyet University

ABSTRACT

In this study, a new cationic P(AAm-AETAC) hydrogels were prepared by a radical addition reaction in aqueous solution with acrylamide and [2-(acryloyloxy)ethyl] trimethylammonium chloride) comonomers in the presence of ethylene glycolmethacrylate. Hydrogels were characterized by spectroscopic, surface, and thermal analysis. The hydrogel does not undergo any structural degradation with the effect of heat up to 250 °C. The adsorption of titan yellow from aqueous solution to the newly prepared cationic hydrogels was evaluated by Freundlich, Langmuir, and Temkin isotherms. The dye adsorption to hydrogels prepared from adsorption isotherms was L type according to the Giles adsorption isotherms. It was determined that the adsorption of titan yellow to the hydrogels prepared from the R_L values calculated for a concentration of 500 mg L⁻¹ titan yellow was favorable. The dye removal efficiency of the hydrogel from the aqueous solution was found to be about 98%. As a result, it can be said that the cationic P(AAm-AETAC) hydrogel, which is prepared at a low cost, can provide a high amount of removal in the adsorption of anionic dyes from aqueous solutions.

Keywords: [2-(acryloyloxy)ethyl] trimethylammonium chloride, Acrylamide, Hydrogel, Titan yellow, Adsorption.

caldiran@cumhuriyet.edu.tr

<https://orcid.org/0000-0001-6481-188X>

isikverali@gmail.com

<https://orcid.org/0000-0003-3871-9435>

Introduction

Water is the most important life component for all living things. Due to the increase in global warming and desertification, the amount of water has become a concern in the world. Population development, rapid industrialization, and inappropriate use of natural water cause serious concerns about the amount and quality of water per capita.

Water pollution is the mixing of unwanted harmful substances in water that can degrade the quality of the water in a measurable amount. Houses, industrial establishments, thermal power plants, fertilizers and chemical pesticides, agricultural industry wastewater, hot water, and substances from nuclear power plants are the main sources of water pollution.

Dyes, which are one of the common water pollutants left by the food, leather, and textile industries, color the water to a great extent even at concentrations as low as 1 ppm. This coloration not only causes an unwanted change in water quality in terms of aesthetic properties but also directly or indirectly affects human and living things' health. Its effects may be in the forms of carcinogenicity, mutagenicity, poisoning, and metabolism in water bodies [1].

Various physical and chemical methods such as flocculation/coagulation, adsorption, and chemical oxidation can be used for the treatment of wastewater. The fact that the removal efficiency varies depending on the type and amount of the pollutant in the wastewater

makes it more difficult to choose the most appropriate method for removal from wastewater.

The adsorption process is one of the most common and effective methods of removing contaminants. Although the most commonly used adsorbent is activated carbon, some easy-to-produce and cheap adsorbents such as zeolite, bentonite, and wood ash are also used for removal. In recent years, studies with composite materials or artificial adsorbents have attracted attention. In particular, cross-linked, networked hydrogels containing functional groups such as amine, hydroxyl, carboxyl, and sulfonyl are used as adsorbents to remove contaminants from aqueous solutions [2,3].

It is an organic triazine azo dye that is widely used in dyeing Titan yellow, nylon, and wool and in some microscopic examinations. El-Azazy et al. studied the removal of Titan yellow with a green adsorbent recycled from Aloe vera leave waste. As a result of their adsorption studies, they found the maximum adsorption capacity of 55.25 mg g⁻¹ with the Langmuir equation [1].

Cheng et al. Prepared a positively charged microporous ceramic membrane and used it for titan yellow removal. The positively charged microporous ceramic membrane exhibited a flow rate of 421 L m⁻² hours at a transmembrane pressure of 0.03 bar. They also stated that between pH 3-8, Titan yellow can be effectively removed with 10 mg L⁻¹ feed concentration [4].

Ghaemi et al. determined the adsorption properties (pH, dye concentration, adsorbent amount, interaction time, ionic

strength, and temperature) of Titan yellow and Congo red from aqueous solution on CoFe_2O_4 magnetic nanoparticles and found the maximum adsorption capacity as 212.8 mg g^{-1} [5].

Dyes, one of the major causes of water pollution, can be anionic, cationic, or amphoteric. There are fewer studies on the removal of anionic dyes than cationic dyes, although they pollute the environment equally.

There are 602738 adsorption studies since 1970 in the Web of Science (WOS) database. 32 of these studies are related to cationic hydrogels and only 11 of them studied dye adsorption. This evaluation on WOS shows the importance of the P(AAm-AETAC) hydrogel prepared in this study for anionic dyes adsorption [6].

In this study, it was aimed that the synthesis and characterization of cationic P(AAm-AETAC) hydrogel with acrylamide and [2-(acryloyloxy) ethyl] trimethylammonium

chloride monomers and its use in the adsorption of titan yellow.

Materials and Methods

Materials

Acrylamide (Merck, Germany) and [2-(acryloyloxy) ethyl] trimethylammonium chloride (Sigma, USA) as monomers, ethylene glycol dimethacrylate (Merck, Germany) as crosslinkers, ammonium persulfate (Merck, Germany) as initiator, N, N, N', N'-tetramethylethylenediamine (Sigma, USA) as accelerator were analytical grade and were used as received. Titan yellow was purchased from Merck (Germany).

The structures of the chemicals used in the study are presented in Table 1.

Table 1. The structures of the chemicals

Chemicals	Representation	Chemical structure
Acrylamide	AAm	
[2-(acryloyloxy) ethyl] trimethylammonium chloride	AETAC	
Ethylene glycol dimethacrylate	EGDMA	
Ammonium persulfate	APS	$(\text{NH}_4)_2\text{S}_2\text{O}_8$
N,N,N',N'-tetramethylethylenediamine	TEMED	
Titan yellow	TY	

Synthesis of Hydrogels

Acrylamide (AAm; 0.8 mol), [2-(acryloyloxy) ethyl] trimethylammonium chloride (AETAC; 0.2 mol) and ethylene glycolmethacrylate (EGDMA; 0.05 mol) were dissolved in water. Then 0.001 mol ammonium persulfate and 0.001 mol N, N, N', N'-tetramethylethylenediamine were added. The mixture was placed into PVC straws. After 24 hours, the hydrogels were removed from the straws, cut into pieces 2-3 mm in length, washed with distilled water, and then dried in air and vacuum. The hydrogels were shown as P(AAm-AETAC) and used in powder form.

Characterization

FTIR/ATR spectra of hydrogels were taken with a Bruker Tensor II model spectrophotometer in the $4000\text{-}400 \text{ cm}^{-1}$ range. SEM images of hydrogels at various magnifications were taken with Tescan-Mira 3 brand Scanning Electron Microscope (SEM). TG thermograms of hydrogels were taken with Shimadzu TG-60 model thermal analyzer. Thermal tests

were performed using a sample mass of 5-10 mg under a nitrogen atmosphere at a scan rate of $10 \text{ }^\circ\text{C min}^{-1}$.

Adsorption Studies

To examine the concentration effect, 0.1 g P(AAm-AETAC) hydrogels were added to 50 mL of titan yellow solutions in the range of $50\text{-}500 \text{ mg L}^{-1}$ and kept in a shaker at $25 \text{ }^\circ\text{C}$ for 24 hours and the equilibrium concentrations were determined. During the adsorption studies, the concentration of titan yellow solutions was recorded at wavelengths of 403 nm, using a Shimadzu A160 model UV-VIS spectrophotometer.

Results and Discussion

Synthesis of Hydrogels

The cationic hydrogels composed of AAm and AETAC were prepared by free radical solution polymerization in the presence of a crosslinker and the possible polymerization mechanism is presented in Figure 1.

In polymerization, the first step is a reaction between APS and TEMED. The activated TEMED molecule can combine with monomers or crosslinker molecules; in the process, the unpaired electron is transferred to the monomeric units so that they, in turn, become reactive. The polymer can continue growing indefinitely, with the active center being continually shifted to the free end of the chain. After 24 h, the hydrogels were cut into pieces of 2–3 mm length, washed with distilled water, and dried.

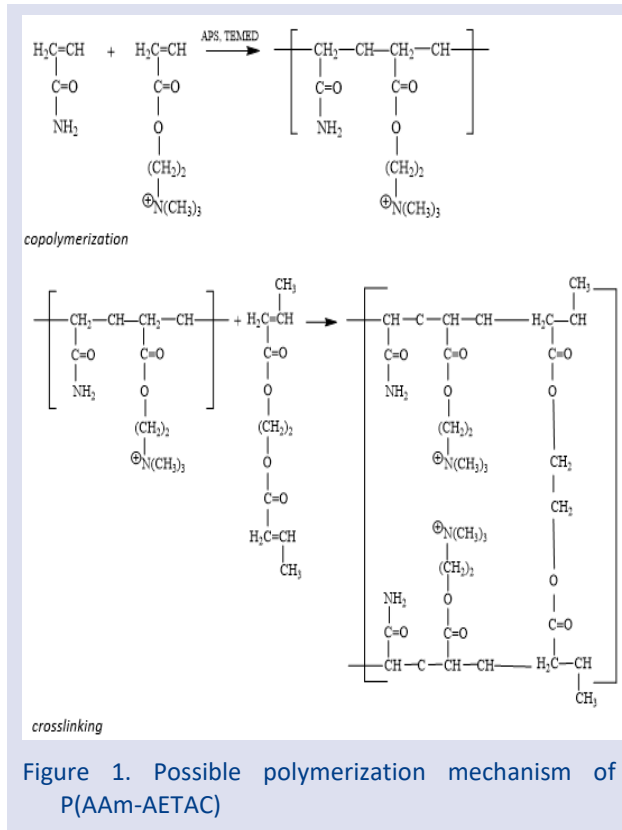


Figure 1. Possible polymerization mechanism of P(AAm-AETAC)

Characterization

FTIR/ATR analysis

ATR spectra of P(AAm-AETAC) hydrogels are presented in Figure 2. The characteristic vibrational bands of the functional groups are as observed: N-H stretch vibration of the amide group at 3200-3600 cm^{-1} , N-H bending vibration in amide structure at 1550 cm^{-1} , C=O stretch vibration in ester structure at 1729 cm^{-1} and $\text{-N}^+(\text{CH}_3)_3$ bending band of the quaternary ammonium pending group at 1476 cm^{-1} . The absence of bands at 900-1000 cm^{-1} , which is evidence of monomeric double bonds, indicates that AAm and AETAC monomers have polymerized successfully [2].

In Figure 2, the presence of new peaks at 1040, 1088, and 1198 cm^{-1} , displacement or variation in peak intensity indicates that the dye molecules are related to the hydrogels [7].

The main interactions between the hydrogel and anionic dye may be electrostatic and hydrophobic.

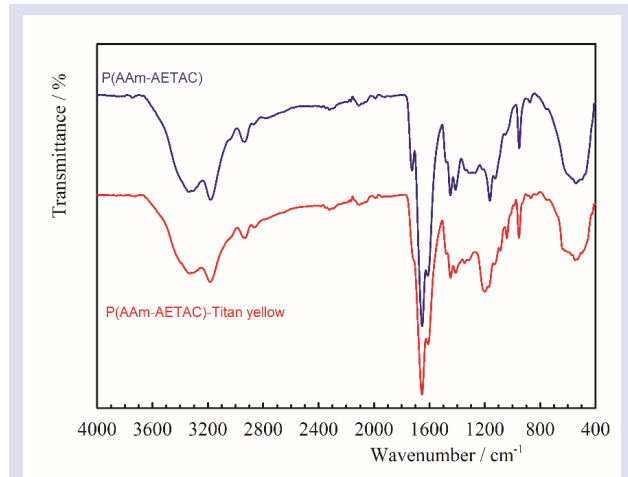


Figure 2. ATR spectra of P(AAm-AETAC) hydrogels.

The possible mechanism of interaction between P(AAm-AETAC) hydrogels and titan yellow is presented in Figure 3.

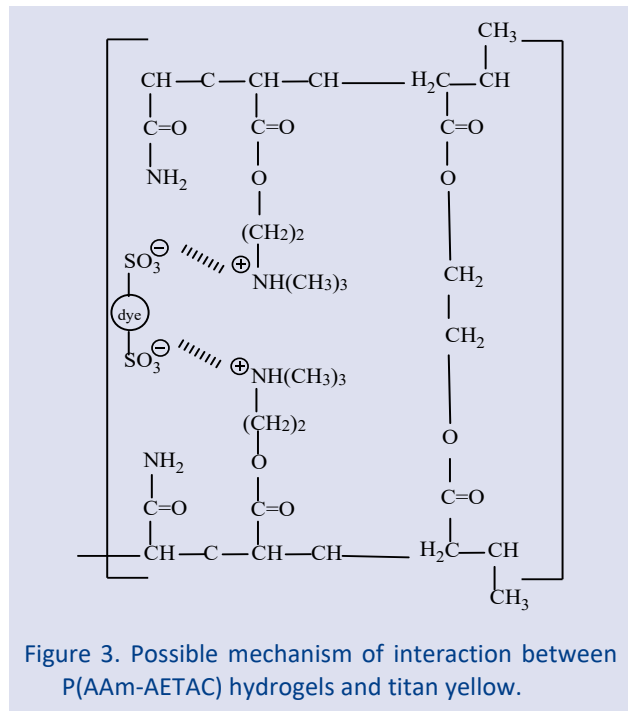


Figure 3. Possible mechanism of interaction between P(AAm-AETAC) hydrogels and titan yellow.

Especially, electrostatic interactions will be expected to occur between -SO_3^- groups on the dye molecules and $\text{-N}^+(\text{CH}_3)_3$ on the monomer unit of the crosslinked polymer.

Hydrophobic effects occur especially in aqueous solution interactions which in the present case will involve aromatic rings on the dye molecules and the methyl groups on the gel. There can be some other interactions such as dipole-dipole and dipole-induced dipole interactions between the dye molecules and the hydrogel chains.

SEM images

SEM images and photographs of the prepared P(AAm-AETAC) hydrogels are presented in Figure 4.

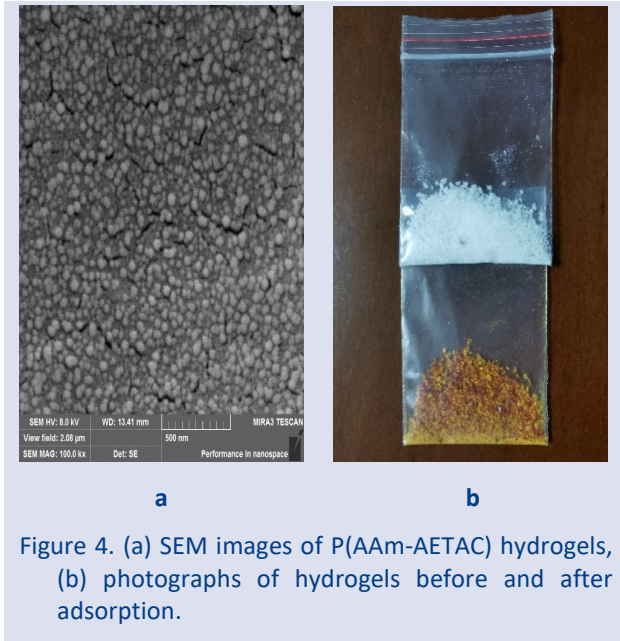


Figure 4. (a) SEM images of P(AAm-AETAC) hydrogels, (b) photographs of hydrogels before and after adsorption.

In the SEM image presented in Figure 4a, it is seen that P(AAm-AETAC) hydrogels have a regular surface structure, there are gaps on the surface of the polymer and these spaces are homogeneous. In the photograph presented in Figure 4b, white-colored P(AAm-AEAC) hydrogels turned brownish-yellow after the dye adsorption.

Thermal analysis

TG and DTA thermograms of P(AAm-AETAC) hydrogels were taken to determine their thermal properties and are presented in Figure 5.

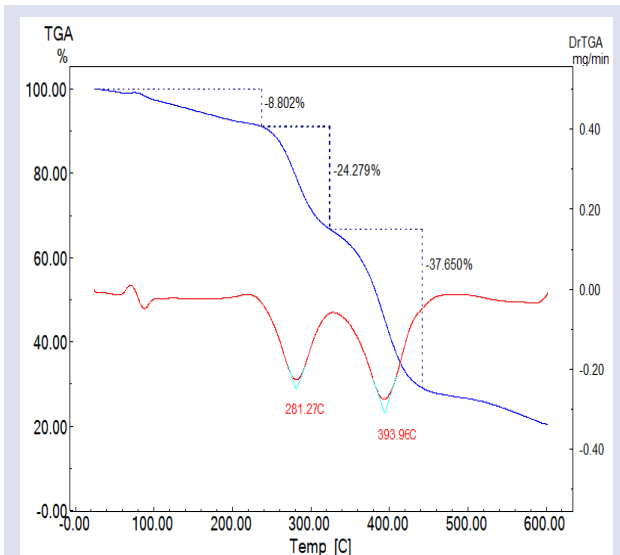


Figure 5. TG thermograms of P(AAm-AETAC) hydrogels.

The initial degradation temperature (T_i), the temperature at the degradation maximum rate (T_m), the degradation final temperature (T_f), the maximum degradation rate (r_m), the residual mass (C_m) at the maximum rate, and the residual mass (C_r) at the end of degradations are given Table 2.

Table 2. Thermogravimetric parameters of P(AAm-AETAC) hydrogels

Degradation region	$T_i/^\circ\text{C}$	$T_m/^\circ\text{C}$	$C_m/\%$	$T_f/^\circ\text{C}$	$r_m/\text{mg min}^{-1}$	$C_r/\%$
1	235	281	79.15	325	0.28	66.36
2	325	393	45.66	440	0.07	28.88

In the TG thermogram of P(AAm-AETAC) given in Figure 5, three different regions are seen such as evaporation of moisture, separation of side groups attached to the main chain due to intramolecular and intermolecular reactions of side groups, and main chain scission. The first stage (25–235°C, 8.802% mass loss) was attributed to the evaporation of moisture from the adsorbed and bound water. The second step (235–325°C, 24.279% mass loss) was attributed to the thermal decomposition of methyl in quaternary ammonium groups as well as the imine reaction of the amide group. The third stage of mass loss occurred at the following intervals. 325–440 °C for P(AAm-AETAC) with approximately 37.65% mass loss from thermal decomposition of the copolymer backbone [8, 9]. It is seen that 50 % of the hydrogels degrade at 387 °C (the half-life temperature, T_h). In addition, 19.71% of P(AAm-AETAC) was found as residue at 600 °C.

Adsorption Studies

In an adsorption system at equilibrium, the total titan yellow concentration (C , mg L^{-1}) can be given as:

$$C = C_b + C_e \quad (1)$$

$$Q = \frac{C_b \cdot V}{m} \quad (2)$$

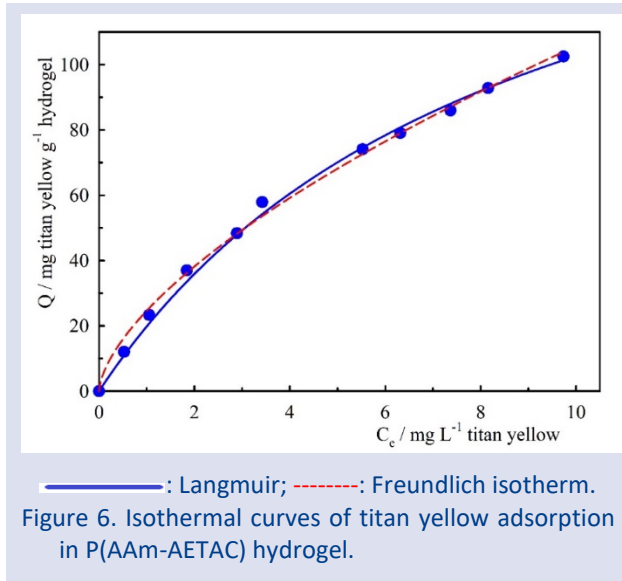
C_b is the equilibrium concentration of titan yellow on the hydrogel (mg L^{-1}) and C_e is the equilibrium concentration of titan yellow in solution (mg L^{-1}). V is the volume of the solution (L) and m is the mass of the hydrogels (g). The amount of substance (Q) adsorbed on the hydrogels was calculated by Equations 1 and 2.

Adsorption isotherm models

The adsorption of a solute from solution to a solid is usually given according to the Giles adsorption isotherm classification. With the Freundlich isotherm model, the type of adsorption (such as S, L, C) and if it is type L, the monolayer adsorption capacity, distribution coefficient, dimensionless dispersion factor, adsorbent dose, and removal efficiency values can be calculated with the Langmuir isotherm model. In addition, with the Temkin isotherm model, adsorption energy change and Temkin equilibrium constant values can be determined. Figure 6 was created for the adsorption of titan yellow in the concentration range of 50-500 mg L^{-1} on P(AAm-AETAC) [2,10,11].

The parameters of Freundlich, Langmuir, and Temkin isotherm models and derived parameters are calculated

from the nonlinear regression of the plots in Figure 6, and have been summarized in Table 3.



The n values of the Freundlich isotherm model are related to the Giles classification, S , L , and C type isotherm. $n < 1$ correspond to S shape, $n=1$ C type, and $n > 1$ to L type [12]. On the other hand, higher values of K_F represent an easy uptake of adsorbate from the solution. The Freundlich exponent n for the P(AAm-AETAC) hydrogel is 1.58, thus suggesting an L -type isotherm. The most characteristic feature of L -type adsorption curves is that the adsorbed molecules have strong intermolecular interactions with the adsorbent.

The Q_m value in the Langmuir isotherm model was calculated as 191.7 mg g^{-1} . It has been observed that the highest monolayer capacity among the organic adsorbents in the studies carried out to date [1,4,5,7].

The efficiency of P(AAm-AETAC) hydrogel for titan yellow adsorption was investigated with dimensionless dispersion factor (R_L) values depending on the initial concentration and the calculated R_L values for 500 mg L^{-1} dye concentration were 0.017. Since the calculated R_L value is $0 < R_L < 1$, it was determined that titan yellow adsorption onto the P(AAm-AETAC) hydrogel was favorable [3].

The adsorbent mass values required for 50% removal from the hypothetical solution containing 500 mg L^{-1} titan yellow and defined as the adsorbent dose were 4.84 g L^{-1} . The amount of adsorbent required for removal is important in terms of cost. From the calculated adsorbent dose value, it is seen that the synthesized cationic hydrogels will provide low-cost removal.

The titan yellow removal efficiency of the P(AAm-AETAC) hydrogel was found to be approximately 98% for all concentrations. This value shows that the P(AAm-AETAC) hydrogel removes the titan yellow with very high efficiency.

The adsorption energy in the Temkin isotherm model was found to be $15.24 \text{ kJ mol}^{-1}$. The b value of $0 < b < 100$ indicates that the adsorption is exothermic and occurs through physical interactions. This result supports the idea that this physical interaction between the prepared cationic P(AAm-AETAC) hydrogels and anionic titan yellow is due to electrostatic forces. [13,14].

Table 3. Isotherm models parameters for titan yellow adsorption onto P(AAm-AETAC) hydrogel

Models	Equations	Values
<i>Freundlich</i>	$Q = K_F C_e^{1/n}$	
Freundlich constant; $K_F ((\text{mg g}^{-1})(\text{L mg}^{-1})^{1/n})$		24.62
heterogeneity factor; n		1.58
correlation coefficient; R		0.998
isotherm type		L -type
<i>Langmuir</i>	$Q = \frac{Q_m K_L C_e}{1 + K_L C_e}$	
monolayer adsorption capacity; $Q_m (\text{mg g}^{-1})$		191.7
distribution coefficient; $K_L (\text{L mg}^{-1})$		0.115
correlation coefficient; R		0.991
adsorbent dose; $AD_L (\text{g L}^{-1})$	$AD_L = \frac{C - C_e}{Q}$	4.84
dimensionless dispersion factor; R_L	$R_L = \frac{1}{1 + K_L C}$	0.017
removal efficiency; $RE\%$	$RE\% = \frac{C_b}{C} \times 100$	98
<i>Temkin</i>	$Q = \left(\frac{RT}{b}\right) \ln(K_T C_e)$	
adsorption energy change, $b (\text{kJ mol}^{-1})$		15.24
Temkin equilibrium constant, $K_T (\text{L mg}^{-1})$		2.09
correlation coefficient; R		0.983
adsorption type		physical
adsorption energy type		exothermic

The maximum adsorption capacities of some adsorbents are presented in Table 4 for comparison with previous studies on titan yellow adsorption.

Table 4. Maximum adsorption capacities of some adsorbents for titan yellow adsorption

Adsorbent	Maximum adsorption capacity	Reference
A green adsorbent recycled from aloe vera leave waste	55.25 mg g ⁻¹	[1]
Positively charged ceramic membrane	99 % (removal efficiency)	[4]
CoFe ₂ O ₄ magnetic nanoparticles	212.8 mg g ⁻¹	[5]
polyaniline@SiO ₂ nanocomposite	141.5 mg g ⁻¹	[7]
P(AAm-AETAC) hydrogel	191.7 mg g ⁻¹ 98% (removal efficiency)	In this study

It is seen that the prepared P(AAm-AETAC) hydrogels are quite good compared to the Aloe vera-based adsorbent used for titan yellow adsorption. In addition, the amount of adsorbed dye is very close to magnetic nanoparticles. In addition, P(AAm-AETAC) hydrogels provided approximately the same amount of dye removal as the positively charged ceramic membrane.

Conclusions

- ✓ P(AAm-AETAC) cationic hydrogel was prepared by a free radical addition reaction in the presence of crosslinker (EGDMA).
- ✓ Although P(AAm-AETAC) hydrogels are glassy in appearance and very hard when dry, they soften when inflated. The gels maintain the geometry of the cylindrical mold in a dry and swollen state.
- ✓ The absence of bands at 900-1000 cm⁻¹, which is evidence of monomeric double bonds, in the ATR spectrum of the P(AAm-AETAC) hydrogel showed that AAm and AETAC monomers were successfully polymerized.
- ✓ The absence of a change in the basebands of the ATR spectra before and after the adsorption of the hydrogel showed that the hydrogel-titan yellow interactions were physical.
- ✓ P(AAm-AETAC) hydrogel gives a two-step thermal decomposition reaction. However, it has been determined that the hydrogel does not undergo any structural deterioration under the influence of heat up to 250 °C and can be used easily up to this temperature.
- ✓ From the SEM image of the P(AAm-AETAC) hydrogel, it was seen that it has a very regular surface structure, there are local voids on the surface of the polymer and these voids are evenly distributed.

- ✓ While the neutral PAAm hydrogel and the anionic titan yellow did not interact, the adsorption of titan yellow was achieved with the [2-(acryloyloxy) ethyl] trimethylammonium chloride comonomer added to the structure.
- ✓ The value of n=1.58 calculated from the Freundlich isotherm proves that the isotherm of the titan yellow adsorption to the P(AAm-AETAC) hydrogel is L-type according to the Giles adsorption isotherms classification, and monolayer adsorption capacities were calculated from Langmuir curves.
- ✓ From the adsorbent dose values calculated from the Langmuir parameters, it was determined that the P(AAm-AETAC) hydrogel would provide the removal of the anionic titan yellow at low cost.
- ✓ It was determined from the R_L value calculated for the 500 mg L⁻¹ titan yellow concentration that the adsorption of titan yellow in the P(AAm-AETAC) hydrogel was favorable.
- ✓ The titan yellow removal efficiency of the P(AAm-AETAC) hydrogel was found to be approximately 98%.
- ✓ From the values of the adsorption energy changes calculated from the Temkin isotherms, it was determined that the adsorption was exothermic and occurred with physical interactions.

As a result, it can be said that the prepared cationic P(AAm-AETAC) hydrogel can be used as a good adsorbent in the removal of anionic dyes from aqueous solutions and high removal can be achieved at low cost.

Conflicts of Interest

The authors declare no conflict of interest.

References

- [1] El-Azazy M., Dimassi S., El-Shafie A., Issa A., Bio-Waste Aloe vera Leaves as an Efficient Adsorbent for Titan Yellow from Wastewater: Structuring of a Novel Adsorbent Using Plackett-Burman Factorial Design, *Appl. Sci.*, 9 (2019) 4856.
- [2] Işıkver Y., Synthesis of Anionic Hydrogels for Uranyl Ion Adsorption, *Cumhuriyet Sci. J.*, 38(4) (2017) 770–780.
- [3] Işıkver Y., Removal of some cationic dyes from aqueous solution by acrylamide- or 2-hydroxyethyl methacrylate-based copolymeric hydrogels, *Fiber. Polym.*, 18(11) (2017) 2070–2078.
- [4] Cheng X., Li N., Zhu M., Zhang L., Deng Y., Deng C., Positively charged microporous ceramic membrane for the removal of Titan Yellow through electrostatic adsorption, *J. Environ. Sci.*, 44 (2016) 204–212.
- [5] Ghaemi M., Absalan G., Shekhan L., Adsorption characteristics of Titan yellow and Congo red on CoFe₂O₄ magnetic nanoparticles, *J. Iran. Chem. Soc.*, 11(6) (2014) 1759–1766.
- [6] Web of Science, WOS. Available at: <https://www.webofscience.com/wos/woscc/summary/36b6867e-d99d-4371-8868-4ac9292c9274-0d0c3701/relevance/1>. Retrieved October 14, 2021.
- [7] Rastgordani M., Zolgharnein J., Mahdavi V., Derivative spectrophotometry and multivariate optimization for simultaneous removal of Titan yellow and Bromophenol blue dyes using polyaniline@SiO₂ nanocomposite, *Microchem. J.*, 155 (2020) 104717.

- [8] Sun J., Ma X., Li X., Fan J., Chen Q., Liu X., Pan J., Synthesis of a Cationic Polyacrylamide under UV Initiation and Its Flocculation in Estrone Removal, *Int. J. Polym. Sci.*, 2018 (2018) 1–11.
- [9] Feng L., Zheng H., Tang X., Zheng X., Liu S., Sun Q., Wang M., The investigation of the specific behavior of a cationic block structure and its excellent flocculation performance in high-turbidity water treatment, *RSC Adv.*, 8(27) (2018) 15119–15133.
- [10] Giles C. H., MacEwan T. H., Nakhwa S. N., Smith D., Studies in adsorption. Part XI. A system of classification of solution adsorption isotherms, and its use in diagnosis of adsorption mechanisms and in measurement of specific surface areas of solids, *J. Chem. Soc.*, 786 (1960) 3973-3993.
- [11] Ivanovska A., Dojčinović B., Maletic S., Pavun L., Asanović K., Kostić M., Waste Jute Fabric as a Biosorbent for Heavy Metal Ions from Aqueous Solution, *Fiber. Polym.*, 21 (2020) 1992-2002.
- [12] Saraydın D., Işıkver Y., Karadağ E., A Study on the Correlation Between Adsorption and Swelling for Poly(Hydroxamic Acid) Hydrogels-Triarylmethane Dyes Systems, *J. Polym. Environ.*, 26(9) (2018) 3924–3936.
- [13] Yabo W., Yi X., Yongkui Z., Siyang T., Chencen G., Jiansheng W., Raymond L., *Chem. Eng. Res. Des.*, 114 (2016) 258-267.
- [14] Nechifor G., Pascu D. E., Pascu M., Traistaru G. A., Albu P. C., *U.P.B. Sci. Bull. Series B*, 77 (2015) 63-72.

CT-DNA/BSA Binding Studies of Thiosemicarbazone-Derived Zn(II) Complex

Asuman Uçar^{1,a,*}, Mükerrerem Fındık^{2,b}, Emine Güler Akgemci^{3,c}¹ Department of Science Education, Education Faculty, Agri Ibrahim Cecen University, Ağrı, Turkey² Department of Chemistry Education, Research Laboratory, A.K. Education Faculty, Necmettin Erbakan University, Konya, Turkey³ Department of Chemistry Education, A.K. Education Faculty, University, Necmettin Erbakan University, Konya, Turkey

*Corresponding author

Research Article

History

Received: 04/10/2021

Accepted: 07/02/2022

Copyright

©2022 Faculty of Science,
Sivas Cumhuriyet University^a asucar340@gmail.com^c egakgemci@gmail.com

ABSTRACT

Zn(II) complex of 2-hydroxy-5-methoxyacetophenone thiosemicarbazone { Zn(HMAT)₂ } was synthesized and characterized by ¹H NMR, UV-Vis and FT-IR spectroscopies. Further, X-ray powder diffraction (XRD) analysis of Zn(HMAT)₂ was carried out to point out the complexation. The binding affinities of Zn(HMAT)₂ with calf thymus DNA (CT-DNA) have been studied by using fluorescence and absorption titration technics. In addition, bovine serum albumin (BSA) binding studies were recorded by fluorescence and UV-Vis spectroscopy. Zn(HMAT)₂ is a strong binders of CT-DNA with binding constant (K_b) 3.65×10⁷ M⁻¹. The binding parameters K_{SV} (for EB), K_q (for BSA) and K_b (for BSA) were determined as 8.2×10⁷ M⁻¹, 1.8×10¹⁴ M⁻¹ s⁻¹ and 2×10⁷ M⁻¹ respectively.

Keywords: DNA, Thiosemicarbazone, Zn(II) complex, Bovine serum albumin binding.^{ib} <https://orcid.org/0000-0003-2674-3120>^{ib} <https://orcid.org/0000-0002-9744-1931>^{ib} mmukerrem@gmail.com^{ib} <https://orcid.org/0000-0002-9441-0814>

Introduction

DNA is the fundamental intracellular target in drug design (1). Combination of DNA and small molecules can give rise to cell death and cancer cells DNA damage (2). However, transition metal complexes are being studied by researchers for DNA binding experiments due to their regulators of gene expression, potential use as drugs and DNA structural probes (3-4). In previous studies, it was reported that, compounds with sulfur content show high DNA/protein binding/cleaving (5-7). Thiosemicarbazones present pharmacological properties due to their C=S and NH moiety for chelating with metal center (8). Metal complexes of thiosemicarbazones exhibit more biological activity than their ligands (9). In previous studies, DNA binding assays, anticancer activity, antimicrobial and cytotoxicity evaluation of some thiosemicarbazones zinc complexes have been investigated (10-12). Zinc differs from other transition metals due to some properties such as the malleable coordination geometry, remarkably high bioavailability and the role as a Lewis acid (13). In the presence of zinc metal, proteins' conformation changes rapidly to carry out biological reactions due to their flexible coordination geometry (14). Understanding the interaction between proteins and metal complexes cause the development of new drugs (15). Bovine serum albumin (BSA), which is the protein in the blood, take place in many researches due to its low cost (16), structural homology to human serum albumin and stability (17).

Synthesis method of 2-hydroxy-5-methoxyacetophenone thiosemicarbazone based Zn(II) complex and its application studies such as evaluation of anticancer activity in breast cancer cell lines, carbonic

anhydrase inhibition and microbiological analysis results were included in our previous study (18,19). In addition, the investigation of binding properties CT-DNA and BSA with the compound have been presented in this article.

Materials and Methods

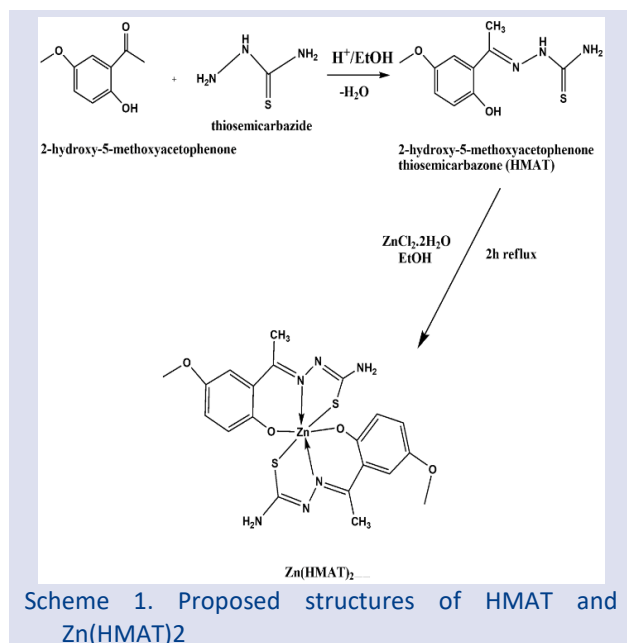
Apparatus

Thiosemicarbazide, 2-hydroxy-5-methoxyacetophenone, DMF (N,N-Dimethylformamide) EtOH (Ethyl alcohol), H₂SO₄ (Sulfuric acid), CT-DNA (Deoxyribonucleic acid from calf thymus) and Trizma base (for Tris/HCl buffer) were obtained from Sigma-Aldrich and Merck. ¹H NMR spectrum was monitored by A Bruker AC 400 (400 MHz) NMR spectrometer. FT-IR spectrum was carried out by using Attenuated Total Reflection-Fourier Transformed Infrared (ATR-FTIR) spectrometer (Perkin Elmer 100). UV-Vis and fluorescence spectra were monitored by Shimadzu UV-1800 double beam spectrophotometer and PTI Quantamaster 400 Fluorometer spectrophotometer, respectively. XRD measurement was recorded using Bruker axis diffractometer (Bruker D8 ADVANCE).

Synthesis of Zn(HMAT)₂

Zn(HMAT)₂ was synthesized (Scheme 1) according to our previous article (18,19). The possible structure of the complex is given in Scheme 1 (20,21).

Zn(HMAT)₂: Yellow crystals, yield 72.5%; mp: 189-191 °C Anal. Calcd. C₂₀H₂₂N₆O₄S₂Zn: H, 4.11; N, 15.56; C, 44.49%. Found: H, 4.19; C, 45.03; N, 15.68%. FT-IR (cm⁻¹) ν : 585, 783, 1030, 1215, 1540, 3192, 3486. ¹H NMR (400 MHz, DMSO-d₆): δ (ppm): 2.35-3.78 (s, 3H, -CH₃), 6.84-6.93 (d, 2H, H_{Ar}), 7.24 (s, 2H, -NH₂).



Dna Binding Experiments

The interactions of Zn(HMAT)₂ with CT-DNA were explored using UV–visible absorption titration experiments. All titration experiments of Zn(HMAT)₂ with CT-DNA were investigated in a pH 7.2 Tris/HCl buffer (5 mM Tris/50 mM NaCl). The emission spectra were recorded with the compound (20 μM in DMF), during which the concentration of CT-DNA (2-5.5 μM) was gradually increased.

Competitive Ethidium Bromide-Dna Binding Fluorescence Measurement

Displacement experiments of EB have been monitored fluorometrically upon gradual addition of Zn(HMAT)₂ (1-4 μM) to the aqueous solution of EB (10 μM) bound CT-DNA (10 μM) in Tris-HCl buffer (5 mM Tris/50 mM NaCl, pH 7.2).

Protein Binding Studies

The absorbance measurements were monitored of 10 μM BSA in phosphate-buffered saline (PBS) and BSA with Zn(HMAT)₂ (4 μM in DMF). The interaction of Zn(HMAT)₂ with BSA was investigated by using fluorescence spectra. The fluorometric measurements were recorded by gradual addition of 0-1 μM Zn(HMAT)₂ to 2 mL, 2 μM BSA with PBS at pH 7.5.

Results and Discussion

Spectroscopic Studies

The ¹H NMR spectrum of Zn(HMAT)₂ was recorded in DMSO-d₆ (Figure 1). A multiple signal for aromatic protons were observed around 6.93-6.84 ppm (22). A singlet was appeared at 7.24, 3.78 and 2.35 ppm was attributed to proton signal of the -NH₂, CH₃ (methoxy group) and -CH₃ (azomethine group), respectively (22-25).

The FT-IR spectrum of Zn(HMAT)₂ (Figure 2) displayed stretching frequency bands for the $\nu(\text{C}=\text{N})$ at 1540 cm⁻¹ (26). The bands attributed to $\nu(\text{Zn}-\text{N})$ vibration was found

at 585 cm⁻¹ (27). $\nu(\text{N}-\text{H})$ stretching frequencies of the NH₂ was observed at 3486 cm⁻¹ (28). $\nu(\text{C}-\text{S})$ vibration at 783 cm⁻¹ was proved the coordination of the NH-C=S group [22]. The band at 1215 cm⁻¹ was appeared due to the $\nu(\text{N}-\text{C}-\text{S})$ vibration (29).

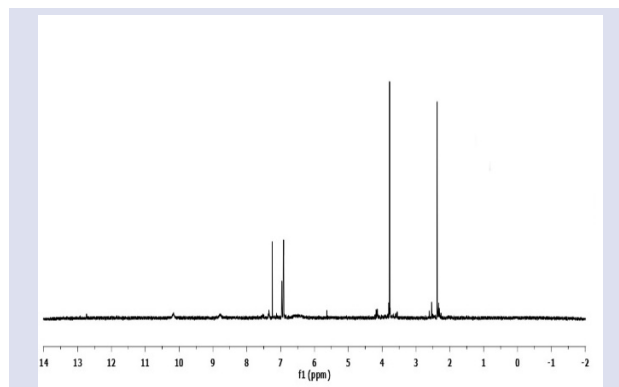


Figure 1. ¹H NMR spectrum of Zn(HMAT)₂.

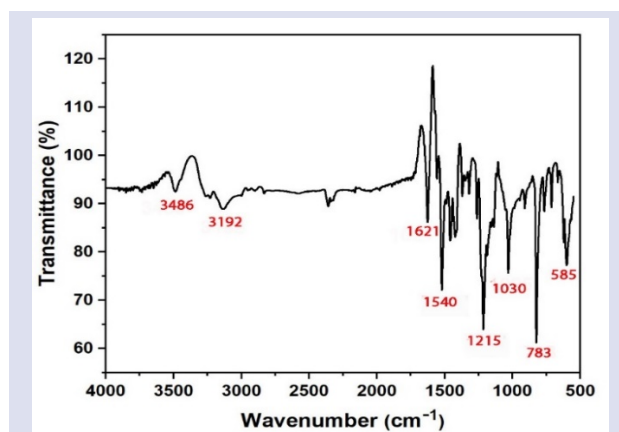


Figure 2. FT-IR spectrum of Zn(HMAT)₂.

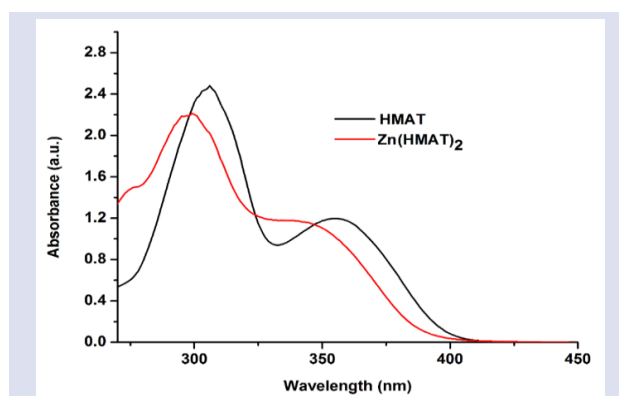


Figure 3. UV-Vis spectra of HMAT and Zn(HMAT)₂.

UV-Vis spectra of HMAT and Zn(HMAT)₂ (in DMF) was presented in Figure 3. In the UV-Vis spectrum of HMAT, the band at 305 nm belongs to azomethine $\pi \rightarrow \pi^*$ transitions, whereas the absorption at 355 nm corresponds to thioamide $n \rightarrow \pi^*$ transitions (19). After the complexation, the first band associated with the carbonyl and azomethine group was observed at 296 nm due to $\pi \rightarrow \pi^*$ transitions (30). The intraligand $n \rightarrow \pi^*$ transition was assigned to band at 346 nm (31). Transformation of the C=S bond to the C-S form due to complexation caused the shift of the bands (32). By comparing the frequency of

HMAT and the corresponding the Zn complex, the electronic transitions of $\pi \rightarrow \pi^*$ are shifted to a lower value due to the formation of the complex and coordination of the ligand to the metal (18).

Powder XRD Analysis

The powder X-ray diffraction pattern of Zn(HMAT)_2 (Figure 4) was monitored over the range 5-80 (2θ). The diffraction peak at $2\theta=24.06$ may have been caused by the bond of Zn-S (33,34). Observing the sharp crystalline peaks arise the crystalline behavior of the samples (35).

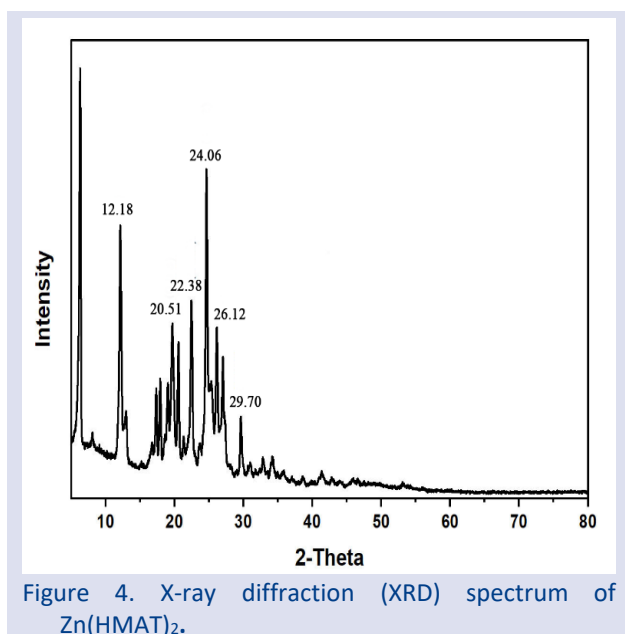


Figure 4. X-ray diffraction (XRD) spectrum of Zn(HMAT)_2 .

DNA Binding Studies

UV absorption spectra of DNA

UV-visible absorption spectra of complex (20 μM) with increasing ratios of CT-DNA (2–5.5 μM ; Tris-HCl 5 mM/NaCl 50 mM, pH: 7.2) were measured to observe the binding interaction (Figure 5A). After increasing the amount of CT-DNA to the complex, the spectrum showed a hypochromism of about 8%, 21% at 275, 344 nm and showed a hypochromism of about 13% with a blue shift of 4 nm at 296 nm. According to the results obtained, the binding to CT-DNA was confirmed from the absorption changes of the complex. The amount of binding interaction between Zn(HMAT)_2 and CT-DNA was described using the binding constant K_b , which is calculated from the Eq. (1).

$$\frac{[\text{DNA}]}{(\epsilon_a - \epsilon_f)} = \frac{[\text{DNA}]}{(\epsilon_b - \epsilon_f)} + \frac{1}{K_b(\epsilon_b - \epsilon_f)} \quad (1)$$

Where $[\text{DNA}]$ is the concentration of CT-DNA, ϵ_f , ϵ_a , and ϵ_b correspond to the extinction coefficient for the free complex, $A_{\text{obsd}}/[\text{complex}]$ and the extinction coefficient for the complex in the fully bound form, respectively. K_b was found by calculating the ratio of slope/intercept in the linear plot of $[\text{DNA}]/(\epsilon_a - \epsilon_f)$ vs $[\text{DNA}]$ (Figure 5B). The binding constant (K_b) value for the interaction of the complex with CT-DNA was found as $3.65 \times 10^7 \text{ M}^{-1}$. The UV-

Vis spectroscopy method provides important data about interaction type on absorbance changes and shift in wavelength in the interaction of small molecules with DNA. Hypochromism with or without a red or blue shift is typically the product of a compound binding to DNA through intercalation. The observed hypochromism with blue shift verified the complex's interaction (36-38).

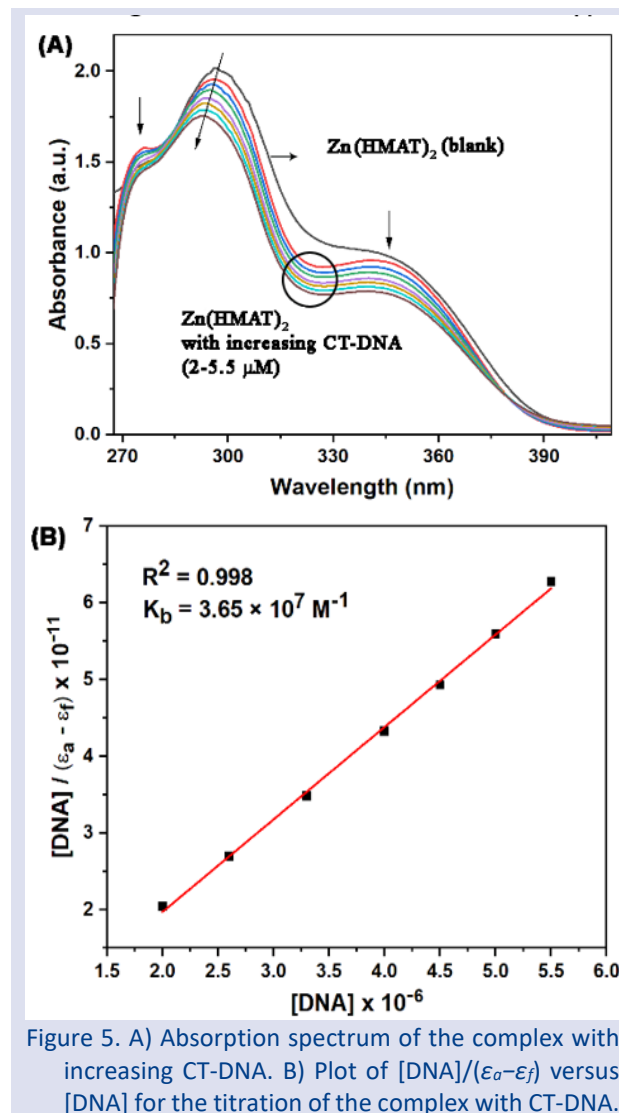


Figure 5. A) Absorption spectrum of the complex with increasing CT-DNA. B) Plot of $[\text{DNA}]/(\epsilon_a - \epsilon_f)$ versus $[\text{DNA}]$ for the titration of the complex with CT-DNA.

Ethidium bromide (EB) displacement

EB is a dye which binds to DNA through intercalation. EB exhibits increased fluorescence intensity after addition of DNA because of the strong intercalation between DNA. EB binding to the DNA by intercalation is cause competition with EB and affect the combination between EB and DNA, giving rise to a decrease in fluorescence intensity (39,40). The study was carried out by titration of the complex varying from 1 to 4 μM into 10 μM CT-DNA and 10 μM EB solution. After addition of each aliquot, 540 nm was used as excitation wavelength for the CT-DNA-EB with Zn(HMAT)_2 (in the range of 550 nm and 780 nm for emission spectra). The fluorescence spectra of the CT-DNA-EB and CT-DNA-EB with Zn(HMAT)_2 (Figure 6a) show the decreasing fluorescence intensity of CT-DNA-EB in each addition with increasing amounts of complex. This result indicated that complex was

able to replace EB in the CT-DNA helix. Thus, this result proves that Zn(HMAT)₂ binds to CT-DNA via intercalative binding mode. The quenching efficiency for Zn(HMAT)₂ was evaluated by the Stern–Volmer constant K_{SV} ,

$$F^0/F = 1 + K_{SV}[Q] \quad (2)$$

where F/F^0 , K_{SV} , $[Q]$ are the fluorescence intensities in the presence/absence of the complex, the linear Stern–Volmer quenching constant and concentration of the complex, respectively. The K_{SV} value calculated from the ratio of slope/intercept in the linear plot of $[Q]$ vs F^0/F and is found to be $8.2 \times 10^7 \text{ M}^{-1}$ (Figure 6b).

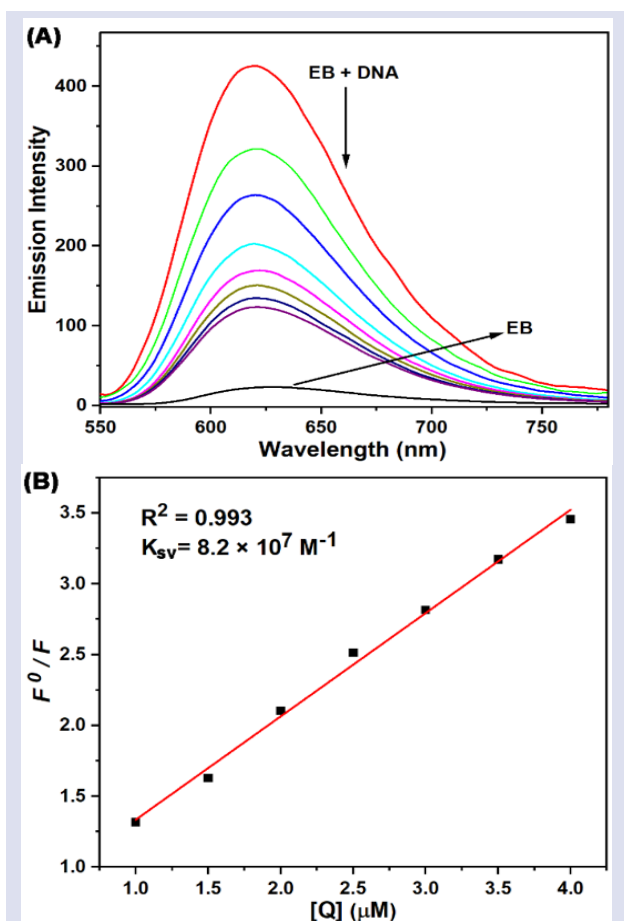


Figure 6. A) Fluorescence quenching curves with increasing complex to DNA/EB. Conditions: [CT-DNA] = 10 μM , [EB] = 10 μM , [complex] = 1–4 μM . B) Stern–Volmer plot of fluorescence titrations of the complex with CT-DNA.

BSA binding studies

Fluorescence quenching of BSA.

Fluorescence of the BSA is due to the fluorophore groups in its structure such as phenylalanine, tyrosine and tryptophan. When any compound interacts with BSA, fluorescence intensity quenches (37,41).

Tryptophan fluorescence quenching study was used to indicate BSA-binding. In this experiment, varied mole ratio of Zn(HMAT)₂ solutions to 2 μM BSA in PBS buffer solution were prepared (pH:7.5). The fluorescence spectra were monitored with emission at 341 nm whereas excitation wavelength is 280 nm. The additions of different concentration of Zn(HMAT)₂ (0–1 μM) solutions to BSA were decrease its fluorescence intensity and a blue shift (341–337 nm) was noticed. The resulting emission behaviour is shown in Figure 7A. The emission spectra demonstrated a definite interaction between BSA and Zn(HMAT)₂. The extent of fluorescence quenching of BSA with the gradual addition of the complex was interpreted by using the Stern–Volmer equation (3).

$$\frac{F_0}{F} = 1 + K_q \tau_0 [Q] = 1 + K_{SV} [Q] \quad (3)$$

Where F/F_0 , K_q , $[Q]$ and τ_0 the fluorescence intensities in the presence/absence of the complex, the bimolecular quenching rate constant, the concentration of the complex and the average lifetime (10^{-8} s) of protein without complex, respectively. K_{SV} is the Stern–Volmer quenching constant and is equal to $K_q \tau_0$. The linear Stern–Volmer plot in Figure 7b indicated that equation (3) is useable for the present system and the numerical values of K_{SV} and K_q were equal to $1.8 \times 10^6 \text{ M}^{-1}$ and $1.8 \times 10^{14} \text{ M}^{-1} \text{ s}^{-1}$, respectively. The calculated K_q value is larger than the limiting diffusion constant K_{dif} ($2.0 \times 10^{10} \text{ M}^{-1} \text{ s}^{-1}$) of the biomolecules (42) which indicated that fluorescence quenching is caused by interaction of BSA with Zn(HMAT)₂ depending on static quenching mechanism. (43).

Constant K_b and the number of binding site n were calculated by using following Scatchard equation (4).

$$\log[(F_0 - F)/F] = \log K_b + n \log [Q] \quad (4)$$

Where F/F_0 , K_b and n are the fluorescence intensity in the presence/absence of the complex, the binding constant of complex with BSA and the number of binding sites. The K_b and n were calculated from the ratio of slope/intercept in the linear plot of $\log[(F_0-F)/F]$ vs $\log [Q]$ and was found to be $2 \times 10^7 \text{ M}^{-1}$ and $n = 0.998$ (Figure 7C). Existence of only one binding site on BSA for complex can be provided with the value for the binding site n which is close to 1. The values of K_q and K_b clearly evidence a strong interaction between BSA and Zn(HMAT)₂. When the related publications are examined, the large K_b and K_q values indicate that the strength of the interaction increases (44,45).

In Table 1, comparison of our work with other studies can be seen by observing the higher values K_b and K_q of Zn(HMAT)₂ indicating a stronger interaction.

Table 1. Comparison with other Zn complexes for Binding constant (K_b) and quenching constant (K_q) values of DNA and BSA

Complex	DNA		BSA		Ref.
	K_b (M^{-1})	K_b (M^{-1})	K_q (M^{-1})		
Zn(HL) ₂	2.85×10^4	4.5×10^4	2.4×10^{13}	(46)	
Zn(L ^{DIOMe} SN) ₂	1×10^5	2.03×10^5	1.67×10^{13}	(47)	
Tp ^{PV} ZnN ₃	6.79×10^4	5.37×10^4	1.19×10^5	(48)	
M(HL) ₂](NO ₃) ₂ (M:Zn)	$2.98 \pm 0.06 \times 10^6$	$\sim 4.68 \times 10^5$	6.31×10^{13}	(49)	
ZnPc-4	1.58×10^5	no data	1.99×10^{13}	(50)	
Zn(H ₂ L)](NO ₃) ₂	5.98×10^3	3.69×10^4	9.69×10^{10}	(51)	
Zn ₂ (L ⁴)(CH ₃ COO)	2.7×10^3	2.4×10^6	$\sim 10^{13}$	(52)	
Zn(II) complex	1.2×10^4	3.5×10^4	2.8×10^{12}	(53)	
2,4-diiodo-6-((2-phenylaminoethylimino)methyl) phenol Zn Complex	1.2×10^4	2.14×10^4	1.66×10^5	(54)	
Zn(HMAT) ₂	3.65×10^7	2×10^7	1.8×10^{14}	This work	

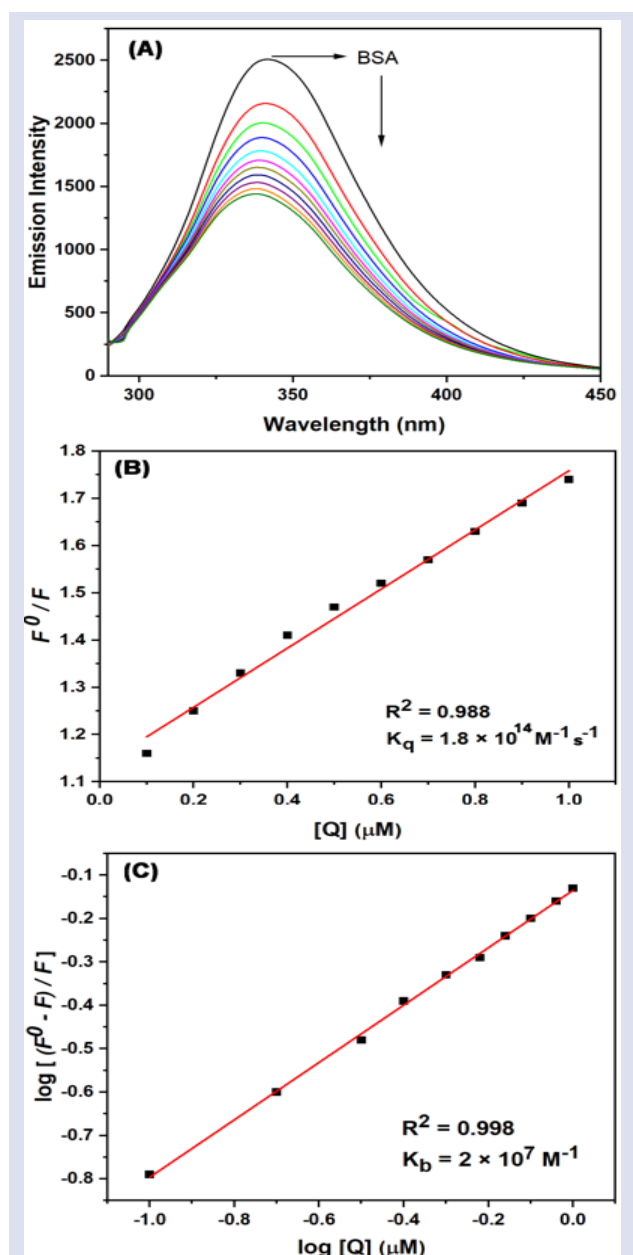


Figure 7. (A) Fluorescence quenching of BSA ($1 \mu M$; $\lambda_{ex} = 280$; $\lambda_{em} = 341$ nm) in the presence/absence of various concentrations of the complex ($0-1 \mu M$); (B) Stern-Volmer plot of the fluorescence titrations of the complex with BSA; (C) Scatchard plot of the fluorescence titrations of the complex with BSA.

UV absorption spectra of BSA.

The BSA solution exhibited a strong band around 278 nm for having the moieties such as phenylalanine, tyrosine and tryptophan. The absorption spectrum of the BSA solution and BSA- Zn(HMAT)₂ were given in Figure 8. The absorbance of BSA ($10 \mu M$) increased with 5 nm red shift with the addition of Zn(HMAT)₂ ($4 \mu M$), which indicated static quenching (36,55,56).

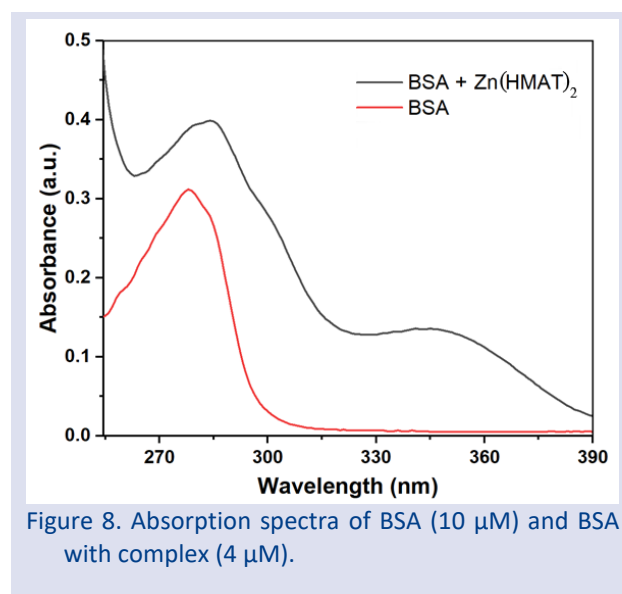


Figure 8. Absorption spectra of BSA ($10 \mu M$) and BSA with complex ($4 \mu M$).

Conclusion

In this study, synthesis and characterization by using spectroscopic methods (FT-IR, ¹H NMR, elemental analysis and UV-Vis spectroscopies) for zinc complex of 2-hydroxy-5-methoxyacetophenone thiosemicarbazone was reported. XRD spectrum of the complex also provided support for the analysis of the structure. BSA and DNA interactions abilities of the Zn(HMAT)₂ were analyzed by fluorescence and UV-Vis spectroscopy. The results showed that Zn(HMAT)₂ binds strongly with CT-DNA via intercalative mode with high binding constant. The results illustrated from absorption titrations as (K_b) $3.65 \times 10^7 M^{-1}$ and ethidium bromide competitive studies as K_{sv} (for CT-DNA): $8.2 \times 10^7 M^{-1}$ were obtained. Protein binding efficiency showed that Zn(HMAT)₂ interact with BSA by

acting as transporters of the complex ($K_f: 1.8 \times 10^{14} \text{ M}^{-1} \text{ s}^{-1}$ and $K_b: 2 \times 10^7 \text{ M}^{-1}$). The reactivity towards BSA exhibited a static emission quenching by the complex. These findings may be useful in determining the mechanism of some Zn complexes' interactions with serum albumin and DNA.

Conflicts of Interest

The authors state that did not have conflict of interests

References

- [1] Deng J.G., Li T., Su G., Qin Q.P., Liu Y., Gou Y., Co(III) complexes based on a-N-heterocyclic thiosemicarbazone ligands: DNA binding, DNA cleavage, and topoisomerase I/II inhibitory activity studies, *J. Mol. Struct.*, 1167 (2018) 33-43.
- [2] Li V.S., Choi D., Wang Z., Jimenez L.S., Tang M.S., Kohn H., Role of the C-10 substituent in mitomycin C-1-DNA bonding, *J. Am. Chem. Soc.*, 118 (10) (1996) 2326–2331.
- [3] Zuber G., Quada J.C., Hecht S.M., Sequence selective cleavage of a DNA octanucleotide by chlorinated bithiazoles and bleomycins, *J. Am. Chem. Soc.*, 120 (36) (1998) 9368–9369.
- [4] Kalaiarasi G., Umadevi C., Shanmugapriya A., Kalaivani P., Dallemer F., Prabhakaran R., DNA(CT), protein (BSA) binding studies, anti-oxidant and cytotoxicity studies of new binuclear Ni(II) complexes containing 4(N)-substituted thiosemicarbazones, *Inorg. Chim. Acta*, 453 (2016) 547-558.
- [5] Giannini F., Suss-Fink G., Furrer J., Efficient Oxidation of Cysteine and Glutathione Catalyzed by a Dinuclear Areneruthenium Trithiolato Anticancer Complex, *Inorg. Chem.*, 50 (21) (2011) 10552-10554.
- [6] Suda Y., Arano A., Fukui Y., Koshida S., Wakao M., Nishimura T., Kusumoto S., Sobel M., Immobilization and Clustering of Structurally Defined Oligosaccharides for Sugar Chips: An Improved Method for Surface Plasmon Resonance Analysis of Protein–Carbohydrate Interactions, *Bioconjugate Chem.*, 17(5) (2006) 1125-1135.
- [7] Mahon A.B., Arora P.S., Design, synthesis and protein-targeting properties of thioether-linked hydrogen bond surrogate helices, *Chem. Commun.*, 48 (2012) 1416-1418.
- [8] shaq M., Taslimi P., Shafiq Z., Khana S., Salmas R.E., Zangeneh M.M., Saeed A., Zangeneh A., Sadeghian N., Asari A., Mohamad H., Synthesis, bioactivity and binding energy calculations of novel 3-ethoxysalicylaldehyde based thiosemicarbazone derivatives, *Bioorg. Chem.*, 100 (2020) 103924-103933.
- [9] Zhang X., Li S., Yang L., Fan C., Synthesis, characterization of Ag(I), Pd(II) and Pt(II) complexes of a triazine-3-thione and their interactions with bovine serum albumin, *Spectrochim. Acta Part A*, 68(3) (2007) 763–770.
- [10] Bessega T., Chaves O.A., Martins F.M., Acunha T.V., Back D.F., Iglesias B.A., Oliveira G.M., Coordination of Zn(II), Pd(II) and Pt(II) with ligands derived from diformylpyridine and thiosemicarbazide: Synthesis, structural characterization, DNA/BSA binding properties and molecular docking analysis, *Inorg. Chim. Acta*, 496 (2019) 119049-119058.
- [11] Kumar S.M., Kesavan M.P., Kumar G.G.V., Sankarganesh M., Chakkaravarthi G., Rajagopal G., Rajesh J., New heteroleptic Zn(II) complexes of thiosemicarbazone and diimine Co-Ligands: Structural analysis and their biological impacts, *J. Mol. Struct.*, 1153 (2018) 1-11.
- [12] Mathews N.A., Kurup M.R.P., In vitro biomolecular interaction studies and cytotoxic activities of copper(II) and zinc(II) complexes bearing ONS donor thiosemicarbazones, *Appl. Organomet. Chem.*, 35(1) (2020) 6056.
- [13] Balakrishnan N., Haribabu J., Krishnan D.A., Swaminathan S., Mahendiran D., Bhuvanesh N.S.P., Karvembu R., Zinc(II) complexes of indole thiosemicarbazones: DNA/protein binding, molecular docking and in vitro cytotoxicity studies, *Polyhedron*, 170 (2019) 188–201.
- [14] Haribabu J., Priyarega S., Bhuvanesh N.S.P., Karvembu R., Synthesis and molecular structure of the zinc(II) complex bearing an N, S donor ligand, *J. Struct. Chem.*, 61(1) (2020) 66-72.
- [15] Zhang Y.Z., Zhou B., Liu Y.X., Zhou C.X., Ding X.L., Liu Y., Fluorescence Study on the Interaction of Bovine Serum Albumin with P-Aminoazobenzene, *J. Fluores.*, 18 (2008) 109-118.
- [16] Zareia L., Asadi Z., Samolova E., Dusek M., Amirghofran Z., Pyrazolate as bridging ligand in stabilization of self-assembled Cu(II) Schiff base complexes: Synthesis, structural investigations, DNA/protein (BSA) binding and growth inhibitory effects on the MCF7, CT-26, MDA-MB-231 cell lines, *Inorg. Chim. Acta*, 509 (2020) 19674-119687.
- [17] Ghosh K.S., Sen S., Sahoo B.K., Dasgupta S., A spectroscopic investigation into the interactions of 3'-O-carboxy esters of thymidine with bovine serum albumin, *Biopolymers: Orig. Res. Biomol.*, 91 (9) (2009) 737–744.
- [18] Ucar A., Findik M., Kuzu M., Pehlivanoglu S., Sayin U., Sayin Z., Akgemci E.G., Cytotoxic effects, microbiological analysis and inhibitory properties on carbonic anhydrase isozyme activities of 2-hydroxy-5-methoxyacetophenone thiosemicarbazone and its Cu(II), Co(II), Zn(II) and Mn(II) complexes, *Res. Chem. Intermed.*, 47 (2021) 533-550.
- [19] Akgemci E.G., Saf A.O., Tasdemir H.U., Türkkan E., Bingol H., Turan S.O., Akkiprik M., Spectrophotometric, voltammetric and cytotoxicity studies of 2-hydroxy-5-methoxyacetophenone thiosemicarbazone and its N(4)-substituted derivatives: A combined experimental-computational study, *Spectrochim. Acta Part A Mol. Biomol. Spectrosc.*, 136 (2015) 719-725.
- [20] Kotian A., Kamat V., Naik K., Kokare D.G., Kumara K., Lokanath N.K., Revankar V.K., Hydroxyacetone derived N4-methyl substituted thiosemicarbazone: Syntheses, crystal structures and spectroscopic characterization of later first-row transition metal complexes, *J. Mol. Struct.*, 1224 (2021) 129055-129062.
- [21] Santoro A., Vileno B., Palacios Ò., Díaz M.D.P., Riegel G., Gaidon C., Krężel A., Faller P., Reactivity of Cu(II)-, Zn(II)- and Fe(II)- thiosemicarbazone complexes with glutathione and metallothionein: from stability to dissociation to transmetallation, *Metallomics*, 11 (2019) 994-1004.
- [22] Cıkla I.K., Güveli S., Yavuz M., Demirci T.B., Ülküseven B., 5-Methyl-2-hydroxy-acetophenone-thiosemicarbazone and its nickel(II) complex: Crystallographic, spectroscopic (IR, NMR and UV) and DFT studies, *Polyhedron*, 105 (2016) 104-114.
- [23] Sharma D., Jasinski J.P., Smolinski V.A., Kaur M., Paul K., Sharma R., Synthesis and structure of complexes (Ni^{II}, Ag^I) of substituted benzaldehyde thiosemicarbazones and antitubercular activity of Ni(II) complex, *Inorg. Chim. Acta*, 499 (2020) 119187-119194.

- [24] Konakanchi R., Haribabu J., Prashanth J., Nishtala V.B., Mallela R., Manchala S., Gandamalla D., Karvembu R., Reddy B.V., Yellu N.R., Kotha L.R., Synthesis, Structural, Biological Evaluation, Molecular Docking and DFT Studies of Co(II), Ni(II), Cu(II), Zn(II), Cd(II) and Hg(II) Complexes bearing Heterocyclic Thiosemicarbazone ligand, *Appl. Organomet. Chem.*, 32 (8) (2018) 4415.
- [25] Arafath M.A., Adam F., Razali M.R., Hassan L.E.A., Ahamed M.B.K., Majid A.M.S.A., Synthesis, characterization and anticancer studies of Ni(II), Pd(II) and Pt(II) complexes with Schiff base derived from N-methylhydrazinecarbothioamide and 2-hydroxy-5-methoxy-3 nitrobenzaldehyde, *J. Mol. Struct.*, 1130 (2017) 791-798.
- [26] Nyawade E.A., Sibuyi N.R.S., Meyer M., Lalancette R., Onani M.O., Synthesis, characterization and anticancer activity of new 2-acetyl-5-methyl thiophene and cinnamaldehyde thiosemicarbazones and their palladium(II) complexes, *Inorg. Chim. Acta*, 515 (2021) 20036-120045.
- [27] Savir S., Wei Z.J., Liew J.W.K., Vythilingam I., Lim Y.A.L., Saad H.M., Sim K.S., Tan K.W., Synthesis, cytotoxicity and antimalarial activities of thiosemicarbazones and their nickel (II) complexes, *J. Mol. Struct.*, 1211 (2020) 128090-128099.
- [28] Amuthakala S., Bharath S., Rahiman A.K., Thiosemicarbazone-based bifunctional chemosensors for simultaneous detection of inorganic cations and fluoride anion, *J. Mol. Struct.*, 1219 (2020) 128640-128654.
- [29] Huseynova M., Farzaliyev V., Medjidov A., Aliyeva M., Taslimi P., Sahin O., Yalçın B., Novel zinc compound with thiosemicarbazone of glyoxylic acid: Synthesis, crystal structure, and bioactivity properties, *J. Mol. Struct.*, 1200 (2020) 127082-127091.
- [30] Kalantari R., Asad Z., DNA/BSA binding of a new oxovanadium (IV) complex of glycylglycine derivative Schiff base ligand, *J. Mol. Struct.*, 1219 (2020) 128664-128675.
- [31] Jacob J.M., Kurup M.R.P., Nisha K., Serdaroglu G., Kaya S., Mixed ligand copper(II) chelates derived from an O, N, S-donor tridentate thiosemicarbazone: Synthesis, spectral aspects, FMO and NBO analysis, *Polyhedron*, 189 (2020) 114736-114746.
- [32] Li Q.X., Tang H.A., Li Y.Z., Wang M., Wang L.F., Xia C.G., Synthesis, characterization, and antibacterial activity of novel Mn(II), Co(II), Ni(II), Cu(II), and Zn(II) complexes with vitamin K3-thiosemicarbazone, *J. Inorg. Biochem.*, 78 (2) (2000) 167-174.
- [33] Palve A.M., Garje S.S., Preparation of zinc sulfide nanocrystallites from single-molecule precursors, *J. Cryst. Growth*, 326 (1) (2011) 157-162.
- [34] Attralarasan S., Febena A.S., Raj M.V.A., Madhavan J., Synthesis, Characterization and DFT Calculations of Thiosemicarbazone 4-Methoxy Benzaldehyde Zinc Chloride, *Mechanics, Materials Science & Engineering*, 9 (2017).
- [35] Kumar L.V., Sundaresan S., Gopinathan R.N., Antioxidant, antidiabetic and anticancer studies of nickel complex of Vanillin-4-Methyl-4-Phenyl-3-Thiosemicarbazone, *Mater. Today* 41 (3) (2021) 669-675.
- [36] Ayyannan G., Mohanraj M., Gopiraman M., Uthayamalar R., Raja G., Bhuvanesh N., Nandhakumar R., Jayabalakrishnan C., New Palladium(II) complexes with ONO chelated hydrazone ligand: Synthesis, characterization, DNA/BSA interaction, antioxidant and cytotoxicity, *Inorg. Chim. Acta*, 512 (2020) 119868.
- [37] Bashiri M., Jarrahpour A.S., Nabavizadeh M., Karimian S., Rastegari B., Haddadi E., Turos E., Potent antiproliferative active agents: novel bis Schiff bases and bis spiro β -lactams bearing isatin tethered with butylene and phenylene as spacer and DNA/BSA binding behavior as well as studying molecular docking, *Medic. Chem. Res.*, 30 (2021) 258-284.
- [38] Amitha G.S., Vasudevan S., DNA binding and cleavage studies of novel Betti base substituted quaternary Cu(II) and Zn(II) phthalocyanines, *Polyhedron*, 190 (2020) 114773-114782.
- [39] Husain M.A., Ishqi H.M., Sarwar T., Rehman S.U., Tabish M., Interaction of indomethacin with calf thymus DNA: a multi-spectroscopic, thermodynamic and molecular modelling approach, *Med. Chem. Comm.*, 8 (2017) 1283.
- [40] Tian Z., Huang Y., Zhang Y., Song L., Qiao Y., Xu X., Wang C., Spectroscopic and molecular modeling methods to study the interaction between naphthalimide-polyamine conjugates and DNA, *J. Photochem. Photobiol. B.*, 158 (2016) 1-15.
- [41] Mo D., Shi J., Zhao D., Zhang Y., Guan Y., Shen Y., Bian H., Huang F., Wu S., Synthesis and characterization of Fe(III)/Co(III)/Cu(II) complexes with Schiff base ligand and their hybrid proteins, SOD activity and asymmetric catalytic oxidation of sulfides, *J. Mol. Struct.*, 1223 (2021) 129229-129238.
- [42] are W.R., Oxygen quenching of fluorescence in solution: an experimental study of the diffusion process, *J. Phys. Chem.*, 66 (3) (1962) 455-458.
- [43] Singh R., Afzal M., Zaki M., Ahmad M., Tabassum S., Bharadwaj P.K., Synthesis, structure elucidation and DFT studies of a new coumarin-derived Zn(II) complex: in vitro DNA/HSA binding profile and pBR322 cleavage pathway, *RSC Adv.*, 4 (2014) 43504.
- [44] Ambika S., Manojkumar Y., Arunachalam S., Gowdhami B., Sundaram K.K.M., Solomon R.V., Venuvanalingam P., Akbarsha M.A., Sundararaman M., Biomolecular Interaction, AntiNCancer and Anti-Angiogenic Properties of Cobalt(III) Schiff Base Complexes, *Sci. Rep.*, 9 (2019) 2721.
- [45] Li Y., Yang Z., Li T., Synthesis, characterisation, in vitro DNA binding properties and antioxidant activities of Ln(III) complexes with chromone-3-carbaldehyde- (2'-hydroxy) benzoyl hydrazone, *Prog. React. Kinet. Mech.*, 40 (4) (2015) 313-329.
- [46] Zhang Y.P., Li Y., Xu G.C., Li J.Y., Luo H.Y., Li J.Y., Zhang Li., Jia D.Z., Synthesis, crystal structure, DNA/bovine serum albumin binding and antitumor activity of two transition metal complexes with 4-acylpyrazolone derivative, *Appl. Organometal Chem.*, 33 (2019) 4668.
- [47] Asadizadeha S., Amirnasra M., Tirani F.F., Mansouria A., Schenk K., DNA-BSA interaction, cytotoxicity and molecular docking of mononuclear zinc complexes with reductively cleaved N_2S_2 Schiff base ligands, *Inorganica Chimica Acta*, 483 (2018) 310-320.
- [48] Narwane M., Dorairaj D.P., Chang Y.L., Karvembu R., Huang Y.H., Chang H.W., Hsu S.C.N., Tris-(2-pyridyl)-pyrazolyl Borate Zinc(II) Complexes: Synthesis, DNA/Protein Binding and In Vitro Cytotoxicity Studies, *Molecules*, 26 (2021) 7341.
- [49] Liu J.J., Liu X.R., Zhao S.S., Yang Z.W., Yang Z., Syntheses, crystal structures, thermal stabilities, CT-DNA, and BSA binding characteristics of a new acylhydrazone and its Co(II), Cu(II), and Zn(II) complexes, *Journal Of Coordination Chemistry*, 73 (2020) 1159-1176.

- [50] Amitha G.S., Vasudevan S., DNA/BSA binding studies of peripherally tetra substituted neutral azophenoxy zinc phthalocyanine, *Polyhedron*, 175 (2020) 114208.
- [51] Bessegaa T., Chaves O.A., Martins F.M., Acunha T.V., Back D.F., Iglesias B.A., Oliveira G.M., Coordination of Zn(II), Pd(II) and Pt(II) with ligands derived from diformylpyridine and thiosemicarbazide: Synthesis, structural characterization, DNA/BSA binding properties and molecular docking analysis, *Inorganica Chimica Acta*, 496 (2019) 119049.
- [52] Ramilo-Gomes F., Addis Y., Tekamo I., Cavaco I., Campos D., Pavan I.R., Gomes C.S.B., Brito V., Santos A.O., Domingues F., Luís A., Marques M.M., Pessoa J.C., Ferreira S., Silvestre S., Correia I., Antimicrobial and antitumor activity of S-methyl dithiocarbazate Schiff base zinc(II) complexes, *Journal of Inorganic Biochemistry*, 216 (2021) 111331.
- [53] Daryanavard M., Jannesari Z., Javeri M., Abyar F., A new mononuclear zinc(II) complex: Crystal structure, DNA- and BSA binding, and molecular modeling; in vitro cytotoxicity of the Zn(II) complex and its nanocomplex, *Spectrochimica Acta Part A: Molecular and Biomolecular Spectroscopy*, 233 (2020) 118175.
- [54] Sakthi M., Ramu A., Synthesis, structure, DNA/BSA binding and antibacterial studies of NNO tridentate Schiff base metal complexes, *Journal of Molecular Structure*, 1149 (2017) 727-735.
- [55] Gacki M., Kafarska K., Pietrzak A., Glowniak I.K., Wolf W.M., Synthesis, characterization, crystal structure and biological activity of metal(II) complexes with theophylline, *J. Saudi Chem. Soc.*, 23 (3) (2019) 346-354.
- [56] Haribabu J., Sabapathi G., Tamizh M.M., Balachandran C., Bhuvanesh N.S.P., Venuvanalingam P., Karvembu R., Water-Soluble Mono- and Binuclear Ru(η^6 -p-cymene) Complexes Containing Indole Thiosemicarbazones: Synthesis, DFT Modeling, Biomolecular Interactions, and In Vitro Anticancer Activity through Apoptosis, *Organomet.*, 37 (8) (2018) 1242-1257.

Chemometric-Based Optimization of Ionic Liquid-Based Dispersive Liquid-Liquid Microextraction for Separation and Preconcentration of Erythrosine from Real Matrices

Adil Elik^{1,a,*}, Nail Altunay^{1,b}¹ Department of Chemistry, Faculty of Science, Sivas Cumhuriyet University, 58140 Sivas, Turkey.

*Corresponding author

Research Article

History

Received: 10/11/2021

Accepted: 16/02/2022

Copyright

©2022 Faculty of Science,
Sivas Cumhuriyet University

ABSTRACT

In this research paper, a simple and economic ionic liquid-based liquid-liquid microextraction (IL-DLLME) procedure was developed to ensure efficient and rapid separation and preconcentration of erythrosine from cosmetic and food samples. Important parameters such as IL volume, temperature, acetone volume, ultrasonic time and pH that may affect the IL-DLLME procedure have been optimized by central composite design (CCD) based on response surface methodology (RSM). The optimum values of IL volume, temperature, acetone volume, ultrasonic time and pH were determined as 440 μL , 35 $^{\circ}\text{C}$, 120 μL , 9 min and 4.2, respectively. Using these optimum conditions, some analytical data obtained for erythrosine were listed below. Working range, limit of detection and enrichment factor were 2-400 ng mL^{-1} , 0.65 ng mL^{-1} and 79, respectively. The relative standard deviation (RSD%) was 2.4% for 50 ng mL^{-1} of erythrosine. The recovery obtained in the analysis of real samples was in the range of 93.2-108.5%. The analytical data obtained showed that the IL-DLLME procedure was successfully applied to the selected samples.

Keywords: Chemometric optimization, Erythrosine, Ionic liquid, Microextraction, Real matrices.^a elik@cumhuriyet.edu.tr^b <https://orcid.org/0000-0002-3942-4711>^b naltunay@cumhuriyet.edu.tr ^b <https://orcid.org/0000-0001-9053-7570>

Introduction

Food dyes, which constitute an important group among food additives, are used in industry for various purposes such as protecting, increasing or modifying the desired and typical existing color, standardizing the appearance by controlling color change and deterioration, adding decorative features, and creating new products [1,2]. Erythrosine is included in the class of xanthine dyes, containing ortho-iodinated phenony groups, in foods (sweets, non-fat confectionery, bakery products, puddings, flavored biscuits and wafer creams, frozen canned crayfish and shrimp, flavored milks, chewing gums, instant jelly mixes, beverage powders, ice products and cookies), pharmaceuticals (tablets and toothpastes) and cosmetics, it is a paint with photoluminous properties, temporarily approved by Food and Drug Administration (FDA) [3-5]. World Health Organization (WHO) and the FDA has recommended an acceptable daily dose of 100 ppm for this dye [6]. It is known that taking more than this dose creates toxic effects for human health [7]. Therefore, it is important to develop accessible, fast and inexpensive methods for monitoring erythrosine in food and cosmetic samples.

Capillary electrophoresis with laser-induced fluorescence detection [8], UV/VIS spectrophotometry [9], cyclic voltammetry [10], ultra-fast liquid chromatography-tandem quadrupole mass spectrometry [11] and high performance liquid chromatography with photo-diode array detector [12] have been used for the determination of erythrosine in different samples. Due to

low detection limit of instruments and matrix effect of real samples, separation and preconcentration procedures such as shaking-based ionic liquid dispersive liquid phase microextraction [13], ultrasonic assisted supramolecular solvent-based dispersion solidification liquid-liquid microextraction [14], ultrasonic-assisted cloud point microextraction [15,16] and magnetic solid phase extraction [17] are necessary for the accurate and sensitive determination of food dyes.

Liquid-liquid extraction methods using organic solvents have disadvantages such as time consuming, consuming large amounts of toxic solvents and solvent evaporation steps [18]. For these reasons, the use of ionic liquids with features such as environmentally friendly, inexpensive, effective phase separation and low steam pressure is becoming widespread in microextraction studies [19,20]. One of the most popular microextraction methods is the dispersive liquid liquid microextraction (DLLME) procedure. DLLME consists of two steps; (1) extraction into the aqueous sample containing the analyte and injection of a suitable mixture of dispersive solvents. In this step, the extraction solvent is well dispersed in the aqueous sample as droplets and the analyte is enriched in it. The large surface area between the extraction solvent and the aqueous sample is achieved, the equilibrium state is quickly reached, and the extraction is time-independent. This is the most important advantage of the method. (2) after centrifugation of the cloudy solution,

the analyte in the precipitated phase is determined by an analytical instrument.

It is necessary to optimize important parameters in microextraction studies. In addition to the disadvantages of traditional univariate optimization approaches such as time consuming and excessive chemical consumption, possible interactions between variables are not taken into account. therefore, an accurate, precise and effective optimization step may not be provided [21]. Therefore, chemometric-based statistical optimization approaches have been frequently used in the optimization step in recent years. These approaches provide significant advantages such as less chemical consumption and fewer experiments required [22].

This study was aimed at developing and validating a fast, selective and sensitive liquid-based liquid-liquid microextraction (IL-DLLME) procedure to separate and preconcentrate erythrosine from foods and cosmetics samples for the determination by UV-VIS spectrophotometer. The IL-DLLME procedure have been optimized by central composite design (CCD) based on response surface methodology (RSM). These results show that the optimized IL-DLLME procedure has the potential to be used as one of the alternatives to conventional analytical methods for determination and extraction of erythrosine from real samples.

Materials and Methods

Reagents

Unless stated otherwise, all chemicals studied were of analytical purity. A stock erythrosine was purchased from Sigma–Aldrich (St. Louis, MO, USA). Working and calibration solutions were daily prepared by diluting this stock solution with water. Dispersive solvents including methanol, ethanol, acetonitrile, tetrahydrofuran and acetone were purchased from Merck (Darmstadt, Germany). 1-octyl–3–methylimidazolium hexafluorophosphate ([OMIM][PF₆]) (as extraction solvent) was bought from Sigma–Aldrich. For pH adjustments in optimization studies, buffer solutions such as acetate, borate, citrate and phthalate were used. To minimize all possible contamination, a diluted HNO₃ solution was used to wash the glassware and finally rinsed with distilled water.

Apparatus

The quantification measures were performed using an UV–VIS Spectrophotometer (Shimadzu UV-1800 PC model, Kyoto, Japan) equipped with 10 mm quartz cuvette. Ultrasonic bath (Kudos, Shanghai, China), centrifuge (Hettich Universal-320 model, Germany) and digital pH-meter (JP Selecta model, Barcelona, Spain) were used to prepare the selected samples, provide phase separation and adjust the pH of the sample solutions, respectively.

Sampling

In this study, two different sample groups including foods and cosmetics were investigated. All samples were collected from supermarkets in Sivas, Turkey. Cherry juice,

pomegranate juice, strawberry juice, pastry cream, jole, and turnip juice were selected as food samples. In addition, lipstick, hair dye, shower gel, and hand cream were chosen as cosmetic samples. Appropriate 0.5 g amounts of the samples were dissolved in the water, filtered, and completed to volume in 50-mL centrifugal tests including 10 mL ethanol. The mixture was stirred in the shaker for about 2 h, as in the case of sausage, to transfer the erythrosine into the ethanol phase. For complete dissolution, the samples were warmed for 5 min and filtered before use. 10 mL of sample solution were then treated using the optimized IL-DLLME procedure for the determination and extraction of erythrosine [5, 23].

Optimization Strategy

A central composite design (CCD) based on response surface methodology (RSM) was created for the optimization of important parameters that may affect the IL-DLLME procedure planned to be developed. After preliminary trials, five parameters (IL volume, temperature, dispersive solvent volume, ultrasonic time and pH) affecting the extraction of erythrosine were determined. A five-variable and three-level CCD was created to optimize these selected parameters effectively and quickly. Design-Expert® trial version 12.0.1. (Stat-Ease Inc., Minneapolis) was used as CCD software. In the CCD design, IL volume, dispersive solvent volume (acetone), temperature, ultrasonic time and pH were symbolized as X₁, X₂, X₃, X₄ and X₅, respectively. In addition, the levels, units and codes of the optimized parameters are given in Table 1.

Table 1. Codes, units, and levels of variables in chemometric-based CCD design

Parameters	Symbol	Unit	Levels		
IL volume	X ₁	μL	50	250	450
Temperature	X ₂	°C	25	40	55
Acetone volume	X ₃	μL	100	500	600
Ultrasonic time	X ₄	min	1	6	11
pH	X ₅		3	6	9

Optimized IL-DLLME Procedure

In this study, 10 mL of sample solution containing the erythrosine at a concentration of 50 ng mL⁻¹ was poured into a centrifugal test tube and the solution pH was adjusted at 4.2 using an acetate buffer solution. Afterwards, 440 μL of [OMIM][PF₆] as extraction solvent was quickly injected into the sample solution. 120 μL of acetone was then added as the dispersing solvent. Following this, the tube was placed in an ultrasonic bath and sonicated for 9 min at 35 °C. The mixture was centrifuged for 5 min at 4000 rpm and then the aqueous phase was thrown away. The final volume of the remaining phase was made up to 500 μL with acetone. Finally, measurements were made using a UV-VIS spectrophotometer at 526 nm. All studies were carried out with the sample blank to exclude possible changes in absorbance from the reagents.

Results and Discussion

Optimization of Parameters in IL-DLLME Step

After preliminary studies, a chemometric-based CCD design was created for five parameters (X1, X2, X3, and X4) affecting the separation and preconcentration of erythrosine. The design results, which include the experimental value and prediction values found as a result of the application of this design, are presented in Table 2. From the results, it is seen that there is no significant difference between the experimental data and the

prediction data of the model. The statistical evaluation of these results is explained in detail below.

Statistical analysis

ANOVA analysis of the experimental data in Table 2 was performed with the CCD statistical program [24,25]. Here, the significance or no significance levels of the microextraction parameters and their interactions are determined. First of all, the p-value must be less than 0.05 for the model to be significance. This explanation is valid for all linear, binary and quadratic interactions.

Table 2. Experimental and estimated values obtained as a result of application of CCD design

Run	X1	X2	X3	X4	X5	Experimental Recovery(%)	Prediction Recovery(%)
1	250	55	350	6	6	65.1	65.56
2	250	40	350	6	6	70.4	70.53
3	250	40	350	6	6	69.7	70.53
4	450	25	600	1	9	52.1	52.15
5	450	25	100	11	9	91.2	91.16
6	50	55	100	11	9	82.7	82.63
7	450	40	350	6	6	70.1	70.47
8	50	25	600	1	3	96.7	96.80
9	250	40	350	6	3	71.2	71.37
10	50	25	100	1	9	76.2	76.28
11	250	40	350	1	6	71.1	70.96
12	450	55	600	1	3	56.7	56.65
13	50	25	600	11	9	85.3	85.34
14	250	40	100	6	6	77.2	77.41
15	450	55	100	11	3	96.8	96.66
16	450	25	100	1	3	87.1	87.11
17	250	40	350	11	6	71.2	71.59
18	50	55	600	11	3	41.9	41.85
19	250	40	600	6	6	63.8	63.83
20	250	40	350	6	6	71.5	70.53
21	50	55	600	1	9	84.2	84.22
22	50	55	100	1	3	70.4	70.39
23	250	40	350	6	6	71.5	70.53
24	50	40	350	6	6	75.2	75.08
25	250	40	350	6	9	71.9	71.98
26	450	25	600	11	3	67.2	67.17
27	450	55	600	11	9	56.9	56.80
28	450	55	100	1	9	69.2	69.14
29	50	25	100	11	3	76.2	76.21
30	250	25	350	6	6	75.0	74.79

Statistical data are presented in Table 3. When the results in Table 3 are evaluated, it is seen that the p-value of the model is much smaller than 0.05. Therefore, it is concluded that the established model has meaning. When the same evaluation is made for other interactions, it is seen that only the p-value of X₄, X₅, X₂², X₃² and X₄² interactions is greater than 0.05. F-values should be considered while evaluating the contribution to the established design. The numerical magnitude of the F-value indicates that the model contribution is large. In the light of this explanation, the

parameters that contribute the most to linear, binary and quadratic interactions are X₃ (F-value: 2251.26) X₁X₃ (F-value: 812.25) and X₁² (F-value:12.39), respectively. R values (R₂, Adjusted R² and Predicted R²) are examined for validation of statistical data. Here, it is desirable that the R²-value be numerically close to 1 and to each other. In addition, for statistical reliability of the results, the difference between Adjusted R² and Predicted R² values should be less than 0.2. When the data in Table 3 is analysed, it is seen that the values of R², Adjusted R² and Predicted R² are 0.9992, 0.9975 and

0.9860, respectively. It can be said that this is in accordance with the above explanations. High agreement of R² values indicates high agreement between experimental values and

predicted values of the model. The quadratic model presented the following equation for the recovery of erythrosine.

$$Recovery (\%) = +70.53 - 2.31X_1 - 4.62X_2 - 6.79X_3 + 0.3167X_4 + 0.3056X_5 + 2.33X_1 X_2 - 7.12X_1 X_3 + 5.53X_1 X_4 - 5.10 X_1 X_5 - 3.2 X_2 X_3 - 0.6250 X_2 X_4 + 3.10 X_2 X_5 - 5.15 X_3 X_4 + 1.70 X_3 X_5 + 3.95 X_4 X_5 + 2.25 X_1^2 - 0.3536 X_2^2 + 0.0964 X_3^2 + 0.7464 X_4^2 + 1.15 X_5^2$$

Table 3. ANOVA analysis result from CCD for erythrosine

Source	Sum of Squares	df	Mean Square	F-value	p-value	
Model	4244.70	20	212.23	575.93	< 0.0001	significant
X ₁ -IL volume	95.68	1	95.68	259.64	< 0.0001	
X ₂ -Temperature	383.64	1	383.64	1041.08	< 0.0001	
X ₃ -Acetone volume	829.60	1	829.60	2251.26	< 0.0001	
X ₄ -Ultrasonic time	1.80	1	1.80	4.90	0.0542	
X ₅ -pH	1.68	1	1.68	4.56	0.0615	
X ₁ X ₂	86.49	1	86.49	234.70	< 0.0001	
X ₁ X ₃	812.25	1	812.25	2204.17	< 0.0001	
X ₁ X ₄	488.41	1	488.41	1325.38	< 0.0001	
X ₁ X ₅	416.16	1	416.16	1129.32	< 0.0001	
X ₂ X ₃	156.25	1	156.25	424.01	< 0.0001	
X ₂ X ₄	6.25	1	6.25	16.96	0.0026	
X ₂ X ₅	153.76	1	153.76	417.25	< 0.0001	
X ₃ X ₄	424.36	1	424.36	1151.57	< 0.0001	
X ₃ X ₅	46.24	1	46.24	125.48	< 0.0001	
X ₄ X ₅	249.64	1	249.64	677.44	< 0.0001	
X ₁ ²	12.39	1	12.39	33.64	0.0003	
X ₂ ²	0.3070	1	0.3070	0.8332	0.3851	
X ₃ ²	0.0228	1	0.0228	0.0620	0.8090	
X ₄ ²	1.37	1	1.37	3.71	0.0861	
X ₅ ²	3.23	1	3.23	8.76	0.0160	
Residual	3.32	9	0.3685			
Lack of Fit	0.9690	6	0.1615	0.2064	0.9518	not significant
Pure Error	2.35	3	0.7825			
Cor Total	4248.01	29				
R ²	0.9992		Adjusted R ²	0.9975	Predicted R ²	0.9860

Effect of factors

The 3D-surface graphics of the binary interactions of the optimized parameters were drawn by the CCD. In this study, the graphs drawn for the 3 most important interactions (pH-IL volume, temperature-IL volume and acetone-ultrasonic time) were interpreted. Figure 1a shows the effect of the interaction between pH and IL volume on recovery % of erythrosine. Here, it is seen that quantitative recoveries% for erythrosine are obtained in the range of ionic liquid volume 325-425 µL when the pH value is in the acidic region. In the basic region, the recovery was reduced. The possible reason for this decrease may be that the binding sites of the ionic liquid are affected.

The effect of the interaction between ionic liquid and temperature on recovery % of erythrosine is presented in Figure 1b.

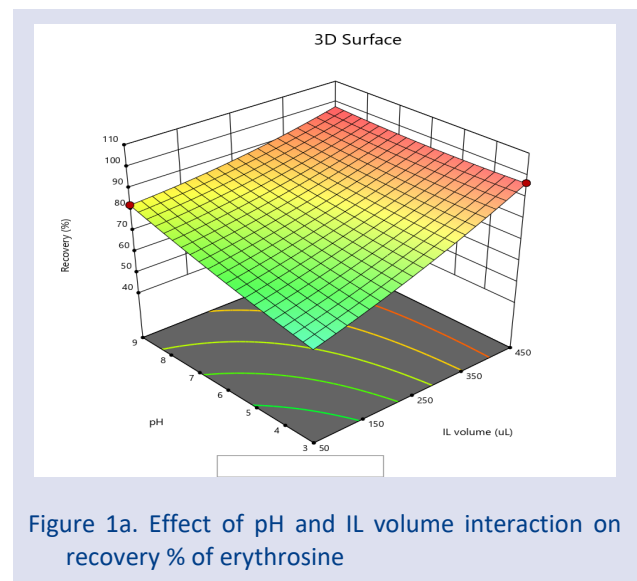


Figure 1a. Effect of pH and IL volume interaction on recovery % of erythrosine

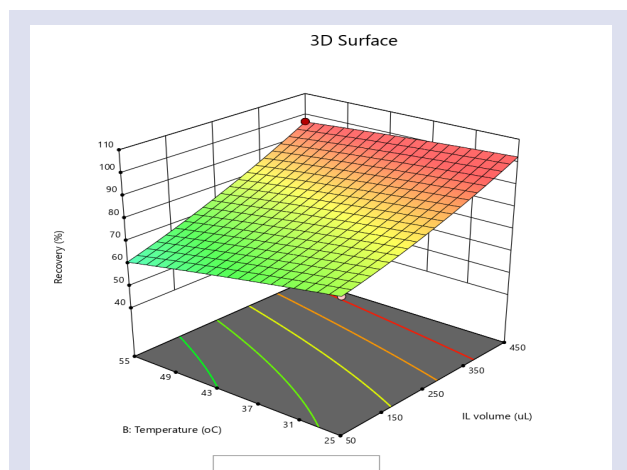


Figure 1b. Effect of temperature and IL volume interaction on recovery % of erythrosine

Here, it can be said that there is a significant decrease in recovery for all ionic liquid volumes above 45 °C. This may be due to a decrease in the separation efficiency of the ionic liquid due to the increase in temperature. For this reason, it is planned to keep the temperature in the works below 45 °C.

The effect of dispersive solvent (acetone) and ultrasonic time on recovery% of erythrosine is presented in Figure 1c. From the related figure, it can be said that the increase in acetone volume does not cause a significant change in recovery, especially above 350 µL. In addition, the best recovery values were obtained in approximately 9 min of ultrasonic time. This shows that the short ultrasonic time is sufficient for the acetone to be effectively dispersed into the sample solution.

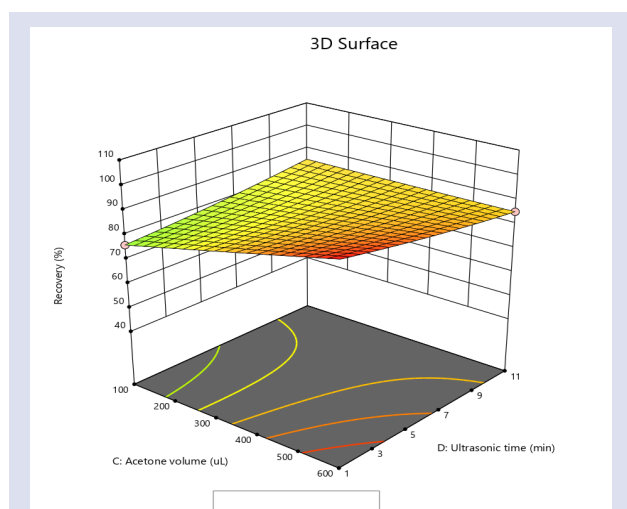


Figure 1c. Effect of acetone and ultrasonic time interaction on recovery % of erythrosine

Optimum conditions

The last step of the chemometric modelling is to determine the optimum conditions of the optimized X1, X2, X3, X4 and X5 parameters. Optimum data for the variables with the highest recovery% for erythrosine were

tested. The optimum values for the parameters X1, X2, X3, X4 and X5 were 440 µL, 35 °C, 120 µL, 9 min and 4.2, respectively, for the estimated recovery of over 90% by the CCD. As a result of the repeated experimental studies carried out, it was seen that the average recovery value was compatible with the predicted value of the model. Therefore, these values were chosen as optimum for the optimized parameters.

Foreign ions effect

Since optimization studies are carried out on model solutions, the effect of foreign ions should be investigated before the analysis of real samples. For this reason, different anions, cations and food dyes were added to the model solutions and then the extraction and determination of erythrosine was performed by applying the optimized method. The recovery% value was calculated for erythrosine in the presence of each foreign ion. As can be seen in the results in Table 4, quantitative recoveries (92.4-103.7%) were obtained in the presence of foreign ions studied, indicating that the optimized IL-DLLME procedure is selective for erythrosine.

Table 4. The effect of some foreign ions on the recovery of erythrosine under optimum conditions

Foreign ions	*Tolerable limit	Recovery (%)
Na(I)	20000	97.4
Mg(II)	20000	97.2
Ca(II)	20000	96.8
C ₂ O ₄ (II)	10000	98.6
SO ₄ (II)	10000	97.1
Fe(II)	10000	98.2
Pb(II)	5000	102.4
Cd(II)	5000	97.8
Sn(II)	5000	101.5
Patent Blue V	1000	96.3
Curcumin	1000	103.7
Azorubine	500	96.2
Tartrazine	500	95.8
Allura Red	250	93.5
Carmine	100	92.4

*[Foreign ions amount]/ [erythrosine amount]

Analytical performance

Under optimal conditions, the analytical performance of the optimized IL-DLLME procedure in terms of working range, limit of detection (LOD), limit of quantification (LOQ), correlation coefficient (R^2), accuracy (as recovery%), precision (as relative standard deviation, RSD%), and enrichment factor were investigated. To investigate the working range of the method, the selected samples were spiked with the erythrosine standard at different concentrations (0.5, 1, 2, 10, 50, 100, 200, 400, 800 and 1000 ng mL⁻¹) and the resulting sample was pretreated with the optimized IL-DLLME procedure before UV-VIS spectrophotometric analysis. As a result, the working range was obtained in the range of 2-400 ng mL⁻¹ with 0.9975 of R^2 . The LOD and LOQ were calculated from the ratio of 3 and 10 times the standard deviation of the

reagent blank to the resulting calibration plot, respectively. The LOD and LOQ was 0.65 ng mL⁻¹ and 2.0 ng mL⁻¹, respectively. The EF value was calculated from the formula below.

$$EF = \text{Slope-1} / \text{Slope-2} \quad (1)$$

Where Slope-1 and Slope-2 were the slope of the calibration graphs obtained before and after applying the optimized IL-DLLME procedure, respectively. The EF was calculated as 79. The accuracy of the optimized IL-DLLME procedure was tested with relative recovery of added selected samples at 20 and 50 ng mL⁻¹ concentrations. The recovery% were ranged from 93.2% to 108.5% (n=3), indicating good reliability and applicability of the optimized IL-DLLME procedure. The precision of the optimized IL-DLLME procedure was tested with RSD%. Intraday precision was tested for three replicate blank analysis of concentrations of 20 and 50 ng mL⁻¹ of erythrosine on the same day, while inter-day precision was tested by analysis of the same concentrations on three consecutive days. In the results of working, the RSD% for intraday precision was in the range of 1.9-3.4%, while the RSD% for interday precision was in the range of 2.2-4.7%. The RSDs% indicate good precision and reproducibility of the optimized IL-DLLME procedure. All results were shown in Table 5.

Table 5. Analytical data of the optimized IL-DLLME procedure using optimum conditions

Analytical parameters	Optimum data
Calibration equation after IL-DLLME	$y = 3.555c + 0.0008$
Calibration equation before IL-DLLME	$y = 0.045c - 0.005$
Working range (ng mL ⁻¹)	2-400
R ²	0.9975
LOD (ng mL ⁻¹)	0.65
LOQ (ng mL ⁻¹)	2.0
Intraday precision	1.9-3.4
Inter-day precision	2.2-4.7
Accuracy (as recovery%), EF	93.2-108.5 79

Real Samples Analysis

The feasibility of the optimized IL-DLLME procedure was tested by applying it to foods (pomegranate juice, strawberry juice, pastry cream, jole, and turnip juice) and cosmetic (lipstick, hair dye, shower gel, and hand cream) samples were investigated. In order to investigate the matrix effect of the optimized IL-DLLME procedure, two standard concentrations (20 and 50 ng mL⁻¹) of the erythrosine were spiked to the selected samples. All measurements were repeated three times. Analysis results of selected samples are given in Table 6. These quantitative recoveries obtained show that the optimized IL-DLLME procedure has low matrix effect. Therefore, the

optimized IL-DLLME procedure can be reliably applied to the extraction and determination of erythrosine from the analyzed samples. Finally, the amounts of erythrosine in the samples were given in detail in Table 6 along with their RSD%.

Table 6. The results of applying the optimized IL-DLLME procedure to selected samples

Sample	Spiked (ng mL ⁻¹)	Found (ng mL ⁻¹)	Recovery (%)
Pomegranate	-	11.2±0.7	-
	20	30.7±1.1	97.4
	50	60.6±2.3	98.9
Juice	-	24.9±0.9	-
	20	43.9±1.5	95.3
	50	73.3±2.7	96.8
Strawberry juice	-	Nd*	-
	20	20.8±1.4	104.0
	50	50.9±1.9	101.8
Pastry cream	-	Nd	-
	20	18.9±0.8	94.6
	50	48.5±2.2	97.0
Jole	-	37.6±2.0	-
	20	56.2±2.7	93.1
	50	85.6±2.9	96.0
Turnip juice	-	Nd	-
	20	20.5±1.3	102.5
	50	50.8±2.0	101.6
Lipstick	-	121.6±5.7	-
	20	141.1±7.2	97.3
	50	170.8±8.3	98.3
Hair dye	-	159.2±6.4	-
	20	180.9±9.5	108.5
	50	211.3±11.8	104.2
Shower gel	-	7.4±0.5	-
	20	26.4±1.1	94.9
	50	55.8±2.3	96.8
Hand cream	-	Nd	-
	20	20.9±0.9	104.5
	50	51.3±1.8	102.6

*could not be determined

Comparison of the Optimized Procedure with the other Reported Methods

Some analytical properties such as working range, LOD, RSD, EF and recovery% of the optimized IL-DLLME procedure were compared with other extraction procedures and detection techniques reported in the literature. Comparison data were made with publications in references (see Table 7). When the relevant publications were examined, it can be said that the optimized IL-DLLME procedure has a higher EF and wider working range than similar determination techniques. It also appears that the proposed method exhibits high precision and low RSD over expensive techniques. From these results it is clear that the optimized IL-DLLME procedure exhibits significant advantages over the compared methods.

Table 7. Comparison of the proposed method with similar analytical methods

Analytical methods	Working range (ng mL ⁻¹)	LOD (ng mL ⁻¹)	RSD (%)	EF	Recovery (%)	Refs.
HIH-LLME-UV-VIS	30-1400	6	≤2.9	37.5	95-101	[5]
UA-SUPRA-MSLLME-UV-VIS	1-100	0.6	≤1.4	142	91-103	[14]
DES-UA-LLME-UV-VIS	0.05–0.25	3.75	≤4.6	40	90-100	[26]
CPE-UV-VIS	30-3000	22	≤3.27	15	-	[27]
VA-DES-DLLME-HPLC	0.5–500	0.1	≤5.6	95	96.8-99	[28]
HP-TLC	20-200 ng/zone	9.8 ng/zone	≤2.7	35	98-101	[29]
IL-DLLME-UV-VIS	2-400	0.65	≤4.7	79	93.2-108.5	Proposed method

HIH-LLME: Heat-induced homogeneous liquid-liquid microextraction, UA-SUPRA-MSLLME: ultrasonic assisted supramolecular solvent based dispersion solidification liquid-liquid microextraction, UA-LLME: Deep eutectic solvent ultrasound assisted liquid-liquid microextraction, CPE: Cloud point extraction, VA-DES-DLLME: Vortex assisted deep eutectic solvent dispersive liquid-liquid microextraction, HP-TLC: high performance thin-layer chromatography

Conclusions

Herein, a simple and economic dispersive liquid-liquid microextraction (DLLME) based on ionic liquid (IL) procedure for the extraction, separation and preconcentration of erythrosine from foods and cosmetics has been optimized using a central composite design (CCD) based on response surface methodology (RSM). In this study, the [OMIM][PF6] (as extraction solvent) and acetone (as dispersive solvent) were used for the extraction of erythrosine for the first time. The optimized IL-DLLME procedure has some advantages including simple, fast, green and economic. As a result of the analysis of the selected samples, it was seen that the optimized method has low matrix effect, high accuracy, wide working range and good sensitivity. These results show that the optimized IL-DLLME procedure has the potential to be used as one of the alternatives to conventional analytical methods for determination and extraction of erythrosine from real samples.

Conflicts of interest

No conflict of interest or common interest has been declared by the authors.

References

- Gomes K. M. S., Oliveira M. V. G. A. D., Carvalho F. R. D. S., Menezes C. C., Peron A. P., Citotoxicity of food dyes sunset yellow (E-110), bordeaux red (E-123), and tartrazine yellow (E-102) on *Allium cepa* L. root meristematic cells, *Food Science and Technology*, 33(1) (2013) 218-223.
- Yamjala K., Nainar M. S., Ramiseti N. R., Methods for the analysis of azo dyes employed in food industry—a review, *Food Chemistry*, 192 (2016) 813-824.
- Lakdawalla, A. A., Netrawali, M.S., Mutagenicity, comutagenicity, and antimutagenicity of erythrosine (FD and C red 3), a food dye, in the Ames/Salmonella assay, *Mutation Research/Genetic Toxicology*, 204(2) (1988) 131-139.
- Ryvolová M., Táborský P., Vrábel P., Krásenský P., Preisler J., Sensitive determination of erythrosine and other red food colorants using capillary electrophoresis with laser-induced fluorescence detection, *Journal of chromatography A*, 1141(2) (2007) 206-211.
- Ozkantar N., Yilmaz E., Soylak M., Tuzen M., Separation, enrichment and spectrophotometric determination of erythrosine (E127) in drug, cosmetic and food samples by heat-induced homogeneous liquid-liquid microextraction method, *International Journal of Environmental Analytical Chemistry*, 99(12) (2019) 1135-1147.
- Rubio L., Sanllorente S., Sarabia L.A., Ortiz M.C., Determination of cochineal and erythrosine in cherries in syrup in the presence of quenching effect by means of excitation-emission fluorescence data and three-way PARAFAC decomposition, *Talanta*, 196 (2019) 153-162.
- World Health Organization. Evaluation of certain food additives: Eighty-sixth report of the joint FAO/WHO expert committee on food additives, World Health Organization, 965 (2019).
- Rubio L., Sanllorente S., Sarabia L. A., Ortiz M.C., Determination of cochineal and erythrosine in cherries in syrup in the presence of quenching effect by means of excitation-emission fluorescence data and three-way PARAFAC decomposition, *Talanta*, 196 (2019) 153-162.
- Hassan M., Uzcan F., Alshana U., Soylak, M., Switchable-hydrophilicity solvent liquid-liquid microextraction prior to magnetic nanoparticle-based dispersive solid-phase microextraction for spectrophotometric determination of erythrosine in food and other samples, *Food Chemistry*, 348 (2021) 129053.
- Nayak D. S., Shetti, N. P., A novel sensor for a food dye erythrosine at glucose modified electrode, *Sensors and Actuators B: Chemical*, 230 (2016) 140-148.
- Chen X.H., Zhao Y.G., Shen H.Y., Zhou L.X., Pan S.D., Jin M.C., Fast determination of seven synthetic pigments from wine and soft drinks using magnetic dispersive solid-phase extraction followed by liquid chromatography-tandem mass spectrometry, *Journal of Chromatography A*, 1346 (2014) 123-128.
- Ma K., Yang Y.N., Jiang X.X., Zhao M., Cai Y.Q., Simultaneous determination of 20 food additives by high performance liquid chromatography with photo-diode array detector, *Chinese Chemical Letters*, 23(4) (2012) 492-495.
- Wu H., Guo J.B., Du L.M., Tian H., Hao C. X., Wang Z.F., Wang J.Y., A rapid shaking-based ionic liquid dispersive liquid phase microextraction for the simultaneous determination of six synthetic food colourants in soft drinks, sugar-and gelatin-based confectionery by high-performance liquid chromatography, *Food Chemistry*, 141(1) (2013) 182-186.

- [14] Shokrollahi A., Pili H.B., Doust K.H., Microspectrophotometric determination of erythrosine in beverage and water samples after ultrasonic assisted supramolecular-based dispersion solidification liquid-liquid microextraction, *Journal of Analytical Chemistry*, 72(6) (2017) 617-623.
- [15] Meral S., Elik A., Ultrasonic-assisted cloud point microextraction and spectrophotometric determination of Ponceau 4R in various beverage samples using Non-ionic surfactant PONPE 7.5, *Food Additives & Contaminants: Part A*, 38(4) (2021) 573-585.
- [16] Elik A., Interference-free determination of carmine in food samples using ultrasonic assisted cloud point extraction coupled with spectrophotometry, *Cumhuriyet Sci. J.*, 40(2) (2019) 305-316.
- [17] Emiroğlu E., Yuvalı D., Sarp G., Yılmaz E., Narin İ., Magnetic solid phase extraction of erythrosine (E127) in pharmaceutical samples with Fe₃O₄/C-nanodots hybrid material prior to spectrophotometric analysis, *Microchemical Journal*, 170 (2021) 106766.
- [18] Canales R.I., Brennecke J.F., Comparison of ionic liquids to conventional organic solvents for extraction of aromatics from aliphatics, *Journal of Chemical & Engineering Data*, 61(5) (2016) 1685-1699.
- [19] Yu H., Merib J., Anderson J. L. (2016). Faster dispersive liquid-liquid microextraction methods using magnetic ionic liquids as solvents, *Journal of Chromatography A*, 1463 (2016) 11-19.
- [20] Nawafa J., Dawidziuk B., Dzedzic D., Gordon D., Popiel S., Applications of ionic liquids in analytical chemistry with a particular emphasis on their use in solid-phase microextraction, *TrAC Trends in Analytical Chemistry*, 105 (2018) 18-36.
- [21] Elik A., Demirbaş A., Altunay N., Experimental design of ligandless sonication-assisted liquid-phases microextraction based on hydrophobic deep eutectic solvents for accurate determination of Pb (II) and Cd (II) from waters and food samples at trace levels, *Food Chemistry*, 371 (2021) 131138.
- [22] Altunay N., Elik A., Unal Y., Kaya S., Optimization of an ultrasound-assisted alcohol-based deep eutectic solvent dispersive liquid-phase microextraction for separation and preconcentration of quercetin in wine and food samples with response surface methodology, *Journal of Separation Science*, 44(9) (2021) 1998-2005.
- [23] Nambiar A.P., Sanyal M., Shrivastav P.S., Performance evaluation and thermodynamic studies for the simultaneous cloud point extraction of erythrosine and tartrazine using mixed micelles in food samples, *Food Analytical Methods*, 10(10) (2017) 3471-3480.
- [24] Stalikas C., Fiamegos Y., Sakkas V., Albanis T., Developments on chemometric approaches to optimize and evaluate microextraction, *Journal of Chromatography A*, 1216(2) (2009) 175-189.
- [25] Mousavi L., Tamiji Z., Khoshayand M.R., Applications and opportunities of experimental design for the dispersive liquid-liquid microextraction method—A review, *Talanta*, 190 (2018) 335-356.
- [26] Yuvalı D., Seyhaneyildizi M., Soylak M., Narin İ., Yılmaz E., An environment-friendly and rapid liquid-liquid microextraction based on new synthesized hydrophobic deep eutectic solvent for separation and preconcentration of erythrosine (E127) in biological and pharmaceutical samples, *Spectrochimica Acta Part A: Molecular and Biomolecular Spectroscopy*, 244 (2021) 118842.
- [27] Shokrollahi A., Zarghampour, F., Determination of erythrosine in food samples by CPE-scanometry as a new method and comparison with spectrophotometric results, *Analytical and Bioanalytical Chemistry Research*, 3(2) (2016) 159-168.
- [28] Faraji M., Determination of some red dyes in food samples using a hydrophobic deep eutectic solvent-based vortex assisted dispersive liquid-liquid microextraction coupled with high performance liquid chromatography, *Journal of Chromatography A*, 1591 (2019) 15-23.
- [29] Nambiar A.P., Sanyal M., Shrivastav, P.S., Simultaneous densitometric determination of eight food colors and four sweeteners in candies, jellies, beverages and pharmaceuticals by normal-phase high performance thin-layer chromatography using a single elution protocol, *Journal of Chromatography A*, 1572 (2018) 152-161.

Blending Effect of Maleic Anhydride-Styrene-Methyl Methacrylate Terpolymer on Polyvinylchloride (Pvc)/Polystyrene (Ps) Mixtures

Ersen Yilmaz ^{1,a,*}

¹ Department of Mechanical and Metal Technology, Tunceli Munzur University, 62100, Tunceli, Turkey

*Corresponding author

Research Article

History

Received: 20/10/2021

Accepted: 28/02/2022

Copyright



©2022 Faculty of Science,
Sivas Cumhuriyet University

chemer80@gmail.com

<https://orcid.org/0000-0002-8567-1668>

ABSTRACT

The blending effect of poly maleic anhydride-styrene-methyl methacrylate (MA-St-MMA) terpolymer on non-miscible PVC and Polystyrene was studied depending on their thermomechanical properties. Depending on the amount of the synthesized and used compatibilizer the tensile strength, modulus, and thermomechanical properties of the blends are enhanced. The unmodified and blends with small amounts of compatibilizer exhibit two-step degradation whereas those containing 6, 8 and 10 percent compatibilizer showed a single glass transition (T_g). All the results reveal that PS/PVC mixtures modified with MA-St-MMA have superior mechanical properties and phase adhesions than mixtures without terpolymer.

Keywords: Polymer blend, Compatibilization, Maleic anhydride, Poly vinylchloride, Polystyrene, Terpolymer

Introduction

From an economic point of view, polymer blending is an important scientific activity because this technique sometimes allows the creation of technical plastics with superior properties. However, for thermodynamic reasons, many polymers do not mix homogeneously at molecular-scale without a suitable compatibilizer. Factors preventing homogeneous mixing are phase separations and interfacial tensions between the two polymers. One of the ways to refine the phase separation morphology of blends composed of two polymers is by adding a compatibilizer [1]. There are many successful studies in which polymer pairs are blended by adding a maleic anhydride based co- or terpolymers as compatibilizers [2-6]. In immiscible binary polymer systems, co- or terpolymers containing maleic anhydride and styrene often act as excellent compatibilizers. In immiscible resins, if such a compatibilizer is used, polar maleic anhydride adds stiffness, thermal stability, and chemical activity to the system, while non-polar styrene contributes to the ease of processing [7, 8]. Polymer mixtures are usually prepared by extruders, banbury mixers, and solution casting.

Due to the synthesizable amount of compatibilizer used in this study, solution casting method was preferred in order to produce test specimens in sufficient quantity. By using the common solvent determined in the study, it was possible to obtain the desired polymer mixtures via solution casting.

Materials and Methods

Apparatus

In the study, DSC measurements were recorded by Shimadzu DSC instrument at a heating rate of 10°C/min under

nitrogen atmosphere. Thermomechanical analysis (TMA) was conducted on Perkin Elmer Pyris Diamond DMTA instrument at penetration mode. The storage (E') and loss ($\tan \delta$) moduli were measured at a heating rate of 5°C/min under nitrogen. All experiments were done on solution cast films.

Chemicals

A commercially available PS compounding grade, and PVC powder with 57 % chlorine content were purchased from PETKIM (Turkey) and used as provided. Maleic anhydride (MA), Styrene (St), and Methyl methacrylate (MMA) and benzoyl peroxide used in the synthesis of MA-St-MMA terpolymer were at analytical grade and Sigma-Aldrich brand. All of the organic solvents used are analytical grade and are Sigma-Aldrich brand.

Synthesis of MA-St-MMA Terpolymer

The terpolymer agent was synthesized according to protocols previously used in our laboratory [9]. The three monomers in molar ratios of 2:1:1 were allowed to react in a glass flask. The volume of the triple mixture prepared as 14.7 g MA 1.5 mol. (dm³)⁻¹, 8,59 mL St 0.75 mol. (dm³)⁻¹ and 7,51 g MMA 0.75 mol. (dm³)⁻¹ was completed to 100 mL with 2-butanone solvent and complete dissolution was achieved. 0.15% by mole Benzoyl peroxide was added and the mixture was reacted at 70 °C for 3 hours. The resulting viscous solution was transferred to a glass beaker and treated with excess ethanol. The precipitated resin was washed 5 times with ethanol. Then placed in a vacuum oven and left to dry at 35 °C.

Co-solvent Determination

Solubility tests of immiscible polymer pairs PS and PVC and the terpolymer were performed to determine the co-solvent. For this test, 0.1 grams of each polymer sample was added separately to 10 mL of selected solvents. Thus, solutions with a concentration of 1g/dL were obtained. Each separate solution was left overnight to complete dissolution by diffusing the solvent. Clear solutions were recorded as soluble, turbid solutions as partially soluble, and solutions with residue at the bottom were recorded as insoluble.

Preparation of PVC/PS Blends

Powdered polymers containing equal parts PS and PVC by mass were dissolved in 25 mL THF solvent. 0, 2, 4, 6, 8, and 10 % compatibilizer terpolymer was added to these solutions. These solutions were poured into a petri dish. The solvent was evaporated. Solid mixtures obtained at the bottom of the Petri dish were used as specimens. The samples obtained are given in Table 1.

Table 1. Prepared PS/PVC and compatibilizer blends

PS/PVC C/g.dL ⁻¹	MA-St-MMA % (w/w)					
	0	2	4	6	8	10
1.0	X	X	X	X	X	X

Thermal Studies

The glass transition temperature (T_g) of pure polymers and their blends were recorded at Shimadzu DSC instrument. The calibration were done with an Indium standard and the measurements carried out under continuous nitrogen flow. The weight of the mixtures used in DSC pan was kept as 10 miligram and the heating rate was set at 10 °C/min.

Mechanical Studies

The mechanical studies were conducted using Universal Tensile Machine (UTM). The measurements of the mechanical properties of the stretched specimens were done at 25 °C.

Results and Discussion

Selection of the Common Solvent

The dissolution experiments showed that the co-solvent of the polymers is THF, The findings are given in Table 2.

Table 2. Dissolution data of PVC, PS and MA-St-MMA polymers.

Polymer	THF	Toluene	MEK	DMSO	DMF
PVC	+	±	+	-	+
PS	+	+	±	-	+
MA-St-MMA	+	-	+	±	±

(+) Soluble (-) Insoluble (±) partially Soluble

Characterization of the Synthesized Compatibilizer

When the infrared peaks are read from Figure 1; The peak at 1780 cm⁻¹ and weak peak at 1825 cm⁻¹ are belong to stretching of anhydride carbonyl (C=O) groups. The peak at 1760 cm⁻¹ belongs to vibrations of the methyl methacrylate (C = O) groups. The two peaks appeared between 2900 cm⁻¹ and 2800 cm⁻¹ in the spectrum are belong to stretching vibration of -CH sp³ of the MMA. Again the vibrations of these methyl groups are observed at 1445 cm⁻¹. The both peaks at 705 cm⁻¹ and 870 cm⁻¹ are C-H stretchings of the styrene part.[6] It can be said that the terpolymer used as compatibilizer was successfully synthesized.

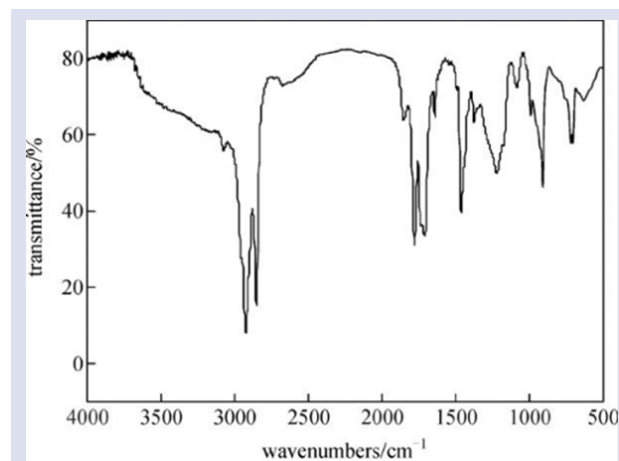


Figure 1. FTIR spectrum of the synthesized MA-St-MMA terpolymer

Thermal Studies

T_g's, obtained from DSC were given at Figure 2. As shown in Fig. 2, two glass transition temperatures were obtained for the blends contained 0, 2 and 4 % MA-St-MMA compatibilizer. The glass transition temperature (T_g) of a polymer blend is often taken as a criterion for determining the miscibility of its components. [10-13] The two T_g's obtained corresponding to their homopolymer glass transitions are due to each component gaining segmental mobility independent of the other as a result of their incompatibility. As can be clearly seen in Figure 2, mixtures with little or no compatibilizer added have two step T_g transitions. However, when the amount of compatibilizer increased and showed its blending effect, specimens showed a single T_g transition. Single T_g's was read for the mixtures with compositions 6, 8 and 10 % MA-St-MMA which refer to compatibility of these blends for these compositions. T_g temperatures read from the DSC thermogram seen in Figure 2; for mixtures where compatibilizer is effective, single and determined as between 88-89 °C.

At Figure 3, it is interesting that in the temperature range of 25-50 °C all the mixture samples expanded and pushed the probe up. It is possible to accept this as an experimental error. However, at later temperatures association of the blending effect of the used compatibilizer particles probably accounts for the decreased penetration. At these temperatures the probe

penetrates the samples at a rate invertedly proportional to their Young modulus' (Fig.4). Again, from Figure 4, as the compatibilizer ratio increases, the Young's modulus, which is a measure of stiffness [14-15], increases.

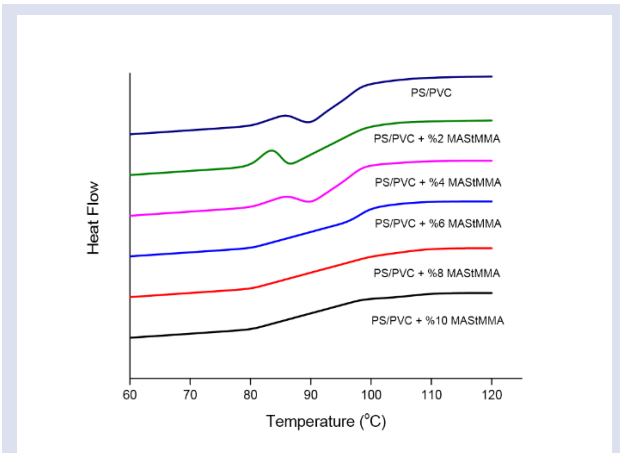


Figure 2. DSC curves of the blends

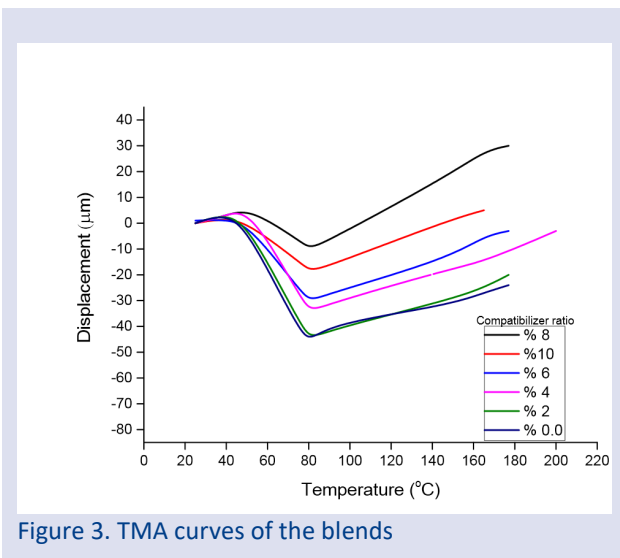


Figure 3. TMA curves of the blends

Mechanical Tests

The addition of MA-St-MMA as compatibilizer for PS/PVC blends increased the tensile strength (Fig. 5), and modulus but reduced the brittleness (Fig. 6). Figure 6 shows typical stress-strain curves of the blends at various compatibilizer compositions.

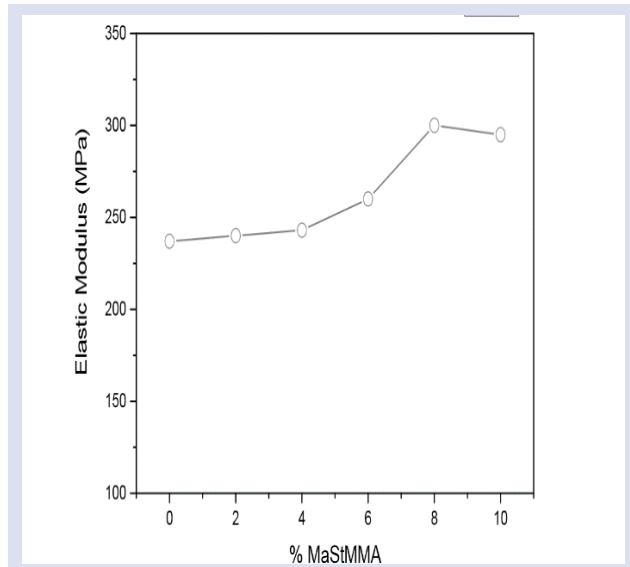


Figure 4. Variation of elastic modulus with compatibilizer rate

With lower MA-St-MMA content, the test specimens of the blends break before reaching the yield point. This clearly demonstrates the high brittleness of unmodified blends. In contrast, 4, 6, 8 and 10 % modified PS/PVC mixtures exhibit ductile behavior; and these samples were not broken before the yield point was reached.

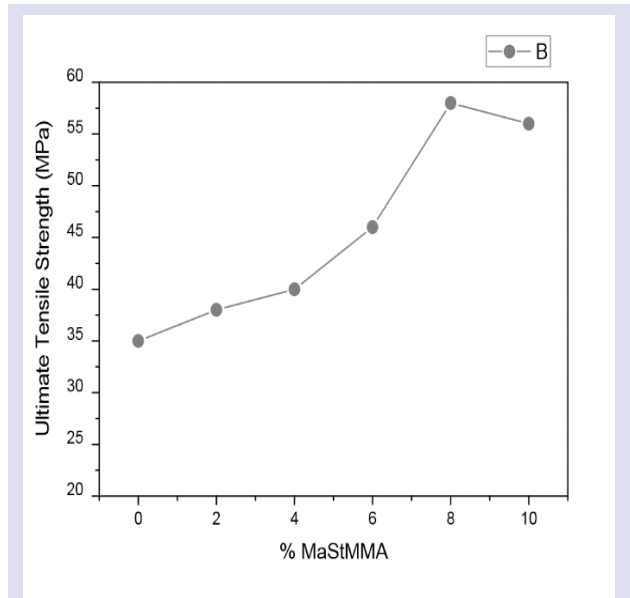


Figure 5. Variation of ultimate tensile strength with compatibilizer rate

When all mechanical findings are evaluated together it can be said that; the terpolymer compatibilizer used, preventing phase separation by acting as a bridge between polymer strands and thus made them miscible, as a result of this increased stiffness, tensile strength and ductile behavior of the blends.

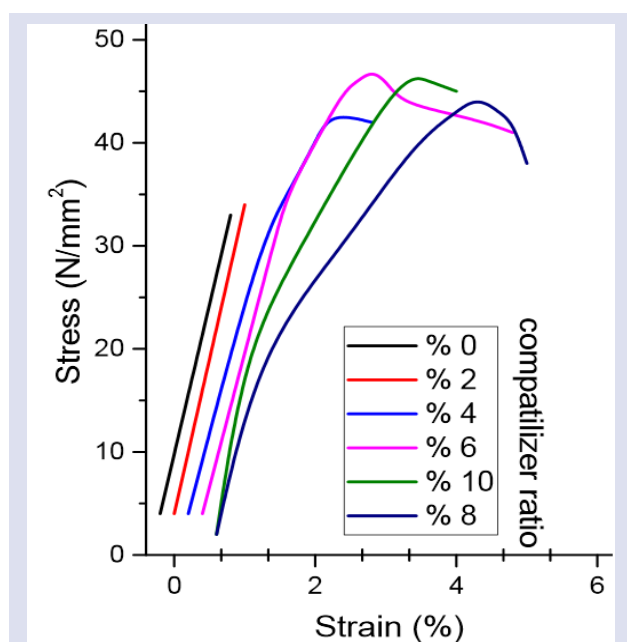


Figure 6. Typical stress-strain behaviour of PS/PVC blends with different compatibilizer ratios

The monomers that the terpolymer is synthesized are shown in Figure 7 below.

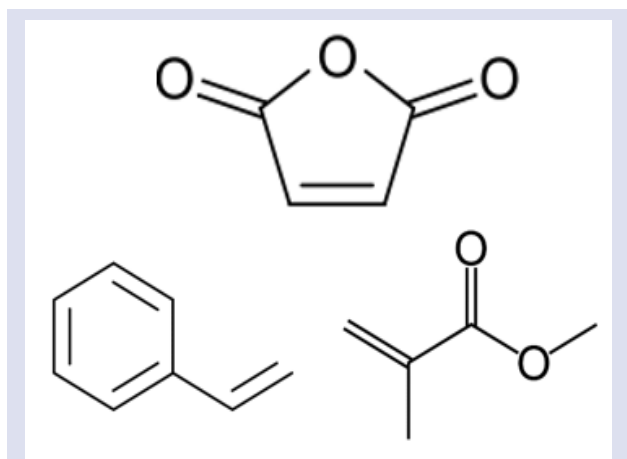


Figure 7. Chemical structures of the terpolymer's monomers (From left to right: MA, St, MMA)

Conclusion

At the end of this study, we showed that the MA-St-MMA terpolymer acts as an effective compatibilizer between polyvinyl chloride and polystyrene. In addition, with this study MA-St-MMA terpolymer not only provided PS/PVC pair mixing, but also improved its thermal and mechanical properties. With the findings it was seen that the thermomechanical properties of the immiscible polystyrene and polyvinyl chloride couple were improved with the compatibilizer used. By this study, it was seen that the terpolymer containing maleic anhydride was a good compatibilizer. Also, using co- or ter-polymers containing reactive polymers such as maleic anhydride to mix immiscible polymers seems to be a viable route.

Finally, it can be stated that, solution casting, and thermomechanical studies, are simple, low-cost and rapid methods which can be used as a useful tests to research the miscibility of polymer blends.

Acknowledgment

The work was supported by MUNIBAP, Reference Grant no MFMUB017-03.

Conflicts of interest

The author state that did not have conflict of interests

References

- [1] Imren D., Boztug A., Yilmaz E., Zengin H.B., Viscometric investigation of compatibilization of the poly(vinyl chloride)/poly(ethylene-co-vinyl acetate) blends by terpolymer of maleic anhydride-styrene-vinyl acetate, *Journal of Molecular Structure*, 891 (2008) 329-332.
- [2] Boztug A., Yilmaz E., Effects of reactive terpolymer containing maleic anhydride on thermomechanical properties of poly(vinyl chloride) based multicomponent blends, *Materials Research Innovations*, 11(3) (2007) 158-160.
- [3] Imren D., Compatibilization of immiscible poly(vinyl chloride) (PVC)/polystyrene (PS) blends with maleic anhydride-styrene-vinyl acetate terpolymer (MAStVA), *Journal of Molecular Structure*, 963 (2010) 245-249.
- [4] Bolayir G., Soygun K., Simsek S, Yilmaz E., Dogan A., Boztug A., Dogan O.M., Effects of the Different Methacrylate Monomers on Bond Strength Between Soft Liner and Acrylic Resin, *Asian Journal of Chemistry*, 25(14) (2013) 8079-80819
- [5] Boztuğ A., Zengin H.B., Basan S., Thermomechanical and thermogravimetric analysis of blends of poly (vinyl chloride)(PVC) with maleic anhydride-allyl propionate copolymer, *Journal of Molecular Structure*, 697 (1-3) (2004) 61-64.
- [6] Boztug A., Preparation and thermomechanical characterization of poly (vinyl chloride) blends compatible with terpolymer-containing maleic anhydride, *J. Appl. Polym. Sci.*, 94 (2004) 1586–1589.
- [7] Aksit A., Menzel T., Aksit M., Altstädt V., Properties of Styrene-Maleic Anhydride Copolymer Compatibilized Polyamide 66/Poly (Phenylene Ether) Blends: Effect of Maleic Anhydride Concentration and Copolymer Content. *Materials (Basel, Switzerland)*, 13(5) (2020) 1237.
- [8] Dharmarajan N., Datta S., Ver Strate G., Ban L., Compatibilized polymer blends of isotactic polypropylene and styrene—maleic anhydride copolymer, *Polymer*, 36(20) (1995) 3849-3861.
- [9] Boztug A., Basan S., The modification and characterization of maleic anhydride-styrene-methyl metacrylate terpolymer by poly(ethylene adipate), *J. Mol. Struct.*, 830 (2007) 126-130.
- [10] Pork J.W., Lm S.S., Miscibility and morphology blends of poly(L-Lactic acid) and poly(vinyl acetate- co-vinyl alcohol), *Polymer*, 44 (2003) 4341-4354.
- [11] Merfeld G.D., Paul D.R., Polymer-polymer interactions based on mean field approximations, In: *Polymer Blend Formulation*, Paul DR, Bucknall CB (Eds). New York: John Wiley, Ch 3, (2000) 55-93.

- [12] Qiu J., Xing C., Cao X., Wang H., Wang L., Zhao L., Li Y., Miscibility and Double Glass Transition Temperature Depression of Poly(l-lactic acid) (PLLA)/Poly(oxymethylene) (POM) Blends, *Macromolecules*, 46 (14) (2013) 5806-5814.
- [13] Aubin M.E., Prud'homme R., Analysis of the glass transition temperature of miscible polymer blends, *Macromolecules*, 21(10) (1988) 2945-2949.
- [14] Hearn E.J., Chapter 1 - Simple stress and strain, Editor(s): E.J. HEARN, *Mechanics of Materials 1*. 3rd. Butterworth-Heinemann, (1997) 1-26.
- [15] Meyers R., *Encyclopedia of Physical Science and Technology*, 3rd ed. California, (2001) 86-92.

Searching for New Natural Inhibitors of Acetylcholinesterase Enzyme

Yasemin Camadan ^{1,a,*}, Ebru Akkemik ^{2,3,b}

¹ Pharmacy Services, Vocational School of Health Services, Artvin Çoruh University, Artvin, Turkey.

² Science and Technology Research and Application Center, Siirt University, Siirt, Turkey.

³ Department of Food Engineering, Faculty of Engineering, Siirt University, Siirt, Turkey.

*Corresponding author

Research Article

History

Received: 17/08/2021

Accepted: 04/03/2022

Copyright



©2022 Faculty of Science,
Sivas Cumhuriyet University

ABSTRACT

Acetylcholinesterase enzyme (AChE) is the enzyme that catalyzes the hydrolysis of the neurotransmitter acetylcholine to choline. Inhibitors of this enzyme (AChE-i) are used to treat Alzheimer's, a neurodegenerative disease. Due to the side effects of the drugs used, there has been an increased interest in investigating the inhibitory potentials of natural products which are presumed to have fewer side effects. For this purpose, the inhibitory effects of highland honey, chestnut honey, royal jelly and the seeds of peach, cherry, plum and apricot on human erythrocyte AChE enzyme was investigated in vitro in the present study. Extracts of the seeds and bee products were prepared in ethanol solvent. In order to determine the inhibitory effect of the extracts, the inhibition concentration (IC₅₀) and K_i values which cause 50% inhibition of the enzyme were calculated using the Ellman method. It was found that among the natural product extracts studied, peach seed had the highest inhibition level (IC₅₀ value 0.05708 mg/ml). IC₅₀ values of highland honey, royal jelly, plum seed and apricot seed were determined as 0.2555 (mg/mL), 0.300 (mg/mL), 0.7049 (mg/mL) and 0.4544 (mg/mL) respectively.

Keywords: Alzheimer', AChE, Inhibition, Bee products, Fruit seeds.

[✉ yaseminc@artvin.edu.tr](mailto:yaseminc@artvin.edu.tr)

[ORCID](https://orcid.org/0000-0002-9000-7761) <https://orcid.org/0000-0002-9000-7761>

[✉ eakkemik@siirt.edu.tr](mailto:eakkemik@siirt.edu.tr)

[ORCID](https://orcid.org/0000-0002-4177-4884) <https://orcid.org/0000-0002-4177-4884>

Introduction

Alzheimer's disease (AD) is the most common form of dementia, which consists of memory loss, cognitive impairment, and difficulty with problem solving and thinking. These symptoms deteriorate over time, becoming severe enough to interfere with daily activities and making the patient need help [1]. Although the etiology of AD is not fully known, according to the cholinergic hypothesis, cognitive and behavioral impairments affecting AD patients are related to a lack of cortical excitability, especially in cholinergic transmission. Acetylcholine levels in the brain can be increased by inhibition of acetylcholinesterase (AChE), thereby improving the cholinergic synapses of AD patients [2].

AD seriously affects the physical and mental health of older people. Aging is the biggest risk factor for the disease, and the incidence doubles every five years after the age of 65 [3]. Today, approximately 50 million people worldwide are affected by neurodegenerative diseases, and this number increases by 10 million each year. About 70% of these patients suffer from AD. This number is estimated to reach 152 million by 2050, and there is currently no treatment to cure neurodegenerative disorders [4].

Acetylcholinesterase (AChE, E.C.3.1.1.7), also called acetylcholine acetylhydrolase, is the carboxylic ester hydrolase which catalyzes the hydrolysis of choline esters [5]. The neurotransmitter hydrolyzes acetylcholine (ACh) and terminates synaptic transmission in cholinergic synapses. Many neurodegenerative diseases such as Alzheimer's and Parkinson's are linked with degeneration

of the cholinergic system, which leads to a reduces neurotransmitters such as acetylcholine [6]. ACh concentration increases by the inhibition of AChE hydrolysis. Thus, inhibition of AChE hydrolysis constitutes an alternative treatment modality. For the treatment of neurodegenerative diseases, AChE inhibitors that can cross the blood-brain barrier, such as rivastigmine, donepezil, tacrine and galantamine, have been successfully used [7].

Since the drugs used as AChE inhibitors have various pitfalls such as poor bioavailability, undesired cholinergic side effects and hepatotoxicity, new compounds either synthetic or from plants are needed to be used as AChE inhibitors [8].

Today, many substances are being investigated as candidate drugs to help slow the rate of both cognitive and functional declines in neurodegenerative diseases such as AD [9]. Since phytochemicals found in plants and vegetables have pharmacological properties such as antioxidants, antiallergics, anti-inflammatory and anticarcinogenic, they are used in the treatment of certain diseases, and their effects have also been investigated in neurological diseases. In previous studies, it was reported that tea, aged garlic extract and ginkgo exhibit protective effects against neurological disorder [10]. In order to investigate the inhibition effects of natural products (bee products such as highland honey, chestnut honey, royal jelly, peach, red cherry, plum and apricot fruits purchased from national companies, and the seeds of these fruits were used) on AChE enzyme associated with

neurodegenerative diseases, were used in the present study. A literature survey revealed no study indicating the inhibition effect of extracts produced from the used material on AChE enzyme.

Honey and bee products have been used in folk medicine since the early years of human history. They were reported to be beneficial in the treatment of gastrointestinal disorders, wounds and burns, to provide protection against acute and chronic gastric lesions and to be effective as antimicrobial agents [11]. Honey, pollen and propolis are highly valuable bee products. The composition of these products is quite variable and depends on many bio-geographical factors such as plant species, climate, environmental conditions and beekeeper contribution [12]. Studies with honey indicate that it has antioxidant, antimicrobial, antiviral, anticancer and antidiabetic properties, and has protective activities on the nervous, cardiovascular, gastrointestinal and respiratory systems [13]. In addition to being a food source, royal jelly also increases the resistance of bees to diseases and pests. It is also an important food for human health. It was reported to have many pharmacological activities such as life-prolonging, antiallergic, anti-inflammatory, antihypercholesterolemic, antihypertensive and anti-inflammatory effects [14].

Various epidemiological studies showed that a diet rich in fruits and vegetables can reduce the incidence of noncommunicable diseases such as cardiovascular diseases, diabetes, cancer and stroke. These protective effects are in part attributed to phenolic secondary metabolites [15]. In addition to being an important source of antioxidants, fruits and vegetables have a significant antioxidant potential for the compounds in their seeds [16]. Anticholinergic, antidiabetic and antimicrobial effects were reported for fruit seed oils and different fruit seed extracts [17]. Thus, fruit seeds seem to have a very important potential in terms of health. However, the effects of peach (*Prunus persica* L.), apricot (*Prunus armeniaca* L.), plum (*Prunus cerasifera* Ehrh) and cherry (*Prunus avium* L.) fruit seeds on AChE enzyme have not been investigated so far.

Peach (*Prunus persica* L.) seeds extracts, one of the seed extracts used in the present study, contains many secondary metabolites such as phenolic compounds, carotenoids and tocopherols, which show biological activity and are considered to be disease-preventing [18]. Apricot (*Prunus armeniaca*) fruit, on the other hand, has antioxidant and anti-inflammatory functions [19]. Plums (*Prunus cerasifera* Ehrh) and cherry (*Prunus avium* L.) fruits are rich in bioactive compounds such as phytochemicals, flavonoids, vitamins A, C, E, anthocyanins, carotenoids and phenolic compounds, which are also considered beneficial for the health [20,21]. Due to the undesirable side effects of the drugs used and the narrow range of therapeutic effects, new AChE inhibitors are needed. To this end, there has been an increasing interest in candidate natural compounds. Based on the effects of certain natural compounds on activities of neural neurotransmitters in the nervous system, the present

study aimed to investigate the potential of various bee products and fruit seeds on AChE enzyme *in vitro*.

Materials and Methods

Chemicals

5,5'-dithio-bis(2-nitrobenzoic acid) (DTNB), AChE from human erythrocytes (50 UN), acetylcholine iodide, ethylenediaminetetraacetic acid (EDTA), sodium citrate and dimethyl sulfoxide (DMSO) were purchased from Sigma Chem. Co. Other chemicals were obtained from either Sigma-Aldrich (St. Louis, MO, USA) or Merck (Kenilworth, NJ, USA).

Preparation of Honey Extracts

About 5 g of samples were weighed and 100 ml ethanol was added as a solvent. Then, the samples were mixed with a shaker at room temperature for 24 hours. The solution was centrifuged at 10,000 g for 15 minutes to remove suspensions. Supernatant was removed with the help of an evaporator (Heldolph-Heizbad-Hei-VAP-517-61000-00-0). The precipitate was dissolved at the minimum volume of the same solvent and kept at 4°C until used [9,12].

Preparation of Seed Extracts

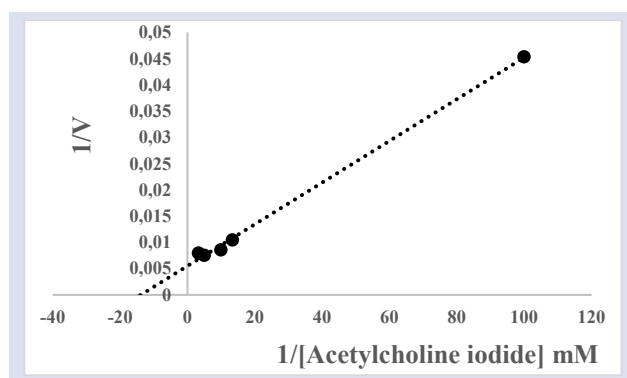
The method described by Velioglu (2007) was used with small modifications depending on laboratory and sample characteristics. A 5 g seed sample was homogenized in 50 mL ethanol using a homogenizer (OVS-VELP Scientifical). Then, the solution was extracted at room temperature in the dark with an orbital shaker for two hours. After filtering from Whatman No.1 filter paper, the mixture was vacuum dried at 40°C using a clear filtrate rotary evaporator (Heldolph-Heizbad-Hei-VAP-517-61000-00-0). The resulting dry crude extract was weighed to calculate extraction efficiency. Then the extract was dissolved in 1 mg/1mL of DMSO and stock solution was prepared. In inhibition studies, extracts were used after dilution with distilled water [22].

Determination of Esterase Activity

Spectrophotometric method described by Ellman et al. (1961) was used with minor modifications to determine the effect of bee products on AChE activity. Hydrolysis of the enzyme which uses acetylcholine iodide (AChI) as substrate produces thiocholine and iodate. The absorption of yellow colored 5-thio-2 nitrobenzoic acid formed by the reaction of thiocholine with 5,5'-dithio-bis(2-nitrobenzoic acid) (DTNB) was measured spectrophotometrically at 412 nm. For the activity measurement, Tris/HCl buffer (1 M, pH: 8.0), sample extracts at different concentrations and human erythrocyte AChE (500 units /mg protein) were added to the reaction. The reaction was allowed for 10 minutes at 25 °C. Finally, acetylcholine iodide (AChI) was added to the reaction and activity measurements were performed [23].

Kinetic Studies

In order to determine the effect of highland honey, chestnut honey, royal jelly and fruit seeds on my AChE enzyme, the activity of the enzyme was measured in five different concentrations of samples (highland honey 0.1315-0.9205 mg/mL, chestnut honey 0.0313-2.191mg/mL, royal jelly 0.0325-0.3900 mg/mL, cherry seed 0.05-0.795 mg/mL, apricot seed 0.05-0.795 mg/mL, plum seed 0.1-1.59 mg/mL, peach seed 0.0112-0.112 mg/mL) mg/mL, in a fixed substrate concentration. The activity of the tube that did not contain sample was used as blank, and its activity was considered 100%. Each experiment was repeated three times. Activity (%)-[I] charts were drawn for each sample to find the IC₅₀ values. IC₅₀ values of the samples were calculated from these charts [24]. Activity measurements were made at five different substrate concentrations to determine the V_{max} and K_m parameters of the enzyme. K_m (0.07272 mM) and V_{max} (181.81 EU) values were calculated by drawing Lineweaver-Burk charts [25].



Using these parameters, the K_i values of the substances were calculated with the following formula [26]:

$$v = \frac{V_{\max}S}{K_m \left(1 + \frac{I}{K_i}\right) + S}$$

In the equation, V_{max} is the maximal speed, K_m is the substrate concentration at which half of the maximum speed is reached, I is the compound concentration, K_i is the inhibition constant, S is the substrate concentration of the substrate. Nonlinear regression was used to calculate the inhibition constant values (K_i) using the equation above.

Results and Discussion

The key role that acetylcholinesterase (AChE) plays on the central nervous system in Alzheimer's disease (AD) encourages research to identify more effective inhibitors and safer drug candidates for the enzyme. However, adverse side effects of AChE inhibitor drugs used in the pharmacological treatment of AD limits their use [27]. Therefore, currently there has been much interest in development of more effective and useful drug candidates.

In the present study, the effect of extracts obtained from natural products on human erythrocyte AChE was investigated in vitro conditions. Extracts of highland honey, chestnut honey, royal jelly and fruit seeds were prepared with ethanol solvent, and their inhibition effects were investigated. IC₅₀ and K_i values of the samples which exerted inhibition effect were calculated (Table 1).

Table 1. Inhibition effects of various natural extracts on AChE enzyme

Sample	Solvent	IC ₅₀ (mg/mL)	K _i (Avg.) (mg/mL)
Highland honey	Ethanol	1.23±0.0077	0.0128±0.0070
Chestnut honey	Ethanol	-	-
Royal jelly	Ethanol	0.397±0.1357	4.22E-06±4.97E-07
Cherry seed	Ethanol	-	-
Plum seed	Ethanol	0.687±0.137	0.095±0.039
Apricot seed	Ethanol	0.460±0.041	0.101±0.033
Peach seed	Ethanol	0.056±0.0037	0.0176±0.0088

IC₅₀ values were 0.2555 mg/mL and 0.3006 mg/ml for ethanol extracts of highland honey and royal jelly, respectively. For chestnut honey, an inhibition effect on the enzyme was observed, but the IC₅₀ value could not be calculated (Table 1, Figure 1). To date, the effects of honey and other bee products were detected only for physiological diseases, while their role in psychological or neurodegenerative diseases is still unknown. Therefore, the effect of bee products on the activity of enzymes attracts the attention of researchers. A study found that the IC₅₀ value of chestnut honey was 41.60 ± 6.05 µg/mL (Galantamine was used as a standard inhibitor for AChE and IC₅₀ value was determined 2.727 ± 0.08 (µg/mL) and it was suggested that bioactive compounds in plants may have inhibitory effects [28]. In different studies found that the extracts of chestnut honey and mad honey had IC₅₀ values ranging from 76 to 129 mg/mL on hyaluronidase enzyme, from 12 to 34 mg/mL on urease enzyme, 1.705 (mg/mL) on hCA I isoenzyme and 2.830 (mg/mL) on hCA II isoenzyme [12, 29]. Akbulut and Akkemik (2018) found that ethanol extracts of highland honey and chestnut had IC₅₀ values ranging from 0.060-2.768 mg/mL on the cancer-related thioredoxin reductase enzyme [9]. It was seen that the results were compatible with our study. Studies of bee products on AChE, a neurotransmitter enzyme, are limited..

The IC₅₀ values of plum, apricot and peach seeds were calculated as 0.7049, 0.4544 and 0.05708 mg/mL, respectively (Table 1). K_i values were in the range of 0.01761-0.1601 (mg/mL). However, IC₅₀ value could not be determined for cherry seed extract because it did not inhibit AChE enzyme activity sufficiently

Although various studies were conducted on the antioxidant, anticancer, antimicrobial, anti-inflammatory effects of fruit seed extracts, studies investigating their effects on enzyme inhibition are limited. Acetylcholinesterase (AChE) and butyrylcholinesterase (BuChE, pseudocholinesterase) enzymes were inhibited by methanolic extracts of grape (*Vitisvinifera* L.) seeds [30]. In studies with *Acacia catechu willd*, *Cola acuminata*, *Cuminum cyminum* and *Lawsonia Inermis* (Henna) seeds, IC_{50} values of seed extracts were found as 204.38 ± 2.54 ($\mu\text{g/mL}$) [31], 14.6 ± 1.04 ($\mu\text{g/mL}$) [32], $0.437\mu\text{g/mL}$ [33] and 66.6 (mg/L) [34] respectively. Similar to the literature, it was observed that selected seed extracts had inhibitory effects on the enzyme activity (Table 1, Figure 2).

As a result of the study, it was observed that natural products showed inhibition against the enzyme at certain ranges, but it was found that the extract obtained from the peach seed exerted the highest inhibition activity (Table 1, Figure 2).

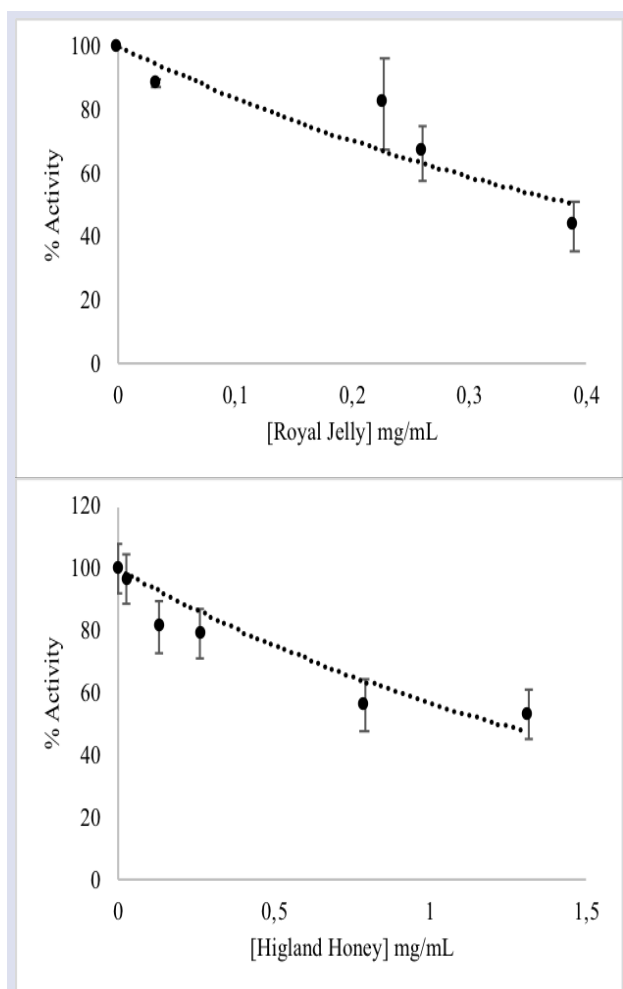


Figure 1. *In vitro* effects of highland honey and royal jelly on AChE enzyme activity

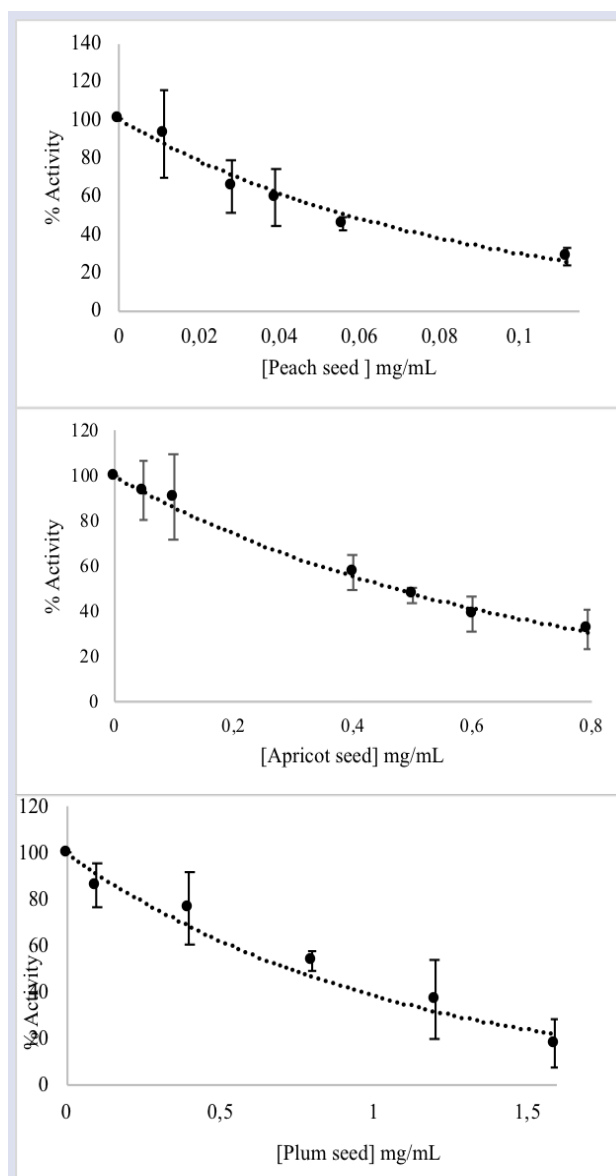


Figure 2. *In vitro* effects of apricot, peach and plum seed on AChE enzyme activity

Conclusion

While dietary intake of some fruits plays a role in delaying the onset of Alzheimer's disease, natural products are also used in the treatment of neurological diseases by altering the activities of neural neurotransmitters in the central nervous system. In order to reduce the side effects of the drugs used today and to obtain more effective and inexpensive drugs, the interest of scientists has shifted towards the extracts and molecules obtained from natural products. For this purpose, the inhibition effect of extracts from natural products on AChE is valuable to guide the future studies. Considering the results of the present study, it could be stated that honey and fruit seeds may have beneficial a role in the treatment for human health. However, more studies are needed to reach a definite conclusion.

Acknowledgements

This article is extended version of a conference presentation entitled “Investigation of The Inhibition Effect Of Honey, Pollen and Royal Jelly On Acetylcholinesterase Enzyme” and presented in “Inesec International Engineering And Natural Sciences Conference (IENSC)”.

Funding

This work was supported by a grant from the Scientific Research Project of Artvin Coruh University of Turkey [Grant Number: BAP. 2016.M80.02.09].

Conflicts of Interest

The authors declared that they have no conflict of interest.

References

- Mantoani S.P., Chierrito P.C.T., Vilela F.L.A., Cardoso L.C., Martínez A., Carvalho I., Novel Triazole-Quinoline Derivatives as Selective Dual Binding Site Acetylcholinesterase Inhibitors, *Molecules*, 193(21) (2016).
- Prasasty V., Radifar M., Istyastono E., Natural Peptides in Drug Discovery Targeting Acetylcholinesterase, *Molecules*, 2344(21) (2018).
- Liu P.P., Xie Y., Meng Y.X., Kang S.J., History And Progress Of Hypotheses And Clinical Trials For Alzheimer’s Disease, *Signal Transduct Target Ther*, 4 (29) (2019).
- Vicente-Zurdo D., Romero-Sánchez I., Rosales-Conrado N., León-González M.E., Madrid Y., Ability Of Selenium Species To Inhibit Metal-Induced A β Aggregation Involved In The Development Of Alzheimer’s Disease, *Anal. Bioanal. Chem.*, 412 (2020) 6485-6497.
- Askar A.K., Kudi C.A., Moody J.A., Purification of Soluble Acetylcholinesterase from Sheep Liver by Affinity Chromatography, *Appl Biochem Biotechnol.*, 165 (2011) 336–346.
- Zhang Y., Hei T., Cai Y., Gao Q., Zhang Q., Affinity Binding-Guided Fluorescent Nanobiosensor for Acetylcholinesterase Inhibitors via Distance Modulation between the Fluorophore and Metallic Nanoparticle, *Anal. Chem.*, 84 (2012) 2830–2836.
- He T., Qi L., Zhang J., Huang L.Y., Zhang Q.Z., Enhanced Graphene Quantum Dot Fluorescence Nanosensor For Highly Sensitive Acetylcholinesterase Assay And Inhibitor Screening, *Sensors and Actuators B*, 215 (2015) 24–29.
- Zhu L.H., Liu W.Y., Liu W.W., Yin J.F., Cao L.Z., Bao J., Lia M., Qina Y.L., Shia H.D., Synthesis, Characterisation And Acetylcholinesterase-Inhibition Activities Of 5-Benzyl-1,3,4-Thiadiazol-2-Amine Derivatives, *J. Chem. Phys.*, 40 (2016).
- Akbulut G., Akkemik E., Investigation of Inhibition Effects Of Honey, Pollen, Propolis And Royal Jelly Extracts On Thioredoxinreductase Enzyme Activity, *SAUJS*, 22(6) (2018) 1585-1590.
- Youdim A. K., Joseph A.J., A Possible Emerging Role Of Phytochemicals In Improving Age-Related Neurological Dysfunctions: A Multiplicity Of Effects, *Free Radical Biology & Medicine*, 30(6) (2001) 583–594.
- Gomez-Caracava A.M., Gomez-Romero M., Arraez-Roman D., Segura-Carretero A., Fernandez-Gutierrez A., Advances In The Analysis Of Phenolic Compounds In Products Derived From Bees, *J. Pharm. Biomed. Anal.*, 41 (2006) 1220–1234.
- Sahin H., Aliyazicioglu R., Yildiz O., Kolayli A., Innocenti A., Supuran T.C., Honey, Polen, And Propolis Extracts Show Potent Inhibitory Activity Against The Zinc Metalloenzyme Carbonic Anhydrase, *J. Enzyme Inhib. Med. Chem.*, 26(3) (2011) 440–444.
- Olas B., Honey and Its Phenolic Compounds as an Effective Natural Medicine for Cardiovascular Diseases in Humans?, *Nutrients*, 283 (12) (2020).
- Kösoğlu M., Yücel B., Gökbulut C., Konak R., Bircan C., The Effect of Harvesting Time on Some Biochemical and Trace Element Compositions of Royal Jelly, *Kafkas Univ. Vet. Fak. Derg.*, 19(2) (2013) 233-237.
- Crozier A., Jaganath B.I., Clifford N.M., Dietary Phenolics: Chemistry, Bioavailability And Effects On Health, *Nat. Prod. Rep.*, 26 (2009) 1001-1043.
- Chen G-L., Chen S-G., Chen F., Xie Y-Q., Han M-D., Luo C-X., Zhao Y-Y., Gao Y-Q., Nutraceutical Potential And Antioxidant Benefits Of Selected Fruit Seeds Subjected To An In Vitro Digestion, *J. Funct. Foods*, 20 (2016) 317–331.
- Alyes E., Simoes A., Domingues R., Fruit Seeds And Their Oils As Promising Sources Of Value-Added Lipids From Agro-Industrial By Products: Oil Content, Lipid Composition, Lipid Analysis, Biological Activity And Potential Biotechnological Applications, *Crit. Rev. Food Sci. Nutr.*, 61(8) (2021) 1305–1339.
- Gasparotto J., Somensi N., Bortolin C.R., Moresco S.K., Girardi S.C., Klafke K., Rabelo K.T., Morrone S.M., Vizzotto M., Raseira B.C.M., Moreira F.C.J., Gelain P.D., Effects Of Different Products Of Peach (*Prunuspersica* L. Batsch) From A Variety Developed In Southern Brazil On Oxidative Stress And Inflammatory Parameters In Vitro And Ex Vivo, *J. Clin. Biochem.Nutr.*, 55(2) (2014) 110–119.
- Rai I., Bachheti K.R., Saini K.C., Joshi A., Satyan S.R., A Review On Phytochemical, Biological Screening And Importance of Wild Apricot (*Prunusarmeniaca* L.), *Orient Pharm. Exp. Med.*, (2015).
- Ozturk B., Kucukera E., Karaman S., Ozkana Y., The Effects Of Cold Storage And Aminoethoxyvinylglycine (AVG) On Bioactive Compounds Of Plum Fruit (*Prunussalicina* Lindell cv. ‘Black Amber’), *Postharvest Biol. Technol.*, 72 (2012) 35–41.
- Yoo M.K., Al-Farsi M., Lee H., Yoon H., Lee Y.C., Antiproliferative Effects Of Cherry Juice And Wine In Chinese Hamster Lung Fibroblast Cells And Their Phenolic Constituents And Antioxidant Activities, *Food Chem.*, 123 (2010) 734–740.
- Velioglu S., Determination Of Antioxidant And Antibacterial Activities And Phenolic Compounds Distribution Of Different Tea Extracts by HPLC, Ankara University Scientific Research Projects, Ankara University, 2007.
- Ellman G.L., Courtney D.K., Andres V., Featherstone M.R., New and Rapid Colorimetric Determination Of Acetylcholinesterase Activity, *Biochem. Pharmacol*, 7 (1961) 88-95.
- Caglayan C., Taslimi P., Türk C., Kandemir M.F., Demir Y., Gulcin İ., Purification And Characterization Of The Carbonic Anhydrase Enzyme From Horse Mackerel (*Trachurus trachurus*) Muscle And The Impact Of Some Metal Ions And Pesticides On Enzyme Activity, *Comp. Biochem. Physiol*, 226 (2019) 108605.

- [25] Lineweaver H., Burk, D., The Determination Of Enzyme Dissociation Constants, *J. Am. Chem. Soc.*, 56 (1934) 658–666.
- [26] Zhang X., Feng P., Gao X., Wang B., Gou C., Bian R., In Vitro Inhibitory Effects Of Cepharanthine On Human Liver Cytochrome P450 Enzymes, *Pharm. Biol.*, 58(1) (2020) 247–252.
- [27] Silva I.J., Moraes C.M., Vieira C.C.L., Corrêa G.A., Cass B.Q., Cardoso L.C., Acetylcholinesterase Capillary Enzyme Reactor For Screening And Characterization Of Selective Inhibitors, *J. Pharm. Biomed.*, 73 (2013) 44– 52.
- [28] Yildiz O., Karahalil F., Can Z., Sahin H., Kolayli S., Total Monoamine Oxidase (MAO) Inhibition By Chestnut Honey, Pollen And Propolis, *J. Enzyme Inhib. Med. Chem.*, 29(5) (2014) 690–694.
- [29] Kolayli S., Can Z., Yildiz O., Sahin H., Karaoglu A. S., A Comparative Study Of The Antihyaluronidase, Antiurease, Antioxidant, Antimicrobial And Physicochemical Properties Of Different Unifloral Degrees Of Chestnut (*Castanea sativa* Mill.) Honeys, *J. Enzyme Inhib. Med. Chem.*, 31(3) (2016) 96–104.
- [30] Tkacz K., Wojdyło A., Nowicka P., Turkiewicz I., Golis T., Characterization In Vitro Potency Of Biological Active Fractions Of Seeds, Skins And Flesh From Selected *Vitisvinifera* L. Cultivars And Interspecific Hybrids, *J. Funct. Foods*, 56 (2019). 353–63.
- [31] Lakshmi Thangavelu T., Ramasamy R., In vitro Acetyl Cholinesterase Inhibitory assay of *Acacia catechu* Willd Ethanolic Seed Extract, *Pharmacognosy J.*, 7(5) (2015).
- [32] Oboh G., J. Akinyemi J.A., Omojokun S.O., Oyeleye S.I., Anticholinesterase and Antioxidative Properties of Aqueous Extract of *Cola acuminata* Seed In Vitro, *Int. J. Alzheimers Dis.*, (2014) 1-8.
- [33] Kumar S., Chowdhury S., Kinetics Of Acetylcholinesterase Inhibition By An Aqueous Extract Of *Cuminum Cyminum* Seeds, *Int. J. Appl. Sci. Biotechnol.*, 2(1) (2014) 64-68.
- [34] Chaibi R., Drine S., Ferchichi A., Chemical Study And Biological Activities Of Various Extracts From *Lawsonia Inermis* (Henna) Seeds, *Acta Medica Mediterr.*, 33 (2017) 981-986.

Mathematical Analysis of Discrete Fractional Prey-Predator Model with Fear Effect and Square Root Functional Response

Prasun Kumar Santra^{1,a,*}

¹ Abada Nsup School, Department of Mathematics, Abada, Howrah-711313, India.

*Corresponding author

Research Article

History

Received: 06/05/2021

Accepted: 24/02/2022

Copyright



©2022 Faculty of Science,
Sivas Cumhuriyet University

^a prasunsantra5@gmail.com

^{id} <https://orcid.org/0000-0002-1857-135X>

ABSTRACT

This paper investigates the dynamics of a discrete fractional prey-predator system. The prey-predator interaction is modelled using the square root functional response, which appropriately models systems in which the prey exhibits a strong herd structure, implying that the predator generally interacts with the prey along the herd's outer corridor. Some recent field experiments and studies show that predators affect prey by directly killing and inducing fear in prey, reducing prey species' reproduction rate. Considering these facts, we propose a mathematical model to study herd behaviour and fear effect in the prey-predator system. We show algebraically equilibrium points and their stability condition. Condition for Neimark-Sacker bifurcation, Flip bifurcation and Fold bifurcation are given. Phase portraits and bifurcation diagrams are portraits that depict the model's behaviour based on some hypothetical data. Numerical simulations reveal the model's rich dynamics as a result of fear and fractional order.

Keywords: Prey-predator, Discrete, Fractional, Bifurcation, Fear effect.

Introduction

Because of their complex behaviour, population models have piqued the interest of researchers. Prey-predator models are an essential component of population models. Based on observed ecological interactions among individuals of the species at various trophic levels, mathematical modelling is a helpful tool for understanding and predicting the long-term survival of various species. There are different types of prey-predator models, such as the continuous model [1-2], discrete model [3-5], fractional model [6-9], etc. Nowadays, the fractional-order system can explain more natural phenomena that were previously ignored by the classical theory of the integer-order dynamical system. Discrete-time population models become more realistic than continuous models when the population sizes are relatively small and in cases where births and deaths occur discrete times or within specific intervals. A discrete form of fractional-order model is now a popular mathematical tool [10]. In this article, we consider the discrete fractional order model.

Din [11] discussed chaos control in a discrete-time prey-predator system. Zhao and Du ([12]) investigated a discrete-time prey-predator model with an Allee effect. Santra and Mahapatra [13] studied the dynamics of a discrete-time prey-predator model under imprecise biological parameters. Santra et al. [14] investigated bifurcation and chaos of a discrete predator-prey model with Crowley-Martin functional response. For more dynamical investigations related to different versions of prey-predator models, we refer to Baydemir et al. [15], Santra et al. [16], Rech [17], Singh and Deolia [18], Khan and Khaliq [19,21], Rozikov and Shoyimardonov [20] and references therein.

In reality, a class of prey population exhibits herd behaviour so that the capturing rate of prey by a predator will be different from usual models. Incorporate this herd behaviour of prey; we consider square root functional response [22-23] in our proposed model. The basic assumption in developing such functional interactions is that the predator hunts on the outskirts of a moving herd. If we assume that the herd has a square shape for simplicity, then the interaction between the predator and the prey will occur on the group's borders, which means that it will hunt one (or more) from four times the square root of the prey density. A similar assumption can be made for the prey population's circle herd shape.

Furthermore, predation fear directly impacts prey reproduction; that's why we modify the prey reproduction term incorporating fear factor [24-25] in our proposed model. Two significant factors are limiting wild animal activity: energy and time constraints. To avoid predation, prey may shorten their activity periods and devote some of their foraging time to vigilance; however, prey must balance defence time and foraging intake. A high level of anti-predator behaviour over a long period causes ageing to be sped up and leads to starvation, impacting growth. As a result, there are costs and benefits for prey in prey defence. In this case, we include the cost as a type of prey growth reduction caused by predation fear. In this paper, we study the prey-predator with fear and herd behaviour using the discrete fractional-order model. The study's intention is: what is the effect of fractional order and fear on the proposed model system?

Mathematical Model

Consider the following fractional-order prey-predator model with square root functional response and fear effect :

$$D^\alpha x = rx \left(1 - \frac{x}{k}\right) \frac{1}{1 + \phi y} - by\sqrt{x}$$

$$D^\alpha y = cy\sqrt{x} - dy$$

with initial condition

$$x(t) \geq 0, y(t) \geq 0$$

Where x and y denote the density of prey and predator populations respectively at any time t . The biological meaning of the system parameters are as follows: r is the intrinsic per capita growth rate of prey population, k is the environmental carrying capacity of prey population, ϕ is the fear effect due to predation, b is the maximal per capita consumption rate of predators, c is the efficiency with which predators convert consumed prey into new predators, d is the per capita death rate of predators, and α is the fractional-order satisfying $\alpha \in (0,1]$ and $D^\alpha \equiv \frac{d^\alpha}{dt^\alpha}$ is in the sense of Caputo derivative.

Using the fractional-order discretization process, we get the following discrete fractional-order system

$$x \rightarrow x + \frac{h^\alpha}{\Gamma(1+\alpha)} \left[rx \left(1 - \frac{x}{k}\right) \frac{1}{1 + \phi y} - by\sqrt{x} \right]$$

$$y \rightarrow y + \frac{h^\alpha}{\Gamma(1+\alpha)} [cy\sqrt{x} - dy]$$

where h is the step size and r, k, ϕ, b, c, d are all positive constants. By the biological meaning of the model variables, we only consider the system in the region $\Omega = \{(x, y) : x \geq 0, y \geq 0\}$ in the (x, y) - plane.

General Stability Analysis

Equilibria

Fixed points of the system (1) are determined by solving the following non-linear system of equations:

$$x = x + \frac{h^\alpha}{\Gamma(1+\alpha)} \left[rx \left(1 - \frac{x}{k}\right) \frac{1}{1 + \phi y} - by\sqrt{x} \right]$$

$$y = y + \frac{h^\alpha}{\Gamma(1+\alpha)} [cy\sqrt{x} - dy]$$

We get three non-negative fixed points by solving the above equations:

(i) $P_0 = (0,0)$

(ii) $P_1 = (k,0)$

(iii) $P_2 = (x_2, y_2)$

here $x_2 = \left(\frac{d}{c}\right)^2$ and y_2 is a positive solution of

$$y^2 + \frac{y}{\phi} - \frac{rd}{\phi bc} \left(1 - \frac{d^2}{kc^2}\right) = 0$$

Local Stability Analysis

The discussion about the dynamical behavior of model (1) is carried out in this sub-section. The Jacobian Matrix J for the system (1) is

$$J = \begin{bmatrix} 1 + \frac{h^\alpha}{\Gamma(1+\alpha)} \left[r \left(1 - \frac{2x}{k}\right) \frac{1}{1 + \phi y} - \frac{by}{2\sqrt{x}} \right] & \frac{h^\alpha}{\Gamma(1+\alpha)} \left[-rx \left(1 - \frac{x}{k}\right) \frac{\phi}{(1 + \phi y)^2} - b\sqrt{x} \right] \\ \frac{h^\alpha}{\Gamma(1+\alpha)} \left[\frac{cy}{2\sqrt{x}} \right] & 1 + \frac{h^\alpha}{\Gamma(1+\alpha)} [c\sqrt{x} - d] \end{bmatrix}$$

The characteristic equation of the matrix J is $\lambda^2 - T\lambda + D = 0$, where

$$T = 2 + \frac{h^\alpha}{\Gamma(1+\alpha)} \left[r \left(1 - \frac{2x}{k}\right) \frac{1}{1 + \phi y} - \frac{by}{2\sqrt{x}} + c\sqrt{x} - d \right]$$

$$D = \left[1 + \frac{h^\alpha}{\Gamma(1+\alpha)} \left[r \left(1 - \frac{2x}{k}\right) \frac{1}{1 + \phi y} - \frac{by}{2\sqrt{x}} \right] \right] \left[1 + \frac{h^\alpha}{\Gamma(1+\alpha)} [c\sqrt{x} - d] \right]$$

$$- \left[\frac{h^\alpha}{\Gamma(1+\alpha)} \left[-rx \left(1 - \frac{x}{k}\right) \frac{\phi}{(1 + \phi y)^2} - b\sqrt{x} \right] \right] \left[\frac{h^\alpha}{\Gamma(1+\alpha)} \left[\frac{cy}{2\sqrt{x}} \right] \right]$$

$$= 1 + \frac{h^\alpha}{\Gamma(1+\alpha)} [c\sqrt{x} - d] + \frac{h^\alpha}{\Gamma(1+\alpha)} \left[r \left(1 - \frac{2x}{k}\right) \frac{1}{1 + \phi y} - \frac{by}{2\sqrt{x}} \right] \left[1 + \frac{h^\alpha}{\Gamma(1+\alpha)} [c\sqrt{x} - d] \right]$$

$$- \left[\frac{h^\alpha}{\Gamma(1+\alpha)} \left[-rx \left(1 - \frac{x}{k}\right) \frac{\phi}{(1 + \phi y)^2} - b\sqrt{x} \right] \right] \left[\frac{h^\alpha}{\Gamma(1+\alpha)} \left[\frac{cy}{2\sqrt{x}} \right] \right]$$

Hence the discrete-time system (1) is said to be:

- (i) a dissipative dynamical system if $|D| < 1$,
- (ii) a conservative dynamical system if and only if $|D| = 1$,
- (iii) an undissipated dynamical system otherwise.

Stability and dynamic behavior at P_1

The Jacobian matrix at the fixed point $P_1 = (k,0)$ is

$$J = \begin{bmatrix} 1 - \frac{rh^\alpha}{\Gamma(1+\alpha)} & -\frac{b\sqrt{k}h^\alpha}{\Gamma(1+\alpha)} \\ 0 & 1 + \frac{h^\alpha}{\Gamma(1+\alpha)} [c\sqrt{k} - d] \end{bmatrix}$$

The equilibrium point P_1 is said to be:

- (i) Sink if $\left| 1 - \frac{rh^\alpha}{\Gamma(1+\alpha)} \right| < 1$, and $\left| 1 + \frac{h^\alpha}{\Gamma(1+\alpha)} [c\sqrt{k} - d] \right| < 1$,
- (ii) Source if $\left| 1 - \frac{rh^\alpha}{\Gamma(1+\alpha)} \right| > 1$, and $\left| 1 + \frac{h^\alpha}{\Gamma(1+\alpha)} [c\sqrt{k} - d] \right| > 1$,

- (iii) Saddle if $\left|1 - \frac{rh^\alpha}{\Gamma(1+\alpha)}\right| > 1$, and $\left|1 + \frac{h^\alpha}{\Gamma(1+\alpha)}[c\sqrt{k} - d]\right| < 1$;
- or $\left|1 - \frac{rh^\alpha}{\Gamma(1+\alpha)}\right| < 1$, and $\left|1 + \frac{h^\alpha}{\Gamma(1+\alpha)}[c\sqrt{k} - d]\right| > 1$,
- (iv) Non-hyperbolic if $\left|1 - \frac{rh^\alpha}{\Gamma(1+\alpha)}\right| = 1$ or $\left|1 + \frac{h^\alpha}{\Gamma(1+\alpha)}[c\sqrt{k} - d]\right| = 1$.

Dynamic behavior around the interior fixed point

From the Jacobian matrix at the interior fixed point

$P_2(x_2, y_2)$, we get

$$\begin{aligned}
 1-T+D &= -1 - \frac{h^\alpha}{\Gamma(1+\alpha)} \left[r \left(1 - \frac{2x_2}{k} \right) \frac{1}{1+\phi y_2} - \frac{by_2}{2\sqrt{x_2}} + c\sqrt{x_2} - d \right] \\
 &+ \left[1 + \frac{h^\alpha}{\Gamma(1+\alpha)} \left[r \left(1 - \frac{2x_2}{k} \right) \frac{1}{1+\phi y_2} - \frac{by_2}{2\sqrt{x_2}} \right] \right] \left[1 + \frac{h^\alpha}{\Gamma(1+\alpha)} [c\sqrt{x_2} - d] \right] \\
 &- \left[\frac{h^\alpha}{\Gamma(1+\alpha)} \left[-rx_2 \left(1 - \frac{x_2}{k} \right) \frac{\phi}{(1+\phi y_2)^2} - b\sqrt{x_2} \right] \right] \left[\frac{h^\alpha}{\Gamma(1+\alpha)} \left[\frac{cy_2}{2\sqrt{x_2}} \right] \right] \\
 1+T+D &= 3 + \frac{h^\alpha}{\Gamma(1+\alpha)} \left[r \left(1 - \frac{2x_2}{k} \right) \frac{1}{1+\phi y_2} - \frac{by_2}{2\sqrt{x_2}} + c\sqrt{x_2} - d \right] \\
 &+ \left[1 + \frac{h^\alpha}{\Gamma(1+\alpha)} \left[r \left(1 - \frac{2x_2}{k} \right) \frac{1}{1+\phi y_2} - \frac{by_2}{2\sqrt{x_2}} \right] \right] \left[1 + \frac{h^\alpha}{\Gamma(1+\alpha)} [c\sqrt{x_2} - d] \right] \\
 &- \left[\frac{h^\alpha}{\Gamma(1+\alpha)} \left[-rx_2 \left(1 - \frac{x_2}{k} \right) \frac{\phi}{(1+\phi y_2)^2} - b\sqrt{x_2} \right] \right] \left[\frac{h^\alpha}{\Gamma(1+\alpha)} \left[\frac{cy_2}{2\sqrt{x_2}} \right] \right]
 \end{aligned}$$

If $1-T+D > 0$, then interior equilibrium point

$P_2(x_2, y_2)$ is:

- (i) Sink if $1+T+D > 0$ and $D < 1$,
- (ii) Source if $1+T+D > 0$ and $D > 1$,
- (iii) Saddle if $1+T+D < 0$,
- (iv) Non-hyperbolic if $1+T+D = 0$ and $T \neq 0, 2$,

or $T^2 - 4D < 0$ and $D = 1$.

Bifurcation Analysis

This section obtains the conditions for Neimark-Sacker bifurcation, flip bifurcation, and fold bifurcation for model (1). Neimark-Sacker bifurcation causes closed invariant curves into the system, which shows more complex behaviour. Another bifurcation, flip bifurcation, occurs when the system switches to a new limit cycle twice the period of the existing one. Fold bifurcation, in which two fixed points collide and disappear into the system.

Neimark-Sacker Bifurcation

Condition for the occurrence of Neimark-Sacker

bifurcation (Elaydi [26]) at an interior fixed point

$P_2(x_2, y_2)$ is $D = 1$.

i.e.

$$\frac{h^\alpha}{\Gamma(1+\alpha)} [c\sqrt{x_2} - d] + h \left[r \left(1 - \frac{2x_2}{k} \right) \frac{1}{1+\phi y_2} - \frac{by_2}{2\sqrt{x_2}} \right] \left[1 + \frac{h^\alpha}{\Gamma(1+\alpha)} [c\sqrt{x_2} - d] \right]$$

$$= \left[\frac{h^\alpha}{\Gamma(1+\alpha)} \left[-rx_2 \left(1 - \frac{x_2}{k} \right) \frac{\phi}{(1+\phi y_2)^2} - b\sqrt{x_2} \right] \right] \left[\frac{h^\alpha}{\Gamma(1+\alpha)} \left[\frac{cy_2}{2\sqrt{x_2}} \right] \right]$$

Flip Bifurcation

Condition for the occurrence of Flip bifurcation

(Elaydi [26]) at an interior fixed point $P_2(x_2, y_2)$ is

$$1+T+D=0.$$

i.e.

$$\begin{aligned}
 &3 + \frac{h^\alpha}{\Gamma(1+\alpha)} \left[r \left(1 - \frac{2x_2}{k} \right) \frac{1}{1+\phi y_2} - \frac{by_2}{2\sqrt{x_2}} + c\sqrt{x_2} - d \right] \\
 &+ \left[1 + \frac{h^\alpha}{\Gamma(1+\alpha)} \left[r \left(1 - \frac{2x_2}{k} \right) \frac{1}{1+\phi y_2} - \frac{by_2}{2\sqrt{x_2}} \right] \right] \left[1 + \frac{h^\alpha}{\Gamma(1+\alpha)} [c\sqrt{x_2} - d] \right] \\
 &= \left[\frac{h^\alpha}{\Gamma(1+\alpha)} \left[-rx_2 \left(1 - \frac{x_2}{k} \right) \frac{\phi}{(1+\phi y_2)^2} - b\sqrt{x_2} \right] \right] \left[\frac{h^\alpha}{\Gamma(1+\alpha)} \left[\frac{cy_2}{2\sqrt{x_2}} \right] \right]
 \end{aligned}$$

Fold bifurcation

Condition for the occurrence of Fold bifurcation

(Elaydi [26]) at an interior fixed point $P_2(x_2, y_2)$ is

$$1-T+D=0$$

i.e.

$$\begin{aligned}
 &-1 - \frac{h^\alpha}{\Gamma(1+\alpha)} \left[r \left(1 - \frac{2x_2}{k} \right) \frac{1}{1+\phi y_2} - \frac{by_2}{2\sqrt{x_2}} + c\sqrt{x_2} - d \right] \\
 &+ \left[1 + \frac{h^\alpha}{\Gamma(1+\alpha)} \left[r \left(1 - \frac{2x_2}{k} \right) \frac{1}{1+\phi y_2} - \frac{by_2}{2\sqrt{x_2}} \right] \right] \left[1 + \frac{h^\alpha}{\Gamma(1+\alpha)} [c\sqrt{x_2} - d] \right] \\
 &= \left[\frac{h^\alpha}{\Gamma(1+\alpha)} \left[-rx_2 \left(1 - \frac{x_2}{k} \right) \frac{\phi}{(1+\phi y_2)^2} - b\sqrt{x_2} \right] \right] \left[\frac{h^\alpha}{\Gamma(1+\alpha)} \left[\frac{cy_2}{2\sqrt{x_2}} \right] \right]
 \end{aligned}$$

Numerical Simulations

In this section, numerical simulations were run using a hypothetical set of parameter values as shown in table 1. These parameter values have biological and mathematical significance. This section numerically analyses the model to investigate more results on fractional-order and the fear effect on prey due to predation. In a specific range, bifurcation diagrams for prey and predator are created for the model. To better understand the system, phase portraits are drawn in a specific section of the bifurcation diagram. This section of the study's parameters are step size, fear effect, and fractional order.

Table 1: Parameter values

r	k	φ	b	c	d	h	α
0.5	1.0	0.1	0.7	0.5	0.3	0.3	0.9

To know the effect of step size in the system dynamics, we draw the bifurcation diagram in figure 1 for $h \in [0.1, 1.0]$ and phase portraits in figure 2 for (A) $h = 0.3$, (B) $h = 0.36$ rest of the parameters from table 1. Neimark-Sacker bifurcation occurs w.r.t. this parameter

and the system enter into an unstable zone when step size h crosses the threshold value 0.3445 .

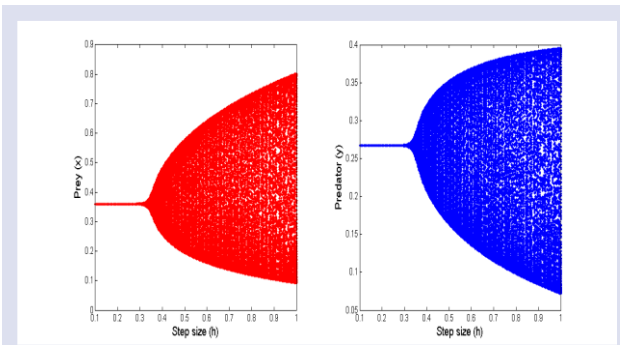


Figure 1. The bifurcation diagram of the system concerning the step size h in the range $[0.1,1]$ and remaining parameters are from Table 1.

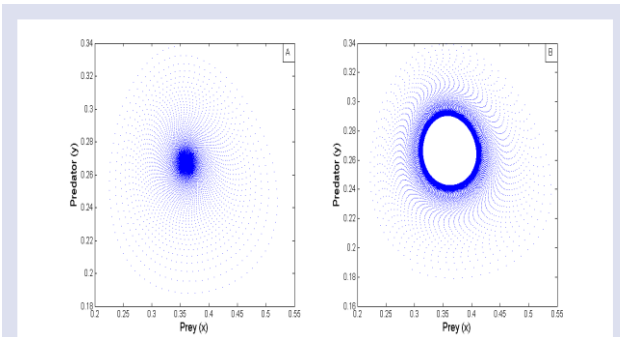


Figure 2. Phase portraits of the system for step size (A) $h = 0.3$, (B) $h = 0.36$, and remaining parameters are from Table 1.

Now, we are interested to know the effect of fear in the system dynamics, and we draw the bifurcation diagram in figure 3 for $\varphi \in [0.1,1.0]$ and phase portraits in figure 4 for (A) $\varphi = 0.6$, (B) $\varphi = 0.9$ rest of the parameters from table 1. Neimark-Sacker bifurcation occurs w.r.t. this parameter and the system enter into an unstable zone when fear effect φ crosses the threshold value 0.7855 .

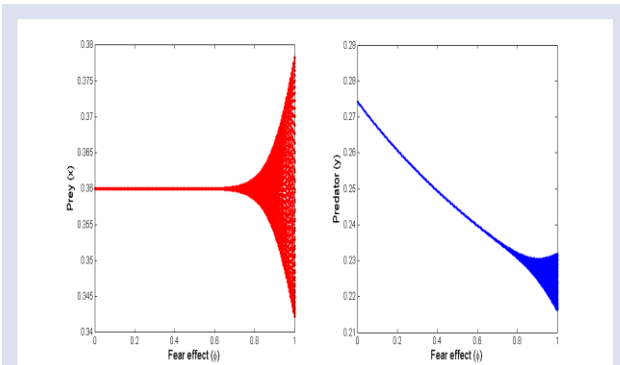


Figure 3. The bifurcation diagram of the system concerning the fear effect φ in the range $[0,1]$ and remaining parameters are from Table 1.

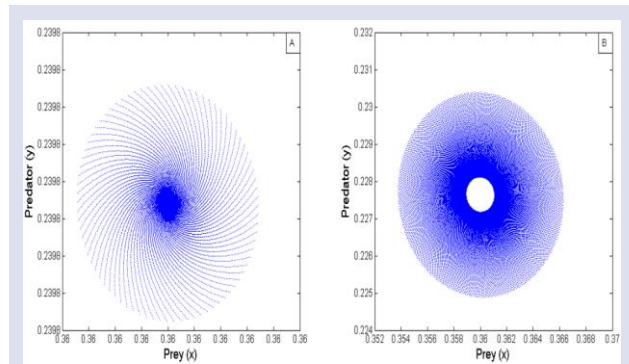


Figure 4: Phase portraits of the system for fear effect (A) $\varphi = 0.6$, (B) $\varphi = 0.9$ and remaining parameters are from Table 1.

Lastly, we are interested to know the effect of fractional-order in the system dynamics. We draw the bifurcation diagram in figure 5 for $\alpha \in [0.1,1.0]$ and phase portraits in figure 6 for (A) $\alpha = 0.8$, (B) $\alpha = 0.9$ the rest of the parameters from table 1. Neimark-Sacker bifurcation occurs w.r.t. this parameter and the system enter into a stable zone when fractional-order α crosses the threshold value 0.8556 . The low weight of α mean strong memory and high value of α mean weak memory. So faint memory can stabilize the model.

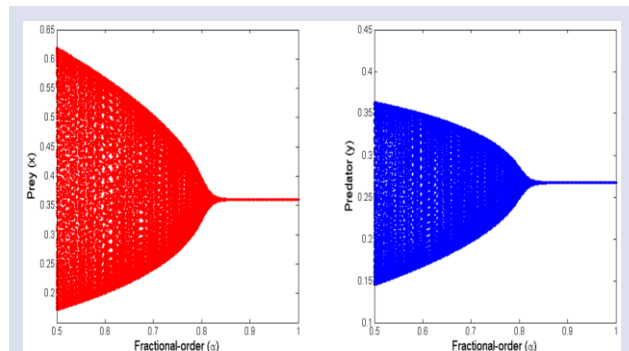


Figure 5. The bifurcation diagram of the system for the fractional-order α in the range $[0,1]$ and remaining parameters are from Table 1.

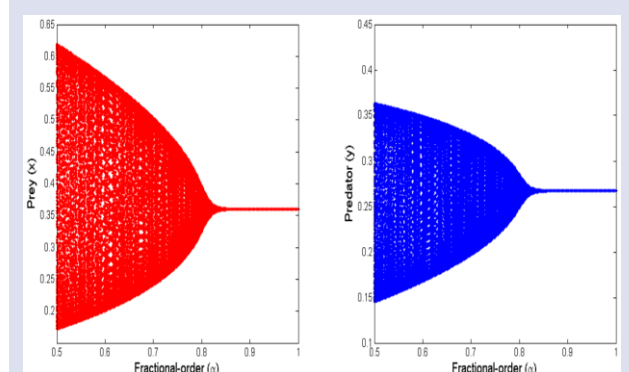


Figure 6. Phase portraits of the system for fractional-order (A) $\alpha = 0.8$, (B) $\alpha = 0.9$ and remaining parameters are from Table 1.

Conclusion

In this work, we investigated the dynamic behaviours of the discrete fractional-order predator-prey system. Fear effect on a prey-predator interaction is studied using the discrete fractional-order model. We established the conditions for a flip bifurcation, fold bifurcation, and a Neimark-Sacker bifurcation of the map at a unique positive fixed point. We have discussed the fear effects concerning the local stability of the interior equilibrium point. Finally, we conclude that fear destabilizes the model, and fear hurts the predator population. Fractional order has to stabilize effect on the model system.

Acknowledgment

The authors are grateful to referees for careful reading, suggestions, and valuable comments, which have substantially improved the paper.

Conflicts of interest

There are no conflicts of interest in this work.

References

- [1] Mahapatra, G.S., Santra, P., Prey-predator model for Optimal Harvesting with Functional Response Incorporating Prey Refuge, *International Journal of Biomathematics*, 09 (2016) ID1650014.
- [2] Pal, D., Santra, P., Mahapatra, G.S., Dynamical behavior of three species predator-prey system with mutual support between non refuge prey, *Ecological Genetics and Genomics*, 3-5 (2017) 1-6.
- [3] Al-Basyouni, K.S., Khan, A.Q., Discrete-Time Predator-Prey Model with Bifurcations and Chaos, *Mathematical Problems in Engineering*, 2020 (2020) ID8845926.
- [4] Kangalgil, F., Isik, S., Controlling chaos and neimark-sacker bifurcation in a discrete-time predator-prey system, *Hacettepe Journal of Mathematics and Statistics*, 49(5) (2020) 1761-1776.
- [5] Liu, W., Jiang, Y., Flip bifurcation and Neimark-Sacker bifurcation in a discrete predator-prey model with harvesting, *International Journal of Biomathematics*, 13(1) (2020) ID1950093.
- [6] Owolabi K.M., Dynamical behaviour of fractional-order predator-prey system of Holling-type, *Discrete and Continuous Dynamical Systems - Series S*, 13 (3) (2020) 823-834.
- [7] Nosrati K., Shafiee M., Dynamic analysis of fractional-order singular Holling type-II predator-prey system, *Applied Mathematics and Computation*, 313 (2017) 159-179.
- [8] El-Saka H.A.A., Lee S., Jang B., Dynamic analysis of fractional-order predator-prey biological economic system with Holling type II functional response, *Nonlinear Dynamics*, 96 (1) (2019) 407-416.
- [9] Bonyah E., Atangana A., Elsadany A.A., A fractional model for predator-prey with omnivore, *Chaos*, 29 (1) (2019).
- [10] Shi Y., Ma Q., Ding X., Dynamical behaviors in a discrete fractional-order predator-prey system, *Filomat*, 32(17) (2018) 5857-5874.
- [11] Din Q., Complexity and chaos control in a discrete-time prey-predator model, *Communications in Nonlinear Science and Numerical Simulation*, 49 (2017) 113-134.
- [12] Zhao M., Du Y., Stability of a Discrete-Time Predator-Prey System with Allee Effect, *Nonlinear Analysis and Differential Equations*, 4 (5) (2016) 225 - 233.
- [13] Santra P. K., Mahapatra G. S., Dynamical study of discrete-time prey-predator model with constant prey refuge under imprecise biological parameters, *Journal of Biological Systems*, 28 (3) (2020) 681-699.
- [14] Santra P. K., Mahapatra G. S., Phaijoo G. R., Bifurcation and Chaos of a Discrete Predator-Prey Model with Crowley-Martin Functional Response Incorporating Proportional Prey Refuge, *Mathematical Problems in Engineering*, (2020) ID 5309814.
- [15] Baydemir P., Merdan H., Karaoglu E., Sucu G., Complex Dynamics of a Discrete-Time Prey-Predator System with Leslie Type: Stability, Bifurcation Analyses and Chaos, *International Journal of Bifurcation and Chaos*, 30(10) (2020) ID2050149.
- [16] Santra P.K., Mahapatra G.S., Phaijoo G.R., Bifurcation analysis and chaos control of discrete prey-predator model incorporating novel prey-refuge concept, *Computational and Mathematical Methods*, (2021) e1185.
- [17] Rech P.C., On Two Discrete-Time Counterparts of a Continuous-Time Prey-Predator Model, *Brazilian Journal of Physics*, 50(2) (2020) 119-123.
- [18] Singh A., Deolia P., Dynamical analysis and chaos control in discrete-time prey-predator model, *Communications in Nonlinear Science and Numerical Simulation*, 90 (2020) ID105313.
- [19] Khan A. Q., Khalique T., Bifurcations and chaos control in a discrete-Time biological model, *International Journal of Biomathematics*, 13(4) (2020).
- [20] Rozikov U.A., Shoyimardonov S.K., Leslie's prey-predator model in discrete time, *International Journal of Biomathematics*, 13(6) (2020) ID2050053.
- [21] Khan A.Q., Khalique T., Neimark-Sacker bifurcation and hybrid control in a discrete-time Lotka-Volterra model, *Mathematical Methods in the Applied Sciences*, 43(9) (2020) 5887-5904.
- [22] Chakraborty P., Ghosh U., Sarkar S., Stability and bifurcation analysis of a discrete prey-predator model with square-root functional response and optimal harvesting, *Journal of Biological Systems*, 28 (1) (2020) 91-110.
- [23] Santra P.K., Discrete-time prey-predator model with θ -logistic growth for prey incorporating square root functional response, *Jambura Journal of Biomathematics*, 1 (2) (2020) 41-48.
- [24] Ma R., Bai Y., Wang F., Dynamical behavior analysis of a two-dimensional discrete predator-prey model with prey refuge and fear factor, *Journal of Applied Analysis and Computation*, 10 (4) (2020) 1683-1697.
- [25] Wang X., Zanette L., Zou X., Modelling the fear effect in predator-prey interactions, *Journal of Mathematical Biology*, 73 (5) (2016) 1-26.
- [26] Elaydi S. N., Discrete chaos: with applications in science and engineering, *Chapman & Hall/CRC*, 2007

Surfaces Using a Common Geodesic Curve With an Alternative Moving Frame in The 3-Dimensional Lie Group

Zühal Küçükarslan Yüzbaşı^{1, a, *}

¹ Department of Mathematics, Faculty of Science, Firat University, Elazığ, Turkey

*Corresponding author

Research Article

History

Received: 28/07/2021

Accepted: 15/12/2021

Copyright



©2022 Faculty of Science,
Sivas Cumhuriyet University

zuhal2387@yahoo.com.tr

<https://orcid.org/0000-0001-7630-5490>

ABSTRACT

Our purpose in this research is to use an alternative moving frame in the 3-dimensional Lie group G to construct the problem of how to characterize a surface family and derive the conditions from a given common geodesic curve as an isoparametric curve. We also derive the relation about developability along the common geodesic of a ruled surface as a member of the surface family. Finally, we will give some examples to show some applications of the method.

Keywords: Alternative Moving frame, Lie group, Geodesic, Ruled surface.

Introduction

The curve and surface theory are the important areas of the different ambient spaces. In particular, these theories and their geometric properties have been examined by many researchers in the Lie group, [1-8].

On the other hand, the geodesic principle has played an important role in lots of areas, such as the geometric design of the hull, multi-scale analysis of images, the relativistic description of gravity. Nowadays, a good deal of research on surface theory is focused on a surface family having a given isogeodesic curve which is both a geodesic and an isoparametric curve. From this aspect, many researchers have derived a parametric representation of a surface family whose members share the same isogeodesic curve, [9-17].

In this paper, we define the surface family as a linear combination of the components of the alternative moving frame in the Lie group by utilizing this $\{N, C, W\}$ frame along the given geodesic and deriving the conditions for the coefficients to satisfy both the geodesic and the isoparametric requirements. We also present some examples to give the surface family and a ruled surface possessing a given common isogeodesic curve.

Materials and Methods

In this section, we will review some concepts related to the Lie group. For general information about the Lie group, we refer to [2, 6, 7].

The Frenet formulas in the Lie Group for a unit speed curve $\alpha(s)$

$$T' = \kappa N,$$

$$N' = -\kappa T + (\tau - \tau_G)B,$$

$$B' = -(\tau - \tau_G)N,$$

where κ and τ are the curvature functions of $\alpha(s)$ and τ_G , which is introduced [2, 7], is the Lie group torsion of $\alpha(s)$.

On the other hand, the alternative moving frame along the $\alpha(s)$ is defined by the three vectors N ,

$$C = \frac{N'}{\|N'\|} = -\frac{1}{\sqrt{1+h^2}}T + \frac{h}{\sqrt{1+h^2}}B$$

and $W = \frac{h}{\sqrt{1+h^2}}T + \frac{1}{\sqrt{1+h^2}}B$, which called the unit principal normal vector, the derivative of the principal normal vector and the unit Darboux vector, respectively. Then the derivatives of this frame is given by

$$N' = f(s)C, \tag{1}$$

$$C' = -f(s)N + g(s)W,$$

$$W' = -g(s)C,$$

where $f(s) = \kappa\sqrt{1+h^2}$, $g(s) = f(s)\frac{1}{\sigma_N} = \frac{h'}{1+h^2}$ and

$$\sigma_N(s) = \frac{\kappa(1+h^2)^{\frac{3}{2}}}{h}.$$

So $f(s)$ and $g(s)$ are curvatures of $\alpha(s)$ in terms of alternative moving frame in Lie Group G , [3, 5].

Here, $h = \frac{\tau - \tau_G}{\kappa}$ is denoted the harmonic curvature function of $\alpha(s)$ which is introduced in [6].

Theorem 1.

The curve is a general helix in the Lie Group G if and only if its harmonic function is a constant, [2,6].

Results

In this section, we will give an algorithm for constructing surfaces from an isogeodesic curve in the Lie Group.

Surfaces

Let $\alpha(s)$ be an arc length parametrized curve on a surface $P(s,t)$ in G . Then the curve α is called an isoparametric curve if it is a parameter curve, that is, there exists a parameter t_0 such that $\alpha(s) = P(s, t_0)$. Also the curve $\alpha(s)$ on the surface $P(s,t)$ is geodesic if and only if $N(s) \parallel \eta(s, t_0)$ where $\eta(s,t)$ is the normal vector of the surface $P(s,t)$. Then, a given curve $\alpha(s)$ is called an isogeodesic of $P(s,t)$ if it is both a geodesic and an isoparametric curve on $P(s,t)$.

Let $P = P(s,t)$ be a parametric surface through a curve $\alpha(s)$. This surface is given based on the curve $\alpha(s)$ and the alternative moving frame $\{N, C, W\}$ as follows

$$P(s,t) = \alpha(s) + \lambda_1(s,t)N(s) + \lambda_2(s,t)C(s) + \lambda_3(s,t)W(s), \quad (2)$$

$0 \leq s \leq L$ and $0 \leq t \leq T$,

where $\lambda_1(s,t)$, $\lambda_2(s,t)$ and $\lambda_3(s,t)$ are all C^1 functions. These functions are called the marching-scale functions.

Since $\alpha(s)$ is an isoparametric curve on this surface, there exists a parameter $t = t_0 \in [0, T]$ such that $\alpha(s) = P(s, t_0)$, $0 \leq s \leq L$, that is,

$$\lambda_1(s, t_0) = \lambda_2(s, t_0) = \lambda_3(s, t_0) = 0, \quad (3)$$

$0 \leq s \leq L$ and $t_0 \in [0, T]$

On the other hand, we know that the curve $\alpha(s)$ on the surface $P(s,t)$ is a geodesic if and only if $N(s) \parallel \eta(s, t_0)$.

To compute $\eta(s, t_0)$, using the alternative Frenet formula (1), one can easily get that

$$\frac{\partial P(s,t)}{\partial s} = \left(\frac{\partial \lambda_1(s,t)}{\partial s} - f(s)\lambda_2(s,t) \right) N(s) + \left(-\frac{\kappa(s)}{f(s)} + f(s)\lambda_1(s,t) + \frac{\partial \lambda_2(s,t)}{\partial s} - g(s)\lambda_3(s,t) \right) C(s)$$

$$+ \left(\frac{\kappa(s)h(s)}{f(s)} + g(s)\lambda_2(s,t) + \frac{\partial \lambda_3(s,t)}{\partial s} \right) W(s)$$

And

$$\frac{\partial P(s,t)}{\partial t} = \frac{\partial \lambda_1(s,t)}{\partial t} N(s) + \frac{\partial \lambda_2(s,t)}{\partial t} C(s) + \frac{\partial \lambda_3(s,t)}{\partial t} W(s),$$

using the value of T in terms of the alternative moving frame as $T = -\frac{\kappa(s)}{f(s)}C + \frac{\kappa(s)h(s)}{f(s)}W$.

So, the normal $\eta(s,t)$ can be calculated as

$$\eta(s,t) = \frac{\partial P(s,t)}{\partial s} \times \frac{\partial P(s,t)}{\partial t}$$

$$= \left[\left(-\frac{\kappa(s)}{f(s)} + f(s)\lambda_1(s,t) + \frac{\partial \lambda_2(s,t)}{\partial s} - g(s)\lambda_3(s,t) \right) \frac{\partial \lambda_3(s,t)}{\partial t} - \left(\frac{\kappa(s)h(s)}{f(s)} + g(s)\lambda_2(s,t) + \frac{\partial \lambda_3(s,t)}{\partial s} \right) \frac{\partial \lambda_2(s,t)}{\partial t} \right] N(s)$$

$$+ \left[-\left(\frac{\partial \lambda_1(s,t)}{\partial s} - f(s)\lambda_2(s,t) \right) \frac{\partial \lambda_3(s,t)}{\partial t} - \left(\frac{\kappa(s)h(s)}{f(s)} + g(s)\lambda_2(s,t) + \frac{\partial \lambda_3(s,t)}{\partial s} \right) \frac{\partial \lambda_1(s,t)}{\partial t} \right] C(s)$$

$$+ \left[\left(\frac{\partial \lambda_1(s,t)}{\partial s} - f(s)\lambda_2(s,t) \right) \frac{\partial \lambda_2(s,t)}{\partial t} - \left(-\frac{\kappa(s)}{f(s)} + f(s)\lambda_1(s,t) + \frac{\partial \lambda_2(s,t)}{\partial s} - g(s)\lambda_3(s,t) \right) \frac{\partial \lambda_1(s,t)}{\partial t} \right] W(s).$$

Then, from (3), we get

$$\eta(s, t_0) = P_1(s, t_0)N(s) + P_2(s, t_0)C(s) + P_3(s, t_0)W(s),$$

where

$$P_1(s, t_0) = -\frac{\kappa(s)}{f(s)} \frac{\partial \lambda_3(s, t_0)}{\partial t} - \frac{\kappa(s)h(s)}{f(s)} \frac{\partial \lambda_2(s, t_0)}{\partial t}, \quad (4)$$

$$P_2(s, t_0) = \frac{\kappa(s)h(s)}{f(s)} \frac{\partial \lambda_1(s, t_0)}{\partial t},$$

$$P_3(s, t_0) = \frac{\kappa(s)}{f(s)} \frac{\partial \lambda_1(s, t_0)}{\partial t}.$$

On the other hand, we know that $N(s) \parallel \eta(s, t_0)$ if and only if

$$P_1(s, t_0) \neq 0, P_2(s, t_0) = 0 \text{ and } P_3(s, t_0) = 0$$

As a result of combining (3) and (4), we have obtained the conditions for $P(s,t)$ to have the curve α as an isogeodesic in the Lie group as shown by the following theorem.

Theorem 2.

The given curve $\alpha(s)$ is an isogeodesic curve on the surface $P(s,t)$ which given by (2) in the Lie group if the following conditions are satisfied

$$\lambda_1(s, t_0) = \lambda_2(s, t_0) = \lambda_3(s, t_0) = 0,$$

$$\frac{\partial \lambda_1(s, t_0)}{\partial t} = 0 \text{ and } \frac{\kappa(s)}{f(s)} \frac{\partial \lambda_3(s, t_0)}{\partial t} + \frac{\kappa(s)h(s)}{f(s)} \frac{\partial \lambda_2(s, t_0)}{\partial t} = \text{const.} \neq 0, \quad (5)$$

where $0 \leq s \leq L$ and $t_0 \in [0, T]$.

For the aim of simplification and analysis, $\lambda_1(s, t)$, $\lambda_2(s, t)$ and $\lambda_3(s, t)$ can be decomposed into two factors

$$\begin{aligned} \lambda_1(s, t) &= \vartheta(s)X(t), \\ \lambda_2(s, t) &= \rho(s)Y(t), \\ \lambda_3(s, t) &= \sigma(s)Z(t), \end{aligned}$$

where $\theta(s), \rho(s), \sigma(s), X(t), Y(t)$, and $Z(t)$ are all C^1 functions and $\theta(s), \rho(s)$ and $\sigma(s)$ are not identically zero.

If $\alpha(s)$ is an isogeodesic curve on the surface $P(s,t)$, then the sufficient conditions can be easily given as follows

$$\begin{aligned} X(t_0) &= Y(t_0) = Z(t_0) = 0, \\ \theta(s) &= 0 \text{ or } \left. \frac{dX}{dt} \right|_{t_0} = 0, \end{aligned} \quad (6)$$

$$\frac{\kappa(s)\sigma(s)}{f(s)} \frac{dZ(t_0)}{dt} + \frac{\kappa(s)h(s)\rho(s)}{f(s)} \frac{dY(t_0)}{dt} = c = \text{const.} \neq 0,$$

where $0 \leq s \leq L$ and $t_0 \in [0, T]$.

Ruled Surface with Common Geodesic Curve in Lie Group

Let $P(s,t)$ be a ruled surface with the directrix $\alpha(s)$ which is also an isoparametric curve on P . Then there exists a parameter $t = t_0$ such that $P(s, t_0) = \alpha(s)$. Thus, the surface $P(s,t)$ can be written as follows

$$P(s, t) - P(s, t_0) = (t - t_0)\zeta(s),$$

where $0 \leq s \leq L$, $0 \leq t \leq T$ and $t_0 \in [0, T]$ and $\zeta(s)$ denotes the direction of the rulings.

By using (2), the surface is equivalent to

$$(t - t_0)\zeta(s) = \lambda_1(s, t)N(s) + \lambda_2(s, t)C(s) + \lambda_3(s, t)W(s). \quad (7)$$

Since the curve $\alpha(s)$ is the isogeodesic curve, by using the conditions given Theorem 2, one can easily write that

$$\lambda_1(s, t) = 0, \lambda_2(s, t) = \mu(s)(t - t_0), \lambda_3(s, t) = \nu(s)(t - t_0),$$

where $\mu(s)$ and $\nu(s)$ are some real functions.

So, substituting these values of $\lambda_1(s, t)$, $\lambda_2(s, t)$ and $\lambda_3(s, t)$ into (7), we easily obtain

$$\zeta(s) = \mu(s)C(s) + \nu(s)W(s), \quad (8)$$

for all $s \in [0, L]$.

The ruled surface with the given isogeodesic directrix $\alpha(s)$ is written by

$$P(s, t) = \alpha(s) + (t - t_0)(\mu(s)C(s) + \nu(s)W(s)), \quad (9)$$

where $\mu(s)$ and $\nu(s)$ are two controlling functions of the surface.

Corollary 3.

If the given ruled surface (9) is developable in the Lie group, then μ equals zero.

Proof. If the surface $P(s,t)$ is developable, then we know that $\det[\alpha', \zeta, \zeta'] = 0$. Using (1), we get

$$\det[\alpha', \zeta, \zeta'] = \mu(s)f(s) \left(\frac{\nu(s)\kappa(s)}{f(s)} + \frac{\mu(s)\kappa(s)h(s)}{f(s)} \right).$$

Since $f(s) \neq 0$ and by using the conditions given Theorem 2, if the above equation equals zero, then we get $\mu(s) = 0$.

So, the developable surface with the curve α as a isogeodesic can be written

$$P(s, t) = \alpha(s) + (t - t_0) \frac{cf(s)}{\kappa(s)} W(s), \quad (10)$$

where $c = \text{const.} \neq 0$. Then $\zeta(s)$ can be given as

$$\zeta(s) = \frac{cf(s)}{\kappa(s)} W(s). \quad (11)$$

Corollary 4.

The developable surface $P(s,t)$ is a cylinder surface if and only if $\alpha(s)$ is a general helix.

Proof. If the developable surface $P(s, t)$ is cylindrical, then we know that $\zeta \times \zeta' = 0$. The derivatives of (11) and from (1), we get

$$\zeta \times \zeta' = \frac{c^2 f^2(s)}{\kappa^2(s)} g(s)N(s) = 0.$$

If the above equation equals zero vector, since $f(s) \neq 0$ and $\kappa(s) \neq 0$, then we get $g(s) = 0$. This means that $h = const$. From Theorem 1, we get that the curve is a general helix.

Conclusion 5. General helices on the cylinder surface in the Lie Group G are isogeodesic.

Example 6. Let

$$\alpha(s) = (0, -\sin s, \cos s) \tag{12}$$

be a unit speed curve. Then the curve α is framed in terms of the alternative frame as follows

$$N(s) = (0, \sin s, -\cos s),$$

$$C(s) = \frac{2}{\sqrt{5}} \left(-\frac{1}{2}, \cos s, \sin s\right),$$

$$W(s) = \frac{2}{\sqrt{5}} \left(1, \frac{1}{2} \cos s, \frac{1}{2} \sin s\right),$$

where $f(s) = \frac{\sqrt{5}}{2}$, $g(s) = 0$ and $\kappa = 1$, $h = -\frac{1}{2}$.

i) Taking $c = 1$, $t_0 = 0$ and from (10), then we get a ruled surface $P_1(s, t)$ that is a developable cylindrical with an isogeodesic curve $\alpha(s)$ as shown in Figure 1:

$$P_1(s, t) = \left(t, -\sin s + \frac{t}{2} \cos s, \cos s + \frac{t}{2} \sin s\right),$$

where $0 \leq s \leq 2\pi$ and $0 \leq t \leq 4$.

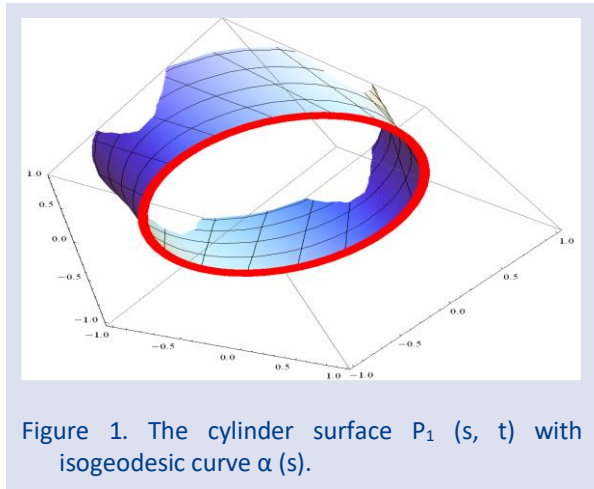


Figure 1. The cylinder surface $P_1(s, t)$ with isogeodesic curve $\alpha(s)$.

ii) Considering $\lambda_1(s, t) = 0$, $\lambda_2(s, t) = \sqrt{5}t$, $\lambda_3(s, t) = \sqrt{5}t$ and $t_0 = 0$ such as the Theorem 2 is satisfied. Then we get another surface $P_2(s, t)$, that is

also the cylinder surface, with an isogeodesic curve $\alpha(s)$ as shown in Figure 2.

$$P_2(s, t) = (t, -\sin s + 3t \cos s, \cos s + 3t \sin s),$$

where $0 \leq s \leq 2\pi$ and $0 \leq t \leq 4$.

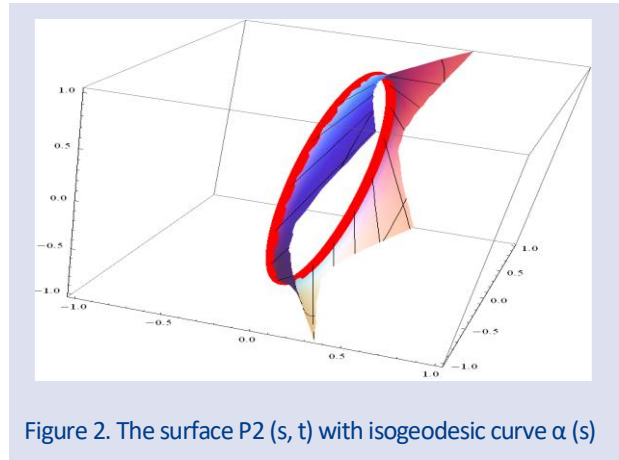


Figure 2. The surface $P_2(s, t)$ with isogeodesic curve $\alpha(s)$

Acknowledgment

We would like to thank the referees and editors who contributed to our article.

Conflicts of interest

The authors state that they did not have conflict of interests.

References

- [1] Bozkurt Z., Gök I, Okuyucu O. Z., Ekmekci F. N., Characterizations of rectifying, normal and osculating curves in three dimensional compact Lie groups, *Life Sci. J.*, 10(3) (2013) 819-823.
- [2] Çiftçi Ü. , A generalization of Lancret's theorem, *J. Geom. Phys.*, 59(12) (2009) 1597-1603.
- [3] Degirmen C., On curves in three dimensional compact Lie Groups, Master's Thesis, Bilecik Seyh Edebali University, 2017.
- [4] do Espirito-Santo N., Fornari S., Frensel K., Ripoll J., Constant mean curvature hypersurfaces in a Lie group with a bi-invariant metric, *Manuscripta Math.*, 111(4) (2003) 459-470.
- [5] Mak M., Natural and Conjugate Mates of Frenet Curves in Three-Dimensional Lie Group, arXiv preprint arXiv:2008.05831 (2020).
- [6] Okuyucu O. Z., Gök İ., Yaylı Y., Ekmekci N., Slant helices in three dimensional Lie groups, *Appl. Math. Comput.*, 221 (2013) 672-683.
- [7] Yoon D. W., General helices of AW(k)-type in the Lie group, *J. Appl. Math.*, (2012) ID 535123.
- [8] Yoon D. W., Tuncer Y., Karacan M. K., On curves of constant breadth in a 3-dimensional Lie group, *Acta Math. Univ. Comenian.*, 85(1) (2016) 81-86.
- [9] Jiang X., Jiang P., Meng J., Wang K., Surface pencil pair interpolating Bertrand pair as common asymptotic curves in Galilean space G_3 , *Int. J. Geom. Methods Mod. Phys.*, 18(7) (2021) 114-459.

- [10] Kasap E., Family of surface with a common null geodesic, *Int. J. Phys. Sci.*, 4(8) (2009) 428–433.
- [11] Kasap E., Akyıldız F.T., Surfaces with a common geodesic in Minkowski 3-space, *Appl. Math. Comp.*, 177 (2006) 260–270.
- [12] Küçükarslan Yüzbaşı Z., Bektaş M., On the construction of a surface family with common geodesic in Galilean space G_3 , *Open Phys.*, 14 (2016) 360–363.
- [13] Küçükarslan Yüzbaşı Z., Yoon D. W., On constructions of surfaces using a geodesic in Lie group, *J. Geo.*, 110(2) (2019) 1-10.
- [14] [Tuncer O.O., Surface pencil with a common isophote curve, Master's Thesis, Ankara University, 2016.
- [15] Wang G. J., Tang K., Tai C. L., Parametric representation of a surface pencil with a common spatial geodesic, *Comput. Aided Des.*, 36 (2004) 447–459.
- [16] Altın M., Kazan, A., Karadağ, H. B., Hypersurface families with Smarandache curves in Galilean 4-space, *Commun. Fac. Sci. Univ. Ank. Ser. A1 Math. Stat.*, 70 (2021) 744-761.
- [17] Ergun E., Bayram E., Surface family with a common natural asymptotic or geodesic lift of a spacelike curve with spacelike binormal in Minkowski 3-space, *Konuralp J. Math.*, 8 (2020) 7-13

On Involutes of Admissible Non-Lightlike Curves in Pseudo-Galilean 3-Space

Arfah Arfah^{1,a,*}

¹ Department of Mathematics, Faculty of Science, Karadeniz Technical University, Trabzon, Turkey.

*Corresponding author

Research Article

History

Received: 02/02/2021

Accepted: 30/01/2022

Copyright



©2022 Faculty of Science,
Sivas Cumhuriyet University

ABSTRACT

This paper aims to investigate the theory of involutes of admissible non-lightlike curves in pseudo-Galilean 3-space. In the second section of this paper, we give fundamental concepts of pseudo-Galilean 3-space and curves over this space together with their casual properties. In section three, the involute of admissible non-lightlike curves in pseudo-Galilean 3-space is defined. Furthermore, the properties of involutes of admissible non-lightlike curves are also investigated by applying the fundamental properties provided in section 2. In the last part but not least, we give some numerical examples as applications of the theorems and corollaries which are derived in the previous section.

Keywords: Involutes, Admissible curve, Non-lightlike, Pseudo-Galilean.

^a arfahn70@gmail.com

^{ORCID} <https://orcid.org/0000-0002-7654-5520>

Introduction

In gravitational theory, one has inevitably to introduce some kind of hypothesis concerning the properties of space as a whole. The simplest and at the same time the most important of these hypotheses is the assumption that, at infinity, space is Galilean. Both properties of uniformity and the whole theory of Galilean space may be formulated in arbitrary coordinates. However, the privileged character of Galilean coordinates manifests itself and in particular simplicity (linearity) of the transformations that relate to the inertial coordinate system, that class of system within which the physical principle of relativity holds. Pseudo-Galilean space possesses a pseudo-Euclidean metric [6]. In pseudo-Galilean space, there are three types of curves, namely spacelike, timelike and null (lightlike) curves. The theory of curves and surfaces in pseudo-Galilean space can be seen in [2, 3, 4, 5, 7, 10, 11, 12, 13, 14].

The theory of involute and evolute was firstly introduced by C. Huygens in 1673 when he tried to build an accurate clock called the isochronous pendulum clock. He found that the isochronous curve is an arc of cycloid and that involute of cycloid [9]. In classical differential geometry, a curve $\alpha^*(s)$ is called an involute of $\alpha(s)$ if it is lying in the tangent surface of $\alpha(s)$ and their tangent lines are perpendicular in all points on the curves. The theory of involutes of curves in Euclidean space has been provided in many books and articles. In this article the author refers to [1, 7, 8].

We organized our present work as follows: after the introduction in Section 1, we provide the basic properties of curves in pseudo-Galilean space in the second section. Then, we define and investigate the properties of the involutes of admissible non-lightlike curves in pseudo-Galilean space G_1^3 in the next section. To close this paper,

we give numerical examples of admissible non-lightlike curves in pseudo-Galilean space with their properties.

Preliminaries

The Pseudo-Galilean geometry is one of the real Cayley-Klein spaces whose projective signature $(0, 0, +, +)$ (see [10]). The absolute of the pseudo-Galilean geometry is an ordered triple $\{\omega, f, I\}$, where ω is the ideal (absolute) plane, f the line in ω and I the fixed elliptic involution of the points of f .

In appropriate affine coordinates for points and vectors (point pairs), the group B_6

$$\begin{aligned} \bar{x} &= a + x, \\ \bar{y} &= b + dx + y \cosh \varphi + z \sinh \varphi, \\ \bar{z} &= c + ex + y \sinh \varphi + z \cosh \varphi \end{aligned}$$

of pseudo-Galilean proper notions will preserve the absolute. Let the group

$$\overline{B}_6 := \langle B_6, \begin{bmatrix} 1 & 0 & 0 \\ 0 & -1 & 0 \\ 0 & 0 & -1 \end{bmatrix} \rangle$$

be called the motion group of the pseudo-Galilean space G_3^1 . The motion group \overline{B}_6 leaves invariant the absolute figure and defines the other invariants of this geometry.

In the affine coordinates, the group \overline{B}_6 acts as follows

$$\begin{aligned} \bar{x} &= a + x, \\ \bar{y} &= b + dx + y\eta \cos \varphi + z\eta \sin \varphi, \\ \bar{z} &= d + ex + y\eta \sin \varphi + z\eta \cos \varphi, \end{aligned}$$

where η is $+1$ or -1 .

Distance between two distinct proper points $P(x_1, y_1, z_1)$ and $Q(x_2, y_2, z_2)$ is given by

$$d(P, Q) = \begin{cases} |x_2 - x_1| & \text{if } x_1 \neq x_2, \\ \sqrt{|(y_2 - y_1)^2 - (z_2 - z_1)^2|} & \text{if } x_1 = x_2. \end{cases}$$

According to the group \overline{B}_6 there are non-isotropic and isotropic vectors. A vector $v(x, y, z)$ is called non-isotropic if $x \neq 0$ and its unit vector can be expressed in $(1, y, z)$ form. On the other hand, vector $v(x, y, z)$ is called isotropic if $x = 0$. In the case of isotropic vector, there are for types of vectors: spacelike ($y^2 - z^2 > 0$), timelike ($y^2 - z^2 < 0$) and two types of lightlike ($y = \pm z$). A non-lightlike vector is a unit vector if $y^2 - z^2 = \pm 1$.

Scalar product of two vectors $v(x_1, y_1, z_1)$ and $w(x_2, y_2, z_2)$ in the pseudo-Galilean 3-space is defined by

$$g(v, w) = \begin{cases} x_1x_2 & \text{if } x_1 \neq 0 \text{ or } x_2 \neq 0, \\ y_1y_2 - z_1z_2 & \text{if } x_1 = 0 \text{ and } x_2 = 0. \end{cases}$$

The norm of P is given by

$$\|x\| = \begin{cases} |x_1| & \text{if } x_1 \neq 0, \\ \sqrt{|y_1^2 - z_1^2|} & \text{if } x_1 = 0. \end{cases}$$

The vector product of v and w in G_3^1 is defined by

$$v \times w = \begin{vmatrix} 0 & -e_2 & e_3 \\ x_1 & y_1 & z_1 \\ x_2 & y_2 & z_2 \end{vmatrix}$$

where $e_2 = (0, 1, 0)$ and $e_3 = (0, 0, 1)$.

A curve $\alpha(t) = (x(t), y(t), z(t))$ is said admissible if it has no inflection points ($\alpha' \times \alpha'' \neq 0$), no isotropic tangent ($x' = 0$) or normal whose projections on the absolute plane would be lightlike vectors ($y'' = \pm z''$). For an admissible curve $\alpha(t)$, the curvature $\kappa(t)$ and the torsion $\tau(t)$ are defined by

$$\kappa(t) = \frac{\sqrt{|(y''(t))^2 - (z''(t))^2|}}{(x'(t))^2},$$

$$\tau(t) = \frac{y''(t)z'''(t) - y'''(t)z''(t)}{\kappa^2(t)}.$$

An admissible curve $\alpha: I \subset \mathbb{R} \rightarrow G_3^1$ which is parametrized by arc length s can be written the form of

$$\alpha(s) = (s, y(s), z(s)).$$

Then, the curvature and torsion of $\alpha(s)$ are given by

$$\kappa(s) = \sqrt{|(y''(s))^2 - (z''(s))^2|},$$

$$\tau(s) = \frac{y''(s)z'''(s) - y'''(s)z''(s)}{\kappa^2(s)}.$$

The orthonormal trihedron of non-null curve $\alpha(s)$ in pseudo-Galilean 3-space is given by

$$\begin{aligned} T(s) &= \alpha'(s), & N(s) &= \frac{\alpha''(s)}{\kappa(s)}, \\ B(s) &= \frac{(0, \epsilon z''(s), \epsilon y''(s))}{\kappa(s)} \end{aligned}$$

where $\epsilon = +1$ if $\alpha(s)$ is a spacelike curve and $\epsilon = -1$ if $\alpha(s)$ is a timelike curve. Here T, N, B are called the tangent, principal normal, and binormal vector fields of α , respectively. Indeed, curve $\alpha(s)$ is spacelike (resp. timelike) if $N(s)$ is spacelike (resp. timelike) vectors. Furthermore, the Frenet formulas of the curve are given by

$$\begin{aligned} T'(s) &= \kappa(s)N(s), & N'(s) &= \tau(s)B(s), \\ B'(s) &= \tau(s)N(s). \end{aligned}$$

(see [2, 3, 11, 13].)

Involutes of Admissible Curves in Pseudo-Galilean Space

In this section, we will define the involute of admissible curves in pseudo-Galilean 3-space and investigate the casual properties of the involute of admissible non-lightlike curves in pseudo-Galilean 3-space.

Definition 3.1. Let $\alpha: I \subset \mathbb{R} \rightarrow G_3^1$ and $\beta: I \subset \mathbb{R} \rightarrow G_3^1$ be curves in pseudo-Galilean space. For all $s \in I$, $\beta(s)$ is called the involute of $\alpha(s)$ if and only if the tangent of α at the point $\alpha(s)$ passes through the tangent at the point $\beta(s)$ of the curve β and

$$g(\bar{T}, T) = 0,$$

where T and \bar{T} are the tangent of curves α and β , respectively.

Theorem 3.1. Let $\beta(s)$ be the involute of an admissible non-lightlike curve $\alpha(s)$ parametrized by arc length s and c be a constant real number. Then,

$$\beta(s) = \alpha(s) + (c - s)T(s) \tag{1}$$

Proof.

Let $\alpha(s)$ be an admissible non-lightlike curve in pseudo-Galilean G_3^1 space. The tangent line of curve $\alpha(s)$ will construct a tangent surface. If $\beta(s)$ is the involute of $\alpha(s)$, then $\beta(s)$ lies on the tangent surface and is orthogonal to all tangent line of $\alpha(s)$. Suppose \bar{p} be the point of $\beta(s)$ which crosses the tangent line $T(s)$ of $\alpha(s)$ at point p . Then, $\bar{p} - p$ is proportional to $T(s)$. Consequently, $\beta(s)$ can be expressed in the form of

$$\beta(s) = \alpha(s) + \lambda(s)T(s). \tag{2}$$

Taking the derivative of (2) yields

$$\beta'(s) = \alpha'(s) + \lambda'(s)T(s) + \lambda(s)\kappa(s)N(s)$$

$$\begin{aligned}
 &= T(s) + \lambda'(s)T(s) + \lambda(s)\kappa(s)N(s) \\
 &= (1 + \lambda'(s))T(s) + \lambda(s)N(s).
 \end{aligned}$$

Consequently, by definition 3.1, we have

$$\begin{aligned}
 g(\beta'(s), T(s)) &= (1 + \lambda'(s))g(T(s), T(s)) + \\
 \lambda(s)\kappa(s)(N(s), T(s)) &= 1 + \lambda'(s) = 0.
 \end{aligned} \tag{3}$$

Integrating (3) gives $\lambda(s) = -s + c$, where c is the real constant. Thus, by (1) there exist an infinite family of involutes of $\alpha(s)$ given by

$$\beta(s) = \alpha(s) + (c - s)T(s). \tag{4}$$

Theorem 3.2. Let $\beta(s)$ be the involute of an admissible non-lightlike curve $\alpha(s)$ parametrized by arc-length s in pseudo-Galilean G_3^1 . Suppose $\{T(s), N(s), B(s)\}$ and $\{\bar{T}(s), \bar{N}(s), \bar{B}(s)\}$ are the orthonormal trihedron of the curve $\alpha(s)$ and $\beta(s)$ respectively. Then,

$$\begin{bmatrix} \bar{T}(s) \\ \bar{N}(s) \\ \bar{B}(s) \end{bmatrix} = \begin{bmatrix} 0 & 1 & 0 \\ 0 & 0 & 1 \\ 0 & 0 & 0 \end{bmatrix} \begin{bmatrix} T(s) \\ N(s) \\ B(s) \end{bmatrix} \tag{5}$$

Proof.

First, taking the derivative of (1) gives

$$\begin{aligned}
 \beta'(s) &= T(s) - T(s) + (c - s)\kappa(s)N(s) \\
 &= (c - s)\kappa(s)N(s).
 \end{aligned}$$

So that,

$$\bar{T} = \frac{(c - s)\kappa(s)N(s)}{\|(c - s)\kappa(s)N(s)\|} = \frac{(c - s)\kappa(s)N(s)}{|(c - s)\kappa(s)|} = \pm N(s).$$

Since \bar{T} and N are both unit vectors, then we can assume that

$$\bar{T}(s) = N(s). \tag{6}$$

Taking the derivative of (6) gives

$$\bar{T}'(s) = \tau(s)B(s),$$

and

$$\|\bar{T}(s)\| = |\tau(s)|. \tag{7}$$

So that

$$\bar{N}(s) = \frac{\tau(s)B(s)}{|\tau(s)|} = \pm B(s).$$

Again since \bar{N} and B are both unit vectors, then we can assume that

$$\bar{N}(s) = B(s). \tag{8}$$

Since $\alpha(s)$ is an admissible curve, then it can be expressed as $\alpha(s) = (s, y(s), z(s))$. As a consequence, we have

$$\begin{aligned}
 \bar{B}(s) &= \bar{T}(s) \times \bar{N}(s) = N(s) \times B(s) = \\
 &\begin{vmatrix} 0 & -e_2 & e_3 \\ 0 & \frac{y''(s)}{\kappa(s)} & \frac{z''(s)}{\kappa(s)} \\ 0 & \frac{\epsilon z''(s)}{\kappa(s)} & \frac{\epsilon y''(s)}{\kappa(s)} \end{vmatrix}
 \end{aligned} \tag{9}$$

Remark 3.1. The theorem above shows that binormal vector of the curve $\beta(s)$ vanishes which imply that $\beta(s)$ is a plane curve.

Theorem 3.3. Let $\beta(s)$ be the involute of an admissible non-lightlike curve $\alpha(s)$ parametrized by arc-length s in pseudo-Galilean G_3^1 . Suppose κ and τ are the curvature and torsion of α , respectively while $\bar{\kappa}$ and $\bar{\tau}$ are the curvature ad torsion of β , respectively, then

$$\bar{\kappa}(s) = |\tau(s)|, \quad \tau(s) = 0. \tag{10}$$

Proof.

It is easy to see that

$$\bar{\kappa}(s) = \|\bar{T}'(s)\| = |\tau(s)|.$$

Since $\beta(s)$ might be a curve not parametrized by arc length so as in the preliminary part,

$$\bar{\tau} = \frac{\det(\beta'(s), \beta''(s), \beta'''(s))}{|\beta'|^5 \bar{\kappa}^2(s)}.$$

From the proof of theorem 3.2 we have

$$\beta' = (c - s)\kappa N.$$

Taking the derivative of $\beta'(s)$ twice again yields

$$\begin{aligned}
 \beta''(s) &= ((c - s)\kappa)'N + (c - s)\kappa\tau B \\
 &= (((c - s)\kappa)'' + (c - s)\kappa\tau^2)N + (((c - s)\kappa)'\tau + \\
 &\quad ((c - s)\kappa\tau)')B.
 \end{aligned}$$

So that

$$\begin{aligned}
 \beta'' \times \beta''' &= -(c - s)\kappa\tau(((c - s)\kappa)'' + (c - \\
 &\quad s)\kappa\tau^2)T + ((c - s)\kappa)'(((c - s)\kappa)'' + (c - \\
 &\quad s)\kappa\tau^2)T + ((c - s)\kappa)'T
 \end{aligned}$$

This implies

$$\det(\beta', \beta'', \beta''') = \beta' \cdot (\beta'' \times \beta''') = 0$$

Since $g(T, N) = 0$. Consequently, $\bar{\tau} = 0$.

Corollary 3.1. Let $\beta(s)$ be the involute of an admissible non-lightlike curve $\alpha(s)$ parametrized by arc-length s in pseudo-Galilean G_3^1 , then $\beta(s)$ is a plane curve.

Corollary 3.2. Let $\alpha(s)$ be an admissible non-lightlike curve parametrized by arc length s in pseudo-Galilean G_3^1 . $\alpha(s)$ has no involute if it is a plane curve.

Corollary 3.3. Let $\beta(s)$ be the involute of an admissible non-lightlike curve $\alpha(s)$ parametrized by arc length s in pseudo-Galilean G_3^1 . If $\alpha(s)$ is a plane curve with constant torsion, then $\beta(s)$ is a circle with radius $r = \frac{1}{|\tau(s)|}$.

Theorem 3.4. Involute of the admissible curve parametrized by arc length s in pseudo-Galilean space is not admissible.

Proof.

Let $\alpha(s)$ be an admissible non-lightlike curve parametrized by arc length s in pseudo-Galilean space. Therefore, $\alpha(s)$ can be written as

$$\alpha(s) = (s, y(s), z(s)).$$

Then, by (1) we have

$$\begin{aligned} \beta(s) &= \alpha(s) + (c - s)T(s) \\ &= (s, y(s), z(s)) + (c - s)(1, y'(s), z'(s)) \\ &= (c, y(s) - (c - s)y'(s), z(s) - (c - s)z'(s)). \end{aligned}$$

Taking the first derivative of the last equation above yields zero in the first component. Hence, its tangent vector is isotropic, and it implies the curve $\beta(s)$ is a non-admissible curve.

Theorem 3.5.

The involute of an admissible spacelike curve in pseudo-Galilean space is a timelike curve and the involute of the timelike curve in pseudo-Galilean space is a spacelike curve.

Proof.

Let $\alpha(s)$ be an admissible spacelike curve parametrized by arc length s in pseudo-Galilean space and expressed by $\alpha(s) = (s, y(s), z(s))$. Then, the principal normal vector field $N(s)$ of $\alpha(s)$ is spacelike and $(y''(s))^2 - (z''(s))^2 > 0$. It implies the binormal vector field $B(s)$ of $\alpha(s)$ become timelike since $(\epsilon z''(s))^2 - (\epsilon y''(s))^2 = (z''(s))^2 - (y''(s))^2 < 0$. By equation (5) we have $\bar{N}(s) = B(s)$ which means that the principal normal vector field $\bar{N}(s)$ of $\beta(s)$ is also timelike. Hence, by definition $\beta(s)$ is a timelike curve. In the same way, if we set $\alpha(s)$ be timelike curve parametrized in pseudo-Galilean space then its involute will be spacelike.

Numerical Examples

Example 4.1. Let $\alpha: I \subset \mathbb{R} \rightarrow G_3^1$ be an admissible non-lightlike curve parametrized by arc length s in pseudo-Galilean space and defined by

$$\alpha(s) = (s, \cosh s, \sinh s).$$

Taking the derivative of $\alpha(s)$ three times yields

$$\begin{aligned} \alpha'(s) &= (1, \sinh s, \cosh s), \\ \alpha''(s) &= (0, \cosh s, \sinh s), \\ \alpha'''(s) &= (0, \sinh s, \cosh s). \end{aligned}$$

Since $(\alpha''(s), \alpha''(s)) = \cosh^2 s - \sinh^2 s = 1 > 0$ then $\alpha(s)$ is a spacelike curve. The curvature and torsion of $\alpha(s)$ are given by

$$\kappa(s) = \sqrt{|(y''(s))^2 - (z''(s))^2|} = \sqrt{|\cosh^2 s - \sinh^2 s|} = 1$$

$$\tau(s) = \frac{y''(s)z'''(s) - y'''(s)z''(s)}{\kappa^2(s)} = \frac{\cosh^2 s - \sinh^2 s}{1} = 1$$

and the orthonormal trihedron of $\alpha(s)$ are

$$T(s) = \alpha'(s) = (1, \sinh s, \cosh s)$$

$$N(s) = \frac{1}{\kappa(s)} \alpha''(s) = (0, \cosh s, \sinh s)$$

$$B(s) = \frac{1}{\kappa(s)} (0, \epsilon z''(s), \epsilon y''(s)) = (0, \sinh s, \cosh s).$$

Note that $\epsilon = 1$ since $\alpha(s)$ is a spacelike curve.

Consequently, the involute of the curve $\alpha(s)$ is given by

$$\begin{aligned} \beta(s) &= \alpha(s) + (c - s)T(s) \\ &= (s, \cosh s, \sinh s) + (c - s)(1, \sinh s, \cosh s) \\ &= \left(c, \cosh s + (c - s) \sinh s, \sinh s + (c - s) \cosh s \right). \end{aligned}$$

The orthogonal dihedron of $\beta(s)$ are

$$\bar{T}(s) = N(s) = (0, \cosh s, \sinh s)$$

$$\bar{N}(s) = B(s) = (0, \sinh s, \cosh s)$$

And the curvature of $\beta(s)$ is $\bar{\kappa}(s) = |\tau(s)| = 1$.

Example 4.2. Let $\gamma: I \subset \mathbb{R} \rightarrow G_3^1$ be an admissible non-lightlike curve parametrized by arc length s in pseudo-Galilean space and defined by

$$\gamma(s) = \left(s, \frac{s^5}{80} + \frac{1}{2s}, \frac{s^5}{80} - \frac{1}{2s} \right).$$

Taking the derivative of $\gamma(s)$ three times yields

$$\begin{aligned} \gamma'(s) &= \left(1, \frac{s^4}{16} - \frac{1}{2s^2}, \frac{s^4}{16} + \frac{1}{2s^2} \right), \\ \gamma''(s) &= \left(0, \frac{s^3}{4} + \frac{1}{s^3}, \frac{s^3}{4} - \frac{1}{s^3} \right), \\ \gamma'''(s) &= \left(0, \frac{3s^2}{4} - \frac{3}{2s^4}, \frac{3s^2}{4} + \frac{3}{2s^4} \right). \end{aligned}$$

Since

$(\gamma''(s), \gamma''(s)) = \left(\frac{s^3}{4} + \frac{1}{s^3} \right)^2 - \left(\frac{s^3}{4} - \frac{1}{s^3} \right)^2 = 1 > 0$, then $\alpha(s)$ is a spacelike curve. The curvature and torsion of $\gamma(s)$ are given by

$$\begin{aligned} \kappa(s) &= \sqrt{|(y''(s))^2 - (z''(s))^2|} \\ &= \sqrt{\left| \left(\frac{s^3}{4} + \frac{1}{s^3} \right)^2 - \left(\frac{s^3}{4} - \frac{1}{s^3} \right)^2 \right|} = 1 \end{aligned}$$

$$\tau(s) = \frac{y''(s)z'''(z) - y'''(s)z''(s)}{\kappa^2(s)}$$

$$= \left(\frac{s^3}{4} + \frac{1}{s^3} \frac{s^3}{4} + \frac{1}{s^3}\right) \left(\frac{3s^2}{4} + \frac{3}{2s^4}\right) - \left(\frac{s^3}{4} - \frac{1}{s^3}\right) \left(\frac{3s^2}{4} - \frac{3}{2s^4}\right) = \frac{3}{s}$$

and the orthonormal trihedron of $\gamma(s)$ are

$$T(s) = \gamma'(s) = \left(1, \frac{s^4}{16} - \frac{1}{2s^2}, \frac{s^4}{16} + \frac{1}{2s^2}\right)$$

$$N(s) = \frac{1}{\kappa(s)}\gamma''(s) = \left(0, \frac{s^3}{4} + \frac{1}{s^3}, \frac{s^3}{4} - \frac{1}{s^3}\right)$$

$$B(s) = \frac{1}{\kappa(s)}(0, \epsilon z''(s), \epsilon y''(s)) = \left(0, \frac{s^3}{4} - \frac{1}{s^3}, \frac{s^3}{4} + \frac{1}{s^3}\right).$$

Note that $\epsilon = 1$ since $\gamma(s)$ is a spacelike curve. Consequently, the involute of the curve $\gamma(s)$ is given by

$$\bar{\gamma}(s) = \gamma(s) + (c - s)T(s)$$

$$= \left(s, \frac{s^5}{80} + \frac{1}{2s}, \frac{s^5}{80} - \frac{1}{2s}\right) + (c - s) \left(1, \frac{s^4}{16} - \frac{1}{2s^2}, \frac{s^4}{16} + \frac{1}{2s^2}\right)$$

$$= \left(c, \frac{s^5}{80} + \frac{1}{2s} + (c - s) \left(\frac{s^4}{16} - \frac{1}{2s^2}\right), \frac{s^5}{80} - \frac{1}{2s} + (c - s) \left(\frac{s^4}{16} + \frac{1}{2s^2}\right)\right).$$

The orthogonal dihedron of $\bar{\gamma}(s)$ are

$$\bar{T}(s) = N(s) = \left(0, \frac{s^3}{4} + \frac{1}{s^3}, \frac{s^3}{4} - \frac{1}{s^3}\right)$$

$$\bar{N}(s) = B(s) = \left(0, \frac{s^3}{4} - \frac{1}{s^3}, \frac{s^3}{4} + \frac{1}{s^3}\right)$$

And the curvature of $\bar{\gamma}(s)$ is $\bar{\kappa}(s) = |\tau(s)| = \left|\frac{3}{s}\right|$

Example 4.3. Let $r: I \subset \mathbb{R} \rightarrow G_3^1$ be an admissible non-lightlike curve parametrized by arc length s in pseudo-Galilean space and defined by

$$r(s) = \left(s, \frac{e^{2s}}{4} - \frac{s^3}{6}, \frac{e^{2s}}{4} + \frac{s^3}{6}\right).$$

Taking the derivative of $r(s)$ three times yields

$$r'(s) = \left(1, \frac{e^{2s}}{2} - \frac{s^2}{2}, \frac{e^{2s}}{2} + \frac{s^2}{2}\right),$$

$$r''(s) = (0, e^{2s} - s, e^{2s} + s),$$

$$r'''(s) = (0, 2e^{2s}, 2e^{2s}).$$

Since $(r''(s), r''(s)) = (e^{2s} - s)^2 - (e^{2s} + s)^2 = -4e^{2s} < 0$ then $\alpha(s)$ is a timelike curve. The curvature and torsion of $r(s)$ are given by

$$\kappa(s) = \sqrt{|(y''(s))^2 - (z''(s))^2|} = \sqrt{|(e^{2s} - s)^2 - (e^{2s} + s)^2|} = \sqrt{|-4e^{2s}|} = 2e^s$$

$$\tau(s) = \frac{y''(s)z'''(z) - y'''(s)z''(s)}{\kappa^2(s)}$$

$$= \frac{(e^{2s} - s)(2e^{2s}) - (2e^{2s})(e^{2s} + s)}{4e^{2s}} = -s$$

and the orthonormal trihedron of $r(s)$ are

$$T(s) = r'(s) = \left(1, \frac{e^{2s}}{2} - \frac{s^2}{2}, \frac{e^{2s}}{2} + \frac{s^2}{2}\right)$$

$$N(s) = \frac{1}{\kappa(s)}r''(s) = \left(0, \frac{e^{2s} - s}{2e^s}, \frac{e^{2s} + s}{2e^s}\right)$$

$$B(s) = \frac{1}{\kappa(s)}(0, \epsilon z''(s), \epsilon y''(s)) = \left(0, -\frac{e^{2s} + s}{2e^s}, -\frac{e^{2s} - s}{2e^s}\right).$$

Note that $\epsilon = -1$ since $r(s)$ is a timelike curve.

Consequently, the involute of the curve $r(s)$ is given by

$$\bar{r}(s) = r(s) + (c - s)T(s)$$

$$= \left(s, \frac{e^{2s}}{4} - \frac{s^3}{6}, \frac{e^{2s}}{4} + \frac{s^3}{6}\right) + (c - s) \left(1, \frac{e^{2s}}{2} - \frac{s^2}{2}, \frac{e^{2s}}{2} + \frac{s^2}{2}\right)$$

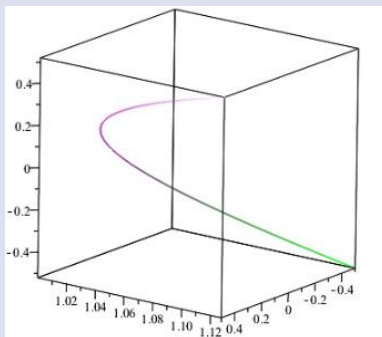
$$= \left(c, \frac{e^{2s}}{4} - \frac{s^3}{6} + (c - s) \left(\frac{e^{2s}}{2} - \frac{s^2}{2}\right), \frac{e^{2s}}{4} + \frac{s^3}{6} + (c - s) \left(\frac{e^{2s}}{2} + \frac{s^2}{2}\right)\right).$$

The orthogonal dihedron of $\bar{r}(s)$ are

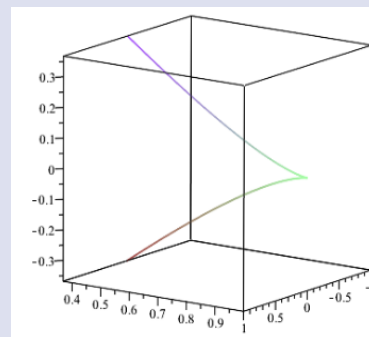
$$\bar{T}(s) = N(s) = \left(0, \frac{e^{2s} - s}{2e^s}, \frac{e^{2s} + s}{2e^s}\right)$$

$$\bar{N}(s) = B(s) = \left(0, -\frac{e^{2s} + s}{2e^s}, -\frac{e^{2s} - s}{2e^s}\right)$$

And the curvature of $\bar{r}(s)$ is $\bar{\kappa}(s) = |\tau(s)| = |s|$

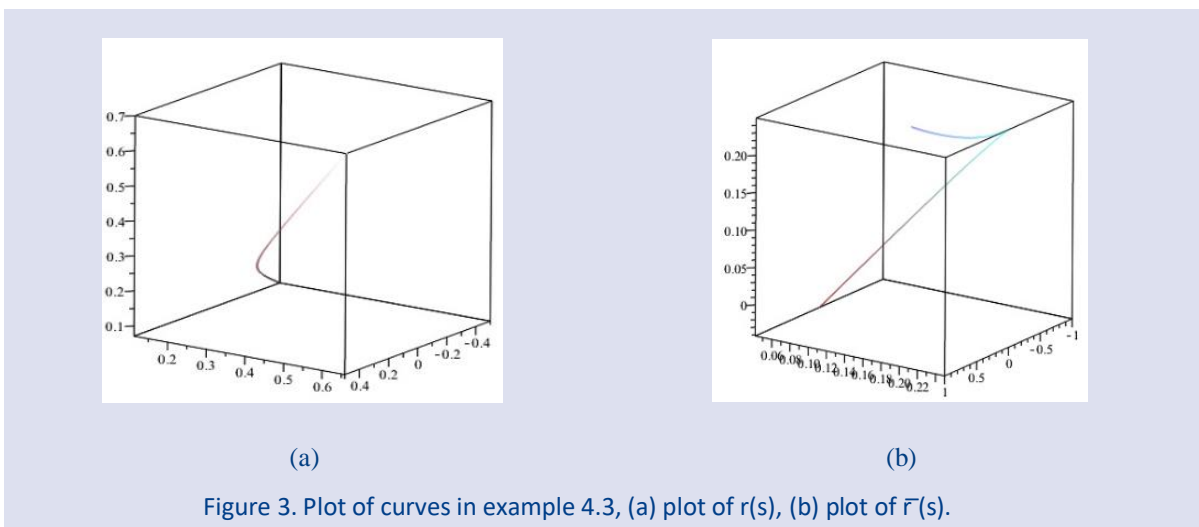
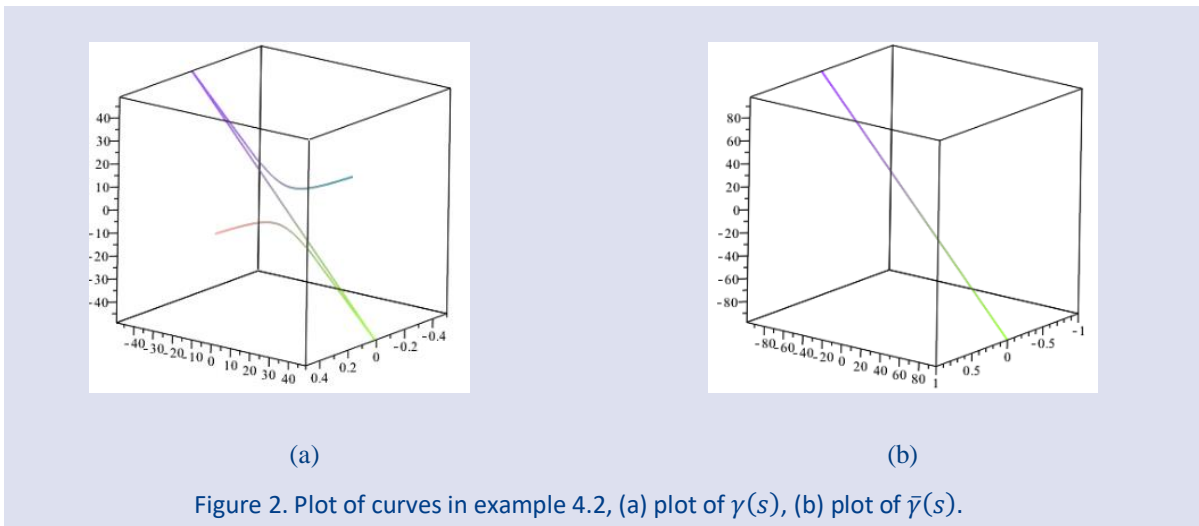


(a)



(b)

Figure 1. Plot of curves in example 4.1, (a) plot of $\alpha(s)$, (b) plot of $\beta(s)$



Acknowledgment

The author would like to thank the referees for all the useful suggestions

Conflicts of interest

The author states that he has no conflict of interest to declare that are relevant to the content of this article.

References

- [1] Carmo M.P.D., Differential Geometry of Curves and Surfaces, Canada: Dover Publication Inc., 2016.
- [2] Divjak B., Curves in Pseudo-Galilean Geometry, *Annales Universitatis Scientiarum Budapestinensis de Rolando Eötvös Nominatae. Sectio Mathematica*, 41 (1998) 117-128.
- [3] Divjak B., The Equiform Differential Geometry of Curves in the Pseudo-Galilean Space, *Mathematical Communications*, 13(2) (2008).
- [4] Divjak B., Sipus M.Z., Some Special Surfaces in the Pseudo-Galilean space. *Acta Mathematica Hungarica*, 118 (2008) 209-226.
- [5] Elzawy M., Mosa M., Helicoidal Surfaces in Galilean Space with Density, *Frontiers in Physics*, 8 (2020) 1-6.
- [6] Fock V., The Theory of Space, Time and Gravitation. 2nd ed. England: Pergamon Press, 1964.
- [7] Fuchs T., Evolutes and Involutes of Spatial Curve. *The American Mathematical Monthly*, 120 (2013) 217-231.
- [8] Lipschutz M.M., Schaum's Outline of Differential Geometry, Canada: McGraw Hill, 1969.
- [9] Merbach U.C., Boyer C.B., A history of Mathematics, New Jersey: John Wiley and Sons Inc., 2011.
- [10] Saad M.K., Spacelike and Timelike Admissible Smarandache Curves in Pseudo-Galilean Space, *Journal of the Egyptian Mathematical Society*, 24(3) (2016) 416-423.
- [11] Sahin T., Intrinsic Equations for a Generalized Relaxed Elastic Line on an Oriented Surface in the Galilean Space, *Acta Math. Sci.*, 33(3) (2013) 701-711.
- [12] Sipus M.Z., Divjak B., Surfaces of Constant Curvature in the Pseudo-Galilean Space, *International Journal of Mathematics and Mathematical Sciences*, 2012 (2012) 1-28.
- [13] Tuncer Y., Canal Surface in Galilean 3-Space, *Kyungpook Mathematical Journal*, 57(2) (2017) 319-326.
- [14] Yuzbasi Z.K., Yoon D.W., Geometry of Isophote Curves in Galilean Space, *AIMS Mathematics*, 6(1) (2021) 66-76.

Period-doubling Bifurcation and Stability in a Two Dimensional Discrete Prey-predator Model with Allee Effect and Immigration Parameter on Prey

Figen Kangalgil ^{1,a}, Feda Gümüşboğa ^{1,b,*}

¹ Bergama Vocational High School, Dokuz Eylul University, 35700, İzmir, Turkey.

² Department of Mathematics, Faculty of Art and Science, Bolu Abant İzzet Baysal University, 14030, Bolu, Turkey.

*Corresponding author

Research Article

History

Received: 10/11/2021

Accepted: 16/02/2022

Copyright



©2022 Faculty of Science,

Sivas Cumhuriyet University

ABSTRACT

This article is about the dynamics of a discrete-time prey-predator system with Allee effect and immigration parameter on prey population. Particularly, we study existence and local asymptotic stability of the unique positive fixed point. Furthermore, the conditions for the existence of bifurcation in the system are derived. In addition, it is shown that the system goes through period-doubling bifurcation by using bifurcation theory and center manifold theorem. Eventually, numerical examples are given to illustrate theoretical results.

Keywords: Prey-predator model, Stability analysis, Fixed point, Allee effect, Period-doubling bifurcation.

 figen.kangalgil@deu.edu.tr

 <https://orcid.org/0000-0003-0116-8553>

 gumusboga_f@ibu.edu.tr

 <https://orcid.org/0000-0003-2867-6304>

Introduction

Modelling the prey-predator interaction of a simple ecosystem is one of the important applications of the nonlinear system of differential equations in mathematical biology and ecology. The dynamics of such a system are observed by using the population data which is obtained by the interaction between a pair of prey-predator. The classical predator-prey system is known as Lotka-Volterra model which is first studied by Lotka [1] and Volterra [2]. For implementing more realistic assumptions in prey-predator model, a lot of modifications and extensions were introduced by several researchers [3-10].

As is well known, differential and difference equations are used in the theory of dynamical population models. Differential equations are used to describe continuous-time models while the discrete-time models are described by difference equations. Recent works showed that, researchers are more interested in discrete-time models than continuous-time models since the dynamics of discrete time models can produce a richer set of patterns. Additionally, many studies have proposed that the mathematical model of population dynamics becomes more suitable and practical when discrete-time equations are used for modelling. Besides they have the basic characteristics of the corresponding continuous-time models, they also provide a significant decrease of numerical simulation duration. Moreover, the discrete time models are more suitable for populations with nonoverlapping generations. In fact, nonlinear continuous models are discretized since nonlinear systems generally do not have analytic solutions expressible in terms of a finite representation of elementary functions. Authors in

[5-11] analyzed dynamical analysis of different types of discrete-time predator-prey systems.

In [12], the discrete-time prey-predator model represented by the following nonlinear system of difference equations is studied:

$$\begin{aligned}x_{n+1} &= \mu x_n(1 - x_n) - x_n y_n \\ y_{n+1} &= y_n(1 - \alpha) + \beta x_n y_n\end{aligned}\tag{1}$$

In (1), x_n and y_n represent prey and predator population densities in the n^{th} generation, respectively. The parameter μ is the intrinsic growth rate of the prey population with carrying ability one in the absence of predator. While α reflects the predators death rate; β denotes the growth rate of predator in the presence of the prey. All the parameters α , β and μ have positive values.

In this study, system (1) is improved with Allee effect and immigration on prey species and the following nonlinear system of difference equations is held:

$$x_{t+1} = \delta x_t(1 - x_t) - x_t y_t \frac{x_t}{x_t + m} + s\tag{2}$$

$$y_{t+1} = y_t(1 - \alpha) + \beta x_t y_t$$

In (2), δ is the intrinsic growth rate of prey population x_t , α and β are the death rate of predator and the growth rate of predator in the presence of the prey.

The parameter $s > 0$ represents the immigration parameter. Prey immigration is the number of individuals of the same species added to the prey population from another place in a certain period of time and it increases

the size of the population of prey. The immigration factor is an effect that makes the predator-prey population model more realistic [13-17]. So, many researchers studied the role of immigration and its impact on population dynamics. Detailed investigations relating to immigration may be found in the papers [18-22].

The term

$$\frac{x_t}{x_t + m}$$

is called Allee effect where $m > 0$ is Allee constant. Allee effects are encountered among many species such as mammals, plants, insects etc. It describes a positive correlation between the density of the population and the per capita growth rate. It means that, as the population gets smaller survivals of individuals and reproductive diversity decrease. In [23], it is pointed out that on different prey predator systems according to different

mechanisms the impact of the Allee effects can vary, too. In [24] and [25], it is shown that a ratio dependent prey predator model including Allee effect removes the possibility of population cycles. In [26] and [27], a new population model and a Lotka-Volterra commensal symbiosis model with Allee effect are studied, respectively. Allee effect and the immigration parameter have an important role in increasing the realism of the population models, besides they help to gain a more accurate description of the model.

This study is organized as follows: In Section 2, we discuss the existence and stability of fixed points of the system (2) and we give some numerical examples. In section 3, the existence of period-doubling bifurcation is shown with the help of bifurcation theory and center manifold theorem. The numerical simulation results are illustrated to confirm our analytical results and display the irregular dynamical behaviors of system (2).

The Existence and Stability of Fixed Points

In this section, the existence of fixed points is studied and the stability properties for system (2) is investigated. With the help of a simple calculation, it can be shown that the following system

$$\delta x(1 - x) - xy \frac{x}{x + m} + s = x \tag{3}$$

$$y(1 - \alpha) + \beta xy = y$$

has three fixed points:

$$P_1 = \left(\frac{\delta - 1 + \sqrt{(\delta - 1)^2 + 4\delta s}}{2\delta}, 0 \right)$$

$$P_2 = \left(-\frac{-\delta + 1 + \sqrt{(\delta - 1)^2 + 4\delta s}}{2\delta}, 0 \right)$$

and

$$P_3 = (x^*, y^*) = \left(\frac{\alpha}{\beta}, \frac{(\alpha^2\beta + \alpha m\beta^2 - \alpha^3 - \alpha^2 m\beta)\delta}{\alpha^2\beta} + \frac{s\alpha\beta^2 + sm\beta^3 - \alpha^2\beta - \alpha m\beta^2}{\alpha^2\beta} \right) \tag{4}$$

P_3 is the unique positive coexistence fixed point of the system (2) where the parameters $\alpha, \beta, \delta, m, s$ are all positive, $\beta - \alpha < 0$ and $(s\beta - \alpha) > 0$. We focus on the coexistence fixed point P_3 when studying stability analysis of the system (2).

It is well known that the local stability of the discrete-time system (2) is determined by calculating the eigenvalues of the Jacobian matrix which is evaluated at the coexistence fixed point P_3 . The Jacobian matrix of system (2) at P_3 is given as follows:

$$J(P_3) = \begin{bmatrix} J_{11} & J_{12} \\ J_{21} & J_{22} \end{bmatrix} \tag{5}$$

where

$$J_{11} = -\frac{\delta\alpha^3 - \alpha^2\beta + (\delta m - 2m + s)\beta^2\alpha + 2sm\beta^3}{\beta(\alpha + m\beta)\alpha}$$

$$J_{12} = -\frac{\alpha^2}{\beta(\alpha + m\beta)}$$

$$J_{21} = \frac{(\alpha(\alpha + m\beta)(\beta - \alpha))\delta + \beta(s\beta - \alpha)(\alpha + m\beta)}{\alpha^2}$$

$$J_{22} = 1$$

The matrix $J(P_3)$ yields the characteristic equation:

$$F(\lambda) = \lambda^2 - \text{tr}(J(P_3))\lambda + \det(J(P_3)) \quad (6)$$

where

$$\text{tr}(J(P_3)) = \frac{\delta\alpha^3 - 2\alpha^2\beta + (s - 3m + \delta m)\beta^2\alpha}{\beta(\alpha + m\beta)\alpha} + \frac{2sm\beta^3}{\beta(\alpha + m\beta)\alpha} \quad (7)$$

and

$$\begin{aligned} \det(J(P_3)) = & \frac{-\delta\alpha^3 + (-\beta - \delta + \delta\beta - \delta m\beta)\alpha^2}{\beta(\alpha + m\beta)} + \frac{(\beta - m\beta^2 + s\beta^2 + \delta m\beta^2)\alpha}{\beta(\alpha + m\beta)} \\ & + \frac{(-\delta m\beta^2 + 2m\beta^2 - s\beta^2 + sm\beta^3)\alpha - 2sm\beta^3}{\beta(\alpha + m\beta)\alpha} \end{aligned} \quad (8)$$

Definition 2.1. Let λ_1 and λ_2 are the roots of the characteristic polynomial $F(\lambda) = \lambda^2 + B\lambda + C$, $B, C \in \mathbb{R}$. Then the fixed point P_3 of the system (3) is called

- i) sink if $|\lambda_1| < 1$ and $|\lambda_2| < 1$,
- ii) source if $|\lambda_1| > 1$ and $|\lambda_2| > 1$,
- iii) saddle if $|\lambda_1| < 1$ and $|\lambda_2| > 1$ or $|\lambda_1| > 1$ and $|\lambda_2| < 1$.
- iv) non-hyperbolic if $|\lambda_1| = 1$ or $|\lambda_2| = 1$.

Definition 2.2. A fixed point is locally asymptotically stable if $|\lambda_1| < 1$ and $|\lambda_2| < 1$.

With the help of the following lemma, the stability of the coexistence fixed point of the system (2) is investigated.

Lemma 2.1. [28] Assume $F(\lambda) = \lambda^2 + B\lambda + C$, where B and C are two real constants and let $F(1) > 0$. Suppose that λ_1 and λ_2 are two roots of $F(\lambda) = 0$. Then the following statements hold:

- i) $|\lambda_1| < 1$ and $|\lambda_2| < 1$ if and only if $F(-1) > 0$ and $C < 1$,
- ii) $|\lambda_1| > 1$ and $|\lambda_2| > 1$ if and only if $F(-1) > 0$ and $C > 1$,
- iii) $|\lambda_1| > 1$ and $|\lambda_2| < 1$ if and only if $F(-1) < 0$,
- iv) λ_1 and λ_2 are a pair of conjugate complex roots and $|\lambda_1| = |\lambda_2| = 1$ if and only if $B^2 - 4C < 0$ and $C = 1$.

By using Lemma 2.1, we determine stability conditions for the fixed point P_3 of the system (2).

$$F(1) = \frac{s\beta^2 + \beta\delta\alpha - \beta\alpha - \delta\alpha^2}{\beta} > 0 \quad (9)$$

If conditions $\delta < \delta_3$, $\beta < \alpha$ and $s > \frac{\alpha}{\beta}$ hold where

$$\delta_3 = \frac{(s\beta - \alpha)\beta}{\alpha(-\beta + \alpha)}$$

$$\begin{aligned} F(-1) = & \left(\frac{-\alpha^3 + (-2 + \beta - m\beta)\alpha^2}{\beta(\alpha + m\beta)} + \frac{m\beta(\alpha - 2)}{(\alpha + m\beta)} \right) \delta + \frac{4\alpha^2 + 6\alpha m\beta - 4sm\beta^2}{(\alpha + m\beta)\alpha} \\ & + \frac{-2s\alpha\beta + s\alpha^2\beta + s\alpha\beta^2m - \alpha^2(\alpha + m\beta)}{(\alpha + m\beta)\alpha} \end{aligned} \quad (10)$$

We define δ_1 as a root of $F(-1) = 0$ where

$$\delta_1 = \frac{(-\alpha^2 + (4 + s\beta - m\beta)\alpha)\beta}{(\alpha^3 + (2 - \beta + m\beta)\alpha^2 - \alpha m\beta^2 + 2m\beta^2)} + \frac{((6m\beta - 2s\beta + sm\beta^2)\alpha - 4sm\beta^2)\beta}{\alpha(\alpha^3 + (2 - \beta + m\beta)\alpha^2 - \alpha m\beta^2 + 2m\beta^2)} \quad (11)$$

Let K is the coefficient of δ in $F(-1)$ where

$$K = \frac{-\alpha^3 + (-2 + \beta - m\beta)\alpha^2}{\beta(\alpha + m\beta)} + \frac{m\beta(\alpha - 2)}{(\alpha + m\beta)}$$

$$F(0) = \left(\frac{-\alpha^3 + (-1 + \beta - m\beta)\alpha^2}{\beta(\alpha + m\beta)} + \frac{m\beta(\alpha - 1)}{(\alpha + m\beta)} \right) \delta + \frac{-2sm\beta^2 + 2am\beta - s\alpha\beta}{(\alpha + m\beta)\alpha} + \frac{\alpha + s\alpha\beta + s\beta^2m - \alpha^2 - \alpha\beta m}{(\alpha + m\beta)} \quad (12)$$

Let us δ_2 is the root of $F(0) - 1 = 0$ where

$$\delta_2 = \frac{(-\alpha^2 + (s\beta - m\beta)\alpha)\beta}{(\alpha^3 + (1 - \beta + m\beta)\alpha^2 - \alpha m\beta^2 + m\beta^2)} + \frac{((m\beta - s\beta + sm\beta^2)\alpha - 2sm\beta^2)\beta}{\alpha(\alpha^3 + (1 - \beta + m\beta)\alpha^2 - \alpha m\beta^2 + m\beta^2)} \quad (13)$$

We assume that S is the coefficient of δ in $F(0) - 1$ where

$$S = \frac{-\alpha^3 + (-1 + \beta - m\beta)\alpha^2}{\beta(\alpha + m\beta)} + \frac{m(\alpha - 1)}{(\alpha + m\beta)} \quad (14)$$

When the sign table according to δ is examined, we conclude the following results:

Theorem 2.1. Assume that $\delta < \delta_3$, $\alpha > \beta$ and $s > \frac{\alpha}{\beta}$. Then for the coexistence fixed point P_3 of the system (2) the following hold true:

- i) P_3 is a sink if the following condition holds
 $K < 0, S < 0$ and $\delta_2 < \delta < \min\{\delta_1, \delta_3\}$
- ii) P_3 is a source if the following condition holds
 $K < 0, S < 0$ and $\delta < \min\{\delta_1, \delta_2, \delta_3\}$
- iii) P_3 is a saddle if the following condition holds
 $K < 0, S < 0$ and $\delta_1 < \delta < \delta_3$
- iv) Assume that λ_1 and λ_2 are roots of $F(\lambda)$ then $\lambda_1 = -1$ and $|\lambda_2| \neq 1$ if and only if
 $K < 0, S < 0, \delta = \delta_1$ and

$$\delta_2 \neq \frac{Q}{P}, \frac{Q}{P} + \frac{2\alpha\beta(m\beta + \alpha)}{P}$$

where

$$Q = (-2sm\beta - s\alpha\beta + s\alpha^2\beta + \alpha sm\beta^2 - \alpha^3 - \alpha^2m\beta + \alpha m\beta)\beta$$

$$P = (m\beta^2 + \alpha^2(1 - \beta) - \alpha m\beta(\beta - \alpha) + \alpha^2(1 + \alpha m\beta))\alpha.$$

Example 2.1. Taking parameters $\alpha = 0.8, \beta = 0.6, m = 0.2, \delta = 0.3, s = 1.8$ and initial condition $(x_0, y_0) = (1.3, 1)$, the coexistence fixed point of the system (2) is obtained as $P_3 = (1.333333333, 0.287500000)$. Using these parameter values, we can get below values:

$\delta_1 = 0.5230142566, \delta_2 = -0.7167597768, \delta_3 = 1.050000000, K = -2.846376811 < 0, S = -1.556521739 < 0$. Characteristic polynomial of the system (2) at fixed point P_3 is obtained as $F(\lambda) = \lambda^2 - 0.2173913044\lambda - 0.5826086952$ and the roots of the characteristic polynomial are $\lambda_1 = 0.8796842643$ and $\lambda_2 = -0.6622929599$ that verify $|\lambda_1| < 1$ and $|\lambda_2| < 1$. Also, the fixed point $P_3 = (1.333333333, 0.287500000)$ of the system (2) is local asymptotically stable for $0 < \delta < 0.5230142566$ which shows the correctness of the Theorem 2.1. From Figure 1, (a)-(b) fixed point P_3 of the system (2) is local asymptotically stable that graphs represent x_t and y_t populations. If the parameter $\delta = 0.8$ is selected, the fixed point $(1.333333333, 0.0958333333)$ of the system (2) is unstable. For this situation, phase portrait of the prey and predator densities are exhibited in Figure 1 (c)-(d).

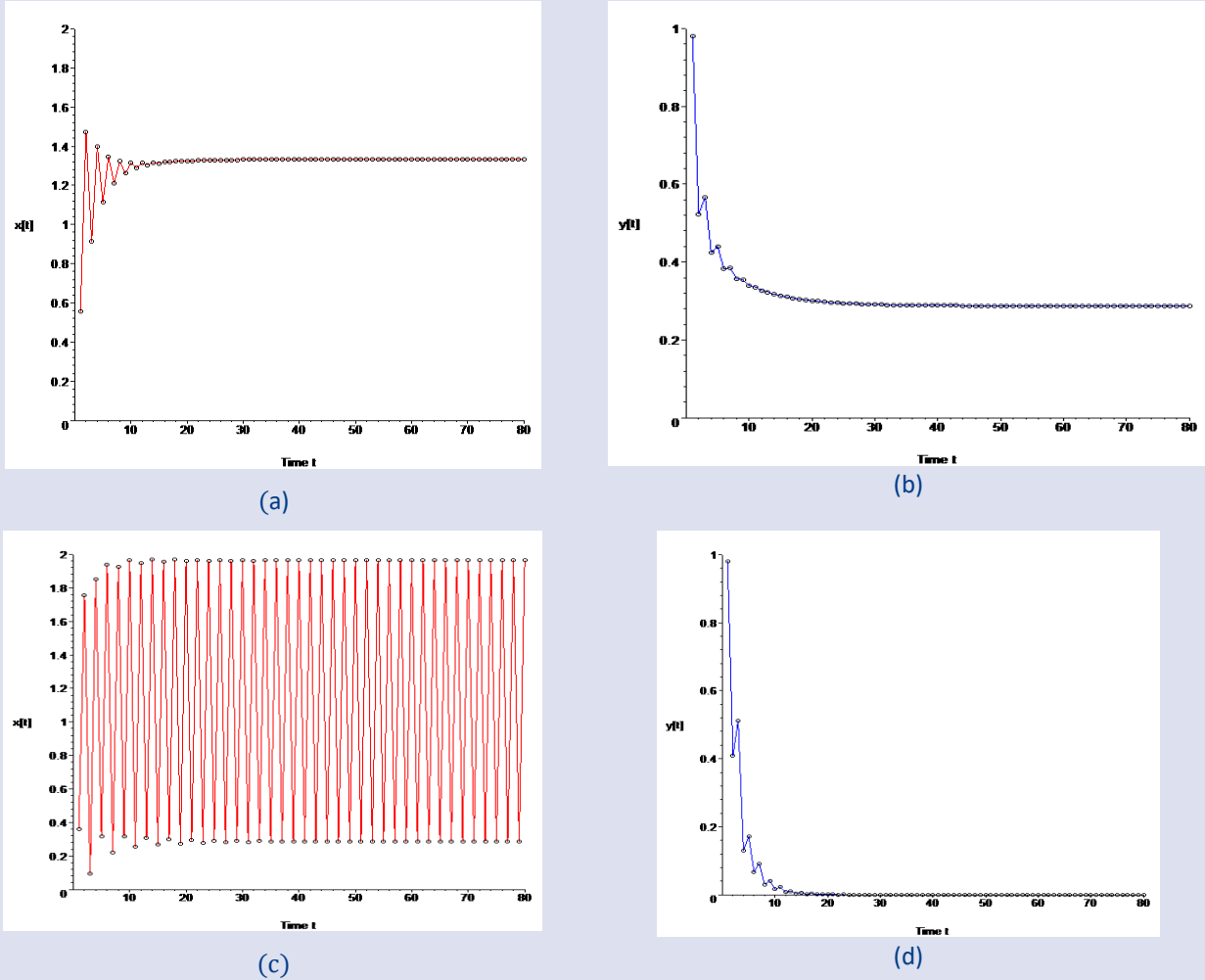


Figure 1. (a)-(b) A stable fixed point of the system (2) for $\alpha = 0.8, \beta = 0.6, m = 0.2, \delta = 0.3, s = 1.8$ and initial condition $(x_0, y_0) = (1.3, 1)$. (c)-(d) An unstable fixed point $(1.333333333, 0.09583333333)$ of the system (2) for $\alpha = 0.8, \beta = 0.6, m = 0.2, \delta = 0.8, s = 1.8$ and initial condition $(x_0, y_0) = (1.3, 1)$.

Period-Doubling Bifurcation

When it comes to case of dynamical systems, various types of bifurcation can occur as a result of changing stability of a fixed point, in other words, when a particular parameter exceeds its critical value. Depending on the bifurcation, various dynamical properties of the system under consideration can be studied. In this section, we investigate the parametric conditions for existence and directions of period-doubling bifurcation for the unique positive fixed point of system (2). When a discrete dynamical system goes through a period-doubling bifurcation, a small change in a parameter value in the system's equations causes a new behavior with twice the period of the original system undergoes.

In references [29-38], similar type of bifurcation analyses for discrete-time dynamical systems are studied. We discuss period-doubling bifurcation of unique positive fixed point P_3 of the system (2) by using bifurcation theory and the center manifold theorem and taking δ as a bifurcation parameter. We suppose the condition

$$\begin{aligned}
 &(-\delta\alpha^3 + 2\alpha^2\beta + (3m - s - \delta m)\beta^2\alpha - 2sm\beta^3)^2 \\
 &> [-4\delta\alpha^4 + (-4\beta - 4\delta + 4\delta\beta - 4\delta m\beta)\alpha^3 + (4\beta - 4m\beta^2 + 4s\beta^2 + 4\delta m\beta^2)\alpha^2 \\
 &+ (-4\delta m\beta^2 + 8m\beta^2 - 4s\beta^2 + 4sm\beta^3)\alpha - 8sm\beta^3](\beta(\alpha + m\beta)\alpha)
 \end{aligned} \tag{15}$$

holds.

Then, λ_1 and λ_2 be distinct real roots of (6). Also, we assume that

$$\delta = \frac{(-\alpha^2 + (4 + s\beta - m\beta)\alpha)\beta}{(\alpha^3 + (2 - \beta + m\beta)\alpha^2 - \alpha m\beta^2 + 2m\beta^2)} + \frac{((6m\beta - 2s\beta + sm\beta^2)\alpha - 4sm\beta^2)\beta}{\alpha(\alpha^3 + (2 - \beta + m\beta)\alpha^2 - \alpha m\beta^2 + 2m\beta^2)} \tag{16}$$

Then, the roots of equation (6) are $\lambda_1 = -1$ and

$$\lambda_2 = -\frac{-4\alpha^3 + (-4m\beta + 2s\beta + 3\beta - 2)\alpha^2}{\alpha^3 + (2 - \beta + m\beta)\alpha^2 + (2 - \alpha)m\beta^2} \tag{17}$$

Furthermore, $|\lambda_2| \neq 1$ under the following conditions:

$$\frac{-4\alpha^3 + (-4m\beta + 2s\beta + 3\beta - 2)\alpha^2}{\alpha^3 + (2 - \beta + m\beta)\alpha^2 + (2 - \alpha)m\beta^2} + \frac{(3m\beta^2 + 2sm\beta^2 - s\beta^2)\alpha - \beta^3sm - 2m\beta^2}{\alpha^3 + (2 - \beta + m\beta)\alpha^2 + (2 - \alpha)m\beta^2} \neq \pm 1 \tag{18}$$

$$\alpha^3 + (2 - \beta + m\beta)\alpha^2 + (2 - \alpha)m\beta^2 \neq 0$$

Let us consider period-doubling set as follows

$$\Omega_{PDB} = \{(\alpha, \beta, \delta, s, m) \in \mathbb{R}_+^5: K, S < 0, (16), (17) \text{ and } (18) \text{ are satisfied}\}.$$

For the aim of discussing the period-doubling bifurcation for the system (2) at its unique positive coexistence fixed point P_3 , we take δ as bifurcation parameter. Then, variation of parameters α, β, δ, m and s in small neighborhood of Ω_{PDB} gives emergence of period-doubling bifurcation. Furthermore, we set

$$\delta_F = \frac{(-\alpha^2 + (4 + s\beta - m\beta)\alpha)\beta}{(\alpha^3 + (2 - \beta + m\beta)\alpha^2 - \alpha m\beta^2 + 2m\beta^2)} + \frac{((6m\beta - 2s\beta + sm\beta^2)\alpha - 4sm\beta^2)\beta}{\alpha(\alpha^3 + (2 - \beta + m\beta)\alpha^2 - \alpha m\beta^2 + 2m\beta^2)} \tag{19}$$

Then, for $(\alpha, \beta, \delta_F, m, s) \in \Omega_{PDB}$, system (2) can be expressed by the following two-dimensional map:

$$\begin{pmatrix} X \\ Y \end{pmatrix} \rightarrow \begin{pmatrix} \delta_F X(1 - X) - XY \frac{X}{X + m} + s \\ Y(1 - \alpha) + \beta XY \end{pmatrix} \tag{20}$$

Let us assume that $\bar{\delta}$ be a small bifurcation parameter such that $|\bar{\delta}| \ll 1$, then corresponding perturbed map for (20) is given by:

$$\begin{pmatrix} X \\ Y \end{pmatrix} \rightarrow \begin{pmatrix} (\delta_F + \bar{\delta})X(1 - X) - XY \frac{X}{X + m} + s \\ Y(1 - \alpha) + \beta XY \end{pmatrix} \tag{21}$$

Then, map (21) has unique fixed point

$$(\bar{X}, \bar{Y}) = \left(\frac{\alpha}{\beta}, \frac{(\alpha^2\beta + \alpha m\beta^2 - \alpha^3 - \alpha^2 m\beta)(\delta_F + \bar{\delta})}{\alpha^2\beta} + \frac{s\alpha\beta^2 + sm\beta^3 - \alpha^2\beta - \alpha m\beta^2}{\alpha^2\beta} \right)$$

For translating the fixed point to the origin, the transformations $x = X - \bar{X}, y = Y - \bar{Y}$ is done at point $(x, y) = (0, 0)$, then we get the following map:

$$\begin{pmatrix} x \\ y \end{pmatrix} \rightarrow \begin{pmatrix} a_{11} & a_{12} \\ a_{21} & a_{22} \end{pmatrix} \begin{pmatrix} x \\ y \end{pmatrix} + \begin{pmatrix} g_1(x, y, \bar{\delta}) \\ g_2(x, y, \bar{\delta}) \end{pmatrix} \tag{22}$$

where

$$g_1(x, y, \bar{\delta}) = a_{13}x^2 + a_{14}xy + b_1x^3 + b_2x^2y + d_1x\bar{\delta} + d_2x^2\bar{\delta} + O((|x| + |y| + |\bar{\delta}|)^4)$$

$$g_2(x, y, \bar{\delta}) = a_{24}xy + O((|x| + |y| + |\bar{\delta}|)^4)$$

where

$$a_{13} = -\frac{(\delta_F + \bar{\delta})\alpha^4 + (2m\delta_F + 2m\bar{\delta})\beta\alpha^3}{(\alpha + \beta m)^2\alpha^2} + \frac{m^2\alpha^2\bar{\delta}\beta^2}{(\alpha + \beta m)^2\alpha^2} + \frac{(m^2\delta_F - m^2)\beta^3\alpha + m^2s\beta^4}{(\alpha + \beta m)^2\alpha^2} \tag{23}$$

$$a_{14} = \frac{(\alpha + 2\beta m)\alpha}{(\alpha + \beta m)^2}$$

$$b_1 = \frac{m^2\beta^3(-\delta_F\alpha^2 + (-\beta + \beta\delta_F)\alpha + \beta^2s)}{\alpha^2(\alpha + \beta m)^3}$$

$$b_2 = -\frac{\beta^3m^2y}{(\alpha + \beta m)^3}$$

$$d_1 = -\frac{(\beta\alpha m(-\beta + 2\alpha) - \alpha^2(\beta + 2\alpha))}{\beta\alpha(\alpha + \beta m)}$$

$$d_2 = -\frac{2\beta\alpha^3m + \alpha^4 + \alpha^2\beta^2m^2}{(\alpha + \beta m)^2\alpha^2}$$

$$a_{24} = \beta$$

For converting the coefficient matrix

$$A = \begin{pmatrix} a_{11} & a_{12} \\ a_{21} & a_{22} \end{pmatrix}$$

in map (22) into normal form, the following translation is used

$$\begin{pmatrix} x \\ y \end{pmatrix} = T \begin{pmatrix} u \\ v \end{pmatrix} \tag{24}$$

where

$$T = \begin{pmatrix} a_{12} & a_{12} \\ -1 - a_{11} & \lambda_2 - a_{11} \end{pmatrix} \tag{25}$$

be an invertible matrix. From (22) and (24), we obtain

$$\begin{pmatrix} u \\ v \end{pmatrix} = \begin{pmatrix} -1 & 0 \\ 0 & \lambda_2 \end{pmatrix} \begin{pmatrix} u \\ v \end{pmatrix} + \begin{pmatrix} g_3(x, y, \bar{\delta}) \\ g_4(x, y, \bar{\delta}) \end{pmatrix} \tag{26}$$

where

$$g_3(u, v, \bar{\delta}) = -\frac{(-\lambda_2 + a_{11})(a_{13} + d_2\bar{\delta})}{a_{12}(\lambda_2 + 1)}x^2 - \frac{(-\lambda_2 + a_{11})a_{14} + a_{12}a_{24}}{a_{12}(\lambda_2 + 1)}xy - \frac{(-\lambda_2 + a_{11})b_1}{a_{12}(\lambda_2 + 1)}x^3$$

$$- \frac{(-\lambda_2 + a_{11})b_2}{a_{12}(\lambda_2 + 1)}x^2y - \frac{(-\lambda_2 + a_{11})d_1\bar{\delta}}{a_{12}(\lambda_2 + 1)}x + O\left((|u| + |v| + |\bar{\delta}|)^4\right)$$

$$g_4(u, v, \bar{\delta}) = \frac{(1 + a_{11})(a_{13} + d_2\bar{\delta})}{a_{12}(\lambda_2 + 1)}x^2 + \frac{(1 + a_{11})a_{14} - a_{12}a_{24}}{a_{12}(\lambda_2 + 1)}xy + \frac{(1 + a_{11})b_1}{a_{12}(\lambda_2 + 1)}x^3 + \frac{(1 + a_{11})b_2}{a_{12}(\lambda_2 + 1)}x^2y$$

$$+ \frac{(1 + a_{11})d_1\bar{\delta}}{a_{12}(\lambda_2 + 1)}x + O\left((|u| + |v| + |\bar{\delta}|)^4\right)$$

$$x = a_{12}(u + v),$$

$$y = -(1 + a_{11})u + (\lambda_2 - a_{11})v.$$

In order to apply the center manifold theorem, we assume that $W^c(0,0,0)$ be the center manifold of (26) evaluated at $(0,0)$ in a small neighborhood of $\bar{\delta} = 0$. We know

$$W^c(0) = \{(x, y) \in R^c \times R^s | y = h(x), |x| < \delta, h(0) = 0, h'(0) = 0\}$$

then $W^c(0,0,0)$ can be approximated as follows:

$$W^c(0,0,0) = \{(\alpha, \beta, \bar{\delta}) \in R^3 : v = h(u) = m_1u^2 + m_2u\bar{\delta} + m_3\bar{\delta}^2\},$$

where

$$m_1 = \left(\frac{a_{12}a_{14}}{\lambda_2^2 - 1}\right)a_{11}^2 + a_{12}a_{11} \left(\frac{a_{12}(a_{24} - a_{13}) + 2a_{14}}{\lambda_2^2 - 1}\right) + a_{12} \left(\frac{a_{14} + a_{12}(a_{24} - a_{13})}{\lambda_2^2 - 1}\right)$$

$$m_2 = -\frac{(a_{11} + 1)d_1}{(\lambda_2 + 1)^2}$$

$$m_3 = 0$$

Therefore, the map is restricted to the center manifold $W^c(0,0,0)$ is given by

$$F: u \rightarrow -u + k_1u^2 + k_2u\bar{\delta} + k_3u^2\bar{\delta}^2 + k_4u\bar{\delta}^2 + k_5u^3 + O\left(\left(|u| + |\bar{\delta}|\right)^4\right) \tag{27}$$

where

$$k_1 = -\frac{(a_{11} - \lambda_2)a_{12}a_{13}}{\lambda_2 + 1} + \left(-\frac{(a_{11} - \lambda_2)a_{14}}{a_{12}(\lambda_2 + 1)} - \frac{a_{24}}{\lambda_2 + 1}\right)(-1 - a_{11})a_{12}$$

$$k_2 = -\frac{(a_{11} - \lambda_2)d_1}{\lambda_2 + 1}$$

$$k_3 = \frac{\left(-\frac{(-\lambda_2 + a_{11})a_{14}}{a_{12}(\lambda_2 + 1)} - \frac{a_{24}}{\lambda_2 + 1}\right)(1 + a_{11})^2d_1a_{12}}{(\lambda_2 + 1)^2} - \left(\frac{\left(-\frac{(-\lambda_2 + a_{11})a_{14}}{a_{12}(\lambda_2 + 1)} - \frac{a_{24}}{\lambda_2 + 1}\right)}{(\lambda_2 + 1)^2}\right)\left(\frac{(\lambda_2 - a_{11})(1 + a_{11})d_1a_{12}}{(\lambda_2 + 1)^2}\right) - \frac{(-\lambda_2 + a_{11})d_1\left(\frac{a_{12}a_{14}}{-1 + \lambda_2^2}\right)a_{11}^2}{\lambda_2 + 1} - \frac{(-\lambda_2 + a_{11})d_1a_{12}^2\left(\frac{(a_{24} - a_{13}) + 2a_{14}}{-1 + \lambda_2^2}\right)a_{11}}{\lambda_2 + 1} - \frac{(-\lambda_2 + a_{11})d_1a_{12}\left(\frac{a_{14} + a_{12}(a_{24} - a_{13})}{-1 + \lambda_2^2}\right)}{\lambda_2 + 1} + \frac{2(-\lambda_2 + a_{11})a_{12}a_{13}(1 + a_{11})d_1}{(\lambda_2 + 1)^3} - \frac{(-\lambda_2 + a_{11})a_{12}d_2}{\lambda_2 + 1}$$

$$k_4 = \frac{(-\lambda_2 + a_{11})d_1^2(1 + a_{11})}{(\lambda_2 + 1)^3}$$

$$k_5 = \left(-\frac{(-\lambda_2 + a_{11})a_{14}}{a_{12}(\lambda_2 + 1)} - \frac{a_{24}}{\lambda_2 + 1}\right)(-1 - a_{11})a_{12} \left(\frac{a_{12}a_{14}}{-1 + \lambda_2^2}\right)a_{11}^2 + a_{12} \left(\frac{2a_{14} + a_{12}(a_{24} - a_{13})}{-1 + \lambda_2^2}\right)a_{11} + a_{12} \left(\frac{a_{12}(a_{24} - a_{13}) + a_{14}}{-1 + \lambda_2^2}\right) + \left(-\frac{(-\lambda_2 + a_{11})a_{14}}{a_{12}(\lambda_2 + 1)} - \frac{a_{24}}{\lambda_2 + 1}\right)(\lambda_2 - a_{11}) \left(a_{12} \left(\frac{a_{14}}{-1 + \lambda_2^2}\right)a_{11}^2 + a_{12} \left(\frac{2a_{14} + a_{12}(a_{24} - a_{13})}{-1 + \lambda_2^2}\right)a_{11} + a_{12} \left(\frac{a_{14} + a_{12}(a_{24} - a_{13})}{-1 + \lambda_2^2}\right)\right)a_{12} - \frac{(-\lambda_2 + a_{11})a_{12}b_2(-1 - a_{11})}{\lambda_2 + 1} - \frac{(-\lambda_2 + a_{11})a_{12}^2b_1}{\lambda_2 + 1} - \frac{2(-\lambda_2 + a_{11})a_{12}a_{13}\left(a_{12}\left(\frac{a_{14}}{-1 + \lambda_2^2}\right)a_{11}^2\right)}{\lambda_2 + 1} - \frac{2(-\lambda_2 + a_{11})a_{11}a_{12}^2a_{13}}{\lambda_2 + 1} - \frac{\left(\frac{2a_{14} + a_{12}(a_{24} - a_{13})}{-1 + \lambda_2^2}\right)}{\lambda_2 + 1} - \frac{a_{12}\left(\frac{a_{14} + a_{12}(a_{24} - a_{13})}{-1 + \lambda_2^2}\right)}{\lambda_2 + 1}.$$

Next, the following two nonzero real numbers are defined:

$$n_1 = \left(\frac{\partial^2 g_3}{\partial u \partial \bar{\delta}} + \frac{1}{2} \frac{\partial F}{\partial \bar{\delta}} \frac{\partial^2 F}{\partial u^2}\right)_{(0,0)} = \frac{(1 + a_{11})d_1}{\lambda_2 + 1};$$

$$n_2 = \left(\frac{1}{6} \frac{\partial^3 F}{\partial u^3} + \left(\frac{1}{2} \frac{\partial^2 F}{\partial u^2}\right)^2\right)_{(0,0)} = k_5 + k_1^2 \neq 0$$

As a result of the above analysis, the following theorem gives the parametric conditions for existence and direction of period-doubling bifurcation for the system (2) at its positive coexistence fixed point P_3 [39].

Theorem 3.1. Suppose that $n_1 \neq 0$ and $n_2 \neq 0$ then system (2) goes through period-doubling bifurcation at the unique positive fixed point P_3 when parameter δ varies in small neighborhood of δ_F . Moreover, if $n_2 > 0$, then the period-two orbits that bifurcate from positive fixed point P_3 are stable, and if $n_2 < 0$, then these orbits are unstable.

Example 3.1. Taking parameters $\alpha = 0.9, \beta = 0.6, m = 0.2, s = 3$ the coexistence fixed point of the system (2) is $(x^*, y^*) = (1.5, 1.020300088)$. The critical value of period-doubling bifurcation point is obtained as $\delta_F = 0.1994704325$. By taking these parameters the characteristic polynomial of the system is obtained as $F(\lambda) = \lambda^2 + 0.405119152\lambda - 0.5948808467$ and the roots of the characteristic polynomial is $\lambda_1 = -1$ and $\lambda_2 = 0.5348808472$ that verifies the theoretical knowledge.

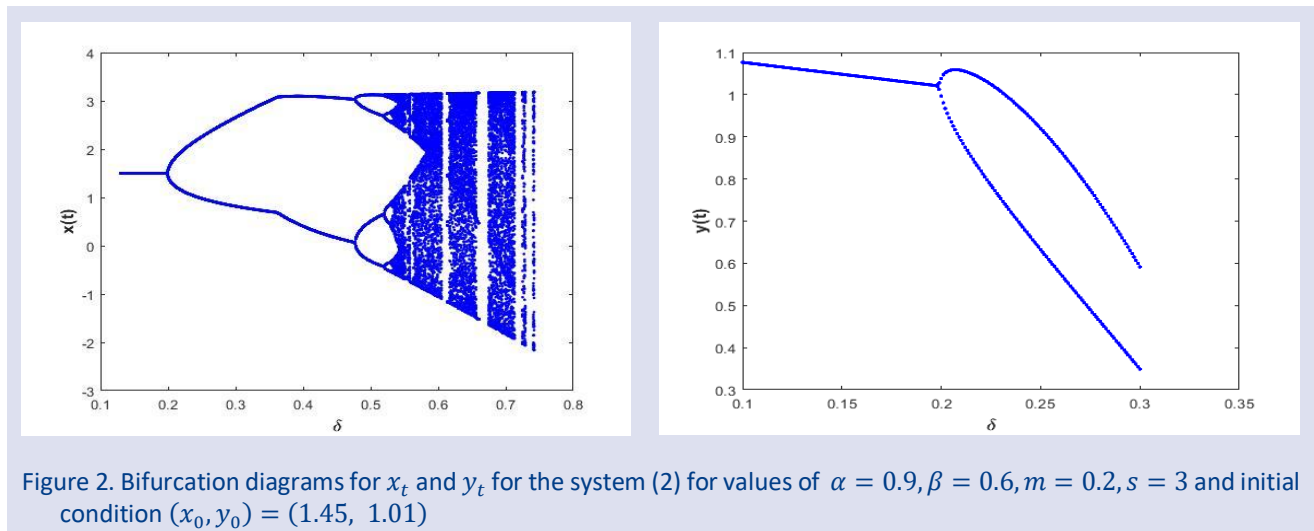


Figure 2. Bifurcation diagrams for x_t and y_t for the system (2) for values of $\alpha = 0.9, \beta = 0.6, m = 0.2, s = 3$ and initial condition $(x_0, y_0) = (1.45, 1.01)$

Conclusion

Allee effect and immigration have an important role in increasing the realism of the prey-predator model. So, we have considered a discrete-time prey-predator model with both Allee effect and immigration in this paper. We have investigated the complex dynamical behaviors of the system (2). Firstly, we have obtained existence conditions of the fixed points of the system (2). We have focused on coexistence fixed point due to biological meaning for showing complex dynamics of the system (2). We have analyzed topological classifications of the coexistence fixed point of the system (2). Later, we have obtained the required conditions on the parameters for period-doubling bifurcation of the system (2) by choosing δ as a bifurcation parameter. For period-doubling bifurcation analyses, we have used center manifold theorem and normal form theory [40]. Finally, we have given numerical simulations to support obtained theoretical finding. In Figure1, we have observed that the coexistence fixed point of the system (2) is local asymptotically stable on some conditions demonstrated in Theorem 2.1 (i). Also, in Figure 2, we have shown that the stability of the fixed point P_3 of the system (2) changes from stable to unstable when the bifurcation parameter δ , crosses a critical value δ_F . Thus, the period-doubling bifurcation arises from the fixed point P_3 .

Conflicts of interest

No conflict of interest or common interest has been declared by the authors.

References

- [1] Lotka A.J., Elements of physical biology, 1st ed. Baltimore: Williams and Wilkins Co., (1925).
- [2] Volterra V., Variazioni e Fluttuazioni del Numero Dindividui in Spece Animali Conviventi, *Mem R Accad Naz dei Lincei*, 2 (6) (1926).
- [3] Murray J.D., Mathematical biology. New York: Springer-Verlag, (1993).
- [4] Walde S.J., Murdoch W.W., Spatial Density Dependence in Parasitoids, *Annu. Rev. of Entomol.*, 33 (1988) 441-466.
- [5] Kangalgil F., Flip Bifurcation and Stability in a Discrete-Time Prey-Predator Model with Allee Effect, *Cumhuriyet Sci. J.*, 40 (2019) 141-149
- [6] Beddington J.R., Free C.A., Lawton J.H., Dynamic Complexity in Predator-Prey Models Framed in Difference Equations, *Nature*, 255 (1975) 58-60.
- [7] Blackmore D., Chen J., Perez J., Savescu M., Dynamical Properties of Discrete Lotka-Volterra Equations, *Chaos Solution. Fract.*, 12 (2001) 2553-2568.
- [8] Danca M., Codreanu S., Bako B., Detailed Analysis of a Nonlinear Prey-Predator Model, *J. Biol. Phys.*, 23 (1997) 11-20.
- [9] Hadelar K.P., Gerstmann I., The Discrete Rosenzweig Model, *Math. Biosci.*, 98 (1) (1990) 49-72.

- [10] Işık S., A Study of Stability and Bifurcation Analysis in Discrete-Time Predator-Prey System Involving the Allee Effect, *Int. J. Biomath.*, 12 (01) (2019).
- [11] Işık S., Kangalgil F., On the Analysis of Stability, Bifurcation, and Chaos Control of Discrete-Time Predator-Prey Model with Allee Effect on Predator, *Hacet. J. Math. Stat.*, 51 (2) (2022) 404-420.
- [12] Selvam A.G.M., Jacintha M., Dhineshbabu R., Bifurcation Analysis and Chaotic Behaviour in Discrete-Time Predator Prey System, *Int. J. Comput. Eng. Res.*, 9 (4) (2019).
- [13] Zhu G., Wei J., Global Stability and Bifurcation Analysis of a Delayed Predator-Prey System with Prey Immigration, *Electron. J. Qual. Theory Differ. Equ.*, 13 (2016) 1-20.
- [14] Sugie J., Saito Y., Uniqueness of Limit Cycles in a Rosenzweig-MacArthur Model with Prey Immigration, *SIAM J. Appl. Math.*, 72 (1) (2012) 299-316.
- [15] Stone L., Hart D., Effects of Immigration on Dynamics of Simple Population Models, *Theor. Popul. Biol.*, 55 (3) (1999) 227-234.
- [16] Ak Gümüş Ö., Kangalgil F., Dynamics of a Host-Parasite Model Connected with Immigration, *New Trend. Math. Sci.*, 5 (3) (2017) 332-339.
- [17] Misra J.C., Mitra A., Instabilities in Single-Species and Host-Parasite Systems: Period-Doubling Bifurcations and Chaos, *Comput. Math. with Appl.*, 52 (3) (2006) 525-538.
- [18] Holt R.D., Immigration and the Dynamics of Peripheral Populations, *Advances in Herpetology and Evolutionary Biology* (Rhodin and Miyata, Eds.), Museum of Comparative Zoology, Harvard University, Cambridge: M.A., (1983).
- [19] McCallum H.I., Effects of Immigration on Chaotic Population Dynamics, *J. Theor. Biol.*, 154 (1992) 277-284.
- [20] Stone L., Hart D., Effects of Immigration on the Dynamics of Simple Population Models, *Theor. Popul. Biol.*, 55 (3) (1999) 227-234.
- [21] Ruxton G.D., Low Levels of Immigration between Chaotic Populations can Reduce System Extinctions by Inducing Asynchronous Regular Cycles, *Proc. Royal Soc. B*, 256 (1994) 189-193.
- [22] Rohani P., Miramontes O., Immigration and the Persistence of Chaos in Population Models, *J. Theor. Biol.*, 175 (2) (1995) 203-206.
- [23] Zhou S., Liu Y., Wang G., The Stability of Predator-Prey Systems Subject to the Allee Effects, *Theor. Popul. Biol.*, 67 (1) (2005) 23-31.
- [24] Sen M., Banarjee M., Morozou A., Bifurcation Analysis of a Ratio-Dependent Prey-Predator Model with the Allee Effect, *Ecol. Complex.*, 11 (2012) 12-27.
- [25] Cheng L., Cao H., Bifurcation Analysis of a Discrete-Time Ratio-Dependent Prey-Predator Model with the Allee Effect, *Commun. Nonlinear Sci. Numer. Simul.*, 38 (2016) 288-302.
- [26] Kangalgil F., Ak Gümüş Ö., Allee Effect in a New Population Model and Stability Analysis, *Gen. Math. Notes*, 35 (1) (2016) 54-65.
- [27] Lin Q., Allee Effect Increasing the Final Density of the Species Subject to Allee Effect in a Lotka-Volterra Commensal Symbiosis, *Model. Adv. Differ. Equ.*, 196 (2018).
- [28] Kangalgil F., Işık S., Controlling Chaos and Neimark-Sacker Bifurcation in a Discrete-Time Predator-Prey System, *Haceteppe J. Mathematics and Statistics*, 49 (5) (2020) 1761-1776.
- [29] Din Q., Global Stability of Beddington Model, *Qual. Theory Dyn. Syst.*, 16 (2017) 391-415.
- [30] Din Q., Global Stability and Neimark-Sacker Bifurcation of a Host-Parasitoid Model, *Int. J. Syst. Sci.*, 48 (6) (2016) 1194-1202.
- [31] Din Q., Neimark-Sacker Bifurcation and Chaos Control in Hassell-Varley Model, *J. Differ. Equ. Appl.*, 23 (4) (2017) 741-762.
- [32] Din Q., Ak Gümüş Ö., Khalil H., Neimark-Sacker Bifurcation and Chaotic Behaviour of a Modified Host-Parasitoid Model, *Z. Naturforsch.*, 72 (1) (2016) 25-37.
- [33] Din Q., Complexity and chaos control in a discrete-time prey-predator model, *Commun. Nonlinear Sci. Numer. Simul.*, 49 (2017) 113-134.
- [34] Elabbasy E.M., Elsadany A.A., Zhang Y., Bifurcation Analysis and Chaos in a Discrete Reduced Lorenz System, *Appl. Math. Comput.*, 228 (2014) 184-194.
- [35] Din Q., Donchev T., Kolev D., Stability, Bifurcation Analysis and Chaos Control in Chlorine Dioxide-Iodine-Malonic Acid Reaction, *MATCH Commun. Math. Comput. Chem.*, 79 (2018) 577-606.
- [36] Allen L.J.S., An introduction to mathematical biology, Texas Tech. University, (2007).
- [37] Kılıç H., Topsakal N., Kangalgil F., Stability Analysis of a Discrete-Time Prey-Predator Population Model with Immigration, *Cumhuriyet Sci. J.*, 41 (4) (2020) 884-900.
- [38] Sucu G., Bir Ayrık Av-Avcı Modelinin Kararlılık ve Çatallanma Analizi, Yüksek Lisans Tezi, TOBB Ekonomi ve Teknoloji Üniversitesi, Fen Bilimleri Enstitüsü, 2016.
- [39] He Z., Lai X., Bifurcation and Chaotic Behavior of a Discrete-Time Prey-Predator System, *Nonlinear Anal. Real World Appl.*, 12 (2011) 403-417.
- [40] Kuznetsov Y.A., Elements of applied bifurcation theory, 2nd ed. New York: Springer-Verlag, (1998).

Investigation of the Asymptotic Behavior of Generalized Baskakov-Durrmeyer-Stancu Type Operators

Gülten Torun ^{1,a}, Meliha Mercan Boyraz ^{1,b}, Ülkü Dinlemez Kantar ^{1,c,*}

¹ Mathematics and Science Education, Faculty of Education, Kastamonu University, Kastamonu, Turkey.

² Department of Mathematics, Graduate School of Natural and Applied Sciences, Gazi University, Ankara, Turkey.

³ Department of Mathematics, Faculty of Sciences, Gazi University, Ankara, Turkey.

*Corresponding author

Research Article

History

Received: 30/11/2021

Accepted: 26/02/2022

Copyright



©2022 Faculty of Science,
Sivas Cumhuriyet University

ABSTRACT

In this manuscript, we firstly find the Korovkin test functions for the Baskakov operators, secondly, we find the generalized Baskakov-Durrmeyer-Stancu type operators. Thirdly, we give the modulus of continuity for the generalized Baskakov-Durrmeyer-Stancu type operators. Then, the asymptotic approach of these operators has been studied by using the Voronovskaja-type theorem. Finally, it is demonstrated that the generalized Baskakov-Durrmeyer-Stancu type operators converge to the considered function by plotting the graphs. Moreover, the convergence of the generalized Baskakov-Durrmeyer-Stancu type operators is compared with that of some other operators to the same function.

Keywords: Voronovskaja type theorem, Baskakov Durrmeyer Stancu type operators, Baskakov operators

^a gtorun@kastamonu.edu.tr
^c ulku@gazi.edu.tr

^{id} <https://orcid.org/0000-0002-1897-0174>
^{id} <https://orcid.org/0000-0002-5656-3924>

^{id} mercanmeliha20@gmail.com ^{id} <https://orcid.org/0000-0002-8288-7949>

Introduction

Weierstrass approximation theorem has played a key role in the development of approximation theory [1]. With the help of this theorem, the approximation theory of linear positive operators has emerged by using suitable sequences defined by several mathematicians.

In [2], Bernstein defined the linear positive operators and showed that these operators converged smoothly to a continuous function in a closed interval.

In [3], for $f \in C[0,1]$, Stancu introduced the following linear positive operators

$$S_n^{\alpha,\beta}(f, x) = \sum_{k=0}^n f\left(\frac{k+\alpha}{n+\beta}\right) \binom{n}{k} x^k (1-x)^{n-k} \quad (1)$$

where $x \in [0,1]$, the parameters α and β satisfy the conditions $0 \leq \alpha \leq \beta$. He examined the convergence properties of the operators (1), which are called Bernstein-Stancu type operators, in the interval $[0,1]$.

In [4], for $f \in C[0, \infty)$, $n \in \mathbb{N}$, Baskakov defined the linear positive operators as follows:

$$B_n(f, x) = \sum_{k=0}^n f\left(\frac{k}{n}\right) P_{n,k}(x) \quad (2)$$

where $P_{n,k}(x) = \binom{n+k-1}{k} x^k (1+x)^{n-k}$, $x \in [0, \infty)$ is the core of the Baskakov operators.

The convergence theorems of the bounded and continuous functions for the operators (2) were studied by Baskakov.

In [5], Mihesan introduced the generalized Baskakov operators with a constant $a \geq 0$ independent of n and defined as follows:

$$B_n^a(f, x) = \sum_{k=0}^n W_{n,k}^a(x) f\left(\frac{k}{n}\right) \quad (3)$$

where

$$W_{n,k}^a(x) = e^{-\frac{ak}{1+x}} \frac{P_k(n, a)}{k!} x^k (1+x)^{-n-k} \quad (4)$$

and

$$P_k(n, a) = \sum_{j=0}^k \binom{k}{j} (n)_j a^{k-j} \quad (5)$$

with $(n)_0 = 1$, $(n)_j = n(n+1)(n+2) \dots (n+j-1)$ for $j \geq 1$.

He proved that these operators converged uniformly on $[0, b]$ for functions that had exponential growth. Also, he discussed a pointwise estimate. In addition, Wafi and Khatoon [6] calculated the rate of convergence of the operators (3) and obtained the Voronovskaja-type theorem. Erencin and Başcanbaz-Tunca [7] studied the weighted approximation properties and estimated the

order of approximation in terms of the usual modulus of continuity for the operators (3). They derived a recurrence relation for the moments of these operators.

To approximate the space of the integrable functions, Durrmeyer [8] defined Durrmeyer operators, which is an integral type generalization of Bernstein operators, and Lupaş [9] developed these operators independently. In [10], for $f \in C_B[0, \infty)$, $n \in \mathbb{N}$, Ercin introduced the Durrmeyer-type modification of the operators (3) as follows:

$$L_n^\alpha(f, x) = \sum_{k=0}^{\infty} W_{n,k}^\alpha(x) \frac{1}{B(k+1, n)} \int_0^\infty \frac{t^k}{(1+t)^{n+k+1}} f(t) dt \quad (6)$$

where $C_B[0, \infty)$ stands for the space of all bounded-continuous functions on the interval $[0, \infty)$, and this space is equipped with the norm $\|f\| = \max_{x \in [0, \infty)} |f(x)|$, and the beta function $B(k+1, n)$ is given by

$$B(x, y) = \int_0^\infty \frac{t^{x-1}}{(1+t)^{x+y}} dt = \frac{\Gamma(x)\Gamma(y)}{\Gamma(x+y)}, \quad x, y > 0 \quad (7)$$

In this study, Ercin gave some approximation properties of the operators (6).

Some Auxiliary Lemmas

In this section, some lemmas will be given for examining the approximation properties of the generalized Baskakov-Durrmeyer-Stancu type operators defined by (8). The proofs of Lemma 2.1 and Lemma 2.2 given below are routine

Lemma 2.1 For $W_{n,k}^a(x)$ given by (4), we have the following equation:

$$\sum_{k=0}^{\infty} W_{n,k}^a(x) = 1.$$

The Korovkin test functions for the Baskakov operators expressed in (3) are given below.

Lemma 2.2 Let $e_m(t) = t^m$, for $m = 0, 1, 2, 3, 4$. For $n \in \mathbb{N}$ and a is a non-negative integer, we have the following equations:

- (i) $B_n^a(e_0(t), x) = 1.$
- (ii) $B_n^a(e_1(t), x) = \frac{x}{n} \left\{ \frac{a}{1+x} + n \right\}.$
- (iii) $B_n^a(e_2(t), x) = \frac{x^2}{n^2} \left\{ \frac{a^2}{(1+x)^2} + \frac{2an}{1+x} + n(n+1) \right\} + \frac{x}{n^2} \left\{ \frac{a}{1+x} + n \right\}.$
- (iv) $B_n^a(e_3(t), x) = \frac{x^3}{n^3} \left\{ \frac{a^3}{(1+x)^3} + \frac{3a^2n}{(1+x)^2} + \frac{3a(n+1)}{1+x} + n(n+1)(n+2) \right\} + \frac{3x^2}{n^3} \left\{ \frac{a^2}{(1+x)^2} + \frac{2an}{1+x} + n(n+1) \right\} + \frac{x}{n^3} \left\{ \frac{a}{1+x} + n \right\}.$

Furthermore, the approximation properties of the modified forms of the operators (6) have been reviewed by Agrawal et al. [11].

In [12], Kumar et al. defined the following Stancu-type generalization of the Durrmeyer-type modification of the operators (6) for $f \in \mathcal{L}$ and $n \in \mathbb{N}$,

$$G_{n,\alpha}^{\alpha,\beta}(f, x) = \sum_{k=0}^{\infty} W_{n,k}^a(x) \frac{1}{B(k+1, n)} \int_0^\infty \frac{t^k}{(1+t)^{n+k+1}} f\left(\frac{nk+\alpha}{n+\beta}\right) dt \quad (8)$$

where α and β are non-negative numbers with $0 \leq \alpha \leq \beta$, and \mathcal{L} denotes the class of all Lebesgue measurable function such that $n > m$ with $\int_0^\infty \frac{|f(t)|}{(1+t)^m} dt < \infty$, $m \in \mathbb{Z}^+$.

They studied some direct local approximation properties of the operators (8). They obtained local direct results in terms of the second-order modulus of smoothness, the rate of convergence in terms of the modulus of continuity. Several studies have been carried out some approximation properties for these types of operators are given in [14-17].

In this study, we examined the asymptotic behavior of the generalized Baskakov-Durrmeyer-Stancu type operators defined by (8) with the help of the Voronovskaja-type theorem.

$$\begin{aligned}
 \text{(v)} \quad B_n^a(e_4(t), x) &= \frac{x^4}{n^4} \left\{ \frac{a^4}{(1+x)^4} + \frac{4a^3n}{(1+x)^3} + \frac{6a^2n(n+1)}{(1+x)^2} + \frac{4an(n+1)(n+2)}{1+x} \right. \\
 &\quad \left. + n(n+1)(n+2)(n+3) \right\} + \frac{6x^3}{n^4} \left\{ \frac{a^3}{(1+x)^3} + \frac{3a^2n}{(1+x)^2} \right. \\
 &\quad \left. + \frac{3a(n+1)}{1+x} + n(n+1)(n+2) \right\} + \frac{7x^2}{n^4} \left\{ \frac{a^2}{(1+x)^2} + \frac{2an}{1+x} \right. \\
 &\quad \left. + n(n+1) \right\} + \frac{x}{n^4} \left\{ \frac{a}{1+x} + n \right\}.
 \end{aligned}$$

Now, we give the following lemmas that give the Korovkin test functions and continuity modules for the generalized Baskakov-Durrmeyer-Stancu type operators defined in (8).

For the sake of shortness, the following abbreviations will be used in the next steps,

$$M_\beta(n) = (n + \beta) \quad , \quad U_s(n) = \prod_{i=1}^s (n - i).$$

Lemma 2.3 Let $e_m(t) = t^m$ for $m = 0, 1, 2, 3, 4$, and we get the following equations for the $G_{n,a}^{\alpha,\beta}(f(t), x)$ operators defined in (8):

$$\text{(i)} \quad G_{n,a}^{\alpha,\beta}(e_0(t), x) = 1.$$

$$\text{(ii)} \quad G_{n,a}^{\alpha,\beta}(e_1(t), x) = x \left\{ \frac{n}{M_\beta(n)U_1(n)} \left(\frac{a}{1+x} + n \right) \right\} + \frac{n}{M_\beta(n)U_1(n)} + \frac{a}{M_\beta(n)}.$$

$$\begin{aligned}
 \text{(iii)} \quad G_{n,a}^{\alpha,\beta}(e_2(t), x) &= x^2 \left\{ \frac{n^2}{[M_\beta(n)]^2 U_2(n)} \left(\frac{a^2}{(1+x)^2} + \frac{2an}{1+x} + n(n+1) \right) \right\} + x \left\{ \frac{4n^2 + 2na(n-2)}{[M_\beta(n)]^2 U_2(n)} \left(\frac{a}{1+x} + n \right) \right. \\
 &\quad \left. + \frac{2n^2 + 2na(n-2)}{[M_\beta(n)]^2 U_2(n)} + \frac{\alpha^2}{[M_\beta(n)]^2} \right\}.
 \end{aligned}$$

$$\begin{aligned}
 \text{(iv)} \quad G_{n,a}^{\alpha,\beta}(e_3(t), x) &= x^3 \left\{ \frac{n^3}{[M_\beta(n)]^3 U_3(n)} \left(\frac{a^3}{(1+x)^3} + \frac{3a^2n}{(1+x)^2} + \frac{3an(n+1)}{1+x} + n(n+1)(n+2) \right) \right\} \\
 &\quad + x^2 \left\{ \frac{9n^3 + 3n^2a(n-3)}{[M_\beta(n)]^3 U_3(n)} \left(\frac{a^2}{(1+x)^2} + \frac{2an}{1+x} + n(n+1) \right) \right\} \\
 &\quad + x \left\{ \frac{18n^3 + 12n^2a(n-3) + 3na^2(n-2)(n-3)}{[M_\beta(n)]^3 U_3(n)} \left(\frac{a}{1+x} + n \right) \right\} \\
 &\quad + \left\{ \frac{6n^3 + 6n^2a(n-3) + 3na^2(n-2)(n-3)}{[M_\beta(n)]^3 U_3(n)} + \frac{a^3}{[M_\beta(n)]^3} \right\}.
 \end{aligned}$$

$$\begin{aligned}
 \text{(v)} \quad G_{n,a}^{\alpha,\beta}(e_4(t), x) &= x^4 \left\{ \frac{n^4}{[M_\beta(n)]^4 U_4(n)} \left(\frac{a^4}{(1+x)^4} + \frac{4a^3n}{(1+x)^3} + \frac{6a^2n(n+1)}{(1+x)^2} \right. \right. \\
 &\quad \left. \left. + \frac{4an(n+1)(n+2)}{1+x} + n(n+1)(n+2)(n+3) \right) \right\} \\
 &\quad + x^3 \left\{ \frac{16n^4 + 4n^3 \alpha(n-4)}{[M_\beta(n)]^4 U_4(n)} \left(\frac{a^3}{(1+x)^3} + \frac{3a^2n}{(1+x)^2} \right. \right. \\
 &\quad \left. \left. + \frac{3an(n+1)}{1+x} + n(n+1)(n+2) \right) \right\} \\
 &\quad + x^2 \left\{ \frac{72n^4 + 36n^3 \alpha(n-4) + 6n^2 \alpha^2(n-3)(n-4)}{[M_\beta(n)]^4 U_4(n)} \left(\frac{a^2}{(1+x)^2} \right. \right. \\
 &\quad \left. \left. + \frac{2an}{1+x} + n(n+1) \right) \right\} + x \left(\frac{a}{1+x} + n \right) \left\{ \frac{96n^4 + 72n^3 \alpha(n-4)}{[M_\beta(n)]^4 U_4(n)} \right. \\
 &\quad \left. + \frac{24n^2 \alpha^2(n-3)(n-4) + 4n \alpha^3(n-2)(n-3)(n-4)}{[M_\beta(n)]^4 U_4(n)} \right\} \\
 &\quad + \frac{24n^4 + 24n^3 \alpha(n-4) + 12n^2 \alpha^2(n-3)(n-4)}{[M_\beta(n)]^4 U_4(n)} \\
 &\quad + \frac{4n \alpha^3(n-2)(n-3)(n-4)}{[M_\beta(n)]^4 U_4(n)} + \frac{a^4}{[M_\beta(n)]^4}.
 \end{aligned}$$

Proof: (i) Taking $e_m(t) = t^m$, $m = 0$ in operators $G_{n,a}^{\alpha,\beta}(e_0(t), x)$ and using the beta function in (7) and Lemma 2.1, we can write the following equation:

$$G_{n,a}^{\alpha,\beta}(e_0(t), x) = \sum_{k=0}^{\infty} W_{n,k}^a(x) \frac{1}{B(k+1, n)} \int_0^{\infty} \frac{t^k}{(1+t)^{n+k+1}} dt,$$

$$= \sum_{k=0}^{\infty} W_{n,k}^a(x) \frac{1}{B(k+1, n)} B(k+1, n) = 1.$$

(ii) Substituting $e_m(t) = t^m$ for $m = 1$ in operators $G_{n,a}^{\alpha,\beta}(e_m(t), x)$, we have

$$G_{n,a}^{\alpha,\beta}(e_1(t), x) = \sum_{k=0}^{\infty} W_{n,k}^a(x) \frac{1}{B(k+1, n)} \int_0^{\infty} \frac{t^k}{(1+t)^{n+k+1}} \left(\frac{nt + \alpha}{n + \beta}\right) dt.$$

Using the beta function in (7), we get

$$G_{n,a}^{\alpha,\beta}(e_1(t), x) = \sum_{k=0}^{\infty} W_{n,k}^a(x) \frac{1}{B(k+1, n)} \frac{1}{(n + \beta)} \left\{ n \frac{(k+1)}{(n-1)} B(k+1, n) + \alpha B(k+1, n) \right\}.$$

Hence, we find

$$G_{n,a}^{\alpha,\beta}(e_1(t), x) = \frac{1}{(n + \beta)} \left\{ \frac{n}{(n-1)} \sum_{k=0}^{\infty} W_{n,k}^a(x) (k+1) + \alpha \sum_{k=0}^{\infty} W_{n,k}^a(x) \right\},$$

$$= \frac{1}{M_{\beta}(n)} \left\{ \frac{n}{U_1(n)} [nB_n^a(t, x) + 1] + \alpha \right\},$$

$$= x \left\{ \frac{n}{M_{\beta}(n)U_1(n)} \left(\frac{a}{1+x} + n\right) \right\} + \frac{n}{M_{\beta}(n)U_1(n)} + \frac{a}{M_{\beta}(n)}.$$

Similarly, (iii)-(v) equations are obtained.

To obtain approximation velocities of generalized Baskakov-Durrmeyer-Stancu type operators with Voronovskaja type theorem, Lemma 2.4, which gives the continuity modules of these operators, will be given first as follows:

Lemma 2.4 We have the following limits;

(i) $\lim_{n \rightarrow \infty} n G_{n,a}^{\alpha,\beta}(t - x, x) = \left(\frac{a}{1+x} + 1 - \beta\right) x + a + 1,$

(ii) $\lim_{n \rightarrow \infty} n G_{n,a}^{\alpha,\beta}((t - x)^2, x) = 2x^2 + x,$

(iii) $\lim_{n \rightarrow \infty} n^2 G_{n,a}^{\alpha,\beta}((t - x)^4, x) = 12x^4 - \left(\frac{12\alpha^2}{1+x} - 24\right) x^3 - (6\alpha^2 - 6\alpha - 12)x^2.$

Proof: (i) Using the linearity property of the $G_{n,a}^{\alpha,\beta}(t; x)$ operators from Lemma 2.3, we have

$$\lim_{n \rightarrow \infty} n G_{n,a}^{\alpha,\beta}(t - x, x) = \lim_{n \rightarrow \infty} n \left\{ x \left(\frac{na}{(1+x)M_{\beta}(n)U_1(n)} + \frac{n^2}{M_{\beta}(n)U_1(n)} - 1 \right) + \frac{n}{M_{\beta}(n)U_1(n)} + \frac{a}{M_{\beta}(n)} \right\},$$

$$\lim_{n \rightarrow \infty} n G_{n,a}^{\alpha,\beta}(t - x, x) = \left(\frac{a}{1+x} + 1 - \beta\right) x + a + 1.$$

(ii) Similarly, using linearity and Lemma 2.3, we obtain

$$G_{n,a}^{\alpha,\beta}((t - x)^2, x) = \left[\left\{ \frac{1}{[M_{\beta}(n)]^2 U_2(n)} \left(\frac{a^2 n^2}{(1+x)^2} + \frac{2an^3}{(1+x)} + n^3(n+1) \right) - \frac{1}{M_{\beta}(n)U_1(n)} \left(\frac{2na}{1+x} + 2n^2 \right) + 1 \right\} x^2 \right.$$

$$\left. + \left\{ \frac{4n^2 + 2n(n-2)\alpha}{[M_{\beta}(n)]^2 U_2(n)} \left(\frac{a}{1+x} + n \right) - \frac{2n}{M_{\beta}(n)U_1(n)} - \frac{2\alpha}{M_{\beta}(n)} \right\} x + \frac{2n^2 + 2n(n-2)\alpha}{[M_{\beta}(n)]^2 U_2(n)} + \frac{\alpha^2}{[M_{\beta}(n)]^2} \right].$$

When necessary arrangements are made in the last equation, the equation is multiplied by n , and the limit is taken as n approaches infinity, we get

$$\begin{aligned} \lim_{n \rightarrow \infty} n G_{n,a}^{\alpha,\beta}((t-x)^2, x) &= \lim_{n \rightarrow \infty} \frac{n}{[M_\beta(n)]^2 U_2(n)} \left[\left\{ \frac{1}{(1+x)^2} (a^2 n^2) \right. \right. \\ &+ \frac{1}{(1+x)} (4an^2 + 4an\beta - 2an^2\beta) + 2n^3 + n^2\beta^2 + 2n^2\beta \\ &+ 2n^2 - 3n\beta^2 - 4n\beta + 2\beta^2 \} x^2 + \left\{ \frac{1}{(1+x)} (4an^2 - 4an\alpha + 2an^2\alpha) \right. \\ &+ 4\alpha\beta - 4n\beta - 4n\alpha + 2n^2\alpha + 2n^2\beta + 4n^2 + 2n^3 - 6n\alpha\beta + 2n^2\alpha\beta \} x \\ &\left. \left. + n^2\alpha^2 + 2n^2\alpha + 2n^2 - 3n\alpha^2 - 4n\alpha + 2\alpha^2 \right\} \right] = 2x^2 + 2x. \end{aligned}$$

(iv) Equation (iii) is easily obtained when the operations in (i) and (ii) are similarly performed in $G_{n,a}^{\alpha,\beta}((t-x)^4, x)$.

We give the weighted Korovkin- type theorems which were proved by Gadzhiev [13]. Let $B_\sigma[0, \infty)$ be the space of all g functions with real values, where function g satisfies the growth condition $|g(x)| \leq N_g \sigma(x)$ and $\sigma(x) = 1 + x^2$, N_g is a constant dependent on g . According to the $\|g\|_\sigma = \sup \left\{ \frac{|g(x)|}{\sigma(x)} : x \in \mathbb{R} \right\}$ norm, $B_\sigma[0, \infty)$ is a normed space. It is a subspace of $B_\sigma[0, \infty)$ space, with $C_\sigma^*[0, \infty)$ being a space of continuous functions satisfying the condition $\lim_{|x| \rightarrow \infty} \frac{|g(x)|}{\sigma(x)} = 0$.

Now, using Lemma 2.3 and Lemma 2.4 we give the following Voronovskaja-type theorem for $G_{n,a}^{\alpha,\beta}(g(t), x)$.

Theorem 2.5: For any $g \in C_\sigma^*[0, \infty)$ such that $g', g'' \in C_\sigma^*[0, \infty)$ we have the following limit:

$$\lim_{n \rightarrow \infty} n(G_{n,a}^{\alpha,\beta}(g(t); x) - g(x)) = g'(x) \left\{ \left(\frac{a}{1+x} + 1 - \beta \right) x + a + 1 \right\} + \frac{1}{2} g''(x) \{ 2x^2 + x \}.$$

Proof: From the Taylor's expansion of g , we get

$$g(t) = g(x) + g'(x)(t-x) + \frac{1}{2} g''(x)(t-x)^2 + \delta(t,x)(t-x)^2 \tag{9}$$

where $\delta(t,x) \rightarrow 0$ as $t \rightarrow x$. If we apply operators $G_{n,a}^{\alpha,\beta}$ to equation (9) using the linearity property of the operators $G_{n,a}^{\alpha,\beta}$, then we obtain

$$G_{n,a}^{\alpha,\beta}(g(t); x) - g(x) = g'(x) G_{n,a}^{\alpha,\beta}((t-x); x) + \frac{1}{2} g''(x) G_{n,a}^{\alpha,\beta}((t-x)^2; x) + G_{n,a}^{\alpha,\beta}(\delta(t,x)(t-x)^2; x) \tag{10}$$

Then, if the $G_{n,a}^{\alpha,\beta}(\delta(t,x)(t-x)^2; x)$ term of the equation (10) is multiplied by n and the Cauchy- Schwarz inequality is applied, we find

$$n G_{n,a}^{\alpha,\beta}(\delta(t,x)(t-x)^2; x) \leq \left(G_{n,a}^{\alpha,\beta} \delta(t,x)^2; x \right)^{\frac{1}{2}} \left(n^2 G_{n,a}^{\alpha,\beta}((t-x)^4; x) \right)^{\frac{1}{2}}. \tag{11}$$

We have $\lim_{n \rightarrow \infty} G_{n,a}^{\alpha,\beta}(\delta(t,x)^2; x) = 0$, and from (iii) of Lemma 4, we have

$$\lim_{n \rightarrow \infty} n^2 G_{n,a}^{\alpha,\beta}((t-x)^4; x) \text{ is finite.}$$

Then, taking the limit of the inequality (11) while n approaching infinity, we get

$$\lim_{n \rightarrow \infty} n G_{n,a}^{\alpha,\beta}(\delta(t,x)(t-x)^2; x) = 0.$$

Therefore, when the limit of both sides of (10) is taken for n approaching infinity, we get

$$\lim_{n \rightarrow \infty} n(G_{n,a}^{\alpha,\beta}(g(t); x) - g(x)) = g'(x) \left\{ \left(\frac{a}{1+x} + 1 - \beta \right) x + a + 1 \right\} + \frac{1}{2} g''(x) \{ 2x^2 + x \}.$$

As a result, it is seen that the proof is complete.

Some Graphical Analysis

In this section, the graphs below show the convergence of the of the Generalized Baskakov-Durmeyer- Stancu type Operators to the considered function

$$g(x) = \sqrt{x}e^{-2x}$$

For different values of n, k, a, α and β .

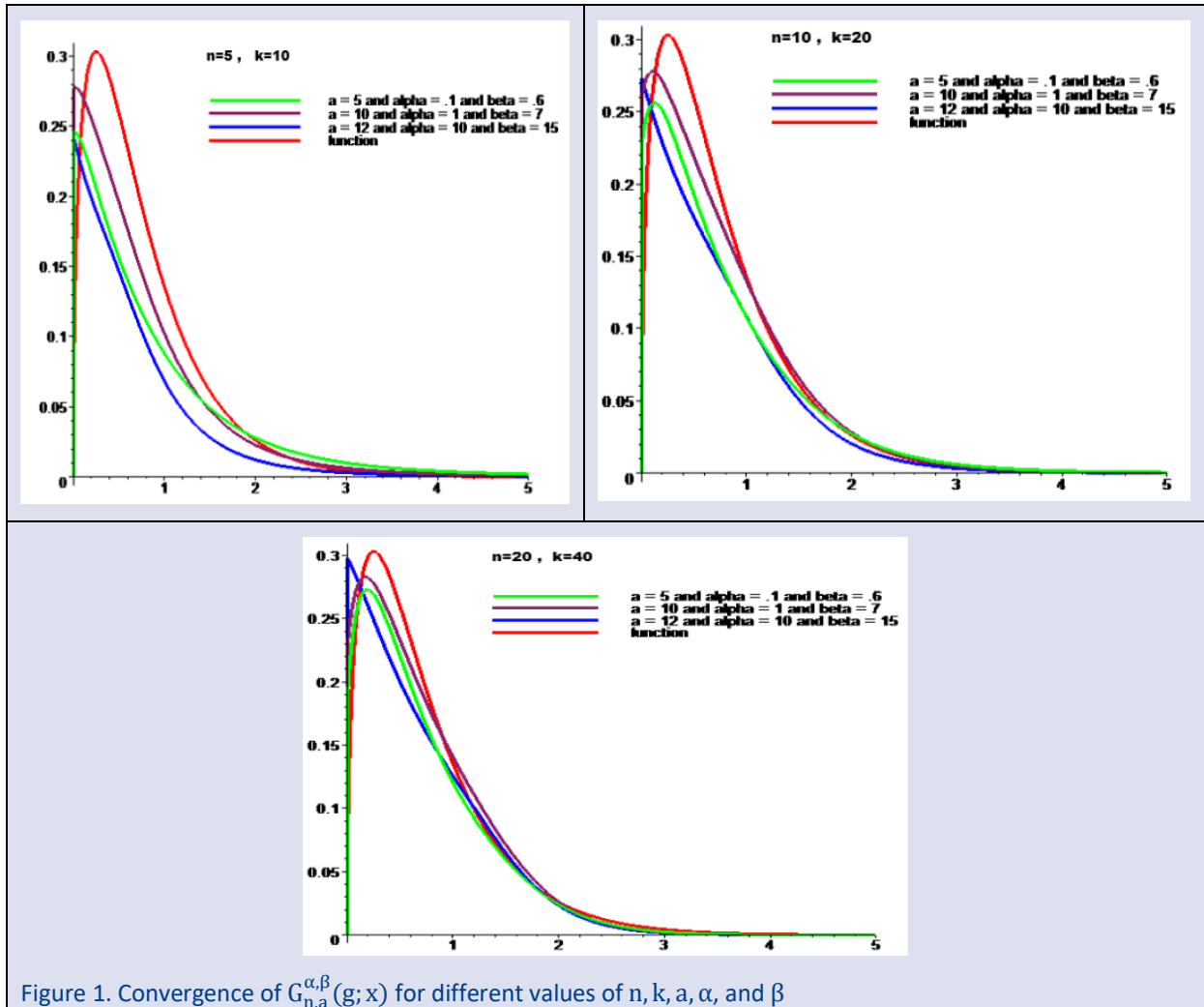


Figure 1. Convergence of $G_{n,a}^{\alpha,\beta}(g; x)$ for different values of $n, k, a, \alpha,$ and β

The graph below shows the convergence of $B_n^a(g, x)$ (BO), $L_n^a(g, x)$ (BDO) and $G_{n,a}^{\alpha,\beta}(g; x)$ (BDSO) to the $g(x)$ function for $n = 20, k = 40, a = 10, \alpha = 1,$ and $\beta = 7$.

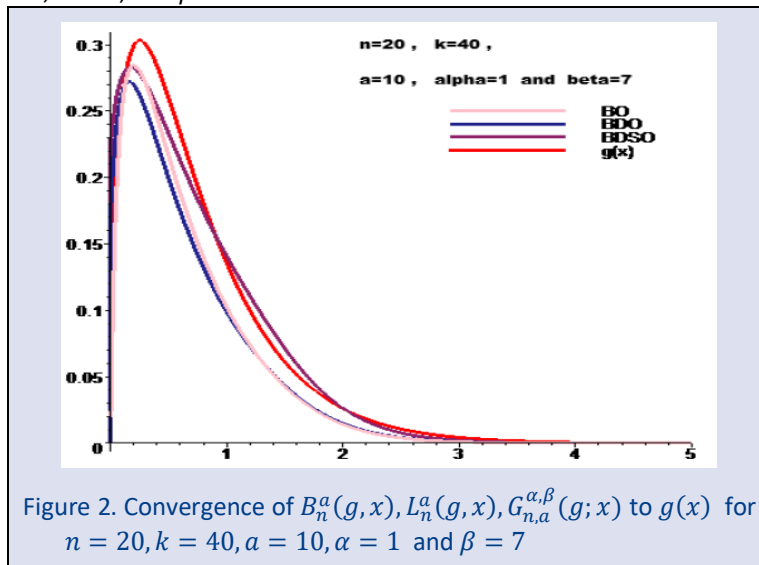


Figure 2. Convergence of $B_n^a(g, x), L_n^a(g, x), G_{n,a}^{\alpha,\beta}(g; x)$ to $g(x)$ for $n = 20, k = 40, a = 10, \alpha = 1$ and $\beta = 7$

Acknowledgement

The authors would like to thank the referee for the careful reading of this paper.

Conflicts of Interest

The authors declared there is no conflict of interest associated with this work.

References

- [1] Weierstrass K., Über die analytische Darstellbarkeit sogenannter willkürlicher Functionen einer reellen Veränderlichen Sitzungsberichteder, *Königlich Preussischen Akademie der Wissenschaften zu Berlin*, (1885) 633-639, 789-805.
- [2] Bernstein S. N., Démonstration du théorème deWeierstrass fondée sur la calcul des probabilités, *Commun. Soc.Math. Charkow Sér.* 13(2) (1912) 1-2 .
- [3] Stancu D.D., Approximation of functions by a new class of linear polynomial operators, *Rev. Roum. Math. Pures Appl.* 13 (1968) 1173-1194.
- [4] Baskakov V. A., An instance of a sequence of positive linear operators in the space of continuous functions, *Doklady Akademii Nauk SSSR*, 113:2 (1957) 249–251,
- [5] Miheşan V., Uniform approximation with positive linear operators generated by generalized Baskakov method, *Automat. Comput. Appl. Math.* 7 (1998).34-37.
- [6] Wafi A., Khatoon S., On the order of approximation of functions by generalized Baskakov operators, *Indian J. Pure Appl. Math.* (2004) 35347-358.
- [7] Erençin A., Başcanbaz-Tunca G., Approximation properties of a class of linear positive operators in weighted spaces. *C. R. Acad. Bulg. Sci.* 63(10), (2010)1397–1404.
- [8] Durrmeyer J. L., Une formule d'inversion de la transformée de Laplace: applications à la théorie des moments, These de 3e cycle, Faculté des Sciences de l'Université de Paris, (1967).
- [9] Lupas A., Die Folge der Betaoperatoren, Dissertation, Universität Stuttgart, (1972).
- [10] Erençin A., Durrmeyer type modification of generalized Baskakov operators, *Appl. Math. Comput.*, 218 (2011) 4384-4390.
- [11] Agrawal P. N., Gupta V., Kumar A. S., Generalized Baskakov-Durrmeyer type operators, *Rend. Circ. Mat. Palermo*, 63 (2014) 193–209.
- [12] Kumar A. S., Finta Z., Agrawal P. N., On generalized Baskakov-Durrmeyer-Stancu type operators, *Demonstr. Math.*, 50 (2017) 144–155.
- [13] Gadhiev A.D., Theorems of the type of P.P. Korovkin type theorems, *Matematicheskie Zametki*, 20(5) (1976) 781-786.
- [14] Erençin A., Olgun A., Taşdelen F., Generalized Baskakov type operators, *Mathematica Slovaca*, 67(5) (2017) 1269-1277.
- [15] Yesildal FT., Bodur M., Bivariate Baskakov type operators, *Revista De La Real Academia De Ciencias Exactas Y Naturales Serie A-Matematicas*, 113(4) (2019) 3269-3281.
- [16] Aktaş R., Söylemez D., Taşdelen F., Stancu type generalization of Szász-Durrmeyer operators involving Brenke-type polynomials, *Filomat*, 33(3) (2019) 855-868.
- [17] Bodur M., Yılmaz O. G., Aral A., Approximation by Baskakov-Szász-Stancu Operators Preserving Exponential Functions, *Constr. Math. Anal.*, 1(1) (2018) 1-8.

Orthogonal Semiderivations and Symmetric Bi-semiderivations in Semiprime Rings

Damla Yılmaz^{1,a,*}

¹ Department of Mathematics, Faculty of Science, Erzurum Technical University, Erzurum, Turkey.

*Corresponding author

Research Article

History

Received: 15/10/2020

Accepted: 05/03/2022

Copyright



©2022 Faculty of Science,
Sivas Cumhuriyet University

ABSTRACT

In this paper, orthogonality for symmetric bi-semiderivations is defined and some results are obtained when two symmetric bi-semiderivations are orthogonal. Also, this paper gives the notion of orthogonality between semiderivations and symmetric bi-semiderivations of a 2-torsion free semiprime ring and offers some results of orthogonality.

Keywords: Semiderivation, Bi-semiderivation, Semiprime ring, Orthogonal derivation.

 damla.yilmaz@erzurum.edu.tr

 <https://orcid.org/0000-0002-6741-8669>

Introduction

The concept of derivation in rings was firstly given by E. C. Posner [1]. An additive mapping $d: R \rightarrow R$ is said to be a derivation if $d(rs) = d(r)s + rd(s)$ for all $r, s \in R$. In the above paper, E. C. Posner examined the commutativity conditions for a prime ring by associating them with derivation. In the following years, different derivations have been defined and the properties of these derivations in prime and semiprime rings have been the subject of many researchers. In these studies, on different derivations, the conditions for the ring to be commutative are examined.

In 1980, the definition of symmetric bi-derivation on a ring was given by Gy. Maksa [2]. A mapping $D(.,.): R \times R \rightarrow R$ is called symmetric if $D(r, s) = D(s, r)$ holds for all $r, s \in R$. A mapping $d: R \rightarrow R$, $d(r) = D(r, r)$ is called trace of D , where $D(.,.): R \times R \rightarrow R$ is a symmetric mapping. It is clear that d the trace of D satisfies the relation $d(r + s) = d(r) + d(s) + 2D(r, s)$ for all $r, s \in R$. A symmetric bi-additive mapping $D(.,.): R \times R \rightarrow R$ is called a symmetric bi-derivation if $D(rs, t) = D(r, t)s + rD(s, t)$ holds for all $r, s, t \in R$. Then the relation $D(r, st) = D(r, s)t + sD(r, t)$ holds for all $r, s, t \in R$. J. Vukman has achieved some conclusions regarding symmetric bi-derivations on prime and semiprime rings [3, 4].

The notion of semiderivation in rings was given by J. Bergen in [5]. An additive mapping f of a ring R into R is called a semiderivation if there exists a function $g: R \rightarrow R$ such that $f(rs) = f(r)g(s) + rf(s) = f(r)s + g(r)f(s)$ and $f(g(r)) = g(f(r))$ for all $r, s \in R$. J. C. Chang generalized some well-known properties to semiderivations in [6]. In the above study, it has been shown that if R is a prime ring and f is a semiderivation associated with function g (not necessarily surjective), then g is a homomorphism.

The definition of orthogonal derivation in rings was given in 1989 by M. Bresar and J. Vukman [7]. Let R be a ring and d, g be nonzero derivations. If for all $r, s \in R$, $d(r)Rg(s) =$

$g(s)Rd(r)$ holds, then d and g are called orthogonal derivations. In the above study, the following theorem has been proved. Let R be a semiprime ring with $\text{char } R \neq 2$, d and g be nonzero derivations. Then, d and g are orthogonal derivations if and only if one of the following conditions holds:

- (i) $dg = 0$,
- (ii) $dg + gd = 0$,
- (iii) For all $r \in R$, $d(r)g(r) = 0$,
- (iv) For all $r \in R$, $d(r)g(r) + g(r)d(r) = 0$,
- (v) d is a derivation.

Similar situations have been proved by many researchers for different derivations. In 2016, C. J. S. Reddy and B. R. Reddy obtained similar results for orthogonal symmetric bi-derivations in semiprime rings [8].

D. Yılmaz and H. Yazarlı, based on the concepts of symmetric bi-derivation and semiderivation, defined a symmetric bi-semiderivation in a prime ring [9]. Moreover, in [9], symmetric Jordan bi-semiderivations are defined, examples are given and when these two concepts are related is examined. Let R be a ring. A symmetric bi-additive function $D: R \times R \rightarrow R$ is called a symmetric bi-semiderivation associated with a function $f: R \rightarrow R$ (or simply a symmetric bi-semiderivation of a ring R) if

$$D(rs, t) = D(r, t)f(s) + rD(s, t) = D(r, t)s + f(r)D(s, t) \text{ and } d(f(r)) = f(d(r)) \text{ for all } r, s, t \in R, \\ \text{where } d: R \rightarrow R \text{ is the trace of } D.$$

Let R be a 2-torsion free semiprime ring, $D_1, D_2: R \times R \rightarrow R$ be two nonzero symmetric bi-semiderivations associated with a surjective homomorphism f . In this paper, some cases are investigated when D_1 and D_2 orthogonal. Also, the notion of orthogonality between semiderivations and symmetric bi-semiderivations of a 2-torsion free semiprime ring is introduced and some features of this concept are examined.

Orthogonal Symmetric Bi-semiderivations in Semiprime Rings

Definition 2.1: Let R be a semiprime ring. Two symmetric bi-semiderivations D_1 and D_2 associated with a surjective function f are called orthogonal if

$$D_1(r, s)RD_2(s, t) = (0) = D_2(s, t)RD_1(r, s)$$

for all $r, s, t \in R$.

Example 2.2: Assume that S is a commutative additively idempotent semiprime ring. Then $R = \left\{ \begin{pmatrix} r & 0 \\ 0 & s \end{pmatrix} : r, s \in S \right\}$ is a semiprime ring with matrix addition and multiplication. We define

$D_1: R \times R \rightarrow R, D_1\left(\begin{pmatrix} r & 0 \\ 0 & s \end{pmatrix}, \begin{pmatrix} t & 0 \\ 0 & w \end{pmatrix}\right) = \begin{pmatrix} rt & 0 \\ 0 & 0 \end{pmatrix}$ and $D_2: R \times R \rightarrow R, D_2\left(\begin{pmatrix} r & 0 \\ 0 & s \end{pmatrix}, \begin{pmatrix} t & 0 \\ 0 & w \end{pmatrix}\right) = \begin{pmatrix} 0 & 0 \\ 0 & sw \end{pmatrix}$. Let $f: R \rightarrow R, f\left(\begin{pmatrix} r & 0 \\ 0 & s \end{pmatrix}\right) = \begin{pmatrix} 0 & 0 \\ 0 & s \end{pmatrix}$. Then D_1 and D_2 are orthogonal symmetric bi-semiderivations associated with function f .

Lemma 2.3: ([7]) Suppose that R is a 2-torsion free semiprime ring and $r, s \in R$. Then, the following conditions are equivalent:

- (i) $rxs = 0$,
- (ii) $sxr = 0$,
- (iii) $rxs + sxr = 0$ for all $x \in R$.

If one of the above conditions holds, then $rs = sr = 0$.

Lemma 2.4: ([8], Lemma 2) Let R be a semiprime ring. Assume that $B, D: R \times R \rightarrow R$ are two bi-additive mappings satisfy $B(r, s)RD(r, s) = 0$ for all $r, s \in R$. Then,

$$B(r, s)RD(s, t) = (0) \text{ for all } r, s, t \in R.$$

Remark 2.5: ([8], Proposition 1) Let B and D be two bi-derivations of a ring R . The following identity holds $(BD)(rs, t) = B(D(rs, t), w) = r(BD)(s, t) + B(r, w)D(s, t) + D(r, t)B(s, w) + (BD)(r, t)s$ for all $r, s, t, w \in R$.

Remark 2.6: Let $D_1, D_2: R \times R \rightarrow R$ be two symmetric bi-semiderivations associated with a surjective function f . Then, for all $r, s, t, w \in R$

$$(D_1D_2)(rs, t) = D_1(D_2(rs, t), w) = (D_1D_2)(r, t)f(s) + f(D_2(r, t))D_1(f(s), w) + D_1(r, w)f(D_2(s, t)) + r(D_1D_2)(s, t). \tag{1}$$

Proof: Assume that D_1 and D_2 are two symmetric bi-semiderivations associated with a surjective function f . For all $r, s, t, w \in R$, we get

$$\begin{aligned} (D_1D_2)(rs, t) &= D_1(D_2(rs, t), w) = D_1(D_2(r, t)f(s) + rD_2(s, t), w) \\ &= D_1(D_2(r, t)f(s), w) + D_1(rD_2(s, t), w) \\ &= D_1(D_2(r, t), w)f(s) + f(D_2(r, t))D_1(f(s), w) + D_1(r, w)f(D_2(s, t)) + rD_1(D_2(s, t), w) \\ &= (D_1D_2)(r, t)f(s) + f(D_2(r, t))D_1(f(s), w) + D_1(r, w)f(D_2(s, t)) + r(D_1D_2)(s, t). \end{aligned}$$

Lemma 2.7: Let R be a 2-torsion free semiprime ring and $D_1, D_2: R \times R \rightarrow R$ be two symmetric bi-semiderivations associated with a surjective function f .

Then, D_1 and D_2 are orthogonal \Leftrightarrow For all $r, s, t \in R, D_1(r, s)D_2(s, t) + D_2(r, s)D_1(s, t) = 0$.

Proof: Firstly, we suppose that for all $r, s, t \in R$,

$$D_1(r, s)D_2(s, t) + D_2(r, s)D_1(s, t) = 0. \tag{2}$$

Replacing t by tr in (2), we have

$$0 = D_1(r, s)D_2(s, tr) + D_2(r, s)D_1(s, tr)$$

$$= D_1(r, s)D_2(s, t)f(r) + D_1(r, s)tD_2(s, r) + D_2(r, s)D_1(s, t)f(r) + D_2(r, s)tD_1(s, r) \\ = D_1(r, s)tD_2(s, r) + D_2(r, s)tD_1(s, r) + (D_1(r, s)D_2(s, t) + D_2(r, s)D_1(s, t))f(r).$$

By using (2) in the last equation, we get

$$D_1(r, s)tD_2(s, r) + D_2(r, s)tD_1(s, r) = 0 \text{ for all } r, s, t \in R. \tag{3}$$

From Lemma 2.3, we obtain $D_1(r, s)RD_2(s, r) = (0)$ for all $r, s \in R$. Since D_1 and D_2 are bi-additive mappings, $D_1(r, s)RD_2(s, t) = (0)$ for all $r, s, t \in R$, by Lemma 2.4.

Using Lemma 2.3, we get $D_2(s, t)RD_1(r, s) = (0)$ for all $r, s, t \in R$. Thus, for all $r, s, t \in R$

$$D_1(r, s)RD_2(s, t) = (0) = D_2(s, t)RD_1(r, s).$$

Therefore, D_1 and D_2 are orthogonal.

Now, we suppose that D_1 and D_2 are orthogonal symmetric bi-semiderivations.

Then, for all $r, s, t, w \in R$

$$D_1(r, s)wD_2(s, t) = 0 = D_2(s, t)wD_1(r, s).$$

By Lemma 2.3, we have $D_1(r, s)D_2(s, t) = 0 = D_2(s, t)D_1(r, s)$. Therefore, we arrive $D_1(r, s)D_2(s, t) + D_2(r, s)D_1(s, t) = 0$ for all $r, s, t \in R$. This completes the proof.

Theorem 2.8: Let R be a 2-torsion free semiprime ring and $D_1, D_2: R \times R \rightarrow R$ be two symmetric bi-semiderivations associated with surjective homomorphism f .

(i) For all $r, s, t \in R$, $D_1(r, s)D_2(s, t) = 0$ or $D_2(r, s)D_1(s, t) = 0$ if and only if D_1 and D_2 are orthogonal.

(ii) If D_1 and D_2 are orthogonal, then D_1D_2 is a symmetric bi-semiderivation associated with function f^2 .

(iii) If D_1 and D_2 are orthogonal, then $D_1D_2 = 0$.

Proof: (i) Assume that for all $r, s, t \in R$, $D_1(r, s)D_2(s, t) = 0$. In this equation replacing r by rw and using hypothesis, we get $D_1(r, s)wD_2(s, t) = 0$ for all $r, s, t, w \in R$. Thus, we obtain $D_1(r, s)RD_2(s, t) = (0)$ for all $r, s, t \in R$. Hence, D_1 and D_2 are orthogonal.

Now, assume that D_1 and D_2 are orthogonal. Then, $D_1(r, s)RD_2(s, t) = (0)$ for all $r, s, t \in R$. By Lemma 2.3, $D_1(r, s)D_2(s, t) = 0$ for all $r, s, t \in R$.

Similarly, it is proved that D_1 and D_2 are orthogonal $\Leftrightarrow D_2(r, s)D_1(s, t) = 0$ for all $r, s, t \in R$.

(ii) Assume that D_1 and D_2 are orthogonal. In view of (i), $D_2(r, s)D_1(s, w) = 0$ for all $r, s, w \in R$. Taking $s = r$ yields that

$$d_2(r)D_1(r, w) = 0 \text{ for all } r, w \in R. \tag{4}$$

Replacing r by $r + v$ in (4), we obtain

$$0 = d_2(r)D_1(r, w) + d_2(r)D_1(v, w) + d_2(v)D_1(r, w) + d_2(v)D_1(v, w) \\ + 2 D_2(r, v)D_1(r, w) + 2 D_2(r, v)D_1(v, w).$$

Since D_1 and D_2 are orthogonal and the equation (2.4), we get

$$d_2(r)D_1(v, w) + d_2(v)D_1(r, w) = 0 \text{ for all } r, v, w \in R.$$

Replacing v by $-v$ in the last equation, we get

$$d_2(r)D_1(v, w) = 0 \text{ for all } r, v, w \in R. \tag{5}$$

Replacing r by $r + t$ in (5), we get $2D_2(r, t)D_1(v, w) = 0$. Since R is a 2-torsion free ring, we have

$$D_2(r, t)D_1(v, w) = 0 \text{ for all } r, t, v, w \in R. \tag{6}$$

Again using (i), we have

$$D_1(r, s)D_2(s, t) = 0 \text{ for all } r, s, t \in R.$$

Taking s for r , we get

$$d_1(s)D_2(s, t) = 0 \text{ for all } s, t \in R. \tag{7}$$

A linearization of (7) gives

$$0 = d_1(s)D_2(s, t) + d_1(s)D_2(u, t) + d_1(u)D_2(s, t) + d_1(u)D_2(u, t)$$

$$+ 2D_1(s, u)D_2(s, t) + 2D_1(s, u)D_2(u, t).$$

Since D_1 and D_2 are orthogonal, we get

$$d_1(s)D_2(u, t) + d_1(u)D_2(s, t) = 0 \text{ for all } s, t, u \in R.$$

Letting $s = -s$ in the last equation, we obtain

$$d_1(s)D_2(u, t) = 0 \text{ for all } s, t, u \in R.$$

Since f is a surjective homomorphism, we get $d_1(f(s))f(D_2(u, t)) = 0$. Putting $s + w$ instead of s in the last equation and using it, we find

$$2D_1(f(s), f(w))f(D_2(u, t)) = 0 \text{ for all } s, t, u, w \in R.$$

Since R is a 2-torion free ring and f is a surjective homomorphism, we get

$$D_1(r, v)f(D_2(u, t)) = 0 \text{ for all } r, t, u, v \in R. \tag{8}$$

On the other hand, for all $r, s, t, w \in R$

$$\begin{aligned} (D_1D_2)(rs, t) &= D_1(D_2(rs, t), w) = D_1(D_2(r, t)f(s) + rD_2(s, t), w) \\ &= D_1(D_2(r, t), w)f^2(s) + D_2(r, t)D_1(f(s), w) \\ &\quad + D_1(r, w)f(D_2(s, t)) + rD_1(D_2(s, t), w). \end{aligned} \tag{9}$$

Using (6) and (8) in the equation (9), we arrive that

$$(D_1D_2)(rs, t) = (D_1D_2)(r, t)f^2(s) + r(D_1D_2)(s, t) \text{ for all } r, s, t \in R.$$

Hence, D_1D_2 is a symmetric bi-semiderivation associated with function f^2 and we conclude that desired result.

(iii) Suppose that D_1 and D_2 are orthogonal. Then, we have

$$D_1(r, s)D_2(s, t) = 0 \text{ for all } r, s, t \in R.$$

This implies that $D_1(D_1(r, s)D_2(s, t), w) = 0$ for all $r, s, t, w \in R$. If this statement is regulated, we get

$$D_1(D_1(r, s), w)f(D_2(s, t)) + D_1(r, s)(D_1D_2)(s, t) = 0.$$

Using the equation (8) in the last expression, we obtain $D_1(r, s)(D_1D_2)(s, t) = 0$ for all $r, s, t \in R$. Replacing r by ru , we get

$$D_1(r, s)u(D_1D_2)(s, t) = 0 \text{ for all } r, s, t, u \in R.$$

In particular, putting $r = D_2(s, t)$ gives $(D_1D_2)(s, t)u(D_1D_2)(s, t) = 0$. Since R is a semiprime ring, we get $D_1D_2 = 0$, the conclusion is obtained.

Orthogonality of Semiderivations and Symmetric Bi-semiderivations

Definition 3.1: Let R be a semiprime ring, g be a semiderivation of R and D be a symmetric bi-semiderivation of R associated with a function f . If

$$D(r, s)Rg(t) = (0) = g(t)RD(r, s) \text{ for all } r, s, t \in R,$$

Then g and D are called orthogonal.

Example 3.2: Let S be a commutative ring and let $M_3(S) = \left\{ \begin{pmatrix} 0 & s & t \\ 0 & 0 & 0 \\ 0 & 0 & w \end{pmatrix} : s, t, w \in S \right\}$.

Define $g: M_3(S) \rightarrow M_3(S)$ by $g\left(\begin{pmatrix} 0 & s & t \\ 0 & 0 & 0 \\ 0 & 0 & w \end{pmatrix}\right) = \begin{pmatrix} 0 & 0 & t \\ 0 & 0 & 0 \\ 0 & 0 & 0 \end{pmatrix}$,

$$D: M_3(S) \times M_3(S) \rightarrow M_3(S) \text{ by } D \left(\begin{pmatrix} 0 & s & t \\ 0 & 0 & 0 \\ 0 & 0 & w \end{pmatrix}, \begin{pmatrix} 0 & a & b \\ 0 & 0 & 0 \\ 0 & 0 & c \end{pmatrix} \right) = \begin{pmatrix} 0 & 0 & tc \\ 0 & 0 & 0 \\ 0 & 0 & 0 \end{pmatrix}$$

$$\text{and } f: M_3(S) \rightarrow M_3(S), \begin{pmatrix} 0 & s & t \\ 0 & 0 & 0 \\ 0 & 0 & w \end{pmatrix} \mapsto \begin{pmatrix} 0 & s & 0 \\ 0 & 0 & 0 \\ 0 & 0 & w \end{pmatrix}.$$

It is obvious that g is a semiderivation of $M_3(S)$ associated with f and D is a symmetric bi-semiderivation of $M_3(S)$ associated with f . Also, g and D are orthogonal.

Lemma 3.3: Let R be a semiprime ring. Suppose that an additive mapping h on R and a bi-additive mapping $f: R \times R \rightarrow R$ satisfy $h(r)Rf(r, s) = (0)$ for all $r, s \in R$. Then, $h(r)Rf(t, s) = (0)$ for all $r, s, t \in R$.

Proof: We have

$$h(r)wf(r, s) = 0 \text{ for all } r, s, w \in R.$$

Linearising the above equation on r gives

$$h(r)wf(r, s) + h(t)wf(r, s) + h(r)wf(t, s) + h(t)wf(t, s) = 0.$$

Then, we get

$$h(r)wf(t, s) + h(t)wf(r, s) = 0 \text{ for all } r, s, t, w \in R.$$

Hence, we obtain $h(r)wf(t, s) = -h(t)wf(r, s)$. Replacing w by $wf(t, s)vh(r)w$ and using hypothesis, we get

$$h(r)wf(t, s)vh(r)wf(t, s) = -h(t)wf(r, s)vh(r)wf(t, s) = 0.$$

Since R is semiprime ring, we get $h(r)wf(t, s) = (0)$ for all $r, s, t, w \in R$.

Lemma 3.4: Let R be a semiprime ring. Suppose that an additive mapping h on R and a bi-additive mapping $f: R \times R \rightarrow R$ satisfy $h(r)Rf(r, s) = (0)$ for all $r, s \in R$. Then, $h(t)Rf(r, s) = (0)$ for all $r, s, t \in R$.

Proof: We have

$$h(r)wf(r, s) = 0 \text{ for all } r, s, w \in R.$$

Linearising the above equation on r gives

$$h(r)wf(r, s) + h(t)wf(r, s) + h(r)wf(t, s) + h(t)wf(t, s) = 0.$$

Then, we get

$$h(r)wf(t, s) + h(t)wf(r, s) = 0 \text{ for all } r, s, t, w \in R.$$

From hypothesis and the last equation, we obtain

$$h(t)wf(r, s)Rh(t)wf(r, s) = -h(t)wf(r, s)Rh(r)wf(t, s) = (0).$$

Since R is semiprime ring, we get $h(t)wf(r, s) = (0)$ for all $r, s, t, w \in R$.

Lemma 3.5: Let R be a 2-torsion free semiprime ring, g be a semiderivation of R and D be a symmetric bi-semiderivation of R associated with a function f . Then, g and D are orthogonal if and only if

$$D(r, s)g(t) + g(r)D(t, s) = 0 \text{ for all } r, s, t \in R.$$

Proof: Suppose g and D satisfy

$$D(r, s)g(t) + g(r)D(t, s) = 0 \text{ for all } r, s, t \in R. \tag{10}$$

Replacing t by tr in (10) and using (10), we get

$$D(r, s)tg(r) + g(r)tD(r, s) = 0 \text{ for all } r, s, t \in R.$$

From Lemma 2.3, we have $g(r)RD(r, s) = (0)$ for all $r, s \in R$.

Then, Lemma 3.4 gives $g(t)RD(r, s) = (0)$ for all $r, s, t \in R$. Using Lemma 2.3 again, we obtain

$$g(t)RD(r, s) = (0) = D(r, s)Rg(t) \text{ for all } r, s, t \in R.$$

Thus, g and D are orthogonal.

Now, suppose that g and D are orthogonal. Then, $D(r, s)g(t) = g(r)D(t, s) = 0$, from Lemma 2.3. This gives the desired result.

Remark 3.6: Let R be a ring. Suppose that g is a semiderivation of R and D is a symmetric bi-semiderivation of R associated with a surjective function f . Then, the following equation holds:

$$(gD)(rs, t) = (gD)(r, t)f^2(s) + D(r, t)g(f(s)) + g(r)f(D(s, t)) + r(gD)(s, t) \text{ for all } r, s, t \in R.$$

Proof: For all $r, s, t \in R$, we have

$$\begin{aligned} (gD)(rs, t) &= g(D(rs, t)) = g(D(r, t)f(s) + rD(s, t)) \\ &= g(D(r, t)f(s)) + g(rD(s, t)) \\ &= (gD)(r, t)f^2(s) + D(r, t)g(f(s)) + g(r)f(D(s, t)) + r(gD)(s, t). \end{aligned}$$

Theorem 3.7: Let R be a 2-torsion free semiprime ring, g be a semiderivation of R and D be a symmetric bi-semiderivation of R associated with a surjective homomorphism f . Then, g and D are orthogonal if and only if $g(r)D(r, s) = 0$ for all $r, s \in R$.

Proof: Suppose g and D such that

$$g(r)D(r, s) = 0 \text{ for all } r, s \in R. \tag{11}$$

A linearization of (11) gives

$$g(r)D(r, s) + g(r)D(t, s) + g(t)D(r, s) + g(t)D(t, s) = 0 \text{ for all } r, s, t \in R.$$

Using (11), we have

$$g(r)D(t, s) + g(t)D(r, s) = 0 \text{ for all } r, s, t \in R. \tag{12}$$

Replacing t by tw in (12), we get

$$g(r)D(t, s)f(w) + g(r)tD(w, s) + g(t)f(w)D(r, s) + tg(w)D(r, s) = 0 \text{ for all } r, s, t, w \in R. \tag{13}$$

By (12), we have $g(r)D(t, s) = -g(t)D(r, s)$ and $g(w)D(r, s) = -g(r)D(w, s)$. Thus, for all $r, s, t, w \in R$, the equation (13) becomes

$$-g(t)D(r, s)f(w) + g(r)tD(w, s) + g(t)f(w)D(r, s) - tg(r)D(w, s) = 0. \tag{14}$$

Taking t by $g(r)$ in (14), we have

$$-g^2(r)D(r, s)f(w) + g(r)^2D(w, s) + g^2(r)f(w)D(r, s) - g(r)^2D(w, s) = 0$$

which implies that

$$g^2(r)[f(w), D(r, s)] = 0 \text{ for all } r, s, w \in R.$$

Since f is a surjective homomorphism, we obtain

$$g^2(r)[u, D(r, s)] = 0 \text{ for all } r, s, u \in R. \tag{15}$$

Letting $u = ut$ in (15), we get $g^2(r)u[t, D(r, s)] + g^2(r)[u, D(r, s)]t = 0$. Using (15) in the last equation, we get $g^2(r)u[t, D(r, s)] = 0$. From Lemma 3.3, we obtain

$$g^2(r)R[t, D(v, s)] = (0) \text{ for all } r, s, t, v \in R. \tag{16}$$

Taking $r = ru$ in (16), we get

$$(g^2(r)f^2(u) + g(r)g(f(u)) + g(r)f(g(u)) + rg^2(u))R[t, D(v, s)] = (0) \text{ for all } r, s, t, u, v \in R.$$

By (16), we have $(g(r)g(f(u)) + g(r)f(g(u)))R[t, D(v, s)] = (0)$ for all $r, s, t, u, v \in R$. Since g is a semiderivation of R associated with f and R is a 2-torsion free ring, we get $g(r)g(f(u))R[t, D(v, s)] = (0)$ for all $r, s, t, u, v \in R$. Since f is a surjective homomorphism, we have

$$g(r)g(w)R[t, D(v, s)] = (0) \text{ for all } r, s, t, v, w \in R. \tag{17}$$

Replacing r by rz in (17), we obtain $g(r)Rg(w)R[t, D(v, s)] = (0)$ for all $r, s, t, v, w \in R$.

In particular,

$$g(r)R[t, D(v, s)]Rg(r)R[t, D(v, s)] = (0) \text{ for all } r, s, t, v \in R.$$

Since R is a semiprime ring, we get $g(r)R[t, D(v, s)] = (0)$ for all $r, s, t, v \in R$. Then, the equation $[g(r), D(v, s)]R[g(r), D(v, s)] = (0)$ holds for all $r, s, v \in R$. Then, we have

$g(r)D(v, s) = D(v, s)g(r)$ for all $r, s, v \in R$. Hence, the equation (12) can be written as

$$D(t, s)g(r) + g(t)D(r, s) = 0 \text{ for all } r, s, t \in R.$$

Therefore, Lemma 3.5 gives the required result.

Now, suppose that g and D are orthogonal. Then we have $g(r)RD(r, s) = (0)$ for all $r, s \in R$. By Lemma 2.3, we get $g(r)D(r, s) = 0$ for all $r, s \in R$.

Theorem 3.8: Let R be a 2-torsion free semiprime ring. Suppose that a semiderivation g of R and a symmetric bi-semiderivation D of R associated with a surjective homomorphism f are orthogonal. Then

$$D(r, t)g(f(s)) + g(r)f(D(s, t)) = 0 \text{ for all } r, s, t \in R.$$

Proof: Let g and D are orthogonal. Hence, we have

$$D(r, t)g(s) = 0 = g(r)D(s, t) \text{ for all } r, s, t \in R. \tag{18}$$

In the equation $D(r, t)g(s) = 0$, replacing s by $f(s)$ yield

$$D(r, t)g(f(s)) = 0 \text{ for all } r, s, t \in R. \tag{19}$$

On the other hand, we have $g(r)D(s, t) = 0$ by (18). Taking $s = t$ in the last equation we get

$$g(r)d(t) = 0 \text{ for all } r, t \in R. \tag{20}$$

Replacing t by $f(t)$ in (20), we get

$$g(r)f(d(t)) = 0 \text{ for all } r, t \in R. \tag{21}$$

Since f is a homomorphism taking $t = t + s$ in (21),

$$g(r)f(d(t)) + g(r)f(d(s)) + 2g(r)f(D(s, t)) = 0 \text{ for all } r, s, t \in R.$$

Using (21), we get $2g(r)f(D(s, t)) = 0$. Since R is 2-torsion free ring, we get

$$g(r)f(D(s,t)) = 0 \text{ for all } r,s,t \in R. \tag{22}$$

The equations (19) and (22) give the required result.

Theorem 3.9: Let R be a 2-torsion free semiprime ring, g be a semiderivation of R and D be a symmetric bi-semiderivation of R associated with a surjective homomorphism f . If g and D are orthogonal, then $gD = 0$.

Proof: We assume that g and D are orthogonal.

Then, we have $g(r)wD(s,t) = 0$ for all $r,s,t,w \in R$. Then,

$$0 = g(g(r))wD(s,t) + g(f(r))g(w)D(s,t) + g(f(r))f(w)(gD)(s,t).$$

Since g and D are orthogonal, we get $g(f(r))f(w)(gD)(s,t) = 0$ for all $r,s,t,w \in R$. Since f is a surjective homomorphism, we get

$$g(u)R(gD)(s,t) = (0) \text{ for all } s,t,u \in R. \tag{23}$$

Let $u = D(s,t)$ in (23). Hence, $(gD)(s,t)R(gD)(s,t) = (0)$ for all $s,t \in R$.

By semiprimeness of R , $(gD)(s,t) = 0$ for all $s,t \in R$. It implies that $gD = 0$.

Theorem 3.10: Suppose R be a 2-torsion free semiprime ring, g be a semiderivation of R and D be a symmetric bi-semiderivation of R associated with a surjective homomorphism f . If g and D are orthogonal, then gD is a symmetric bi-semiderivation associated with f^2 function.

Proof: Let g and D be orthogonal. By Remark 3.6, we have for all $r,s,t \in R$,

$$(gD)(rs,t) = (gD)(r,t)f^2(s) + D(r,t)g(f(s)) + g(r)f(D(s,t)) + r(gD)(s,t). \tag{24}$$

Also, by Theorem 3.8, we have $D(r,t)g(f(s)) + g(r)f(D(s,t)) = 0$ for all $r,s,t \in R$. From the last two expression, we get $(gD)(rs,t) = (gD)(r,t)f^2(s) + r(gD)(s,t)$ for all $r,s,t \in R$. It implies that gD is a symmetric bi-semiderivation of R associated with f^2 function.

Conflicts of interest

The author declares no conflict of interest

Acknowledgments

The author wish to thank the anonymous reviewers for their valuable suggestions.

References

[1] Posner E. C., Derivations in prime rings, *Proc. Amer. Math. Soc.*, 8 (1957) 1093-1100.
 [2] Maksa Gy., A remark on symmetric biadditive functions having nonnegative diagonalization, *Glasnik. Mat.*, 15(35) (1980) 279-282.
 [3] Vukman J., Symmetric biderivations on prime and semiprime rings, *Aequa. Math.* 38 (1989) 245-254.
 [4] Vukman J., Two results concerning symmetric biderivations on prime rings, *Aequa. Math.*, 40 (1990) 181-189.
 [5] Bergen J., Derivations in prime rings, *Canadian Math. Bull.*, 26(3) (1983) 267-270.
 [6] Chang J. C., On semiderivations of prime rings, *Chinese Journal Mathematics*, 12(4) (1984) 255-262.
 [7] Bresar M., Vukman J., Orthogonal derivation and extension of a theorem of Posner, *Rad. Mat.* 5(2) (1989) 237-246.
 [8] Reddy C. J. S., Reddy B. R., Orthogonal symmetric biderivations in semiprime rings, *International Journal of Mathematics and Statistics Studies*, 4(1) (2016) 22-29.
 [9] Yılmaz D., Yazarlı H., (to appear), On symmetric bi-semiderivations of prime rings.

Calculating Entropy of Some Solid Metals by Using n-Dimensional Debye Approximation

Ebru Çopuroğlu^{1, a, *}¹ Department of Physics, Faculty of Arts and Sciences, Tokat Gaziosmanpaşa University, Tokat, Turkey

*Corresponding author

Research Article

History

Received: 11/03/2021

Accepted: 27/12/2021

Copyright

©2022 Faculty of Science,
Sivas Cumhuriyet University

ABSTRACT

The entropies of some solid metals (*Ni*, *Ag*, *Zr*, *Al*, and *Fe*) have been analytically calculated by the use of n-dimensional Debye approximation in this study. The obtained formula is valid for all temperature ranges from low to melting temperature. We have compared our results with available numerical and experimental data for room temperature (298 K). As can be seen that our results are in good agreement with literature.

Keywords: Debye approximation, Thermodynamic properties, Entropy, Solid metals.ebrucopuroglu@gmail.com<https://orcid.org/0000-0002-4363-5730>

Introduction

Thermodynamics is a physical science that studies energy and energy transformations, entropy and the relationships between the physical properties of matter [1]. As it is known there are many different types of energy (mechanical, electrical, heat, chemical, nuclear, etc.). Thermodynamics is also defined as the science of energy and entropy today. For many years, people struggled to invent self-propelled machines against the laws of thermodynamics. Thermodynamics has a wide range of applications from automobiles to aircraft and spacecraft, from thermal power plants to nuclear power plants, from air conditioning systems to computers. The design of most of the vehicles we use in homes has been carried out using the principles of thermodynamics. As examples we can show the electric or gas oven, pressure cooker, kettle, iron, air conditioner, computer, and television.

The first law of thermodynamics explains the principle of conservation of energy, and the second law of thermodynamics states that besides the quantity (quantity) of energy, its quality must also be taken into account. In other words, it states that the changes in nature occur in the direction that decreases the quality of the energy [2, 3].

It is also well known that determining thermodynamic properties of materials plays an efficient role in explaining metallurgical behavior with respect to temperature. The most important thermodynamic properties are heat capacity, entropy and enthalpy which should be evaluated accurately for a wide range of temperature parameters [4-6]. From this point of view suggesting new approximations for one of these properties is very important in thermodynamic calculations.

In literature there are limited studies for the calculation of entropy in a wide range of temperatures [7-9]. Also, the most of these studies based on numerical and

experimental methods. For this purpose we have evaluated entropy by n-dimensional Debye approximation which is with full analytically method. It is easy to say that our formulation and calculation method have no restriction in their uses. Also obtained formula is valid for all temperature values from low to melting temperatures.

Materials and Methods

The definition of entropy at constant volume is given as following [10]:

$$S = - \left(\frac{\partial F}{\partial T} \right)_V \quad (1)$$

Here F is free energy and T is temperature. The integral form of free energy can be written as:

$$F = E_0 + 3Nk_0T \ln(1 - e^{-\theta/T}) - 3Nk_0T \left(\frac{T}{\theta} \right)^3 \int_0^{\theta/T} \frac{x^3 dx}{e^x - 1} \quad (2)$$

where $E_0 = \frac{9}{8} Nk_0\theta$ is the zero energy, N is the Avagadro number, k is the Boltzman constant, θ is the Debye temperature of solids and T is the absolute temperature. By considering Eq. (2) in Eq. (1), we get the expression as following:

$$S = -3Nk_0 \ln(1 - e^{-\theta/T}) + 4Nk_0 D \left(\frac{\theta}{T} \right) \quad (3)$$

The quantity $D_n(\beta, x)$ occurring in Eq. (3) for $\beta = 1$ is the n-dimensional Debye function defined by [10, 11]

$$D_n(\beta, x) = \frac{n}{x^n} \int_0^x \frac{t^n}{(e^t - 1)^\beta} dt \quad (4)$$

$$D_n(\beta, x) = \frac{n}{x^n} \lim_{N \rightarrow \infty} \sum_{i=0}^N (-1)^i F_i(-\beta) \times \frac{\gamma(n+1, (i+\beta)x)}{(i+\beta)^{n+1}} \quad (5)$$

As can be seen from Eq. (3) the choice of reliable formulas for evaluation of n-dimensional Debye functions is of prime importance in the accurate calculation of the entropy for solids. The series relation for the calculation of n-dimensional Debye functions has the following form [11, 12]:

where the quantity N is the upper limit of summation, $F_i(-\beta)$ and $\gamma(\alpha, x)$ are the binomial coefficients and incomplete gamma functions, respectively [13, 14].

Table 1. The comparisons of entropy calculations for some solid metals at room temperatures (298° K) for upper limit of summation N=200.

Solid Metal	Analytical results for Eq.(3) (J / K * mol)	Experimental results from Refs. [15, 16] (J / K * mol)
Ni	30.42	29.87
Ag	41.05	42.6
Zr	38.07	39
Al	27.58	28.3
Fe	28.61	27.3

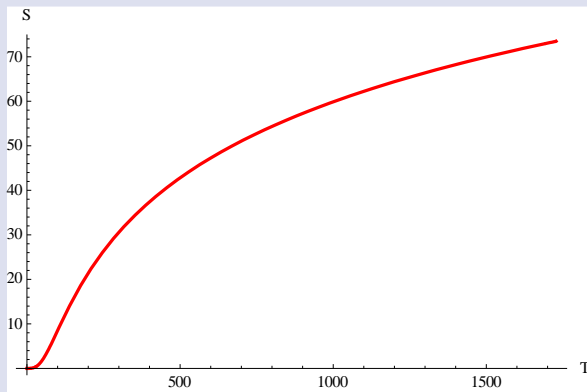


Figure 1. Temperature dependence of entropy of solid Ni metal from low to melting point (0°→1728° K)

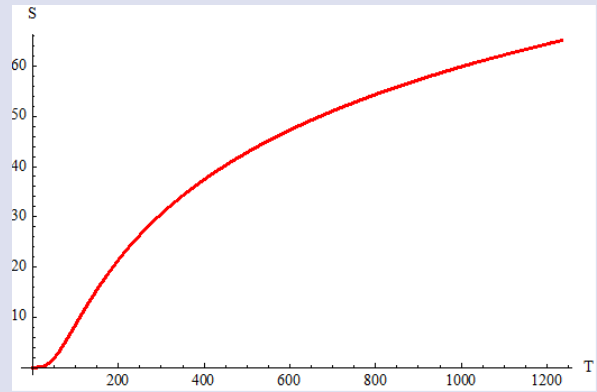


Figure 2. Temperature dependence of entropy of solid Ag metal from low to melting point (0°→1234° K)

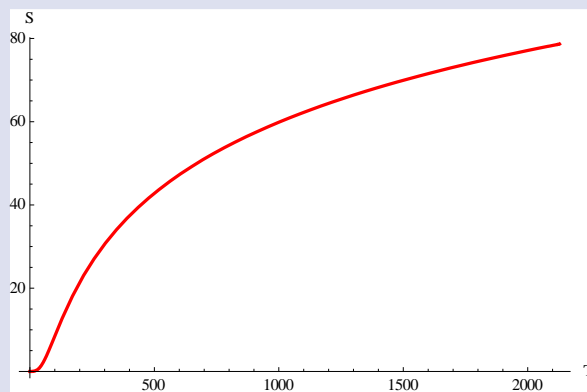


Figure 3. Temperature dependence of entropy of solid Zr metal from low to melting point (0°→2128° K)

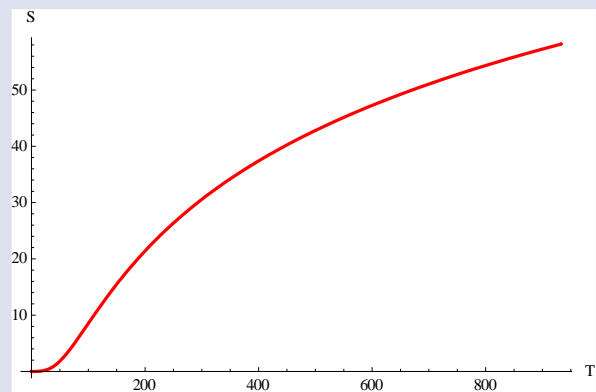


Figure 4. Temperature dependence of entropy of solid Al metal from low to melting point (0°→933° K)

Numeric Results and Conclusion

By the use of n-dimensional Debye functions, the calculation of Ni, Ag, Zr, Al, and Fe solid metals entropies have been performed.

The computational results and their comparisons (for room temperature 298° K) with literature [15, 16] data have been shown in Table 1. As can be seen from Table 1 that our approximation is satisfactory. In calculations the θ Debye temperatures of Ni, Ag, Zr, Al, and Fe solid metals have been taken as $\theta_{Ni} = 345^\circ \text{K}$, $\theta_{Ag} = 221^\circ \text{K}$, $\theta_{Zr} = 250^\circ \text{K}$, $\theta_{Al} = 390^\circ \text{K}$ and $\theta_{Fe} = 373^\circ \text{K}$, respectively [15, 16]. As we mentioned, our method for entropy calculations can be applied to temperature dependency studies of these solid metals, since our formula is valid for all temperature ranges from low to melting temperatures. Also, to show the temperature dependencies of Ni, Ag, Zr, Al, and Fe solid metal entropies, the Figures 1-5 have been plotted. Notice that our calculations and comparisons of entropy have been made in SI unit system.

As a conclusion, this method for the calculating entropy by the use of n-dimensional Debye function can be easily applied other solids for determining thermodynamically properties.

Conflicts of interest

No conflict of interest or common interest has been declared by the authors.

References

- [1] Chaplot S. L., Mittal R., Choudhury N., Thermodynamic properties of solids: Experiment and modeling, *Thermodynamic Properties of Solids*, 1(2010).
- [2] Ventura G., Perfetti M., Thermal properties of solids at room and cryogenic temperatures. Berlin, Germany: Springer, (2014) 81-91.
- [3] Kittel C., McEuen P., McEuen P., Introduction to solid state physics. New York: Wiley, 8 (1996) 105-130.
- [4] Cankurtaran M., Askerov B. M., Equation of state, isobaric specific heat, and thermal expansion of solids with polyatomic basis in the Einstein-Debye approximation, *Physica Status Solidi (b)*, (2) (1996) 499-507.
- [5] Abu-Eishah S. I., Correlations for the thermal conductivity of metals as a function of temperature, *International journal of Thermophysics*, (6) (2001)1855-1868.
- [6] Hatta I., Heat capacity per unit volume, *Thermochimica acta*, (1-2) (2006) 176-179.
- [7] Gao M. C., Widom M., Information entropy of liquid metals, *The Journal of Physical Chemistry B*, (13) (2018) 3550-3555.
- [8] Desjarlais M. P., First-principles calculation of entropy for liquid metals, *Physical Review E*, (6) (2013) 062145.
- [9] Uspenskaya, I. A., & Kulikov, L. A., Method for the estimation of standard entropy of crystal phases at 298.15 K on the limited temperature range of heat capacity measurements, *Journal of Chemical & Engineering Data*, (8) (2015) 2320-2328.
- [10] Askerov B. M., Figarova S., Thermodynamics, Gibbs Method and Statistical Physics of Electron Gases, Springer Science & Business Media, (57) (2009) .
- [11] Debye P., Zur theorie der spezifischen wärmen, *Annalen der Physik*, (14) (1912) 789-839.
- [12] Guseinov I. I., Mamedov B. A., Calculation of integer and noninteger n-dimensional debye functions using binomial coefficients and incomplete gamma functions, *International Journal of Thermophysics*, (4) (2007) 1420-1426.
- [13] Mehmetoglu T., Use of Einstein-Debye method in the analytical and semi empirical analysis of isobaric heat capacity and thermal conductivity of nuclear materials, *Journal of Nuclear Materials*, 527 (2019)151827.
- [14] Gradshteyn I. S., Ryzhik I. M., Tables of integrals, sums, series, and products. Elsevier, (1971).
- [15] Gordon England. Periodic Table of the Elements. Available at: <https://www.gordonengland.co.uk/elements/> Retrieved March 11, 2021.
- [16] Knowledge Door Element Handbook. Available at: <http://www.knowledgedoor.com/> Retrieved March 11, 2021.

On the Lyapunov Time Estimations For Comet 1/P Halley

Murat Kaplan^{1, a, *}¹ Department of Space Science and Technologies, Faculty of Science, Akdeniz University, Antalya, Turkey

*Corresponding author

Research Article

History

Received: 06/07/2021

Accepted: 28/12/2021

Copyright

©2022 Faculty of Science,
Sivas Cumhuriyet Universitymuratkaplan@akdeniz.edu.tr<https://orcid.org/0000-0003-2595-5463>

ABSTRACT

In three consecutive articles published in recent years, quite different estimates were made for the Lyapunov time of comet 1/P Halley, whose orbit is known to have high precision. In this work, we examined the Lyapunov time of the comet 1/P Halley using the MEGNO method and compared our results with previous studies. To investigate the effects of numerical overflows on the results that may have occurred during the calculations, we conducted tests with and without the renormalization procedure. We used various renormalization intervals to see their possible effects on the results and to avoid improper ones. We reached the maximum Lyapunov exponents at renormalization times for 2250 yr, 2265 yr, and 3000 yr. In both cases where renormalization is used and not used, the Lyapunov time is calculated as 119 yr and 190 yr, respectively. Besides, we performed orbital integrations for ∓ 10 kyr for comet 1/P Halley with the clone orbits produced by the MCM method and compared the standard errors of the means of the orbital parameters with the Lyapunov times. We conclude that calculated different Lyapunov times correspond to different levels of the standard errors of the means.

Keywords: N-body integration, Lyapunov time, Comets.

Introduction

For the first time in history, Edmund Halley [1] found that some historical comet observations belonged to the same object, as it is known today, comet 1/P Halley. Since that time, comet 1/P Halley is one of the most well-known objects of both popular and dynamical astronomy. It has been observed repeatedly by different civilizations since 240 BC in its every visit. Edmund Halley calculated its orbit and predicted for the next apparition as late 1758 or the beginning of 1759 [2, 3]. It turned back with a perihelion passage in 1759 March 13.1. It was the first solar system object whose periodicity was discovered other than planets and their natural satellites. During its last apparition in 1986, it was observed by seven spacecraft [4]. It is the first comet observed by spacecraft. Today, short-period comets with a period between 20 yr and 200 yr are also called Halley type comets (HTC). There are 14 numbered, 80 unnumbered HTC listed (JPL's SBDB [5-7]) as of 27/12/2021. Unnumbered comets were observed only in 1 apparition. Among the numbered HTCs, 1/P Halley is the second object with the smallest perihelion distance (0.586 au).

Although comet 1/P Halley perhaps is the best known, long studied, and most observed comet, its orbit continues to attract attention in terms of dynamical astronomy. One of the most important reasons for this is that it is in a chaotic orbit, as it has been known since the work of [8]. The future trajectory of 1/P Halley cannot be determined with great accuracy, even if non-gravitational and relativistic effects are well known or can be calculated [9]. The measure of the dynamical predictability of a chaotic trajectory is given by the Lyapunov time calculated by taking the inverse of the maximum Lyapunov exponent. No matter how well the trajectory of the object is known and

how advanced the computing tools at hand are, long term evolution of the orbit cannot be predicted for longer than Lyapunov time. Therefore, statistical methods should be preferred for trajectory calculations that go beyond Lyapunov time.

The oldest estimate we can reach for the Lyapunov time of comet 1/P Halley is in [10] and is given as approximately 34 yr, indicating the lower limit. Three consecutive publications [11-13] in recent years show that the dynamic study of 1/P Halley's orbit still deserves attention. In these three articles, different Lyapunov time estimations were made varying between 70 yr and 562 yr. In [11], unlike previous studies, indirect numerical integration was used for the first time to calculate the Lyapunov exponent. A total of 30 simulations were run for 3000 yr. All planets except Mercury, all dwarf planets except Sedna and 5 dwarf planet candidates were included in the simulation. Integrated ghost particles were produced by applying $\mp 10^{-6}$ perturbations to the position vectors. A total of 30 simulations were run. In [12], ghost particles were produced similar to [11], but initial perturbations were added to the velocity vectors in addition to the position vectors and 13 initial conditions were used together with the nominal orbit. However, the integration time was kept longer (10 kyr). As a result of the 3-body tests, it was stated that the influence of Mercury, Uranus and Neptune is negligible. In [13], first-order variational equations were used instead of the ghost particle approach in previous studies. In the simulations, test objects were integrated with the major planets and the Moon. Integration time was quite long compared to previous studies (2×10^5 yr).

Various methods, initial conditions, integration schemes and indicators were used in each of these studies. Naturally, their approaches are different. Besides, there are fine-tuning points during the application of these methods-e.g., renormalization that can lead to different results. However, calculated various Lyapunov exponents for the same object should give similar time scales regardless of method. So that would be the limit of dynamical computability of the orbit. The fundamental question is: how long can the dynamics of the movement be followed, and which one of the previous estimations for the Lyapunov time are the most accurate?

In this study, we worked on the calculation of Lyapunov time for comet 1/P Halley using the MEGNO (the Mean Exponential Growth factor of Nearby Orbits) method and comparing the calculated Lyapunov times with orbital integrations. In Section 2, the numerical methods and initial conditions are given. In Section 3, Lyapunov time calculations and orbital integration results of clone orbits are discussed and presented. Section 4 summarizes the comments and results.

Materials and Methods

In this work, we used the publicly available REBOUND integrator package [14] with first-order variational equations. We used MEGNO function included in the REBOUND integrator package to calculate Lyapunov time. Besides, we tested renormalization in the calculation of MEGNO (the detail is given in subsection 2.1). We chose high accuracy integrator IAS 15 based on the 15th-order Gauß-Radau quadrature as the integration method [15]. The integrals included dwarf planets Pluto and Ceres in addition to eight major planets. We ignored the masses for the test objects outside these bodies. Also, all kind of non-gravitational effects and relativistic corrections that can be important in comet dynamics are ignored as in previous papers [11-13].

The initial conditions for all small and big Solar system bodies have been obtained using the Jet Propulsion Laboratory's Solar System Dynamics Group Small-Body Database (JPL's SSDG SBDB) and JPL's Horizons ephemeris system [16-18] for the epoch JD 2449400.5 (1994-Feb-17.0) TDB (Barycentric Dynamical Time).

Clone orbits were used to see the dynamically reliable computability time of the orbit. The orbital elements of the clone orbits were produced at the same precision level as the uncertainties of the orbit obtained from observations. For this, MCCM (Monte Carlo using Covariance Matrix) method [19-21] using the covariance matrix of orbital elements was used.

MEGNO Technique

MEGNO technique was first proposed in [22] and [23] publications. Since then it has been applied for various dynamic systems such as irregular satellites of Jupiter [24], double and binary asteroids [25, 26], planetary systems [27-29], and galaxy dynamics [30]. It has been discussed and compared with previously well-known LCE

calculations [24, 31]. Compared to other methods, it has been seen that it gives good results with relatively short integration times [27, 31].

The MEGNO technique has been repeatedly presented with similar formulations in various sources. Here, we summarize the method using the notation in [25]. When a dynamic system in the form below is considered;

$$\frac{dx}{dt} = f(x(t)), \text{ with } x \in R^{6n} \quad (1)$$

where the solution of the system is $\varphi(t)$. For a defined tangent vector $\delta_\varphi(t)$ along with $\varphi(t)$, the evolution of this vector is given by;

$$\dot{\delta}_\varphi = \frac{df}{dx}(\varphi(t))\delta_\varphi(t). \quad (2)$$

Here, the MEGNO indicator is defined as;

$$Y_\varphi(t) = \frac{2}{t} \int_{t_0}^t \frac{\|\delta_s\|}{\|\delta_s\|} ds, \quad (3)$$

and the time-averaged mean value of the MEGNO is;

$$\bar{Y}_\varphi(t) = \frac{1}{t} \int_{t_0}^t Y_\varphi(s) ds. \quad (4)$$

If the orbit is chaotic, the two quantities Y_φ and \bar{Y}_φ increase linearly in time and goes to infinity. If the orbit is quasi-periodic, \bar{Y}_φ converges to 2, and if the orbit is stable and periodic, it converges to 0. In addition, a linear least-squares fit \bar{Y}_φ gives half of the Lyapunov exponent (γ) where the Lyapunov time (T_γ) is $T_\gamma = 1/\gamma$.

In many cases, since δ diverges exponentially during integration, the norm of the variational vector grows too much in a short time, causing a numerical overflow. To avoid this situation, it is recommended that the variational vector is renormalized at certain time intervals according to Eq.5 as in [27]. However, there are no specific criteria for determining the length of renormalization intervals. It was shown in [24] that in some cases the choice of renormalization time does not affect the calculation of maximum Lyapunov exponent. However, this may not be the case in all situations as shown in [32]. It should be decided by performing tests at different renormalization ranges.

$$\gamma = \lim_{k \rightarrow +\infty} \frac{1}{k\tau} \sum_{i=1}^k \ln \frac{\|\delta(k\tau)\|}{\|\delta_0(k\tau)\|} \quad (5)$$

Results and Discussion

Lyapunov Time Calculations

In the calculation of the MEGNO indicator, it is suggested to take 10^3 to 10^4 times the period of the largest or outmost planet in the system in [27, 32] as the integration time, which gives the characteristics of the

system. Considering Jupiter, the largest planet, this time can be taken in the range of 1.2×10^4 yr to 1.2×10^5 yr for the solar system. In our case, the frequency of interaction of the planets with the targeted body mainly depends on the comet's period, not the major planet Jupiter. Considering the orbital period of comet 1/P Halley, integration time should go up to 7.5×10^5 yr as far as possible. It is stated in various papers that the required minimum integration time for the MEGNO technique to estimate the maximum Lyapunov exponent is $10 - 10^2$ times shorter than any classical method [27, 31].

In [13] the integration time was taken as 2×10^5 yr, and first-order variational equations were preferred to calculate Lyapunov exponents. Lyapunov times corresponding to the calculated positive Lyapunov exponents range from 385 yr to 702 yr. However, it was considered an estimation for the Lyapunov time taking the average value of the maximum and minimum Lyapunov exponents and obtained averaged Lyapunov time as 562 yr. In [12], Lyapunov time was estimated with an integration time of 10 kyr using ghost particles produced by applying $\mp 10^{-6}$ and $\mp 4.4 \times 10^{-8}$ perturbations to the position and velocity vectors, respectively. Lyapunov time obtained by these approaches is 300 yr. A similar approach was used in [11], but for a quite short (3000 yr) integration time. In this case, they obtained the Lyapunov time as the interval of 70-100 years.

Renormalization is highly recommended not only for the MEGNO method but also Lyapunov exponent calculations for various techniques. Interestingly non of the three papers [11-13] which calculated Lyapunov time for comet 1/P Halley mentioned whether the renormalization is used or not. In cases where short integration times are used, it may be reasonable not to use renormalization. However, short integration time also has other drawbacks as mentioned earlier, therefore it is not recommended in Lyapunov calculations for classical approaches.

Using different renormalization times during the calculation of the maximum Lyapunov exponent from the MEGNO indicator has been examined in various publications [24, 32], and it has been shown that the renormalization period does not change the results in some cases. On the other hand, depending on the initial conditions, it is possible to get incorrect results with improper applications [27].

Here, Lyapunov time is calculated in two different ways using the linear characteristic of the MEGNO indicator, with and without renormalization. Randomly generated 100 variational particle sets were used for each test. In the absence of renormalization, the integrations were allowed to continue until they produced numerical overflows. Various trials were conducted here with different renormalization intervals ranging from 75 yr to 3000 yr.

Figure 1 shows the $\log(\gamma)$ - $\log(\text{yr})$ graph for two methods with and without renormalization. In both graphs, maximum Lyapunov exponents are at the same level. However, without renormalization, numerical overflows are produced in shorter periods for variational

particles as predicted in [24, 27, 32]. Therefore, it is necessary to keep the integration times at levels of 10^4 yr even shorter.

We calculated the Lyapunov time as 190 yr by using the linearly increasing characteristic of the MEGNO parameter in the integrations that continued until the numerical overflow. When we take the integration time as 1×10^4 yr, 2×10^4 yr, and 3×10^4 yr to avoid numerical overflows, we obtained the Lyapunov times as 96 yr, 121 yr and 164 yr, respectively.

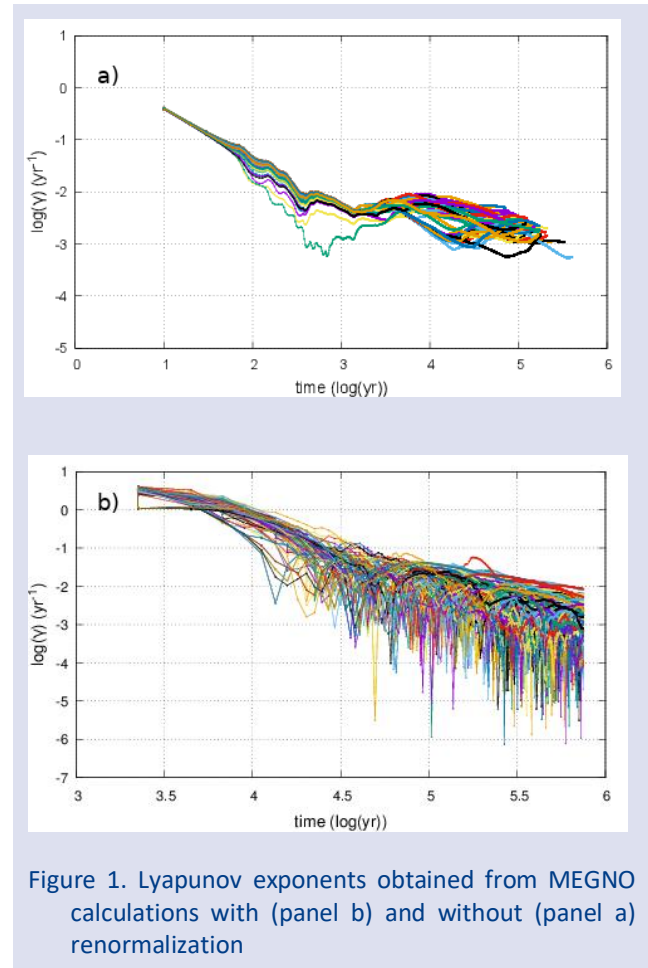


Figure 1. Lyapunov exponents obtained from MEGNO calculations with (panel b) and without (panel a) renormalization

Since we can keep the integration time longer when renormalization is applied, we tried to obtain the maximum convergent Lyapunov exponent. We reached the minimum and quite similar (119 yr, 124 yr, and 123 yr respectively) Lyapunov times with renormalization intervals of 2250 yr, 2265 yr, and 3000 yr.

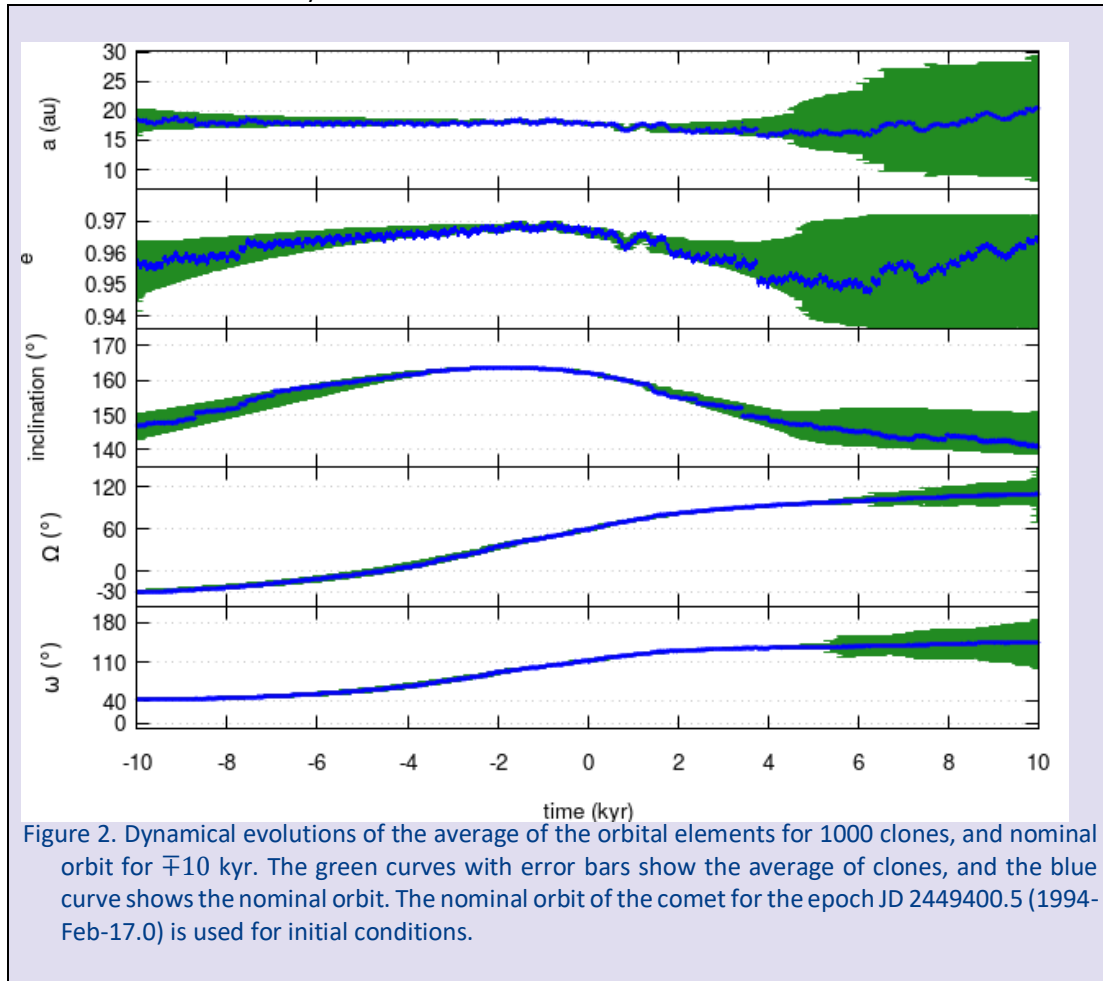
N-Body Simulations for Comet 1/P Halley with Clon Orbits

It is well-known that long-term simulations made only for the nominal orbits are not very reliable in chaotic regions. Trajectories with very close initial conditions can follow very different paths in a simulation of longer duration than Lyapunov time. Therefore, using clone orbits in long-term dynamic analysis of orbits is a more reliable approach for long simulation times.

The easiest and most general approach to generate clone orbits is to distribute the orbital elements or position and velocity components with small dispersion. Even though the clone orbits obtained in this way are very close to the nominal one, they will not be compatible with the uncertainties of the nominal orbital elements. Such clones have similar but independent orbits near the nominal one. Thus, they may not reflect the change of orbital elements well over time [21].

For these reasons, in this study, clone orbits produced by the MCCM method were used. Thus, all clones produced have the same sensitivity level as the orbital

parameters obtained from the observations. In other words, they are not only in the close vicinity of the nominal orbit but also dispersed in the same sensitivity range. Thus, the initial parameters will be as accurate as of the nominal orbital elements. This is a better approach than classical methods to follow the change of clone orbits in time and compare them with the nominal orbit. Besides, the divergence time of the parameters due to chaotic motion can give us a norm for the Lyapunov time.



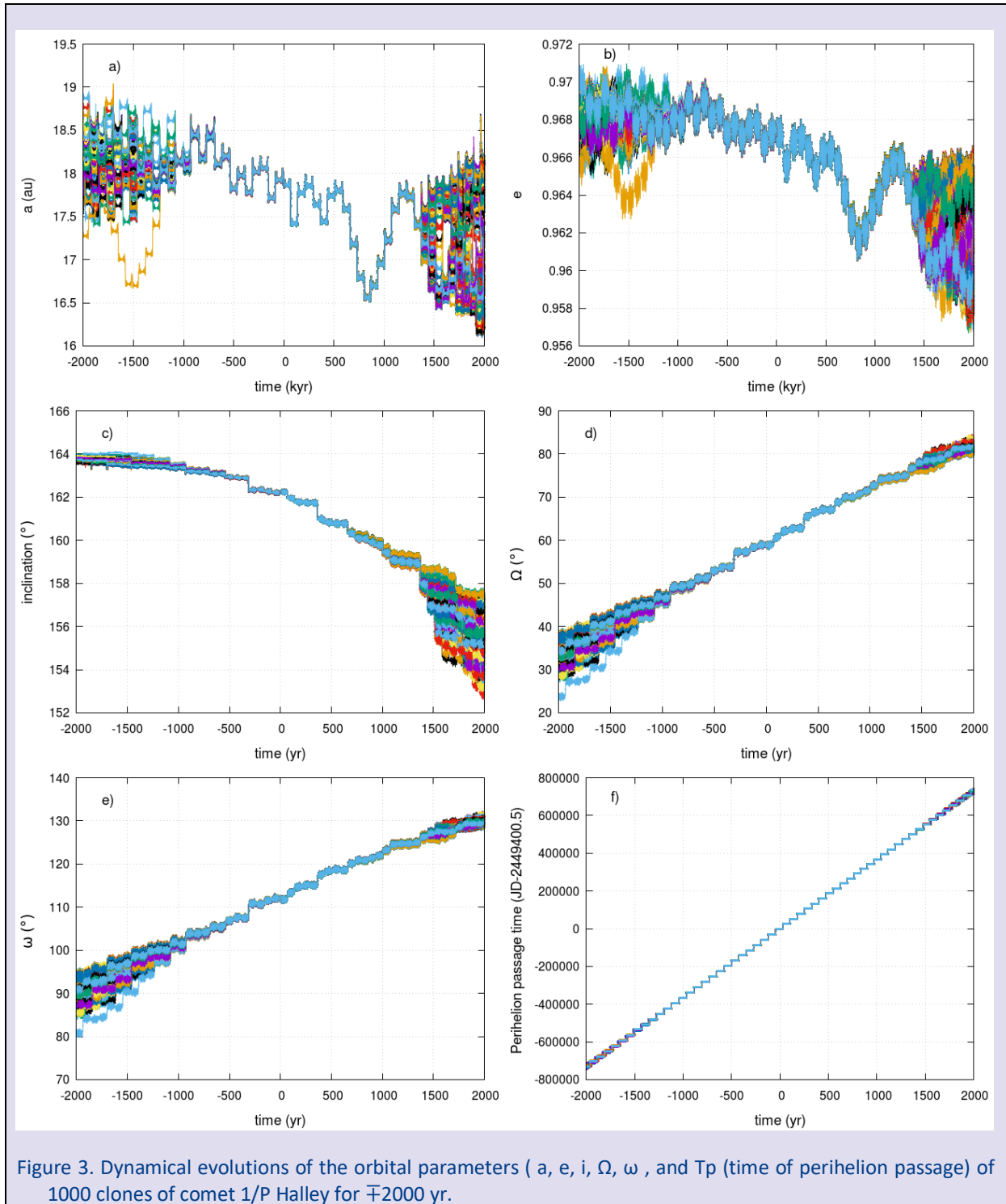
In Figure 2, comet 1/P Halley's nominal orbital elements are given comparatively with the averages of the clone orbits. The clone orbits in the approximately ∓ 1500 yr range are in great coherence with the nominal orbit. In this range, all clone orbits provide almost the same orbit shape, size and orientation. When we look at the error bars of the average of clone orbits, a larger error range is seen in future simulations than in the past. This situation can be interpreted as an indication that the comet's orbit has evolved into a more chaotic orbit in time.

Figure 3 shows the change of basic orbital elements of all clones to time in the ∓ 2000 yr interval. Similar to Figure 2, all orbital elements support the same orbital shape and orientation with very small changes over the range of about -1000 yr to +1300 yr. However, similar to what is mentioned in [11], the time it takes for the differences

between orbital elements to start to be greater than their initial sensitivity ranges is 108 yr. This definition also gives us an approximation for the Lyapunov time.

Our primary motivation here is to see footprints of the forward Lyapunov time in the orbital dynamics of clones. Figure 4 portrays the standard deviations of the mean of the clone orbital elements for the time interval 0-2000 yr. The y axis (standard deviations) is in log scaled so that any sudden increase in dispersions can be noticed easily. By definition, the required time where the nearby orbits begin to diverge exponentially is Lyapunov time. That time limit is 108 yr in Figure 4.

After the exponential increase at 108 yr, there is no sudden growth till 1300 yr even though the standard deviation for 1000 clones remains in the same band.



For almost all orbital elements, the separations that start after about 1300 yr become more evident around 1400 yr, and standard deviations start to increase exponentially one more time. Nevertheless, all clones retain more or less the same trajectory shape between 108 yr and 1400 yr. Although various Lyapunov times can be obtained using different methods for this range, no distinctly different results are seen in terms of dispersion range.

For the 108 yr to 1400 yr range, it seems that it will be easier and much more clear to do a detailed examination on T_p (time of perihelion passage). In Figure 4f, the smallest

dispersions for each time interval belongs to the value calculated at the perihelion of the comet. The standard deviations calculated at the aphelion are much higher. However, it should be noted here that the dispersions formed during the calculation of T_p when the body is at perihelion are more determinant and distinct. For this reason, the standard deviations of T_p close to the perihelion are taken as a basis in these analyses. Here, the standard deviation calculated at perihelions between 109 yr and 289 yr is less than 1 day, between 290 yr and 589 yr is less than 5 days. Between 590 yr and 1027 yr, it is still less than 20 days.

Standard deviations start to increase exponentially after 1396 yr.

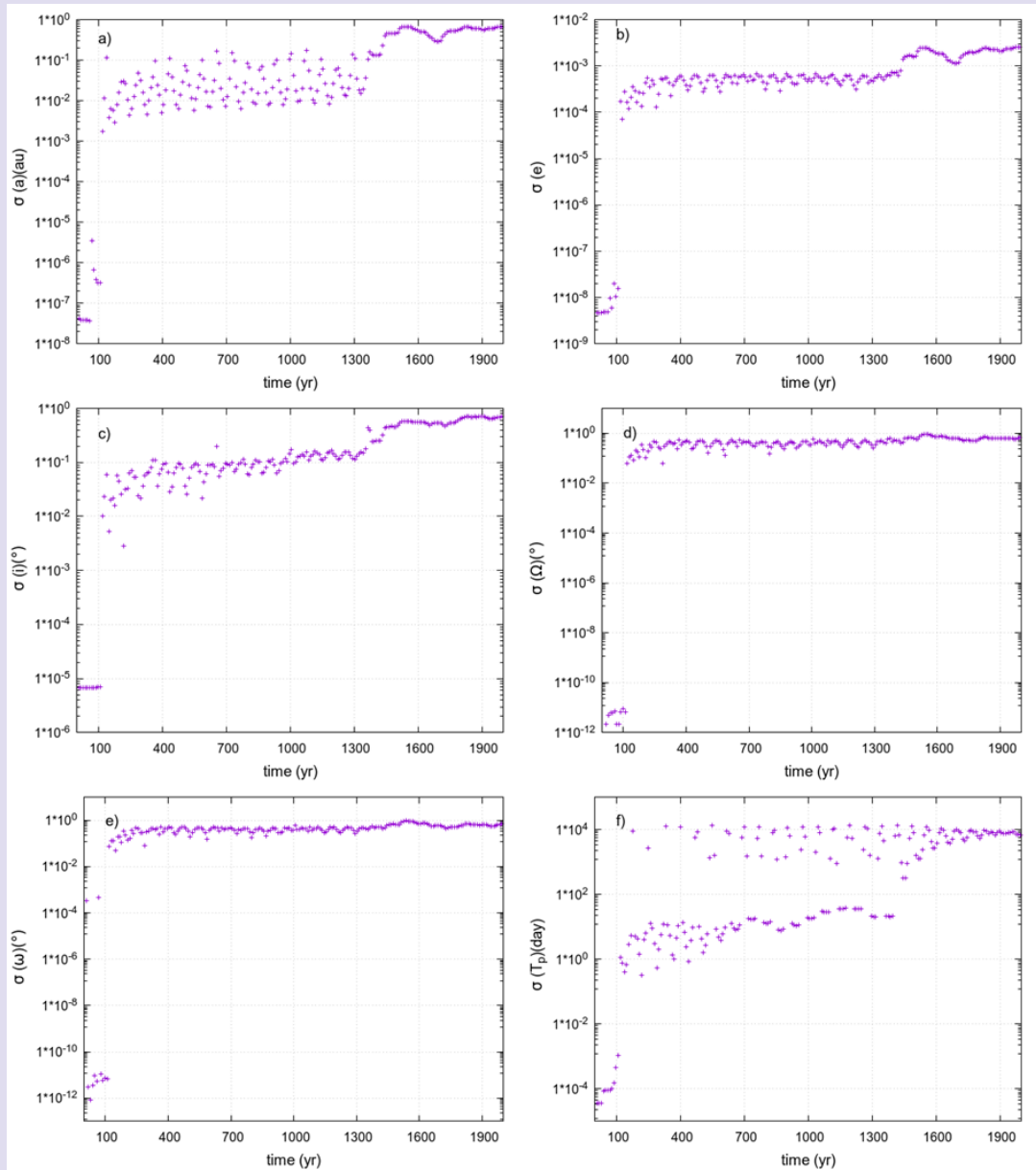


Figure 4. Standard deviations for the mean of the orbital elements (a, e, i, Ω , ω and T_p (time of perihelion passage) of the clones for comet 1/P Halley.

Conclusion

In this study, we calculated the Lyapunov time for comet 1/P Halley using the MEGNO indicator. Estimated Lyapunov times with and without renormalization are 119 yr and 190 yr, respectively. This result showed us the effect of renormalization in calculating the Lyapunov time for a high eccentric orbit. Depending on the different integration levels (1×10^4 yr, 2×10^4 yr, and 3×10^4 yr), varying results were also obtained, such as 96 yr, 121 yr and 164 yr respectively. Besides, to see the reflection of Lyapunov time in dynamic analysis, we performed orbital integrations for ∓ 10 kyr interval of the 1000 clone orbits produced using the MCM method. We compared the

means of the orbital elements of the clones and the time-dependent variations of their standard deviations with the Lyapunov times in the literature.

These results lead us to conclude that when we calculate different Lyapunov times at different levels, that can give us different scales: if our measure is at the initial precision range, Lyapunov time should not be more than 108 yr (such as 70-100 yr in [11]), for a standard deviation of less than one day at T_p , it should not be more than 289 yr (such as 300 yr in [12]), and for a standard deviation of fewer than five days on T_p , it should not be more than 589 yr (such as 562 yr in [13]). Moreover, for a measure where

the shape and orientation of the orbit are still similar, and for a standard deviation of up to 20 days at Tp is acceptable, approximately 1300 yr can be taken as the limit for dynamical studies. It seems that Lyapunov times obtained from different methods using various assumptions can correspond to different levels in the dynamical analysis of the body.

Conflicts of interest

The authors state that did not have conflict of interests

References

- [1] Hughes D. W., Green, D. W., Halley's first name: Edmond or Edmund, *International Comet Quarterly* 29 (2007) 7-14.
- [2] Yeomans D. K., Comet Halley-The orbital motion, *The Astronomical Journal*, 82 (1977) 435-440.
- [3] Yeomans D. K., Kiang T., The long-term motion of comet Halley, *Monthly Notices of the Royal Astronomical Society*, 197 (1981) 633-646.
- [4] Stelzried C., Efron L., Ellis J., Halley comet missions, *Nature*, 321 (1986) 240-242.
- [5] Giorgini J., Chodas P., Yeomans D., Orbit uncertainty and close-approach analysis capabilities of the horizons on-line ephemeris system, *In Bulletin of the American Astronomical Society*, 33 (2001) 1562.
- [6] Giorgini J., New challenges for reference systems and numerical standards in astronomy, *Proceedings of the Journées 2010 "Systèmes de Référence Spatio-Temporels"*, N. Capitaine (ed.), Observatoire de Paris, 2011..
- [7] Giorgini J., IAU General Assembly, Meeting# 29, 22 (2015).
- [8] Chirikov R., Vecheslavov V., Chaotic dynamics of comet Halley, *Astronomy and Astrophysics*, 221 (1989) 146-154.
- [9] Bailey M., Emel'Yanenko V., Dynamical evolution of halley-type comets, *Monthly Notices of the Royal Astronomical Society*, 278 (1996) 1087-1110.
- [10] Shevchenko I. I., On the lyapunov exponents of the asteroidal motion subject to resonances and encounters, *Proceedings of the International Astronomical Union*, 2 (2006) 15-30.
- [11] Muñoz-Gutiérrez M., Reyes-Ruiz M., Pichardo B., Chaotic dynamics of comet 1P/Halley: Lyapunov exponent and survival time expectancy, *Monthly Notices of the Royal Astronomical Society*, 447 (2015) 3775-3784.
- [12] Boekholt T. C., Pelupessy F., Heggie D. C., Portegies Zwart S., The origin of chaos in the orbit of comet 1P/Halley, *Monthly Notices of the Royal Astronomical Society*, 461 (2016) 3576-3584.
- [13] Pérez-Hernández J. A., Benet L., On the dynamics of comet 1P/Halley: Lyapunov and power spectra, *Monthly Notices of the Royal Astronomical Society*, 487 (2019) 296-303.
- [14] Rein H., Liu S.-F., Rebound: An open-source multi-purpose n-body code for collisional dynamics, *Astronomy & Astrophysics*, 537 (2012) A128.
- [15] Rein H., Spiegel D. S., IAS15: A fast, adaptive, high-order integrator for gravitational dynamics, accurate to machine precision over a billion orbits, *Monthly Notices of the Royal Astronomical Society*, 446 (2014) 1424-1437.
- [16] Giorgini J., Yeomans D.K., Chamberlin A.B., Chodas P.W., Jacobson R.A., Keesey M.S., Lieske J.H., Ostro S.J., Standish E.M., Wimberly R.N., JPL's On-line Solar System Data Service, *In Bulletin of the American Astronomical Society*, 28 (1996) 1158.
- [17] Standish E., JPL Planetary and Lunar Ephemerides, de405/le405, interoffice memo. Memorandum 312. F-98-048, Jet Propulsion Laboratory, Pasadena, California (1998).
- [18] Giorgini J., Yeomans D., On-line system provides accurate ephemeris and related data. NASA TECH BRIEFS, NPO-20416 48 (1999).
- [19] Bordovitsyna T., Avdyushev V., Chernitsov A., New trends in numerical simulation of the motion of small bodies of the solar system, *Celestial Mechanics and Dynamical Astronomy*, 80 (2001) 227-247.
- [20] Avdyushev V., Banschikova M., Regions of possible motions for new jovian satellites, *Solar System Research*, 41 (2007) 413-419.
- [21] de la Fuente Marcos C., de la Fuente Marcos R., Asteroid 2015 DB216: A recurring co-orbital companion to Uranus, *Monthly Notices of the Royal Astronomical Society*, 453 (2015) 1288-1296.
- [22] Cincotta P. M., Simó C., Simple tools to study global dynamics in non-axisymmetric galactic potentials-I, *Astronomy and Astrophysics Supplement Series*, 147 (2000) 205-228.
- [23] Cincotta P. M., Giordano C. M., Simó C., Phase space structure of multi-dimensional systems by means of the mean exponential growth factor of nearby orbits, *Physica D: Nonlinear Phenomena*, 182 (2003) 151-178.
- [24] Hinse T. C., Christou A. A., Alvarellos J. L., Goździewski K., Application of the megno technique to the dynamics of jovian irregular satellites, *Monthly Notices of the Royal Astronomical Society*, 404 (2010) 837-857.
- [25] Compère A., Lemaître A., Delsate N., Detection by megno of the gravitational resonances between a rotating ellipsoid and a point mass satellite, *Celestial Mechanics and Dynamical Astronomy*, 112 (2012) 75-98.
- [26] Compère A., Farrelly D., Lemaître A., Hestroffer D., A possible mechanism to explain the lack of binary asteroids among the plutinos, *Astronomy & Astrophysics*, 558 (2013) A4.
- [27] Goździewski K., Bois E., Maciejewski A., Kiseleva-Eggleton, L., Global dynamics of planetary systems with the megno criterion, *Astronomy & Astrophysics*, 378 (2001) 569-586.
- [28] Goździewski K., Stability of the 47 uma planetary system, *Astronomy & Astrophysics*, 393 (2002) 997-1013.
- [29] Satyal S., Quarles B., Hinse T., Application of chaos indicators in the study of dynamics of s-type extrasolar planets in stellar binaries, *Monthly Notices of the Royal Astronomical Society*, 433 (2013) 2215-2225.
- [30] Maffione N. P., Darriba L. A., Cincotta P. M., Giordano C. M., Chaos detection tools: application to a self-consistent triaxial model, *Monthly Notices of the Royal Astronomical Society*, 429 (2013) 2700-2717.
- [31] Maffione N. P., Giordano C. M., Cincotta P. M., Testing a fast dynamical indicator: The MEGNO, *International Journal of Non-Linear Mechanics*, 46 (2011) 23-34.
- [32] Hinse T., Michelsen R., Jørgensen U., Goździewski K., Mikkola S., Dynamics and stability of telluric planets within the habitable zone of extrasolar planetary systems-numerical simulations of test particles within the hd 4208 and hd 70642 systems, *Astronomy & Astrophysics*, 488 (2008) 1133-1147.

The Modeling of Radioactive Cobalt Adsorption on Molecular Sieves

Ekrem Çiçek ^{1,a,*}

¹ Department of Physics, Faculty of Science and Letters, Mehmet Akif Ersoy University, Burdur, Turkey

*Corresponding author

Research Article

History

Received: 07/09/2020

Accepted: 13/01/2022

Copyright



©2022 Faculty of Science,
Sivas Cumhuriyet University

 ekrcicek@gmail.com

 <https://orcid.org/0000-0001-6724-9423>

ABSTRACT

Radioactive wastes are products of nuclear activities around the world. Radioactive cobalt is one of the usually found radionuclide in nuclear waste. It is crucial to separate radioactive cobalt from aqueous media. The removal of radioactive cobalt (Cobalt-60) was investigated using molecular sieves in this study. The molecular sieves structure comprises of a microporous and aluminosilicate framework. Due to their chemical composition and structures molecular sieves have excellent sorption capacities. The response surface methodology was utilized to constitute the predictive regression model. The experimental minimum and maximum decontamination factor 2.5 and 11.1 was obtained, respectively. The predicted maximum decontamination factor was 10. Molecular sieves present a high adsorbent capacity for the disposal radioactive cobalt from water solution

Keywords: Adsorption, Radioactive cobalt, Response surface methodology, Molecular sieves.

Introduction

The nuclear power stations and nuclear laboratories are increasing [1]. Nuclear activities have produced too much amount of radioactive waste. These wastes cause to significant risks to the environments [2]. They always have been recognized as a serious threat for human health. Owing to their health implications the public concerns are raising on nuclear safety. Disposal of radioactive waste are receiving more attention since nuclear application increased globally [3]. Radioactive contamination is severely dangerous and it is not easy task to handling. For protection against radioactive wastes the new methods were developed by researchers [4,5].

A great quantity of nuclear waste has been produced from nuclear facilities with the fast development of the nuclear field [6]. Cobalt-60 is produced artificially and described as a major environmental contaminant at nuclear region [7]. Radioactive isotope of cobalt has many useful applications [8].

Radioactive isotope of cobalt (Cobalt-60) employed in medicine and industry. The radioactive cobalt is used commonly in radiotherapy units as gamma source for treatment. In nuclear medicine, it (so low activity) is just used as to be flat gamma source to check gamma camera quality control [9]. It is also used to investigate materials and sterilization. The half-life of cobalt-60 is 5.27 years [8].

The disposal of radioisotopes from the environment comprises a number of methods such as filtration, reverse osmosis, precipitation, vacuum evaporation, extraction and adsorption by cation exchange [10]. Adsorption has received rising attention because of its advantages in radioactive wastewater treatment [6].

Different types of sorbents have been utilized to remove nuclear waste. Because of its excellent removal capacity, zeolite is the one of the best choice for radioactive waste adsorption [3].

Zeolites are crystalline materials with three dimensional frameworks [11]. They have micro porous and their frameworks are charged [3]. Alkaline metallic cations and porosity made the zeolite hydrophilic and excellent adsorptive material [2,4,12]. The advantages of zeolites are extensive ion exchange capacity, perfect selectivity and low cost are [6]. The sorption capacity of zeolite is generally depending to pore size [3].

Zeolite is a porous mineral with exchangeable ions. The cavities and channels of zeolites can capture cations, water, and radionuclides. Due to their high cation-exchange capacities, they have been considered for radioactive waste treatment [13]. Removal of radionuclides from aqueous solution is particularly important in cleaning for environmental contamination [3]. Cations exchange and adsorption are the major mechanism for discharging radioisotopes from water solution. Since zeolite comprises uniform small pores they present excellent adsorption and exchange capacity [6].

Adsorption modelling is examined and decontamination factor (response) is predicted by response surface methodology (RSM). The experimental input variables are amount of adsorbent and initial activity of solution.

In this study, molecular sieves (a kind of zeolite) were exploited for the discharging of radioactive cobalt from aqueous media.

Materials and Methods

Experimental procedure

We used molecular sieve obtained from Merck (105705) in this study. In order to remove water from molecular sieve, it was activated with temperature for two hours at 873 K. After activation process, molecular sieve was added to the radioactive cobalt and suspensions were mixed for 4 h. Thereafter the mixtures were filtered with a syringe filter (Whatman Syringe Filter 25 mm diameter, 0,2 µm pore size). The activities of radioactive cobalt were measured with Polon Warszawa Analyzer (A-22p HT Power supply ZW N-21M HT Control 0/2000V). For all liquid radioactive cobalt measurements, a volume of 10 mL solution was utilized. The measurements were repeated for 10 times. The experimental decontamination factor was presented as below:

$$DF = A_0 / A_f \tag{1}$$

where A_0 was the initial activity of radioactive cobalt feed solution (Bq L⁻¹) and A_f was the final radioactivity (Bq L⁻¹).

More details concerning experiment can be found in previous studies [13-15].

We utilized RSM for analysis and modeling. It is a useful statistical and mathematical technique as described previous studies in details [13-17]. The decontamination factor (response) can be described which is influenced by controllable various input values in RSM model.

The general form of RSM can be demonstrated as below:

$$\hat{DF} = \beta_0 + \beta_1 x_1 + \beta_2 x_2 + \beta_{11} x_1^2 + \beta_{22} x_2^2 + \beta_{12} x_1 x_2 \tag{2}$$

$$\beta = [\beta_0 \beta_1 \beta_2 \beta_{11} \beta_{22} \beta_{12}]^T \tag{3}$$

$$\beta = (X^T \cdot X)^{-1} \cdot X^T \cdot DF \tag{4}$$

where: β – present regression coefficients;

X – input variables;

DF – decontamination factor (response).

Adsorption of radioactive cobalt upon molecular sieves;

- regression model with actual variables:

$$\hat{DF} = 5.63 - 56.3SD - 0.0005A_0 + 764SD^2 - 0.00256SDA_0 \tag{5}$$

valid for the range: $0.05 \leq SD \leq 0.15$ (%w v⁻¹); $7600 \leq A_0 \leq 15200$ (Bq L⁻¹)

The modeling details can be seen in previous studies [13-18]. All calculations were done by means of Minitab 19 software.

Results and Discussion

The ANOVA was used to examine the accuracy of the calculated model. According to the results the model was compatible where the probability value was 0.028. F value was 8.75, it was pointed out that the experimental decontamination factor obtained by changing the factor levels were statistically meaningful at the 92% confidence limit. R² value should be close to 1 for a good statistical model. The mathematical model is adequate for the prediction radioactive cobalt removal by molecular sieves sorption since R² = 0.92 > (0.75). Lack of fit F and p values are 38.71 and 0.117 (P > 0.05), respectively. Lack of fit was not significant and this means that the model is good [18,19].

Table 1. Radioactive cobalt experimental design for molecular sieves

Run number (N)	Factors (input values)				Final activity Bq L ⁻¹	Response	
	Amount of sorbent (g 100ml ⁻¹)		Initial activity of radioactive cobalt Bq L ⁻¹			Decontamination Factor (DF)	
	Sorbent Dosage (%w v ⁻¹)	level a x1	CO (mg L ⁻¹)	level a x2		Experimental DF	Predicted DF
1	0.15	1	15200	1	1492.61	10.2	10.0
2	0.05	-1	15200	1	4317.62	3.5	4.2
3	0.15	1	7600	-1	683.32	11.1	9.9
4	0.05	-1	7600	-1	3026.31	2.5	2.2
5	0.15	1	11400	0	1433.73	8.0	9.4
6	0.05	-1	11400	0	3732.90	3.1	2.7
7	0.1	0	15200	1	2678.49	5.7	5.2
8	0.1	0	7600	-1	2875.68	2.6	4.2
9	0.1	0	11400	0	2568.94	4.4	4.1
10	0.1	0	11400	0	2378.59	4.8	4.1

^a -1 = low. 0 = center. +1 = high.

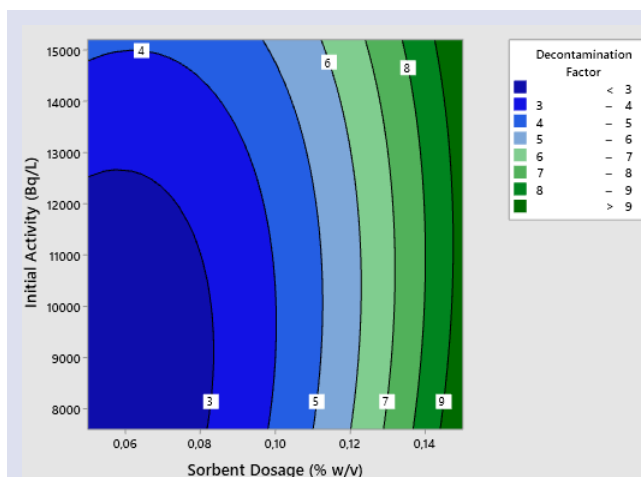


Figure 1. Contour plot of decontamination factor for molecular sieves - radioactive cobalt

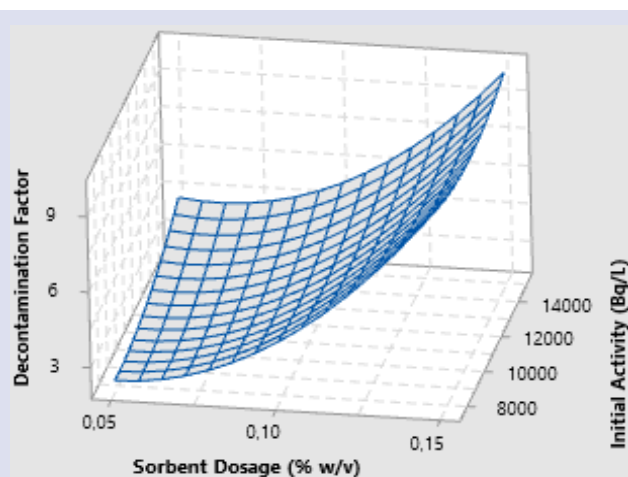


Figure 2. 3D-Response surface plot of decontamination factor for molecular sieves- radioactive cobalt

Conclusion

We examined the ability of removal of the radioactive cobalt by molecular sieves in aqua solution in this study. Initial cobalt activity and the influence of molecular sieves amount on decontamination factor were investigated by means of RSM. RSM can predict decontamination factor for different amount of sorbent dosage and initial activity. We suggested that molecular sieves might be used as an adsorbent for the removal of radioactive cobalt in nuclear waste. Also. RSM can prevent many experimental runs.

Conflicts of interest

The authors declare no conflict of interest.

References

- Zhong Q.Q., Zhao Y.Q., Shen L., Hao B., Xu X., Gao B.Y., Shang Y.N., Chu K.Z., Zhang X.H., Yue Q.Y., Single and binary competitive adsorption of cobalt and nickel onto novel magnetic composites derived from green macroalgae, *Environ. Eng. Sci.*, 37(3) (2020) 188-200.
- Lee H.Y., Kim H.S., Jeong H.K., Park M., Chung D.Y., Lee K.Y., Lee E.H., Lim W.T., Selective removal of radioactive cesium from nuclear waste by zeolites: on the origin of cesium selectivity revealed by systematic crystallographic studies, *J. Phys. Chem. C*, 121(19) (2017) 10594–10608.
- Ovhal S., Butler I.S., Xu S., The potential of zeolites to block the uptake of radioactive strontium-90 in organisms, *Contemporary Chemistry*, 1(1) (2018) 1-13.
- Sadeghi M., Yekta S., Ghaedi H., Babanezhad E., Effective removal of radioactive ^{90}Sr by CuO NPs/Agclinoptilolite zeolite composite adsorbent from water sample: isotherm. kinetic and thermodynamic reactions study, *Int. J. Ind. Chem.*, 7 (2016) 315–331.
- Olatunji M.A., Khandakar M.U., Mahmud H.N.M.E., Amin Y.M., Influence of adsorption parameters on cesium uptake from aqueous solutions- a brief review, *RSC Adv.*, 5 (2015) 71658-71683.
- Fang X.H., Fang F., Lu C.H., Zheng L., Removal of Cs, Sr²⁺ and Co²⁺ ions from the mixture of organics and suspended solids aqueous solutions by zeolites, *Nucl Eng Technol.*, 49(3) (2017) 556-561.
- Handley-Sidhu S., Mullan T.K., Grail Q., Albadameh M., Ohnuki T., Macaskie L.E., Influence of pH, competing ions and salinity on the sorption of strontium and cobalt onto biogenic hydroxyapatite, *Sci. Rep.*, 6 (2016) 1-8.
- Herrfinez-Barrales E., Granados-Correa F., Sorption of radioactive cobalt in natural Mexican clinoptilolite, *J. Radioanal. Nucl. Chem.*, 242(1) (1999) 111-114.
- Myers M.J., Lavender J. P., de Oliveira, J. B., Maseri, A., A simplified method of quantitating organ uptake using a gamma camera, *Br. J. Radiol.*, 54(648) (1981) 1062–1067.
- Munthali M.W., Johan E., Aono H., Matsue N., Cs⁺ and Sr²⁺ adsorption selectivity of zeolites in relation to radioactive decontamination, *J. Asian Ceram. Soc.*, 3(3) (2015) 245-250.
- Yeritsyan H., Sahakyan A., Harutyunyan V., Nikoghosyan S., Hakhverdyan E., Grigoryan N., Hovhannisyan A., Atoyan V., Keheyanyan Y., Rhodes C., Radiation-modified natural zeolites for cleaning liquid nuclear waste (irradiation against radioactivity), *Sci. Rep.*, 3 (2013) 2900.
- Frising T., Leflaive P., Extraframework cation distributions in X and Y faujasite zeolites: a review, *Microporous Mesoporous Mater.*, 114(1–3) (2008) 27–63.
- Çicek E., Cojocar C., Zakrzewska-Trznadel G., Harasimowicz M., Miskiewicz A., Response surface methodology for the modeling of ^{85}Sr adsorption on zeolite 3A and pumice, *Environ. Technol.*, 33(1) (2012) 51–59.
- Çicek E., Cojocar C., Zakrzewska-Trznadel G., Jaworska A., Harasimowicz M., Response surface methodology for cobalt removal from aqua solutions using Isparta pumice and zeolite 4A adsorbents, *Nukleonika* 53(S2) (2008) 121-128.
- Çicek E., Response surface methodology for cobalt removal from aqua solutions using nevsehir and kayseri pumice adsorbents, *Asian J. Chem.*, 21(7) (2009) 5727-5736.
- Khayet M., Cojocar V., Zakrzewska-Trznadel G., Response surface modelling and optimization in pervaporation, *J. Membr. Sci.*, 321 (2008) 272–283.
- Cojocar C., Macoveanu M., Modeling and Optimization of Diesel Oil Spill Removal from Water Surface Using Shredded Strips of Polypropylene as the Sorbent, *Environ. Eng. Manage. J.*, 2(2) (2003) 145-154.
- Le M.H., Behera S.K., Park H.S., Optimization of operational parameters for ethanol production from Korean food waste leachate, *Int J Environ Sci Te*, 7 (2010) 157–164.
- Chauhan B., Gupta R., Application of statistical experimental design for optimization of alkaline protease production from *Bacillus* sp. RGR-14, *Process Biochem.*, 39(12) (2004) 2115–2122.

Effect of Ring Radius and Electric Field on the Relative Refractive Index of a GaAs Quantum Ring

Aysevil Salman Durmuşlar^{1,a,*}

¹ Department of Naval Architecture and Marine Engineering, Faculty of Engineering, Piri Reis University, 34940 Istanbul, Turkey.

*Corresponding author

Research Article

History

Received: 22/11/2021

Accepted: 11/02/2022

Copyright



©2022 Faculty of Science,
Sivas Cumhuriyet University

ABSTRACT

The influence of inner ring radius and in-plane electric field on the relative refractive index of a GaAs-AlGaAs single circular quantum ring is theoretically studied. The energy levels and corresponding wave functions are obtained by solving the Schrödinger equation within effective mass and envelope wave function approximations. The changes in the intraband transition energies are presented in terms of varying ring radius and external electric fields. Relative refractive index changes are calculated through the compact-density matrix approach. The results show that both ring radius and electric field significantly affect the location and also the peak intensities of relative refractive index changes on the incident photon energy.

Keywords: Quantum ring, Refractive index, Electric field.

^a asdurmuslar@pirireis.edu.tr

^{id} <https://orcid.org/0000-0001-6998-5942>

Introduction

Constraining charge carriers in low-dimensional structures and then modifying the electronic and optical properties have reached great attention due to improvements in technological devices. Semiconductor quantum rings (QR) are one of the topological geometries that confine charge carriers within different shapes such as circular, elliptic or oval. The shape of QR together with the geometrical parameters and the applied external fields lead the changes in the potential profile of QR and so the optical properties. The effect of eccentricity on the electronic spectrum of QRs is handled in some studies [1-8]. In addition to deviations from circular curves of QRs, the exposure to electric field [1-5] and magnetic field [6-8] have been impressively used to tailor the electronic properties. Chakraborty and co-workers present the possibility of tuning the electronic spectrum by adjusting the ring radius, ring shape and as well as exposing the QR intense laser fields and external magnetic fields [9]. The influence of ring geometry on the electronic properties of QR is investigated by Vinasco and co-authors [10]. Xie has studied the influence of the ring radius of QR on the optical absorptions within subbands for two-electron [11]. In another study performed by Barticevic et al., the role of ring radius and the magnetic field is investigated for a QR [12]. Radu and co-workers have examined the responses of electronic spectra and absorption properties to the intense laser field for a single QR [13]. The simultaneous effect of laser radiation and electric field to the electronic and optical absorption properties of the GaAs/AlGa_{0.7}As_{0.3} QR has been studied for single QR again by Radu and co-workers [14] and for double QR by Baghramyan et al. [15]. The influence of lateral electric field on the variations of intraband optical absorption changes for a concentric

double QR is handled by Baghramyan et al. [16] and to the possibility of controlling the optoelectronic properties with the applied electric field and as well as light polarization are reported [16]. The effect of electric field on the optical responses in the presence of donor impurity is presented by Restrepo and co-workers [17] and also by Duque and co-workers [18]. The impact of donor impurity together with the hydrostatic pressure on the nonlinear optical properties of GaAs QR is analyzed in the other study of Restrepo and his group [19].

Apart from circular QRs, the optical properties are examined in a triangular QR designed by Nasri and Bettahar [20]. In that study, they conclude that both transition energies between the first two excited states and ground state and optical matrix are significantly influenced by the changes in the side length of the inner triangle [20]. Due to technological applications of low-dimensional quantum systems, theoretical studies are densely performed with low-dimensional systems to support or encourage experimental studies. Here only some of these studies which are carried out on the relative refractive index changes in quantum dots will be referred. The changes in the relative refractive index are investigated for spherical quantum dots in [21-22] and cylindrical quantum dots in [23-25]. In the study with the spherical quantum dot performed by Karabulut and Baskoutas, the influences of impurities, electric field, size, and optical intensity on the change in refractive index as well as absorption coefficient are analyzed [25]. The influence of size variation and donor position on linear, nonlinear and total refractive index changes of a spherical quantum dot is handled by Al [26]. His results indicate the significant changes on these coefficients for donor intersubband transitions [26].

This study was inspired by the studies [13, 14] that investigate the effect of electric field and intense laser field on the absorption coefficients for a single GaAs ring. The novelty of the present study lies in the investigations on the first-order relative refractive index changes with varying electric field and inner ring radius. The theoretical description of the problem is given in Section 2. Obtained results and related discussion are presented in Section 3 and the main conclusion of the study is given in Section 4.

Materials and Methods

We have investigated the influence of varying ring radius and electric field on the intraband transitions, dipole moment matrix elements as well as relative refractive index changes for a single circular GaAs-GaAlAs QR. For the determination of electronic states and related wavefunctions of structure, the Schrödinger equation is solved within the framework of effective mass and envelope wave function approximation. Time-independent Schrödinger equation for the confined electron in a QR in the presence of an x -oriented external electric field has the following form:

$$E \phi(x, y) = \left[-\frac{\hbar^2}{2m^*} \nabla^2 + V(x, y) - eFx \right] \phi(x, y), \quad (1)$$

where \hbar is the Planck's constant, m^* is the effective electron mass, e is the charge of electron and F is the applied static electric field along the negative x direction. Here E stands for the Eigen energies of energy levels and $\phi(x, y)$ denotes the corresponding wave functions of these levels. $V(x, y)$ is the potential term and for a circular single ring and defined as below:

$$V(x, y) = \begin{cases} 0, & \text{if } R_1 \leq \sqrt{x^2 + y^2} \leq R_2, \\ V_0, & \text{if } \sqrt{x^2 + y^2} < R_1, \text{ or } \sqrt{x^2 + y^2} > R_2. \end{cases} \quad (2)$$

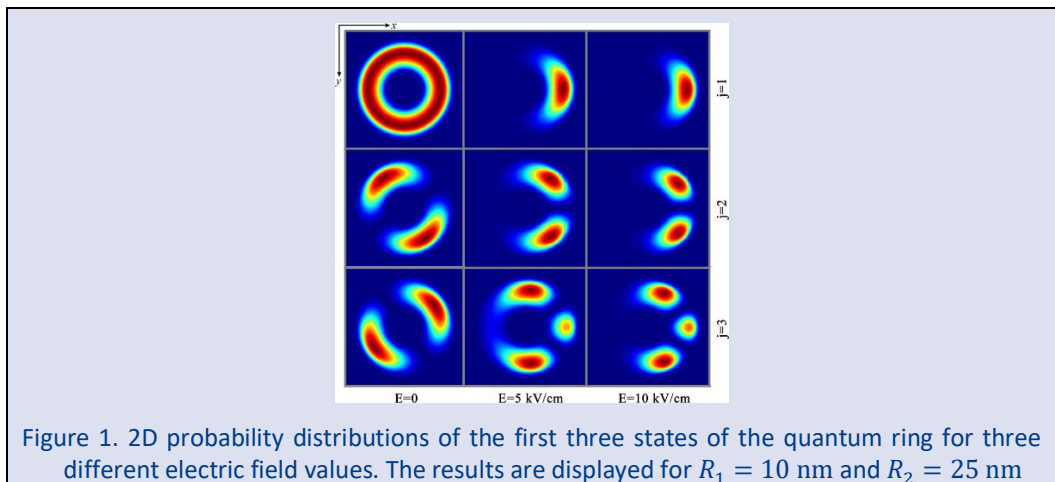


Figure 1. 2D probability distributions of the first three states of the quantum ring for three different electric field values. The results are displayed for $R_1 = 10$ nm and $R_2 = 25$ nm

Figure 1 displays the electron probability densities for the first three states of the circular quantum ring for the inner radius $R_1 = 10$ nm and outer radius $R_2 = 25$ nm. The densities of $j=1, 2$, and 3 electron states are displayed through the rows of Figure 1, respectively. Influences of three in-plane electric field values on the probability densities are shown through the columns of Figure 1.

where R_1 and R_2 are the inner and outer radii of circular ring and V_0 is the maximum value of potential. The solution of Eq. (1) with the potential given in Eq. (2) will lead the energies of levels, E and the corresponding wave functions $\phi(x, y)$ and thereby the electronic spectrum of QR will be obtained. After the determination of the electronic structure of QR, the first order coefficient of relative refractive index changes can be calculated with the help of the density-matrix approach and the analytical expression for it is given as follows [27-29],

$$\frac{\Delta n^{(1)}(\omega)}{n_r} = \frac{\sigma_v |M_{ij}|^2}{2n_r^2 \varepsilon_0} \left[\frac{\Delta E - \hbar\omega}{(\Delta E - \hbar\omega)^2 + (\hbar\Gamma)^2} \right] \quad (3)$$

Here $n_r = \sqrt{\varepsilon_r}$ is the relative refractive index of the system, ε_0 is the permittivity of vacuum, σ_v is the carrier density of the system and Γ is the relaxation rate. ω is the angular frequency of incident photon and ΔE is the energy difference between excited states and lowest-lying state. $M_{ij} = \langle \psi_i(z) | ez | \psi_j(z) \rangle$ stands for the dipole moment matrix element for the transitions between excited states and ground state.

Results and Discussion

This numerical study represents the first order relative refractive index changes of a single circular GaAs QR for varying inner ring radius and electric field application. In the calculations the used parameters are as follows: $m^* = 0.067m_0$ (where m_0 is the free electron mass), $\sigma_v = 3 \times 10^{22} \text{ m}^{-3}$, $n_r = 3.2$, $\varepsilon_r = 12.58$, $\Gamma = 0.14 \text{ ps}^{-1}$ and $V_0 = 228 \text{ meV}$. First, we present the probability densities and energy eigenvalues and then relative refractive index changes for different values of inner ring radius and electric field.

oriented electric field disturbs the densities of states by changing the probabilities of wave functions. Electric field application through the $-x$ direction destroys the axial symmetry of the confining potential. Electrons begin to accumulate along the $+x$ direction and therefore the right side of the well get deepen. Thus, the wave functions are aimed to localize to the right side of the ring as seen in Figure 1.

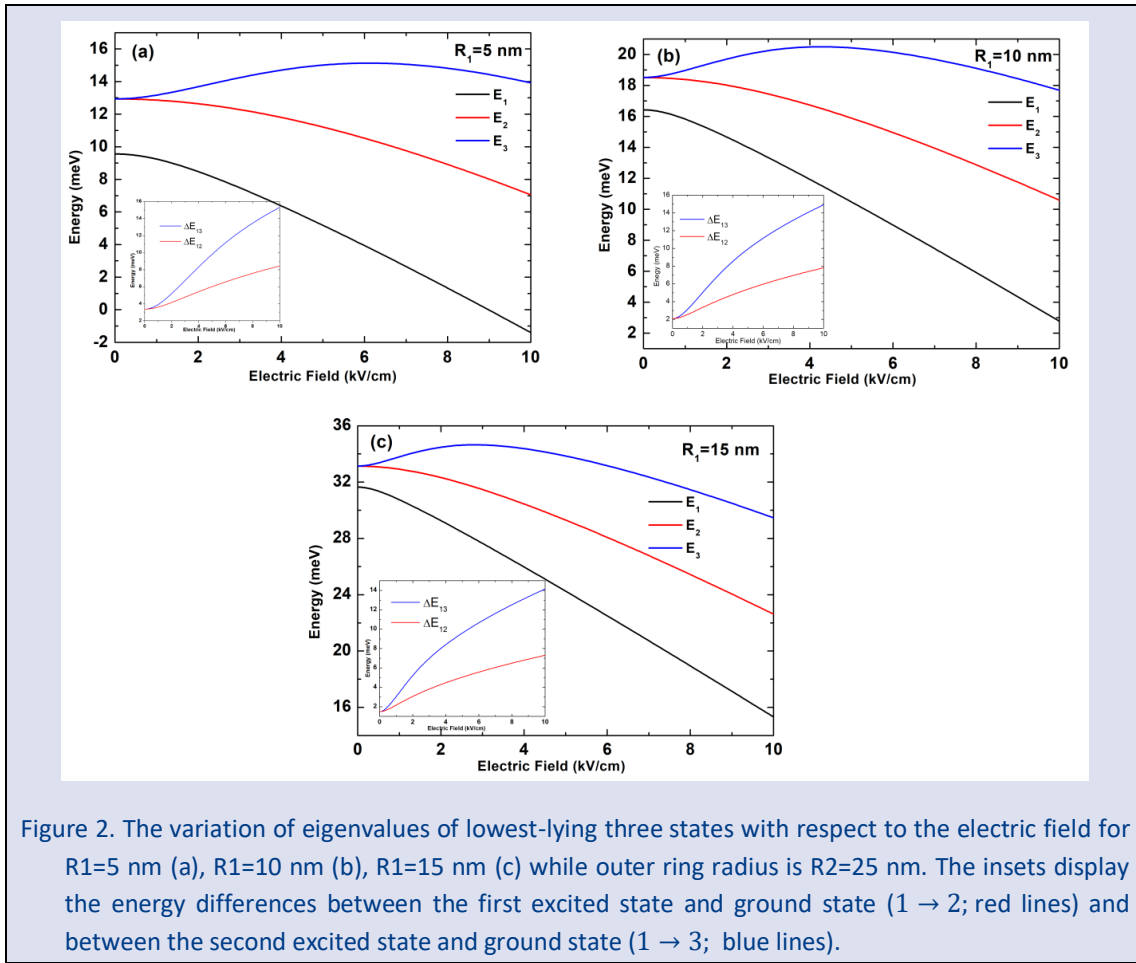


Figure 2. The variation of eigenvalues of lowest-lying three states with respect to the electric field for $R_1=5$ nm (a), $R_1=10$ nm (b), $R_1=15$ nm (c) while outer ring radius is $R_2=25$ nm. The insets display the energy differences between the first excited state and ground state ($1 \rightarrow 2$; red lines) and between the second excited state and ground state ($1 \rightarrow 3$; blue lines).

In figure 2, we display the energies of the first three states as a function of the electric field for three different inner ring radius. The first excited state has double degeneracy in the absence of an external field. The presence of electric field removes that degeneracy by breaking the axial symmetry. The responses to the increase in the electric field have similar behaviors in terms of energy variations and the energy differences between first/second excited states and ground state while inner ring radius is varying. The energies of states go to higher values as a result of widening inner ring in other words narrowing well widths. While inner ring radius is increasing, although the state energies remarkably soars up, the energy differences between excited states and the ground state are slightly scales down. The augmentation in the electric fields lowers the energies of the first three lowest-lying states as a consequence of more confinement.

Breaking the symmetry of QR by applying an in-plane electric field requires taking into consideration of selection rules between states. The allowed transition for the x-polarization occurs between the second excited state and ground state ($1 \rightarrow 3$). For the y-polarization, it is between the first excited state and ground state ($1 \rightarrow 2$) [13, 14].

Figure 3 represents the variations in the relative refractive index coefficients with respect to photon energies for three different inner ring radius with the augmentation of the electric field. The changes in the light polarization direction are indicated in Figure 3 by considering the allowed transitions between excited states and ground state. As mentioned above, Figure 3(a-c) represents the changes in relative refractive index coefficients for intraband transition energies between ($1 \rightarrow 3$) and Figure 3(d-f) represent these changes between ($1 \rightarrow 2$) states. The peak position of these coefficients moves to lower photon energies not only for the x-polarization but also for the y-polarization for increasing inner ring radius at a fixed electric field. This red-shift can be attributed to the reduction in the intraband transition energies while the inner ring is expanding, as mentioned in the explanations of Figure 2. Due to the degeneracy in the energy of first and second excited states in the absence of an electric field, both x-polarized and y-polarized incident light display the same results. The application of x-orientated electric field moves the relative refractive index peak positions to higher energies for both polarization, however the movement is more pronounced for x-polarized light concerning the differences of state energies, ΔE_{13} and ΔE_{12}

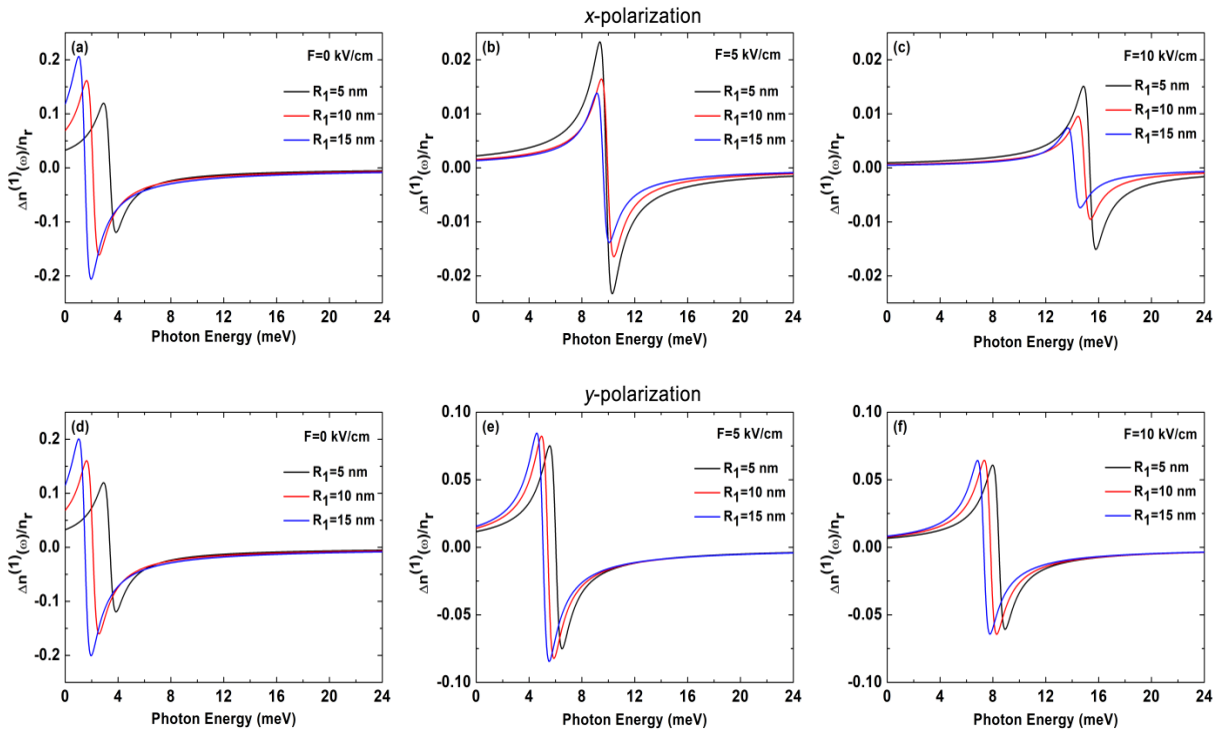


Figure 3. The relative refractive index changes as a function of photon energy with varying inner ring radius for three different electric field values: (a) $F = 0$ kV/cm, (b) $F = 5$ kV/cm, (c) $F = 10$ kV/cm. The figures (a-c) and (d-f) display the results for x-polarization and y-polarization of the incident light, respectively

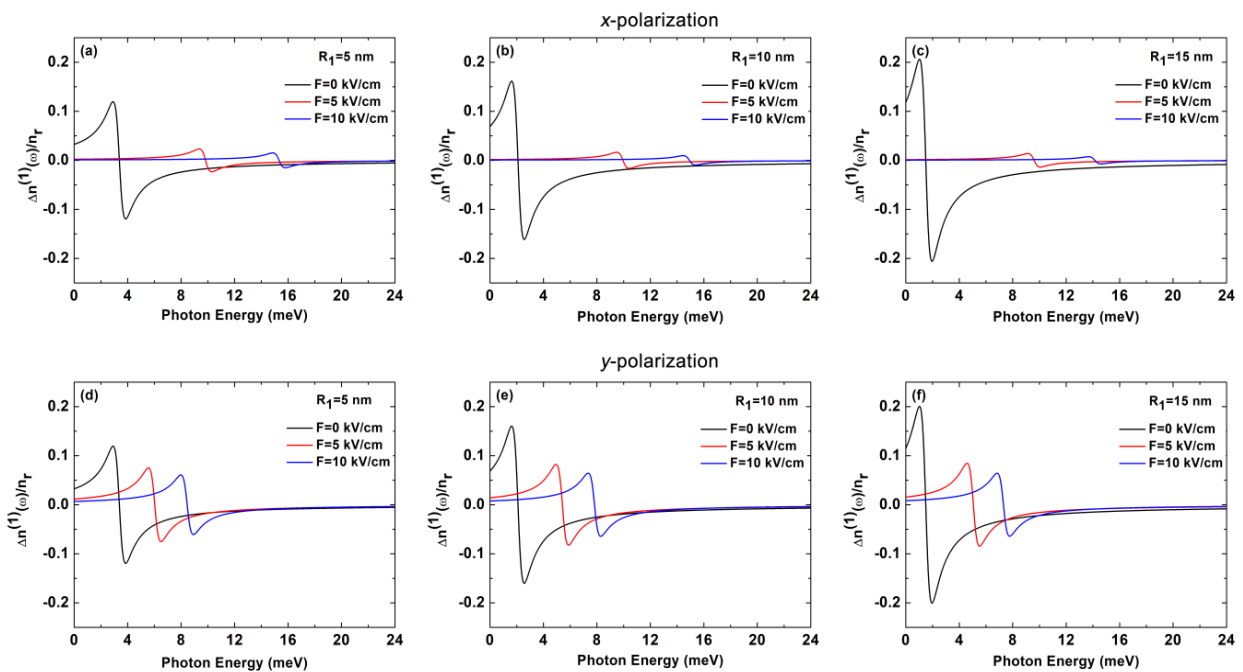


Figure 4. The variations in the relative refractive index coefficients as a function of incident photon energy with three different electric field values. The inner ring radius in (a, d) is $R_1 = 5$ nm, in (b, e) is $R_1 = 10$ nm and in (c, f) $R_1 = 15$ nm. The rows represent the results of x-polarization and y-polarization of the incident light, respectively.

The changes in the relative refractive index coefficients concerning photon energy while the electric field is changing are shown in Figure 4 for three different inner ring radius. The increase in the inner ring radius shifts the relative refractive index peaks to lower energies by increasing the magnitudes of peaks for y-polarized light. For x-polarized light, the increase in the inner ring radius enhances the peak magnitudes when the electric field is absent but slightly diminishes with the augmentation of the electric field. The remarkable reduction in the intensities of relative refractive index changes can be clearly seen for the increasing values of electric field for a fixed ring radius not only for x-polarized light but also y-polarized light. The declines in the peak intensities are consequences of the diminishing overlap between wave functions and as can be noticed here, the subjection of increasing x-oriented electric field has a so strong impact on these peaks for the same light polarization direction.

Conclusion

The energies and corresponding density probabilities of a single circular quantum ring with varying inner ring radius and in-plane static electric field are investigated by solving the Schrödinger equation within the effective mass and envelope band approximation. The obtained electronic spectrum is used to get relative refractive index change coefficients for different inner ring radius as well as for varying electric fields. The increases in the inner ring radius cause the relative refractive index peaks to appear at lower incident photon energies. On the other hand the augmentation in the electric field acts on these peaks by shifting them to blue for both x-polarized and y-polarized light. Both inner ring radius and electric field as well as light polarization lead to significant changes not also in the position of relative refractive index coefficients but also in the intensities of these peaks.

Acknowledgments

The author deeply thank Prof. Dr. Fatih UNGAN for his precious discussions on the paper

Conflicts of interest

The author states that did not have a conflict of interest

References

- [1] Lavenère-Wanderley L. A., Bruno-Alfonso A., Latge A., Electronic states in quantum rings: Electric field and eccentricity effects, *Journal of Physics Condensed Matter*, 14 (2002) 259-270.
- [2] Bruno-Alfonso A., Latgé A., Aharonov-Bohm oscillations in a quantum ring: Eccentricity and electric-field effects, *Physical Review B*, 71 (2005) 125312.
- [3] Niculescu E. C., Stan C., Bejan D., Cartoaje C., Impurity and eccentricity effects on the nonlinear optical rectification in a quantum ring under lateral electric fields, *Journal of Applied Physics*, 122 (2017) 144301.
- [4] Bejan D., Stan C., Niculescu E. C., Optical properties of an elliptic quantum ring: Eccentricity and electric field effects, *Optical Materials*, 78 (2018) 207-219.
- [5] Nasri D., On the eccentricity effects on the intraband optical transitions in two dimensional quantum rings with and without donor impurity, *Physica B: Condensed Matter*, 540 (2018) 51-57.
- [6] Silva J. C., Ferreira R., Chaves A., Farias G. A., Eccentricity effects on the quantum confinement in double quantum rings, *Solid State Communications*, 151 (2011) 1200-1204.
- [7] Vinasco J. A., Radu A., Niculescu E., Mora-Ramos M. E., Feddi E., Tulupenko V., Restrepo R. L., Kasapoglu E., Morales A. L., Duque C. A., Electronic states in GaAs-(Al,Ga)As eccentric quantum rings under nonresonant intense laser and magnetic fields, *Scientific Reports*, 9 (2019) 1427.
- [8] Nasri D., Electronic and optical properties of eccentric quantum ring under parallel magnetic field, *Physica B: Condensed Matter*, 615 (2021) 413077.
- [9] Chakraborty T., Manaselyan A., Barseghyan M., Laroze D., Controllable continuous evolution of electronic states in a single quantum ring, *Physical Review B*, 97 (2018) 041304(R).
- [10] Vinasco J. A., Radu A., Kasapoglu E., Restrepo R. L., Morales A. L., Feddi E., Mora-Ramos M. E., Duque C. A., Effects of Geometry on the Electronic Properties of Semiconductor Elliptical Quantum Rings, *Scientific Reports* 8, (2018) 13299.
- [11] Xie W., Intersubband optical absorptions of a two-electron quantum ring, *Physics Letters A*, 374 (2010) 1188-1191.
- [12] Barticevic Z., Pacheco M., Latge A, Quantum rings under magnetic fields: Electronic and optical properties, *Physical Review B*, 62 (2000) 6963-69660.
- [13] Radu A., Kirakosyan A. A., Laroze D., Baghrmalyan H. M., Barseghyan M. G., Electronic and intraband optical properties of single quantum rings under intense laser field radiation, *Journal of Applied Physics*, 116 (2014) 093101.
- [14] Radu A., Kirakosyan A. A., Laroze D., Barseghyan M. G., The effects of the intense laser and homogeneous electric fields on the electronic and intraband optical properties of a GaAs/Ga_{0.7}Al_{0.3}As quantum ring, *Semiconductor Science and Technology*, 30 (2015) 045006.
- [15] Baghrmalyan H. M., Barseghyan M. G., Kirakosyan A. A., Ojeda J. H., Bragard J., Laroze D., Modeling of anisotropic properties of double quantum rings by the terahertz laser field, *Scientific Reports* 8, (2018) 6145.
- [16] Baghrmalyan H. M., Barseghyan M. G., Laroze D., Kirakosyan A. A., Influence of lateral electric field on intraband optical absorption in concentric double quantum rings, *Physica E*, 77 (2016) 81-89.
- [17] Restrepo R. L., Morales A. L., Martínez-Orozco J. C., Baghrmalyan H. M., Barseghyan M. G., Mora-Ramos M. E., Duque C. A., Impurity-related nonlinear optical properties in delta-doped quantum rings: Electric field effects, *Physica B: Condensed Matter*, 453 (2014) 140-145.
- [18] Duque C. M., Acosta R. E., Morales A. L., Mora-Ramos M. E., Restrepo R. L., Ojeda J. H., Kasapoglu E., Duque C. A., Optical coefficients in a semiconductor quantum ring: Electric field and donor impurity effects, *Optical Materials*, 60 (2016) 148-158.
- [19] Restrepo R. L., Barseghyan M. G., Mora-Ramos M. E., Duque C. A., Effects of hydrostatic pressure on the nonlinear optical properties of a donor impurity in a GaAs quantum ring, *Physica E*, 51 (2013) 48-54.

- [20] Nasri D., Bettahar N., Linear and nonlinear intersubband optical properties in a triangular quantum ring, *Physica B*, 478 (2015) 146-152.
- [21] Çakır B., Yakar Y., Özmen A., Refractive index changes and absorption coefficients in a spherical quantum dot with parabolic potential, *Journal of Luminescence*, 132 (2012) 2659-2664.
- [22] Lu L., Xie W., Hassanabadi H., Linear and nonlinear optical absorption coefficients and refractive index changes in a two-electron quantum dot, *Journal of Applied Physics*, 109 (2011) 063108.
- [23] Vahdani M. R. K., Rezaei G., Intersubband optical absorption coefficients and refractive index changes in a parabolic cylinder quantum dot, *Physics Letters A*, 374 (2010) 637-643.
- [24] Liu C.-H., Xu B.-R., Theoretical study of the optical absorption and refraction index change in a cylindrical quantum dot, *Physics Letters A*, 372 (2008) 888-892.
- [25] Karabulut I., Baskoutas S., Linear and nonlinear optical absorption coefficients and refractive index changes in spherical quantum dots: Effects of impurities, electric field, size, and optical intensity, *Journal of Applied Physics*, 103 (2008) 073512.
- [26] Al E. B., Effect of size modulation and donor position on intersubbands refractive index changes of a donor within a spherical core/shell/shell semiconductor quantum dot, *Cumhuriyet Science Journal*, 42 (3) (2021) 694.
- [27] Dakhlaoui H., Nefzi M., Simultaneous effect of impurities, hydrostatic pressure, and applied potential on the optical absorptions in a GaAs field-effect transistor, *Results in Physics*, 15 (2019) 102618.
- [28] Li K., Guo K., Jiang X., Hu M., Effect of position-dependent effective mass on nonlinear optical properties in a quantum well, *Optik*, 132 (2017) 375.
- [29] Prasad V., Silotia P., Effect of laser radiation on optical properties of disk shaped quantum dot in magnetic fields, *Physics Letters A*, 375 (2011) 3910-3915.

Dynamics of the Dirac Particle in an Anisotropic Rainbow Universe

Evrım Ersin Kangal ^{1,a,*}

¹ Computer Technology and Information Systems, School of Applied Technology and Management of Erdemli, Mersin University, Mersin, Turkey..

*Corresponding author

Research Article

History

Received: 03/01/2022

Accepted: 24/02/2022

Copyright



©2022 Faculty of Science,
Sivas Cumhuriyet University

evrimersin@gmail.com.

<https://orcid.org/0000-0001-5906-3143>

ABSTRACT

An alternative way of understanding physical effects in curved space time is to solve the associated particle equation such as the Dirac equation. It is a first-order relativistic wave equation and defines spin- $\frac{1}{2}$ massive particles like electrons and quarks. In this study, we solved the Dirac equation in an anisotropic rainbow universe. Subsequently, the reduced wave equation is obtained by making use of the asymptotic property of the Whittaker function. In the final stage, we calculate each component of the spin current density and then graphically evaluate their behavior according to the rainbow function. According to our results, the spin current density only depends on the z component of the momentum. In addition, the sign of both spin current densities is not changing with time. Finally, the current density amplitude in the high energy state or high scale parameter ($\epsilon = 0.9$) is rapidly decreasing faster than in $\epsilon = 0.6$ and $\epsilon = 0.3$.

Keywords: Dirac equation, Rainbow function, Spin current density.

Introduction

Generally, a well-known shortcoming of the Klein-Gordon theory is a negative quantum probability that is considered to be physically meaningless[1]. To overcome such a challenge, Dirac proposed a first-order relativistic wave equation that plays an important role in many branches including those in nuclear and high energy physics. It is commonly believed that this idea is the most effective mathematical method to analyze the relativistic quantum mechanical behavior of the spin- $\frac{1}{2}$ particles (electron, proton, and their corresponding antiparticles)[2]. Therefore, one can easily see that there are lots of papers where some solutions of the Dirac equation are illustrated in various spacetimes[3-7].

Investigating the effects of the rainbow functions in different research areas is still a very attractive topic in recent years. The dynamics of the photon equation are discussed in the cosmic string spacetime[8]. Bakke and Mota evaluate the Aharonov-Bohm effect in the context of rainbow gravity[9]. Junior and his co-authors investigate regular black holes in rainbow gravity [10]. Ling derives the kinematics of particles moving in rainbow spacetime[11]. The idea behind it is the Planck scale (or the Planck energy $E_{pl} \approx 10^{19}$ GeV)[12]. It plays a vital role while determining the boundary between the classical and quantum gravity regimes[13-14]. However, the existence of such a scale forces us to consider the Planck energy as an invariant quantity for all observers in momentum space whereas the invariance of light's speed c is valid in Special Relativity (SR). This result points out the existence of a Deformed Special Relativity (DSR)[15-16]. Smolin and Magueijo presented a modified energy and momentum relation as the following formulation[17]:

$$f^2(\epsilon)E^2 - g^2(\epsilon)P^2 = m^2 \quad (1)$$

Here $\epsilon = \frac{E}{E_{pl}}$ is a scale parameter, where E_{pl} represents the Planck energy, and E denotes particle's energy. Furthermore, both $f(\epsilon)$ and $g(\epsilon)$ are called rainbow functions obeying the following relation

$$\lim_{\epsilon \rightarrow 0} f(\epsilon) = \lim_{\epsilon \rightarrow 0} g(\epsilon) = 1 \quad (2)$$

Thus, the DSR formalism can be reduced to the SR framework with the help of the above condition. In literature, there are several proposals[15,17] for the rainbow functions:

$$1^{st} \text{ Scenario: } f(\epsilon) = \sqrt{1 - \epsilon^2} \quad g(\epsilon) = 1 \quad (3)$$

$$2^{st} \text{ Scenario: } f(\epsilon) = 1 \quad g(\epsilon) = 1 + \frac{\epsilon}{2} \quad (4)$$

Following Refs[17,18-20], one can write the rainbow type line-elements by making use of the transformations $dt \rightarrow \frac{dt}{f(\epsilon)}$ and $dx^i \rightarrow \frac{dx^i}{g(\epsilon)}$. From this point of view, the energy-independent tetrads defined in the Minkowski spacetime are transformed mathematically into energy-dependent ones. For this reason, in the rainbow formalism of gravity (RFG), the metric tensor of a given line-element is rewritten in terms of the energy-dependent tetrad[17]s:

$$g_{\mu\nu} = e_{\mu}^{(i)}(\epsilon) \otimes e_{\nu}^{(j)}(\epsilon) \quad (5)$$

where the Greek and Latin indices show the curved($\mu: 0, 1, 2, 3$) and flat spacetime($i: 0, 1, 2, 3$), respectively. Therefore, all components of energy-dependent tetrads are divided into two main groups according to time and space components:

$$e_0^{(0)}(\epsilon) = \frac{1}{f(\epsilon)} \tilde{e}_0^{(0)} \tag{6}$$

$$e_i^{(i)}(\epsilon) = \frac{1}{f(\epsilon)} \tilde{e}_i^{(i)} \tag{7}$$

where the tilde denotes the Minkowski spacetime.

One of the most important scenarios, where the effects of Quantum Gravity (QG) are tested in an anisotropic universe, is associated with the subsequent metric[21]:

$$ds^2 = -dt^2 + t^2(dx^2 + dy^2) + dz^2 \tag{8}$$

Applying the procedure of RFG to the metric gives

$$ds^2 = -\frac{1}{f^2} dt^2 + \frac{t^2}{g^2} (dx^2 + dy^2) + \frac{1}{g^2} dz^2 \tag{9}$$

As a result, we can easily write the covariant and contravariant forms of the metric tensor as given below

$$g_{\mu\nu} = \begin{pmatrix} -\frac{1}{f^2} & 0 & 0 & 0 \\ 0 & \frac{t^2}{g^2} & 0 & 0 \\ 0 & 0 & \frac{t^2}{g^2} & 0 \\ 0 & 0 & 0 & \frac{1}{g^2} \end{pmatrix} \tag{10.a}$$

$$g^{\mu\nu} = \begin{pmatrix} -f^2 & 0 & 0 & 0 \\ 0 & \frac{g^2}{t^2} & 0 & 0 \\ 0 & 0 & \frac{g^2}{t^2} & 0 \\ 0 & 0 & 0 & g^2 \end{pmatrix} \tag{10.b}$$

According to the general transport theory, spin current, one of the most significant physical quantities in quantum physics, is accompanied by a spin continuity equation which includes additional torque terms like the spin operator $\hat{s} = \frac{\hbar}{2} \hat{\sigma}$ which are the Pauli matrices. If we compare $\rho_e = \Psi^\dagger e \Psi$ (charge density) with $\rho_s = \Psi^\dagger \hat{s} \Psi$ (spin density), \hat{s} is thought of as the spin-charge. In the fermion state, the spin current is converted into the Dirac current and it consists of the Gordon decomposition and spin magnetization. Further, both currents are precisely discussed in [22-24]. From the point of the physical interpretation, the Gordon current arises from a moving point charge while the spin magnetization one is created by the spin of the elementary particles.

The layout of the study is as follows: in the second section, we solve the Dirac equation for the anisotropic universe. In the third section, we rewrite the asymptotic wave function. Then, the Dirac current is calculated with

the help of the rainbow function and is graphically illustrated. The last section is devoted to the conclusion part.

The Solution of Dirac Equation

The Dirac equation in curved spacetime is given by [25]

$$[i\gamma^\lambda (\partial_\lambda + \Gamma_\lambda) - m] \Psi(t, \vec{r}) = 0 \tag{11}$$

where m is the particle's mass, $\Psi(t, \vec{r})$ is the particle's wave function, and Γ_λ is the spinor affine connections as given below

$$\Gamma_\lambda = -\frac{1}{8} g_{\mu\alpha} \Gamma_{\mu\lambda}^\alpha [\gamma^\mu, \gamma^\nu] \tag{12}$$

$\Gamma_{\mu\lambda}^\alpha$ denotes the Christoffel symbols and are defined by the following equation

$$\Gamma_{\mu\lambda}^\alpha = \frac{1}{2} g^{\alpha\sigma} (\partial_\nu g_{\lambda\sigma} + \partial_\lambda g_{\nu\sigma} - \partial_\sigma g_{\nu\lambda}) \tag{13}$$

The non-zero components of the Christoffel symbol for the given line element are expressed in terms of time and the rainbow functions as follows

$$\begin{aligned} \Gamma_{11}^0 &= \Gamma_{22}^0 = \frac{tf^2}{g^2} \\ \Gamma_{01}^1 &= \Gamma_{10}^1 = \frac{1}{t} \\ \Gamma_{02}^2 &= \Gamma_{20}^2 = \frac{1}{t} \end{aligned} \tag{14}$$

Substituting Eq.14 into Eq.12 gives

$$\Gamma_0 = \frac{f}{2g} \gamma^{(0)} \gamma^{(2)}, \quad \Gamma_1 = \frac{f}{2g} \gamma^{(0)} \gamma^{(1)} \tag{15}$$

where the brackets () represents the Minkowski spacetime. If Eq.15 is inserted into Eq.11, the Dirac equation becomes

$$[\gamma^{(0)} (\partial_0 + \frac{f}{t}) + \frac{g}{tf} (\gamma^{(1)} \partial_1 + \gamma^{(2)} \partial_2) + \frac{g}{f} \gamma^{(3)} \partial_3 + \frac{im}{f}] \Psi = 0 \tag{16}$$

Subsequently, Eq. 16 is reduced to the following form by setting $\Psi = t^{-1} \psi$ to eliminate the contribution from the spinor connections

$$[\gamma^{(0)} \partial_0 + \frac{g}{tf} (\gamma^{(1)} \partial_1 + \gamma^{(2)} \partial_2) + \frac{g}{f} \gamma^{(3)} \partial_3 + \frac{im}{f}] \psi = 0 \tag{17}$$

By using $\gamma^{(3)} \gamma^{(0)} \gamma^{(3)} \gamma^{(0)} = 1$, Eq. 17 can be easily expressed as a sum of two first-order differential operators after some mathematical steps

$$[L_1 + L_2] \Phi = 0 \tag{18}$$

Where

$$L_1 = t \left(\gamma^{(3)} \partial_0 + \frac{g}{f} \gamma^{(0)} \partial_3 + \frac{im}{f} \right)$$

$$L_2 = \frac{g}{f} (\gamma^{(1)} \partial_1 + \gamma^{(2)} \partial_2) \tag{19}$$

$$\Phi = \gamma^{(3)} \gamma^{(0)} \psi$$

We chose the following representation of the Dirac matrices[21]:

$$\gamma^{(0)} = \begin{pmatrix} -i\sigma^1 & 0 \\ 0 & i\sigma^1 \end{pmatrix}, \quad \gamma^{(1)} = \begin{pmatrix} 0 & i \\ i & 0 \end{pmatrix} \tag{20.a}$$

$$\gamma^{(2)} = \begin{pmatrix} \sigma^2 & 0 \\ 0 & -\sigma^2 \end{pmatrix}, \quad \gamma^{(3)} = \begin{pmatrix} \sigma^3 & 0 \\ 0 & -\sigma^3 \end{pmatrix} \tag{20.b}$$

With

$$\sigma^1 = \begin{pmatrix} 0 & 1 \\ 1 & 0 \end{pmatrix}, \quad \sigma^2 = \begin{pmatrix} 0 & -i \\ i & 0 \end{pmatrix} \tag{21.a}$$

$$\sigma^3 = \begin{pmatrix} 1 & 0 \\ 0 & -1 \end{pmatrix} \tag{21.b}$$

By using a separation constant λ , Eq.18 can be written as

$$L_1 \Phi = -\lambda \Phi \tag{22}$$

$$L_2 \Phi = \lambda \Phi \tag{23}$$

Since the particle moves freely in x, y, and z coordinates, the spinor Φ is given by

$$\Phi = e^{i(k_1x+k_2y+k_3z)} \chi(t) \tag{24}$$

where

$$\chi(t) = \begin{pmatrix} \chi_1 \\ \chi_2 \end{pmatrix} \tag{25}$$

If we insert Eq.25 and Eq.24 into Eq.23 and apply some mathematical steps, we get the following relation between components of the bispinor

$$\chi_2 = \frac{k_1 \sigma^2}{ik_2 + \frac{f}{g} \lambda} \chi_1 \tag{24}$$

where $\lambda = \mp i \frac{g}{f} \sqrt{k_1^2 + k_2^2}$. Then, if the same procedure is applied for Eq. 22, we find two coupled differential equations as below

$$\frac{\partial \Phi_2}{\partial t} + \frac{\lambda}{t} \Phi_2 - \left(\frac{gk_3}{f} + \frac{m}{f} \right) \Phi_1 = 0 \tag{27}$$

$$\frac{\partial \Phi_1}{\partial t} - \frac{\lambda}{t} \Phi_1 + \left(\frac{gk_3}{f} + \frac{m}{f} \right) \Phi_2 = 0 \tag{28}$$

where the bispinor χ_1 is chosen by the following form

$$\chi_1 = \begin{pmatrix} \Phi_1 \\ \Phi_2 \end{pmatrix} \tag{29}$$

If we perform some algebra between these coupled equations, we get the following second-order differential equation:

$$\left[\frac{\partial^2}{\partial t^2} + \frac{\lambda - \lambda^2}{t^2} - \left\{ \left(\frac{m}{2} \right)^2 - \left(\frac{gk_3}{f} \right)^2 \right\} \right] \Phi_1 = 0 \tag{30}$$

Defining a new variable $t = \alpha u$ takes Eq.30 to the form of the well-known Whittaker Equation and thus, the corresponding solutions are written as [26]

$$\Phi_1 = N_1 M_{\kappa, \mu}(t/\alpha) + N_2 W_{\kappa, \mu}(t/\alpha) \tag{31}$$

which $M_{\kappa, \mu}$ and $W_{\kappa, \mu}$ are called as Whittaker functions, $\kappa = 0$, $\mu = \mp \left(\lambda - \frac{1}{2} \right)$ and $\alpha = \frac{f}{2gk_3} \left(1 - \left(\frac{m}{gk_3} \right)^2 \right)^{-1}$. If we analyze the asymptotic behavior of Whittaker functions as $t \rightarrow \infty$ [26], N_1 must be zero since $M_{\kappa, \mu}$ leads to the divergence of Φ_1 in that limit. Therefore, Eq.31 is reduced to the following form

$$\Phi_1 = W_{0, \mu}(t/\alpha) \tag{32.a}$$

$$\Phi_2 = \frac{f}{m - gk_3} \left(\partial_t + \frac{\lambda}{t} \right) W_{0, \mu}(t/\alpha) \tag{32.b}$$

With the help of the differential definition of the Whittaker function[26], the explicit form of Eq.32 can be written as

$$\Phi_1 = W_{0, \mu}(t/\alpha) \tag{33.a}$$

$$\Phi_2 = \frac{f}{m - gk_3} \left[\left(\frac{1}{2\alpha} - \frac{\lambda}{t} \right) W_{0, \mu}(t/\alpha) - \frac{1}{t} W_{1, \mu}(t/\alpha) \right] \tag{33.b}$$

Similarly, if we use the asymptotic property of the Whittaker function[26] for Eq. 33, we get

$$\Phi_1 = e^{-\frac{t}{2\alpha}} \tag{34.a}$$

$$\Phi_2 = \beta e^{-\frac{t}{2\alpha}} \tag{34.b}$$

where

$$\beta = \sqrt{\frac{k_3 + \frac{m}{g}}{k_3 - \frac{m}{g}}} \tag{35}$$

Thus, the total associated Dirac wave function is in the following form:

$$\Psi(t, \vec{r}) = N \begin{pmatrix} 1 \\ \beta \\ -\gamma\beta \\ \gamma \end{pmatrix} \frac{e^{i(\vec{k}\cdot\vec{r} - \frac{t}{2\alpha})}}{t} \tag{36}$$

where $\gamma = \frac{igk_1}{igk_2 + f\lambda}$ and N is a normalization coefficient as follows

$$N = i \sqrt{\frac{g^3}{\alpha(1+\beta^2)(1+|\gamma|^2)}} \quad (37)$$

Spin Current Density

From the quantum mechanical perspective, the spin current density associated with the flow of its probability is known as the Dirac current and is given by [27,28]

$$J_D^\mu = J_G^\mu + J_M^\mu \quad (38)$$

With

$$J_G^\mu = ie[\bar{\Psi}\partial^\mu\Psi - \Psi\partial^\mu\bar{\Psi}] \quad (39)$$

$$J_M^\mu = ie\partial_\nu[\bar{\Psi}\gamma^\mu\gamma^\nu\Psi - \bar{\Psi}\gamma^\nu\gamma^\mu\Psi] \quad (40)$$

where $\bar{\Psi} = \Psi^\dagger\gamma^{(0)}$, G, and M denote the Gordon and spin magnetization current. If we calculate the spin current for the line element given in Eq.9, we obtain

$$J_D^\mu = e\left(\frac{g}{f}\right)^2 e^{-\frac{g}{f}k_3 t} k_{sum} \quad (41)$$

where $k_{sum} = k_1 + k_2 + k_3 > 0$ and also k_3 must be positive because this enables us to avoid divergence of spin current in high time. If making a plot of Eq.41 in terms of charge value ($e = 1$ and $e = -1$) by considering two rainbow scenarios, we get the following figure:

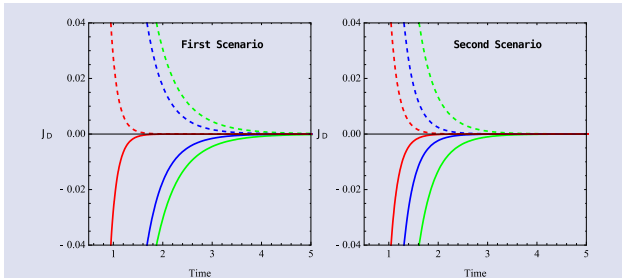


Figure 1. In the both figures, dashed line shows $e=1$ (positron) state while line indicates $e=-1$ (electron) one at $k_3=0.5$ and $k_{sum}=1$. Furthermore, red(high scale), green(medium one), and blue(low one) color of both dashed and line represent $\epsilon = 0.9$, $\epsilon = 0.6$ and $\epsilon = 0.3$ and respectively

It can be seen that the current density defined for both positron and electron decreases over time. However, the second scenario's slope is much bigger than the first one since Eq.40 is linearly dependent on g while it is inversely proportional to f . Also, any particle creation is not observed in either of the scenarios since they do not have any critical turning point whose sign-magnitudes lead to change through the time axis in both current densities.

Conclusion

In this work, we propose a solution to the Dirac equation in the anisotropic rainbow universe. By rewriting the Dirac wave function considering the asymptotic property of the Whittaker function, we calculate the spin current density using the asymptotic limit. According to our results, no particle creation event occurred in any of the rainbow scenarios. To understand their effects on particle creation, we, therefore, need to discuss the different rainbow scenarios listed in the literature.

Acknowledgment

I would like to thank the anonymous reviewer for giving such constructive comments which substantially helped improving the quality of the paper.

Conflicts of interest

The authors declares no conflict of interest.

References

- [1] Nyambuya G. G., General Spin Dirac Equation (II), *Journal of Modern Physics*, 4 (2013) 1050-1058.
- [2] Tokmehdashi H., Rajabi A.A., Hamzavi M., Dirac Equation with Mixed Scalar–Vector–Pseudoscalar Linear Potential under Relativistic Symmetries, *Zeitschrift für Naturforschung A*, 70 (2015) 713-720.
- [3] Rubinow S. I., Joseph B. K., Asymptotic Solution of the Dirac Equation, *Phys. Rev.*, 87 (1963) 2789-2796.
- [4] Thaller B., The Dirac Equation, *Texts and Monographs in Physics*. 1st ed. Berlin, (1992).
- [5] Hassanabadi H., Zare S., Montigny, M., Relativistic spin-zero bosons in a Som–Raychaudhuri space–time, *Gen. Relat. Grav.*, 50 (2018) 104-129.
- [6] Mozaffari F.S., Hassanabadi H., Sobhani H., Chung J., Investigation of the Dirac Equation by Using the Conformable Fractional Derivative, *Korean Phys. Soc.*, 72 (2018) 987-990.
- [7] Sargolzaeipor S., Hassanabadi H., Chung W.S., Superstatistics of the Klein–Gordon equation in deformed formalism for modified Dirac delta distribution, *Mod. Phys. Lett. A*, 33 (2018) 1850060-1850071.
- [8] Sogut K., Salti M., Aydogdu O., Quantum dynamics of the photon in rainbow gravity, *Annals of Physics*, 431 (2021) 168556-168566.
- [9] Bakke K., Mota H., Aharonov–Bohm effect for bound states in the cosmic string spacetime in the context of rainbow gravity, *General Relativity, and Gravitation*, 52 (2020) 52-67.
- [10] Junior E.L.B., Rodrigues M.E., Regular black holes in Rainbow Gravity, *Nuclear Physics B*, 961 (2020) 15244-15258.
- [11] Ling Y., Song H., Hongbao Z., The Kinematics of Particles Moving in Rainbow Spacetime, *Modern Physics Letters A*, 22 (2007) 2931–2938.
- [12] Lobo I.P., Christian P., Reaching the Planck scale with muon lifetime measurements, *Phys. Rev. D*, 103, (2021) 106025-106033.
- [13] Giovanni A.C., Testable scenario for relativity with minimum length, *Physics Letter B*, 510 (2001) 255-263.

- [14] Giovanni A.C., Relativity in spacetimes with short-distance structure governed by an observer-independent (Planckian) length scale, *International Journal of Modern Physics D*, 11 (2002) 35-59.
- [15] Leiva C., Saavedra J., Villanueva J., Geodesic structure of the schwarzschild black hole in rainbow gravity, *Modern Physics Letters A*, 24(2009) 1443-1451.
- [16] Giovanni A.C., Phenomenology of doubly special relativity, *International Journal of Modern Physics A*, 20 (2005) 6007-6037.
- [17] Magueijo J., Smolin L., Generalized Lorentz invariance with an invariant energy scale, *Physical Review D*, 67 (2003) 044017-044029.
- [18] Kimberly D., Magueijo J., Medeiros, J., Nonlinear relativity in position space, *Physical Review D*, 70 (2004) 084007-084014.
- [19] Magueijo J., Smolin L., Gravity's rainbow, *Class. Quant. Grav.*, 21(2004) 1725-1736.
- [20] Feng Z.W., Yan S.Z., Thermodynamic phase transition of a black hole in rainbow gravity, *Phys. Lett. B*, 772(2017) 737-742.
- [21] Villalba V.M., Greiner W., Creation of scalar and Dirac particles in the presence of a time varying electric field in an anisotropic Bianchi type I universe, *Physical Review D*, 65(2001) 025007- 025013.
- [22] Pauli W., *Handbuch der Physik*, 24 (1933).
- [23] Sakurai J.J., *Advanced Quantum Mechanics*. 1nd ed. USA, (1967).
- [24] Gurtler R., Hestenes D., Observables, operators, and complex numbers in the Dirac theory, *J. Math. Phys.*, 16 (1974) 556-572.
- [25] Dirac P. A. M., The quantum theory of the electron, *Proceedings of the Royal Society of London A*, 117 (1928) 610-626.
- [26] Abramowitz M., Stegun I.A., *Handbook of Mathematical Functions*, (1964).
- [27] Tiwari S.,C., Gordon decomposition of Dirac current: a new interpretation, arXiv:1206.3643, 2017.
- [28] W. Gordon, Über den Stoß zweier Punktladungen nach der Wellenmechanik, *Z.Phys.*, 48(1928) 180-191.

The Investigation of Photovoltaic and Electrical Properties of Bi Doped CTS/Si Hetero-Junction Structure for the Solar Cell Application

Serap Yiğit Gezgin^{2,a}, Amina Houimi^{1,b}, Bedrettin Mercimek^{3,c}, Hamdi Şükür Kiliç^{2,4,5,d,*}

¹Department of Nano-technology and developed materials, Faculty of Science, University of Selçuk, 42031, Konya, Türkiye.

²Department of Physics, Faculty of Science, University of Selçuk, 42031, Konya, Türkiye.

³Department of Chemistry Education, Faculty of Ahmet Keleşoğlu Education, Necmettin Erbakan University, 42090, Konya, Türkiye.

⁴Directorate of High Technology Research and Application Center, University of Selçuk, 42031, Konya, Türkiye.

⁵Directorate of Laser Induced Proton Therapy Application and Research Center, University of Selçuk, 42031, Konya, Türkiye.

*Corresponding author

Research Article

History

Received: 05/09/2021

Accepted: 05/03/2022

Copyright



©2022 Faculty of Science,
Sivas Cumhuriyet University

ABSTRACT

In this study, we have produced Cu-Sn-S (CTS) and Bi doped CTS powder composite structures by mixing CuS and SnS₂ powders and adding %3 Bi into CuS-SnS₂ (1:1) powder mixture. These raw powders were mixed and milled by a ball milling device and then CTS and Bi doped CTS target pellets have been produced by cold pressing using a mold prepared in special dimensions. The morphology and crystal structure of target pellets have analysed by SEM and XRD techniques. The target pellets contain different crystalline phases such as: Cu₂SnS₃, Cu₂Sn₃S₇, Cu₄Sn₇S₁₆ and SnS. It has been experienced that Bi doped CTS target pellet has better morphology compared to CTS target pellet. Using PLD technique, the target pellets have been ablated by laser beam to deposited thin film on soda lime glass substrates. According to AFM analysis, the particle size that forms Bi doped CTS thin film is larger than that of CTS thin film. Bi doped CTS thin film has poor crystal structure, while the pure CTS thin film were amorphous. The band gap of Bi doped CTS thin film is slightly lower than that of CTS thin film. While the produced Ag/CTS/Si/Al hetero-junction has not shown diode feature, Ag/Bi dop CTS/Si/Al hetero-junction has exhibited photovoltaic behaviour. The ideality factor, the barrier height, serial resistivity of Ag/Bi dop CTS/Si/Al hetero-junction have been calculated by the conventional $J - V$, Cheung-Cheung and Norde methods in the darkness and under the illumination (AM 1.5 solar radiation in 80 mW/cm²). The photovoltaic parameters of the hetero-junction have been determined and interpreted in detail in this article.

Keywords: Target pellet, Doped, Bi doped CTS, Thin film, Ball milling, PLD.

^a serap.gezgin@selcuk.edu.tr

^b <https://orcid.org/0000-0003-3046-6138>

^c bedrettinmercimek@gmail.com

^d <https://orcid.org/0000-0002-3407-6906>

^e aminahouimi@gmail.com

^f <https://orcid.org/0000-0002-2621-2250>

^g hamdisukurkili@selcuk.edu.tr

^h <https://orcid.org/0000-0002-7546-4243>

Introduction

In recent years, many studies have been actualised on Cu-Sn-S (CTS) system consisting of ternary components such Cu₂SnS₃, Cu₄SnS₄, Cu₃SnS₄, Cu₂Sn₃S₇, Cu₄Sn₇S₁₆ [1-4] for thin film solar cells. Cu₂SnS₃, which has the most stable structure among these ternary components, is a p-type semiconductor in high absorption coefficient, 0.9-1.35 eV direct band gap and it also consists of non-toxic and low cost elements. It is foreseen that use of CZTS (Cu₂ZnSnS₄) as an absorber layer will be replaced in thin film solar cell. In order to realise this, advanced studies have been actualised on the optical, crystal and morphological properties of Cu₂SnS₃ material. At this point, a significant increase has been succeed in the efficiency of solar cells by doping Ge (6%) and Na (4.6%) atoms into Cu₂SnS₃ [5]. Among the prospective doping elements, Bismuth (Bi) is a V group element that offers an acceptor dopant property to p-type semiconductor material. Bi element has been used as a dopant for p-type materials such as CIS (CuInS₂), CIGS (CuInGaS₂) and CZTS resulting in an increase in particle size of materials, passivation of the donor defects, improvement in their crystal structure, and an increase in the number of charge carriers [6-8]. Furthermore, these parameters have been improved the open circuit voltage

(V_{oc}), filling factor (FF) and power conversion efficiency (η) of produced solar cells [9]. With this point of view, Antimony (Sb) element, which shares the same group element with Bi atom, has developed the crystal structure of Cu₂SnS₃ [10] showing that Bi doping element can increase the efficiency of Cu₂SnS₃ based solar cell to be produced.

The deposition techniques such as electron beam evaporation, sputtering and pulse laser deposition (PLD) techniques have been used to produce Cu₂SnS₃ thin film [5]. PLD is a simple system consisting of vacuum chamber and laser system. PLD system is a very power full technique serving very prominent advantageous for stoichiometric transfer and homogeneous thin film growth. By changing PLD parameters such as laser fluency, background gas pressure, laser wavelength and substrate temperature, we can adjust the optical, crystalline, morphological and electrical properties of the growth thin film [11-13].

In this study, in order to produce Bi doped CTS material, we have added Bi powder into CTS powder mixture, mixed it by a ball milling technique and then we have formed target pellets of pure CTS and Bi doped CTS

components. Bi doped CTS target pellet has been ablated by a laser beam and its thin film has been deposited on n-Si wafer and soda lime glass (SLG) substrate using PLD technique. We have performed production and characteristic analyses of CTS and Bi doped CTS target pellets and their thin films. Al and Ag contacts have been coated on the rear side of Si wafer and Bi doped CTS thin film in produced Si/Bi doped CTS hetero-junction, respectively. $J - V$ graphs of Ag/Bi doped CTS/Si/Al hetero-junctions were determined at dark and under illumination conditions and their electrical and photovoltaic properties have also been investigated.

Experimental

Produce of Cts, Bi Doped Cts Target Pellets and Ag/Bi Doped Cts (And Non Doped Cts)/Si/Al Hetero-Junctions

CTS and Bi doped CTS powder components have been formed by $\text{Cu}_x\text{S-SnS}_2$ powder mixture and adding %3 Bi into $\text{Cu}_x\text{S-SnS}_2$ (1:1) powder mixture, respectively (Fig. 1a). The raw powders have been mixed and milled for 9 hour by a ball milling device shown in Fig 1b. CTS and Bi doped CTS powder mixture have been annealed at 600 °C for 1 hour in a quartz tube furnace under vacuum. The target

pellets (Fig 1e) have been produced by cold pressing the resulted powders (Fig 1d) using a special mould (Fig 1c). The diameter and thickness of the target pellet are 12 mm and 2mm, respectively. The target pellets have been annealed at 700°C for 6 hours under argon ambient gas environment.

Before starting the thin film production process, SLG and silicon wafer substrate were cleaned. After cleaning the SLGs with foamy soap, they were soaked in acetone and isopropyl alcohol for 15 minutes *via* ultrasonic bath, respectively. Si wafer was first cleaned with foamy soap and then kept in HF: distilled water (1:24) solution mixture for 2 minutes to remove the oxide layer. Then, Si wafer was soaked in distilled water for 5 minutes. SLG and Si wafers were dried with nitrogen gas jet just before the deposition process started. n-Si wafer used to form hetero-junction, has 10 $\Omega\cdot\text{cm}$ resistance, 500 μm thickness and (100) crystalline orientation.

In order to produce thin film with PLD technique, the target-substrate distance was adjusted to 45mm. The pressure of vacuum chamber was reduced down to 3×10^{-6} mbar. Pure CTS and Bi doped CTS target pellets were ablated by laser beam using 1.6 J/cm^2 laser fluency and 1064 nm wavelength for 90 minutes.

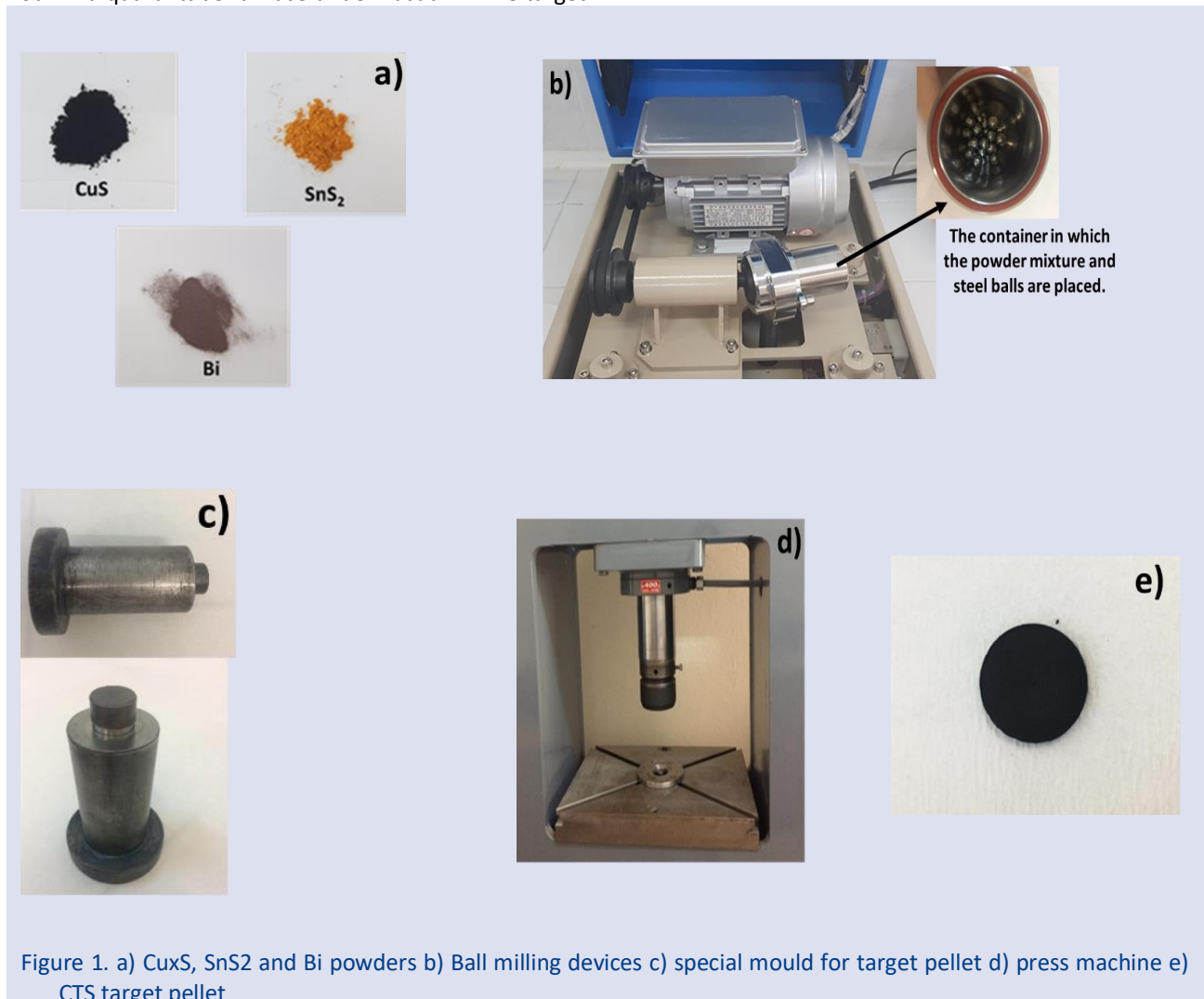


Figure 1. a) Cu_xS , SnS_2 and Bi powders b) Ball milling devices c) special mould for target pellet d) press machine e) CTS target pellet

The thin films were deposited on SLG and the front face of n-Si wafer at room temperature *via* the plasma in Fig 2a. Al metal contacts were deposited on rear face of n-Si wafer using Physical Vapour Deposition (PVD) and then, CTS and Bi doped thin films were placed next to 50 mg of sulphur powder in a quartz tube and annealed at 400°C temperature under vacuum. Ag finger front contact was deposited on Bi doped CTS (and CTS) thin films by PVD technique, forming Ag/Bi doped CTS (and non doped CTS)/Si/Al heterojunctions. The thickness of back (Al) and front (Ag) contacts was measured to be 150 nm. The active area and size of the heterojunction diodes, which are 0.2 cm² and 1 cm², respectively.

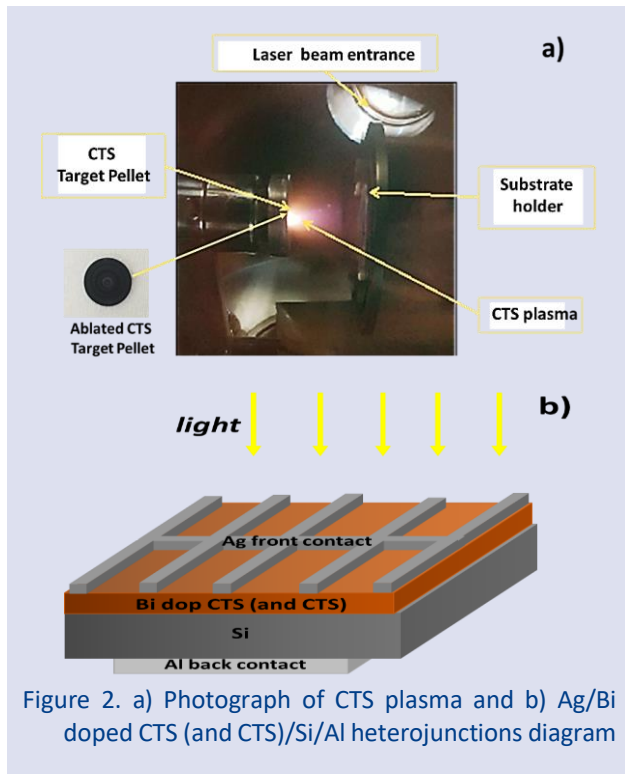


Figure 2. a) Photograph of CTS plasma and b) Ag/Bi doped CTS (and CTS)/Si/Al heterojunctions diagram

Material Characterization

The crystal structure and morphology of CTS and Bi doped CTS target pellets have been determined by XRD (X-Ray Diffraction) and SEM (Scanning Electron Microscopy) analyses, while the crystal, optical and morphological properties of their thin films structures have been determined by XRD, UV-vis spectra and AFM (Atomic Force Microscopy), respectively. $J - V$ characteristics of pure and Bi doped CTS/Si hetero-junctions were obtained in the darkness and the illumination conditions. The ideality factor (n), barrier height (Φ_B) and series resistance (R_s) have been calculated by conventional $J - V$, Cheung-Cheung, Norde methods and V_{oc} , J_{sc} , FF and η photovoltaic (PV) parameters have been obtained.

Discussion

XRD Analysis of CTS and Bi Doped CTS Target Pellets

Fig 3a and 3b show XRD Spectra of CTS and Bi doped CTS target pellets. Both target pellets contain different

ternary phases of Cu-Sn-S sulphides, such as; Cu_2SnS_3 (JCPDS 00-027-0198), Cu_3SnS_4 (JCPDS 00-036-0218), $Cu_2Sn_3S_7$ (JCPDS 00-039-0970) and $Cu_4Sn_7S_{16}$ (JCPDS 01-089-4713), in addition one binary phase SnS (JCPDS 00-039-0354) phases [1-3, 5, 14-17]. These phases indicate that the target pellets have been found as Sn rich [4, 13, 16, 18, 19]. At temperatures above 400°C, the formation of SnS phase is probable [20] leading to an obvious SnS peak at the XRD diagram at both pure and doped CTS pellet targets. Also, it is likely for SnS phase to appear at Sn rich precursors [16, 21, 22]. However, the crystal structure of CTS target pellet has been weakened by the addition of the Bi atom [23-26]. We have also noticed a decrease in the density of peaks referring to SnS phase. Addition of Bi atom into CTS as a dopant can cause undesirable defects in CTS and it may cause deterioration of the crystal structure. Furthermore, Bi atoms (117 pm) are more likely to occupy Cu (91 pm), Sn (83 pm) and S (51 pm) vacancies. Since the ionic radius of Bi atoms is higher than that of other atoms, it can lead to surface strain, which adversely affects the crystal structure. Therefore, when Bi atoms are doped into CTS target pellet, the crystal structure of CTS target pellet can be weakened.

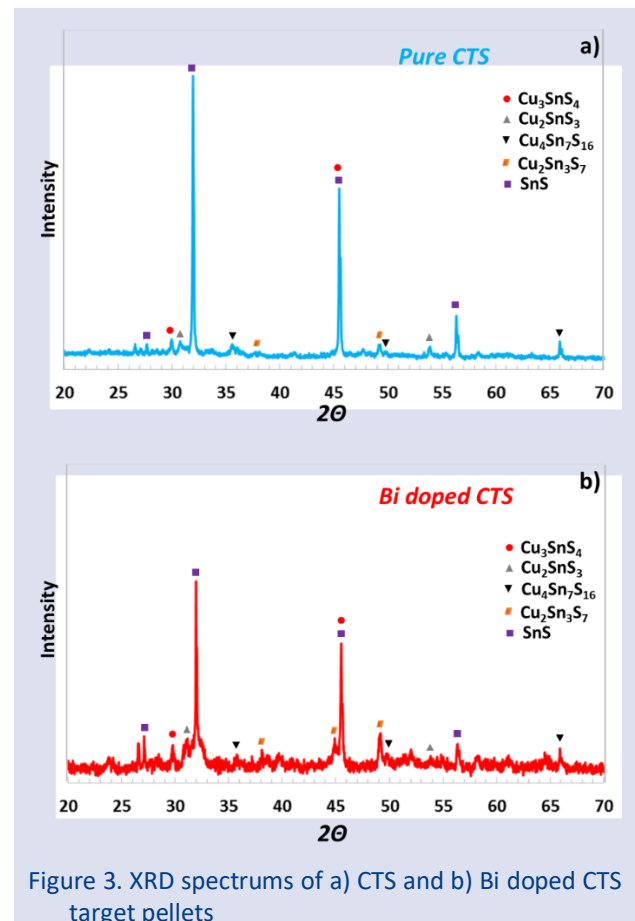


Figure 3. XRD spectrums of a) CTS and b) Bi doped CTS target pellets

The crystalline size of CTS target pellets have been obtained using Scherrer equation (eq.1):

$$D = 0.94\lambda/\beta\cos\theta \quad (1)$$

Where D is the size of crystalline, λ is wavelength of X-Ray, β is full-width at half-maximum of diffraction peak and θ is Bragg diffraction angle. The main crystalline size of CTS and Bi doped CTS target pellets, which were calculated to be 76.24 nm and 59.08 nm using Scherrer equation, respectively. Due to the possibility of surface strain, the crystalline size of the Bi-doped CTS target pellet is smaller than the crystalline size of the CTS target pellet.

Morphologic Analyses of CTS and Bi Doped CTS Target Pellets

Bi doped CTS target pellet consists of larger particles compared to CTS target pellets, according to SEM images given in Fig. 4a and 4b. The reason behind this increase can be explained by the possibility of Bi (117 pm) atom occupying Sn (83 pm) and S (51 pm) vacancies and can cause an enlargement in the particle size. Furthermore, Bi doped CTS target pellet indicates more homogeneous and uniform particle distribution compared to CTS target pellet through Bi doping. Thus, an ideal laser ablation can be achieved using Bi doped CTS target pellet with its the smoother morphological structure.

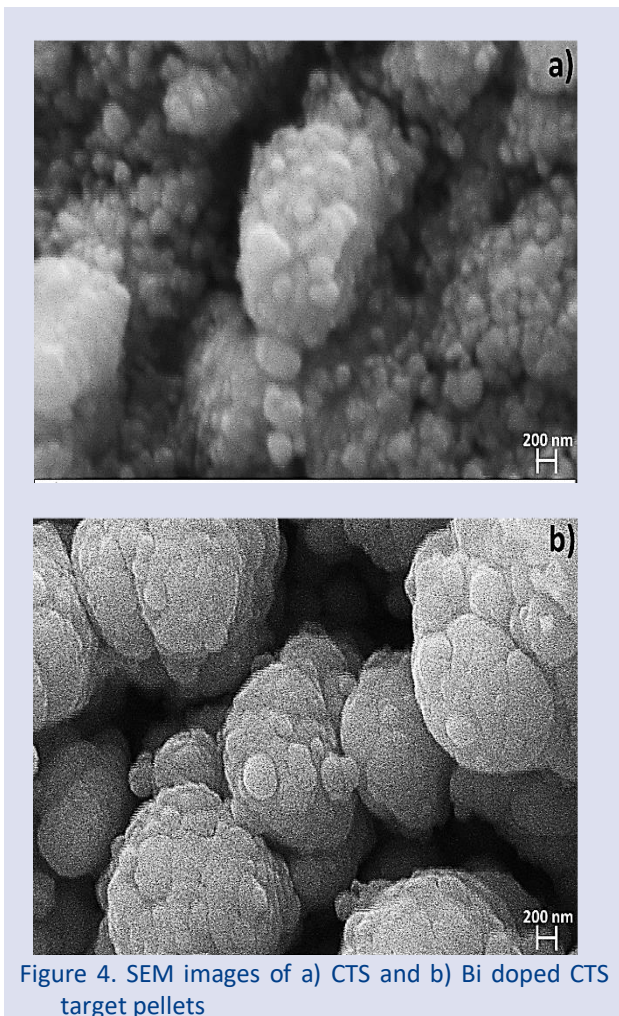


Figure 4. SEM images of a) CTS and b) Bi doped CTS target pellets

XRD Analysis of CTS and Bi Doped CTS Thin Films

XRD spectra of CTS and Bi doped CTS thin films are shown in Fig. 5. Bi doped CTS thin film has a very poor crystalline structure while CTS thin film is amorphous.

Similar to the target pellet, a peak with a very low intensity was formed at $2\theta = 32^\circ$ indicating SnS phase [27] in XRD pattern of Bi doped CTS thin film. The cause of the amorphous structure of pure CTS thin film can be based to the fact that the CTS target pellet is not uniform and inhomogeneous compared to Bi doped CTS target pellet, and therefore, an ideal laser ablation process cannot be achieved. Annealing of Bi doped CTS thin film at low sulfurization temperature can cause a poor crystalline structure of thin film. In addition, Bi doped CTS thin film can be exposed to the wetting problem as it grown on Si wafer surface at higher sulfurization temperature and it can't completely cover the surface of Si wafer [28, 29]. Therefore, high annealing temperature is not preferred.

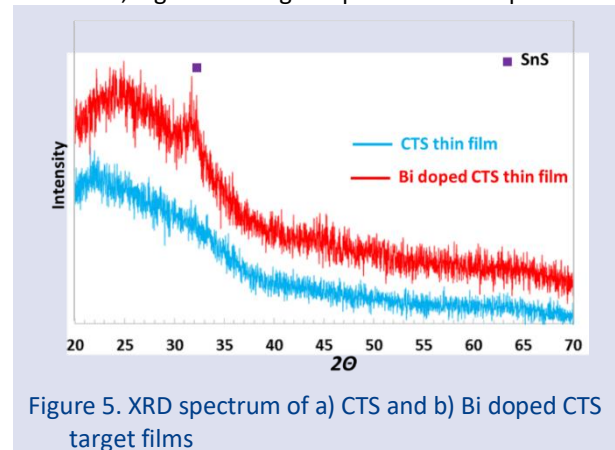


Figure 5. XRD spectrum of a) CTS and b) Bi doped CTS target films

Morphologic Analyses of CTS and Bi Doped CTS Thin Films

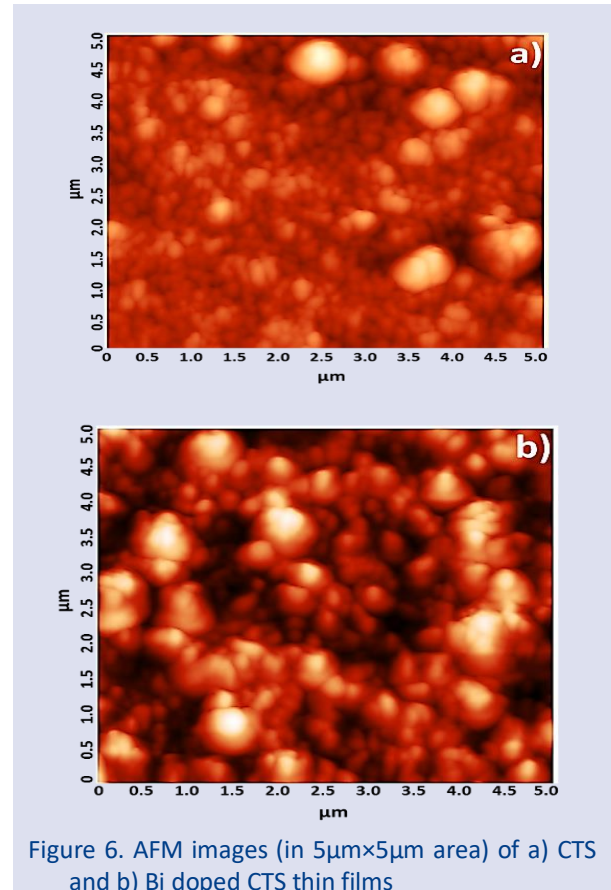


Figure 6. AFM images (in $5\mu\text{m}\times 5\mu\text{m}$ area) of a) CTS and b) Bi doped CTS thin films

AFM images of CTS and Bi-doped CTS thin films in 420 nm thickness are given in Fig 6a and 6b, respectively. The particle size of Bi doped CTS thin film is larger than that of CTS thin film. The fact that Bi atom (117 pm) can occupy Cu (68 pm) and S (51 pm) vacancies and then increase the particle size of Bi doped CTS thin film. The large particle size of Bi doped CTS thin film causes the reduction of the numbers of grain boundaries and the passivation of defects and traps within the boundaries. This provides some improvement in the crystal structure of Bi doped CTS thin film compared to pure CTS thin film [11, 30].

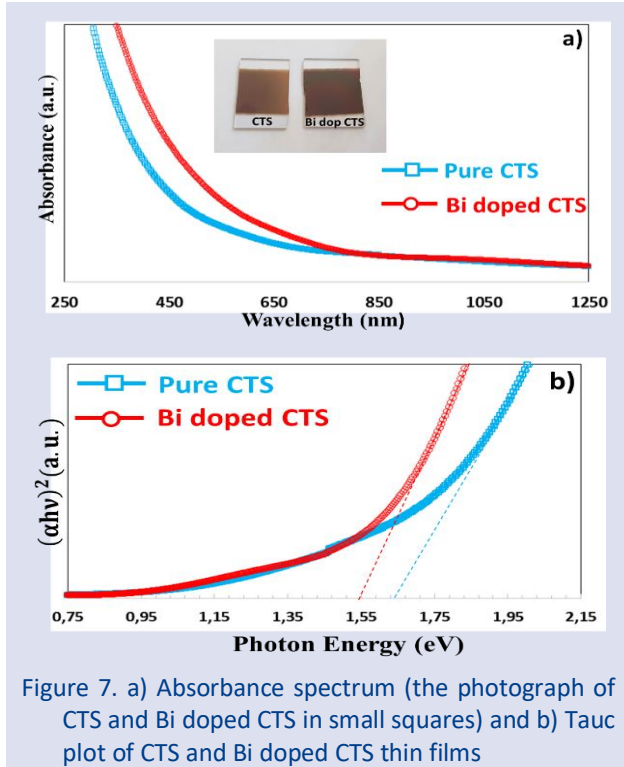


Figure 7. a) Absorbance spectrum (the photograph of CTS and Bi doped CTS in small squares) and b) Tauc plot of CTS and Bi doped CTS thin films

Bi doped CTS thin film absorbs slightly more light than CTS thin films, according to absorbance spectra shown in Fig. 7a. As shown in AFM image in Fig 6b, Bi atom has increased the particle size of Bi doped CTS thin film causing more light absorption. In addition, according to the photographs of CTS and Bi doped CTS thin films have been given in the small square in Fig. 7a, it appears that Bi doped CTS thin film is darker than CTS thin film and it can be foreseen that Bi doped CTS thin film can absorb more photons.

The band gaps of thin films have been calculated by Tauc Eq (2) expressed below:

$$(\alpha hv)^2 = A(hv - E_g)^{1/2} \quad (2)$$

where A, hv , E_g are a constant, the photon energy and the band gap of thin film, respectively. The band gaps of CTS and Bi doped CTS thin films have been determined as 1.64 eV and 1.55 eV from Tauc graph in Fig. 7b, using Eq (1), respectively. The photon absorption of Bi doped CTS thin film is slightly higher since its band gap is slightly lower. The band gap of Bi doped CTS thin film is more consistent with the value has been reported in the literature [31, 32].

The electrical characteristics of Ag/Bi doped CTS/Si/Al hetero-junctions in darkness and under illumination

Since the crystal structure of CTS thin film is amorphous, there are excessive defects and traps in this thin film structure. Because the charge carriers are recombined in these traps and defects, Ag/CTS/Si/Al hetero-junction could not show any diode features.

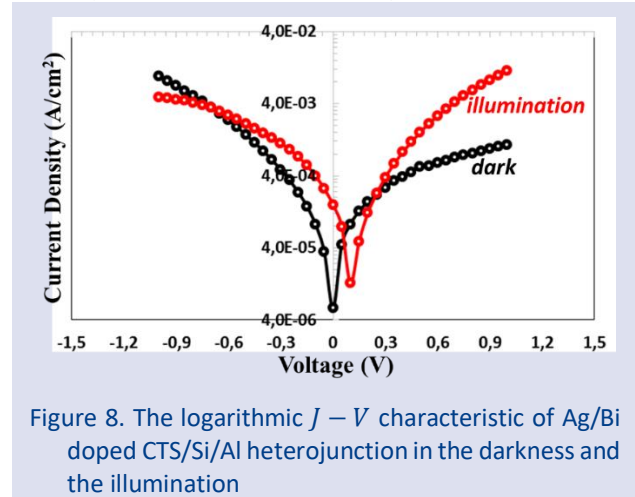


Figure 8. The logarithmic $J - V$ characteristic of Ag/Bi doped CTS/Si/Al hetero-junction in the darkness and the illumination

However, Ag/Bi doped CTS/Si/Al hetero-junction has exhibited PV behaviour according to the logarithmic $J - V$ characteristics shown in Fig 8. The rectification ratio (RR) of a diode, which is expressed by Eq (3):

$$RR = \frac{I_F(+V)}{I_R(-V)} \quad (3)$$

Where, I_F is forward current in +1V, I_R is reverse current in -1V. Rectification rate of Bi doped CTS hetero-junction ($RR = 2.34$) under the darkness is higher than the rectification ratio ($RR = 0.11$) of the hetero-junction in the light. The increase in forward current due to photo-excited electron-hole pair formation lead to a better rectification behaviour of the hetero-junction [33]. However, the weak crystalline structure of Bi doped CTS thin film and the large number of defects and traps in its crystal structure cause more recombination of the charge carriers. Therefore, the rectification rates of the hetero-junction are low in the darkness and under the illumination.

The current of a diode is determined by Eq (4) in thermionic emission theory,

$$I = I_0[\exp(qV/nkT) - 1] \quad (4)$$

V is applied forward bias voltage applied, I_0 is saturation current, n is the ideality factor, q is electric charge, T is the absolute temperature and k is Boltzman constant. Ideality factor of a diode is given by Eq (5):

$$n = \frac{q}{kT} \frac{dV}{d(\ln I)} \quad (5)$$

The ideality factor is determined by the drawn straight line in forward bias region in the logarithmic $J - V$ graph

seen in Fig 8. The ideality factors of the hetero-junction in darkness and the illumination conditions have been calculated to be $n_{dark} = 3.71$ and $n_{illum.} = 3.36$, respectively. The ideality factors of the hetero-junction in both environment conditions have been found to be rather high [34]. The reasons behind it might be referred to the leakage current and dangling-bonds that can occur at the interfaces of the depletion region where the recombination of charge carriers is high due to the existence of defects, traps and interface states formed due to the poor crystalline of Bi doped CTS thin film [11, 35, 36].

The barrier height (Φ_b) of a diode is obtained by using the following equation:

$$\Phi_b = \frac{kT}{q} \ln \left(\frac{AA^*T^2}{I_0} \right) \quad (6)$$

A and A* are the active area of diode and Richardson constant ($112 \text{ A cm}^{-2}\text{K}^{-2}$ to n-Si), respectively. I_0 saturation current is determined by the straight line drawn intersects y-axis of the reverse bias region in the logarithmic $J - V$ characteristic in Fig 8. The barrier heights of Bi doped CTS thin film in darkness and illumination conditions have been found to be $\Phi_{b(dark)} = 0.60 \text{ eV}$ and $\Phi_{b(illum.)} = 0.56 \text{ eV}$, respectively. The photo current result in that a decrease in both the ideality factor and barrier height of Bi doped CTS hetero-junction due to the photo excited charge carriers under illumination conditions [35, 37].

Serial resistance of a diode has been calculated using $R_s = \frac{\Delta V_{forward\ bias\ voltage}}{\Delta I_{forward\ bias\ current}}$ formula for the forward bias region of the logarithmic J-V curve [38]. We have obtained $R_s - V$ curve given in Fig. 9 using this formula and determined the saturated value of R_s serial resistances at high voltage.

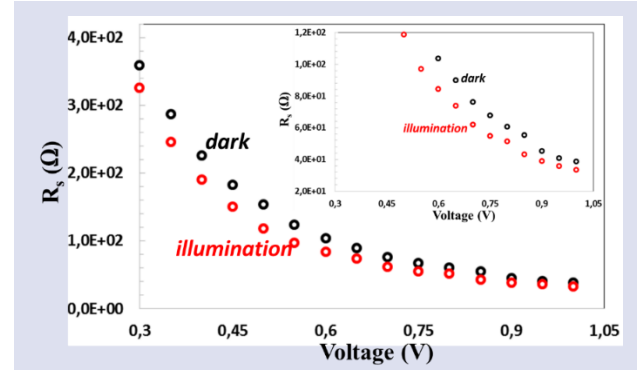


Figure 9. $R_s - V$ curve of Bi doped CTS hetero-junction in the darkness and the illumination

R_s values have been determined to be 38.84Ω and 33.57Ω in the darkness and the illumination conditions. Electrons excited by the photon in the valence band of Bi doped CTS have been transmitted to the conduction band under the illumination conditions and cause the formation of charge carriers, thus the series resistance has been reduced [39, 40].

Table 1. The electrical parameters of Ag/Bi doped CTS/Si/Al hetero-junction in the darkness and the illumination

Bi doped CTS/Si hetero-junction	J-V Method			Cheung Cheung Method				Norde Method	
	dln(J)-V			dV/dln(J)-J		H(J)-J		F(V)-V	
	n	$R_s(\Omega)$	$\Phi_b(\text{eV})$	n	$R_s(\Omega)$	$R_s(\Omega)$	$\Phi_b(\text{eV})$	$R_s(\Omega)$	$\Phi_b(\text{eV})$
Darkness	3.71	38.84	0,60	6.68	17.49	21.91	0.61	49.63	0.65
Illumination	3.36	33.57	0.56	5.37	20.28	23.49	0.63	43.63	0.70

n, R_s and Φ_b parameters have been calculated by Cheung-Cheung method, Norde Method as well as the conventional J-V method and the result are presented in Table 1. Cheung-Cheung functions have been expressed by Eq 7), Eq (8) and Eq (9):

$$\frac{dV}{d(\ln I)} = IR_s + n \left(\frac{kT}{q} \right) \quad (7)$$

$$H(I) = V - \left(\frac{nkT}{q} \right) \ln \left(\frac{I}{AA^*T^2} \right) \quad (8)$$

$$H(I) = IR_s + n\Phi_b \quad (9)$$

$dV/d(\ln J) - J$ and $H(J) - J$ characteristics of Bi doped CTS hetero-junction are given in Fig 10a and 10b, respectively. y-axis intercept and the slope of $dV/d(\ln J) - J$ graphic obtained by Eq (7) show nkT/q and IR_s , respectively. The ideality factors of the hetero-junction have been calculated to be $n_{dark} = 6.68$ and $n_{illum.} = 5.37$, while the serial resistances have been calculated to be $R_{s(dark)} = 17.49\Omega$ and $R_{s(illum.)} = 20.28\Omega$ in the darkness and the under illumination conditions, respectively. The ideality factors and serial resistance determined by $dV/d(\ln J) - J$ characteristics are higher compared to that calculated by the conventional $J - V$ characteristics.

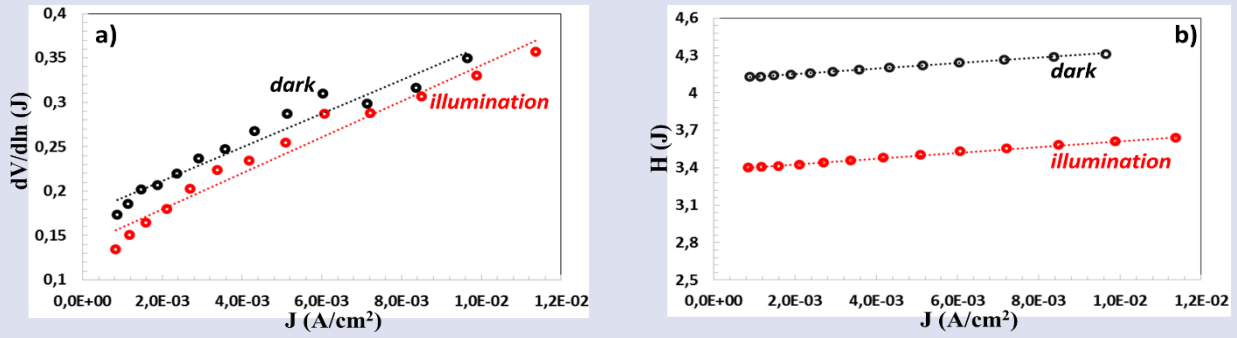


Figure 10. a) $dV/d(\ln J) - J$ and b) $H(J) - J$ curves of Bi doped CTS hetero-junctions in darkness and the illumination

γ -axis intercept and the slope of $H(J) - J$ graphic obtained by Eq (8) present $n\Phi_b$ and IR_s in Eq (9). The serial resistance of Bi doped CTS hetero-junction have been calculated to be $R_{s(dark)} = 21.91\Omega$ and $R_{s(illum.)} = 23.49\Omega$, while its barrier height have been calculated to be $\Phi_{b(dark)} = 0.61$ eV and $\Phi_{b(illum.)} = 0.63$ eV in the darkness and the illumination conditions, respectively. R_s values obtained by $H(J) - J$ characteristic have been found to be slightly higher than that obtained by $dV/d(\ln J) - J$ characteristics. However, R_s values obtained by $H(J) - J$ characteristics have been found to be lower than that of the conventional $J - V$ characteristics. The ideality factors and serial resistance calculated by both conventional $J - V$ and Cheung-Cheung methods for the darkness have been found to be higher than those of the illumination conditions. However, the barrier heights determined by conventional $J - V$ and Cheung-Cheung methods have been recorded to be lower and higher to the darkness and the illumination conditions, respectively. This conflict might be referred to the fact that the barrier height has been obtained from the reverse bias region of $J - V$ curve using the conventional $J - V$ method, while it has been determined from the forward bias region of $J - V$ curve by Cheung-Cheung method.

resistance have been calculated by Norde method [41] expressed in Eq (10);

$$F(V, \gamma) = \frac{V}{\gamma} - \frac{kT}{q} \ln \left(\frac{I(V)}{AA^*T^2} \right) \quad (10)$$

In Eq (10), γ is the first constant higher than ideality factor which was determined by logarithmic $J - V$ curve. Φ_b and R_s values can be calculated by Eq (11) and Eq (12) in Norde method;

$$\Phi_b = F(V_o) + \frac{V_o}{\gamma} - \frac{kT}{q} \quad (11)$$

$$R_s = \frac{\gamma - n}{I_{min}} \frac{kT}{q} \quad (12)$$

$F(V_o)$ is the minimum value of $F(V) - V$ curve, V_o is voltage corresponding to $F(V_o)$ value, I_{min} is current corresponding to V_o value in $J - V$ curve. R_s and Φ_B values of the Bi doped CTS hetero-junction have been calculated using Eq (11) and Eq (12) to be 49.63 Ω , 0.65 eV and 43.63 Ω , 0.70 eV in the darkness and under the illumination conditions, respectively. R_s and Φ_B values determined by Norde method are higher than that obtained by Cheung Cheung method. The reason for this situation is that Cheung Cheung methods are only implemented to nonlinear region (in high voltage area) in forward bias of $J - V$ curve while Norde method is implemented to all forward bias region of $J - V$ curve [37].

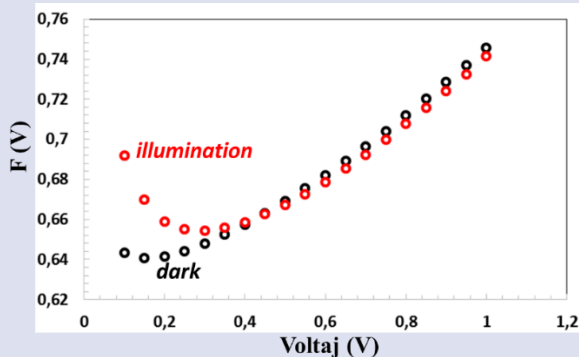


Figure 11. $F(V) - V$ characteristic of Bi doped CTS hetero-junction in the darkness and the illumination.

In Fig 11, we have presented $F(V) - V$ characteristics of Bi doped CTS hetero-junction in darkness and the illumination conditions. The barrier height and serial

Table 2. The photovoltaic parameters of Bi doped CTS hetero-junction under the illumination

Hetero-junction	J_{sc}	V_{oc}	FF	η
Bi doped CTS	0,158 mA/cm ²	100 mV	0,24	0,0049 %

Bi doped CTS/n-Si hetero-junction has exhibited photovoltaic behaviour as seen in logarithmic $J - V$ curve in Fig 8 and the photovoltaic parameters of the hetero-junction are presented in Table 2. Since Bi doped CTS thin film has a weak crystalline structure, photo-excited charge carriers undergo more recombination [12, 42, 43]. Thus, the charge transfer to the depletion region is limited and the charge accumulation is less. This situation causes the short circuit current to be lower [30]. The photo excited charge carriers can cause leakage current at the interface. In addition, when Bi doped CTS

semiconductor with 1.55 eV band gap grown over Si semiconductor of 1.1 eV band gap, a low built in potential can occur in the depletion region [12]. Furthermore, it is also seen in Table 1 that a low barrier height is formed in the conventional $J - V$ characteristic to illumination. All these factors can lead to lower the open circuit voltage. Low J_{sc} , V_{oc} and FF values cause low power conversion efficiency. However, the work functions of n-Si semiconductor and metal contacts such as Ag, Al which are important for the contacts to exhibit ohmic property and affect photovoltaic performance of the heterojunction diode. To the metal contact to be ohmic for the n-type semiconductor, the metal's work function must be smaller than n-type semiconductor's work function ($\phi_M < \phi_S$). For a contact metal to be ohmic for a p-type semiconductor, the work function of the metal must be higher than that of the p-type semiconductor ($\phi_S < \phi_M$) [12, 44]. Al back contact (4.06 eV) tends to exhibit ohmic behaviour for n-Si (4.58 eV) semiconductors. Thus, charge flow can be easily achieved through the contact and a contribution to charge collection can be made [45-47]. As a result, Ag/Bi doped CTS/n-Si/Al hetero-junction shows the photovoltaic property and the higher efficiency can be achieved in CTS thin film solar cells with the improvement studies on CTS and Bi doped CTS thin film.

Conclusions

In this study, we have added Bi powder to Cu_xS and SnS_2 powder mixture and milled it by ball milling, and then we have produced CTS and Bi doped CTS target pellets by cold press. It has been noticed that these target pellets are Cu poor and Sn rich containing Cu_2SnS_3 , Cu_2SnS_3 , $Cu_2Sn_3S_7$, $Cu_4Sn_7S_{16}$ and SnS crystal phases. Bi atoms have weakened the crystal structure of CTS target pellet. However, Bi doped CTS target pellet consists of larger and homogeneously distributed particles compared to non-doped CTS target pellet. The target pellets have been ablated by laser beam and their thin films have been formed using PLD technique. CTS thin film has been produced with an amorphous structure while Bi thin film has been formed in a poor crystalline structure. These Bi doped thin films were Cu poor and Sn rich with a weak peak of SnS phase. Bi doped CTS thin film consist of larger particles compared to CTS thin film and their E_g band gap is lower than that of pure CTS thin film.

Since CTS thin film is in amorphous structure, Ag/CTS/n-Si/Al hetero-junction produced could not exhibit diode feature. On the other hand, Ag/Bi doped CTS/Si/Al hetero-junction has exhibited diode characteristics and PV behaviours. Electrical parameters of Bi doped CTS/Si hetero-junction have been calculated by the conventional $J - V$, Cheung Cheung and Norde methods in the darkness and under the illumination conditions. The ideality factors of the hetero-junction have been found somehow higher which can be attributed to the leakage current, weak crystal structure and the recombination of the charge carriers. Series resistance of

the hetero-junction under the illumination conditions has been found to be lower compared to dark conditions. This situation is based on the transfer of the photo excited electron from the valence band to the conduction band which increases the number of charge carriers. The series resistance and barrier height calculated by Cheung-Cheung and Norde methods have been found to be lower and higher compared to the conventional $J - V$ method. PV parameters Bi doped CTS heterojunctions have been determined to be $J_{sc}=0.158 \text{ mA/cm}^2$, $V_{oc}=100 \text{ mV}$, $FF=0.24$ and $\eta=0.0049\%$. The low power conversion efficiency of the hetero-junction device can be attributed to the leakage current, too much recombination of the charge carriers, the interface states and the low built in potential in the hetero-junction.

Acknowledgements

Authors kindly would like to thank,
 - Selçuk University, High Technology Research and Application Center and Selçuk University, *Laser Induced Proton Therapy Application and Research Center* for supplying with Infrastructure and
 - Selçuk University, Scientific Research Projects Coordination (BAP) Unit for grants via projects with references of 18401178 and 20401018

Conflicts of interest

The author states that he has no conflict of interest to declare that are relevant to the content of this article.

References

- [1] Berg D.M., et al., Raman analysis of monoclinic Cu_2SnS_3 thin films. *Applied Physics Letters*, 100(19) (2012) 192103.
- [2] Bourgès C., et al., Low thermal conductivity in ternary $Cu_4Sn_7S_{16}$ compound. *Acta Materialia*, 97 (2015) 180-190.
- [3] Fu L., et al., Graphene-encapsulated copper tin sulfide submicron spheres as high-capacity binder-free anode for lithium-ion batteries. (2017).
- [4] Alias M., et al., Synthesis Cu_2SnS_3 and Cu_3SnS_4 nanopowder and studying the composition, structural and morphological properties. *Journal of Non-Oxide Glasses*, 8(4) (2016) 93-97.
- [5] Lokhande A., et al., Development of Cu_2SnS_3 (CTS) thin film solar cells by physical techniques: A status review. *Solar Energy Materials and Solar Cells*, 153 (2016) 84-107.
- [6] Akaki Y., Matsuo H., Yoshino K., Structural, electrical and optical properties of Bi-doped $CuInS_2$ thin films grown by vacuum evaporation method. *physica status solidi c*, (8) (2006) 2597-2600.
- [7] Chantana J., et al., Bismuth-doped Cu (In, Ga) Se_2 absorber prepared by multi-layer precursor method and its solar cell. *physica status solidi (c)*, 12(6) (2015) 680-683.
- [8] Rawat K., Shishodia P., Enhancement of photosensitivity in bismuth doped Cu_2ZnSnS_4 thin films. *Physica status solidi (RRL)–Rapid Research Letters*, 10(12) (2016) 890-894.

- [9] Chen F.-S., et al., Cu (In, Ga) Se₂ thin films codoped with sodium and bismuth ions for the use in the solar cells. *Journal of Nanomaterials*, 2015. 2015.
- [10] Chalapathi U., Poornaprakash B., Park S. H., Antimony induced crystal growth for large-grained Cu₂SnS₃ thin films for photovoltaics. *Journal of Power Sources*, 426 (2019) 84-92.
- [11] Gezgin S.Y., Kiliç H. Ş., Determination of electrical parameters of ITO/CZTS/CdS/Ag and ITO/CdS/CZTS/Ag heterojunction diodes in dark and illumination conditions. *Optical and Quantum Electronics*, 51(11) (2019) 360.
- [12] Gezgin S.Y., Kiliç H. Ş., The electrical characteristics of ITO/CZTS/ZnO/Al and ITO/ZnO/CZTS/Al heterojunction diodes. *Optik*, 182 (2019) 356-371.
- [13] Ettliger R.B., et al. Pulsed laser deposition of Cu-Sn-S for thin film solar cells. in World Conference on Photovoltaic Energy Conversion 6 (2014).
- [14] Zhou W., et al., Sustainable thermoelectric materials fabricated by using Cu₂Sn_{1-x}Zn_xS₃ nanoparticles as building blocks. *Applied Physics Letters*, 111(26) (2017) 263105.
- [15] Chen X., et al., SnS/N-Doped carbon composites with enhanced Li⁺ storage and lifetime by controlled hierarchical submicron-and nano-structuring. *CrystEngComm*, 22(9) (2020) 1547-1554.
- [16] Hossain E.S., et al., Fabrication of Cu₂SnS₃ thin film solar cells by sulphurization of sequentially sputtered Sn/CuSn metallic stacked precursors. *Solar Energy*, 177 (2019) 262-273.
- [17] Wang C.-J., et al., Fabrication and sulfurization of Cu₂SnS₃ thin films with tuning the concentration of Cu-Sn-S precursor ink. *Applied Surface Science*, 388 (2016) 71-76.
- [18] He T., et al., The role of excess Sn in Cu₄Sn₇S₁₆ for modification of the band structure and a reduction in lattice thermal conductivity. *Journal of Materials Chemistry C*, 5(17) (2017) 4206-4213.
- [19] Cui J., et al., Improved thermoelectric performance of solid solution Cu₄Sn_{7.5}S₁₆ through isoelectronic substitution of Se for S. *Scientific reports*, 8(1) (2018) 1-9.
- [20] Weber A., Mainz R., Schock H., On the Sn loss from thin films of the material system Cu-Zn-Sn-S in high vacuum. *Journal of Applied Physics*, 107(1) (2010) 013516.
- [21] Jackson A.J., Walsh A., Ab initio thermodynamic model of Cu₂ZnSnS₄. *Journal of Materials Chemistry A*, 2(21) (2014) 7829-7836.
- [22] Berg D.M., et al., Thin film solar cells based on the ternary compound Cu₂SnS₃. *Thin Solid Films*, 520(19) (2012) 6291-6294.
- [23] Andrade Jr, M.A., Mascaro L. H., Bismuth doping on CuGaS₂ thin films: structural and optical properties. *MRS COMMUNICATIONS*, 8(2) (2018) 504.
- [24] Liu N., et al., Synthesis and characterization of (Cu_{1-x}Ag_x)₂ZnSnS₄ nanoparticles with phase transition and bandgap tuning. *Journal of Materials Science: Materials in Electronics*, (2020) p. 1-9.
- [25] Zhao Y., et al., Effect of Ag doping on the performance of Cu₂SnS₃ thin-film solar cells. *Solar Energy*, 201 (2020) 190-194.
- [26] Alijani M., Ilkhechi N. N., Effect of Ni Doping on the Structural and Optical Properties of TiO₂ Nanoparticles at Various Concentration and Temperature. *Silicon*, 10(6) (2018) 2569-2575.
- [27] Ammar I., Gassoumi A., Turki-Kamoun N., The Effect of TSC and Nickel Doping on SnS Thin Films. *Silicon*, 2020: p. 1-6.
- [28] Song N., et al., Epitaxial Cu₂ZnSnS₄ thin film on Si (111) 4 substrate. *Applied Physics Letters*, 106(25) (2015) 252102.
- [29] Shin B., et al., Epitaxial growth of kesterite Cu₂ZnSnS₄ on a Si (001) substrate by thermal co-evaporation. *Thin Solid Films*, 556 (2014). 9-12.
- [30] Gezgin S.Y., Houimi A., Kiliç H. Ş., Production and photovoltaic characterisation of n-Si/p-CZTS heterojunction solar cells based on a CZTS ultrathin active layers. *Optik*, 199 (2019) 163370.
- [31] Jia Z., et al., The photovoltaic properties of novel narrow band gap Cu₂SnS₃ films prepared by a spray pyrolysis method. *RSC Advances*, 5(37) (2015) 28885-28891.
- [32] Welatta F., et al. Fabrication and characterization of copper-tin-sulfide thin film. in *AIP Conference Proceedings*. (2018) AIP Publishing LLC.
- [33] Uslu H., et al., The interface states and series resistance effects on the forward and reverse bias I-V, C-V and G/ω-V characteristics of Al-TiW-Pd₂Si/n-Si Schottky barrier diodes. *Journal of alloys and compounds*, 503(1) (2010) 96-102.
- [34] Elhouichet H., Othmen W. B. H., Dabboussi S., Effect of Sb, Tb 3+ Doping on Optical and Electrical Performances of SnO₂ and Si Based Schottky Diodes. *Silicon*, 12(3) (2020) 715-722.
- [35] Tataroğlu A., Altındal Ş., Azizian-Kalandaragh y., Electrical and photoresponse properties of CoSO.
- [36] Lambada D.R., et al., Investigation of Illumination Effects on the Electrical Properties of Au/GO/p-InP Heterojunction with a Graphene Oxide Interlayer. *Nanomanufacturing and Metrology*, (2020) 1-13.
- [37] Özerli H., et al., Electrical and photovoltaic properties of Ag/p-Si structure with GO doped NiO interlayer in dark and under light illumination. *Journal of Alloys and Compounds*, 718 (2017). 75-84.
- [38] Soliman H., et al., Electronic and photovoltaic properties of Au/pyronine G (Y)/p-GaAs/Au: Zn heterojunction. *Journal of alloys and compounds*, 530 (2012) 157-163.
- [39] Karataş Ş., Yakuphanoglu F., Effects of illumination on electrical parameters of Ag/n-CdO/p-Si diode. *Materials Chemistry and Physics*, 138(1) (2013) 72-77.
- [40] Bedia F., et al., Electrical characterization of n-ZnO/p-Si heterojunction prepared by spray pyrolysis technique. *Physics Procedia*, 55 (2014) 61-67.
- [41] Norde H., A modified forward I-V plot for Schottky diodes with high series resistance. *Journal of Applied Physics*, 50(7) (1979) 5052-5053.
- [42] Shi Z., Jayatissa A. H., One-pot hydrothermal synthesis and fabrication of kesterite Cu₂ZnSn(S, Se)₄ thin films. *Progress in Natural Science: Materials International*, 27(5) (2017) 550-555.
- [43] Zedan I., El-Menyawy E., Mansour A., Physical Characterizations of 3-(4-Methyl Piperazinylimino Methyl) Rifampicin Films for Photodiode Applications. *Silicon*, 11(3) (2019) 1693-1699.
- [44] Gezgin S.Y., Kiliç H. Ş., Determination of electrical parameters of ITO/CZTS/CdS/Ag and ITO/CdS/CZTS/Ag heterojunction diodes in dark and illumination conditions. *Optical and Quantum Electronics*, 51(11) (2019) 1-22.
- [45] Yao Z., et al., High-Performance and Stable Dopant-Free Silicon Solar Cells with Magnesium Acetylacetonate Electron-Selective Contacts. *physica status solidi (RRL)–Rapid Research Letters*, 14(6) (2020) 2000103.
- [46] Kang J., et al., Electron-Selective Lithium Contacts for Crystalline Silicon Solar Cells. *Advanced Materials Interfaces*, (2021) 2100015.
- [47] Ali M., et al., Optimization Of Monoclinic Cu₂sn₃ (Cts) Thin Film Solar Cell Performances Through Numerical Analysis. *Chalcogenide Letters*, 17(2) (2020) 85-98.

Investigating the COVID19 Characteristics of the Countries Based on Time Series Clustering

Muhammet Oguzhan Yalçın ^{1,a,*}, Nevin Güler Dincer ^{1,b}, Öznur İşçi Güneri ^{1,c}

¹Department of Statistics, Faculty of Science, Muğla Sıtkı Kocman University, Muğla, Turkey

*Corresponding author

Research Article

History

Received: 10/07/2021

Accepted: 05/03/2022

Copyright



©2022 Faculty of Science,
Sivas Cumhuriyet University

ABSTRACT

The objective of this study is to reveal the COVID19 characteristics of the countries by using time series clustering. Up to now, various studies have been conducted for similar objectives. But, it has been observed that these studies belong to early time of pandemic and are involved limited number of countries. To analyze the characteristic of COVID19 more, this study has considered 111 countries and time period between the 4th of April 2020 and the 1st of January 2021. Fuzzy K-Medoid (FKM) is preferred as clustering method due to its three abilities: i) FKM enables to determine the similarities and differences between the countries in more detail by utilizing the membership degrees, ii) In FKM, cluster centers are selected among from objects in the data set. Thus, it has the ability of detecting the countries which represent the behavior of all countries, iii) FKM is a robust method against to outliers. Thanks to this ability, FKM prevents that the countries exhibiting abnormal behavior negatively affect to the clustering results. At the results of the analyses, it is observed that 111 countries have three different behaviors in terms of confirmed cases and five different behaviors in terms of deaths.

Keywords: Fuzzy K-medoids, Cluster validity, Time series clustering, COVID19

^a moguzhanyalcin@mu.edu.tr

^b <https://orcid.org/0000-0003-4017-5588>

^c nguler@mu.edu.tr

^d <https://orcid.org/0000-0003-0361-1803>

^e oznur.isci@mu.edu.tr

^f <https://orcid.org/0000-0003-3677-7121>

Introduction

Coronavirus which emerged in China's Hubei province in December 2019 and spread to the all over the world in a short time has been declared as pandemic by World Health Organization (WHO) on the March 11, 2020. As of 5 March 2021, 115,598,160 confirmed COVID19 cases and 2,569,011 deaths have been reported in all of the world. Therefore, the countries have developed various strategies to fight COVID19 such as lockdown, obligation of mask, closing down of cafés and restaurants, restricting international air traffic etc. But, these kinds of restrictions affect the countries quite negatively in terms of economy. Determining correct strategies having the least impact on the economy depends on a good understanding of the COVID19 behavior of countries. In this study, some statistical properties of COVID19 are investigated for each country separately and the countries having similar COVID19 behavior are determined by using time series clustering. Thus, it is hoped to detect the countries that need to take more serious precautions individually and the countries that can develop common strategies.

So far, several studies have been conducted to determine the countries having similar behavior of COVID19. Some of these studies can be summarized as follows: Imtyaz et al.[1] have clustered thirty countries in terms of percentage of their elderly population and, COVID19 mortality rate. They have applied k-means clustering algorithm to the data set of the thirty countries for the time period between 22 January 2020 and 01 June 2020. At the result of the analyses, they have found that mortality rates in countries in Western Europe are high

while the mortality rates in countries in South Asia and Middle East are low. Zariakas et al.[2] have used the hierarchical clustering methods to divide the countries into the homogenous groups with respect to active cases, active cases per population and active cases per population and per area for the time period between 22 January 2020 and 4 April 2020. Mahmoudi et al.[3] have clustered the high-risk countries including United States America, Spain, Italy, Germany, United Kingdom, France and Iran with respect to the number of confirmed cases, the number of death cases, cumulative number of confirmed cases and cumulative number of deaths using fuzzy clustering. The data sets they used involve the time period from 22 February 2020 up to 18 April 2020. They also have investigated the correlation between the population size and spread of COVID19. Alvarez et al. [4] have used non-parametric techniques based on correlation distance and Minimal Spanning tree in order to cluster 191 countries in terms of COVID19 dynamics. Hutagalung et al.[5] have focused on the grouping of the 11 countries located in Southeast Asia in terms of the number of confirmed cases and the number of deaths observed on the date of April 2020. They have used the k-means clustering algorithm. Virgantari and Faridhan[6] have applied k-means clustering algorithm to the data set covering COVID19 cases in 34 provinces of Indonesia. Rojas et al.[7] have used the hierarchical clustering algorithm based on dynamic time warping distance measure to determine behavioral relationships between different states of the US with respect to COVID19.

Azarafza et al.[8] have investigated the spatiotemporal distribution and spread pattern of COVID19 in Iran. For this objective, they have utilized k-means clustering algorithm. Crnogorac et al.[9] have carried out a study based on clustering the cumulative relative number of the European countries and territories. They have used three clustering algorithms, including K-Means, agglomerative and BIRCH. Sadeghi et al. [10] used hierarchical clustering algorithm to rank and score 180 countries in terms of COVID19 cases and fatality in 2020. Putra ve Kadyanan[11] have clustered 9 provinces in Bali by using K-Means clustering algorithm. They have used four clustering variables, consisting of number of cases, dead rate, the number of recovered and the number of isolated people. Utomo[12] has applied k-means and k-medoids clustering algorithms to data set, consisting of confirmed and death cases for grouping 34 provinces in Indonesia. Abdullah et al.[13] also clustered provinces in Indonesia of the risk of the COVID19. They used the K-Means clustering algorithm and three clustering variable, including confirmed, death and recovered cases.

The most of these studies are based on the classical clustering approach. But, the clustering approaches based on classical logic have some disadvantages: i) Classical clustering approaches force that each object to be clustered in such a way as to belong to only one cluster. In case an object is approximately equidistant from more than one cluster, the object is assigned to the cluster that is the closest one. Thus, the fact that the object has also the characteristics of other clusters with certain degree is ignored. ii) In classical clustering, there is no difference between the objects within the same cluster. Whereas some objects carry the characteristics of the cluster more, some less. Besides, in most of the studies summarized above, short periods at the beginning of the pandemic and limited number of countries have been considered. In the current study, FKM clustering algorithm is applied to cumulative number of confirmed cases (CCOP) and deaths (DOP) per one million persons of 111 countries. The time period studied covers the period between 1 April 2020 and

22 January 2021. The contributions of this study can be sorted as follows:

- This study uses FKM clustering algorithm based on fuzzy logic. The fuzzy clustering approaches allow assigning a country to more than one cluster with different membership degrees. Thus, it is possible to identify the countries having the characteristics of more than one cluster and the differences between the countries within the same cluster.

- FKM clustering algorithm selects the cluster centers among from the countries. This ability of FKM allows determining a representative country for each cluster separately in order to form an opinion about the COVID19 behavior of the other countries which are assigned to the same cluster with high membership degrees.

- FKM clustering algorithm is robust to outliers. It's this ability considerably decreases the negative effect on the clustering of the countries having abnormal COVID19 pattern.

- Five cluster validity indexes have been considered simultaneously to reveal the number of different COVID19 behavior.

This study is organized as follows. Section 2 gives brief information about the data set and methods used. Section 3 includes the experimental results and in the last section, the study is concluded.

Materials and Methods

Data Set

The raw data sets used in this study are downloaded from the web site of <https://www.kaggle.com/sudalairajkumar/novel-coronavirus-2019-dataset>. Data sets consist of the cumulative number of confirmed cases and cumulative number of deaths. 111 countries and the time period between the 4th of April 2020 and the 19th of January 2021 are considered. Before the clustering process, the raw data are standardized as follows:

$$CCOP_{ij} = \frac{\text{Cumulative number of Confirmed Cases}_{ij}}{\text{Population Size}_i} * 1000000 \quad i = 1,2, \dots, N \quad j = 1,2, \dots, n \quad (1)$$

$$DOP_{ij} = \frac{\text{Cumulative number of deaths}_{ij}}{\text{Population Size}_i} * 1000000 \quad i = 1,2, \dots, N \quad j = 1,2, \dots, n \quad (2)$$

Where n (294) is the length of time series, N (111) is the number of countries.

Time Series Clustering

Clustering analysis is a data mining technique used for dividing the objects into homogenous groups according to their characteristic properties. According to this method, while objects with the same properties are in the same group, objects with a large difference from each other are placed in different groups. While increasing the difference between groups to the maximum is aimed by the method, the difference between groups is minimum.

Clustering methods are generally divided into two groups as hierarchical and partitioning methods. Hierarchical clustering techniques are the process of combining clusters gradually. In order to perform hierarchical cluster analysis, researchers have to decide how to define similarity or distance and how to merge or separate clusters[14][15].

Partitioning clustering algorithms take c input parameters and divide N objects into c clusters. These techniques perform operations that find single-level clusters instead of working on a nested clustering structure like a dendrogram[16]. All techniques are based on the cluster center representing the cluster. To improve cluster quality, the algorithm is run multiple times with

different starting points and the best configuration from total runs is used as output clustering. Partitioning clustering algorithms are widely used due to their easy applicability and efficient results. Partitioning methods are divided into classical clustering and fuzzy clustering [17]. In classical clustering, each object of the data set is assigned to one and only one cluster. In fuzzy clustering, it allows objects to belong to two or more clusters. According to the fuzzy logic principle, each object belongs to each of the clusters with a membership value varying between [0,1].

Time series clustering (TSC) is a special type of clustering in which the objects to be clustered correspond to the time series. Time series can be defined as a set consisting of the observations measured at the successive time points. TSC methods can be collected under three main headings i) distance-based, ii) feature-based and iii) model-based[18]. Distance-based TSC methods directly works with time series themselves without any transforming or preprocessing on them. Therefore, this kind of TSC methods provide the best clustering performance since they do not lead to information lost.

In feature-based TSC methods, time series are converted into feature space with lower dimension which represents its behavior. Clustering algorithm is applied to the features extracted. Lastly, in the model-based TSC methods, a model is predicted for each time series by using statistical or other modeling techniques. To determine similar time series, model parameters are used as a clustering variable.

Distance-based time series clustering is preferred in this study due to its advantage mentioned above. In these methods, data set is organized as follows:

$$Y = \begin{bmatrix} y_{11} & y_{12} & \dots & y_{1n} \\ y_{21} & y_{22} & \dots & y_{2n} \\ \vdots & \vdots & \vdots & \vdots \\ y_{N1} & y_{N2} & \dots & y_{Nn} \end{bmatrix} \quad (3)$$

Where N is the number of time series, n is the length of time series. In matrix Y, each row corresponds to a time series. In this study, each row is the time series of a country consisting of CCOP or DOP values.

Fuzzy Clustering and Fuzzy K-Medoids Algorithm

Fuzzy clustering algorithms have the ability of assigning an time series to more than one clusters via membership degrees. In fuzzy clustering, the membership degrees must satisfy following conditions:

$$\begin{aligned} 0 \leq u_{ij} \leq 1 \quad i=1,2,\dots,N, \quad j=1,2,\dots,c \quad (a) \\ 0 < \sum_{i=1}^N u_{ij} < N \quad j=1,2,\dots,c \quad (b) \\ \sum_{j=1}^c u_{ij} = 1 \quad i=1,2,\dots,N \quad (c) \end{aligned} \quad (4)$$

Where u_{ij} is the membership degree of i^{th} time series to j^{th} cluster, c is the number of clusters and N is the number of time series. 4(a) indicates that membership degrees are between 0 and 1, 4(b) states that the sum of membership degrees of the time series in j^{th} cluster must be between 0 and N . Lastly, 4(c) states that sum of membership degrees of i^{th} time series to all clusters must be equal to one.

Fuzzy clustering methods are based on minimizing the following objective function:

$$J_F = \sum_{j=1}^c \sum_{i=1}^N u_{ij}^m d^2(y_i, v_j) \quad (5)$$

m : fuzziness index, v_j : j^{th} cluster center, $d^2(y_i, v_j)$: distance between j^{th} cluster and i^{th} time series.

When the given objective function is tried to be minimized, in other words, when the derivatives are taken for u_{ij}^m and set to 0, the following update equation is obtained.

$$u_{ij} = \left[\sum_{s=1}^c \left(\frac{d^2(y_i, v_j)}{d^2(y_i, v_s)} \right)^{\frac{1}{m-1}} \right]^{-1} \quad j = 1, 2, \dots, c, \quad i = 1, 2, \dots, N \quad (6)$$

Fuzzy clustering algorithms differ according to form of the cluster centers and distance measure used. Fuzzy C-Means (FCM)[19], Gustafson-Kessel (GK)[20], Fuzzy C-Regression Model (FCRM) [21] and Fuzzy K-Medoids (FKM)[22] are most popular fuzzy clustering algorithms. The form of cluster centers and the distance measure used are given in Table 1.

Table 1. Properties of Widely Used Fuzzy Clustering Algorithms

Clustering algorithm	Distance Measure	Cluster Centers
FCM	$d^2(y_i, v_j) = \sqrt{\sum_{k=1}^n (y_{ik} - v_{jk})^2}$	$v_j = \frac{\sum_{i=1}^N u_{ij}^m y_i}{\sum_{i=1}^N u_{ij}^m}$
FCRM	$d^2(y_i, v_j) = \sqrt{(y_{in} - v_{ij})^2}$	$v_{ij} = \beta_{0j} + \beta_{1j}y_{i1} + \dots + \beta_{j(n-1)}y_{i(n-1)}$
FKM	$d^2(y_i, v_j) = \sqrt{\sum_{k=1}^n (y_{ik} - v_{jk})^2}$	$q = \underset{1 \leq k \leq N}{\operatorname{argmin}} \sum_{j=1}^N u_{ij}^m d^2(y_k, y_j) \quad v_j = y_q$
GK	$d^2(y_i, v_j) = \sqrt{(y_i - v_j)^T \Sigma_j^{-1} (y_i - v_j)}$	$v_j = \frac{\sum_{i=1}^N u_{ij}^m y_i}{\sum_{i=1}^N u_{ij}^m}$

According to Table 1, FCM, FCRM and FKM use the Euclidian distance measure while GK use the Mahalanobis distance measure. In Mahalanobis distance, Σ_j is the variance-covariance matrix of j^{th} cluster. The cluster centers in FCM and GK correspond to the arithmetic means weighted by membership degrees. Thus, FCM and GK algorithms are negatively affected from the outliers because these points pull cluster centers towards to themselves. In FCRM, the cluster center is a hyperplane. This algorithm is generally used in the modeling the data set generating by more than one stochastic process.

Lastly in FKM, the cluster centers are called as medoid. In fact, the medoids correspond to time series in the data set that minimizes its distance from all time series in the datasets depending on the cluster membership[23]. The most important property of the FKM algorithm is to more robust to the outliers when comparing with FCM, GK and FCRM. Besides, the correspondence of cluster centers to time series in the data set in FKM allows to select a representative time series for the time series within the same cluster. In this study, FKM algorithm is used to cluster CCOP or DOP values due to these properties of it. The pseudo code of the FKM is given in Table 2.

Table 2. Pseudo code of FKM[22]

```

Fix the number of clusters c; Randomly select to initial values of the medoids,
V = {v1, v2, ..., vc} from Y (defined in Eq. 3)
Iter = 1;
Repeat
  for i=1:N
    for j=1:c
      calculate uij by using Eq. (6)
    end;
  end;
  Viter = V
  for j=1:c
    q = argmin1 ≤ k ≤ N ∑j=1N uijm d2(yk, yj)
    vj = yq
  end;
  iter = iter+1;
  Viter = V
Until Viter = Viter-1
    
```

The most important problem in partitioning clustering methods is to determine the number of clusters. Many algorithms have been proposed to determine the number of clusters. Next subsection gives the cluster validity indexes used in this study.

Cluster Validity Indexes

Cluster validity are techniques used to find the optimal number of clusters without any prior knowledge.

Fuzzy silhouette index (FS)

The Silhouette index technique was first proposed by Peter J. Rousseeuw in 1987[24]. It provides a graphical representation of how well each time series is in its own set. In this technique, a silhouette score is calculated for each number of clusters, and silhouette scores above the average determine the number of clusters. The silhouette score is the score that calculates how well the data is clustered and is calculated to evaluate the quality of clustering algorithms. This score is calculated separately for each time series of the different clusters. For this, the silhouette score (S) is calculated as follows:

$$S = \frac{b_i - a_i}{\max(a_i - b_i)} \tag{7}$$

Where **a** is average of the distances between the time series and other cluster elements (intra-cluster distance) and **b** is average distances of the distances between the time series

and the data of the other closest cluster (average closest cluster distance).

Silhouette score ranges from -1 to 1. If the score is 1, it is said that the cluster is a dense cluster and is better separated from other clusters. If the score is close to 0, we can say that it is very close to neighboring clusters. When negative values are seen, it can be said that there is a wrong clustering. The overall average of the entire data set is found, and the largest overall mean silhouette shows the best cluster. The number of clusters with the maximum silhouette width is determined as the optimum number of clusters.

The fuzzy version of the silhouette index is calculated as follows:

$$I_{FS}(X; V, U) = \frac{\sum_{i=1}^n (u_{ij} - u_{ij'})^\alpha \left(\frac{b_i - a_i}{\max(b_i, a_i)}\right)}{\sum_{i=1}^n (u_{ij} - u_{ij'})^\alpha} \tag{8}$$

b, a: weighting coefficients of fuzzy

The fuzzy silhouette index is designed in such a way that the optimal number of clusters (c) takes the maximum value.

Xie-beni index (XB)

The Xie-Beni (XB)[25] index is a popular measure of fuzzy set validity. It is an index that truly measures

compactness and separation. This proposed index generally focuses on two features. These are the closeness of object to each other and the difference of clusters from each other. The numerator part in the formula shows the density and the denominator part shows the strength of the separation. The value that makes the index minimum is selected.

$$I_{XB}(Y; V, U) = \frac{\sum_{j=1}^c \sum_{i=1}^N u_{ij}^m |y_i - v_j|^2}{N \min_{1 \leq j, k \leq c, j \neq k} \{||v_j - v_k||^2\}} \quad (9)$$

Partition coefficient (PC)

Bezdek[28] proposed the partition coefficient, which measures the amount of overlap between clusters. A performance measure based on minimizing the fuzzy intercept is defined.

$$I_{PC}(U) = \frac{1}{N} (\sum_{j=1}^c \sum_{i=1}^N u_{ij}^m) \quad (10)$$

The range of values for PC is (1/c, 1). The PC index has two disadvantages: it tends to decrease as the number of clusters increases and is sensitive to fuzzier; it prevents the data set from correctly determining the underlying cluster number[27]. Accordingly, the best performance is the value at which the function takes the maximum value.

Partition entropy (PE)

$$I_{PE}(U) = \frac{1}{N} (\sum_{j=1}^c \sum_{i=1}^N u_{ij}^m \log_b(u_{ij})) \quad (11)$$

The PE[28] index is a scalar measure of the amount of fuzziness in a given U. The best performance in the index is found when it takes the minimum value.

Modified partition coefficient (MPC)[29]

$$I_{MPC}(U) = (c * I_{PC}(U) - 1)/(c - 1) \quad (12)$$

The number of clusters which MPC value is maximum corresponds to optimal number of clusters.

Experimental Results

Clustering process is performed at two steps. In the first step, optimal number of clusters is determined by using five cluster indexes defined in Section 2.4. In the second step, clustering is performed with the optimal number of clusters and the lengths of clusters (CL) are calculated to determine the risk levels of clusters. The following equation is used for CL:

$$CL_j = \sqrt{\sum_{i=1}^n v_{ij}^2} \quad j = 1, 2, \dots, c \quad (13)$$

Where n is the length of the cluster center (is equal to the length of the time series). The CL values are sorted in descending order. The cluster having maximum CL values is labelled as high risk and the cluster having minimum CL value is labelled as low risk.

The Clustering Results for CCOP

In order to determine the optimal number of clusters, FKM clustering algorithm is executed for all numbers of clusters between 3 and 10. Table 3 gives the values of cluster validity indexes.

According to Table 3, the optimal number of clusters is found as 3. When clustering process is repeated for the optimal number of clusters and CL values are calculated, low risk countries are obtained as seen in Table 4

The results given in Table 4 can be summarized as follows:

- Low risk cluster consists of 52 countries.
- The cluster center corresponds to Uzbekistan. This states that information about COVID19 characteristics of the other countries can be obtained by only monitoring Uzbekistan.
- Greece, Mexico, Kazakhstan, Saudi Arabia, Singapore, and Tunisia also belong to the cluster of middle risk countries with approximately 0.3 membership degrees.
- The membership degrees of the other countries to low risk countries are generally bigger than 0.8.

Descriptive statistics for low risk countries are given in Figure 1

According to Figure 1,

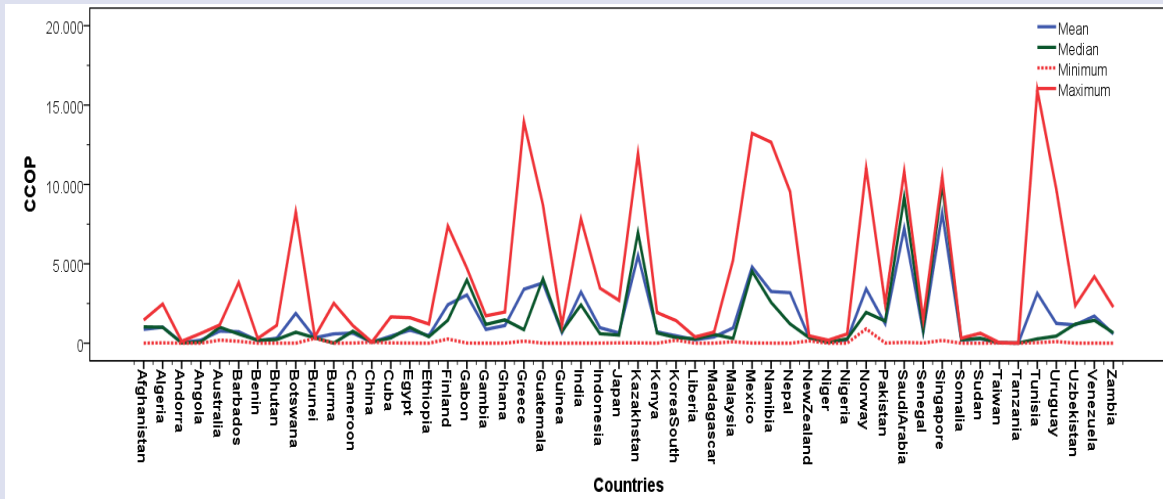
- The countries which have the highest mean and median in terms of the CCOP in the low risk cluster are Kazakhstan, Saudi Arabia and Singapore. Tanzania, Taiwan and Andorra have the smallest mean and median CCOP values. Besides, the maximum value (maximum of maximum CCOP values of the countries) of CCOP value is observed in Tunisia while minimum value is observed in Sudan.
- Variation coefficients given in Figure 1(b) indicate the variability of CCOP values observed in the date of 1 April 2020 - 19 January 2021. Accordingly, the countries having the highest variability are Greece and Tunisia. The smallest variabilities are observed in CCOP values of China, Brunei, New Zealand, Taiwan and Tanzania.
- In Figure 1(c), lines in the middle of boxes show the median values of the countries. Based on this, it can be said that the CCOP values in the countries of Angola, Bhutan, Cuba, Ethiopia, Finland, Greece, India, South Korea, Malaysia, Namibia, Nepal, Norway, Tunisia and Uruguay have increased considerably since 26 August 2020 (the mid of the time period considered) since the median values are at the bottom of the boxes.
- The CCOP values in the countries of Afghanistan, Algeria, Australia, Benin, Cameroon, Egypt, Gabon, Gambia, Ghana, Guinea, Kazakhstan, Mexico, Pakistan, Saudi Arabia, Senegal and Singapore have started to increase at the beginning of the time period considered.

Table 3. Cluster Validity Indexes for CCOP

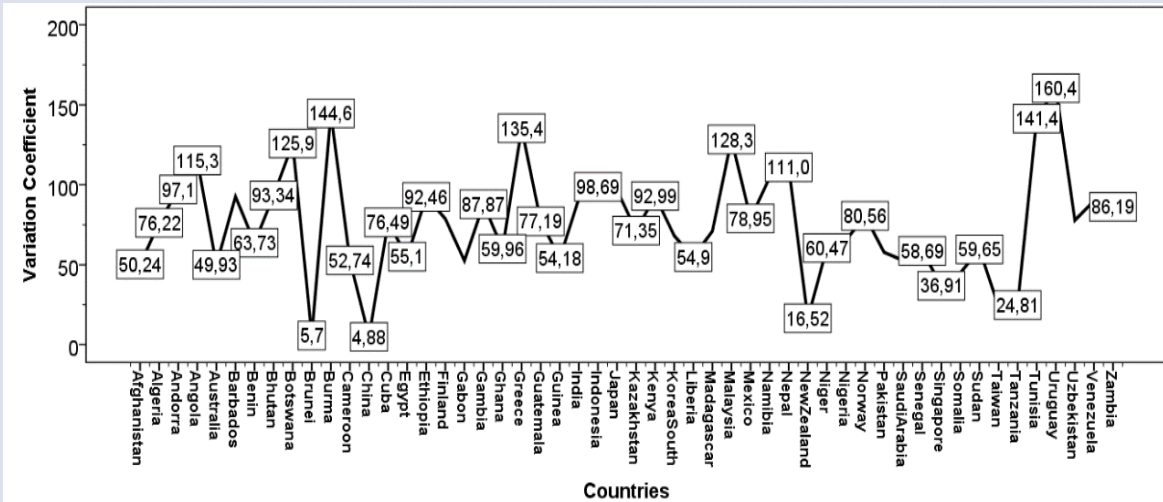
Index/NC	3	4	5	6	7	8	9	10
FS	0.75	0.75	0.73	0.72	0.71	0.65	0.65	0.67
XB	0.17	0.83	0.59	5.95	3.74	4.83	4.47	3.99
PC	0.73	0.65	0.61	0.59	0.54	0.53	0.52	0.51
PE	0.46	0.66	0.83	0.90	0.96	1.06	1.13	1.19
MPC	0.60	0.56	0.52	0.49	0.49	0.49	0.46	0.46

Table 4. Low Risk Countries in terms of CCOP

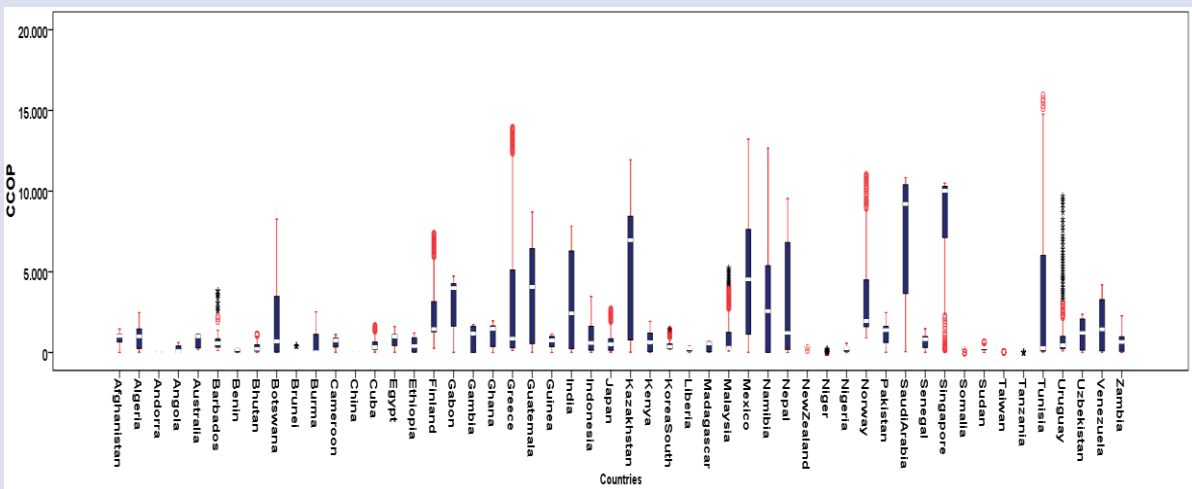
CL		25001.3			Low Risk				
No	Countries	U1	U2	U3	No	Countries	U1	U2	U3
1	Afghanistan	0.99	0.00	0.00	27	Kazakhstan	0.53	0.39	0.06
2	Algeria	0.99	0.00	0.00	28	Kenya	0.99	0.00	0.00
3	Andorra	0.98	0.01	0.00	29	South Korea	0.99	0.00	0.00
4	Angola	0.98	0.01	0.00	30	Liberia	0.98	0.01	0.00
5	Australia	0.99	0.00	0.00	31	Madagascar	0.99	0.00	0.00
6	Barbados	0.99	0.00	0.00	32	Malaysia	0.99	0.00	0.00
7	Benin	0.98	0.01	0.00	33	Mexico	0.58	0.36	0.05
8	Bhutan	0.98	0.00	0.00	34	Namibia	0.78	0.18	0.03
9	Botswana	0.94	0.04	0.00	35	Nepal	0.77	0.19	0.03
10	Brunei	0.98	0.01	0.00	36	New Zealand	0.98	0.01	0.00
11	Burma	0.99	0.00	0.00	37	Niger	0.98	0.01	0.00
12	Cameroon	0.99	0.00	0.00	38	Nigeria	0.98	0.01	0.00
13	China	0.98	0.01	0.00	39	Norway	0.82	0.15	0.02
14	Cuba	0.9	0.00	0.00	40	Pakistan	0.99	0.00	0.00
15	Egypt	0.99	0.00	0.00	41	Saudi Arabia	0.46	0.44	0.09
16	Ethiopia	0.99	0.00	0.00	42	Senegal	0.99	0.00	0.00
17	Finland	0.95	0.04	0.00	43	Singapore	0.45	0.42	0.11
18	Gabon	0.94	0.05	0.01	44	Somalia	0.98	0.01	0.00
19	Gambia	0.99	0.00	0.00	45	Sudan	0.98	0.01	0.00
20	Ghana	0.99	0.00	0.00	46	Taiwan	0.98	0.01	0.00
21	Greece	0.58	0.36	0.04	47	Tanzania	0.98	0.01	0.00
22	Guatemala	0.80	0.16	0.03	48	Tunisia	0.63	0.31	0.04
23	Guinea	0.99	0.00	0.00	49	Uruguay	0.96	0.02	0.00
24	India	0.84	0.13	0.02	50	Uzbekistan	1	0	0
25	Indonesia	0.99	0.00	0.00	51	Venezuela	0.99	0.00	0.00
26	Japan	0.99	0.00	0.00	52	Zambia	0.99	0.00	0.00



(a) Mean, Median, Minimum and Maximum Values For Low Risk Countries



(b) Variation Coefficients for Low Risk Countries



(c) Box-Plot for Low Risk Countries

Figure 1. Descriptive Statistics for Low Risk Countries

According to CL value, middle risk countries are obtained as in Table 5.

As can be seen in Table 5,

- This cluster includes 33 countries.
- The cluster center of middle risk countries is Ukraine. The behavior of Ukraine in terms of CCOP can be used to gain insight about the CCOP behavior of the countries which belong to this cluster with especially high membership degrees.
- Many countries such as Bolivia, Canada, Ecuador, Kyrgyzstan etc. have the characteristics of low risk countries at the same time since the membership degrees of these countries to low risk clusters are bigger than 0.2.
- Bosnia and Herzegovina (BH) and Serbia also belong to cluster of high risk with membership values of 0.304 and 0.441 respectively.
- The other countries belong with high membership degrees to middle risk cluster.
- Fig 2. illustrates the descriptive statistics of the middle risk countries
- When examined Figure 2, it can be seen that

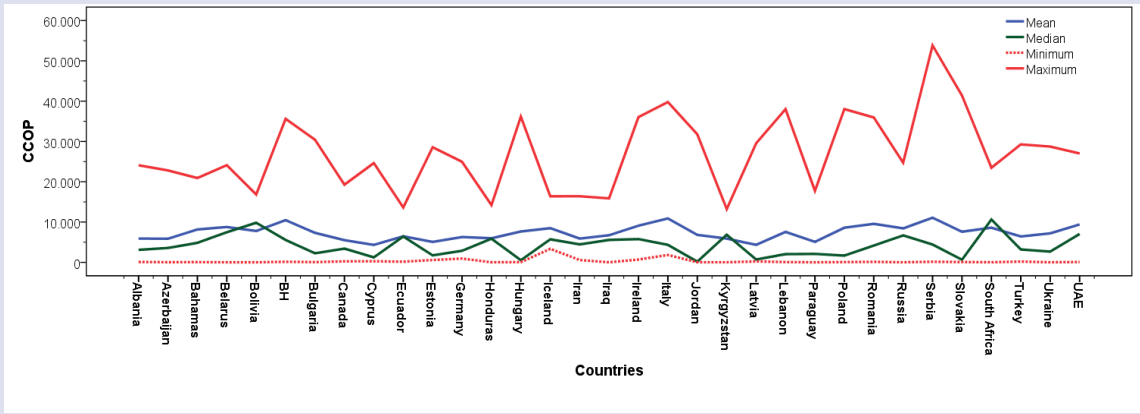
- The country having the highest CCOP value in mean is Serbia.
- According to median values, the country having the highest CCOP value is South Africa.
- The highest CCOP value is observed in Serbia while the smallest CCOP value is in Paraguay.
- The countries having the highest variation coefficients are Latvia, Jordan, Slovakia and Hungary. This states that CCOP values of these countries show the most variation over time. The minimum variations are observed in Iceland, Ecuador and Bolivia.
- In Albania, Bahamas, BH, Bulgaria, Canada, Cyprus, Estonia, Germany, Hungary, Iceland, Ireland, Italy, Jordan, Latvia, Lebanon, Paraguay, Poland, Romania, Slovakia, Ukraine and UAE, CCOP values have increased much since 26 August 2020.
- In Bolivia, Kyrgyzstan and South Africa, high CCOP values have been observed at the beginning of the time period considered.

In the other countries assigned to this cluster, CCOP values have showed a more homogenous distribution.

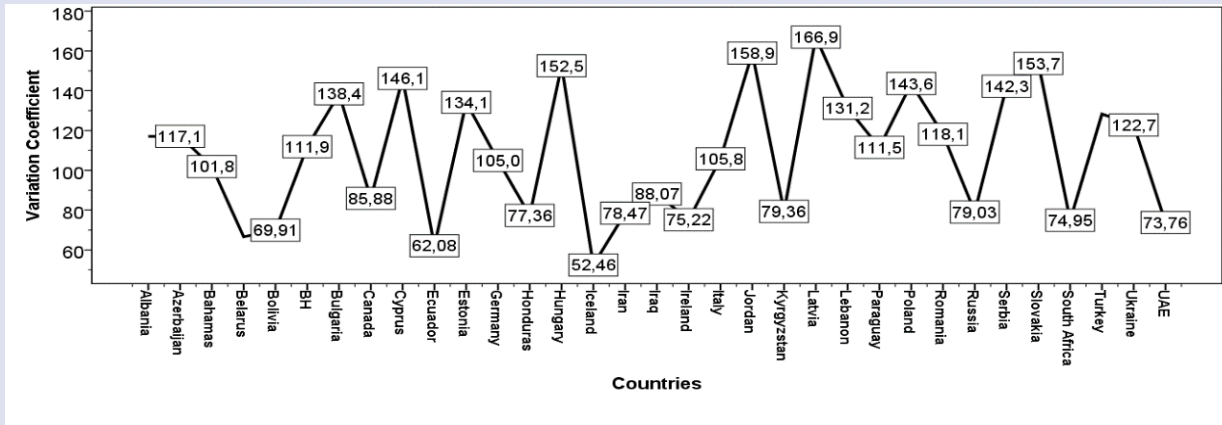
High risk countries for CCOP are given in Table 6

Table 5. Middle Risk Countries in terms of CCOP

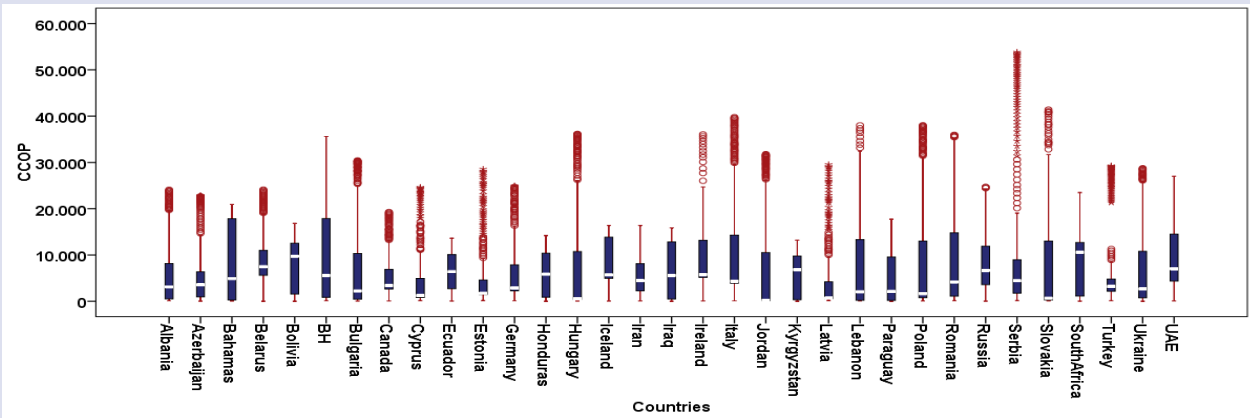
CL		195048.6			Middle Risk				
N	Countries	U1	U2	U3	N	Countries	U1	U2	U3
1	Albania	0.08	0.88	0.03	18	Ireland	0.11	0.78	0.10
2	Azerbaijan	0.10	0.85	0.03	19	Italy	0.06	0.63	0.29
3	Bahamas	0.11	0.78	0.10	20	Jordan	0.04	0.90	0.05
4	Belarus	0.14	0.76	0.09	21	Kyrgyzstan	0.41	0.51	0.07
5	Bolivia	0.30	0.58	0.11	22	Latvia	0.22	0.71	0.05
6	BH	0.06	0.63	0.30	23	Lebanon	0.02	0.95	0.02
7	Bulgaria	0.02	0.95	0.02	24	Paraguay	0.28	0.65	0.05
8	Canada	0.34	0.59	0.05	25	Poland	0.06	0.76	0.16
9	Cyprus	0.28	0.65	0.05	26	Romania	0.05	0.78	0.16
10	Ecuador	0.41	0.50	0.07	27	Russia	0.08	0.85	0.06
11	Estonia	0.20	0.74	0.05	28	Serbia	0.10	0.45	0.44
12	Germany	0.10	0.86	0.03	29	Slovakia	0.05	0.84	0.09
13	Honduras	0.40	0.52	0.07	30	South Africa	0.19	0.68	0.12
14	Hungary	0.05	0.85	0.09	31	Turkey	0.11	0.82	0.05
15	Iceland	0.24	0.65	0.10	32	Ukraine	0	1	0
16	Iran	0.33	0.60	0.06	33	UAE (United Arab Emirates)	0.08	0.88	0.03
17	Iraq	0.23	0.68	0.08					



(a) Mean, Median, Minimum and Maximum Values For Middle Risk Countries



(b) Variation Coefficients for Middle Risk Countries

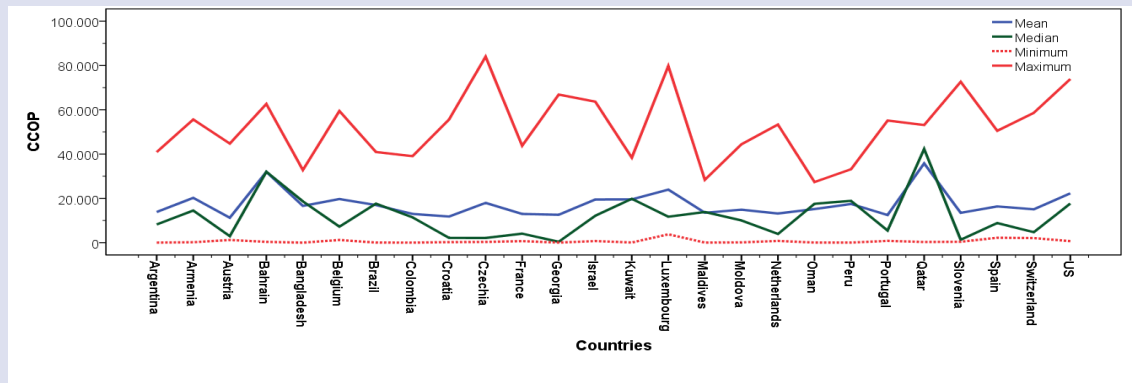


(c) Box-Plot for Middle Risk Countries

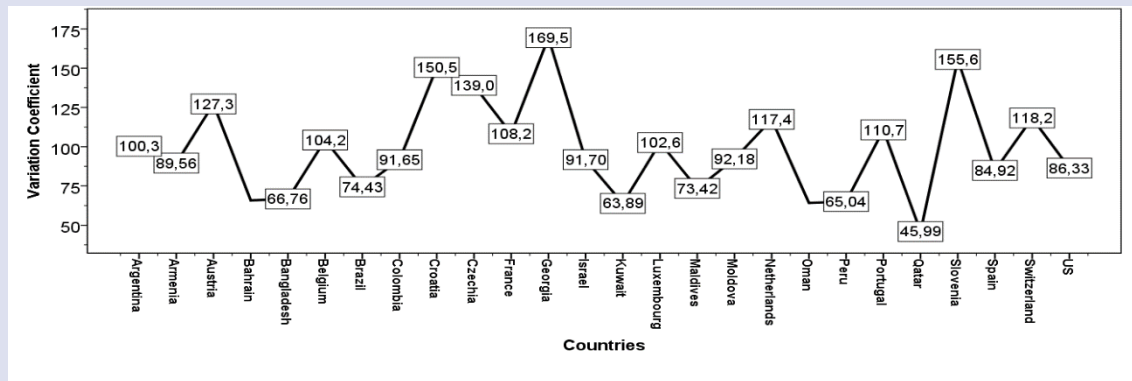
Figure 2. Descriptive Statistics for Middle Risk Countries

Table 6. High Risk Countries in terms of CCOP

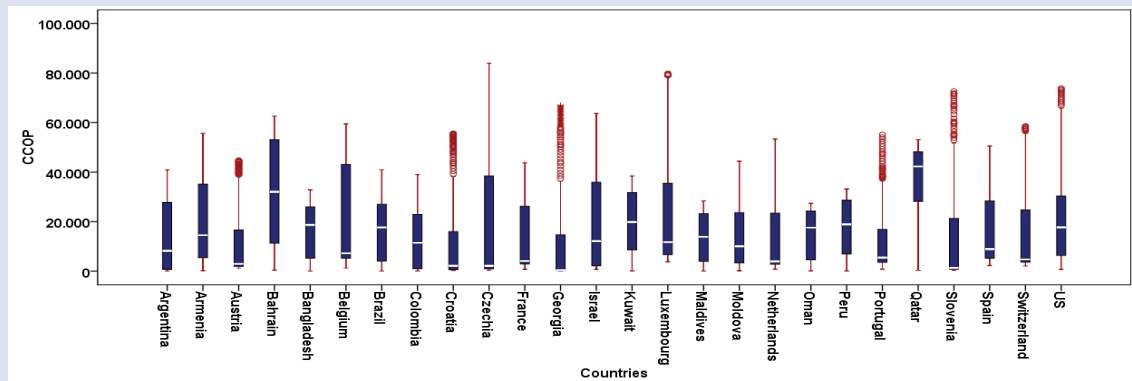
CL			High Risk						
No	Countries	U1	U2	U3	No	Countries	U1	U2	U3
1	Argentina	0.030	0.118	0.853	14	Kuwait	0.072	0.171	0.757
2	Armenia	0.052	0.130	0.819	15	Luxembourg	0.115	0.236	0.649
3	Austria	0.073	0.427	0.501	16	Maldives	0.107	0.370	0.523
4	Bahrain	0.155	0.255	0.589	17	Moldova	0.016	0.066	0.918
5	Bangladesh	0.087	0.236	0.677	18	Netherlands	0.047	0.208	0.745
6	Belgium	0.068	0.165	0.766	19	Oman	0.125	0.333	0.542
7	Brazil	0.055	0.157	0.789	20	Peru	0.085	0.213	0.702
8	Colombia	0.061	0.287	0.652	21	Portugal	0.061	0.334	0.605
9	Croatia	0.089	0.345	0.567	22	Qatar	0.190	0.281	0.529
10	Czechia	0.105	0.240	0.655	23	Slovenia	0.098	0.288	0.614
11	France	0.038	0.185	0.777	24	Spain	0.000	0.000	1.000
12	Georgia	0.113	0.328	0.559	25	Switzerland	0.055	0.185	0.759
13	Israel	0.052	0.128	0.820	26	US	0.075	0.172	0.753



(a) Mean, Median, Minimum and Maximum Values For High Risk Countries



(b) Variation Coefficients for High Risk Countries



(c) Box-Plot for High Risk Countries

Figure 3. Descriptive Statistics for High Risk Countries

- According to Table 6,
- High risk cluster contains 26 countries.
 - The cluster center of high risk cluster is Spain. The CCOP characteristics of Argentina, Armenia, Belgium, Brazil, France, Moldova, Israel, Kuwait, Netherlands, Peru, Switzerland and US show high similarity with those of Spain since the membership degrees of these countries are bigger than 0.7.
 - Argentina, Armenia, Austria, Brazil, Colombia, Georgia and US are assigned to high risk cluster with high membership values. Therefore, it can be said that these countries are the most risk countries in terms of CCOP.
 - Bahrain, Bangladesh, Maldives, Oman, Peru, Croatia, Czechia, Portugal, Qatar, and Slovenia also belong to the Middle Risk cluster with membership values which are bigger than approximately 0.2
 - Descriptive statistics for high risk cluster are given in Figure 3.
 - Figure 3 can be summarized as follows:
 - According to mean and median values of CCOPs in the time period monitored, the highest CCOP values are observed in Qatar and Bahrain.
 - The countries seen in the maximum CCOP values are Czechia, Luxembourg and US.
 - The countries whose CCOP values show the most variation are Georgia, Slovenia and Croatia while the smallest variations are obtained from Qatar, Kuwait and Oman.
 - According to Fig 3(c), CCOP values observed in the countries of Argentina, Armenia, Austria, Belgium, Croatia, Czechia, France, Georgia, Israel, Luxembourg, Moldova, Netherlands, Portugal, Slovenia, Spain and Switzerland have increased much after the second half

of the time period considered. In the Bangladesh, Brazil, Oman, Peru and Qatar, the increase in the CCOP values has started in the first half of the time period. In the other countries, increase in the CCOP values is more regular.

The Results for Cumulative Number of Deaths

Cluster validity indexes for DOP are given in Table 7. According to Table 7, it is decided that the optimal number of clusters is equal to 5 when all cluster validity indexes are evaluated simultaneously. Low risk countries in terms of DOP are given in the Table 8.

- When looking at the Table 8, it can be seen that
- Low risk cluster in terms of DOP consists of 56 countries.
 - The cluster center of low risk cluster is Sudan.
 - Azerbaijan, Belarus, Estonia, Kazakhstan and Lebanon are also element of clusters of middle risk1 and middle risk 2 with different membership degrees. All countries except these countries show the highest similarity with Sudan in terms of DOP values.

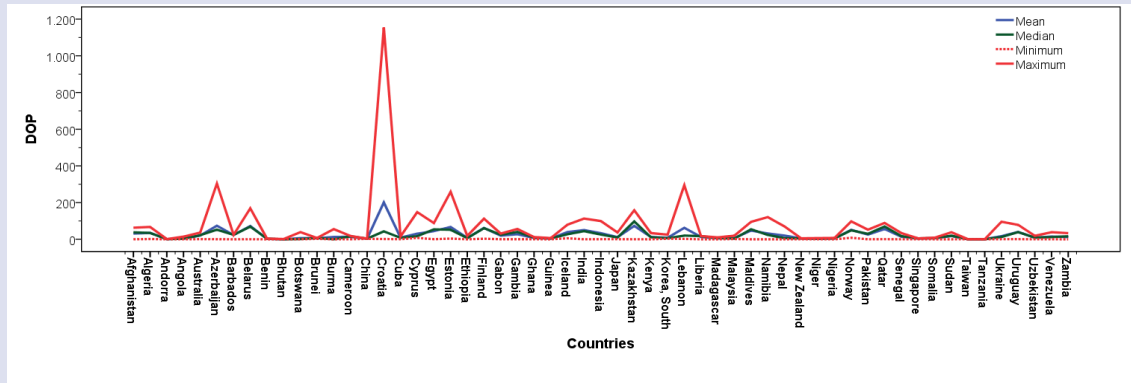
Figure 4 shows the descriptive statistics for low risk cluster.

Table 7. Cluster Validity Indexes for DOP

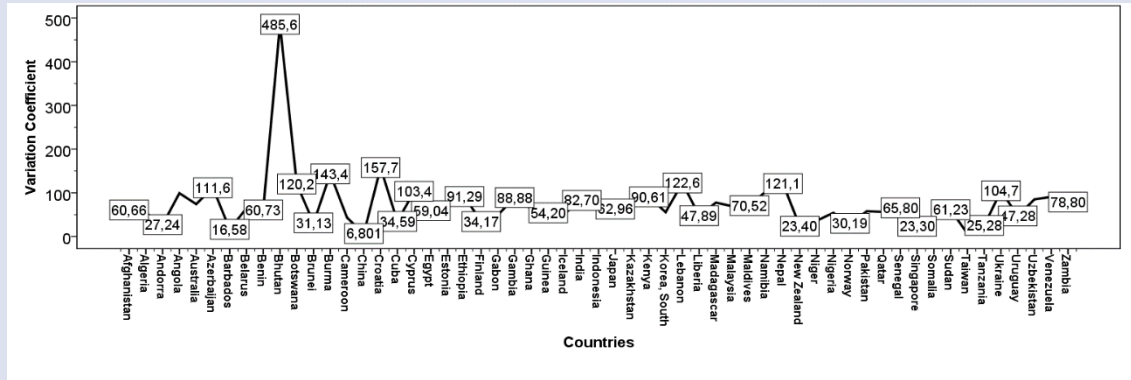
Index/NC	3	4	5	6	7	8	9	10
FS	0.76	0.77	0.77	0.73	0.72	0.70	0.70	0.67
XB	29.26	2.31	0.75	0.62	6.96	1.04	5.63	5.61
PC	0.39	0.70	0.68	0.61	0.58	0.57	0.54	0.56
PE	0.42	0.61	0.71	0.86	0.95	0.99	1.07	1.13
MPC	0.65	0.57	0.59	0.55	0.51	0.54	0.48	0.48

Table 8. Low Risk Countries in terms of DOP

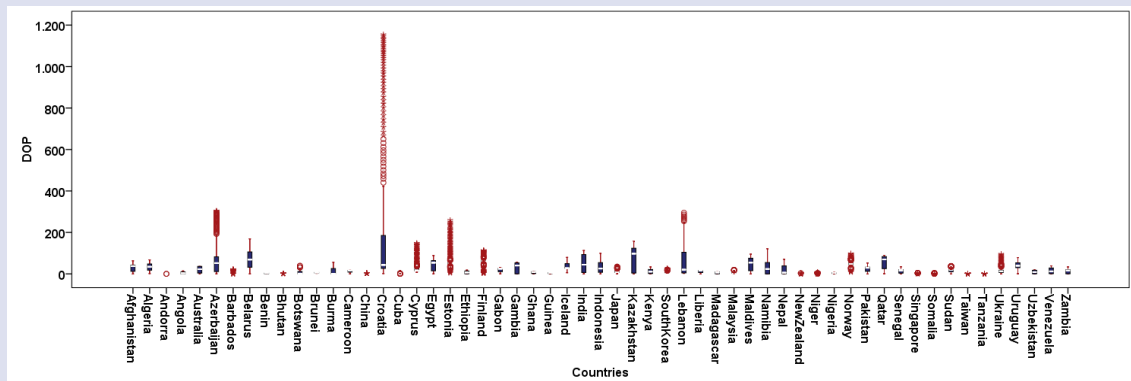
CL		356.82 Low Risk											
No	Countries	U1	U2	U3	U4	U5	No	Countries	U1	U2	U3	U4	U5
1	Afghanistan	0.98	0.01	0.01	0.00	0.00	29	Japan	0.99	0.00	0.00	0.00	0.00
2	Algeria	0.97	0.01	0.01	0.00	0.00	30	Kazakhstan	0.53	0.19	0.22	0.04	0.02
3	Andorra	0.98	0.01	0.01	0.00	0.00	31	Kenya	0.99	0.00	0.00	0.00	0.00
4	Angola	0.99	0.01	0.01	0.00	0.00	32	South Korea	0.99	0.00	0.00	0.00	0.00
5	Australia	0.99	0.00	0.00	0.00	0.00	33	Lebanon	0.47	0.28	0.19	0.04	0.02
6	Azerbaijan	0.36	0.35	0.22	0.04	0.03	34	Liberia	0.99	0.00	0.00	0.00	0.00
7	Barbados	0.99	0.00	0.00	0.00	0.00	35	Madagascar	0.99	0.01	0.01	0.00	0.00
8	Belarus	0.61	0.16	0.17	0.03	0.02	36	Malaysia	0.99	0.00	0.00	0.00	0.00
9	Benin	0.98	0.01	0.01	0.00	0.00	37	Maldives	0.87	0.05	0.06	0.01	0.01
10	Bhutan	0.97	0.01	0.01	0.00	0.00	38	Namibia	0.94	0.03	0.03	0.01	0.00
11	Botswana	0.99	0.00	0.00	0.00	0.00	39	Nepal	0.98	0.01	0.01	0.00	0.00
12	Brunei	0.99	0.01	0.01	0.00	0.00	40	N. Zealand	0.98	0.01	0.01	0.00	0.00
13	Burma	0.99	0.00	0.00	0.00	0.00	41	Niger	0.98	0.01	0.01	0.00	0.00
14	Cameroon	0.99	0.00	0.00	0.00	0.00	42	Nigeria	0.98	0.01	0.01	0.00	0.00
15	China	0.98	0.01	0.01	0.00	0.00	43	Norway	0.90	0.04	0.04	0.01	0.01
16	Cuba	0.99	0.00	0.00	0.00	0.00	44	Pakistan	0.99	0.00	0.00	0.00	0.00
17	Cyprus	0.94	0.03	0.02	0.01	0.00	45	Qatar	0.83	0.07	0.08	0.02	0.01
18	Egypt	0.91	0.04	0.04	0.01	0.01	46	Senegal	0.99	0.00	0.00	0.00	0.00
19	Estonia	0.66	0.16	0.13	0.03	0.02	47	Singapore	0.98	0.01	0.01	0.00	0.00
20	Ethiopia	0.99	0.00	0.00	0.00	0.00	48	Somalia	0.99	0.01	0.01	0.00	0.00
21	Finland	0.82	0.07	0.08	0.02	0.01	49	Sudan	1.00	0.00	0.00	0.00	0.00
22	Gabon	0.99	0.00	0.00	0.00	0.00	50	Taiwan	0.98	0.01	0.01	0.00	0.00
23	Gambia	0.97	0.01	0.01	0.00	0.00	51	Tanzania	0.98	0.01	0.01	0.00	0.00
24	Ghana	0.99	0.00	0.00	0.00	0.00	52	Uruguay	0.95	0.02	0.02	0.01	0.00
25	Guinea	0.98	0.01	0.01	0.00	0.00	53	Ukraine	0.99	0.00	0.00	0.00	0.00
26	Iceland	0.95	0.02	0.02	0.01	0.00	54	Uzbekistan	0.99	0.00	0.00	0.00	0.00
27	India	0.81	0.08	0.08	0.02	0.01	55	Venezuela	0.99	0.00	0.00	0.00	0.00
28	Indonesia	0.95	0.02	0.02	0.01	0.00	56	Zambia	0.99	0.00	0.00	0.00	0.00



(a) Mean, Median, Minimum and Maximum Values For Low Risk Countries



(b) Variation Coefficients for Low Risk Countries



(c) Box-Plot for Low Risk Countries

Figure 4. Descriptive Statistics for Low Risk Countries

According to Figure 4.

- Although Croatia has the highest DOP value (mean=200.86, median=43.12) according to mean values, the country having the highest DOP value (mean =73.12, median =97.43) according to median values is Kazakhstan.
- According to variation coefficients, the highest variations are observed in the countries of Bhutan and Croatia. The reason for this high variation in Bhutan is that no DOP value is reported at the beginning of the time period. The countries whose DOP values show the least variability are China and Taiwan.
- In the countries of Angola, Croatia, Lebanon, Nepal, Uruguay and Venezuela, DO values have increased

since 26 August 2020. The DOP values of Afghanistan, Egypt, Gambia, Kazakhstan, Maldives, Qatar, Senegal and Zambia started to increase before August 2020

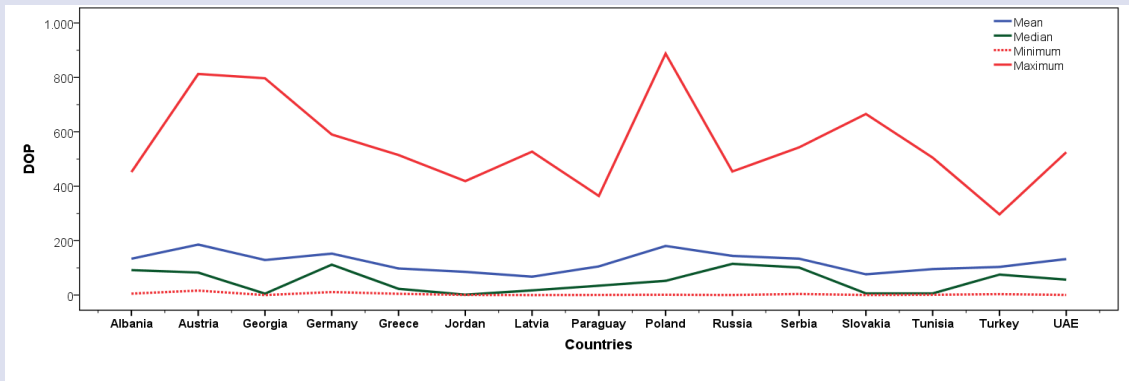
Middle risk1 countries are given in Table 9. As shown in Table 9,

- The cluster of middle risk1 consists of 16 countries and its cluster center is UAE. The countries that are the closest to UAE in terms of DOP are Albania, Greece, Jordan, Serbia and Tunisia. The other countries also have the characteristics of the other clusters with different membership degrees.

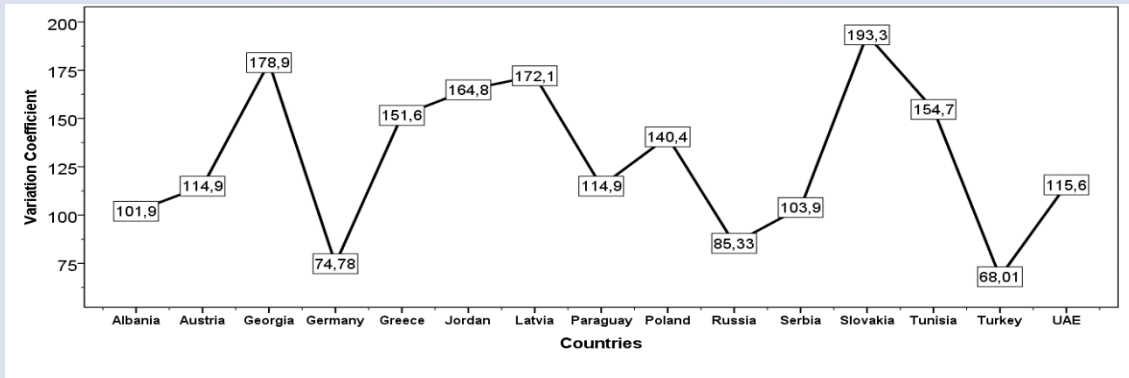
Descriptive statistics for the cluster of middle risk1 are given in Figure 5

Table 9. Middle Risk 1 Countries in terms of DOP

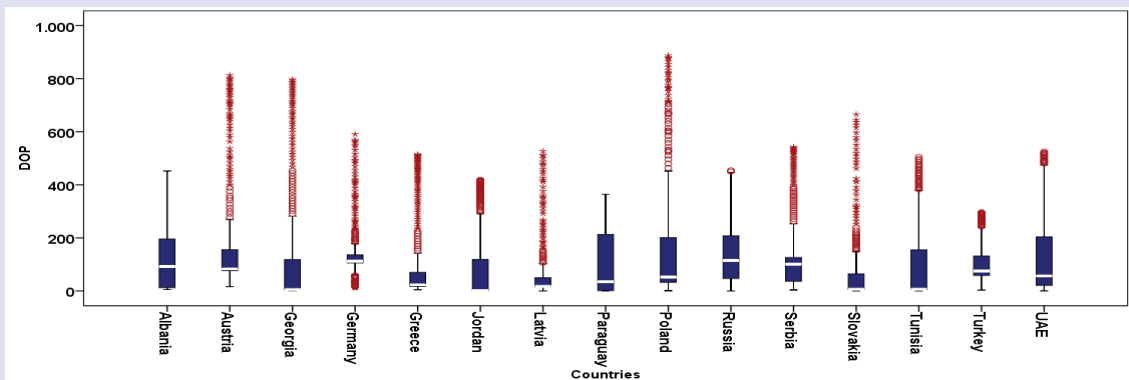
CL		Middle Risk 1											
No	Countries	U1	U2	U3	U4	U5	No	Countries	U1	U2	U3	U4	U5
1	Albania	0.02	0.85	0.11	0.02	0.01	9	Paraguay	0.09	0.60	0.26	0.04	0.02
2	Austria	0.06	0.49	0.18	0.17	0.10	10	Poland	0.07	0.41	0.17	0.21	0.14
3	Croatia	0.08	0.29	0.16	0.25	0.23	11	Russia	0.04	0.61	0.31	0.03	0.02
4	Georgia	0.08	0.58	0.16	0.11	0.07	12	Serbia	0.04	0.79	0.13	0.03	0.02
5	Germany	0.09	0.55	0.27	0.06	0.03	13	Slovakia	0.17	0.57	0.17	0.06	0.04
6	Greece	0.08	0.73	0.12	0.04	0.02	14	Tunisia	0.06	0.79	0.10	0.03	0.02
7	Jordan	0.10	0.70	0.14	0.04	0.02	15	Turkey	0.26	0.36	0.31	0.05	0.03
8	Latvia	0.28	0.45	0.19	0.05	0.03	16	UAE	0.00	1.00	0.00	0.00	0.00



(a) Mean, Median, Minimum and Maximum Values For Middle Risk Countries



(b) Variation Coefficients for Middle Risk Countries



(c) Box-Plot for Middle Risk Countries

Figure 5. Descriptive Statistics for Middle Risk Countries

Based on Figure 5, it can be said that

- The highest DOP values are observed from the countries of Poland and Austria.
- According to mean values, the countries having the highest mean of DOP values are also Austria and Poland
- While the countries that variation coefficients are the highest are Slovakia and Georgia, the smallest are Turkey and Germany.
- DOPs in the all countries except for Russia and Serbia have increased in the second time period (after 26 August 2020).
- Russia has the most regular behavior in terms of DOP. In the Serbia, the increase of DOPs has generally occurred in the first time period.

The countries in the cluster of middle risk2 are given Table 10. According to Table 10,

- Middle risk2 cluster includes 13 countries.
- The cluster center of middle risk2 cluster is Honduras. The countries belonging to this cluster with high membership degrees are Guatemala, Iraq and Oman. Thus, it can be said that information about DOP values of these countries can be obtained by monitoring Honduras.
- All countries also belong to the cluster of middle risk1 with different membership degrees except the countries of Guatemala, Iraq and Oman.
- In Figure6, the countries of middle risk 2 cluster are shown. When looking at the Figure 6, it can be seen that

- According to mean and median values, while the highest DOP values are observed in the countries of Bangladesh and Canada, Saudi Arabia is the country which has the smallest DOP values.
- Maximum DOP value in the time period monitored is observed in the country of South Africa.
- The country having maximum variation coefficient is Bahamas. Canada exhibits more stable behavior in terms of DOP values. Therefore, minimum variation coefficient is obtained for Canada.
- In the countries of Bahamas and Israel, the increase of DOPs is higher in the second time period. Bahrain, Canada, Honduras, Iraq, Kuwait, Oman and Saudi Arabia have more stable behavior in terms of increase of DOP values. In the other countries, high DOP values have been observed in the first time period.

Table 11 shows the countries which belong to cluster of high risk1

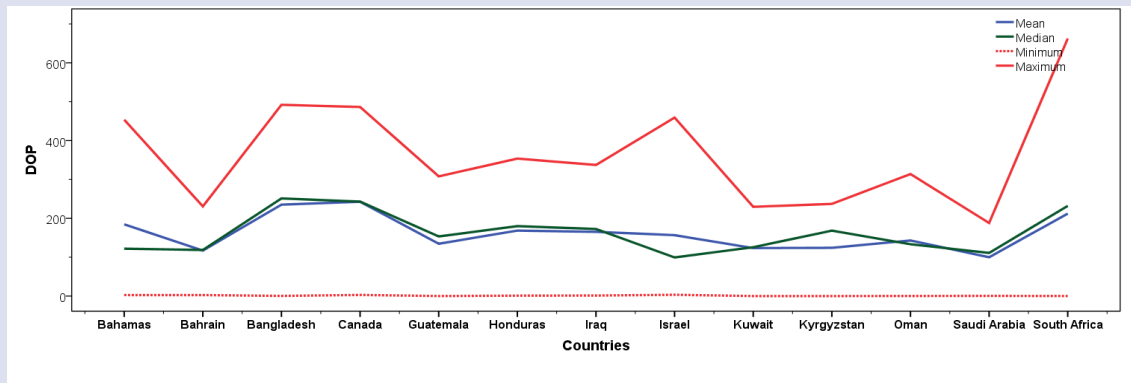
As shown in Table 11,

- The cluster of high risk1 contains 8 countries and the cluster center of this cluster is Iran.
- Hungary, Luxembourg, Netherlands, Romania and Switzerland also have the characteristics of the cluster of high risk 2.
- Ireland also belongs to the clusters of middle risk 2 and high risk with approximately 0.2 membership degrees.
- Portugal exhibits a more unstable behavior in terms of being assigned to the clusters.

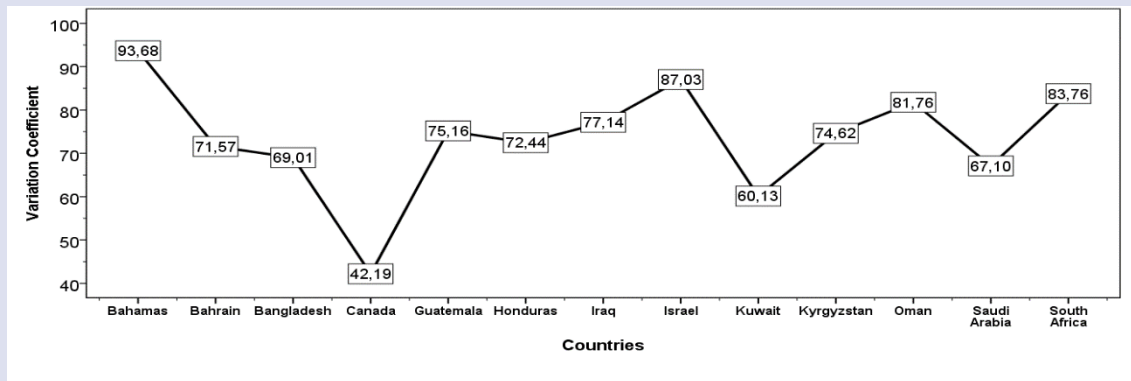
Figure 7 demonstrates the descriptive statistics of this cluster

Table 10. Middle Risk2 Countries in terms of DOP

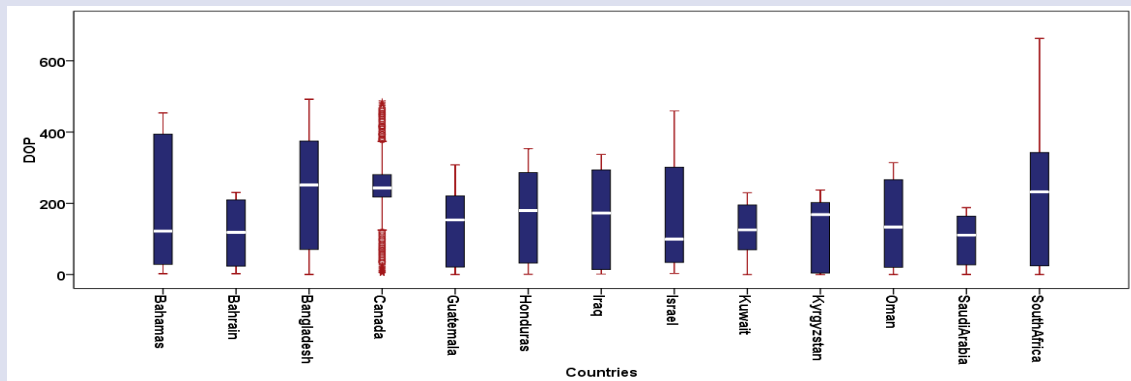
CL							3563.41585							Middle Risk 2				
No	Countries	U1	U2	U3	U4	U5	No	Countries	U1	U2	U3	U4	U5					
1	Bahamas	0.05	0.32	0.44	0.14	0.06	8	Israel	0.03	0.39	0.51	0.04	0.02					
2	Bahrain	0.15	0.25	0.54	0.04	0.02	9	Kuwait	0.16	0.25	0.51	0.05	0.03					
3	Bangladesh	0.04	0.15	0.43	0.28	0.09	10	Kyrgyzstan	0.16	0.21	0.54	0.05	0.03					
4	Canada	0.07	0.21	0.43	0.20	0.09	11	Oman	0.03	0.14	0.79	0.02	0.01					
5	Guatemala	0.06	0.17	0.73	0.03	0.02	12	Saudi Arabia	0.30	0.24	0.38	0.05	0.03					
6	Honduras	0.00	0.00	1.00	0.00	0.00	13	South Africa	0.04	0.22	0.43	0.22	0.08					
7	Iraq	0.00	0.01	0.98	0.00	0.00												



(a) Mean, Median, Minimum and Maximum Values For Middle Risk2 Countries



(b) Variation Coefficients for Middle Risk2 Countries

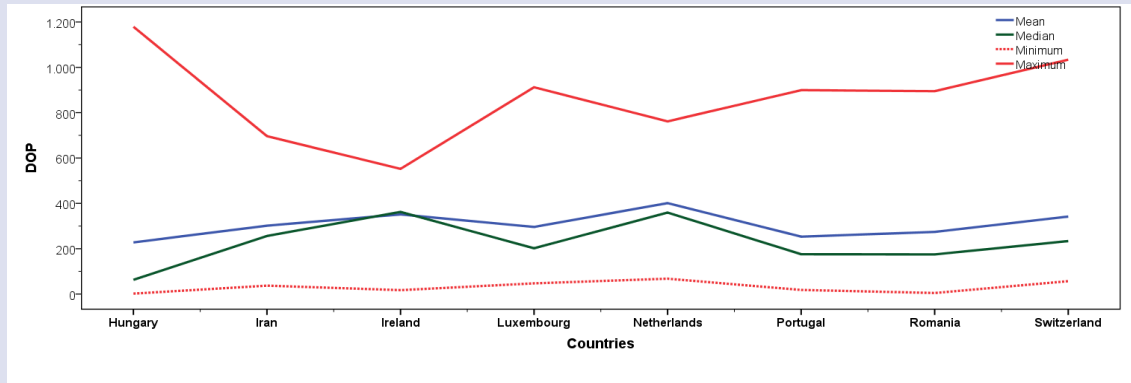


(c) Box-Plot for Middle Risk2 Countries

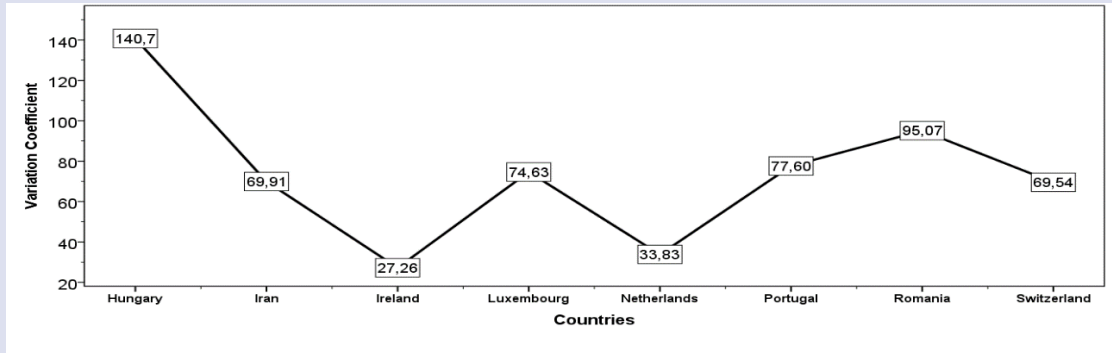
Figure 6. Descriptive Statistics for Middle Risk2 Countries

Table 11. High Risk1 Countries in terms of DOP

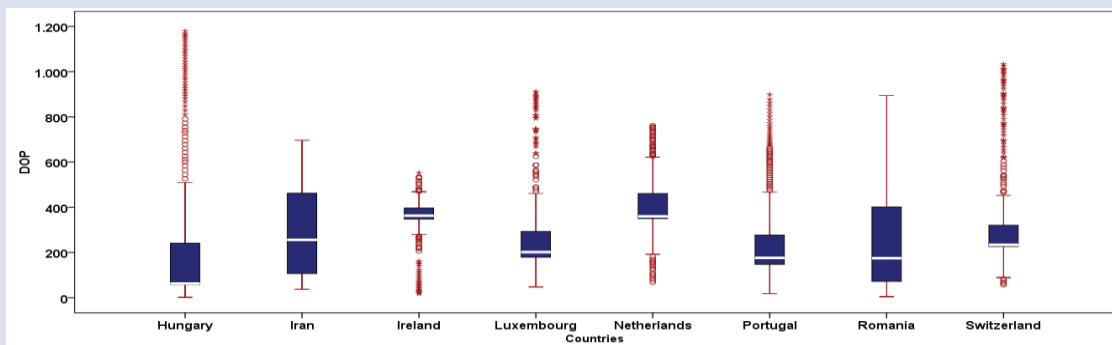
CL		High Risk 1												
No	Countries	U1	U2	U3	U4	U5	No	Countries	U1	U2	U3	U4	U5	
1	Hungary	0.07	0.24	0.14	0.28	0.27	5	Netherlands	0.05	0.11	0.13	0.41	0.30	
2	Iran	0.00	0.00	0.00	1.00	0.00	6	Portugal	0.04	0.22	0.16	0.41	0.17	
3	Ireland	0.08	0.15	0.23	0.35	0.20	7	Romania	0.02	0.08	0.07	0.50	0.33	
4	Luxembourg	0.04	0.13	0.11	0.46	0.26	8	Switzerland	0.04	0.11	0.09	0.39	0.37	



(a) Mean, Median, Minimum and Maximum Values For High Risk1 Countries



Variation Coefficients for High Risk1 Countries



(c) Box-Plot for Middle Risk2 Countries

Figure 7. Descriptive Statistics for High Risk1 Countries

Table 12. High Risk2 Countries in terms of DOP

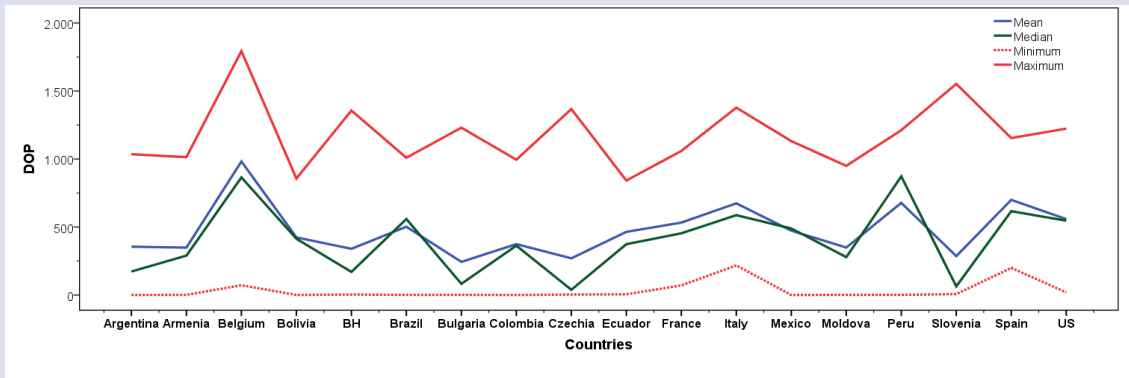
CL	7623.690332 High Risk 2												
No	Countries	U1	U2	U3	U4	U5	No	Countries	U1	U2	U3	U4	U5
1	Argentina	0.03	0.08	0.08	0.26	0.55	10	Ecuador	0.04	0.08	0.10	0.29	0.49
2	Armenia	0.01	0.03	0.03	0.15	0.79	11	France	0.06	0.11	0.12	0.31	0.41
3	Belgium	0.12	0.16	0.17	0.25	0.30	12	Italy	0.08	0.14	0.14	0.28	0.36
4	Bolivia	0.04	0.09	0.11	0.29	0.48	13	Mexico	0.04	0.08	0.09	0.26	0.53
5	BH	0.05	0.12	0.10	0.26	0.48	14	Moldova	0.00	0.00	0.00	0.00	1.00
6	Brazil	0.05	0.09	0.11	0.28	0.47	15	Peru	0.09	0.14	0.16	0.26	0.35
7	Bulgaria	0.07	0.20	0.13	0.28	0.32	16	Slovenia	0.08	0.18	0.14	0.26	0.34
8	Colombia	0.02	0.05	0.05	0.22	0.66	17	Spain	0.09	0.14	0.15	0.28	0.34
9	Czechia	0.06	0.17	0.13	0.28	0.36	18	US	0.06	0.10	0.11	0.28	0.45

As can be seen from Figure 7,

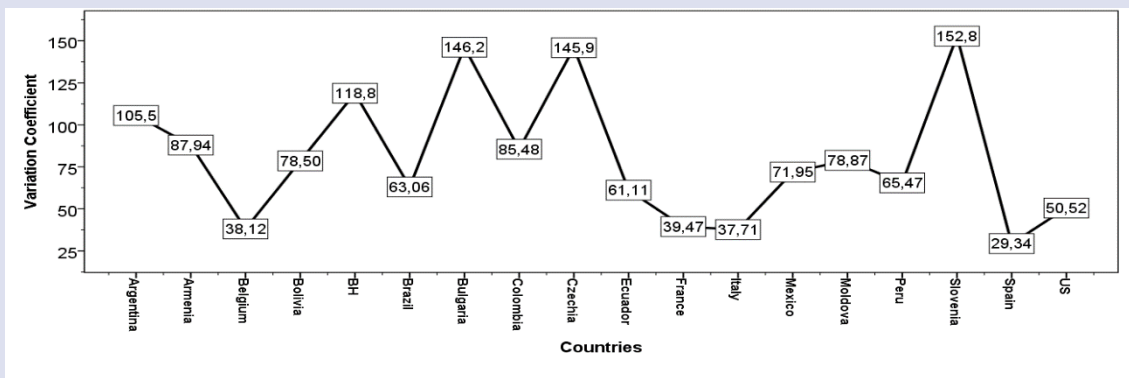
- When mean and median values of the countries are examined, it is seen that Netherlands has the highest DOP values; Hungary has the smallest DOP values.
- The country whose DOP values change the most is Hungary. When the reason for this is investigated, it is observed that the DOP values of Hungary have increased dramatically since 2 October 2020.
- In the all countries except Iran, DOP values have increased in the second time period.
- Lastly, high risk2 countries are given in Table 12

- As shown in Table 12,
- The cluster of high risk2 consists of 18 countries and the cluster center is Moldova. Armenia and Colombia have high membership degrees. Thus, information about the DOP values of Armenia and Colombia can be obtained by monitoring the behavior of Moldova.
- All the countries except Armenia and Colombia belong to the cluster of high risk2 with small membership degrees. These countries also are members of the cluster of high risk 1.

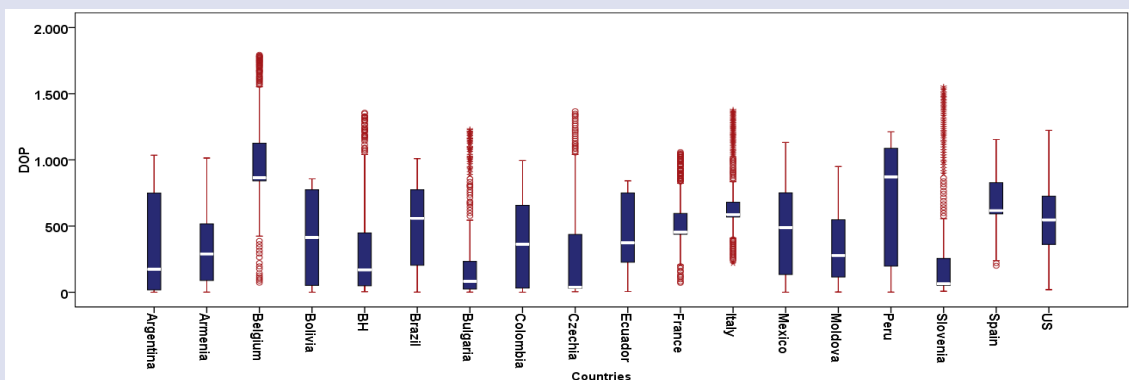
Fig 8. shows the descriptive statistics for this cluster.



(a) Mean, Median, Minimum and Maximum Values For High Risk2 Countries



(b) Variation Coefficients for High Risk2 Countries



(c) Box-Plot for Middle Risk2 Countries

Figure 8. Descriptive Statistics for High Risk2 Countries

As seen in Figure 8,

- According to mean and median values, the highest DOP values are reported from Belgium.
- Czechia and Bulgaria have the smallest DOP values in mean.
- The highest DOP value is observed in the Belgium.
- The highest variation coefficients are obtained from the countries of Bulgaria, Czechia and Slovenia. The smallest variations are observed in Belgium, France, Italy and Spain.
- According to Figure 8(c), Armenia, Bolivia, Colombia, Mexico and US have exhibited a more regular behavior in terms of DOP in the time period considered.
- In Argentina, Belgium, BH, Bulgaria, Czechia, Ecuador, France, Italy, Moldova, Slovenia and Spain, the increases in DOP values have been observed in the second time period.

Conclusions

In this study, it is aimed to determine the countries exhibiting similar and different behavior in terms of spread of COVID19. For this objective, the data set consisting of CCOP and DOP values of 111 countries are used. Firstly, the optimal number of clusters is found by using five cluster validity indexes for each variable (CCOP and DOP). The number of clusters is determined as 3 and 5 for CCOP and DOP respectively. FKM clustering algorithm is executed with the optimal number of clusters and CL value is calculated for each cluster separately. CL values are used to reveal the risk levels of the countries with respect to COVID19. The results obtained for CCOP values are as follows:

- The cluster of low risk includes 52 countries. The cluster center of this cluster is Uzbekistan. All the countries except Greece, Mexico, Kazakhstan, Saudi Arabia, Singapore, and Tunisia have been assigned to this cluster with high membership degrees. From here, it can be said that the information about the spread of COVID19 spread in 45 countries can be obtained by following the spread of COVID19 in Uzbekistan.
- The cluster of middle risk contains 33 countries. The cluster center of this cluster is Ukraine. The COVID19 behavior of the countries of Albania, Azerbaijan, Bahamas, Belarus, Bulgaria, Estonia, Germany, Hungary, Ireland, Jordan, Latvia, Lebanon, Poland, Romania, Russia, Slovakia, Turkey and UAE show high similarity with that of Ukraine.
- High risk cluster consists of 26 countries and its cluster center is Spain. Argentina, Armenia, Belgium, Brazil, France, Israel, Kuwait, Moldova, Netherlands, Peru, Switzerland and US are assigned to this cluster with membership degrees which are bigger than 0.7 and thus, it can be said that these countries have similar COVID19 behavior with Spain.

According to DOP values, following results are obtained:

- Low risk cluster consists of 56 countries and the cluster center of this cluster is Sudan. All the countries except Azerbaijan, Belarus, Estonia, Kazakhstan and Lebanon belong to this cluster with high membership degrees. In other words, 51 countries have similar DOP behavior with Sudan.
- The cluster of middle risk 1 includes 16 countries. The cluster center is found as UAE. Albania, Greece, Jordan, Serbia and Tunisia have high similarity with UAE in terms of DOP behavior.
- Middle risk2 cluster contains 13 countries and the cluster center is Honduras. All the countries except Guatemala, Iraq and Oman also belong to the other clusters with different membership degrees.
- High risk1 cluster contains 8 countries. The cluster center is Iran. All the countries in this cluster are also assigned to the other clusters. Thus, it can be said that the countries in this cluster exhibit unstable behavior in terms of DOP.
- Lastly, the cluster of high risk2 consists of 18 countries and the cluster center is Moldova. All the countries except Armenia and Colombia are the element of the other clusters with different membership degrees. When the clusters of CCOP and DOP are compared, the following results are obtained:
 - Although the countries of Greece, Guatemala, Saudi Arabia and Tunisia are element of low risk cluster in terms of CCOP, they belong to middle risk cluster in terms of DOP values.
 - Mexico belongs to low risk cluster according to CCOP values while it is the element of high risk cluster according to DOP values.
 - Azerbaijan, Belarus, Cyprus, Estonia, Iceland, Lebanon and Ukraine are assigned to low risk cluster with respect to DOP. But, these countries are the element of middle risk cluster with respect to CCOP.
 - Lastly, while Maldives and Qatar belong to low risk cluster with respect to DOP, they are assigned to high risk cluster with respect to CCOP.

In the future work, we planned that countries are clustered by considering three COVID19 behavior, including the number of active cases, the number of deaths and the number of recovered cases, simultaneously

Conflicts of Interest

Sample sentences if there is no conflict of interest: The authors state that did not have conflict of interests.

References

- [1] Imtyaz A, Haleem A, Javaid M, Analysing Governmental Response to The COVID19 Pandemic, *Journal of Oral Biology and Craniofacial Research*, 10 (2020) 504-513.
- [2] Zarikas V, Pouloupous SG, Gareiou Z, Zervas E, Clustering Analysis of the Countries COVID19 Data Sets, *Data in Brief*, (2020) 31.

- [3] Mahmoudi MR, Baleanu D, Mansor Z, Tuan BA, Pho K, Fuzzy Clustering Method to Compare The Spread Rate of COVID19 in The High-risk Countries, *Chaos, Solitons and Fractals*, (2020) 140.
- [4] Alvarez E, Brida JG, Limas E, Comparisons of COVID19 dynamics in the different countries of the World using time series clustering, (2020), medRxiv
- [5] Hutagalung J, Ginantra NLWSR, Bhawika GW, Parwita WGS, Wanto A, Panjaitan PD. COVID19 Cases and Deaths in Southeast Asia Clustering Using K-means Clustering, Annual Conference on Science and Technology Research, Journal of Physics: Conference Series, (2021) 1783.
- [6] Virgantari F, Faridhan YE. K-means clustering of COVID19 cases in Indonesia's provinces, Proceedings of the International Conference on Global Optimization and Its Applications, Jakarta, Indonesia, November 21-22, (2020).
- [7] Rojas F, Valenzuela O, Rojas I., Estimation of COVID19 dynamics in the different states of the United States using time series clustering, (2020), medRxiv.
- [8] Azarafza M, Azarafza M, Akgün H, Clustering Method for Spread Pattern Analysis of Corona-virus (COVID19) Infection in Iran, *Journal of Applied Science, Engineering, Technology, and Education*, 3(1) (2021).
- [9] Crnogorac V, Grbic M, Dukanovic M, Matic D, Clustering of European countries and territories based on cumulative relative number of COVID19 patients in 2020, 20th International Symposium INFOTEH, (2021).
- [10] Sadeghi B, Cheung RCY, Hanbury M, using hierarchical clustering analysis to evaluate COVID-19 pandemic preparedness and performance in 180 countries in 2020, *BMJ Open*, (2021).
- [11] Putra PMA, Kadyanan GAGA, Implementation of K-Means clustering algorithm in determining classification of the spread of the COVID19 virus in Bali, *Jurnal Elektronik Ilmu Komputer Udayanan*, 10(1) (2021).
- [12] Utomo W, The comparison of k-means and k-medoids algorithms for clustering the spread of the COVID19 outbreak in Indonesia, *ILKOM Jurnal Ilmiah*, 13(1) (2021).
- [13] Abdullah D, Susilo S, Ahmar AS, Rusli R, Hidayat R, The application of K-Means clustering for province clustering in Indonesia of the risk of the COVID-19 pandemic based on COVID-19 data, *Quality and Quantity*, (2021).
- [14] Everitt B, Landau S, Leese M, Cluster analysis, 4th ed. London: Arnold, (2001).
- [15] Hair J, Black W, Babin B, Anderson R, Tatham R, Multivariate data analysis. 6th ed. Uppersaddle River, N.J.: Pearson Prentice Hall, (2006).
- [16] Jain A, Murty M, Flynn P, Data Clustering: A Review, *ACM Computing Surveys*, 31(3) (1999) 264-323.
- [17] De Carvalho FAT, De Melo FM, Lechevallier Y, A Multi-view Relational Fuzzy C-medoid Vectors Clustering Algorithm, *Neurocomputing*, 163 (2015) 115-123.
- [18] Rani S, Sikka G, Recent Techniques of Clustering of Time Series Data: A Survey, *International Journal of Computer Applications*, 52 (2012).
- [19] Bezdek JC, Pattern Recognition with Fuzzy Objective Function Algorithms. New York: Plenum Press, (1981)
- [20] Gustafson DE, Kessel WC, Fuzzy Clustering with a Fuzzy Covariance Matrix. IEEE CDC San Diego, (1979) 761-766.
- [21] Hathaway RJ, Bezdek JC, Switching regression models and fuzzy clustering, *IEEE Transactions On Fuzzy Systems*, 1(3) (1993) 195-204.
- [22] Krishnapuram R, Joshi A, Yi L, A fuzzy relative of the k-medoids algorithm with application to web document snippet clustering, IEEE International Fuzzy Systems, Conference Proceedings, (1999).
- [23] Labroche N, New incremental fuzzy C medoids clustering algorithms, Annual Conference of the North American Fuzzy Information Processing Society—NAFIPS; Toronto, ON, Canada, (2010).
- [24] Rousseeuw PJ, Silhouettes: a Graphical Aid to the Interpretation and Validation of Cluster Analysis, *Computational and Applied Mathematics*, 20 (1987) 53-65.
- [25] Xie X, Beni G, A Validity Measure for Fuzzy Clustering, *IEEE Transactions on Pattern Analysis and Machine Intelligence*, 3(8) (1991) 841-846.
- [26] Bezdek JC, Numerical taxonomy with fuzzy sets, *Journal of Mathematical Biology*, 1(1) (1974) 57-71.
- [27] Li CS, The Improved Partition Coefficient, *Procedia Engineering*, 24 (2011) 534-538.
- [28] Bezdek, JC, Cluster validity with fuzzy sets. Journal of cybernetics, 3(3) (1974) 58-72.
- [29] Dave RN, Validating fuzzy partitions obtained through c-shells clustering, *Pattern Recognition Letters*, 17(6) (1996) 613-623.

AUTHOR GUIDELINES

Thank you for choosing to submit your paper to Cumhuriyet Science Journal. The following instructions will ensure we have everything required so your paper can move through pre-evaluating, peer review, production and publication smoothly. Please take the time to read and follow them as closely as possible, as doing so will ensure your paper matches the journal's requirements.

Submission

Cumhuriyet Science Journal is an international, peer-reviewed, free of charge journal covering the full scope of both natural and engineering sciences. Manuscripts should be submitted by one of the authors of the manuscript as online submission after registration to the Cumhuriyet Sciences Journal. Microsoft Word (.doc, .docx, .rtf), files can be submitted. There is no page limit. If there is a problem while uploading the files of manuscript, please try to reduce their file size, especially manuscripts including embedded figures. Submissions by anyone other than one of the authors will not be accepted. The submitting author takes responsibility for the paper during submission and peer review. If for some technical reason submission through the online submission system is not possible, the author can contact csj@cumhuriyet.edu.tr for support.

Submission or processing charges

Cumhuriyet Science Journal does not charge any article submission, processing charges, and printing charge from the authors.

Terms of Submission

Papers must be submitted on the understanding that they have not been published elsewhere (except in the form of an abstract or as part of a published lecture, review, or thesis) and are not currently under consideration by another journal. The submitting author is responsible for ensuring that the article's publication has been approved by all the other coauthors. It is also the authors' responsibility to ensure that the articles emanating from a particular institution are submitted with the approval of the necessary institution. Only an acknowledgment from the editorial office officially establishes the date of receipt. Further correspondence and proofs will be sent to the author(s) before publication unless otherwise indicated. It is a condition of submission of a paper that the corresponding author permit editing of the paper for readability. All enquiries concerning the publication of accepted papers should be addressed to csj@cumhuriyet.edu.tr. Please note that Cumhuriyet Science Journal uses iThenticate software to screen papers for unoriginal material. By submitting your paper to Cumhuriyet Science Journal are agreeing to any necessary originality checks your paper may have to undergo during the peer review and production processes. Upon receiving a new manuscript, the Editorial office conducts initial pre-refereeing checks to ensure the article is legible, complete, correctly formatted, original, within the scope of the journal in question, in the style of a scientific article and written in clear English. Any article that has problems with any of the journal criteria may be rejected at this stage.

Peer Review

This journal operates a single blind review process. All contributions will be initially assessed by the editor for suitability for the journal. Papers deemed suitable are then typically sent to a minimum of two independent expert reviewer to assess the scientific quality of the paper. The author is required to upload the revised article to the system within 15 days by making the corrections suggested by the referee. The article will be rejected if there are no fixes in it. The Editor is responsible for the final decision regarding acceptance or rejection of articles. The Editor's decision is final

Title and Authorship Information

The following information should be included

Paper title

Full author names

Full institutional mailing addresses

Corresponding address

Email address

Abstract

The manuscript should contain an abstract. The researchers who are native speakers of Turkish have to add Turkish title and abstract as well. The abstract should be self-contained and citation-free and should be 250-300 words.

Keywords

Keywords of the scientific articles should be selected from the web address of www.bilimadresleri.com

Introduction

This section should be succinct, with no subheadings.

Materials and Methods

This part should contain sufficient detail so that all procedures can be repeated. It can be divided into subsections if required.

Conflicts of interest

Sample sentence if there is no conflict of interest: The authors stated that did not have conflict of interests.

Acknowledgements

Sample sentences for acknowledgements: The work was supported by grants from CUBAP (T-1111). We would like to acknowledge Prof. Mehmet Sözer, MD, for his precious technical and editorial assistance. We would like to thank

References

References to cited literature should be identified by number in the text in square brackets and grouped at the end of the paper in numerical order of appearance. Each reference must be cited in the text. Always give inclusive page numbers for references to journal articles and a page range or chapter number for books. References should be styled and punctuated according to the following examples

- [1] Karaca E., Ulusoy S., Morgül Ü., Ulusoy H.I., Development of Analytical Method for Sensitive Determination of Streptozotocin based on Solid Phase Extraction, Cumhuriyet Sci. J., 41 (4) (2020) 826-831. (sample reference for journals)
- [2] Keskin B., Ozkan A.S., Inverse Spectral Problems for Dirac Operator with Eigenvalue Dependent Boundary and Jump Conditions, Acta Math. Hungar., 130 (2011) 150-159(sample reference for journals)
- [3] Mazur M.T., Kurman R.J., Dysfunctional Uterine Bleeding. In: Mazur M.T., Kurman R.J., (Eds). Diagnosis of endometrial biopsies and curettings, A practical approach. 2nd ed. Berlin: Springer, (2005) 100-120. (sample reference for book chapters)
- [4] Mazur M.T., Kurman R.J.,Diagnosis of endometrial biopsies and curettings, A practical approach. 2nd ed. Berlin, (2005) 100-120. (sample reference for book)
- [5] National Cancer Institute, Surveillance Epidemiology and End Results. Cancer of the Corpus and Uterus, NOS. Available at: http://seer.cancer.gov/statfacts/html/corp.html?statfacts_page=corp. Retrieved March 2, 2008. (sample reference for websites)
- [6] Surname N., Title of thesis, PD or master thesis, Name of university, name of institue, year. (sample reference for thesis)
- [7] Surname N., Title of fulltext conference paper, name of conference, city, year, pages. (sample reference for Abstratcs in conferences are not accepted as a valid reference except full text)

Preparation of Figures

Each figure can be integrated in the paper body or separately uploaded and should be cited in a consecutive order. Figure widths can be 4-6 inch as 300 dpi. The labels of the figures should be clear and informative. The name and the subtitles of the figures must be 9-point font.

Preparation of Tables

Tables should be cited consecutively in the text. Every table must have a descriptive title and if numerical measurements are given, the units should be included in the column heading. Tables should be simple with simple borders and text written as left text. The name and the subtitle of the tables must be 9-point font

Proofs

Corrected proofs must be returned to the publisher within 2 weeks of receipt. The publisher will do everything possible to ensure prompt publication. It will therefore be appreciated if the manuscripts and figures conform from the outset to the style of the journal.

Copyright

Open Access authors retain the copyrights of their papers, and all open access articles are distributed under the terms of the Creative Commons Attribution license, which permits unrestricted use, distribution and reproduction in any medium, provided that the original work is properly cited.

The use of general descriptive names, trade names, trademarks, and so forth in this publication, even if not specifically identified, does not imply that these names are not protected by the relevant laws and regulations.

While the advice and information in this journal are believed to be true and accurate on the date of its going to press, neither the authors, the editors, nor the publisher can accept any legal responsibility for any errors or omissions that may be made. The publisher makes no warranty, express or implied, with respect to the material contained herein.

Ethical Guidelines

New methods and ethically relevant aspects must be described in detail, bearing in mind the following:

Human Experiments. All work must be conducted in accordance with the Declaration of Helsinki (1964). Papers describing experimental work on human subjects who carry a risk of harm must include:

A statement that the experiment was conducted with the understanding and the consent of the human subject.

A statement that the responsible Ethical Committee has approved the experiments.

Animal Experiments. Papers describing experiments on living animals should provide:

A full description of any anaesthetic and surgical procedure used.

Evidence that all possible steps were taken to avoid animal suffering at each stage of the experiment. Papers describing experiments on isolated tissues must indicate precisely how the donor tissues were obtained.

Submission Preparation Checklist

As part of the submission process, authors are required to check off their submission's compliance with all of the following items, and submissions may be rejected that do not adhere to these guidelines.

The submission has not been previously published, nor is it before another journal for consideration (or an explanation has been provided in Comments to the Editor).

The submission file is in Microsoft Word document file (Times New Roman) format.

Where available, URLs for the references have been provided.

The text is single-spaced; uses a 11-point font; employs italics, rather than underlining (except with URL addresses); and all illustrations, figures, and tables are placed within the text at the appropriate points, rather than at the end.

The text adheres to the stylistic and bibliographic requirements outlined in the Author Guidelines, which is found in About the Journal.

If submitting to a peer-reviewed section of the journal, the instructions in Ensuring a Double-Blind Review have been followed.